Influence of laser parameters on the relativistic short electron bunches dynamics in linear accelerators based on RF-guns and development of associated diagnostics

Thomas Vinatier

UNIVERSITÉ PARIS SUD

Comprendre le monde, construire l'avenir®

Université Paris-Sud 11 ED 534 MIPEGE

Modélisation et Instrumentation en Physique, Energies, Geosciences et Environnement

Université Paris-Sud

Ecole Doctorale 534 : MIPEGE
Laboratoire de l'Accélérateur Linéaire

Discipline : Physique

Spécialité : Physique des accélérateurs

Thèse de doctorat

Soutenue le 23 Septembre 2015 par

Thomas Vinatier

Influence des paramètres du laser sur la dynamique des paquets courts d'électrons relativistes dans des accélérateurs linéaires basés sur des canons RF et développement de diagnostics associés

Directeur de thèse :	M. Patrick Puzo	Professeur (Université Paris Sud)
Encadrant :	Mme. Christelle Bruni	Docteur (Université Paris Sud)

Composition du jury :

Président du jury :	M. Achille Stocchi	Professeur (Université Paris Sud)
Rapporteurs :	M. Frank Zimmermann	Docteur (CERN)
	M. Serge Bielawski	Professeur (Université Lille 1)
Examinateurs :	M. Alban Mosnier	Ingénieur (CEA)
	M. Patrick Puzo	Professeur (Université Paris Sud)
	Mme. Christelle Bruni	Docteur (Université Paris Sud)
Invités :	Mme. Anne Oppelt	Docteur (DESY)

UNIVERSITÉ PARIS SUD

Comprendre le monde, construire l'avenir®

Université Paris-Sud 11
ED 534 MIPEGE
Modélisation et Instrumentation en Physique, Energies, Geosciences et Environnement

Université Paris-Sud

Ecole Doctorale 534 : MIPEGE
Laboratoire de l'Accélérateur Linéaire

Field : Physics

Speciality : Accelerator Physics

Doctoral Thesis

Defended the September 23rd, 2015 by

Thomas Vinatier

Influence of laser parameters on the relativistic short electron bunches dynamics in linear accelerators based on RF-guns and development of associated diagnostics

Thesis director :	M. Patrick Puzo	Professor (Université Paris Sud)
Supervisor :	Mme. Christelle Bruni	Doctor (Université Paris Sud)

Committee members :

Committee President :	M. Achille Stocchi	Professor (Université Paris Sud)
Referees :	M. Frank Zimmermann	Doctor (CERN)
	M. Serge Bielawski	Professor (Université Lille 1)
Examiners :	M. Alban Mosnier	Engineer (CEA)
	M. Patrick Puzo	Professor (Université Paris Sud)
	Mme. Christelle Bruni	Doctor (Université Paris Sud)
Guest :	Mme. Anne Oppelt	Doctor (DESY)

Résumé

Dans de nombreuses applications, des paquets d'électrons relativistes sub-ps sont requis : Accélération laser-plasma, Lasers à électrons libres, Génération de rayonnement THz intense, Etude des phénomènes ultra-rapides dans la matière, etc.
L'aspect court des paquets et la nécessité d'un fort courant crête pour les applications impliquent de fortes forces de charge d'espace conduisant à une dégradation des propriétés du faisceau, telles que son émittance transverse et sa longueur. La principale difficulté est de caractériser, modéliser et prendre en compte ces effets.
Ma thèse s'inscrit dans ce cadre à travers l'étude de la dynamique et des diagnostics associés à ces paquets courts, à savoir ceux dont la durée rms n'est pas directement mesurable par une méthode électronique situant la frontière à quelques dizaines de picosecondes.

Le chapitre 2 rassemble des mesures de plusieurs propriétés de ces paquets courts : charge, émittance transverse, énergie et longueur. L'originalité de mon travail réside dans l'utilisation de méthodes simples, des points de vues théoriques (analytiques au maximum) et technologiques (utilisant seulement des éléments communs sur les accélérateurs d'électrons). Ces méthodes, plus adaptées pour des faisceaux moins extrêmes, permettent néanmoins d'obtenir de très bons résultats.
J'ai en particulier développé une méthode de mesure de charge à partir de la mesure de l'intensité lumineuse émise par un écran scintillant suite à l'interaction avec le faisceau. Cette méthode permet de mesurer précisément des charges inférieures à 100 fC, ce qui surpasse les capacités des diagnostics classiques (ICT et Coupe de Faraday) limités au picoCoulomb à cause du bruit électronique. Cette méthode est utile, du fait que les paquets courts sont souvent faiblement chargés pour limiter l'effet des forces de charge d'espace. Elle sera aussi utilisée pour la calibration de détecteurs, qui requiert de faibles charges.
J'ai développé une méthode pour mesurer l'énergie moyenne du faisceau avec un steerer et un écran scintillant, via le déplacement du barycentre du faisceau en fonction du champ magnétique du steerer. Cette méthode a prouvé être fiable pour des énergies de quelques MeV en sortie d'un canon RF, puisque les énergies moyennes de faisceau mesurées sont totalement compatibles avec celles déduites des spectres en énergies du faisceau mesurés par un dipôle. C'est aussi le cas quand seulement deux valeurs du champ magnétique du steerer sont utilisées, ce qui rend cette méthode très rapide.
J'ai aussi adapté des méthodes multiparamétriques pour mesurer l'émittance transverse et la longueur des paquets d'électrons. Ces méthodes indirectes permettent de déterminer ces propriétés à partir de la mesure d'autres propriétés plus accessibles : les dimensions transverses pour l'émittance et la dispersion en énergie pour la longueur. La mesure de longueur (méthode des 3 phases) donne de très bons résultats, puisqu'elle permet de mesurer avec une précision meilleure que 10% des longueurs rms inférieures à la picoseconde. La mesure d'émittance sans prise en compte des forces de charge d'espace donne des résultats mitigés, puisque la précision varie de 20% (méthode des 3 gradients) à plus de 100% (méthode des 3 écrans). Une amélioration significative de la précision, jusqu'à un facteur

5, peut être obtenue en prenant en compte les forces de charge d'espace via une équation d'enveloppe en considérant une densité de charge 3D gaussienne pour le faisceau, ce qui constitue l'originalité de mon travail.
J'ai finalement grandement contribué à l'implémentation, au développement et au commissioning d'un diagnostic de mesure de longueur de faisceau basé sur l'effet Cherenkov sur l'accélérateur PHIL au LAL. J'ai tout particulièrement établi les conditions de transport du faisceau d'électrons qui permettent de maximiser l'intensité de la lumière Cherenkov extraite de la ligne faisceau et transportée jusqu'à la caméra à balayage de fente. J'ai également participé au développement de la ligne de transport optique entre le cristal de saphir et la camera à balayage de fente, en achetant un nouveau type de miroir qui a amené un gain significatif d'un facteur 50 sur l'intensité de la lumière Cherenkov à l'entrée de la caméra à balayage de fente.

Le chapitre 3 consiste en une comparaison des propriétés des paquets courts d'électrons, unique ou longitudinalement modulé, générés par trois méthodes différentes : Utilisation d'une impulsion laser courte ou longitudinalement modulée dans un canon RF ; Compression magnétique dans une chicane ; Compression RF dans une structure accélératrice (velocity bunching). J'ai en particulier montré que, à charge égale, la génération de paquets courts via une impulsion laser courte dans un canon RF est désavantageuse, des points de vue de la longueur et de l'émittance transverse du faisceau, par rapport à la compression magnétique ou RF d'un paquet déjà accéléré. Cela est expliqué par les forces de charge d'espace plus importantes juste après l'émission du faisceau par la photocathode. A l'inverse, j'ai démontré que l'utilisation directement dans un canon RF d'une impulsion laser longitudinalement modulée et constituée de parquets courts est plus appropriée pour générer un faisceau d'électrons longitudinalement modulé et composé de paquets courts que la compression magnétique ou RF d'un faisceau d'électrons longitudinalement modulé et composé de paquets initialement plus longs. En particulier, cela permet de réduire les fluctuations sur l'espacement des paquets et sur la longueur des paquets.
Il est également consacré au développement et au test de modèles analytiques de la dynamique longitudinale des faisceaux. J'ai développé une matrice de transfert longitudinale pour un canon RF, en partant du modèle de K. J. Kim. Ce modèle a été comparé avec plusieurs mesures effectuées à PITZ et PHIL et a prouvé être précis sur les aspects énergétiques et temporels, mais pas totalement sur l'aspect de la dispersion en énergie. J'ai également développé un modèle analytique du phénomène de velocity bunching dans des structures accélératrices à onde progressive, en partant d'un modèle simple développé par P. Piot.

Mots-clés: Canons RF ; Diagnostics faisceau ; Dynamique faisceau ; Modélisation analytique ; Mise en forme du laser

Abstract

In several applications, quasi-relativistic sub-ps electron bunches are required : Laser-plasma acceleration, Free electron lasers, Generation of intense THz radiation, Study of ultra-fast phenomena in matter, etc.
The short nature of the bunch and the necessity of a high peak current for the applications imply strong space-charge forces leading to a degradation of beam properties, as its transverse emittance and duration. The main difficulty is to characterize, model and take into account these effects.
My thesis falls within this context through the study of dynamics and diagnostics related to these short bunches, namely whose rms duration is not directly measurable by an electronic method locating the border at a few tens of picoseconds.

The chapter 2 consists in the measurements of several properties of these bunches : charge, transverse emittance, energy and duration. The originality of my work is that I use simple methods, both on the theoretical (analytical at maximum) and technological (using only common elements of electron accelerators) point of view. These methods, more suitable for less extreme bunches, allow however obtaining very good results.
I especially developed a method of charge measurement from the measurement of the light intensity emitted by a scintillating screen following the interaction with an electron beam. This method allows precisely measuring charges lower than 100 fC. This is better than the capabilities of classical diagnostics (ICT and Faraday Cup) limited to the picoCoulomb because of electronic noise. This method is useful since the short bunches are often low-charged to minimize the effects of space-charge forces. This will also be used for detectors calibration, which requires low charges.
I developed a method to measure the bunch mean energy with a steering magnet and a scintillating screen, via the displacement of the bunch centroid as a function of the field of the steering magnet. This method has proven to be reliable for energies of few MeV at the exit of an RF-gun, since the measured bunch mean energies are fully compatible with the ones deduced from the bunch energy spectra measured by a dipole magnet. This is also the case when only two values of the steering magnet field are used, which makes this method very fast.
I also adapt multiparametric methods to measure the transverse emittance and duration of electron bunches. These indirect methods allow determining these properties from the measurement of other more accessible properties : the transverse dimensions for the transverse emittance and the energy spread for the duration. The duration measurement (3-phase method) gives very good results, since it allows determining with accuracy better than 10% rms durations lower than one picosecond. The emittance measurement without taking into account the space-charge forces in the modeling gives mixed results, since the accuracy is from 20% (3-gradient method) to more than 100% (3-screen method). A significant accuracy improvement, up to a factor of 5, can be obtained by taking the space-charge forces into account through a beam envelope equation and considering a 3D Gaussian charge density for the bunch, which constitutes the originality of my work.
I finally greatly contributed to the implementation, development and commissioning of a

Cherenkov-based bunch length measurement device on the PHIL accelerator at LAL. I especially established the electron bunch transport conditions to maximize the intensity of the Cerenkov light extracted from the beamline and transported up to the streak camera. I also participated to the development of the optical transport line between the Sapphire crystal and the streak camera, by purchasing a new type of mirror which led to a significant gain of a factor 50 on the Cerenkov light at the streak camera entrance.

The chapter 3 consists in the comparison of the properties of short electron beams, single or longitudinally modulated, generated by three different methods : Injection of a short or longitudinally modulated laser pulse in an RF-gun ; Magnetic compression in a chicane ; RF-compression in an accelerating structure (Velocity Bunching). I particularly shown that, at equal conditions of charge, the generation of short bunches thanks to a short laser pulse driving an RF-gun is disadvantageous, both from the beam duration and transverse emittance point of view, with respect to a magnetic or RF compression of an already accelerated beam. This is explained by the more important space-charge forces just after the beam emission by the photocathode. On the contrary, I have shown that the use of a longitudinally modulated laser pulse with short bunches directly in an RF-gun is more suitable to obtain a longitudinally modulated electron beam with short bunches than the magnetic or RF compression of a longitudinally modulated electron beam with longer bunches. In particular, this allows reducing the fluctuations in the bunch spacings and in the bunch lengths.
It also consists in the development and test of analytical models for longitudinal beam dynamics. I developed a longitudinal transfer matrix for RF-gun, starting from a Kim-like model. This model has been compared with several measurements performed at PITZ and PHIL and shown to be accurate on the energy and temporal aspects, but not totally on the energy spread aspect. I also developed an analytical model of the velocity bunching phenomenon in traveling wave accelerating structures, starting from a simple model developed by P. Piot.

Keywords: RF-guns ; Beam diagnostics ; Beam dynamics ; Analytical modeling ; Laser shaping.

Remerciements

Je tiens tout d'abord à remercier Patrick Puzo pour avoir accepté d'être mon directeur de thèse pendant ces trois années ainsi que pour ses conseils avisés dans le moment clé qu'est la préparation de la soutenance. Je le remercie également de m'avoir encouragé, pendant mes deux ans d'études au Magistère de Physique Fondamentale d'Orsay, à m'inscrire dans le Master 2 APIM et à ainsi me spécialiser dans le domaine de la physique des accélérateurs de particules. C'est un choix dont je suis très heureux aujourd'hui.

Je remercie aussi les directeurs de l'école doctorale MIPEGE Bruno Espagnon et Xavier Quidelleur qui ont acceptés de financer mon sujet de thèse et qui ont également suivis l'évolution de mon travail de thèse. Je remercie également le directeur du LAL Achille Stocchi pour m'avoir accueilli au sein de son laboratoire où l'environnement de travail s'est avéré très agréable. Je le remercie aussi d'avoir accepté de présider mon jury de thèse.

Je remercie sincèrement Serge Bielawski et Frank Zimmermann pour avoir accepté d'être les rapporteurs de mon travail de thèse. Leurs relectures avisées et très attentives ainsi que leurs nombreuses suggestions ont permi d'améliorer la qualité de ce manuscrit, tant du point de vue scientifique que de la qualité de l'anglais employé. Elles permettront aussi, dans le futur, d'améliorer les outils et modèles développés durant ma thèse. Je remercie également Alban Mosnier pour avoir accepter de faire parti de mon jury de thèse, pour sa relecture de mon manuscrit et pour les suggestions qu'il a apportées pour améliorer mon travail de thèse.

Je remercie Anne Oppelt pour m'avoir offert la possibilité de passer deux mois dans le groupe PITZ à Zeuthen durant ma thèse. Je la remercie pour s'être occupée de tous les détails de mon séjour, en particulier le logement, ainsi que de m'avoir offert la possibilité de réaliser des expériences sur PITZ. Je la remercie aussi d'avoir acceptée de faire partie de mon jury de thèse, ainsi que pour sa relecture avisée de mon manuscrit de thèse et pour ses suggestions qui ont permi de l'améliorer. Je remercie également tous les membres du groupe PITZ pour leur accueil ainsi que leur aide durant mon séjour.

Je remercie profondément Christelle Bruni qui a encadré quotidiennement mon travail pendant trois ans. Je la remercie de m'avoir laissé une grande autonomie dans mon travail, tout en étant présente dès que j'en avais besoin. Elle m'a laissé une grande latitude dans le choix de mes activités et des domaines à explorer, tout en veillant bien à ce que ces différentes activités se recoupent et forment un ensemble cohérent. Cela m'a permi de travailler dans de nombreux domaines différents de la physique des accélérateurs (Dynamique faisceau, Diagnostics faisceau, Modélisation analytique, Réalisation d'expériences, etc.) sans pour autant me disperser. Je la remercie également de m'avoir fait découvrir le domaine de la physique des accélérateurs durant mon stage de Master 1 sur PHIL. C'est ce stage qui m'a décidé à m'engager définitivement dans le domaine de la physique des accélérateurs. J'associe également Pierre Lepercq, qui a co-encadré ce stage, à ce remerciement.

Je remercie également tous les membres du département accélérateurs, actuels et passés, pour l'aide qu'ils m'ont apportés durant mon travail de thèse et pour leur sympathie qui a contribuée à faire de ma thèse une expérience très agréable et enrichissante, tant sur le plan scientifique que sur le plan humain. Je remercie en particulier : Agnès, Walid, Pierre, Hugues, Philip, Nicolas, Cécile, Mohamed, Cynthia, Thomas, Noureddine, Iryna, Viktor, Vincent, Jean-Luc, Robert, Joël, Didier, Alexandre, Mathilde, Leila, Isabelle, Jean-François, Raphaël, Julien, Olivier et Emilienne. Parmi tout les membres du département accélérateurs il en est deux, outre Christelle, que je souhaite remercier encore plus chaleureusement. Le premier est Jean-Noël Cayla qui m'a apporté une aide technique vitale sur PHIL et qui a toujours répondu présent pour m'assister lorsque je souhaitais réaliser des expériences. Sans son soutien une part importante de ce travail de thèse n'aurait tout simplement pas pu être effectuée. Le second est Sophie Chancé, qui s'est intéressée de très près à mon travail et à son avancement ce qui m'a énormément motivé. Durant nos nombreuses discussions, sur PHIL ou pendant le repas, elle m'a également appris beaucoup de choses sur les bonnes pratiques à avoir dans le milieu scientifique et m'a ainsi permi d'être moins direct et d'acquérir un minimum de sens de la diplomatie. Tout n'est certes pas encore parfait mais, comme elle dit, on partait de très loin avec moi.

Je remercie tous les doctorants du département accélérateurs, actuels et passés, qui ont contribués à rendre l'ambiance de travail très agréable : Illya, Mélissa, Luca, Ping et Nuria. Parmi tous ces doctorants je souhaite particulièrement remercier Dima pour les nombreuses discussions que j'ai eu avec elle, pour ses indéniables qualités vocales et pour son soutien indéfectible et très précieux. Merci mon amie. Je remercie également Vagelis et Brice pour les nombreuses discussions, plus ou moins sérieuses, que l'on a eu ensemble sur nos expériences de thèse respectives.

Je remercie avec une grande affection mes parents Patrick et Tania, ainsi que ma soeur Julie, qui m'ont supportés quotidiennement pendant ces trois ans (et même beaucoup plus que trois ans) où mon humeur n'a pas toujours été des plus agréables. Ils ont su être toujours présents pour me soutenir et me changer les idées par rapport à mon travail.

Je remercie finalement ma Shan chérie. Tu m'as toujours soutenue pendant la période de rédaction de ma thèse et, malgré la distance, la période de préparation de ma soutenance. Je suis très heureux que cette thèse m'ait aussi permi de te rencontrer. Tu en es la plus belle découverte.

Table des matières

Chapitre 1
Introduction

1.1 Applications of the short electron bunches . . . 1
1.2 Electron guns state of the art . . . 5
1.2.1 The basic principles of an electron gun . . . 5
1.2.2 Thermionic guns . . . 6
1.2.3 Photocathode guns . . . 8
1.2.4 Field-emission guns . . . 11
1.2.5 Photocathode RF-guns working principles . . . 13
1.3 Beam diagnostics state of the art . . . 18
1.3.1 Beam charge diagnostics . . . 18
1.3.1.1 Faraday Cup . . . 18
1.3.1.2 Current transformers . . . 20
1.3.2 Transverse beam profile diagnostics . . . 23
1.3.2.1 Scintillating screens . . . 23
1.3.2.2 OTR screens . . . 25
1.3.2.3 Other devices . . . 27
1.3.3 Beam transverse emittance measurement . . . 29
1.3.3.1 Definition of the beam transverse emittance . . . 29
1.3.3.2 The moving slit method . . . 30
1.3.3.3 The pepper-pot method . . . 32
1.3.4 Measurement of the beam energy spectrum . . . 33
1.3.5 Bunch length measurement . . . 34
1.3.5.1 Methods using light emission . . . 34
1.3.5.2 Transverse deflecting cavity . . . 35
1.3.5.3 The electro-optical sampling (EOS) method . . . 36

1.4 Facilities used to perform experiments and simulations 38
1.4.1 PHIL at LAL 38
1.4.2 PITZ at DESY 39
1.4.3 HELIOS Linac at SOLEIL 40
1.4.4 SPARC at INFN 41

Chapitre 2
Diagnostics of short electron bunches

2.1 Low-charge bunch measurements 46
2.1.1 The experimental layout 46
2.1.2 Calibration of the scintillating screen 47
2.1.3 Influence of the transverse bunch size on the calibration 50
2.1.4 Bunch charge measurement as a function of the optical density . . . 51
2.1.5 Comparison with the diamond detector 53
2.1.6 The case of the bunches with wide energy spectra 55
2.1.7 Conclusions 56
2.2 Transverse emittance measurements 58
2.2.1 The 3-screen method for bunch transverse emittance measurement . 58
2.2.1.1 Theoretical principles 58
Without space-charge forces 58
With space-charge forces 59
2.2.1.2 Evaluation of the precision on PHIL 62
2.2.1.3 Experimental measurements 65
Example measurement 65
Systematic measurements 72
2.2.1.4 Conclusions 74
2.2.2 The 3-gradient method for bunch transverse emittance measurement 74
2.2.2.1 Theoretical principles 74
2.2.2.2 Evaluation of the precision on PHIL 77
2.2.2.3 Experimental measurements 79
Example measurement 79
Systematic measurements 82
2.2.2.4 Conclusions 84
2.3 Longitudinal measurements 86
2.3.1 Measurement of the bunch kinetic energy thanks to a steerer magnet 86

2.3.1.1 Theoretical calculation . . . 86
2.3.1.2 Determination of the PHIL steerers magnetic length . . . 87
2.3.1.3 Experimental measurements on PHIL . . . 89
2.3.1.4 Measurement of the bunch mean energy with two bunch positions . . . 93
2.3.1.5 Conclusions . . . 94
2.3.2 Measurement of the bunch length thanks to the 3-phase method . . 95
2.3.2.1 Theoretical principles . . . 95
2.3.2.2 The used longitudinal transfer matrices . . . 96
The longitudinal drift space . . . 97
The accelerating structures . . . 97
2.3.2.3 Proof-of-principle measurement on the HELIOS Linac at SOLEIL . . . 99
2.3.2.4 Measurements performed at PITZ, DESY, Zeuthen . . . 104
2.3.3 Measurement of the bunch length thanks to a Cerenkov detector . . 110
2.3.3.1 Physical principle . . . 110
2.3.3.2 Experimental layout . . . 113
2.3.3.3 Calibration of a CCD camera . . . 114
2.3.3.4 Extraction of the Cerenkov photons from the Cerenkov station . . . 115
2.3.3.5 Transport of the Cerenkov radiation up to the streak camera entrance . . . 118
2.3.3.6 Resolution of the measurement . . . 119
2.3.3.7 Bunch length measurement with the streak camera . . . 124

Chapitre 3
Different methods for generating short electron bunches 131

3.1 Short laser pulse in an RF-gun . . . 132
3.1.1 Principles and limitations . . . 132
3.1.2 Analytical modeling of beam dynamics in an RF-gun . . . 132
3.1.2.1 Calculation of the RF-gun longitudinal transfer matrix . . 132
3.1.2.2 Test of the analytical model on the beam mean energy aspect . . . 136
3.1.2.3 Test of the analytical model on the time aspect . . . 142

3.1.2.4 Test of the beam energy spread dependence on the gun RF-phase . . . 148
3.1.3 Simulations on PHIL . . . 152
3.1.3.1 Influence of the Gun RF-phase . . . 153
3.1.3.2 Influence of the Gun peak accelerating field . . . 154
3.1.3.3 Influence of the laser pulse duration . . . 155
3.1.3.4 Influence of the laser pulse transverse radius . . . 156
3.1.3.5 Influence of the laser shape . . . 157
3.1.3.6 Influence of the bunch charge . . . 158
3.1.3.7 Influence of a booster cavity . . . 160
3.1.3.8 Propagation of a longitudinally modulated electron beam . 165
3.2 Magnetic compression in a chicane . . . 170
3.2.1 Principles and limitations . . . 170
3.2.2 Compression of a single electron bunch . . . 171
3.2.2.1 Evolution of the bunch mean energy . . . 172
3.2.2.2 Evolution of the final rms bunch length . . . 173
3.2.2.3 Evolution of the final bunch rms transverse emittance . . 174
3.2.2.4 Evolution of the bunch time profile and longitudinal phase-space . . . 177
3.2.2.5 Design of the magnetic chicane . . . 180
3.2.3 Compression of a longitudinally modulated electron beam . . . 180
3.2.3.1 Compression of a "perfect" modulated electron beam . . . 182
3.2.3.2 Compression of a longitudinally modulated electron beam coming from ASTRA simulations . . . 184
3.2.3.3 Use of a negative curvature for the correlation in the time/energy phase space . . . 186
3.2.3.4 Optimization of the compression of a modulated beam coming from ASTRA simulations . . . 192
3.2.3.5 Design of the magnetic chicane . . . 195
3.3 RF compression by velocity bunching in an accelerating cavity . . . 197
3.3.1 Principles and limitations . . . 197
3.3.2 Analytical modeling of the velocity bunching . . . 199
3.3.2.1 Model of P.Piot . . . 199
3.3.2.2 Evolution of the model of P.Piot . . . 201

3.3.2.3 Comparison of the analytical models with PARMELA simulations . . . 203
Model of P. Piot . . . 204
Evolved analytical model . . . 206
3.3.3 Simulations on SPARC for the compression of a single bunch by velocity bunching . . . 207
3.3.3.1 Influence of the Gun RF-phase . . . 209
3.3.3.2 First scheme of ultra-short electron bunch generation . . . 211
Influence of the injection phase in S1 . . . 211
Influence of the S1 and S2 mean accelerating field . . . 213
Influence of the bunch charge . . . 216
Influence of the laser pulse parameters . . . 216
Study at 10 pC with a 1 ps - 4 mm laser pulse . . . 221
3.3.3.3 Second scheme of ultra-short electron bunches generation . 222
Influence of the S1 and S2 mean accelerating field . . . 222
Comparison of the two compression schemes . . . 223
Influence of the bunch charge . . . 224
Influence of the laser pulse parameters . . . 225
Study at 10 pC with a 1 ps - 4 mm laser pulse . . . 226
3.3.3.4 Conclusions and prospects . . . 227
3.4 Conclusion : comparison of the three methods . . . 228
The rms bunch length . . . 228
The bunch rms transverse emittance . . . 228
The case of a longitudinally modulated electron beam . . . 230

Conclusion **231**

Annexe A
Demonstration of the beam magnetic rigidity

Annexe B
Additional information on the modes

Annexe C
Code for the analysis of the images produced by the YAG screens of the PHIL facility

Annexe D
Relative variation of the travel time in a magnetic structure between electrons of different energies

Annexe E
The ASTRA beam dynamics code

Bibliographie **257**

Chapitre 1

Introduction

Contents

1.1 Applications of the short electron bunches 1
1.2 Electron guns state of the art 5
1.2.1 The basic principles of an electron gun 5
1.2.2 Thermionic guns 6
1.2.3 Photocathode guns 8
1.2.4 Field-emission guns 11
1.2.5 Photocathode RF-guns working principles 13
1.3 Beam diagnostics state of the art 18
1.3.1 Beam charge diagnostics 18
1.3.2 Transverse beam profile diagnostics 23
1.3.3 Beam transverse emittance measurement 29
1.3.4 Measurement of the beam energy spectrum 33
1.3.5 Bunch length measurement 34
1.4 Facilities used to perform experiments and simulations . . . 38
1.4.1 PHIL at LAL 38
1.4.2 PITZ at DESY 39
1.4.3 HELIOS Linac at SOLEIL 40
1.4.4 SPARC at INFN 41

1.1 Applications of the short electron bunches

The short electron bunches are nowadays necessary for several applications in various domains, mainly in chemical [1] and physical [2] domain, which give them great interest.

One can quote as first example the future light sources, called fourth-generation sources, which are based on free electron lasers and will require electron bunches with an rms length of 100 fs or lower. These sources must allow achieving, among others, two objectives. First of all, they must allow generating ultra-short X-rays pulses (duration of

a few femtoseconds) [3]. Then, they also must allow increasing the average brightness [1] of the generated radiation, a factor of 10000 being expected with respect to the third-generation sources as the synchrotron SOLEIL for example [4]. However, it is not the only intended solution to increase the radiation brightness. In fact, the Diffraction Limited Storage Rings (DLSR) would be able to deliver a brightness between 100 and 1000 times higher than the one of the third generation sources [5].

Still in the radiation generation domain, the short electron bunches should allow fulfilling the current lack of intense radiation source in the frequency domain around the Terahertz [6]. This would be possible thanks to the coherent emission of synchrotron radiation. In fact, the synchrotron radiation emission at a wavelength significantly larger than the length of the electron bunch is in phase, therefore in a coherent way, for the different electrons of the bunch. It allows multiplying the intensity of the emitted radiation by the number of electrons in the bunch (10^8 to 10^{10}). Yet, the THz corresponds to a wavelength of 300 μm. The injection of relativistic electron bunches with an rms length around 100 fs, corresponding to 30 μm, in a magnetic structure (dipole magnet, undulator ...) adapted such that the emitted synchrotron radiation is centered around the THz [2] should allow producing an intense source in the THz domain. Besides, when a longitudinally modulated electron beam made of short bunches is used, the frequency is tunable through a change in the beam longitudinal modulation [7].

Another important application for short electron bunches is the imaging techniques, which aim to observe the ultra-fast phenomena in matter, namely taking place at a time scale significantly lower than one picosecond [8]. For example, in pulse radiolysis phenomenon, the short electron bunches should allow studying the transient species created during chemical reactions, which frequently have lifetimes lower than one picosecond. This will allow a better understanding of the processes involved in a chemical reaction. For example, the REGAE (Relativistic Electron Gun for Atomic Exploration) facility at Hamburg is used to produce low energy (< 5 MeV) and low charged (down to 10 fC) short (< 100 fs rms) electron bunch, to study the atomic dynamics at the femtosecond time scale [9, 10].

The production of RF power is also an issue where the short electron bunches are expected to play an important role. For example, the CLIC project is based on an innovative two-beam system for the next large electron/positron linear collider [11]. In this project, the high-gradient (80 MV/m) 30 GHz accelerating cavities of the main accelerator would be supplied by the RF power created during the deceleration of strongly-charged (between 10 nC and 20 nC) short (rms length between 2 ps and 3 ps) electron bunches in a 30 GHz decelerating structure placed in parallel with the main accelerator.

Finally some laser-plasma acceleration patterns, currently extensively studied for generating very energetic electron bunches on very short accelerating distances, require the use of short electron bunches. One of the studied patterns is to inject an electron bunch in a wave with a strong field (possibly higher than GV/m) and a short wavelength (less

1. The radiation brightness is defined as the number of photons emitted per second per mm^2 per mrad^2 and in 0.1% of frequency bandwidth around a central frequency ν_0, the latter meaning that to determine the radiation brightness, we count all the photons such as their frequencies ν verify $\frac{\nu-\nu_0}{\nu_0} < 0.1\%$.

2. This is not at all the case in the current light sources.

than 100 μm) which was previously created in the plasma by the interaction between the plasma and an intense laser [12]. The injected electron bunch must then be short, with a length significantly lower than the wavelength of the wave in the plasma (100 μm or 333 fs). Otherwise the electrons of the bunch will undergo very different fields (even of opposite sign). This would strongly deteriorate the bunch quality and particularly its energy spread, which is defined as the standard deviation of the energy distribution of the electron bunch.

Considering the numerous and various applications of the short electron bunches, previously introduced, the study of their generation and their diagnostics are nowadays two major fields of research and development in the accelerator physics. These two domains constitute the scope of my thesis, which is divided into three chapters with three main sections in each chapters.

The first one is the remainder of Chapter 1. The state of the art of the electron beam sources is presented in this part. The state of the art of the low energy (< 100 MeV) electron beam diagnostics is also presented in this part. Finally, the facilities where I performed experiments and simulations are introduced.

The second one is the Chapter 2, which presents the diagnostics that I used and developed during my thesis for the short electron bunches, as well as the applications of these diagnostics to measure short electron bunch properties. The first section is about the development and test of a method allowing measuring very low bunch charge (< 100 fC) with a scintillating screen. The second section is about the measurement of the transverse emittance of a few MeV electron bunch by using the 3-screen and 3-gradient methods, which are classically used for high energy electron bunches. I also include the effects of space-charge forces in the 3-screen method through the beam envelope equation. The third section is about the measurement of the bunch longitudinal properties. I developed and tested a method allowing the measurement of the bunch energy with a steering magnet and a scintillating screen. I applied the 3-phase method, classically used for high energy electron bunches, to measure the rms length of a 20 pC few MeV electron bunch down to 900 fs. Finally, I present the development and test of a bunch length measurement device, using the Cerenkov emission, that I greatly contributed to implement on the PHIL facility at LAL.

The third one is the Chapter 3, which deals with the three methods used nowadays to generate short electron bunches. The first section is about the use of a short laser pulse to drive an RF-gun. Starting from the model of K. J. Kim [13], I first developed and tested an analytical model describing the beam dynamics in an RF-gun with a simple transfer matrix. I also performed simulations to study the achievable bunch properties by this method. I finally study the possibility to generate a longitudinally modulated electron beam made of short bunches by this method. The second section is about the longitudinal compression of an electron bunch in a magnetic structure. I performed simulations to study the impact of the synchrotron radiation emitted by the bunch on its properties. My main work in this second section has been to study the possibility to compress a

longitudinally modulated electron beam in a magnetic structure without destroying this modulation. The third section is about the compression of an electron bunch by velocity bunching in an accelerating structure. Starting from the model of P. Piot [14], I first developed and tested an analytical model describing this phenomenon in a traveling wave accelerating structure. Finally, I performed simulations on the SPARC facility to study the achievable bunch properties with two different schemes of velocity bunching.

During my thesis, I principally use the ASTRA code to perform my beam dynmics simulations [42]. A brief description of the principal features of ASTRA I used during my thesis are presented in the Appendix E. I also use the CSRTrack code [113], which is fully compatible with the ASTRA code, to perform the simulations of beam magnetic compression. I finally use the PARMELA code [120] to perform the simulations of beam compression by the velocity bunching phenomenon in traveling wave accelerating sections. The reason is that it is easier to include traveling wave accelerating sections in the PARMELA code than in the ASTRA code.

1.2 Electron guns state of the art

In this section, I present at first the basic principles of an electron gun, regardless of the emission process. I then introduce the various types of electron sources which can be found in an accelerator. For each type, I briefly explain its physical and technological principles. In particular, the conditions for the electron emission are presented.

It is noteworthy that all the laws of electron emission given in this section do not take into account the limitation due to the space-charge forces, namely the fact that the already emitted electrons create an electric field which limits the emission of new electrons.

1.2.1 The basic principles of an electron gun

An electron gun is made of a cathode, which is the electron emitter, placed under vacuum (typically between 10^{-5} mbar and 10^{-10} mbar). The emitted electrons have then to be collected and accelerated by an electric field to constitute the beam. This electric field can be an electrostatic one, created by an anode having an electrostatic potential different from the one of the cathode. In this case the gun is called a DC-gun. The electric field can also be an oscillating one, created by an electromagnetic standing wave resonating in a cavity. In this case the gun is called an RF-gun, where RF means Radio Frequency. Then a hole has to be made in the anode or in the cavity, to extract the electron beam from the gun. The design of these apertures is a crucial point in the design of an electron gun. Indeed, they have to distort the electric field the less possible with respect to the ideal case of a closed gun. Finally the electron beam is divergent because of the space-charge forces, namely the Coulomb interaction between the electrons of the beam. A focusing system has therefore to be implemented to transport the beam without losing electrons. This focusing system is most of the time magnetic (solenoid and/or quadrupole magnet), but can sometimes be electrostatic (Einzel lens [15]) for a beam energy in the keV range. Fig. 1.1 summarizes these facts by showing a simplified layout of an electron gun.

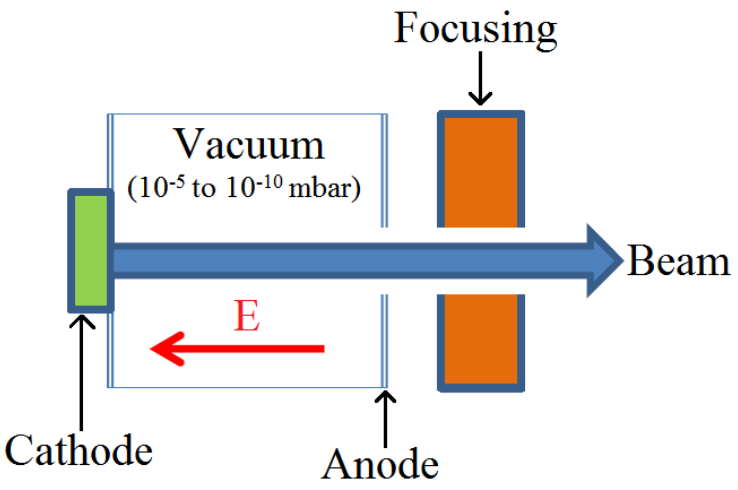

FIGURE *1.1 – Simplified layout of an electron gun.*

The main and general advantage of the RF-guns with respect to the DC-guns is that the accelerating electric field can be much higher, and therefore the beam energy too, without electrical breakdowns in the gun [16]. The maximum voltage currently achievable in a DC-gun is around 750 kV for the Cornell gun [17], corresponding to a beam energy of 750 keV at the exit. The maximum accelerating field currently achievable in an RF-gun is around 200 MV/m [18], corresponding to a beam mean energy between 6 MeV and 7 MeV at the exit. This higher and faster energy gain in an RF-gun with respect to the DC one allows minimizing the effects of space-charge forces, which scale like the inverse square of the energy [19], and therefore reaching much lower values of the beam transverse emittance (see Sec. 1.3.3.1).

1.2.2 Thermionic guns

The first type of electron gun which has been historically built is the thermionic electron gun. In this kind of gun, the electrons are emitted from a cathode whose surface is heated up to a temperature typically between 1000 K and 2500 K. This is called the thermionic emission. The basic physical principle of the thermionic emission is shown in Fig. 1.2, where the kinetic energy distributions of the electrons in the cathode material, following the Fermi-Dirac distribution [20], are depicted for three temperatures.

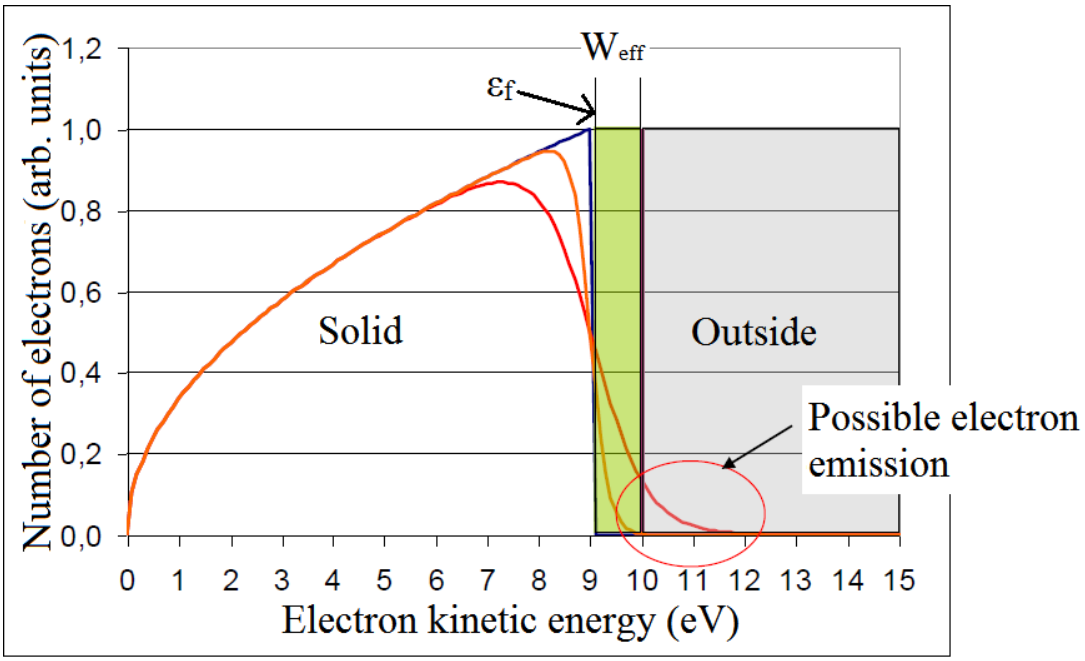

FIGURE *1.2 – The basic physical principle of the thermionic emission. W is the work function of the material and ϵ_f is the Fermi level. Blue curve : 0 K ; Orange curve : 2000 K ; Red curve : 5000 K.*

The blue curve in Fig. 1.2 represents the kinetic energy distribution of the electrons in the cathode material at 0 K. It shows an increasing number of electrons up to the Fermi

level ϵ_f, and no electrons at higher kinetic energies. No electron can therefore be emitted in this condition, since the emission requires an electron kinetic energy higher than $\epsilon_f + W$, where W is the work function of the cathode material. When the temperature is increasing the kinetic energy distribution of the electrons is deforming, as shown in Fig. 1.2, implying that a fraction of the electrons, also increasing with the temperature, has kinetic energies higher than $\epsilon_f + W$ and can therefore be emitted from the cathode. This is due to the growing thermal agitation in the cathode material.

The current surface density J_R which can be extracted from a cathode having the work function W and heated up at a temperature T is given by the Richardson law [21] :

$$J_R = AT^2 e^{-\frac{W}{k_b T}} \tag{1.1}$$

where k_b =1.38∗10^{-23} J/K is the Boltzmann constant and A is the Richardson constant which actually depends on the material and has a value typically between 0.3 A.cm^{-2}.K^{-2} and 330 A.cm^{-2}.K^{-2}.

One can see that the emitted current J_R increases when the temperature T increases and when W decreases. The good material should then have a high melting temperature and a low work function. These two properties are not fulfilled together for the pure materials. Practically, the cathode is often made of a matrix of refractory material in which are included materials lowering the work function of the cathode. The Tungsten, which has a melting temperature around 3700 K and a work function around 4.5 eV, is often used as the matrix. For example, some Cesium can be included in it to decrease W. For a certain amount of Cesium W can be lowered down to 1.4 eV, which is even lower than the work function of the pure Cesium (around 1.9 eV). The spread of the various possibilities is large and also depends on the applications, making the development and preparation of the cathodes a full-fledged scope of research.

The material work function W has to be replaced in Eq. 1.1 by the effective work function W_{eff}, namely the work function in the conditions of the experiment. In fact, the work function of a material changes with the temperature and with the electric field applied on its surface. The work function can be lowered or increased by an increase of the temperature, it depends on the material. The work function is lowered by an increase in the electric field applied on the material surface. This is called the Schottky effect [22]. In the case of the metals, the lowering δW of the work function is given by [22, 23] :

$$\delta W = \sqrt{\frac{e^3}{4\pi\epsilon_0}}\sqrt{E} \tag{1.2}$$

where ϵ_0 is the dielectric permittivity of vacuum and E is the applied electric field. δW starts to become significant at the 10 MV/m scale, where it reaches 0.4 eV.

Currently most of the thermionic electron guns are DC-guns, as it is for example the case on the HELIOS Linac at SOLEIL (see Sec. 1.4.3). However, quite recently, the thermionic RF-guns start to be used, as it is the case for example at the MAX-lab Linac injector [24].

The advantage of the thermionic RF-guns with respect to the DC ones is that the duration of the electron beam can be much shorter. In fact, the thermionic emission being a continuous process, the beam duration is driven by the oscillating frequency of the accelerating field for a thermionic RF-gun. This is due to the simple fact that no electrons are emitted when the electric field on the cathode is decelerating. For example, for a 3 GHz RF-field, the beam duration is shorter than a half period of this field, ie shorter than 180 ps. On the other hand, for a thermionic DC-gun, the beam duration is driven by a device (a grid for example), located in front of the cathode, in which a switching voltage stopping the electron emission is applied. Due to the limitation in the speed of this switching voltage, the beam duration is currently limited around 1 ns for a thermionic DC-gun.

The thermionic RF-guns have the drawback that a fraction of the electrons are emitted by the cathode and thereafter submitted to a decelerating field, which sends them back to the cathode. This is called the cathode back-bombardment. This bombardment with energetic electrons can damage the cathode and the gun if its intensity is too high. The current density which can be extracted from the cathode of a thermionic RF-gun is therefore limited for this reason. Another drawback is that the thermionic RF-guns produce an electron beam with a high energy spread, because of the time variation of the accelerating field during the electron emission. However, this energy spread can be lowered below 1% FWHM by choosing the appropriate amplitudes and phases, with respect to the gun accelerating field, of the accelerating field in the accelerating sections directly following the thermionic RF-gun [25, 26].

1.2.3 Photocathode guns

A later developed but nowadays widely used type of electron gun is the photocathode gun, where the electrons are emitted from the cathode by the photoelectric effect following the impact of a laser pulse on the cathode, which is then called photocathode.

Fig. 1.3 shows the basic physical principles of the photoelectric emission. The photoemission occurs when an electron of the cathode absorbs a photon having an energy higher than the effective work function W_{eff} of the material and subsequently leaves the material. It is noteworthy that not all the photons of a laser pulse impacting the photocathode will lead to the emission of an electron. The ratio between these two numbers is called the Quantum Efficiency (QE) of the photocathode. It is an important feature of a photocathode, since it sets the energy needed in the laser pulse to emit a given amount of charge in the electron beam. The QE depends on the material and is higher for the semiconductor than for the metals. For example, it is around 10^{-4}% for the Copper [23] and around 1% to 10% for the Cs_2Te [27, 23] at a wavelength of 266 nm for the laser pulse. The QE also depends on the wavelength of the laser pulse. For example, it increases to around 10^{-2}% for the Copper at 213 nm and decreases to around 10^{-5}% at 308 nm [23].

The photoemission can also happen if an electron absorbs simultaneously [3] several photons of the laser pulse, having each an energy lower than W_{eff}, such that the sum of their energies is higher than W_{eff}. This is called the multiphoton photoemission [28, 29], the order being given by the number of photons needed to emit one electron.

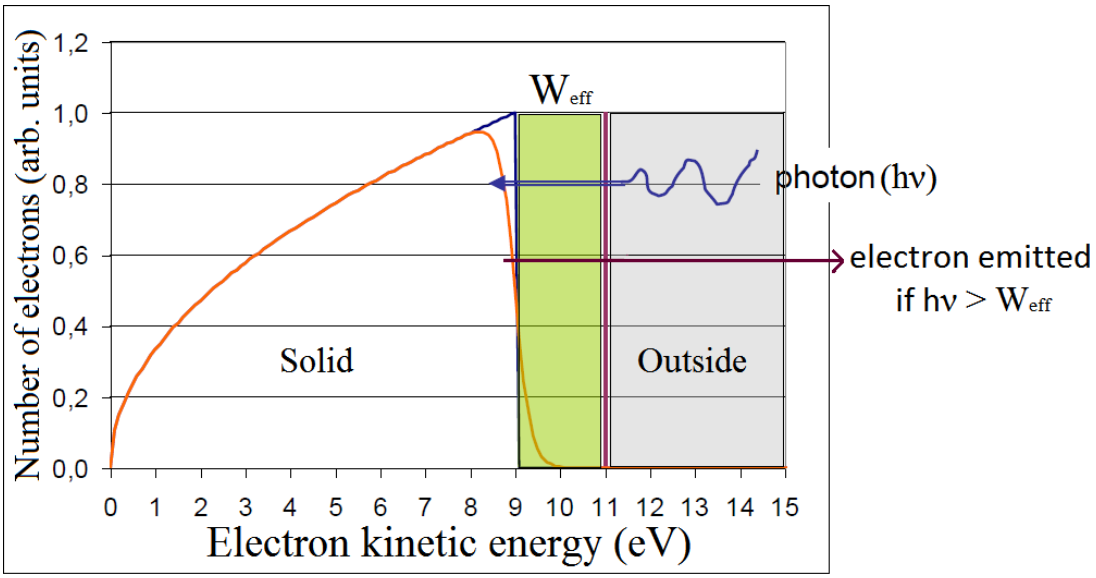

FIGURE *1.3 – The basic physical principle of the photoelectric emission. W_{eff} is the effective work function of the material and $h\nu$ is the photon energy, with ν the photon frequency and the Planck constant $h = 6.626 * 10^{-34}$ J.s. Blue curve : 0 K ; Orange curve : 2000 K. [23].*

The current surface density J_{FD} which can be extracted from a photocathode having the effective work function W_{eff}, the temperature T and illuminating by photons having the energy $h\nu$ is given by the Fowler-Dubridge law [23] :

$$J_{FD} = \sum_n J_n, \text{ with } J_n = A a_n T^2 I^n (1-R)^n F\left(\frac{nh\nu - W_{eff}}{k_b T}\right)\left(\frac{e}{h\nu}\right)^n \qquad (1.3)$$

where A is the Richardson constant, I is the laser pulse power surface density, R is the reflectivity of the cathode material and n is the order of multiphoton photoemission. The order $n = 0$ corresponds to the thermionic emission and J_0 is the Richardson law (see Eq. 1.1). a_n is a constant depending on the cathode material, roughly scaling like 10^{-12n}, which represents the cross section of the n^{th} order multiphoton absorption process. F is the Fowler function, which is a positive and increasing function approximately scaling like :

3. More precisely in a time shorter than the time of deexcitation of an electron having absorbed a photon.

$$F(x) \sim \begin{cases} x < 0 & e^x \\ x = 0 & \frac{\pi^2}{12} \\ x > 0 & \frac{\pi^2}{6} + \frac{x^2}{2} - e^{-x} \end{cases}$$

F is therefore a fast varying function, having very low values when $x < 0$ ie when $nh\nu < W_{eff}$. It means that this type of photoemission, by tunneling, is always possible but very unlikely compared to the photoemission with $nh\nu > W_{eff}$ $(x > 0)$.

Both photocathode DC-guns and photocathode RF-guns are currently used as sources for accelerators. They are used for different kind of applications, due to their different advantages and drawbacks.

The main advantage of the photocathode guns compared to the thermionic ones is that the electron beam duration is given by the duration of the laser pulse illuminating the cathode. It allows therefore producing electron beam with a duration in the picosecond range, and even of a few tens of femtoseconds, directly in the gun without using subsequent RF structures to bunch the beam [4].

The power injected in an RF-gun to generate the accelerating field is very high, typically from a few MW to more than 10 MW, and therefore generates a lot of heat in the gun walls which has to be evacuated. It implies that a lot of cooling power is required for the operation of a photocathode RF-gun, which complicates its mechanical design. Even with these cooling devices, the need to evacuate the heat limits the repetition rate of a photocathode RF-gun. In a photocathode DC-gun, the repetition rate is given by the one of the laser pulse and can therefore be higher. This limitation of the repetition rate in a photocathode RF-gun could be overcome by using superconducting materials (SRF-gun) instead of normal conducting materials, because the power injected and dissipated in an SRF-gun is order of magnitudes lower than in a normal conducting photocathode RF-gun. An SRF-gun is for example currently developed at Rossendorf [32]. However, the SRF-gun technology is at its very beginning and is currently not used as electron source for applications. The production of a polarized electron beam requires the use of special photocathodes, typically $GaAs$ photocathode. This type of cathode has currently never been used in any photocathode RF-gun. The first reason is that it is very sensitive to contamination and requires a vacuum pressure lower than 10^{-10}mbar, while it is around 10^{-8} to 10^{-9}mbar in a photocathode RF-gun. The second reason is that a lot of electrons are emitted from the gun walls and cathode in the absence of laser pulse (dark current), because the high electric field in the gun causes an important field emission (see Sec. 1.2.4). These electrons can hit and therefore destroy the cathode. The photocathode DC-guns are therefore used in the applications requiring a high repetition rate of the electron beam and/or a polarized electron beam. This is for example the case of the linear colliders

4. This is true as long as the response time of the cathode to the laser is shorter than the laser pulse. Otherwise the beam duration starts to be influenced by the cathode time response and becomes dominated by it if it is much longer than the laser pulse duration. The metallic cathodes like Copper and Magnesium have a response time in the femtosecond range [30]. The semiconductor cathodes have a longer response time, which is typically in the picosecond range but can be of the order of several tens of picosecond [31].

for particle physics studies, the electron source for the ILC project being intended to be a photocathode DC-gun [33].

The photocathode RF-guns combine the advantages of the RF-technology compared to the DC one and of the photoemission compared to the thermionic one. It allows therefore creating directly at the exit of the gun an electron beam of very high quality. Namely an electron beam with a high energy (up to 6-7 MeV), a short duration (potentially lower than 100 fs rms), a low energy spread (around 0.1% rms), a high charge (up to more than 10 nC in one bunch) and a low normalized transverse emittance (a few π.mm.mrad for a 100 pC, 100 fs rms and 6 MeV electron beam). The combination of all these properties cannot be achieved with the other electron sources. The photocathode RF-guns are therefore used as electron sources for applications requiring a high peak current, but not affected by a low average current, and high brightness electron beam [5]. This is for example the case for the X-ray free electron lasers like LCLS [35], FLASH [36] and the European XFEL [4].

The scope of my thesis is the dynamics and diagnostics of the short electron beams with an energy of a few MeV. The photocathode RF-guns are the only type of electron sources able to generate this kind of electron beam. As a consequence, a large majority of the simulations and experiments presented in the chapters 2 and 3 of my thesis has been performed with a photocathode RF-gun as electron source. In these chapters, the term "gun" or "RF-gun" will always define a photocathode RF-gun unless otherwise stated. Further explanations on the working principles of this kind of electron guns are given in Sec. 1.2.5.

1.2.4 Field-emission guns

Another type of electron emission is the field-emission, also called cold emission, where the electrons are emitted from the material by quantum tunneling due to the application of a strong electric field E on the material surface. Fig. 1.4 shows the basic physical principles of the field emission.

When a strong electric field E is applied on the material surface the potential barrier, which prevents the emission of electron when no electric field is applied, is lowered by a quantity δW and deformed as it schematically shown in Fig. 1.4. This distortion of the potential barrier implies that electrons from the material can go through by quantum tunneling, and therefore escape from the material [22]. A current of electron is then emitted. The current surface density J_{FN} which can be emitted from a material by the field emission process is given by the Fowler-Nordheim formula [37] :

$$J_{FN} = \frac{e^3}{8\pi h t^2(y)} \frac{E^2}{W_{eff}} e^{-\frac{8\pi\sqrt{2m_e}}{3eh}\frac{W_{eff}^{1.5}}{E}v(y)}, \text{ with } y = \frac{\delta W}{W_{eff}} \tag{1.4}$$

5. The brightness B_b is a parameter representing the overall quality of an electron beam. It is defined as $B_b = \frac{Q}{\epsilon_x \epsilon_y \epsilon_z}$ [34], where Q is the beam charge and $\epsilon_{x\ (y)}$ and ϵ_z are respectively the rms normalized transverse horizontal (vertical) and longitudinal emittances (see Sec. 1.3.3.1).

where $t(y)$ is a function very close to 1 and $v(y)$ is a function which remains very close to 1 as long as y is not too high since $v(y) = 1$ when $y = 0$ and $v(y) = 0.907$ when $y = 0.25$. One has to note that, strictly speaking, Eq. 1.4 is established only at 0 K. But it is a very good approximation at ambient temperature (around 300 K) for high electric field (of the GV/m order). For example, for the Tungsten at 1000 K, the discrepancy is about the order of 10% for a field of 3.33 GV/m applied on the material surface. The field emission can be used, as previously described, with just an electric field applied on the material surface. But it can also be improved by exciting the electrons of the material. The latter can be done by heating up the material and/or illuminating the material with photons having an energy lower than W_{eff}.

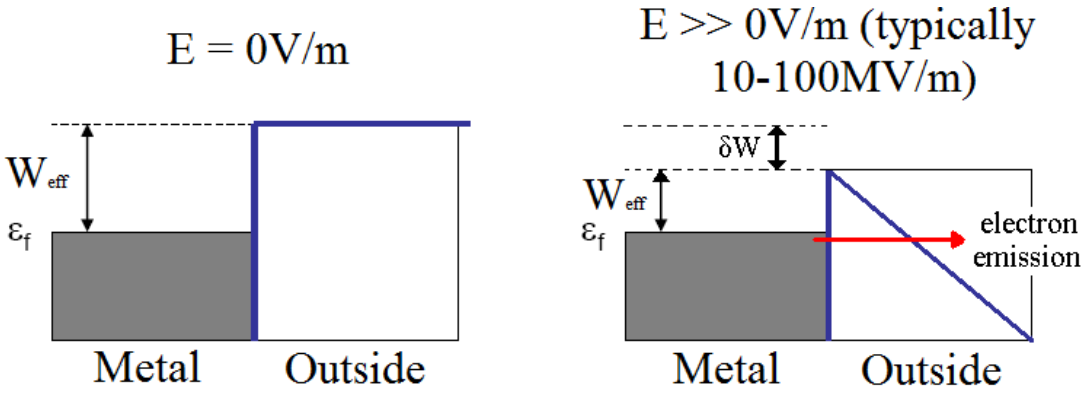

FIGURE *1.4 – Basic physical principles of the field emission. W_{eff} is the material effective work function, δW is the variation of W_{eff} due to the applied electric field E (see Eq. 1.2) and ϵ_f is the material Fermi energy.*

The two parameters influencing J_{FN} are W_{eff} and the applied electric field E. J_{FN} is increasing when W_{eff} decreases. The search for cathode with a low W_{eff} is a full-fledged scope of research, as briefly described in Sec. 1.2.2. J_{FN} is increasing when the electric field E applied on the material surface increases. To increase E, the lightning rod effect close to a sharp tip is used. In fact, close to a sharp tip, the electric field lines are concentrated leading to an increase of the electric field value by a factor β_c, called the field enhancement factor, with respect to the value on a perfectly flat surface. E has then to be replaced by $\beta_c E$ in Eq. 1.4. β_c depends on the tip geometry and can be very high (up to 10000). The emitting surface of a tip is very small, of the nm^2 order, implying that a mesh of tips is required to obtain a high electron current. The density of tips can be very high, up to 10^9 tips per cm^2, and thus the cathode can remain very small (of the mm^2 order). The materials used for this cathode can be metals, like Mo (Spindt cathodes), or semiconductors, like $GaAs$, because they are better field emitters than the metals. Carbon nanotubes are also used, because they are naturally very sharp (diameter in the nanometer range for a length in the micrometer range) thus generating a strong lightning rod effect.

The field-emission electron guns are used in several applications because of their compactness, the high current density that can be generated and the non necessity of

heating up the cathode. They are for example used in the RF-tubes embedded in the satellites, in the flat TV screens and in the electron microscopes. The field emission guns are currently not used as electron sources for the accelerators encountered in industrial and scientific applications, but some studies have recently been started on this topic [38, 39].

The field emission also occurs in the thermionic and photocathode electron guns. It is especially important in the RF ones, because the electric field can be up to 200 MV/m without taking into account the field enhancement factor β_c. It is then a parasitic electron emission which comes in addition to the electron beam and has to be minimized. This emission comes from the spikes and ruggedness, which can be found on the cathode and on the gun walls, which creates a local increase in the electric field. In a photocathode RF-gun this parasitic emission is called the dark current, since it happens even in the absence of the laser pulse. Fig. 1.5 shows an example of dark current measurement performed at the PHIL facility (see Sec. 1.4.1), as a function of the peak accelerating field in the photocathode RF-gun, for a Copper photocathode. The fitting of this data with Eq. 1.4 allows estimating the field enhancement factor of the photocathode to $\beta_c = 107$, implying a local electric field of a few GV/m on the photocathode surface which is a typical value to observe a significant field emission.

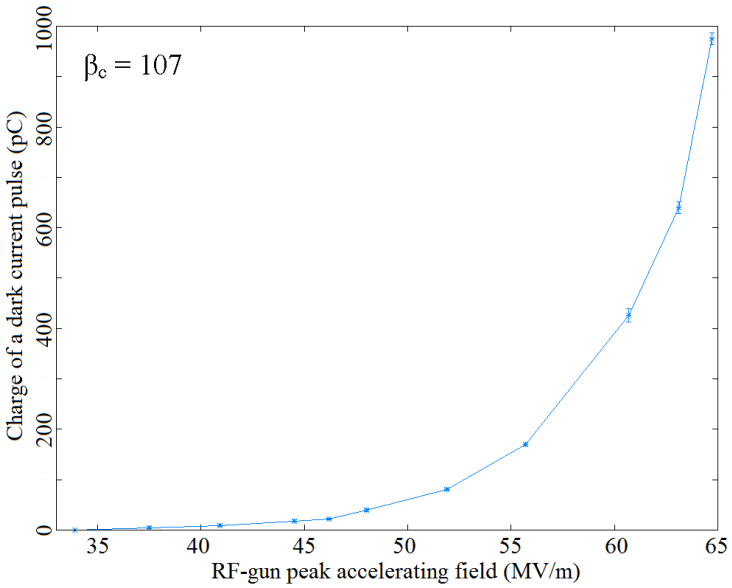

FIGURE *1.5 – Dark current measurement performed at the PHIL facility, as a function the photocathode RF-gun peak accelerating field, for a Copper photocathode. The duration of the dark current pulse is given by the one of the RF power pulse fed into the photocathode RF-gun.*

1.2.5 Photocathode RF-guns working principles

A large majority of the accelerators currently producing short electron beams contains a photocathode RF-gun as electron source. It is therefore important to expose here the working principles of these guns and the state-of-the-art of this domain. The photocathode

RF-guns generate electron beams accelerated at an energy of a few MeV (up to 7 MeV) on very short accelerating distances (typically between 10 and 20 cm).

A photocathode RF-gun is made of an electron donor photocathode and of RF cavities, located just after the photocathode, where the electrons will be accelerated. The currently two most popular designs are the 1.6 cells and 2.5 cells photocathode RF-guns where the non-entire cell, namely the shorter cell, is located just after the photocathode. Fig. 1.6 shows as an example a section of the 2.5 cells Alpha-X photocathode RF-gun which was mounted on the PHIL accelerator at LAL (see Sec. 1.4.1) between November 2009 and May 2012.

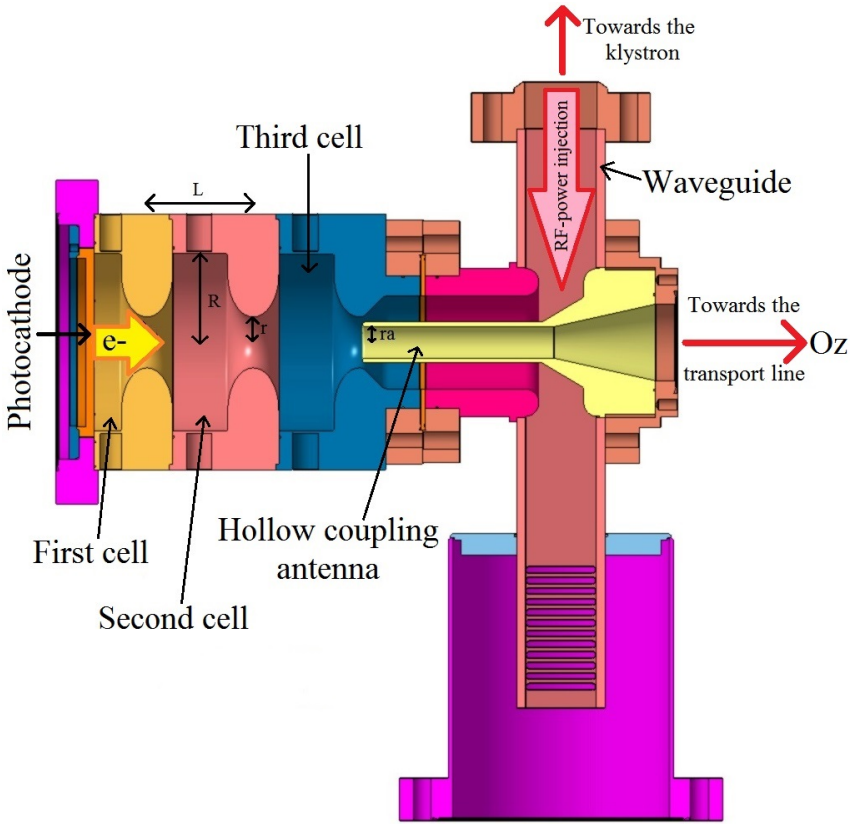

FIGURE *1.6 – Section of the Alpha-X photocathode RF-gun and of its coupling system to the klystron [40]. L = 5 cm ; R = 42 mm ; r = 12 mm ; ra = 7.4 mm. Note that the first cell is half the length of the other.*

The electrons are extracted from the photocathode, by photoelectric emission, thanks to the impact of a laser pulse. The emitted charge is adjustable via the energy contained in this laser pulse. It varies linearly with the energy of the laser pulse as long as the emitted surface charge density is not too high. Indeed, when the surface charge density is too high, the space charge forces prevent the extraction of new electrons and the emitted charge starts to saturate. The used wavelength of the laser pulse is frequently in the UV range (262 nm for the Alpha-X gun at PHIL) because, for most of materials used in the photocathodes, the quantum efficiency is maximum at these wavelengths, thus allowing

emitting more electrons for the same energy in the laser pulse.

RF power of typically several MW, produced by a klystron [41], is injected in the photocathode RF-gun through a coupling system. In the cells of the photocathode RF-gun standing electromagnetic waves, called the modes, will then be established. They oscillate at discrete frequencies, one per mode, which are a function of cavities dimensions (length and radius). It is therefore important to precisely tune the frequency of the injected RF power, and the cavities parameters, in order to only have the mode of interest established in the photocathode RF-gun. The selected mode is used to accelerate the beam just after its emission from the photocathode. The mode used in most part of the photocathode RF-guns to accelerate the electrons is the $TM_{010-\pi}$ mode, because its electric field is essentially oriented along the cell symmetry axis (Oz axis in Fig. 1.6) which is the desired direction of acceleration for the electrons. Besides, it is invariant under rotation around the Oz axis which allows keeping a cylindrical symmetry for the electron beam. Fig. 1.7 shows the normalized profile of the electric field on the Oz axis for the $TM_{010-\pi}$ mode in the SPARC (see Sec. 1.4.4) 1.6 cells photocathode RF-gun. The Appendix B contains additional information on the modes.

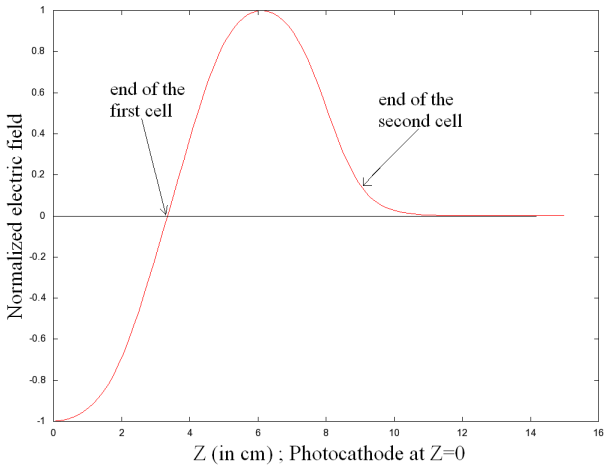

FIGURE *1.7 – Normalized profile of the longitudinal electric field E_z along the Oz axis of the SPARC 1.6 cells photocathode RF-gun.*

The longitudinal field along the Oz axis in the photocathode RF-gun is of the form $E_0(z)\sin(2\pi ft+\phi)$, where f is the mode frequency and ϕ the RF-phase which is adjustable. Fig. 1.7 shows well that in the $TM_{010-\pi}$ mode the field is phase shifted by π, so that it is at any time of opposite sign for two adjacent cells. Maximizing the electron energy gain along the photocathode RF-gun thus requires that the electric field changes sign at the time the electron beam changes cell. The RF-phase ϕ must therefore be adjusted such that the electrons undergo an accelerating field all along the first cell and leave it just when the field changes sign. Since the rest mass energy (m_ec^2) of the electrons is small compared to the energy provided by the electric field, about 2 MeV in the first cell, they are quickly accelerated to velocities close to c, the speed of light in vacuum. This allows considering that all along their motion after the first cell they have an almost constant velocity equal to c. This fixes the length of the cells other than the first to $L = \frac{c}{2f}$ so

that the field changes sign when the bunch is moving from one cell to the next. It should be noted that once again the $TM_{010-\pi}$ mode is perfectly suitable because its frequency f is independent on L and depends only on the cells radii. The first cell has to be shorter than the others because otherwise the accelerating field E_z would be at all times zero on the photocathode. It would then be impossible to correctly collect and accelerate the emitted electrons. Under these conditions of RF-phase and cells lengths the energy of the electrons is maximum at the exit of the photocathode RF-gun.

It is important to note that the RF-phase ϕ can be chosen differently if we want to optimize other beam properties than the energy. For example, as it will be shown in Sec. 2.3.2.5, the RF-phases minimizing the energy spread or the bunch length are not the same than the one maximizing the energy.

The choice of the RF-phase ϕ also affects the charge Q of the emitted electron beam. Indeed, the electric field value at the cathode is dependent on the value of ϕ (see Fig. 1.8). It implies therefore that the effective work function W_{eff} of the photocathode is also dependent on ϕ because of the Schottky effect (see Eq. 1.2). As a result the charge of the emitted beam, given by Eq. 1.3, depends on ϕ. The curve of Q as a function of ϕ is called the dephasing curve and is used to characterize the photocathode RF-guns. The impact of the Schottky effect on the dephasing curve can be very important, since Q can be more than doubled compared to the emitted charge Q_0 with no Schottky effect (see Fig. 1.8). The shape of the dephasing curve is also strongly affected, since the charge plateau visible with no Schottky effect gives way to a continuous increase in the emitted beam charge up to the RF-phase where the electric field on the cathode is maximal (see Fig. 1.8).

The dephasing curve can be used to quantify the importance of the Schottky effect in the electron emission. It is shown in Fig. 1.8 where experimental data, acquired on the PHIL facility with a Copper photocathode, are compared with several beam dynamics simulations performed with the ASTRA code [42]. The fitting of the experimental data with the dephasing curves coming from the ASTRA simulations shows that Q_0 is around 85 pC, while the maximum emitted beam charge is 210 pC. The Schottky effect is therefore responsible for 60% of the electron emission for this photocathode at maximum. The (negative) accelerating field on the photocathode, at the moment of the beam emission, as a function of ϕ is also depicted in Fig. 1.8.

One can remark in Fig. 1.8 that the RF-phase maximizing the beam energy, defined as 0°, is not at all the same as the one maximizing the beam charge. There is a difference of $-60°$, due to the fact that the emitted beam charge is maximal when the electric field on the cathode is maximal, while the maximum energy gain requires that the beam undergoes an accelerating field all along the first cell of the gun.

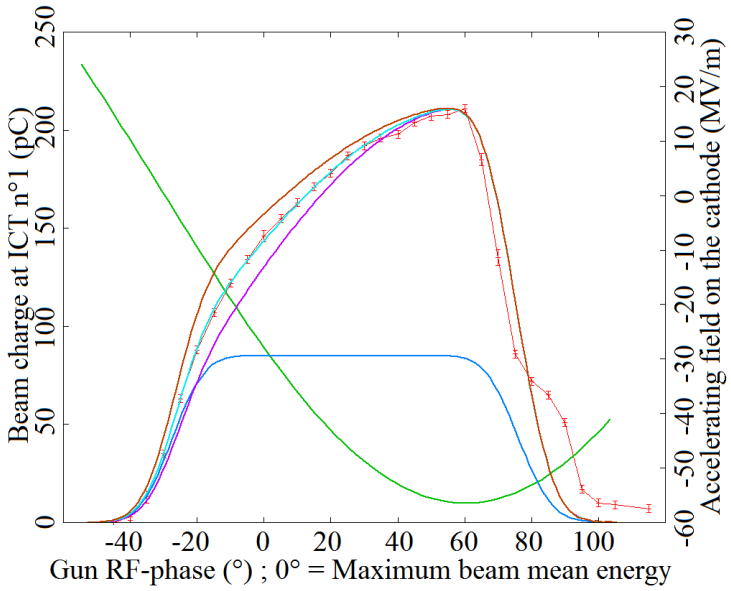

FIGURE *1.8 – Dephasing curve acquired on the PHIL facility, with a Copper photocathode, compared with some coming from ASTRA simulations. RF-gun peak accelerating field : 56.7 MV/m. Red curve : Experimental data ; Purple curve : ASTRA curve with $Q_0 = 60$ pC ; Cyan curve : ASTRA curve with $Q_0 = 85$ pC ; Brown curve : ASTRA curve with $Q_0 = 110$ pC ; Blue curve : ASTRA curve with no Schottky effect ; Green curve : Accelerating field on the photocathode at the moment of the beam emission.*

1.3 Beam diagnostics state of the art

Beam diagnostics is an essential ingredient of any kind of accelerator, since it is used to measure the properties and the behavior of the beam. These measurements have several goals. They are used to evaluate the characteristics of the beam delivered by the accelerator. They are also used to detect malfunctions of the accelerator, namely to detect the origin and location of these malfunctions, and they help to solve them. Finally, they can also be used to perform live modifications of some beam properties through a feedback system. In this kind of system, the beam measurement performed by the diagnostics is an input to another device which acts on the beam to modify its properties.

The measurement of beam properties requires to interact with the beam through different physical processes : interaction of the beam with external electric/magnetic field ; electromagnetic influence of the beam on the environment ; emission of photons as a result of interaction with matter (Cerenkov radiation, Transition radiation, Fluorescence radiation ...) ; energy loss through interaction with matter .... The diagnostics will be called destructive if it modifies significantly the beam properties during the measurement, and non-destructive if the beam properties are not or only slightly modified.

In this section, I will introduce the most common beam diagnostics, found on the low energy linear electron accelerator that I used during my thesis.

1.3.1 Beam charge diagnostics

1.3.1.1 Faraday Cup

A Faraday Cup is a beam stopper which is used to measure the electric charge contained in the beam. A schematic layout of a Faraday Cup and of its working principle is shown in Fig. 1.9.

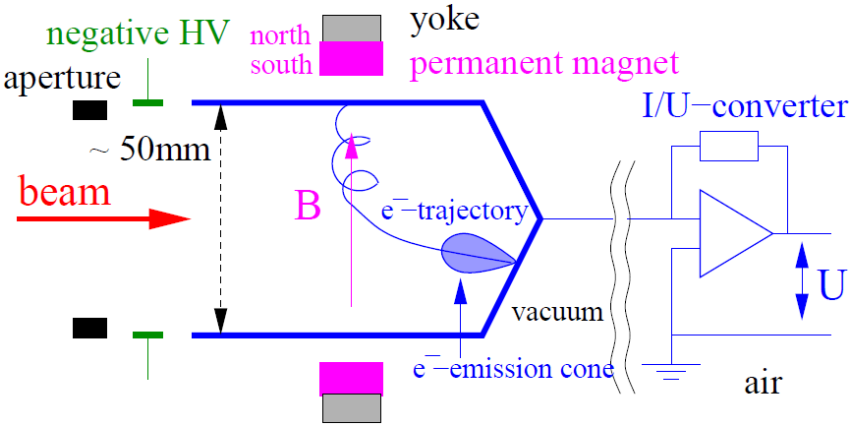

FIGURE *1.9 – Schematic layout and working principle of a Faraday Cup [43].*

It consists in an isolated metal cup which intercepts and stops all the electrons of the beam. It is therefore a destructive diagnostics. The generated current is linked to the

charge in the beam and is sent to a current sensitive pre-amplifier to which the cup is connected. This pre-amplifier is used to amplify the signal and also to convert it from current to voltage. The reading of the resulting voltage allows determining the beam charge.

Fig. 1.10 shows, as an example, the display on an oscilloscope of a signal produced by a Faraday Cup on the PHIL facility (see Fig. 1.24 in Sec. 1.4.1). The beam charge is deduced from this signal by computing the area under the curve.

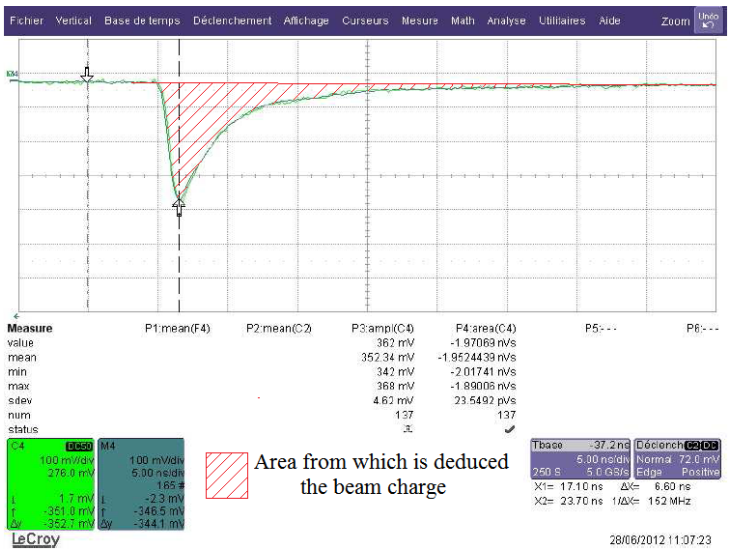

FIGURE *1.10 – Typical signal produced by a Faraday Cup on the PHIL facility (see Fig. 1.24 in Sec. 1.4.1).*

When the electron beam hits the wall of the Faraday Cup, secondary electrons are emitted from this wall. If these electrons manage to escape the insulated cup, the reading of the beam charge is wrong by the same amount. It is therefore necessary to ensure that the secondary electrons cannot leave the Faraday Cup and return to the wall. This can be achieved in three ways, whether or not combined. First, if the cup length in the beam propagation direction is much larger than the cup diameter, the number of escaping secondary electrons is geometrically very low. Secondly, a negative high-voltage can be applied close to the entrance of the Faraday Cup. If the voltage value is well above the mean energy of the secondary electrons, which is below 10 eV, they are pushed back to the cup surface. It is noteworthy that the high-voltage value is always far lower than the electron beam energy, implying that it is not affected. Finally, a magnetic field B perpendicular to the electron beam propagation direction created by permanent magnets can be used. In this field, the secondary electrons spiral around the magnetic field lines and are channeled towards the cup surface. The extension of this motion is approximately given by the classical cyclotron radius r_c :

$$r_c = \frac{\sqrt{2mE_{kin}}}{eB} = 3.37\frac{\sqrt{E_{kin}(eV)}}{B(mT)}(mm)$$

with m the electron mass and E_{kin} the secondary electron kinetic energy component perpendicular to the magnetic field lines. r_c has to be small compared to the mechanical dimensions of the Faraday Cup, to maximize the secondary electrons collection efficiency.

The use of Faraday Cups to measure the beam charge on linear electron accelerator encounters two main limitations. The first one is that the energy lost by the beam will heat up the material, which can lead to damages and degradations of its properties. A cooling system has therefore to be provided to evacuate this heat. The second one is that the penetration depth of the electron beam in the material should be much shorter than the mechanical dimension for a practical cup design, in order to completely stop the beam. When the beam energy becomes too high, typically higher than a few tens of MeV, the penetration depth becomes too large and the Faraday Cup is therefore not used anymore. For these two reasons the use of Faraday Cup is limited to the beginning of linear electron accelerators, namely within the first few accelerating modules.

1.3.1.2 Current transformers

The current transformers are a non-destructive diagnostics, which allows measuring the beam current through the detection of the magnetic field generated by the beam during its motion. A schematic layout of a current transformer and of its working principle is shown in Fig. 1.11.

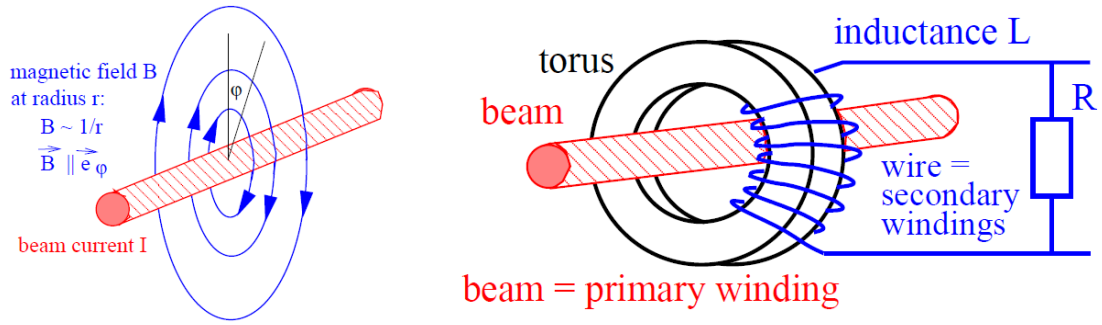

FIGURE *1.11 – Schematic layout and working principle of a current transformer [43].*

The beam is considered as the primary winding of the transformer, and passes through a torus with a high magnetic permeability μ. An insulated wire is wound around the torus with N_{sec} turns and is the secondary winding of the transformer. It has the inductance L given by :

$$L = \frac{\mu}{2\pi} l N_{sec}^2 \ln\left(\frac{r_o}{r_i}\right)$$

where l is the torus thickness in the beam propagation direction, r_i is the inner radius of the torus and r_o is its outer radius. The reason to choose the torus shape is to guide the beam magnetic field-lines, which are mainly along the azimuthal direction $\vec{e}_\phi$ as shown in Fig. 1.11. It allows maximizing the output signal, with a strength nearly independent on the beam transverse position inside the vacuum pipe.

For an ideal current transformer, loaded with a low value of ohmic resistor R (typically 50 Ω), the ratio between the primary current I_{beam}, namely the one of the beam, and the secondary current I_{sec} in the winding around the torus is given by :

$$I_{sec} = \frac{N_{prim}}{N_{sec}} I_{beam} \Rightarrow I_{sec} = \frac{1}{N_{sec}} I_{beam}$$

with $N_{prim} = 1$ since the beam passes only one time through the torus. In most practical cases, the measurement of the voltage U across the resistor R is performed leading to :

$$U = RI_{sec} = \frac{R}{N_{sec}} I_{beam} \tag{1.5}$$

A more realistic, but still simplified, representation of the equivalent circuit for the secondary transformer side is shown in Fig. 1.12, where the current is modeled by a current source delivering $I_{sec}(t)$. Some stray capacitances, modeled by C_s, have also to be taken into account. They come from the capacitance between the windings, between the torus and the windings and along the shielded cable to the resistor R. The voltage $U(t)$ is given by $ZI_{sec}(t)$, where the impedance Z for the three elements in parallel is given by :

$$\frac{1}{Z} = \frac{1}{i\omega L} + \frac{1}{R} + i\omega C_s \Rightarrow Z = \frac{i\omega L}{1 + i\omega \frac{L}{R} + \omega \frac{L}{R} \omega R C_s} \tag{1.6}$$

with i the complex number such that $i^2 = -1$ and ω the excitation frequency of the circuit. A typical value for ω is given by $\omega = \frac{2\pi}{T}$, where T is the duration of the beam.

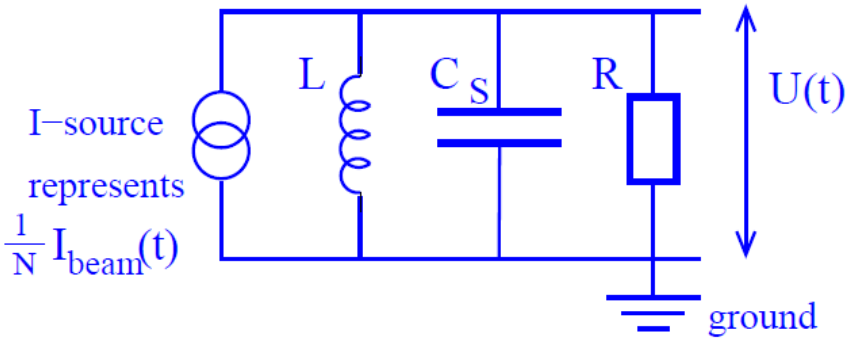

FIGURE *1.12 – Simplified equivalent circuit for the secondary transformer side [43].*

Eq. 1.6 points to the existence of three regions of excitation frequency ω. The low frequency region, for $\omega << \omega_{low} = \frac{R}{L}$, in which $Z \approx i\omega L$. In this region, the inductance L acts as a short circuit and I_{sec} mainly flows through it. The high frequency region, for $\omega >> \omega_{high} = \frac{1}{RC_s}$, in which $Z \approx \frac{1}{i\omega C_s}$. In this region, I_{sec} mainly flows through the capacitor. The intermediate frequency region, for $\omega_{low} << \omega << \omega_{high}$, in which $Z \approx R$. In this region, the measured voltage U across the resistor R is significant. It is therefore the working region of the current transformer.

The time response of a current transformer is illustrated by Fig. 1.13. It is described by the rise time constant τ_{rise} and the droop time constant τ_{droop}, which are given by :

$$\tau_{droop} = \frac{1}{\omega_{low}} = \frac{L}{R} \qquad \text{and} \qquad \tau_{rise} = \frac{1}{\omega_{high}} = RC_s$$

If the beam time profile is rectangular, the signal amplitude increases in proportion to $\left(1 - e^{-t/\tau_{rise}}\right)$ and τ_{rise} corresponds to the time for an increase by $e^{-1} = 37\%$. τ_{droop} is the typical time for the signal droop observed in Fig. 1.13.

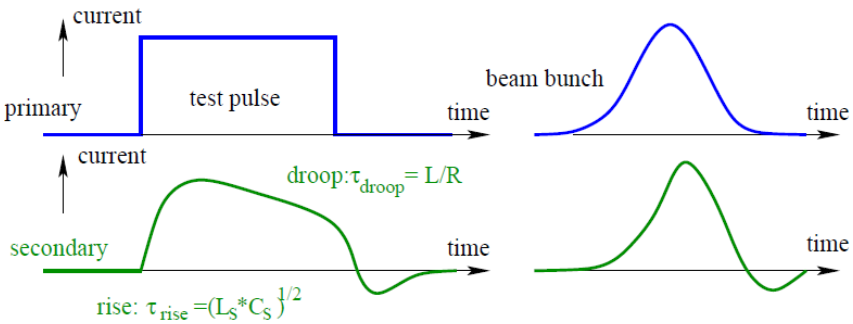

FIGURE *1.13 – Time response of a current transformer to a temporally rectangular beam and to a temporally Gaussian beam [43].*

There are three main requirements for the design of a current transformer, which imply constraints on its parameters. The first is that a large voltage U across the resistor R is needed to have a high sensitivity. It implies that the number of windings N_{sec} around the torus should remain small, since U scales like $1/N_{sec}$ according to Eq. 1.5. The second is to have a long droop time constant τ_{droop}, to minimize the decrease in the response of the transformer to the beam. It allows measuring long beams. The inductance L must therefore be large. It implies that N_{sec} should nevertheless not be too small, since L scales like N_{sec}^2, and that materials with high magnetic permeability μ have to be used for the torus, since L scales like μ. The third is to have a fast response, meaning that the rise time τ_{rise} has to be low. It implies that the stray capacitance C_s should be minimized, since $\tau_{rise} = RC_s$.

The last important point is that the electrical conductivity of the beam pipe has to be interrupted by an insulator insertion close to the current transformer, as shown in Fig. 1.14. Otherwise, the image current generated by the beam in the beam pipe would flow inside of the torus, resulting in a zero current by addition with the beam current. A high permeability metallic housing is used to bypass the image current outside the torus and to shield the current transformer against the external magnetic fields.

Fig. 1.15 shows, as an example, the display on an oscilloscope (green curve) of a signal produced by an ICT (Integrated Current Transformer) on the PHIL facility (see Fig. 1.24 in Sec. 1.4.1). The beam charge is then deduced by computing the voltage difference between the bottom and the top of the signal.

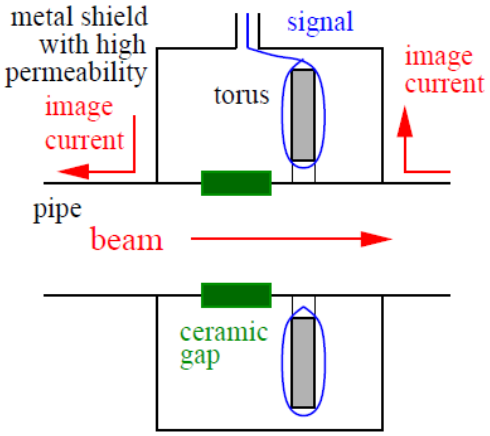

FIGURE 1.14 – *Scheme of a typical current transformer housing [43].*

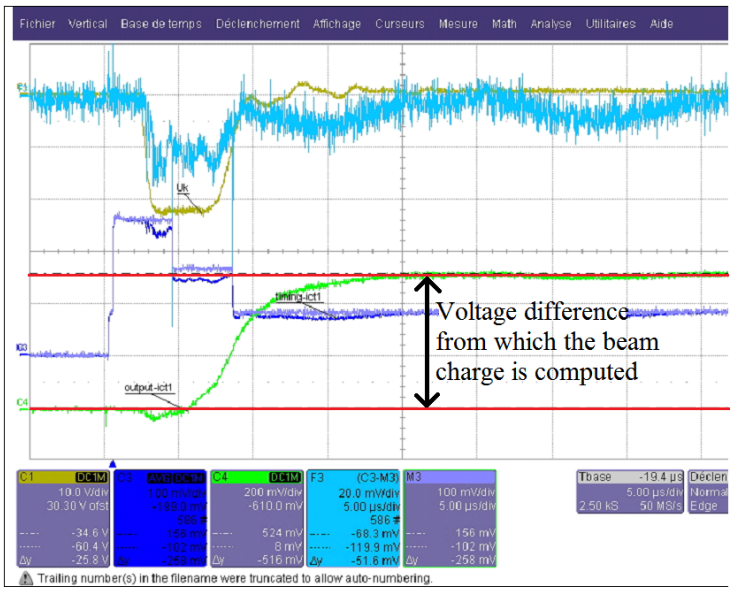

FIGURE 1.15 – *Typical signal (green curve) produced by an ICT on the PHIL facility (see Fig. 1.24 in Sec. 1.4.1).*

1.3.2 Transverse beam profile diagnostics

1.3.2.1 Scintillating screens

At low energy, the most used diagnostics to perform measurements of the transverse beam profile is a scintillating screen monitored by a video or CCD camera. The fluorescence light emitted by the scintillator, following the interaction with the beam, is sent to the camera through an optical line, thus giving an image of the projected transverse beam profile. I developed at the beginning of my thesis a code to analyze such images and extracted the beam transverse sizes from them. It is presented in Appendix C.

Fig. 1.16 shows a schematic representation of the two typical setups generally encountered for these devices on the low energy electron accelerators. The first one has a screen oriented at 45° with respect to the beam trajectory, implying a direct observation of the light emitted by the screen. In the second one, the screen is perpendicular to the beam trajectory and the light is sent to the camera by a reflective mirror. The second scheme is preferentially used when the scintillation screen is made of a transparent material. The reason is that some of the fluorescence light, which is emitted in all the directions, will undergo a reflection on the exit face of the scintillator and exits it by the entry face. In the first scheme, this reflected light is recorded by the camera and results in a double image of the beam, as shown in Fig. 1.17, which disturbs the analysis of the beam transverse profile. On the opposite, in the second scheme, this reflected light is not recorded by the camera and therefore does not pollute the measured beam transverse profile.

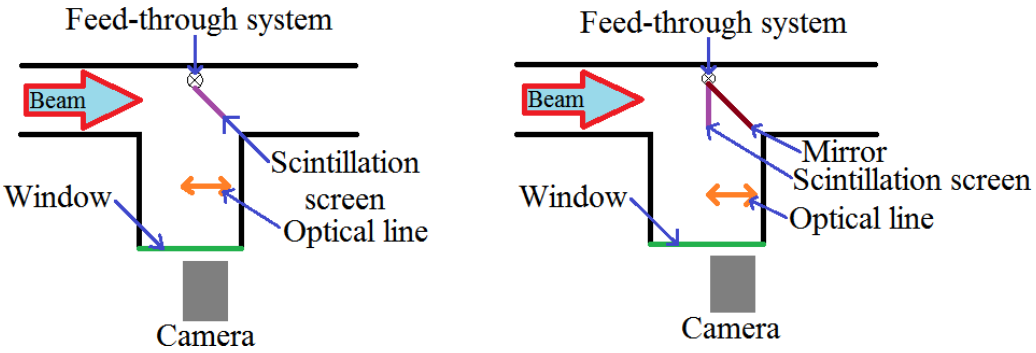

FIGURE *1.16 – The two typical setups for beam transverse profile measurements using a scintillating screen.*

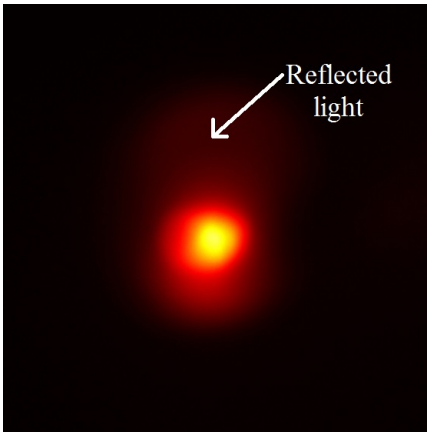

FIGURE *1.17 – Beam transverse profile measured with the YAG1 screen of PHIL (see Sec. 1.4.1).*

Several properties are required for the scintillators used to perform beam transverse profile measurements. The first one is to have a good radiation hardness, to prevent damages. For this reason inorganic scintillators are used instead of organic scintillators.

They must also have good mechanical properties for producing large screens (typically up to several centimeters of diameter). They have to deliver a high light output in the wavelength range in which the camera has the highest sensitivity, typically between 400 nm and 800 nm. The dynamic range of the scintillator should be as high as possible, namely the linearity between the incident beam charge and the light output has to be effective for the highest possible beam charge. The reason is that the saturation of the light emission, occurring for too high incident beam charge, leads to deformation of the beam transverse profile. For example, a saturation has been observed from 20 pC/mm^2 for LANEX screens [44] while it appears only above 1 nC/mm^2 for the YAG screens [45]. The scintillator should not absorb the light it emits, otherwise stray light will be emitted leading to a distortion of the beam transverse profile. Finally, the decay time of the scintillator has to be fast, to enable measurements at a high repetition rate for monitoring the transverse beam size variations. Tab. 1.1 shows the properties of some scintillators currently used for beam transverse profile measurements.

Name	Chemical formula	Density (g/cm^3)	Hardness (Mho)	Maximum emission (nm)	Decay time (ns)	Light output (% of NaI:Tl)
NaI:Tl	NaI (doped with Tl)	3,67	2	415	230	100
YAG:Ce	$Y_3Al_5O_{12}$ (doped with Ce)	4,57	8,5	550	70	40
BGO	$Bi_4(GeO_4)_3$	7,13	5	480	300	20
CaF:Eu	CaF_2 (doped with Eu)	3,18	4	435	940	50

TABLE *1.1 – Some properties of common scintillation screens used for beam transverse profile measurements [46].*

YAG screens are often used, as on the PHIL facility (see Sec.1.4.1), because of their high radiation hardness, fast decay time, high saturation threshold and because of their wavelength of maximum emission (550 nm) which is close to the wavelength of maximum sensitivity of the standard CCD cameras (see Fig. 2.45 for example).

A general drawback of the scintillator screens is that they intercept the beam. The screen is in most cases so thick (> 1 mm) that it implies strong degradations of the beam properties, which practically lead to the destruction of the beam. This is particularly true on a low energy electron linear accelerator such as the PHIL facility, where the electron energies are of the order of a few MeV.

1.3.2.2 OTR screens

The beam transverse profile can also be determined from the light emitted when the beam crosses a thin metallic foil. This light has to be monitored by a CCD camera, as for a scintillating screen. It is called the Optical Transition Radiation (OTR), and it is emitted when a charged particle passes the boundary between two media of different dielectric permittivities. It results from the fact that the configuration of the beam electromagnetic field is different in the vacuum of the beam pipe and in the metallic foil. It implies that when the beam is approaching the foil, a time-dependent polarization appears at the foil boundary. The change of this polarization leads to the emission of radiation, which concentrates in two lobes centered around the directions forming an angle of $\frac{1}{\gamma}$ with the

beam trajectory (see Fig. 1.18 forward light), where $\gamma = \frac{1}{\sqrt{1-\frac{v^2}{c^2}}}$ is the Lorentz relativistic factor, v is the beam velocity and c is the speed of light in vacuum. Two lobes are also emitted perpendicularly to the beam trajectory, because the metallic foil surface acts as a mirror (see Fig. 1.18 backward light).

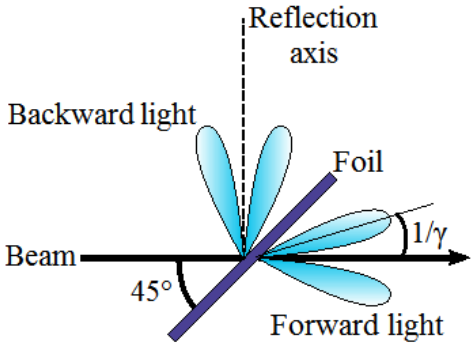

FIGURE *1.18 – Scheme of the Optical Transition Radiation emission [47].*

The energy dW radiated into a solid angle $d\Omega$ and per frequency interval $d\omega$ can be approximated by [43] :

$$\frac{d^2W}{d\Omega d\omega} = \frac{\mu_0 c e^2}{4\pi^3} \frac{\theta^2}{(\gamma^{-2} + \theta^2)^2}$$

where $\mu_0 = 4\pi 10^{-7}$ kg.m.A^{-2}.s^{-2} is the permeability of vacuum and θ is the angle of observation with respect to the beam trajectory. It shows by differentiation that the radiated energy is zero for $\theta = 0°$, increases up to two symmetrical maxima at $\theta = \pm\frac{1}{\gamma}$ and decreases for larger observation angles. It is also demonstrable by differentiation that the radiated energy is concentrated in a narrower region around $\theta = \pm\frac{1}{\gamma}$ when γ increases.

The observation of the OTR can be used to perform two types of measurements on the beam. First, if the focus of the CCD optics coincides with the OTR screen, the transverse profile of the beam is measured. Second, if the focus is set to infinity, the angular distribution of the photons can be measured, from which the beam angular distribution can be evaluated. By combining these two types of measurements, a measurement of the beam transverse emittance can be performed [48]. This is one of the OTR screen advantages with respect to the scintillating screens, which can only perform beam transverse profile measurements.

The OTR screen has other advantages. First, it is based on a classical electrodynamic process. It implies a strict linearity between the incident beam charge and the number of emitted photons, in contrast to the scintillating screens where a saturation appears for too high incident beam charge. Then, the photons are emitted only by the surface of the OTR screen and their number and distribution are independent of the metallic foil thickness. It implies that very thin metallic foil (< 1 μm) can be used, thus limiting the degradation of the beam properties when it passes through the OTR screen. Furthermore, the surface aspect of OTR emission leads to a more precise measurement of the beam transverse

profile. Indeed, the volume emission of fluorescence light in the scintillating screens and the transparency of a majority of them lead to an enlargement of the measured beam transverse profile with respect to the real one. This is called the "size-blurring" effect and has been for example studied at the ALBA Linac [45].

But the OTR screen has some drawbacks. The most important is that, for the same incident beam charge, the light produced by an OTR screen is orders of magnitude lower than for a scintillating screen. It implies that the OTR screens can only be used with heavy-charged beam, or that advanced and expensive techniques of image amplification have to be used. The other major drawback is that the OTR screens can practically only be used on high energy accelerators ($>$ 100 MeV for the electrons and $>$ 20 GeV for the protons). The reason is that at lower energy the photon angular distribution becomes too wide, implying that too few photons are collected by the optics and transported to the CCD camera, to perform a precise transverse beam profile measurement.

1.3.2.3 Other devices

The transverse beam profile can also be measured using devices such as secondary electron emission (SEM) grids, wire scanners and semiconductor detectors (like diamond detectors). Fig. 1.19 shows an example of a SEM grid device, Fig. 1.20 shows an example of a wire scanner device.

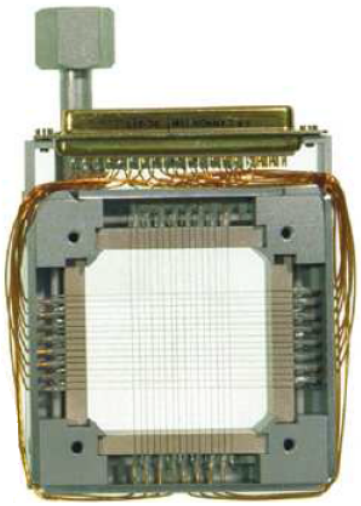

FIGURE *1.19 – Example of a SEM grid device [43].*

The basic physical principle of the SEM grid is that, when the beam crosses a wire or a flat ribbon, secondary electrons are generated and escape from the surface of the material. It generates an electrical current in the wire, which is directly proportional to the number of escaping secondary electrons, which is itself directly proportional to the number of beam particles impacting the wire. This current is then collected and converted into a voltage by a current-to-voltage amplifier. In a SEM grid, several wires (ten or so), having each their individual readout electronics, are located side by side in the horizontal

and vertical directions, thus interacting with the beam at different transverse positions. It allows then determining the beam horizontal and vertical profiles by combining the data coming from all the wires.

The wires are often made of Tungsten or Tungsten-Rhenium alloys, which are used for their excellent refractory properties. This is important, because no cooling can be applied on a SEM grid because of the geometry. The diameter of the wires varies between 0.01 mm and 0.5 mm and their spacing between 0.5 mm and 2 mm typically.

A wire scanner works on the same principle as a SEM grid. The difference is that only one wire, or one wire in horizontal direction and one wire in vertical direction, is used and swept through the beam to measure its transverse profile.

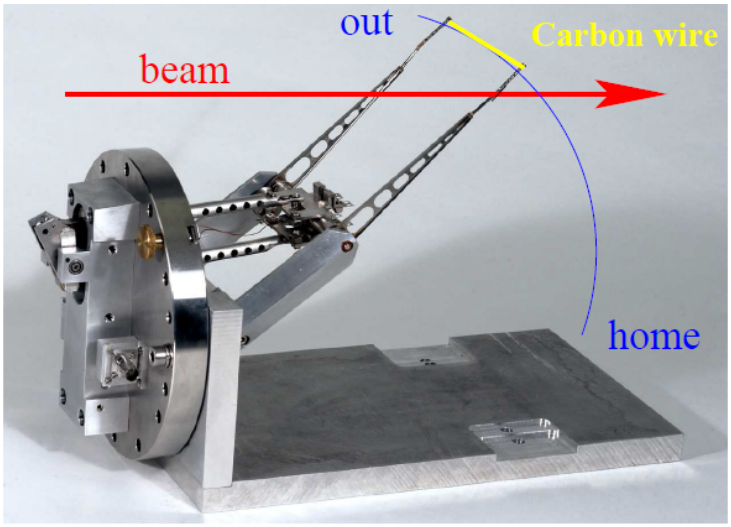

FIGURE *1.20 – Example of a wire scanner device [43].*

The first advantage compared to the SEM grid is that only one or two reading electronics channels are used instead of a few tens, thus lowering the costs and the complexity of the device. The other advantage is that the resolution is not limited by the wire spacing, as it is the case for a SEM grid, but only by the wire diameter which can be down to 4 μm [49] and is similar to the resolution of a scintillating screen. It is therefore often preferred to the SEM grids in electron accelerators, where sub-mm transverse beam size are often encountered. The SEM grid is no more suitable in this range, since the spacing between the wires cannot be much lower than 0.5 mm to avoid interactions between the wires.

As a drawback, due to the fact that a single wire is scanned through the beam, the beam transverse profile is not determined on a single beam but on several successive beams, each contributing for different transverse positions. As a result, only time-averaged beam transverse profile can be measured with a wire scanner. On the opposite, the SEM grids and scintillating screens allow monitoring beam by beam fluctuations of the transverse profile. Besides, the wire scanner motion has to be exactly synchronized with the crossings of the beams to perform the measurement, which induces technological complexities.

Compared with the scintillating screens, the SEM grids and wire scanners have the advantage of providing a larger dynamic range. The secondary electron emission, on which is based the measurement with the SEM grids and wire scanners, is a surface phenomenon. It allows putting very thin wires (down to 10μm) into the beam path without penalizing the strength of the signal. As a result, the degradation of the beam properties remains quite low and these diagnostics can be considered as nearly non-destructive. This is not the case for the scintillating screens which are much thicker (see Sec. 1.3.2.1). But the scintillating screens allow measuring the entire 2D beam transverse profile, while the SEM grids and wire scanners allows measuring only the projections of this profile along the horizontal and vertical directions.

In a semiconductor detector, like a diamond detector for example, electron-hole pairs are generated when a particle beam passes through, because of the ionization processes. The application of a bias voltage to metallic electrodes on the surfaces of the semiconductor generates an electric field in the bulk of the semiconductor. This electric field allows collecting the created electrons and holes to opposite electrodes, thus creating a current which is recorded and treated by a readout electronics to generate a signal. The strength of the generated signal is then used to determine the number of incident beam particles. For beam transverse profile measurement purpose, a thin strip of semiconductor, which can be down to 100 μm width, is used and swept through the beam, similarly to a wire scanner, to perform the measurement. For example, Shan Liu from LAL used diamond detectors to perform such measurements within the context of her thesis on PHIL and ATF2 [50].

Semiconductor detectors have the advantages to provide a wide dynamic range and to be able to detect a very low number of particles. For example, the range of measurement for a diamond detector goes to theoretically one electron up to 10^9 electrons thanks to the use of various electronic amplifiers and attenuators [50, 51]. It is therefore perfectly suitable to perform a precise measurement of the beam halo, which typically contains a thousand times less charge than the beam core. This has been done for example in the thesis of Shan Liu on ATF2 [50].

1.3.3 Beam transverse emittance measurement

1.3.3.1 Definition of the beam transverse emittance

The transverse phase-space of the beam is defined by the position of all its particles in the planes (x, x') and (y, y'). x and y are respectively the horizontal and vertical coordinates of the particles in the plane transverse to the motion of the beam, which is longitudinal. The origin of this plane is very often defined such that $< x >= 0$ and $< y >= 0$, where $<>$ denotes the average taken on all the beam particles. x' and y' are respectively the horizontal and vertical divergences of the particles with respect to the beam trajectory. The origin of this plane is also very often defined such that $< x' >= 0$ and $< y' >= 0$. The transverse dynamics of the particles is then studied with respect to a virtual particle, called the reference particle, which has $x = y = 0$ and $x' = y' = 0$ at all times and defines the beam trajectory.

The beam transverse horizontal and vertical rms emittance ϵ_x and ϵ_y are then mathematically defined by :

$$\begin{cases} \epsilon_x = \sqrt{< x^2 >< x'^2 > - < xx' >^2} \\ \epsilon_y = \sqrt{< y^2 >< y'^2 > - < yy' >^2} \end{cases} \tag{1.7}$$

The emittances are expressed in the unit of π.mm.mrad. Geometrically speaking, ϵ_x (respectively ϵ_y) represents the area covered by a certain fraction of the beam particles in the (x, x') plane (respectively (y, y') plane). For example, for a beam having Gaussian particle distributions both in terms of position and divergence, the rms transverse emittance corresponds to an area containing 39% of the particles.

The expressions given by Eq. 1.7 are called the geometrical emittances of the beam. These quantities are naturally decreasing when the beam is accelerated. The reason is that the beam divergences, which are defined as the ratios between the transverse particles velocities and the longitudinal one, are strongly decreasing because the acceleration is almost totally performed in the longitudinal direction. To obtain emittances which are invariant under beam acceleration, the geometrical emittances have to be multiplied by $\beta\gamma$, where $\gamma = \frac{1}{\sqrt{1-\beta^2}}$ is the relativistic Lorentz factor and $\beta = \frac{v}{c}$ is the normalized beam velocity (v is the longitudinal beam velocity). These are then called the normalized emittances. They are constant as long as the beam dynamics is linear, but can increase under the action of non linear forces such as the space charge forces. In the remainder of this manuscript, the term emittance will always refer to the normalized one unless otherwise specified.

The physical meaning of the transverse emittance is to reflect the quality of the beam, which becomes better when the transverse emittance decreases. More precisely, the transverse emittance reflects the easiness to transport and to transversely focus the beam. The smaller the transverse emittance is, the smaller the beam can be transversely focused and the slower the increase of beam size is after passing the focusing point. It is also a crucial parameter in the definition of the brightness of an electron beam [34]. It is therefore a key beam property to measure.

1.3.3.2 The moving slit method

One method to measure the beam transverse emittance is to use a movable slit together with a beam transverse profile measurement device (see Sec. 1.3.2). The slit has a very thin aperture d_{slit} (which can be down to 10 μm [52]) along the direction in which it can be moved, for instance the horizontal direction x in the following. In the perpendicular direction, the vertical one y in the following, the slit is very wide in order to fully transmit the beam to get a large and exploitable signal. Fig. 1.21 shows a schematic layout of a moving slit device.

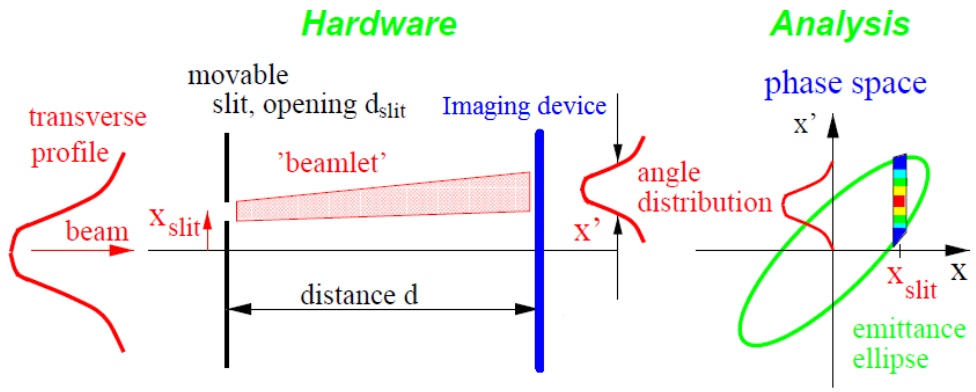

FIGURE 1.21 – *Schematic layout of a moving slit device for the measurement of the beam transverse emittance [43].*

Let x_{slit} be the horizontal position of the slit, x_{meas} be the horizontal position of a beam particle on the imaging device placed after the slit and d be the longitudinal distance between the slit and the imaging device. The divergence x' of a particle passing the slit is then determined as :

$$x' \approx \tan(x') = \frac{x_{meas} - x_{slit}}{d}$$

where the approximation $x' \approx \tan(x')$ is justified by the fact that the divergence is always small. By measuring, with the imaging device, the horizontal distribution of the particle passing the slit, it is therefore possible to get the distribution of the particle divergence at the level of the slit and for the horizontal position x_{slit}. By performing this measurement for several horizontal positions x_{slit} of the slit, the beam horizontal transverse phase-space (x, x') is reconstructed at the level of the slit. From the obtained phase-space, the beam transverse horizontal rms emittance ϵ_x can then be determined using Eq. 1.7. A similar measurement has to be performed with a slit moving in the vertical direction to measure ϵ_y.

The resolution of the moving slit method is limited for the horizontal coordinate x by the slit aperture, such as $\Delta x = d_{slit}$. For the horizontal divergence x' the resolution is limited by the slit aperture and by the resolution of the imaging device $\sigma_{imaging}$, such as $\Delta x' = \frac{d_{slit}+\sigma_{imaging}}{d}$. The measured transverse phase-space (x, x') is actually made of discrete elements with a size given by $\Delta x * \Delta x'$. This can induce large errors in the case of a tightly focused beam or of an almost parallel beam, namely with an almost zero divergence.

The distance d between the slit and the imaging device has to be carefully adjusted. In fact, it must not be too short, in order to have a good resolution on the measurement of the beam divergence. But, on the other hand, it must not be too large. The reason is that the impact of the space charge forces on the particles motion between the slit and the imaging device would become significant in this case, thus distorting the measurement of the beam divergence. A compromise has therefore to be found between these two requirements.

A limitation to the use of a moving slit device to measure the beam transverse emittance is that the beam particles which are not entering the slit have to be stopped to not disturb the measurement. It implies that the material in which the slit is drilled has to be sufficiently thick to stop them. But, when the energy of the incident beam increases the thickness of the material has also to increase to stop the particles. However, when the thickness of the material increases, the particles entering the slit have less and less probability to escape the slit, because they have a non zero divergence. This probability decreases as the electron enters the slit away from its center. As a result, the effective width of the slit becomes significantly smaller than the mechanical one implying an underestimation of the transverse emittance. Besides, the signal measured by the imaging device decreases when the thickness of the material increases. As a result, the moving slit device becomes unusable for too high energy of the incident beam ($>$ 100 MeV for an electron beam).

1.3.3.3 The pepper-pot method

The moving slit device presents the drawback, since the slit has to be scanned through the beam, that the emittance measurement performed is not a single-shot measurement. It means that several successive beams are necessary to perform the measurement, implying that only the average beam transverse emittance can be determined in this way. This may be insufficient if there are significant beam to beam fluctuations, as it is the case for the beams generated and accelerated by laser-plasma interaction.

To solve this difficulty, it is possible to use a single-shot device to measure the beam transverse emittance. This is called a pepper-pot device and a simplified layout of it is shown in Fig. 1.22.

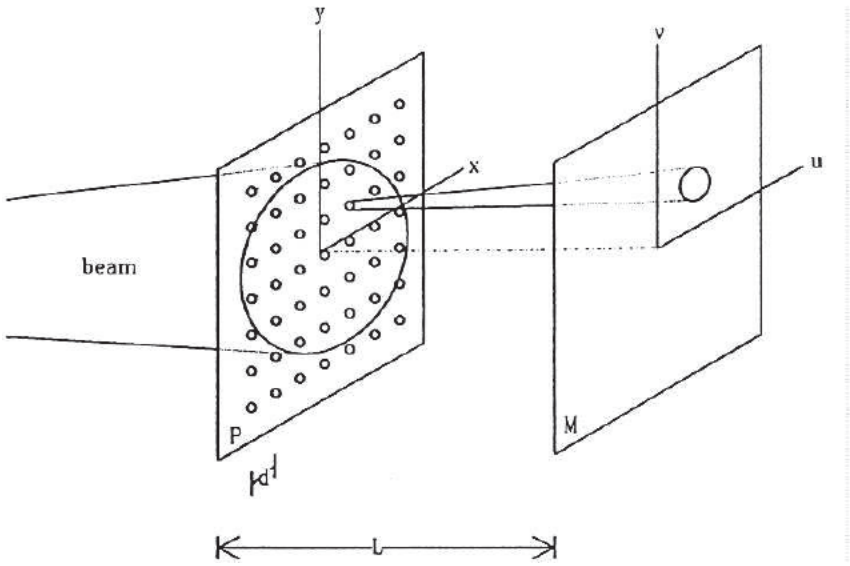

FIGURE *1.22 – Simplified layout of a pepper-pot device for the measurement of the beam transverse emittance [53].*

The pepper-pot device simply consists in the substitution of the moving slit previously presented by a square matrix of holes drilled in a plate. By this way, and following the same physical principles as for the moving slit method, the horizontal and vertical beam transverse emittances are determined simultaneously for one beam. The single-shot aspect of the pepper-pot device requires to precisely know the position of the plate. This can be done, for example, by illuminating the plate with a laser and recording the image generated by the imaging device, which will be then used as a calibration for the image generated by the particle beam.

Compared with the moving slit method, the pepper-pot has less resolution because of two facts. The first one is that, to have enough signal on the imaging device, the diameter of the holes drilled in the plate has to be larger than the aperture of the slit used in the moving slit method (because the slit transmits all the beam in the direction perpendicular to its thin aperture). A typical diameter is around 100 μm. The second one is that the spacing between the holes is generally much larger than the increment in the slit motion, which can be as small as the slit aperture. This quite high spacing is required to avoid the superposition of the beamlets coming from the different holes at the level of the imaging device and also to reduce at maximum the Coulomb interactions between the different beamlets. These two effects can indeed distort the beam transverse emittance measurement.

For the same reason as for the moving slit method, the pepper-pot method is limited to relatively low energy ($<$ 100 MeV for an electron beam). For higher energies, other methods like the 3-screen and 3-gradient method are generally used. These methods are described in detail in Sec. 2.2. I widely used these methods during my thesis, because of the absence of dedicated beam transverse emittance diagnostics on the PHIL facility (see Sec. 1.4.1 and Fig. 1.24). It is noteworthy that I used them to measure few MeV electron beams, which is not the standard and optimal case to apply these methods.

1.3.4 Measurement of the beam energy spectrum

The beam energy spectrum is the distribution of the particle of the beam as a function of their kinetic energies. It allows determining the beam mean energy, which is the average of this distribution, and the beam rms energy spread, which is the standard deviation of this distribution.

It is in most cases determined using the dispersive power of a dipole magnet. In fact, for a fixed magnetic field B, perpendicular to the beam trajectory, in the dipole magnet, the particles are more or less deviated according to their energies. This fact is depicted in the following relation, which defines the beam magnetic rigidity $B\rho$ (see Appendix A) :

$$B\rho = \frac{p}{q} = \frac{\sqrt{T(T + 2mc^2)}}{qc} \tag{1.8}$$

where ρ is the curvature radius of the particle path in the dipole magnet, which is a circle arc. p is the momentum of the particle, q is its electric charge, T is its kinetic energy and m is its mass. After the dipole magnet the particles are therefore distributed according to

their energies along one direction, called the dispersive direction, in the transverse plane. This is the horizontal direction if the magnetic field is vertical and the vertical direction if the magnetic field is horizontal.

Several methods can then be used to determine the beam energy spectrum. A first one is to place an imaging device (see Sec. 1.3.2) after the dipole magnet at its focal point. The beam transverse profile measured by this device along the dispersive direction is then translated into the beam energy spectrum. A second one is to set after the dipole magnet, at its focal point, a slit having a thin aperture along the dispersive direction, and a charge measurement device (see Sec. 1.3.1) just after the slit. If the slit is fixed, the beam energy spectrum can be measured by varying the magnetic field B of the dipole, in order to vary the energy of the particles passing the slit, and measuring each time the charge passing the slit. If the magnetic field B is fixed, the beam energy spectrum can be measured by moving the slit along the dispersive direction, in order to vary the energy of the particles passing the slit, and measuring each time the charge passing the slit. This last method is presented in detail for its application on the HELIOS Linac at SOLEIL (see Sec. 1.4.3 and Sec. 2.3.2.4).

The method with an imaging device located after the dipole magnet has the advantage to provide the energy spectrum for a single beam, while several successive beams are required with the methods using a slit placed after the dipole magnet implying that only the average beam energy spectrum can be determined in this case. As a drawback, the imaging device has to be sufficiently wide to measure all the beam transverse profile along the dispersive direction, which is not always possible.

1.3.5 Bunch length measurement

In this part, I will only consider the short electron bunches. That is to say the electron bunches for which the rms length is too short to be measured with classical electronic devices like pick-ups or wall current monitors [43]. The threshold is then located at a few tens of ps rms.

1.3.5.1 Methods using light emission

A first type of method to measure the length of a short electron bunch is to use the light emitted by the bunch under specific conditions. If the emission process is fast enough, namely much faster than the bunch length, the time profile of the emitted light pulse will then reproduce the one of the electron bunch. A measurement of the time profile of the emitted light pulse with a streak camera (see Sec. 2.3.3.1) allows finally a determination of the electron bunch time profile. The resolution of the measurement is limited, but not necessarily defined, by the time resolution of the streak camera which is around 1 ps for the standard cameras but can be down to 200 fs for the best ones in the visible wavelengths [54].

As an example, the synchrotron radiation emitted by an electron bunch when its trajectory is curved by a dipole magnet can be used to perform this kind of measurement.

It is often used on the synchrotron rings (like SOLEIL) or on the transfer lines between a linear injector and a synchrotron ring. The synchrotron radiation being a wide spectrum radiation, it has to be filtered (to obtained a width ≤ 10 nm) before being measured by the streak camera to avoid chromatic effects. This type of measurement has for example been performed at the SOLEIL synchrotron [55].

Another kind of radiation which can be used to perform the bunch length measurement is the OTR, already presented in Sec. 1.3.2.2 for beam transverse profile measurement purpose. It has for example been used at the SCSS (Spring-8 Compact SASE Source) test accelerator to measure a bunch length around 100 fs rms [56].

The Cerenkov radiation, emitted when the bunch travels through a dielectric medium with a velocity higher than the speed of light in this medium, can also be used to measure the bunch time profile with a streak camera. I perform this kind of measurement during my thesis on the PHIL facility (see Sec. 1.4.1). The physical principles, the experimental layout, the limitations as well as the obtained results are presented in detail in Sec. 2.3.3.

1.3.5.2 Transverse deflecting cavity

A second type of method to measure the length of a short electron bunch is to use an RF structure in which a transverse electric field is resonating. This kind of structure is called a Transverse Deflecting Cavity (TDC). This transverse electric field induces a transverse deflection of the bunch which corresponds to a rotation of the bunch between the transverse and longitudinal directions, as shown in Fig. 1.23. This rotation transfers therefore a part of the bunch time profile towards the transverse plane. A measurement of the bunch transverse profile, with an imaging device (see Sec. 1.3.2) located downstream of the TDC, with the TDC turned off and with the TDC turned on allows determining the rms bunch length σ_z thanks to the following formula [57] :

$$\sigma_z = \frac{\lambda}{2\pi} \frac{\sqrt{E_d E_s}}{|eV_0 \sin(\Delta\psi)\cos(\varphi)|} \sqrt{\frac{\left(\sigma_x^2 - \sigma_{x_0}^2\right)}{\beta_d \beta_s}} \tag{1.9}$$

where λ is the wavelength of the transverse electric field, E_d is the bunch energy at the TDC entrance, E_s is the bunch energy at the level of the imaging device, V_0 is the voltage of the field in the TDC and φ is the RF-phase of the TDC. $\varphi = 90°$ is the RF-phase where the field is maximum in the TDC. Usually, the bunch is injected close to $\varphi = 0°$ in the TDC, otherwise a global transverse deviation of the bunch appears in addition to the rotation [6]. $\Delta\psi$ is the betatron phase-advance between the TDC and the imaging device, β_d is the β-function at the TDC entrance and β_s is the β-function at the level of the imaging device. σ_{x_0} is the rms transverse bunch size when the TDC is turned off and σ_x is the rms transverse bunch size when the TDC is turned on.

One can see in Eq. 1.9 that, to have a good resolution on the bunch length measurement with a TDC, σ_x has to be much higher than σ_{x_0}. In other words, the TDC has

6. If the bunch is not centered on the axis of the TDC, a global transverse deviation of the bunch also appears in addition to the rotation

to sufficiently spread out transversely the bunch at the level of the imaging device, such that the rms transverse bunch size σ_{x_0} does not dominate the measurement. If L is the distance between the TDC and the imaging device, m_e is the electron mass and γ is the Lorentz relativistic factor, the time resolution Δt for the bunch length measurement with the TDC is given by [58] :

$$\Delta t = \sigma_{x_0} \frac{\gamma m_e c \lambda}{\pi e L V_0}$$

When the bunch travels into the TDC, its time profile is transfered towards a transverse direction, let's say the vertical one for instance. By using a dipole magnet, located after the TDC, to transfer the energy spectrum towards the horizontal transverse direction, it is possible to determine the longitudinal phase-space of the bunch by measuring the bunch transverse profile with an imaging device placed after the dipole magnet.

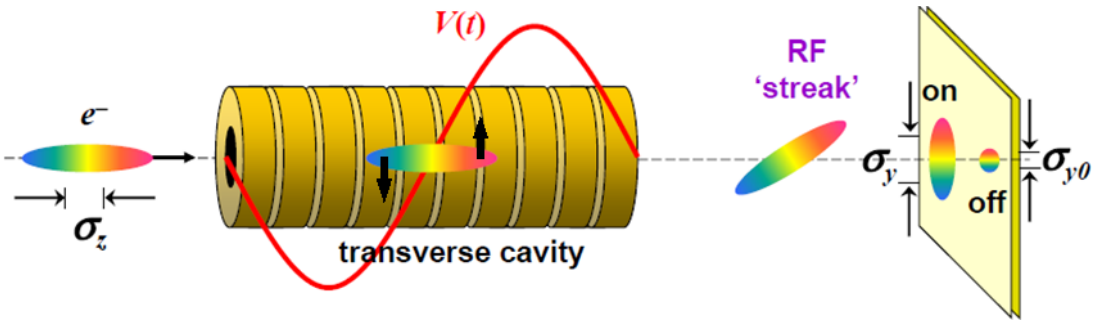

FIGURE *1.23 – Working principle of a transverse deflecting cavity (TDC) used for the bunch length measurement [43].*

The TDC has been already used to measure bunch lengths in the picosecond range. For example, an rms bunch length of 1.2 ps has been measured at SLAC [59]. Some studies are currently ongoing to allows bunch length measurement in the femtosecond range with a TDC. This is for example the case on the LCLS (Linac Coherent Light Source) at Stanford [60] and on the VELA facility at Daresbury [61].

1.3.5.3 The electro-optical sampling (EOS) method

Another type of method to measure the length of a short electron bunch is to use the birefringence induced by the bunch electric field in an electro-optical crystal, like the ZnTe for example.

When a relativistic electron bunch is passing close to an electro-optical crystal, its electric field induces in the crystal a birefringence phenomenon. Namely the crystal refractive index, which is isotropic with no electric field, becomes dependent on the direction of polarization of the incident light. Besides, the strength of this induced birefringence is proportional to the strength of the bunch electric field, that is to say to the bunch charge if all the other parameters are fixed.

To reconstruct the longitudinal profile of the bunch charge, namely the bunch time profile, it is possible to sample the birefringence induced in the crystal with a femtosecond laser pulse having initially a linear polarization. In fact, when passing through the birefringent crystal, the linear polarization of the laser pulse will be converted into an elliptical polarization. The characteristics of this elliptical polarization, which can be measured with optical devices [62], are a function of the crystal birefringence, therefore of the bunch electric field strength and therefore of the bunch charge.

To determine the bunch time profile, the relative delay between the arrival time of the laser pulse at the crystal and the one of the electron bunch has therefore to be varied by steps which can be down to a few tens of femtoseconds. This variation of the delay allows, by measuring the elliptical polarization of the laser pulse for many successive electron bunches, scanning over the bunch longitudinal charge profile and therefore reconstructing the bunch time profile. The determined length is therefore the average length of the electron bunches, and not the length of a single bunch.

The EOS method is a rather complex method, since it needs several advanced technological requirements to perform a precise measurement of the bunch length. A major one is that the laser pulse has to be much shorter than the electron bunch, to have a good resolution on the bunch time profile. Anyway, the resolution of the EOS method is improved when the duration of the laser pulse decreases. For these reasons, infrared laser pulses of a few tens of fs rms are used to perform the EOS method. Another crucial requirement is to have a very precise synchronization between the arrival time of the laser pulse and the one of the electron bunch at the level of the crystal, otherwise the determination of the bunch time profile will be distorted.

It is possible to perform the length measurement of a single electron bunch with an EOS method. This is done by using a chirped laser pulse, namely a laser pulse having a varying frequency along its time profile. By performing the analysis previously described for each frequency component of the laser pulse, the time profile of a single electron bunch can be reconstructed [63].

1.4 Facilities used to perform experiments and simulations

1.4.1 PHIL at LAL

PHIL accelerator is a 3 GHz RF-gun test bench located at LAL [64]. Its main objective is to test and characterize new RF-guns to obtain very bright electron bunches, in other words very dense and slightly divergent bunches. These bunches will be for example useful in the future plasma and laser/plasma accelerators which are currently under study or for future linear colliders. PHIL is also dedicated to the training of PhDs, young engineers and Doctors in accelerator physics and technologies and also in the driving of an accelerator. Finally, the PHIL electron beam is available for user experiments requiring an electron bunch around 5 MeV such as : Test and calibration of detectors ; sample irradiation ; parametric X-ray generation ....

A layout of PHIL, with the main elements and diagnostics composing it, is shown in Fig. 1.24.

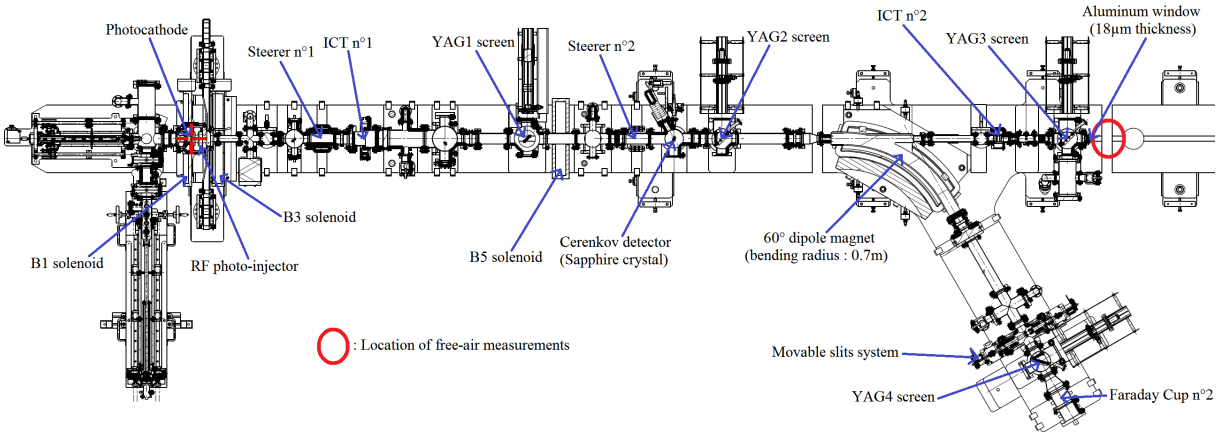

FIGURE *1.24 – Layout of the PHIL accelerator at LAL with the PHIN RF-gun.*

The electron bunch is generated and accelerated by the RF-gun (see Sec. 1.2). This RF-gun is driven by a 3D Gaussian laser pulse. PHIL is made of a straight beamline, going from the RF-gun to the Aluminum window 5.8 m away. It corresponds to the bunch path when the dipole magnet is turned off. When the dipole magnet is turned on, the bunch path corresponds to the deviated beamline. The pumps located all along the beamline allows creating the ultra-high vacuum required for PHIL operation. It corresponds to a static pressure, namely with no bunch in the accelerator, around 10^{-9} mbar.

The two ICT (Integrated Current Transformer) and the Faraday Cup $n°2$ are used to measure the bunch charge. The two steerer magnets are used to modify and correct the bunch trajectory and transverse misalignments, thanks to a transverse magnetic field. 3 solenoid magnets are inserted along the beamline : B1, B3 and B5. The B3 solenoid is located 14 cm after the photocathode, namely just at the RF-gun exit. The B5 solenoid is located 2.1 m after the photocathode, namely in the middle of the beamline. B3 can be

used either to transversely focus the electron bunch, to transport it without losses, or to optimize the bunch transverse emittance at the RF-gun exit by the emittance compensation process [65, 66]. The field values are not the same for these two uses. B5 is used only to transversely focus the electron bunch, to transport it without losses. The B1 solenoid is used to cancel the magnetic field on the photocathode, which is non-zero when B3 is activated, otherwise this non-zero magnetic field would induce an increase of the initial bunch transverse emittance.

The 3 YAG screens (YAG1, YAG2 and YAG3) of the direct beamline are used to produce images of the bunch in the transverse plane, to measure the bunch transverse sizes. The Sapphire crystal is used to produce Cerenkov light when the bunch goes through. This light is sent to a streak camera, to measure its duration which reproduces the electron bunch duration. The dipole magnet, whose entrance is located 3.91 m after the photocathode, allows measuring the bunch energy and energy spread thanks to YAG4 screen and slit system. Finally, an Aluminium window of 18 μm thickness is located at the end of the direct beamline. It allows the use of the bunch in free air (see red circle in Fig. 1.24) by letting the bunch passing through.

1.4.2 PITZ at DESY

PITZ [67] is a 1.3 GHz RF-gun test bench located at DESY (Zeuthen). It has for example conditioned and characterized several RF-guns for the FLASH [36] and XFEL [4] projects, and also reached a record value of 1 π.mm.mrad for the normalized rms transverse emittance of a 1 nC electron bunch. Fig. 1.25 shows a shortened layout of PITZ with the elements used in the measurements performed on this facility.

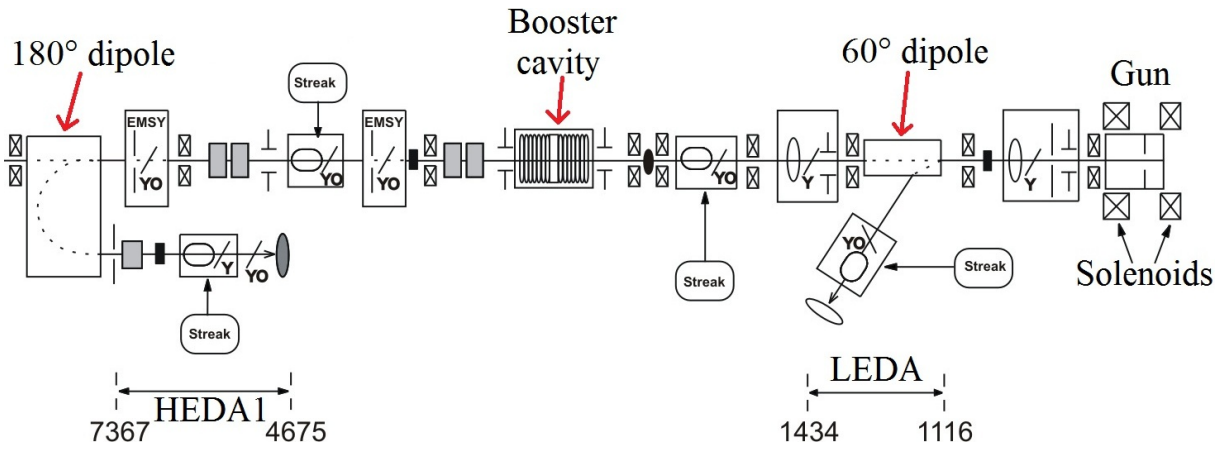

FIGURE *1.25 – Layout of the first part of the PITZ accelerator at DESY, Zeuthen [67].*

The gun is a 18.5 cm long 1.6 cells RF-gun. The maximal reachable peak accelerating field is around 62 MV/m, which corresponds to a beam mean kinetic energy of 6.25 MeV at the gun exit. This RF-gun is driven by a laser, whose time profile is adjustable with various possibilities between a short Gaussian pulse of 0.85 ps rms (= 2 ps FWHM) and a long flat-top pulse of 24 ps FWHM with 2 ps rise/fall time (σ_t = 6.8 ps rms). The

laser transverse profile is radial uniform with a radius adjustable via a mechanical beam shaping aperture (BSA) from 0.1 mm to 2 mm.

The 60° dipole magnet is used to measure the beam energy and energy spread in the LEDA (Low Energy Dispersive Arm) station located about 1 m after the RF-gun exit. A 1.7 m long booster cavity (CDS booster) is located about 3 m after the gun. The maximal reachable peak accelerating field of this booster is about 18 MV/m, which allows reaching a maximal mean beam energy around 22 MeV at its exit. Finally, the 180° dipole magnet is used to measure the beam energy and energy spread after the CDS booster in the HEDA1 (High Energy Dispersive Arm 1) station located about 5 m after the photocathode.

1.4.3 HELIOS Linac at SOLEIL

SOLEIL synchrotron (Source Optimisée de Lumière d'Energie Intermédiaire du LURE) is a third generation light source, allowing generating high-brightness photon beams (up to 10^{20} photon/s/mm^2/ mrad^2/0.1%bw at 2 keV) within a very broad spectral range (from the far-infrared (1 eV) to the hard X-rays (50 keV)). These photon beams are used for several applications, since their high brightness allows obtaining far more precise results than with a standard light source (like X-rays tube). One can mention as an example X-ray diffraction and scattering which are used to study the matter structure in a sample [68, 69, 70], or the IR, UV and X spectroscopies which give chemical informations on the studied sample [68, 71, 72, 73]. The photon beams are also used to characterize the detectors and devices used in X-ray imaging [74].

Fig. 1.26 shows a general layout of SOLEIL. The accelerating injection chain and the 30 light lines are depicted.

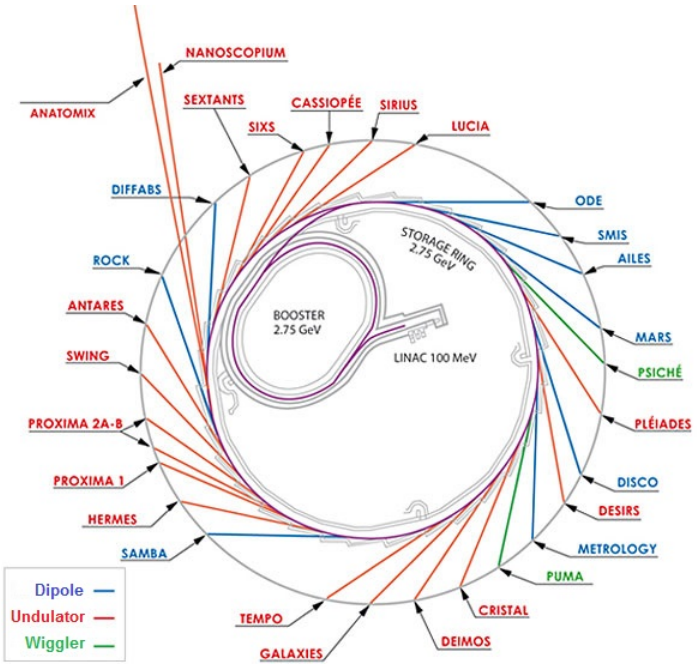

FIGURE *1.26 – Layout of SOLEIL at Saint-Aubin, France [75].*

The accelerating injection chain is made of 3 main parts. The electrons coming from the thermionic DC-gun are first bunched and accelerated up to around 100 MeV in the HELIOS (Hundred MeV Electron Linac Injector Of SOLEIL) Linac. These 100 MeV bunches are then injected in a 157 m circumference synchrotron ring (Booster), where they are accelerated up to their nominal energy of 2.75 GeV. The bunches are finally injected in the 354 m circumference storage ring where they turn and produce light for the lines via several magnetic structures (dipole magnets, undulators and wigglers). The electron bunches have a lifetime of around 15 h in the storage ring. The mean current is generally of 500 mA in the storage ring and it works in top-up mode, namely there is regular electron reinjection by the Linac-Booster system to keep almost constant the current in the storage ring. This allows a high stability for the emitted photon beams.

I performed experiments for my thesis only on the HELIOS Linac, which operates in S-band at a resonant frequency of 2998.30 MHz. A simplified layout of HELIOS is depicted in Fig. 1.27.

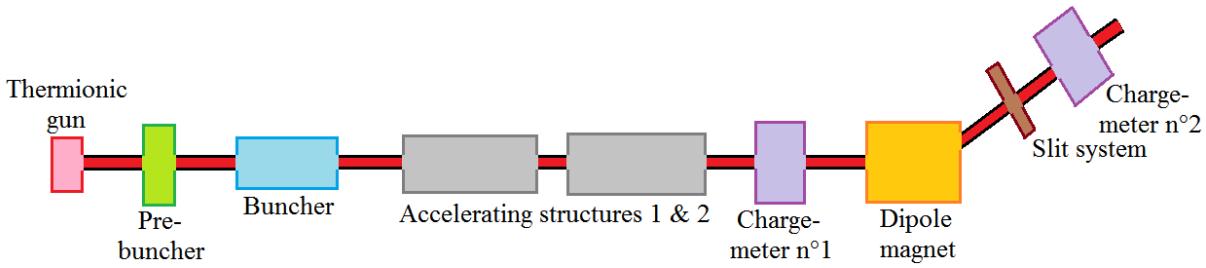

FIGURE *1.27 – Simplified layout of the HELIOS Linac at SOLEIL.*

The mode available to perform my experiments is the Short-Pulse Mode (SPM). In this mode the thermionic gun generates a square-pulse of electrons with 1.4 ns FWHM duration, a total charge adjustable up to 2.3 nC and an energy of 90 keV. This pulse is pre-bunched in the prebuncher, which is a single-cell standing wave cavity with a peak field of 0.75 MV/m. It is then bunched in the buncher, which is a 1 m long standing wave cavity with a peak field of 32.5 MV/m allowing an energy gain of 15 MeV. Four main bunches and one microbunch are obtained at the buncher exit. The bunches are then accelerated up to around 100 MeV by two 4.5 m long traveling wave accelerating structures working in the $TM_{010-\frac{2\pi}{3}}$ mode and allowing each an energy gain of 45 MeV. The two charge-meters (ICTs) are used to measure the beam charge, namely the total charge of the five bunches. The dipole magnet, slit system and charge-meter n°2 are used to measure the beam energy spectrum, from which the beam energy and energy spread are extracted.

1.4.4 SPARC at INFN

The SPARC (Sorgente Pulsata Auto-amplificata di Radiazione Coerente : Pulsed Self-amplified Source of Coherent Radiation) project is based at Frascati in Italy and is jointly driven by the INFN (Instituto Nazionale di Fisica Nucleare) and the ENEA

(Ente Nazionale per l'Energia Atomica) [76]. SPARC is intended to be a test bench for the SPARX proposal [77]. Its main goal is the development of a fourth-generation X-ray source coming from a FEL (Free Electron Laser) working in self-amplified regime (SASE FEL), meaning that the radiation amplified by interaction with the electron beam in the FEL is the radiation emitted by the beam itself in undulators placed on the beamline [78, 79].

The accelerator used in this project offers however the possibility to perform other types of experiments. In particular, a laser-plasma acceleration experiment, joint between LPGP (Laboratoire de Physique des Gaz et des Plasmas) at Orsay, LAL and INFN of Frascati was intended on SPARC. Fig. 1.28 shows a simplified layout of the SPARC photo-injector where the elements of interest for my study are depicted.

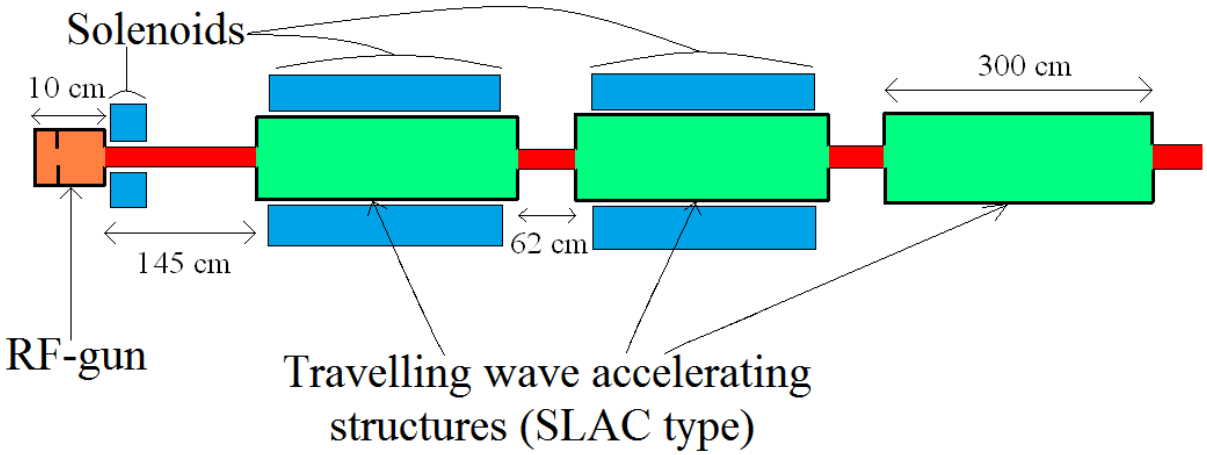

FIGURE *1.28 – Simplified layout of the SPARC photo-injector.*

The RF-gun used at SPARC is a 1.6 cells RF-gun operating in the $TM_{010-\pi}$ mode at a resonant frequency of 2856 MHz. The maximum peak accelerating field achievable on the axis of this gun is 130 MV/m, which corresponds to a maximum mean accelerating field of 53 MV/m along the gun axis [7]. It allows a maximum beam mean energy around 6 MeV at the gun exit. The laser pulse used to drive the gun has a wavelength of 266 nm and allows extracting 250 pC of charge from a Copper photocathode in typical operation, but it can be adjusted via the energy contained in the laser pulse.

The three traveling wave accelerating structures are 3 m long SLAC-type sections operating at a frequency of 2856 MHz. Pierced disks are periodically located in the cylindrical structure to slow down the wave and bring back its phase velocity close to c, which allows an optimal acceleration of the beam. Thus, a SPARC accelerating structure is divided into 86 cells with a length of 3.5 cm and a phase shift of $\psi = 120°$ between two adjacent cells. It is a $\frac{2\pi}{3}$ mode operation, meaning that the wave is periodic with a 3 cells period. The mean field in the first two sections can be set up to 21 MV/m, while it is limited to 13 MV/m in the third section. It allows a maximum mean beam energy

7. The mean field is defined as $\frac{1}{L}\int_0^L |E_0(z,\varphi)|\,\mathrm{d}z$, where L is the RF-gun length and $E_0(z,\varphi)$ is the maximum accelerating field as a function of z. It is a function of the time through the Gun RF-phase φ.

of 170 MeV at the exit of the third section. For technical reasons, the mean field has to be the same in the first two sections, while it can be adjusted independently in the third. In contrast, the RF-phases of the traveling waves can be controlled independently for the three sections.

Solenoid magnets are located at the RF-gun exit and around the first two accelerating sections to transversely focus the electron beam and to perform beam transverse emittance compensation. The coils constituting the SPARC's solenoids are arranged in a particular configuration, the "Holtzhelm" configuration. They are identical, traversed by currents of equal value but with opposite direction and separated by one magnetic length [8]. This allows greatly reducing the coupling between the two transverse directions, horizontal and vertical, generated by a single coil. In fact the coils traversed by opposite currents induce opposite transverse rotations of the electrons which almost compensate each other, without affecting the beam focusing which is independent on the current sign. The solenoid at the gun exit is made of four coils, with opposite currents between the first two and the two last. Fig. 1.29 (a) shows the associated magnetic field normalized profile on the accelerator Oz axis. The solenoids around the first two SLAC sections are each made of thirteen coils. There is one coil at the section entrance followed by four triplets between which the current is of alternating sign. Fig. 1.29 (b) shows the associated magnetic field normalized profile on the accelerator Oz axis.

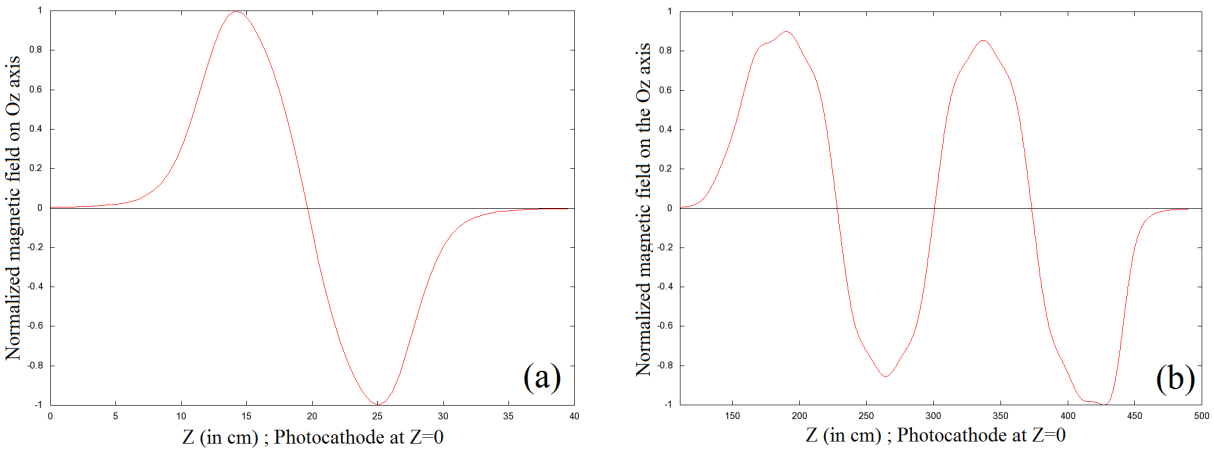

FIGURE *1.29 – Normalized magnetic field on the SPARC accelerator Oz axis ; (a) : Solenoid at the RF-gun exit (maximum current of 250 A → peak field of 0.4 T) , (b) : Solenoid around the first SLAC section (maximum current of 180 A → peak field of 0.3 T).*

The magnetic peak field generated by the solenoid magnet located at the RF-gun exit is of 0.28 T for an injected current of 185 A. The scaling law with respect to this value can be considered as linear, provided that the injected current is not too high compared to 185 A.

8. The magnetic length of a coil is defined by $L_m = \frac{1}{B_0}\int_{-\infty}^{+\infty} B_z(z)\,\mathrm{d}z$, where $B_z(z)$ is the longitudinal field on the coil axis and B_0 the peak value of this field

Chapitre 2

Diagnostics of short electron bunches

Contents

2.1 Low-charge bunch measurements 46
2.1.1 The experimental layout 46
2.1.2 Calibration of the scintillating screen 47
2.1.3 Influence of the transverse bunch size on the calibration 50
2.1.4 Bunch charge measurement as a function of the optical density 51
2.1.5 Comparison with the diamond detector 53
2.1.6 The case of the bunches with wide energy spectra 55
2.1.7 Conclusions 56
2.2 Transverse emittance measurements 58
2.2.1 The 3-screen method for bunch transverse emittance measurement 58
2.2.2 The 3-gradient method for bunch transverse emittance measurement 74
2.3 Longitudinal measurements 86
2.3.1 Measurement of the bunch kinetic energy thanks to a steerer magnet 86
2.3.2 Measurement of the bunch length thanks to the 3-phase method 95
2.3.3 Measurement of the bunch length thanks to a Cerenkov detector 110

This chapter describes the diagnostics developed during my PhD to measure the properties of a few MeV electron bunch generated by an RF-gun. The objective is to mainly use methods which are simple from both the theoretical and technological point of view.

2.1 Low-charge bunch measurements

The need to measure low charge, namely close to or below 1 pC, is particularly strong for the short electron bunches field. Indeed short bunches often contain a low charge to limit the space-charge force effects, which can deteriorate the bunch properties and particularly cause a lengthening of the bunch. For example, the REGAE (Relativistic Electron Gun for Atomic Exploration) facility at Hamburg is used to produce a low-energy (< 5 MeV) and low-charge (down to 10 fC) short (< 100 fs rms) electron bunch, to study the atomic dynamics at the femtosecond scale [9, 10].

Measuring electron bunches with a charge lower than 1 pC in an accelerator is quite challenging since the traditional diagnostics, like ICT (Integrated Current Transformer) or Faraday Cup, have a resolution limited to a few pC because of electronic noise. Special devices, like a cavity resonating at 1.3 GHz in the TM_{01} mode at the REGAE facility [10], can be used to measure lower bunch charges. A simpler and cheaper way to measure bunch charge below 1 pC would be to determine and then use the linear relation, existing before the saturation regime, between the incident charge on a scintillating screen and the light intensity emitted in response by this screen. This has for example been used at the REGAE facility, to measure a bunch charge as low as 10 fC with an ICCD [9].

Demonstration measures has been performed at LAL on the PHIL accelerator, for charges lower than 200 pC, with YAG and LANEX screens located close to an ICT or a Faraday Cup to enable their calibrations. Comparative measurements with a diamond detector installed on PHIL have also been carried out in collaboration with Shan Liu in the context of her thesis [50].

This powerful and simple measurement method could thereafter be used as a single-shot diagnostic for the bunch generated and accelerated by laser-plasma interaction. In fact, these bunches are non-reproducible from one shot to another and generally contain a low charge. This method will be for example employed in the framework of the DACTOMUS project. However there is an inevitable drawback using this method rather than ICT, which is the interception and destruction of the electron bunch.

2.1.1 The experimental layout

The PHIL accelerator is a 3 GHz RF-gun test bench located at LAL, Orsay, France. A layout of PHIL, with the main elements composing it, is shown in Fig. 1.24.

From the point of view of the measurements presented in this section, PHIL contains essentially 3 bunch charge diagnostics (ICT n°1, ICT n°2 and Faraday Cup n°2) and 4 bunch transverse imaging diagnostics (YAG1, YAG2, YAG3 and YAG4). It is therefore possible to perform our charge measurements on PHIL with the 3 following sets : "ICT n°1 + YAG1" ; "ICT n°2 + YAG3" ; "Faraday Cup n°2 + YAG4". However, none of these 3 sets allows doing measurements either with a LANEX screen or comparative measurements with those coming from a diamond detector since these 2 elements cannot currently be placed under-vacuum in the PHIL beamline, due to a too high outgassing rate which is not compatible with the use of a photocathode RF-gun.

To perform measurements with these elements we have therefore to place the experimental setup in free air, just after the 18 μm thickness Aluminum window located 5.8 m after the photocathode (see red circle in Fig. 1.24). Fig. 2.1 shows a scheme of the experimental setup located just after the exit window. It is possible to put a 2 mm diameter collimator on this window, to limit the transverse size and the charge of the extracted bunch. The measurements are performed thanks to a translator, moving in the horizontal plane perpendicularly with respect to the exit window, allowing us to successively put a movable Faraday Cup (Faraday Cup n°1), a LANEX or YAG screen and a diamond detector in front of the exit window, therefore in the electron bunch path. It is noteworthy that the ICT n°2 can also be used for these measurements since, considering the thickness of the Aluminium window (18 μm) and the bunch energy ($>$ 3 MeV) involved, there are almost no electron losses when the bunch goes through the window. It is also very close to the exit window (around 40 cm upstream), which prevents from losses due to the space-charge forces during the bunch transport, the bunch charge being moderate ($<$ 350 pC) in my measurements. The YAG screen (see Sec. 1.3.2.1) is a 100 μm thick screen produced by Crytur. It is made of a matrix of YAG crystal ($Y_3Al_5O_{12}$) doped with Cerium. The LANEX screen is produced by Kodak (Kodak LANEX Fine). It is constituted of two protective coatings of 10 and 5 μm thickness made of cellulose acetate ($(C_6H_{10}O_5)_n$), between which is placed a plastic substrate of 180 μm thickness made of mylar ($(C_{10}H_8O_2)_n$) on which is deposited the scintillating element (80 μm of Gd_2O_2S :Tb).

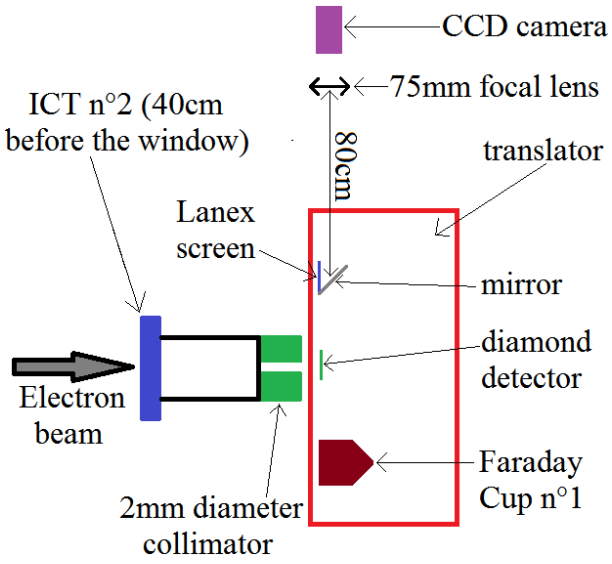

FIGURE *2.1 – Scheme of the experimental setup located just after the exit window*

2.1.2 Calibration of the scintillating screen

The method used to calibrate a scintillating screen for charge measurement purposes is simple. In fact it is sufficient to acquire, for several values of the bunch charge Q known thanks to an ICT or a Faraday Cup, images of the same bunch generated by the

scintillating screen and recorded by a CCD camera (MatrixVision BlueCougar S-123 [80]). We have then to determine the total intensity I collected by the CCD.

The determination of the total intensity I requires several steps of analysis. First of all, ten successive images of the bunch are recorded by the CCD camera, to later compute the statistical fluctuation of I. The second step is the subtraction of the dark current (see Sec. 1.2.4). To do that, ten images without the electron bunch, that is to say without laser pulse impacting the photocathode of the RF-gun, are taken in the same conditions as the images of the bunch. The mean of these ten images is computed and subtracted from each of the ten images of the bunch previously taken. The following step is the subtraction of the background noise from the resulting CCD signal. This noise is a mix between the thermal noise and the reading noise of the CCD camera. To subtract it, an area of interest not including the signal due to the bunch is selected on each of the ten bunch images corrected from the dark current. This area has to be chosen above or below the signal due to the bunch, and has an extension similar to the one of the signal due to the bunch along the horizontal direction. The reason is that, for the used CCD camera, the reading of the signal is performed horizontal line by horizontal line. The generated reading noise can therefore be varying along the horizontal direction. The previously mentioned way to select the area of interest for the noise subtraction allows taking this fact into account. The intensity of each pixel in this area is then summed and the sum divided by the number of pixels constituting it. It allows obtaining the mean noise intensity per pixel. Finally, an area of interest including the signal due to the bunch is selected on each of the ten bunch images subtracted from the dark current. The intensity of each pixel in this area is then summed and subtracted by the mean noise intensity per pixel multiplied by the number of pixels constituting the area. We thus obtain ten values of I, one for each of the ten bunch images. The final value of I is the mean of these ten values and the error bars on it is the standard deviation of these ten values. This analysis code is currently implemented on the PHIL facility.

This measurement has been performed for several values of the incident bunch charge. The incident bunch charge has each time been modified by changing, via the use of known optical densities, the energy of the laser pulse generating the electron bunch. All the other experimental conditions, especially the accelerating and focusing conditions, remained unchanged.

The $I(Q)$ curve then obtained is linear as long as we are not in the saturated regime of the scintillating screen fluorescence emission. This saturation appears only for surface charge densities impacting the screen higher than a few nC/mm^2 for a YAG screen [45], and above 100 pC/mm^2 for the Kodak Lanex Fine screen used at PHIL [44]. It is therefore not encountered for the low-charge bunches we want to measure. A linear fit performed on the $I(Q)$ curve can be then extrapolated and used to measure low charges by a simple determination of the light intensity collected by a CCD camera following the impact of an electron bunch on the scintillating screen.

As it will be shown later, the resolution in this case is far better than the ones of the ICTs and Faraday Cups. It is important to note that the calibration performed is valid only if the configuration of the imaging system remains strictly the same, otherwise

a new calibration law will be necessary. Strictly speaking, the calibration is valid only at a fixed gain X of the CCD camera. However, it is easily transposable to another gain Y. In fact, it is sufficient to take the same picture for both the gain X and the gain Y and to determine the intensity ratio between the two images. The calibration ratio will then be the same between the gain X and the gain Y. It allows simply performing bunch charge measurements with different gain of the CCD camera without redoing the entire calibration.

It is interesting to compare the results obtained with different types of scintillating screens. At PHIL, we have compared the measurements with the LANEX screen previously mentioned and with a YAG screen of 100 μm thickness. Fig. 2.2 shows the calibration measurements allowing the determination of the relative respective light yield of the LANEX screen and of the 100 μm thickness YAG screen. These measurements have been performed strictly in the same conditions (see Fig. 2.2).

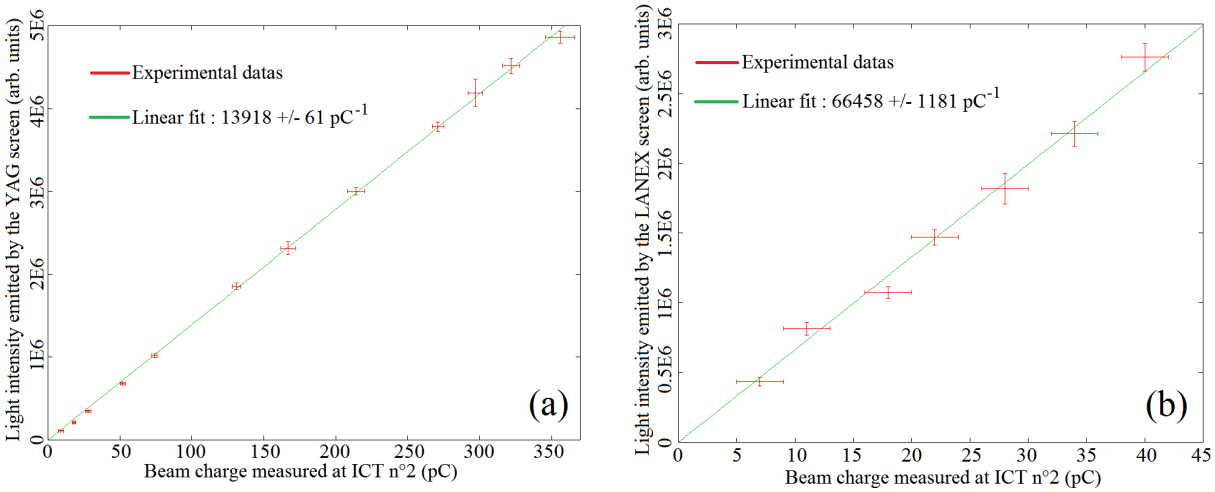

FIGURE *2.2 – Comparison of light yields between a LANEX screen (b) and a 100 μm thickness YAG screen (a). RF-gun peak accelerating field : 62 MV/m ; Gun RF-phase : maximizing the bunch energy ; Bunch energy : 3.55 MeV ; CCD gain = 10.*

Fig. 2.2 shows a very good linearity of the LANEX and YAG screens responses for incident charges between 7 pC and 350 pC. The linear fits obtained can therefore be used to perform lower charges measurements via the extraction, with the CCD camera, of the light intensity emitted by the scintillating screen. It is noteworthy that the uncertainty on the charge measured by this method will mainly come from the CCD signal fluctuations, which are typically around 10%, since the uncertainties on the linear fits of Fig. 2.2 are very small ($< 2\%$).

Fig. 2.2 shows also that the light yield of the LANEX screen mounted on PHIL is approximately 5 times higher than the one of a 100 μm thickness YAG screen. The fluorescence emission in a YAG screen being in volume, this can be compensated by using a 5 times thicker YAG screen. However, a thicker YAG screen will be less accurate for the bunch transverse sizes measurement. Indeed, it will introduce an increase of the apparent bunch transverse size growing with the YAG thickness. It is due to the fact that the

bunch will undergo a increasingly strong scattering at the YAG screen crossing, which will enlarge its apparent transverse size. The enlarging effects due to the emitted light reflections between the two YAG screen faces will also be amplified by an increase in its thickness. Then, the LANEX screen is more suitable than the YAG screen for low-charge bunch measurements due to its higher light yield. I will therefore use this screen to perform the measurements presented hereafter.

2.1.3 Influence of the transverse bunch size on the calibration

To study the influence of the transverse bunch size, the calibration of the LANEX screen has been performed in two different configurations allowing to obtain very different transverse bunch sizes. The first without collimator on the exit window, giving rms transverse sizes of $\sigma_x * \sigma_y = 1.65 * 2.02$ mm^2 on the LANEX screen, with charge measurement on the ICT n°2. The second with an Aluminum collimator of 2 mm diameter putted on the exit window, giving rms transverse sizes of $\sigma_x * \sigma_y = 0.85 * 0.95$ mm^2 on the LANEX screen, with charge measurement on the Faraday Cup n°1.

Fig. 2.3 shows the LANEX screen calibration obtained without collimator (a) and the LANEX screen calibration obtained with collimator (b). The incident charge on the LANEX screen has each time been modified by changing, via the use of known optical densities, the energy of the laser pulse generating the electron bunch.

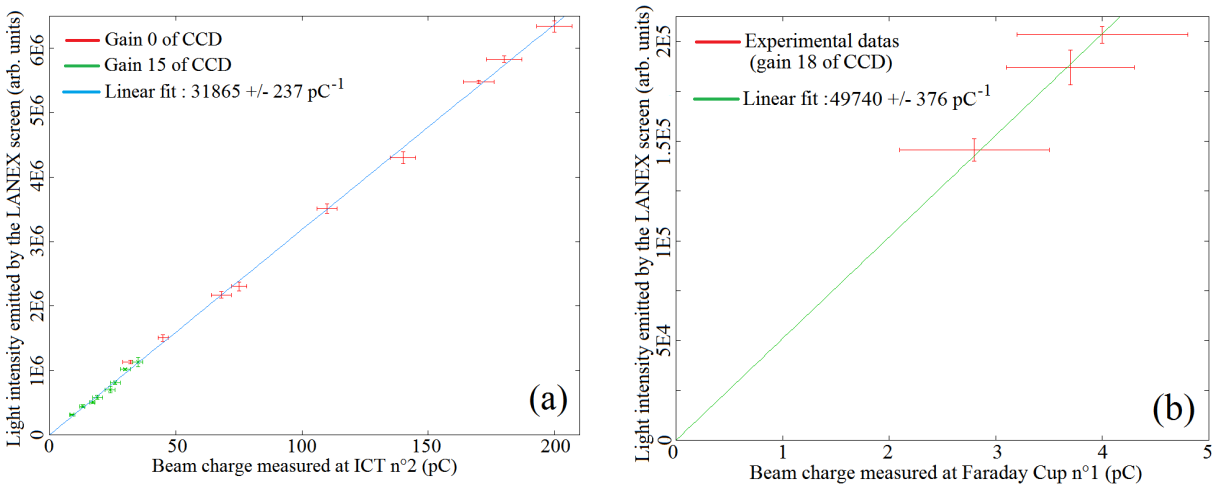

FIGURE *2.3 – Calibration of the LANEX screen without collimator (a) and with collimator (b). All the intensities are normalized to be bring back to the same scale as for the gain 0 of the CCD. RF-gun peak accelerating field : 62 MV/m ; Gun RF-phase : maximizing the bunch energy ; Bunch mean energy : 3.55 MeV.*

The important fact to notice in Fig. 2.3 is that the calibration factors are not the same in the configuration without collimator and in the configuration with collimator. There is indeed a gap of 35% in favor of the configuration with collimator. This is due to the fact that the transverse size of the electron bunch impacting the LANEX screen is not the same. It is indeed much bigger without collimator than with collimator. As a result, since

the fluorescence light is emitted isotropically, a smaller part of the light emitted by the LANEX screen is then collected by the lens and brought to the CCD camera. This explains the lower calibration factor subsequently observed. It is therefore important to note that the LANEX screen calibration, and consequently all subsequent charge measurement via this screen, will depend on the transverse size of the electron bunch impacting the screen. A way to limit this impact of the bunch transverse size is to have a large distance, much larger than the scintillating screen size, between the scintillating screen and the lens collecting the light [9]. However, this comes with a decrease of the intensity of the CCD camera signal and therefore an increase of the lowest measurable bunch charge. A compromise has therefore to be found concerning the distance between the scintillating screen and the lens collecting the light.

It should also be noted that the configuration with a collimator allows us measuring lower charge than the one without collimator. It is explained by the fact that the signal is more focused on the CCD and can therefore more easily be extracted from the noise. The configuration allowing one measuring the lowest possible charges with the setup of Fig. 2.1 will therefore be with the collimator on the exit window and the CCD gain fixed to its maximal value of 18. However this configuration cannot be used to measure charges higher than 5 pC, since the signal obtained on the CCD is then saturated at a gain of 18. As a result, only a small charge range could be used to calibrate the LANEX screen in this configuration before reaching the Faraday Cup n°1 resolution limit around 3 pC (see Fig. 2.3 (b)).

The signal is more diluted on the CCD in the configuration without collimator, allowing the acquisition of much more measurement points for charges up to 200 pC (see Fig. 2.3 (a)). It allows a far better check of the linearity of the LANEX screen response to the electron bunch. To measure higher charges a less sensible screen, like a 100 μm thickness YAG screen, can be used. Indeed, with such a YAG and a CCD gain fixed to 10, it is possible to measure charges higher than 350 pC (see Fig. 2.2 (a)) and therefore even higher for a CCD gain fixed to 0. This possibility is of no use here, because we want to use the previous calibrations to measure lower charges.

2.1.4 Bunch charge measurement as a function of the optical density

The first type of measurement I performed is the one of the bunch charge via a scintillating screen as a function of the optical density placed in the path of the laser pulse generating the electron bunch. The used optical densities are the NDUV ones fabricated by Thorlabs, which work in a spectral range between 200 nm and 1200 nm [81]. Knowing that an optical density x (in logarithmic units) mitigates the energy of the laser pulse by 10^{-x}, it is then possible via a fit by the function $a * 10^{-x}$ to determine the viability of the scintillating screen charge measurement.

It is important to note that this possibility is allowed by 2 factors. First of all we

9. In this way the source of fluorescence light is almost point-like whatever the bunch transverse size.

are not in the space-charge saturated regime for the photoemission in the RF-gun, which allows to have a linear variation of the charge of the generated bunch with the energy of the used laser pulse. If this had not been the case, the charge decrease should have not at all followed the one of the laser pulse energy. It is also necessary to ensure that there are no charge losses during the bunch transport from the cathode to the LANEX screen at the end of the beamline. This is the case, since the space-charge forces are not too strong, for the low bunch charges used here (< 250 pC).

This measurement has been performed for optical densities from $x = 1.0$ to $x = 3.5$ with a LANEX screen located just after the exit window with no collimator mounted. A fit of the data by the function $a * 10^{-x}$ has then been performed. Fig. 2.4 shows the results obtained during these measurements. Fig. 2.5 shows other measurements of the same type performed with optical densities from $x = 1.0$ to $x = 3.05$ with a LANEX screen located after the exit window with the 2 mm diameter collimator mounted.

Fig. 2.4 and Fig. 2.5 show a good agreement between the bunch charge values measured by the LANEX screen and those deduced from values of used optical densities. It is a proof that the use of a scintillating screen is perfectly suitable and reliable for the determination of the charge of a low-charge electron bunch. There is a small discrepancy (25% at maximum) which can be observed between the density $x = 1.6$ and the density $x = 2.4$ in Fig. 2.4. But this discrepancy remains small and does not call into question the viability of bunch charge measurement by a LANEX screen.

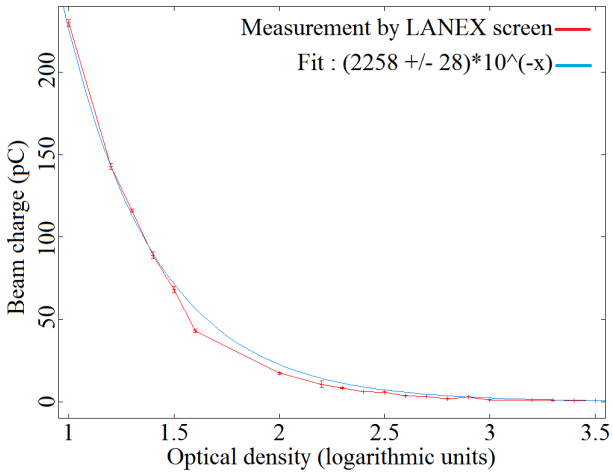

FIGURE *2.4 – Bunch charge measurement by a LANEX screen, without collimator, as a function of the optical density (Thorlabs NDUV [81]) placed in the path of the laser pulse (4th April 2014). Calibration of Fig. 2.3 (a) used. Fit via Gnuplot. RF-gun peak accelerating field : 62 MV/m ; Gun RF-phase : maximizing the bunch energy ; Bunch mean energy : 3.55 MeV.*

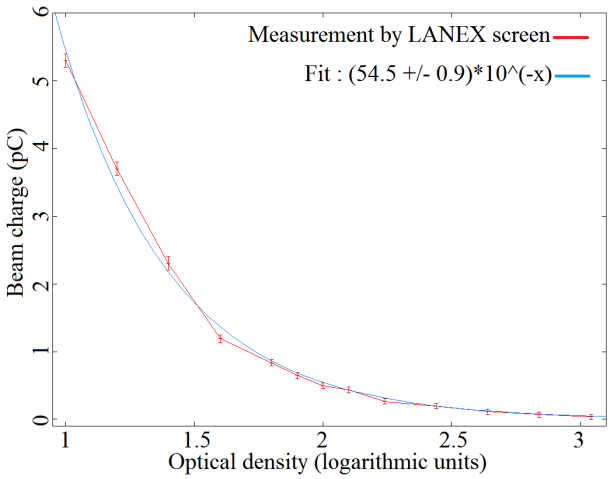

FIGURE *2.5 – Bunch charge measurement by a LANEX screen, with collimator, as a function of the optical density (Thorlabs NDUV [81]) placed in the path of the laser pulse (25th April 2014). Calibration of Fig. 2.3 (b) used. Fit via Gnuplot. RF-gun peak accelerating field : 62 MV/m; Gun RF-phase : maximizing the bunch energy; Bunch mean energy : 3.55 MeV.*

2.1.5 Comparison with the diamond detector

The diamond detector used on PHIL is a single-crystalline detector produced by CIVIDEC [82] thanks to the CVD (Chemical Vapor Deposition) technique, which allows one obtaining high-purity diamonds leading to a better charge collection efficiency [83]. Two important features of the diamond detector are its quite high thermal conductivity, allowing a fast evacuation of the heat caused by radiation which prevents damages, and its high radiation hardness.

The measurement range for this kind of detector goes theoretically from one single electron up to 10^9 electrons thanks to the use of various electronic amplifiers and attenuators. A calibration in clean room with β-sources allows determining a yield of 2.88 fC/MIP (Minimum Ionizing Particle) for a complete collection of the charge created in the detector. As the PHIL electrons (3 MeV) are very close to the MIP energy, the yield of 2.88 fC/MIP has been used to compute the incident bunch charge on the diamond detector.

I therefore performed comparative measurements of the bunch charge between the LANEX screen and the diamond detector developed for the PhD thesis of Shan Liu on ATF2 [50]. I progressively lowered the bunch charge in the range 0.8 pC - 15 fC and measured each time the charge with the LANEX screen and the diamond detector under the same conditions. Fig. 2.6 shows the results of these measurements.

It shows an agreement between the measurements by the LANEX screen and by the diamond detector only for the lowest bunch charges, namely around 10^5 electrons per bunch. To explain the discrepancy at higher charge, the diamond detector yield should be increased up to around 8.2 fC/MIP namely 3 times higher than the theoretical value measured in clean room with β-sources.

The origin of this discrepancy is still under investigation, but it is unlikely to come from the bunch charge measurement via the LANEX screen. In fact we know, thanks to the calibrations of Fig. 2.3, that the charge measurement by LANEX screen is perfectly linear below 200 pC. There is no known physical reason in favor of a variation of this behavior at very low charge. Furthermore, the charge measurement as a function of the optical density placed in the path of the laser pulse generating the bunch (see Fig. 2.4 and Fig. 2.5) shows no deviation with respect to the expected charge, even at very low charge.

The most reasonable explanation is that the diamond detector response is still not well understood. In particular its calibration has not been performed in an accelerator environment but with β-sources, which deliver very low electron currents compared to the ones on PHIL, which are around 100 A when averaged over one rms bunch length. It is perfectly possible that the diamond detector response varies, for the same incident charge, with the incident electron flux. This is supported by the fact that the diamond detector measurement differs from the one of the LANEX screen only from a certain charge value, namely around $3*10^5$ electrons.

Measurements under ultra-high vacuum are intended on PHIL, with a new diamond detector, to investigate the origin of the discrepancy between the LANEX screen and the diamond detector at high incident charge.

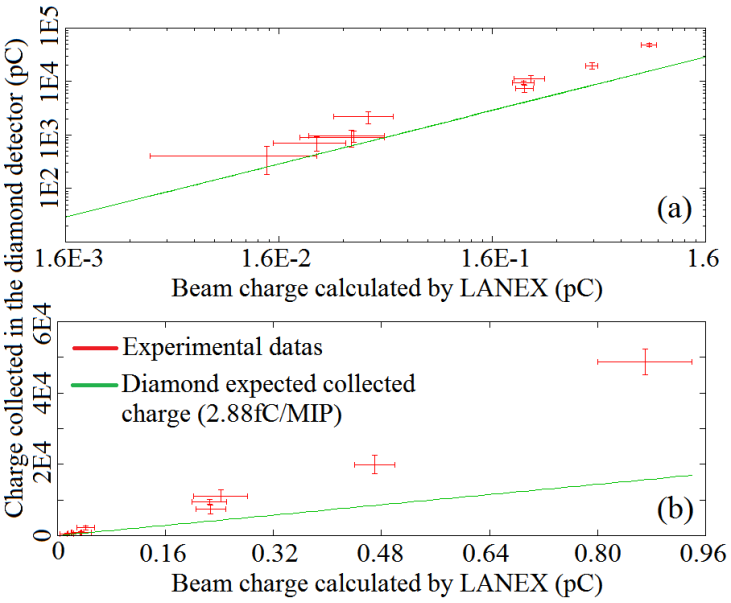

FIGURE *2.6 – Comparison of the bunch charge measured with the LANEX screen and the diamond detector. (a) : Logarithmic scale ; (b) : Linear scale. RF-gun peak accelerating field : 62 MV/m ; Gun RF-phase : maximizing the bunch energy ; Bunch mean energy : 3.55 MeV.*

The lowest charge measured by the LANEX screen is 15 $\pm$ 10 fC, and it has otherwise been confirmed by the diamond detector (see Fig. 2.6). The resolution for charge measurement with a LANEX screen is therefore 10 fC in the current experimental conditions

on PHIL. This resolution can however be lowered, by shielding the CCD camera against the X-rays produced on PHIL, by cooling it down to reduce the thermal noise and also by improving the collection and transport of the light by the optical line between the scintillating screen and the CCD camera.

2.1.6 The case of the bunches with wide energy spectra

The measurements shown in Sec. 2.1 has been performed on PHIL with a mean bunch kinetic energy around 3.5 MeV and a bunch rms energy spread around 0.2%. It allows therefore calibrating the screens, and performing the charge measurements, in a precise way without taking into account the variation of the fluorescence radiation quantity emitted for the different electron energies constituting the bunch. This remark is valid for the most part of the electron accelerators, since the bunch energy spread is often only of a few percents at maximum. The only case where this variation must be taken into account is when the electron bunch has a very wide energy spectrum. This is for example the case for the bunches generated by laser-plasma interaction, which have energy spectra with dispersions up to 100%. Fig. 2.7 shows the energy deposited by an electron in the scintillator layer of the Kodak Lanex fine screen used at PHIL as a function of the electron energy.

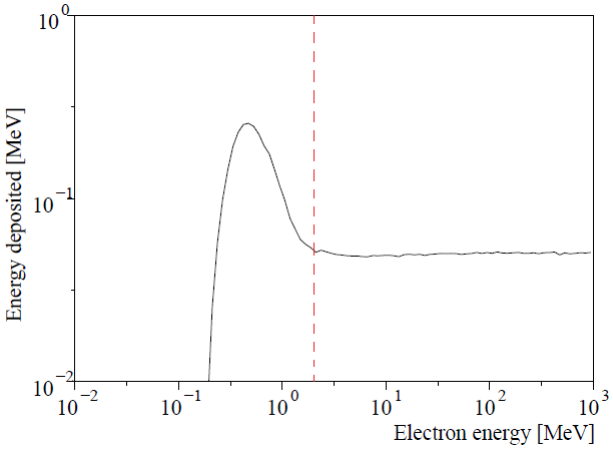

FIGURE *2.7 – Simulation of the energy deposited by an electron in the scintillator layer of the Kodak Lanex fine screen as a function of its energy [84]. The red line corresponds to an energy of 2 MeV for the incident electron.*

It is visible in Fig. 2.7 that for energies higher than 2 MeV the energy deposited by an electron in the scintillator layer of the Kodak Lanex fine screen, and therefore the quantity of fluorescence emitted by this Lanex, is almost constant whatever its energy. This is due to the fact that the Lanex screen is rather thin (280 μm). It implies that the most part of the secondary particles generated by the electron in the Lanex are not stopped in the Lanex, escape it and deposit their energies further away [10]. There is a peak

10. The standard collisional stopping power cannot be used in this case.

of deposited energy, and therefore of emitted fluorescence by the Lanex screen, around 450 keV. The fast decrease at lower energies is explained by the fact that the electron loses all its energy or nearly all its energy in the protective layer and in the substrate constituting the Lanex screen in addition to the scintillator layer. All the thin scintillator screens have this same behavior, except for the fast decrease at low energies if there is no substrate, with different deposited energy values and values of the energy above which the deposited energy becomes almost constant.

This behavior of the deposited energy by an electron bunch in a scintillating screen implies that if no low energy electrons, namely below 2 MeV for the Kodak Lanex fine screen [11], are present in the bunch, the bunch charge measurement method presented in Sec. 2.1 can directly be used whatever the energy spread of the bunch is. This is for example the case for the bunches generated in the DACTOMUS experiment [85], which are generated by the interaction of an intense laser with a plasma and have energies around 50 MeV.

If low energy electrons are present in the bunch, two solutions are possible to nevertheless measure the bunch charge thanks to the image produced by a scintillating screen. The first one is to filter these low energy electrons by putting an aluminum foil with a few millimeters of thickness before the scintillating screen. The bunch charge is then determined directly by the method presented in Sec. 2.1. The second one is to send the bunch in a dipole magnet and to acquire its image with a scintillating screen placed after this dipole magnet. The electrons will in this case be separated according to their energies, along the dipole magnet dispersive direction, on the obtained image (see Sec. 1.3.4). The image projected profile along the dipole magnet dispersive direction is then the bunch energy spectrum (see Sec. 1.3.4). By using a calibration of the scintillating screen made at a known energy and applying a correction factor to take into account the variation of the emitted fluorescence quantity with the incident electron energy, the bunch charge spectrum as a function of its energies is reconstructed. The total bunch charge is finally simply given by the integral of this bunch charge spectrum.

2.1.7 Conclusions

The calibrations of LANEX and YAG screens (see Fig. 2.2 and Fig. 2.3) shows that the light response of these scintillating screens is perfectly linear for incident bunch charges between 3 pC and 350 pC and probably above. It is then possible to extrapolate this linearity to measure lower bunch charges from the light intensity emitted by a scintillating screen.

The charge measurements as a function of the optical density placed in the path of the laser pulse generating the electron bunch (see Fig. 2.4 and Fig. 2.5) allow demonstrating that the use of a scintillating screen is perfectly reliable and suitable to measure the charge of a low-charge electron bunch.

The lowest charge measured with the LANEX screen on PHIL, and confirmed by

11. It depends on the used scintillating screen.

the diamond detector, is 15 fC with a resolution around 10 fC, which is mainly due to the noise (thermal and X-rays noises) on the signal coming from the CCD imaging the LANEX screen and to the configuration of the optical line collecting and transporting the light between the scintillating screen and the CCD camera.

There is however a very important limitation for using a LANEX screen to measure low-charge bunches in an accelerator. Indeed the LANEX cannot be placed under ultra-high vacuum ($< 10^{-6}$ mbar) because of too high an outgassing rate, especially on an accelerator based on an RF-gun as PHIL is. This therefore prevents it to be used in the large majority of electron accelerators. However, a sufficiently thick YAG screen ($>$ 500 μm thickness) can be used under ultra-high vacuum and produce a light intensity equivalent to the one of a LANEX screen (see Sec. 1.1.2), thus allowing the measurement of charges lower than 100 fC.

The measurements with the diamond detector do not match with those coming from the LANEX screen for an incident charge higher than $3*10^5$ electrons. A misunderstanding of the diamond detector response in accelerator environment is strongly suspected. This could especially come from the fact that the diamond detector yield has been determined from measurements with β-sources, having a far lower flux than an electron bunch in an accelerator like PHIL.

The charge measurement with a scintillating screen, developed in Sec. 2.1, is a single-shot method. It can therefore be used to measure the charge of electron bunches generated and/or accelerated through a laser-plasma interaction. It can even be used when the energy spread of the bunch is very large, as it has been shown in Sec. 2.1.6.

2.2 Transverse emittance measurements

2.2.1 The 3-screen method for bunch transverse emittance measurement

2.2.1.1 Theoretical principles

The 3-screen method is a multiparametric method allowing measuring the bunch transverse emittance from the measurement of its transverse sizes at three different points of the beamline. The classical 3-screen method, which I will present hereafter, corresponds to the case where the space between these three points is a pure drift space. The reconstructed bunch emittance is then the one at the level of the first point where the bunch transverse sizes are measured. However, any known linear optics could be included, through their transfer matrices, before, between and after the three bunch transverse sizes measurement points.

Without space-charge forces

To establish the classical 3-screen method, it is necessary to perform several approximations. Firstly, we have to neglect the effect of space-charge forces between the first and third point of transverse sizes measurement. This approximation becomes more consequent as the bunch energy decreases, since the space-charge force effects are then increasing. It allows assuming that the bunch transverse emittance is invariant between these points and that the bunch transport can be determined thanks to the classic transfer matrix for a drift space of length L_i, given by :

$$M_{L_i} = \begin{pmatrix} 1 & L_i \\ 0 & 1 \end{pmatrix}$$

The other approximation is to neglect the coupling between the two transverse directions, horizontal and vertical. This is particularly an approximation when a solenoid magnet is used before the first point of transverse sizes measurement. In fact, this kind of magnet strongly couples the two transverse directions. Even in the case where this coupling is compensated by a second solenoid magnet, as on the SPARC facility (see Sec. 1.4.4), there is always a residual coupling. Neglecting this coupling allows separating the bunch transport along the two transverse directions, by transporting two beam matrices of the following form :

$$\Sigma_x = \begin{pmatrix} \epsilon_x\beta_x & -\epsilon_x\alpha_x \\ -\epsilon_x\alpha_x & \epsilon_x\gamma_x \end{pmatrix} \qquad \text{and} \qquad \Sigma_y = \begin{pmatrix} \epsilon_y\beta_y & -\epsilon_y\alpha_y \\ -\epsilon_y\alpha_y & \epsilon_y\gamma_y \end{pmatrix}$$

where ϵ_x and ϵ_y are respectively the bunch horizontal and vertical transverse emittances and β_x, β_y, α_x, α_y, γ_x, γ_y are the bunch horizontal and vertical Twiss parameters.

The calculation being the same along the two transverse directions, I will develop thereafter only the calculation along the horizontal direction x. Let Σ_{x_i} be the horizontal beam matrix at the point number i of the transverse sizes measurement and M_{L_1} and M_{L_2} the transfer matrices, respectively between the first and second point of transverse sizes measurement and between the second and third point of transverse sizes measurement. We have by definition : $\Sigma_{x_2} = M_{L_1}\Sigma_{x_1}M_{L_1}^t$, $\Sigma_{x_3} = M_{L_2}\Sigma_{x_2}M_{L_2}^t$ and $\sigma_{x_i}^2 = \epsilon_x\beta_{x_i}$ where σ_{x_i} is the bunch horizontal transverse size at the i^{th} measurement point. We obtain the following system of equations :

$$\begin{cases} -2L_1A + BL_1^2 = \sigma_{x_2}^2 - \sigma_{x_1}^2 \\ \\ -2L_2A + (2L_1L_2 + L_2^2)\,B = \sigma_{x_3}^2 - \sigma_{x_1}^2 \end{cases}$$

where $A = \epsilon_x\alpha_{x_1}$ and $B = \epsilon_x\gamma_{x_1}$. The system above finally gives by inversion :

$$\begin{cases} A = \frac{BL_1^2+\sigma_{x_1}^2-\sigma_{x_2}^2}{2L_1} \\ \\ B = \frac{\sigma_{x_3}^2-\sigma_{x_1}^2+\left(1+\frac{L_1}{L_2}\right)\left(\sigma_{x_1}^2-\sigma_{x_2}^2\right)}{L_2(L_1+L_2)} \end{cases}$$

Knowing that $\beta_{x_i}\gamma_{x_i} - \alpha_{x_i}^2 = 1$, by unitarity of the beam matrix Σ_{x_i}, we can determine the bunch transverse emittance by :

$$\epsilon_x = \sqrt{\sigma_{x_1}^2 B - A^2} \tag{2.1}$$

The bunch transverse emittance ϵ_x is then determined, but it remains to determine the error bars on it. To do that, I chose to use the 3-screen method explained above in combination with a Monte-Carlo algorithm. Concretely, I drew 100000 triplets of bunch transverse sizes $(\sigma_{x_1}\,;\sigma_{x_2}\,;\sigma_{x_3})$ according to Gaussian distributions having as mean values the measured values of bunch transverse sizes and as standard deviations the uncertainties on these measurements. I then applied Eq. 2.1 for each of the 100000 triplets. I obtained in this way 100000 values of ϵ_x. The value of ϵ_x is finally the mean of these 100000 values and the uncertainty on it is the standard deviation of these 100000 values.

With space-charge forces

The simplest method to take into account the space-charge forces in the 3-screen method is to use the envelope equations, which give the evolution of the bunch transverse rms properties. Since the two transverse directions, horizontal (x) and vertical (y), are equivalent, I will only treat the case of the horizontal direction thereafter.

The first step is to establish the transverse beam envelope equation. To do that, I work in the position-divergence transverse phase-space denoted by $(x\,;x')$. The independent variable is the longitudinal position s along the accelerator. Thereafter, I will denote by a ' the first derivative with respect to s and by a " the second derivative with respect to s.

The divergence is defined as the angle between the electron trajectory and the s direction. It is always small, typically a few mrad, and is given by $x' \approx \tan(x') = \frac{\beta_x}{\beta_s}$, where $\beta_\alpha c$ is the electron velocity along the α direction. One can remark that we also have $x' = \frac{dx}{ds}$. The two variables describing the electrons of the bunch are the gap in position $X = \Delta x = x - x_0$ and in divergence $X' = \Delta x' = x' - x'_0$ with respect to the bunch reference particle, which is the mean particle of the bunch.

By definition of the bunch reference particle we have $< X >= 0$ and $< X' >= 0$, where $<>$ denotes the average over all the electrons of the bunch. The bunch transverse rms properties are then simply given by :

$$\begin{cases} \sigma_X = \sqrt{< X^2 >} = \text{ bunch rms transverse size} \\ \sigma_{X'} = \sqrt{< X'^2 >} = \text{ bunch rms transverse divergence} \\ \sigma_{XX'} =< XX' >= \text{ bunch rms transverse eccentricity} \end{cases}$$

The bunch transverse rms emittance is defined by :

$$\epsilon_X = \sqrt{< X^2 >< X'^2 > - < XX' >^2} = \sqrt{\sigma_X^2 \sigma_{X'}^2 - \sigma_{XX'}^2}$$

In the framework of the classical 3-screen method, the bunch moves freely and straight in a drift space. It is not subject to external focusing magnetic forces. The only force acting on any electron of the bunch is therefore the space-charge force $\vec{F}_{SC}$ created by all the others bunch electrons. Electrons dynamics is then governed by the following equation, where $\vec{p}$ is the electron momentum :

$$\frac{d\vec{p}}{dt} = \vec{F}_{SC} \Rightarrow \frac{d\vec{p}}{ds} = \frac{\vec{F}_{SC}}{\beta_s c} \tag{2.2}$$

As previously mentioned, the divergence remains small and the bunch motion is for the most part in the s direction. It allows applying the paraxial approximation, which consists in supposing $\beta_x^2 + \beta_y^2 << \beta_s^2 \approx \beta^2$ where βc is the total electron velocity. I also assume that the electron energy is a constant during its motion. This is not totally true since the space-charge force induces slight variations of the electron energy. Using these approximations, the projection of Eq. 2.2 along the x direction leads to :

$$\frac{dX'}{ds} = X'' = \frac{F_{SC,x}}{\gamma \beta^2 mc^2}$$

where $(\gamma - 1)mc^2$ is the electron kinetic energy. It is noteworthy that $F_{SC,x}$ does not depend only on the X coordinates of the electrons, but also on the Y and Z coordinates where $Z = z - z_0$ denotes the longitudinal position of the electron in the bunch (z_0 is the reference particle longitudinal position).

We now want to establish the equation describing the evolution of σ_X along s. Noting that $\frac{d}{ds}$ and $<>$ commute, we have :

$$\sigma_X^{'} = \frac{\frac{d<X^2>}{ds}}{2\sigma_X} = \frac{<XX'>}{\sigma_X}$$

and :

$$\sigma_X^{''} = \frac{\sigma_{X'}^2}{\sigma_X} + \frac{<XX''>}{\sigma_X} - \frac{\sigma_{XX'}^2}{\sigma_X^3}$$

This equation can be rewritten as :

$$\sigma_X^{''}\sigma_X^3 = \left(\sigma_X^2\sigma_{X'}^2 - \sigma_{XX'}^2\right) + < X\frac{F_{SC,x}}{\gamma\beta^2 mc^2} > \sigma_X^2$$

We finally obtain the transverse beam envelope equation [19, 86] :

$$\sigma_X^{''} - \widetilde{K}_{SC,x}\sigma_X - \frac{\epsilon_X^2}{\sigma_X^3} = 0 \tag{2.3}$$

where $\widetilde{K}_{SC,x} = \frac{<X\frac{F_{SC,x}}{\gamma\beta^2 mc^2}>}{\sigma_X^2}$ is called the linearization coefficient of the space-charge force, since it allows linearizing the effect of the space-charge force in the transverse beam envelope equation. $-\widetilde{K}_{SC,x}\sigma_X$ is the space-charge defocusing term, and $-\frac{\epsilon_X^2}{\sigma_X^3}$ is the emittance defocusing term.

For a bunched beam having an uniform ellipsoidal charge distribution, $\widetilde{K}_{SC,x}$ is given by [19, 87] :

$$\widetilde{K}_{SC,x_{unif}} = \frac{3eQ}{4\pi\epsilon_0\beta^2\gamma^2 mc^2}\int_0^{+\infty}\frac{dt}{\sqrt{\left(5\sigma_X^2+t\right)^3\left(5\sigma_Y^2+t\right)\left(5\gamma^2\sigma_Z^2+t\right)}} \tag{2.4}$$

where Q is the bunch charge, σ_Z the bunch rms longitudinal size and ϵ_0 is the dielectric permittivity of vacuum.

For a 3D round Gaussian bunch, namely a bunch with Gaussian charge distributions in the three directions and $\sigma_X = \sigma_Y$, the charge density is given by :

$$\rho(X,Y,Z) = \rho_0 e^{-\frac{1}{2}\left(\frac{X^2+Y^2}{\sigma_X^2}+\frac{Z^2}{\sigma_Z^2}\right)}$$

with $\rho_0 = \frac{Q}{2\pi\sqrt{2\pi}\sigma_X^2\sigma_Z}$.

The x component of the space-charge electric field is then given by [13] :

$$E_{SC,x_{gauss}} = \frac{QX}{4\pi\epsilon_0\sqrt{2\pi}\sigma_X^2\sigma_Z}\int_0^{+\infty}\frac{e^{-\frac{1}{2}\left(\frac{X^2+Y^2}{\sigma_X^2(1+t)}+\frac{Z^2}{\sigma_Z^2(1+A^2t)}\right)}}{(1+t)^2\sqrt{1+A^2t}}dt$$

where $A = \frac{\sigma_X}{\sigma_Z}$. The linearization coefficient of the space-charge force is by definition given by :

$$\widetilde{K}_{SC,x_{gauss}} = \frac{< XF_{SC,x_{gauss}} >}{\sigma_X^2}$$

with $F_{SC,x_{gauss}} = \frac{eE_{SC,x_{gauss}}}{\beta^2\gamma^3mc^2}$. We finally have :

$$\widetilde{K}_{SC,x_{gauss}} = \frac{eQ}{4\pi\epsilon_0\sqrt{2\pi}\sigma_Z\sigma_X^4\beta^2\gamma^3mc^2} < X^2\int_0^{+\infty}\frac{e^{-\frac{1}{2}\left(\frac{X^2+Y^2}{\sigma_X^2(1+t)}+\frac{Z^2}{\sigma_Z^2(1+A^2t)}\right)}}{(1+t)^2\sqrt{1+A^2t}}dt > \qquad (2.5)$$

We now want to apply Eq. 2.3 for the determination of the bunch transverse emittance ϵ_X by the 3-screen method, namely using only the three measured bunch rms transverse sizes σ_{X_1}, σ_{X_2} and σ_{X_3}.

Four quantities are necessary to solve Eq. 2.3 : The initial bunch rms transverse size σ_{X_0} ; Its derivative σ'_{X_0} which is the initial bunch rms transverse divergence ; The bunch rms transverse emittance ϵ_X ; The linearization coefficient of the space-charge force $\widetilde{K}_{SC,x}$.

Practically, σ_{X_0} is experimentally determined and is equal to σ_{X_1}. $\widetilde{K}_{SC,x}$ is numerically calculated from the analytical expressions Eq. 2.4 or Eq. 2.5. σ'_{X_0} is unequivocally determined by fitting the points $(s_1 = 0\,;\sigma_{X_1})$, $(s_2\,;\sigma_{X_2})$ and $(s_3\,;\sigma_{X_3})$ with a second order polynomial $as^2 + bs + c$. σ'_{X_0} is then chosen equal to b.

Eq. 2.3 is then numerically solved, using a Runge-Kutta algorithm of fourth order, for several values of ϵ_X. A curve of σ_X as a function of s is obtained each time. The bunch rms transverse emittance is finally determined as the one for which the distance between the three measured bunch rms transverse sizes $(\sigma_{X_1}\,;\sigma_{X_2}\,;\sigma_{X_3})$ and this curve is minimal.

2.2.1.2 Evaluation of the precision on PHIL

The goal of this section is to present the results obtained by applying the 3-screen method to measure the bunch transverse emittance, via Eq. 2.1, on simulations performed with the ASTRA beam dynamics code. This allows estimating the accuracy that one can hope to achieve experimentally with this method, provided that the operation of the used accelerator is well understood and correctly modeled in ASTRA. The 3-screen method was thus tested in the context of PHIL accelerator at LAL (see Fig. 1.24). The theoretical principles of this method have already been presented previously (see Sec. 2.2.1). The bunches simulated in this study are transversely round and have therefore very close

transverse emittances along the two transverse directions x and y. I will only present the transverse emittances along x hereafter.

To test the 3-screen method, it is sufficient to pick up the bunch rms transverse sizes calculated by ASTRA at the positions of the 3 YAG screens located on the PHIL beamline (see Fig. 1.24), to extract from it by the 3-screen method the bunch rms transverse emittances (see Eq. 2.1) and to compare these values with the statistical rms transverse emittances values directly calculated by ASTRA. Tab. 2.1 gathers the obtained results. It is noteworthy that I check that the rms transverse sizes are correctly calculated by ASTRA. To do that, I analyze the ASTRA particle distribution with an image analysis code developed with MATLAB (see Appendix C) and find the same results as in ASTRA. I use a Gaussian initial particles distribution with $\sigma_t = 3.6$ ps rms, $\sigma_x = \sigma_y = 1$ mm rms and a typical bunch charge of 100 pC.

case number	focusing	beam energy (MeV)	space-charge force in ASTRA	IB3 (A)	ε_x ASTRA (π.mm.mrad)	ε_x 3-screens (π.mm.mrad)	relative deviation
1	underfocusing	3,16	yes	110	4,713	22,87	385%
2	underfocusing	3,16	yes	120	3,925	13,153	235,00%
3	waist before YAG1	3,16	yes	126	3,741	9,885	164,20%
4	underfocusing	3,16	no	112	0,7288	0,7503	2,95%
5	waist on YAG2	3,16	no	117	0,7293	0,731	0,23%
6	overfocusing	3,16	no	121	0,7357	0,7324	0,45%
7	underfocusing	4,13	yes	140	4,072	20,525	404%
8	underfocusing	4,13	yes	155	3,527	8,529	141,80%
9	waist on YAG1	4,13	yes	159	3,22	6,286	95,20%
10	overfocusing	4,13	yes	166	2,756	6,258	127,10%
11	underfocusing	4,13	no	149	0,8426	0,8501	0,89%
12	waist on YAG2	4,13	no	155	0,8567	0,8613	0,54%
13	overfocusing	4,13	no	159	0,8688	0,864	0,55%
14	underfocusing	5,09	yes	177	3,395	15,703	363%
15	waist on YAG2	5,09	yes	193	3,074	5,302	72,50%
16	overfocusing	5,09	yes	204	2,48	5,061	104,10%
17	underfocusing	5,09	no	186	1,028	1,064	3,50%
18	waist on YAG2	5,09	no	193	1,049	1,056	0,70%
19	overfocusing	5,09	no	198	1,073	1,068	0,47%

TABLE *2.1 – Results of ASTRA simulations for evaluating the classical 3-screen method (without space-charge forces included and with a pure drift space) accuracy. Bunch charge : 100 pC; Gun RF-phase : maximizing the bunch mean energy.*

This study has been performed for 3 different peak accelerating fields in the PHIN RF-gun on PHIL : 50 MV/m, 65 MV/m and 80 MV/m. It corresponds respectively to mean bunch energies of 3.16 MeV, 4.13 MeV and 5.09 MeV. This has been done each time taking into account and not taking into account the space-charge force, and for different magnetic fields in the B3 solenoid at the gun exit. One has to remind that to use the 3-screen method the B5 solenoid in the beamline middle cannot be used, since it is not upstream the first of the 3 YAG screens. The idea was to have a magnetic field value where the bunch presents a waist on the YAG2 screen (central screen used in the emittance measurement), or as close as possible when it was impossible (at 50 MV/m and

65 MV/m with space-charge force actually), a value where the bunch is focused before YAG2 (overfocusing) and a value where the bunch is slightly focused and keeps a positive and almost constant divergence during its motion downstream B3 (underfocusing). Fig. 2.8 shows 3 images illustrating the bunch transverse sizes evolution in these 3 cases.

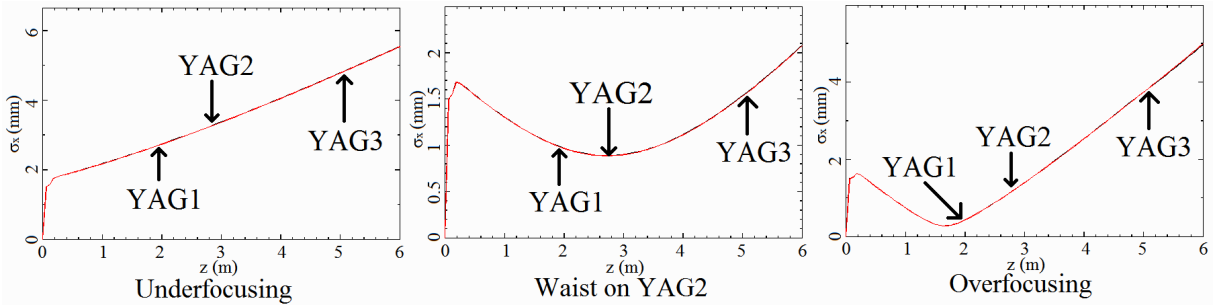

FIGURE *2.8 – The 3 focusing cases studied in ASTRA*

It is noteworthy that for the cases at 50 MV/m with space-charge force, no overfocusing case has been studied because important particles losses appears in the beamline at the dipole magnet entrance point, which is located before YAG3 (see Fig. 1.24). Tab. 2.1 contains some very instructive results which I will now develop.

In the cases without space-charge forces (cases 4, 5, 6, 11, 12, 13, 17, 18 and 19 in Tab. 2.1), the relative deviation with respect to the rms transverse emittances computed by ASTRA is always very close from zero. It is expected, since the transverse emittance is determined unequivocally with the classical 3-screen method when exactly three screens in a pure drift space are used. It must therefore always be determined exactly by this method in the absence of space-charge forces, which is observed in Tab. 2.1. One can observe that for the underfocusing cases (cases 4, 11 and 17 in Tab. 2.1) the relative deviation of the 3-screen method with the ASTRA predictions is slightly higher (typically a few percents). This is explained by the loss of a few electrons of the bunch during its transport up to the YAG3 screen of PHIL (5.09 m after the photocathode) in these cases [12].

In the cases with space-charge forces (cases 1, 2, 3, 7, 8, 9, 10, 14, 15 and 16), one first remarks that the relative deviation of the 3-screen measurements with the ASTRA predictions is never zero. This is due to the effects of space-charge forces, which are not taken into account in the classical 3-screen method. One also remarks that the deviation is much more important in the case at 3.16 MeV (164.2% : case 3 in Tab. 2.1) than in the case at 4.13 MeV (95.2% : case 9 in Tab. 2.1) and in the case at 5.09 MeV (72.5% : case 15 in Tab. 2.1). The agreement becomes therefore better when the bunch energy increases. This was expected since the space-charge forces, not taking into account in the classical 3-screen method, are then less and less important. It is also visible and noteworthy that the deviation with the ASTRA predictions increases in the overfocusing and especially underfocusing cases with respect to the ones with a bunch waist on, or close to, the YAG2 screen of PHIL (see for example the cases 14, 15 and 16 in Tab. 2.1).

12. The 3-screen method requires that there are no charge losses during the bunch transport.

Thus it could be said that, on PHIL, the ASTRA simulations predict that the classical 3-screen method (with a pure drift space and without taking into account the space-charge forces) would allow a transverse emittance measurement with an accuracy better than 100% if the bunch energy exceeds 4.13 MeV and better than 75% if the bunch energy exceeds 5.09 MeV. However the accuracy would quickly deteriorate, since it would be only 164.2% at 3.16 MeV.

2.2.1.3 Experimental measurements

All the experimental bunch transverse emittance measurements that I performed by the 3-screen method have been carried out on the PHIL facility, with the YAG1, YAG2 and YAG3 screens (see Fig. 1.24). The precise measurement of the bunch rms transverse horizontal size with the YAG1 screen is impossible because of a parasitic light due to reflection (see Fig. 1.17 in Sec. 1.3.2.1) [13]. I will therefore only treat the case of the vertical bunch rms transverse emittance ϵ_y measurement in this section.

Example measurement

I will first of all detail the determination of ϵ_y through an example. In the selected example, the bunch rms vertical transverse sizes measured on the three PHIL YAG screens are : $\sigma_{y_1} = 1.99 \pm 0.05$ mm (YAG1), $\sigma_{y_2} = 2.33 \pm 0.02$ mm (YAG2) and $\sigma_{y_3} = 4.47 \pm 0.04$ mm (YAG3).

The bunch rms transverse emittance ϵ_y is then first extracted from these sizes by using Eq. 2.1 and the Monte-Carlo algorithm detailed in Sec. 2.2.1.1. This determination of ϵ_y is the one with the classical 3-screen method, namely with the drift transport matrix and without including the space-charge forces. Fig. 2.9 shows the histogram obtained for ϵ_y in the selected example. This histogram allows determining $\epsilon_y = 21.7 \pm 0.8$ π.mm.mrad. This experimental value is quite far from the $\epsilon_y = 2.03$ π.mm.mrad predicted by the ASTRA simulation, the discrepancy being of 969%. This large discrepancy is explained by the numerous approximations used to establish Eq. 2.1 (see Sec. 2.2.1.1) and shows that the classical 3-screen method is not appropriate to compute the rms transverse emittance of a 100 pC and few MeV electron bunch with the current position of the YAG screens on PHIL.

Once ϵ_y is determined, the Twiss parameters of the bunch, β_y, γ_y and α_y can also be determined. Finally, the Twiss ellipse of the bunch can be computed in the plane $(y; y')$ because it is the one defined by the following equation : $\gamma_y y^2 + 2\alpha y y' + \beta_y y'^2 = \epsilon_y$. The Twiss ellipse contains 39% of the bunch particles, around the bunch center, if the bunch has a Gaussian distribution for the particles transverse positions and divergences. This Twiss ellipse is very useful, since it allows visualizing at a glance the bunch rms transverse size, the bunch rms transverse divergence and the orientation of the bunch in its transverse phase-space. This last point allows deducing if the bunch is convergent, divergent or at a

13. The CCD camera viewing the YAG screen is rotated by 90° and the horizontal and vertical directions are therefore inverted on the image.

waist. The knowledge of the Twiss parameters and ellipse is also very important to adapt the bunches coming from a transfer line to a storage ring like THOM-X [88].

Fig. 2.10 shows the histogram obtained for β_y (a), γ_y (b) and α_y (c) in the selected example. It also shows the vertical bunch Twiss ellipse deduced from this calculation (d). It is clearly visible in Fig. 2.10 (d) that the bunch is slightly convergent, but almost at a waist, at the position of the YAG1 screen. It is verified by a further use of the beam envelope equation (see Fig. 2.11), which shows that the derivative of the beam envelope is almost zero at the position of the YAG1 screen (0 m).

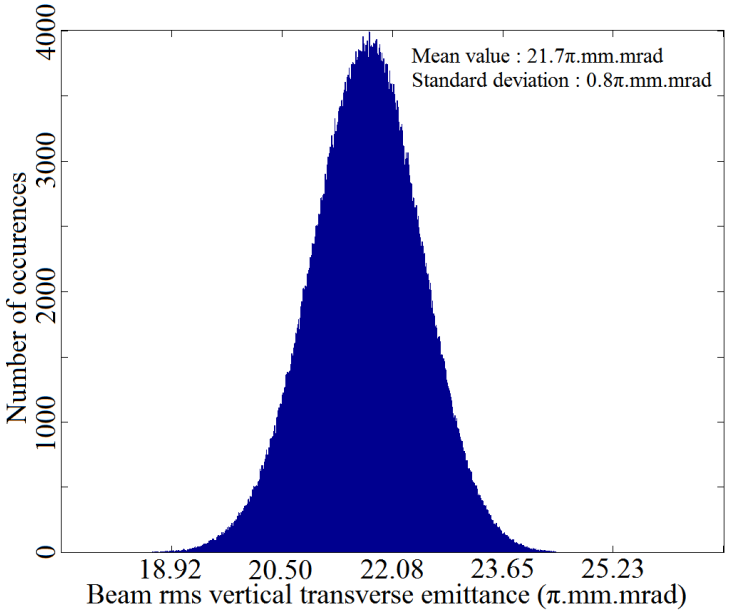

FIGURE *2.9 – Histogram of ϵ_y obtained with the classical 3-screen method in the selected example. RF-gun peak accelerating field : 62 MV/m ; Gun RF-phase : minimizing the bunch energy spread ; Bunch energy : 3.55 MeV ; Bunch charge : 100 pC ; Current injected in B3 : 165 A.*

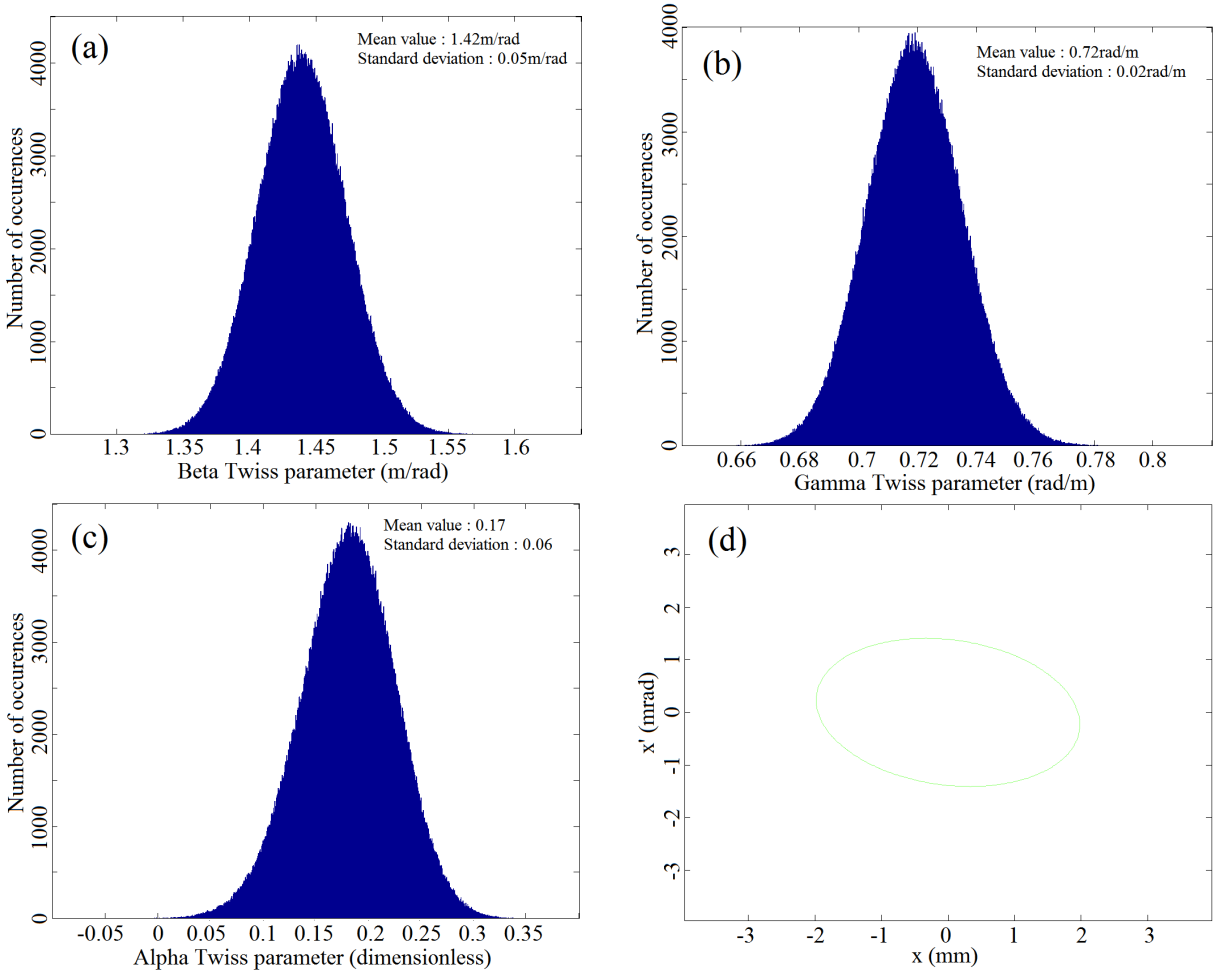

FIGURE *2.10 – Histograms obtained for β_y (a), γ_y (b) and α_y (c) with the classical 3-screen method in the selected example. Vertical Twiss ellipse obtained (d). Experimental conditions : see Fig. 2.9.*

The next step is to determine ϵ_y by using the beam envelope equation (see Eq. 2.3) and the algorithm presented at the end of Sec. 2.2.1.1. I choose to perform a first determination without taking into account the space-charge forces [14], to see if there are some differences between the classical 3-screen method with the transport matrix and the one with the beam envelope equation. Fig. 2.11 shows some bunch size curves, computed using the beam envelope equation without space-charge forces included, with different values of ϵ_y.

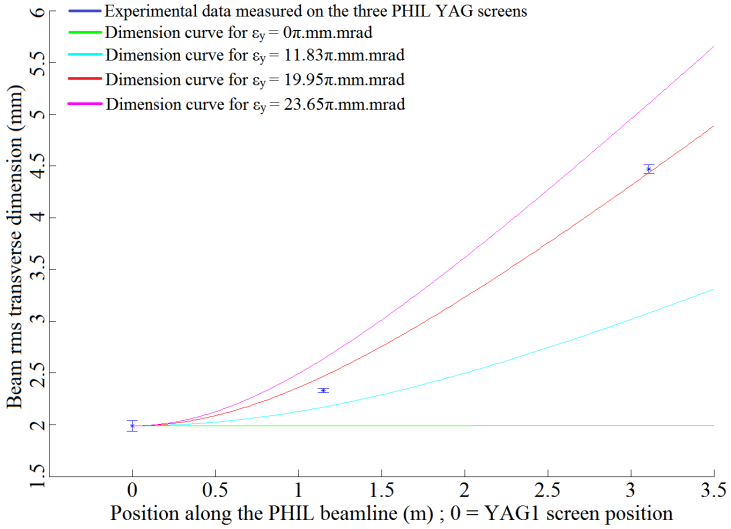

FIGURE *2.11 – Determination of ϵ_y by the 3-screen method using the beam envelope equation, without space-charge forces included, for the selected example. Experimental conditions : see Fig. 2.9.*

Fig. 2.11 allows determining a value of $\epsilon_y = 19.95$ π.mm.mrad. This value is still very far from the $\epsilon_y = 2.03$ π.mm.mrad predicted by the ASTRA simulation, the discrepancy being of 883%. It shows that the inclusion of the space-charge forces is essential to perform a more realistic measurement of the transverse emittance, with the 3-screen method, for a 100 pC and few MeV electron bunch generated by an RF-gun.

However, one can note that the ϵ_y values are not the same when determined by the classical 3-screen method or by the one using the beam envelope equation. ϵ_y is indeed a little bit lower and closer to the ASTRA simulation when determined by the beam envelope equation. This discrepancy is explained by the fact that, as shown in Fig. 2.11, the waist of the bunch is not positioned on the YAG2 screen but on the YAG1 screen for the selected example. The classical 3-screen method is a least square based method [15] implying that its accuracy is improved when the minimum of the bunch transverse sizes is located on, or close to, the YAG2 screen. It has been shown in Tab. 2.1 in Sec. 2.2.1.2 (see cases 7, 8, 9 and 10 for example). The 3-screen method based on the beam envelope equation relies on the numerical solving of Eq. 2.3, and is therefore not submitted to this behavior.

14. It means that the term $\widetilde{K}_{SC,x}$ in Eq. 2.3 is set equal to zero.
15. The least square inversion is unique and unequivocal in my examples, since there are three unknown quantities and three measurements.

To prove this, it is relevant to compare the ϵ_y values coming from these two methods for a case where the bunch waist is close to the YAG2 screens. I do this for a case where the bunch rms vertical transverse sizes measured on the three PHIL YAG screens are : $\sigma_{y_1} = 1.74 \pm 0.07$ mm (YAG1), $\sigma_{y_2} = 1.54 \pm 0.08$ mm (YAG2) and $\sigma_{y_3} = 3.14 \pm 0.10$ mm (YAG3). In this case, I determine $\epsilon_y = 13.7 \pm 0.7$ π.mm.mrad with the classical 3-screen method and $\epsilon_y = 13.72$ π.mm.mrad with the one based on the beam envelope equation, as shown in Fig. 2.12. There is no more discrepancy in this case, proving that the accuracy of the classical 3-screen method is sensitive to the position of the bunch waist, while this is not the case of the one based on the beam envelope equation.

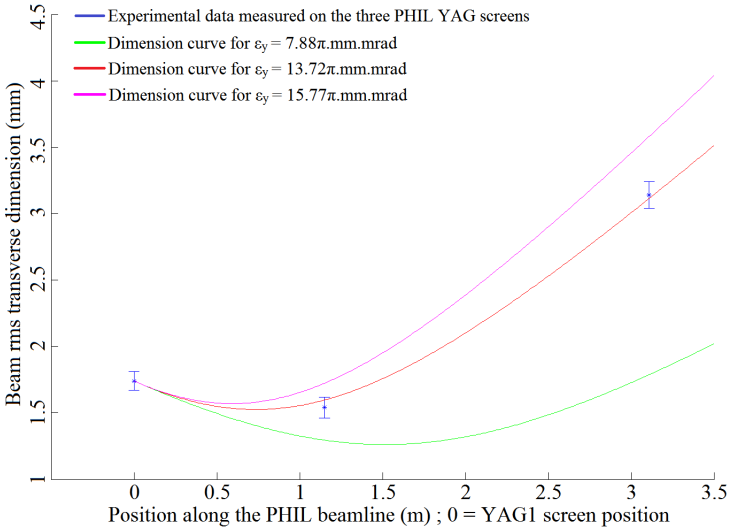

FIGURE *2.12 – Determination of ϵ_y by the 3-screen method using the beam envelope equation without space-charge forces included. RF-gun peak accelerating field : 62 MV/m ; Gun RF-phase : minimizing the bunch energy spread ; Bunch energy : 3.55 MeV ; Bunch charge : 8 pC ; Current injected in B3 : 150 A.*

Let us now return to the previously selected example and see what happens when the space-charge forces are included in the beam envelope equation. Fig. 2.13 shows some bunch size curves, computed using the beam envelope equation supposing a 3D ellipsoid uniform bunch charge density (see Eq. 2.4), with different values of ϵ_y. Fig. 2.14 shows some bunch size curves, computed using the beam envelope equation supposing a 3D Gaussian bunch charge density (see Eq. 2.5), with different values of ϵ_y.

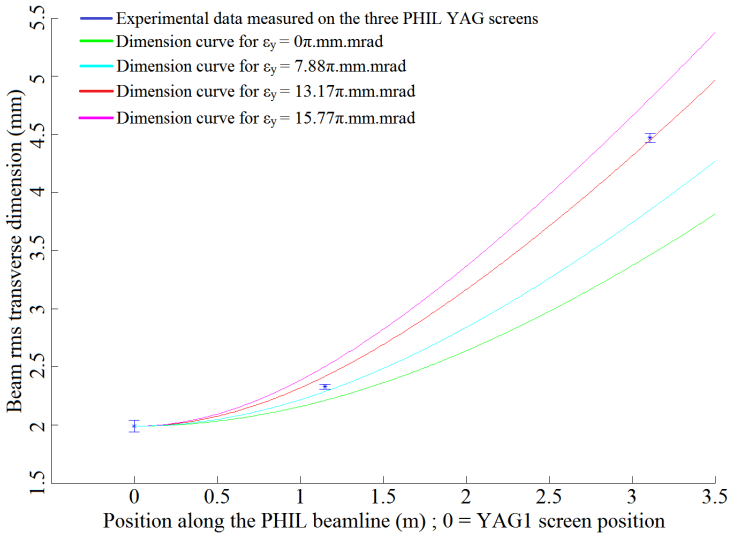

FIGURE *2.13 – Determination of ϵ_y by the 3-screen method using the beam envelope equation, with space-charge forces included assuming a 3D ellipsoid uniform bunch charge density (see Eq. 2.4), for the selected example. Experimental conditions : see Fig. 2.9.*

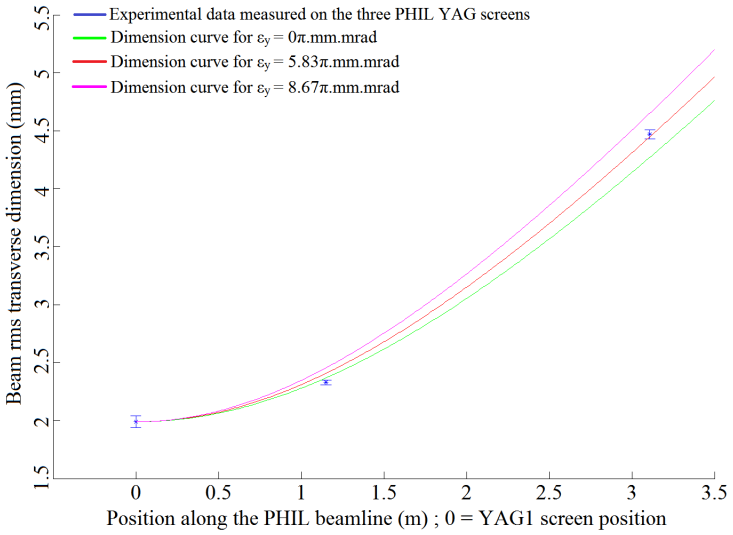

FIGURE *2.14 – Determination of ϵ_y by the 3-screen method using the beam envelope equation, with space-charge forces included assuming a 3D Gaussian bunch charge density (see Eq. 2.5), for the selected example. Experimental conditions : see Fig. 2.9.*

The values of ϵ_y extracted from the calculation with a 3D ellipsoid uniform bunch charge density and with a 3D Gaussian bunch charge density are respectively of 13.17 π.mm.mrad and 5.83 π.mm.mrad. These results prove that the inclusion of the space-charge forces in the 3-screen method, via the beam envelope equation, brings a significant improvement in the determination of the transverse emittance of a 100 pC and few MeV electron bunch generated by an RF-gun. In fact, the discrepancies with the $\epsilon_y = 2.03$ π.mm.mrad predicted by the ASTRA simulation are lowered to respectively 549% and 187%.

One can note that the 3D Gaussian charge density is much more suited than the 3D ellipsoid uniform one to model the space-charge forces within the PHIL electron bunch. This was expected, since the laser pulse driving the PHIL RF-gun presents a 3D Gaussian energy density.

One can also remark that there is still a large discrepancy with the ASTRA simulations, despite the inclusion of the space-charge forces in the 3-screen method. This remaining large discrepancy is not mainly due to a mismodeling of the PHIL bunch and beamline in the ASTRA simulations. Indeed, as it will be shown in Sec. 2.2.2.3, the bunch rms transverse emittance measurement performed with the 3-gradient method are much closer to the predictions of ASTRA, the discrepancy being typically of only 30%. There are several hypotheses which may explain this larger discrepancy observed for the 3-screen method on PHIL.

A first one is that, to compute the space-charge forces, I assume a constant rms bunch length σ_t during the bunch motion between YAG1 and YAG3. This is not true, since it can vary under the actions of the space-charge forces and of the longitudinal focusing effect due to the RF-gun accelerating field. Furthermore, as it will be shown in Sec. 2.3.3.7, the real rms length of the PHIL electron bunch is still unknown and the ASTRA simulations cannot be used to estimate it. I chose therefore to fix σ_t at 4.5 ps for all the measurement of ϵ_y I performed with the 3-screen method. I chose this value because it is the one of the laser pulse driving the PHIL RF-gun (see Fig. 2.55), which is the only reliable experimental value to estimate the rms bunch length. This choice is rather conservative, because most of my ϵ_y measurements with the 3-screen method have been performed at the Gun RF-phase minimizing the bunch energy spread. At this phase, the bunch is longitudinally compressed in the RF-gun and in the longitudinal drift space following it. The bunch rms length is therefore lower than the one of the laser pulse driving the RF-gun. As a result, the PHIL electron bunch rms length is likely to be lower than 4.5 ps in my 3-screen method measurements. The consequence of fixing it to 4.5 ps rms is therefore a probable underestimation of the space-charge forces, resulting in an overestimation of ϵ_y.

A second one is that I use only three measurements of the bunch rms transverse sizes, which is the minimal number, to determine ϵ_y. Increasing the number of points used to determine ϵ_y would improve the accuracy of this determination. The estimation of the initial bunch rms transverse divergence, namely at the level of the YAG1 screen, would also be improved by an increase in the number of measurement points. In fact, as a reminder, it is determined by fitting the measured bunch rms transverse sizes with a second order polynomial (see end of Sec. 2.2.1.1). When only three measurements are

used, it is therefore determined unequivocally and the accuracy of the determination is minimal.

The last one is that the way I choose to include the effect of the space-charge forces, namely to compute the average of the forces experienced by each individual electron of the bunch, is not accurate enough to model their real effect. In the ASTRA simulations, the effect of the space-charge forces is taken into account by computing them with a Particle In Cell (PIC) algorithm, and then by applying them separately to each individual electron of the bunch.

Systematic measurements

I then perform some systematic measurements of the bunch rms transverse emittance ϵ_y using the 3-screen method, to see if I manage to retrieve the behavior predicted by the ASTRA simulations in Sec. 2.2.1.2.

I first measure ϵ_y for different magnetic field of the B3 solenoid magnet located at the exit of the PHIL RF-gun, that is to say for different focusing of the bunch. To perform the measurements, I use the 3-screen method based on the beam envelope equation with a 3D Gaussian bunch charge density to model the effect of space-charge forces. The reason is this has previously been shown to be the most accurate of the 3-screen methods I used, with an uncertainty on the space-charge forces due to the unknown rms bunch length. Fig. 2.15 shows the results obtained for four different focusing of the bunch, as well as the prediction of the ASTRA simulations.

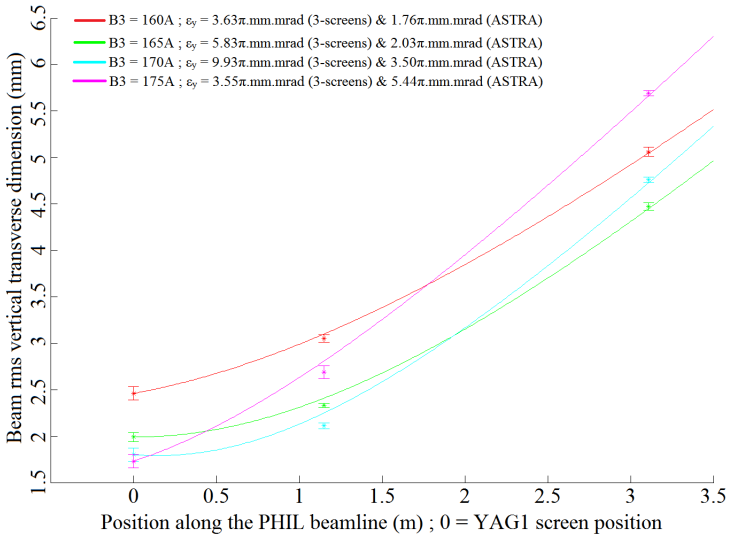

FIGURE *2.15 – Determination of ϵ_y by the 3-screen method using the beam envelope equation, with space-charge forces included assuming a 3D Gaussian bunch charge density (see Eq. 2.5). RF-gun peak accelerating field : 62 MV/m ; Gun RF-phase : minimizing the bunch energy spread ; Bunch energy : 3.55 MeV ; Bunch charge : 100 pC.*

It is visible in Fig. 2.15 that the relative discrepancy with the ASTRA simulations is lower for the two extreme focusing of the bunch, namely B3 = 160 A (red curve) and B3 = 175 A (magenta curve). On the contrary, it is the highest for the two intermediate focusing of the bunch, namely B3 = 165 A (green curve) and B3 = 170 A (cyan curve), in other words when the bunch waist is the closest from the YAG2 screen position. This does not correspond to the behavior which was predicted in Sec. 2.2.1.2 by the ASTRA simulations. In fact, the prediction of Tab. 2.1 was that the relative discrepancy is the lowest when the bunch waist is the closest possible from the YAG2 screen position. The reason explaining this different behavior in the experimental measurements is that, as previously mentioned, I likely underestimate the space-charge forces by fixing the bunch rms length to 4.5 ps during all the bunch motion. As a result, the cases showing the lowest discrepancy with the ASTRA simulations are experimentally the ones where the space-charge forces are the less intense. It is therefore logical that the cases with B3 = 160 A (red curve) and B3 = 175 A (magenta curve) present the lowest discrepancy, since it is for these cases that the bunch rms transverse sizes are the highest all along the bunch motion.

I then measure ϵ_y for two different bunch mean energies, namely 3.55 MeV and 4.47 MeV, in similar focusing conditions of the B3 solenoid magnet. Once again, I use the 3-screen method based on the beam envelope equation with a 3D Gaussian bunch charge density to model the effect of space-charge forces to perform these measurements. Fig. 2.16 shows the results obtained for these two energies, as well as the prediction of the ASTRA simulations.

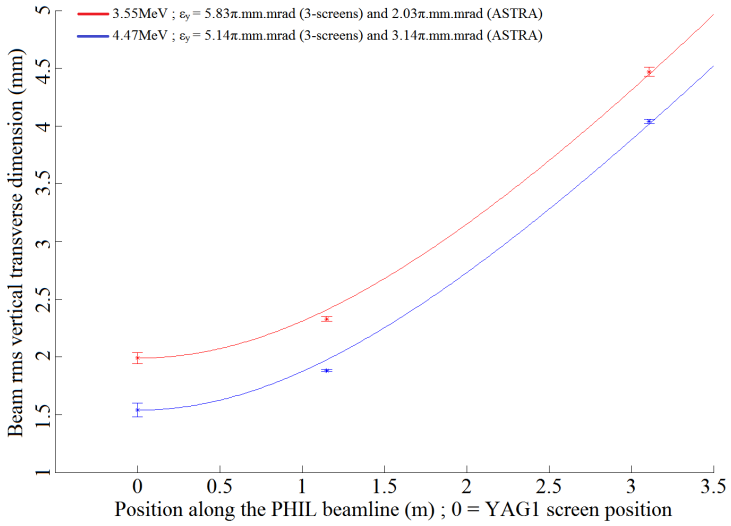

FIGURE *2.16 – Determination of ϵ_y by the 3-screen method using the beam envelope equation, with space-charge forces included assuming a 3D Gaussian bunch charge density (see Eq. 2.5). RF-gun peak accelerating field : 62 MV/m (red curve) and 78 MV/m (blue curve) ; Gun RF-phase : minimizing the bunch energy spread ; Bunch charge : 100 pC (red curve) and 135 pC (blue curve). Current injected in the B3 solenoid magnet at the RF-gun exit : 165 A (red curve) and 205 A (blue curve).*

Fig. 2.16 shows that the relative discrepancy between the experimental measurements and the ASTRA simulations decreases when the bunch energy increases. Indeed, it is 187% at 3.55 MeV and 63.7% at 4.47 MeV which starts to become acceptable. This decrease is simply due to the decrease in space-charge forces and has been predicted in Tab. 2.1 of Sec. 2.2.1.2.

2.2.1.4 Conclusions

The classical 3-screen method, namely with a pure drift space between the 3 screens and without inclusion of the space-charge forces, is not at all suitable to perform the measurement of the rms transverse emittance of a 100 pC and few MeV electron bunch generated by an RF-gun. In fact, the discrepancy with the ASTRA simulations can be up to 900% (namely a factor of ten). The two main reasons for this large discrepancy are the omission of the space-charge forces and the fact that I use only three measurement points, which is the minimum, to perform this classical 3-screen method.

The inclusion of the space-charge forces via the formalism of the beam envelope equation leads to a significant gain by strongly decreasing the discrepancy with the ASTRA simulations, especially when a 3D Gaussian bunch charge density is used to model the effects of space-charge forces [16]. However, the agreement with the ASTRA simulations is still not satisfactory since the discrepancy is 63.7% at minimum for a bunch energy of 4.47 MeV and a bunch charge of 135 pC. It is only a little lower than the prediction of ASTRA simulations in Tab. 2.1 of Sec. 2.2.1.2, which has been performed for the classical 3-screen method with no space-charge forces included. However, it does not mean that the model and the algorithm developed at the end of Sec. 2.2.1.1 are not suitable to perform the measurement of the bunch rms transverse emittance. Indeed, as previously mentioned, the measurements are limited on PHIL by the current impossibility to precisely know the rms bunch length. It required me to fix it to the one of the laser pulse driving the RF-gun (4.5 ps rms), which is very likely to underestimate the space-charge forces effects and therefore to overestimate the bunch rms transverse emittance.

2.2.2 The 3-gradient method for bunch transverse emittance measurement

2.2.2.1 Theoretical principles

The 3-gradient method is a multiparametric method allowing measuring the bunch transverse emittance from the measurement of its transverse sizes at one measurement point of the beamline for different focusing forces of a magnetic element located before this measurement point. The classical 3-gradient method, which I will present hereafter, corresponds to the case where the space between the focusing magnetic element and the bunch transverse sizes measurement point is a pure drift space of length L_α. The reconstructed bunch transverse emittance is then the one at the entrance of the magnetic

16. The laser of PHIL has a 3D Gaussian energy density.

element from which we vary the focusing force. However, any known linear optics could be included, through their transfer matrices, before this magnetic element, between this magnetic element and the bunch transverse sizes measurement point and after the bunch transverse sizes measurement point.

During my thesis, I perform the 3-gradient method only with solenoid magnets. We will only consider this kind of magnet thereafter. The transverse transfer matrix for this kind of magnet is given by [89, 90] :

$$\begin{pmatrix} C^2 & \frac{2SC}{K} & SC & \frac{2S^2}{K} \\ -\frac{KSC}{2} & C^2 & -\frac{KS^2}{2} & SC \\ -SC & -\frac{2S^2}{K} & C^2 & \frac{2SC}{K} \\ \frac{KS^2}{2} & -SC & -\frac{KSC}{2} & C^2 \end{pmatrix}$$

where $C = cos(\theta)$ and $S = sin(\theta)$. We have $\theta = \frac{eB_m l_m c}{2pc}$ where B_m is the peak magnetic field of the solenoid, l_m the magnetic length of the solenoid, p the mean momentum of the bunch and c the speed of light in vacuum. Finally, $K = \frac{eB_m c}{pc}$ is the strength parameter of the solenoid.

To establish the model it is necessary to perform several approximations. First of all, we neglect the effect of space-charge forces between the entrance of the solenoid magnet from which we vary the focusing force and the point of transverse sizes measurement. This approximation is becoming more important as the bunch energy decreases, since the space-charge forces effect is then increasing. It allows assuming that the bunch transverse emittance is invariant between these points and that the bunch transport is linear and can be determined thanks to a transfer matrix M_T which is the product of the transfer matrix of the drift with length L_α by the transfer matrix of the used solenoid magnet :

$$M_T = \begin{pmatrix} 1 & L_\alpha & 0 & 0 \\ 0 & 1 & 0 & 0 \\ 0 & 0 & 1 & L_\alpha \\ 0 & 0 & 0 & 1 \end{pmatrix} \begin{pmatrix} C^2 & \frac{2SC}{K} & SC & \frac{2S^2}{K} \\ -\frac{KSC}{2} & C^2 & -\frac{KS^2}{2} & SC \\ -SC & -\frac{2S^2}{K} & C^2 & \frac{2SC}{K} \\ \frac{KS^2}{2} & -SC & -\frac{KSC}{2} & C^2 \end{pmatrix} = \begin{pmatrix} a & c & d & e \\ -f & b & -g & h \\ -d & -e & a & c \\ g & -h & -f & b \end{pmatrix}$$

with $a = C^2 - \frac{KL_\alpha SC}{2}$, $b = C^2$, $c = \frac{2SC}{K} + L_\alpha C^2$, $d = SC - \frac{KL_\alpha S^2}{2}$, $e = \frac{2S^2}{K} + L_\alpha SC$, $f = \frac{KSC}{2}$, $g = \frac{KS^2}{2}$ and $h = SC$.

The other approximation is to neglect the coupling between the two transverse directions, horizontal (x) and vertical (y). This is particularly an approximation when a solenoid magnet located upstream of the one performing the 3-gradient method is used. Indeed, this kind of magnet strongly couples the two transverse directions. Anyway, there is always at least a residual coupling. It allows assuming that the bunch transport is separated along the two transverse directions, namely that the beam matrix Σ is of the following form :

$$\Sigma = \begin{pmatrix} \epsilon_x\beta_x & -\epsilon_x\alpha_x & 0 & 0 \\ -\epsilon_x\alpha_x & \epsilon_x\gamma_x & 0 & 0 \\ 0 & 0 & \epsilon_y\beta_y & -\epsilon_y\alpha_y \\ 0 & 0 & -\epsilon_y\alpha_y & \epsilon_y\gamma_y \end{pmatrix}$$

where ϵ_x and ϵ_y are respectively the bunch horizontal and vertical transverse emittances and β_x, β_y, α_x, α_y, γ_x, γ_y are the bunch horizontal and vertical Twiss parameters.

The transport of the beam matrix Σ between the entrance of the solenoid magnet from which we vary the focusing force (i subscript) and the point of transverse sizes measurement (f subscript) is given by :

$$\Sigma_f = M_T \Sigma_i M_T^t$$

The experimentally exploitable equations are those concerning $\epsilon_x\beta_{x_f}$ and $\epsilon_y\beta_{y_f}$, since these two quantities are actually the bunch transverse sizes σ_{x_f} and σ_{y_f} squared. They are linked to the components of Σ_i by :

$$\begin{cases} \sigma_{x_f}^2 = a^2\epsilon_x\beta_{x_i} - 2ac\epsilon_x\alpha_{x_i} + c^2\epsilon_x\gamma_{x_i} + d^2\epsilon_y\beta_{y_i} - 2de\epsilon_y\alpha_{y_i} + e^2\epsilon_y\gamma_{y_i} \\ \sigma_{y_f}^2 = d^2\epsilon_x\beta_{x_i} - 2de\epsilon_x\alpha_{x_i} + e^2\epsilon_x\gamma_{x_i} + a^2\epsilon_y\beta_{y_i} - 2ac\epsilon_y\alpha_{y_i} + c^2\epsilon_y\gamma_{y_i} \end{cases}$$

By measuring σ_{x_f} and/or σ_{y_f} for at least 6 different experimental conditions, namely 6 different focusing force of the solenoid magnet, the least squares method allows extracting the components of Σ_i from the two equations above. However, it has been shown by M'Garrech Slah in his thesis that using the two equations above separately leads to an inaccurate determination of these parameters [90]. To improve the accuracy of the obtained results, it is preferable to use the following system of equations :

$$\sigma_{x_f}^2 - \sigma_{y_f}^2 = (a^2 - d^2)(\epsilon_x\beta_{x_i} - \epsilon_y\beta_{y_i}) + 2(ac - de)(\epsilon_y\alpha_{y_i} - \epsilon_x\alpha_{x_i}) + (c^2 - e^2)(\epsilon_x\gamma_{x_i} - \epsilon_y\gamma_{y_i})$$

$$\sigma_{x_f}^2 + \sigma_{y_f}^2 = (a^2 + d^2)(\epsilon_x\beta_{x_i} + \epsilon_y\beta_{y_i}) + 2(ac + de)(\epsilon_y\alpha_{y_i} - \epsilon_x\alpha_{x_i}) + (c^2 + e^2)(\epsilon_x\gamma_{x_i} + \epsilon_y\gamma_{y_i})$$

It is now sufficient to measure the bunch transverse sizes σ_{x_f} and σ_{y_f} for at least 3 different focusing force of the solenoid magnet, hence the name of 3-gradient method. The least squares method allows then extracting, from the two equations above, the sums and differences of the Σ_i components along the x and y directions. It is subsequently easy to deduce the components of Σ_i. Knowing that $\beta_{x_i}\gamma_{x_i} - \alpha_{x_i}^2 = \beta_{y_i}\gamma_{y_i} - \alpha_{y_i}^2 = 1$, the bunch transverse emittances are finally given by these formulas :

$$\begin{cases} \epsilon_x = \sqrt{(\epsilon_x\beta_{x_i})(\epsilon_x\gamma_{x_i}) - (\epsilon_x\alpha_{x_i})^2} \\ \epsilon_y = \sqrt{(\epsilon_y\beta_{y_i})(\epsilon_y\gamma_{y_i}) - (\epsilon_y\alpha_{y_i})^2} \end{cases}$$

It is important to note that, to optimize the accuracy of the least squares method, it is necessary to maximize the number of different focusing forces used for the solenoid magnet and to symmetrize these forces with respect to the one minimizing the bunch transverse sizes.

The bunch transverse emittances ϵ_x and ϵ_y are then determined, but it remains to determine the error bars on them. To do that, I chose to use the 3-gradient method explained above in combination with a Monte-Carlo algorithm. Concretely, I drew 100000 series of bunch transverse sizes according to Gaussian distributions having as mean values the measured values of bunch transverse sizes and as standard deviations the uncertainties on these measurements. I then deduced ϵ_x and ϵ_y for each of the 100000 series. I obtained in this way 100000 values of ϵ_x and ϵ_y. The values of ϵ_x and ϵ_y are finally the means of these 100000 values and the uncertainties on them are the standard deviations of these 100000 values.

2.2.2.2 Evaluation of the precision on PHIL

The goal of this section is to present the results obtained by applying the 3-gradient method to measure the bunch transverse emittance on simulations performed with the ASTRA beam dynamics code. This allows estimating the accuracy that one can hope to achieve experimentally with this method, provided that the operation of the used accelerator is well understood and correctly modeled in ASTRA. The 3-gradient method was thus tested in the context of PHIL accelerator at LAL (see Fig. 1.24). The theoretical principles of this method have already been presented previously (see Sec. 2.2.1). The bunches simulated in this study are transversely round and have therefore very close transverse emittances along the two transverse directions x and y. I will only present the transverse emittances along x thereafter.

To test the 3-gradient method, it is sufficient to pick up the bunch rms transverse sizes computed by ASTRA at the position of one of the PHIL beamline YAG screens for different values of the focusing magnetic field of a solenoid located upstream this screen (See Fig. 1.24). We then obtain a transverse sizes scan as a function of the solenoid magnetic field, from which the bunch rms transverse emittances can be extracted. These values are then compared with those computed by ASTRA. I used a Gaussian initial particles distribution with $\sigma_t = 3.6$ ps rms, $\sigma_x = \sigma_y = 1$ mm rms and a typical bunch charge of 100 pC.

This study has been performed for 3 different peak accelerating fields in the PHIN RF-gun on PHIL : 50 MV/m, 65 MV/m and 80 MV/m. It corresponds respectively to mean bunch energies of 3.16 MeV, 4.13 MeV and 5.09 MeV. I test the method on the YAG2 and YAG3 screens while varying the magnetic field of the B5 solenoid at the middle of PHIL beamline, such that the elevation in either side of the transverse sizes minimum is the same. This has been done each time taking into account and not taking into account the space-charge force in the ASTRA simulations. Tab. 2.2 gathers the obtained results without taking into account the space-charge forces in the ASTRA simulations.

case	beam energy (MeV)	space-charge force in ASTRA	screen	ε_x ASTRA (π.mm.mrad)	εx 3-gradients (π.mm.mrad)	relative deviation
1	3,16	no	YAG2	0,8527	1,285	50,70%
2	3,16	no	YAG3	0,8527	0,7138	19,46%
3	4,13	no	YAG2	0,8582	1,655	92,80%
4	4,13	no	YAG3	0,8582	1,03	20,00%
5	5,09	no	YAG2	1,035	2,477	139,00%
6	5,09	no	YAG3	1,035	1,478	42,80%

TABLE *2.2 – Results of ASTRA simulations for evaluating the 3-gradient method accuracy without space-charge forces. Gun RF-phase : maximizing the bunch mean energy.*

These cases are very informative about the accuracy of the transfer matrix used to model the effect of the solenoid magnet on the electron bunch. In fact, in all these cases we observe that the relative deviation between the emittances deduced by the 3-gradient method and the emittance predicted by ASTRA is smaller when using YAG3 screen than when using YAG2 screen. The only difference is the distance between the B5 solenoid and the YAG screen, which is around 0.73 m for YAG2 and around 3.1 m for YAG3. In other words, the only difference is that the magnetic field used to focus the bunch on YAG3 is smaller (by a factor around 2) than the one used to focus the bunch on YAG2. We can therefore conclude that the transfer matrix used to model a solenoid magnet becomes less accurate when its magnetic field is increasing. This conclusion is bolstered by the fact that the relative deviation is increasing when the bunch energy is increasing. Indeed, when the bunch energy is increasing it becomes more rigid and an higher magnetic field is required to focus it.

Tab. 2.3 gathers the obtained results when the space-charge force is taken into account in the ASTRA simulations.

case	beam energy (MeV)	space-charge force in ASTRA	screen	ε_x ASTRA (π.mm.mrad)	εx 3-gradients (π.mm.mrad)	relative deviation
1	3,16	yes	YAG2	4,716	1,823	159,00%
2	3,16	yes	YAG3	4,716	4,186	12,66%
3	4,13	yes	YAG2	4,082	2,011	103,00%
4	4,13	yes	YAG3	4,082	3,947	3,42%
5	5,09	yes	YAG2	3,562	2,117	68,26%
6	5,09	yes	YAG3	3,562	3,161	12,69%

TABLE *2.3 – Results of ASTRA simulations for evaluating the 3-gradient method accuracy with space-charge forces. Bunch charge : 100 pC ; Gun RF-phase : maximizing the bunch mean energy.*

We observe the same behavior between YAG2 and YAG3 screen as without space-charge forces, and the reason is the same. We also observe that the relative deviation between the emittances deduced by the 3-gradient method and the emittance predicted by ASTRA is first decreasing between 3.16 MeV bunch energy (12.7%) and 4.13 MeV bunch energy (3.4%), and then increasing again between 4.13 MeV bunch energy (3.4%) and 5.09 MeV bunch energy (12.7%). The decrease between 3.16 MeV and 4.13 MeV is

explained by the decrease in space-charge forces, which are not taken into account in the 3-gradient method. There is also a decrease in space-charge forces between 4.13 MeV and 5.09 MeV, but this decrease is compensated by the increase in the magnetic field required to focus the bunch which causes a degradation of the 3-gradient method accuracy as previously mentioned.

One can remark, by comparing Tab. 2.1 and Tab. 2.3, that the accuracy achieved in the transverse emittance reconstruction with the 3-gradient method is better than the one achieved with the 3-screen method, especially at low bunch energy (3.16 MeV). It is explained by the fact that these two methods are least-squares based methods, and become therefore more accurate when the number of used measurement points increases. The number of used measurement points in 3-gradient method is typically 10 or more [17], while it is only 3 (on PHIL) for the 3-screen method. This explains the better accuracy of the 3-gradient method predicted by ASTRA.

Finally it could be said that, on PHIL, the 3-gradient method could allow a transverse emittance measurement with an accuracy better than 15% between 3 MeV and 5 MeV bunch energy, and even better than 5% around 4 MeV, if the B5 solenoid magnet and the YAG3 screen are used to perform this measurement (see Fig. 1.24).

2.2.2.3 Experimental measurements

All the experimental bunch transverse emittance measurements that I performed by the 3-gradient method have been carried out on the PHIL facility, with the B5 solenoid magnet and the YAG2 screen or with the B5 solenoid magnet and the YAG3 screen (see Fig. 1.24). I choose not to perform this measurement with the B3 solenoid magnet and the YAG1 screen. The reason is that the magnetic field of B3 acts in the RF-gun, where the bunch energy is not constant. It is therefore impossible to apply the 3-gradient method, which requires the knowledge of the bunch energy at the solenoid.

Example measurement

I will first of all detail the bunch rms transverse emittances ϵ_x and ϵ_y determination through an example. Fig. 2.17 shows an example of the bunch transverse sizes σ_x and σ_y, measurement with the YAG2 screen as a function of the peak magnetic field generated by the B5 solenoid magnet.

The bunch rms transverse emittances are then extracted from Fig. 2.17 by using the Monte-Carlo algorithm detailed in Sec. 2.2.2.1. Fig. 2.18 shows the histogram containing all the values obtained for the bunch rms transverse vertical emittance ϵ_y, in the selected example, after application of this Monte-Carlo algorithm on the data of Fig. 2.17. This histogram allows determining $\epsilon_y = 2.78 \pm 0.07\ \pi$.mm.mrad. This experimental value is quite close to the $\epsilon_y = 1.64\ \pi$.mm.mrad predicted by the ASTRA simulation, the

17. It could therefore better be renamed multi-gradient method but the term 3-gradient method is conventional.

discrepancy being of 65.2%.

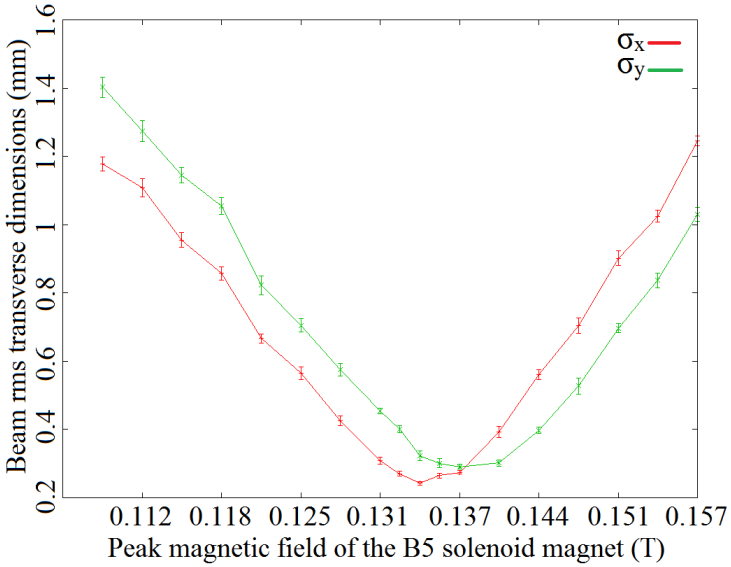

FIGURE *2.17 – Bunch transverse rms sizes σ_x and σ_y measured with the YAG2 screen as a function of the peak magnetic field generated by the B5 solenoid magnet. RF-gun peak accelerating field : 63 MV/m ; Gun RF-phase : minimizing the bunch energy spread ; Bunch energy : 3.67 MeV ; Bunch charge : 46 pC ; Current injected in B3 : 155 A.*

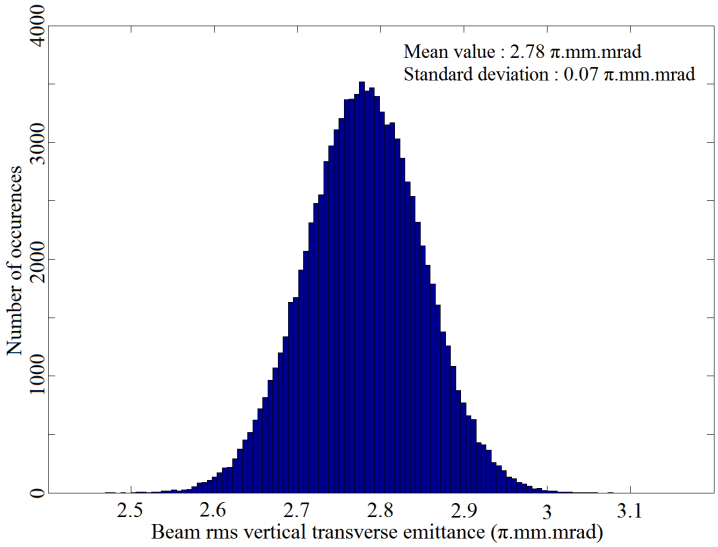

FIGURE *2.18 – Histogram of ϵ_y obtained after application of the Monte-Carlo algorithm described in Sec. 2.2.2.1 on the data of Fig. 2.17. Experimental conditions : see Fig. 2.17.*

Once ϵ_y is determined, the Twiss parameters of the bunch, β_y, γ_y and α_y can also be determined. Finally, the Twiss ellipse of the bunch can be computed in the plane $(y; y')$ because it is the one defined by the following equation : $\gamma_y y^2 + 2\alpha y y' + \beta_y y'^2 = \epsilon_y$.

The Twiss ellipse contains 39% of the bunch particles, around the bunch center, if the bunch has a Gaussian distribution for the particle transverse positions and divergences. This Twiss ellipse is very useful, since it allows visualizing at a glance the bunch rms transverse size, the bunch rms transverse divergence and the orientation of the bunch in its transverse phase space. This last point allows deducing if the bunch is convergent, divergent or at a waist. Fig. 2.19 shows the histogram obtained for β_y (a), γ_y (b) and α_y (c) in the selected example. It also shows the horizontal and vertical bunch Twiss ellipses deduced from this calculation (d).

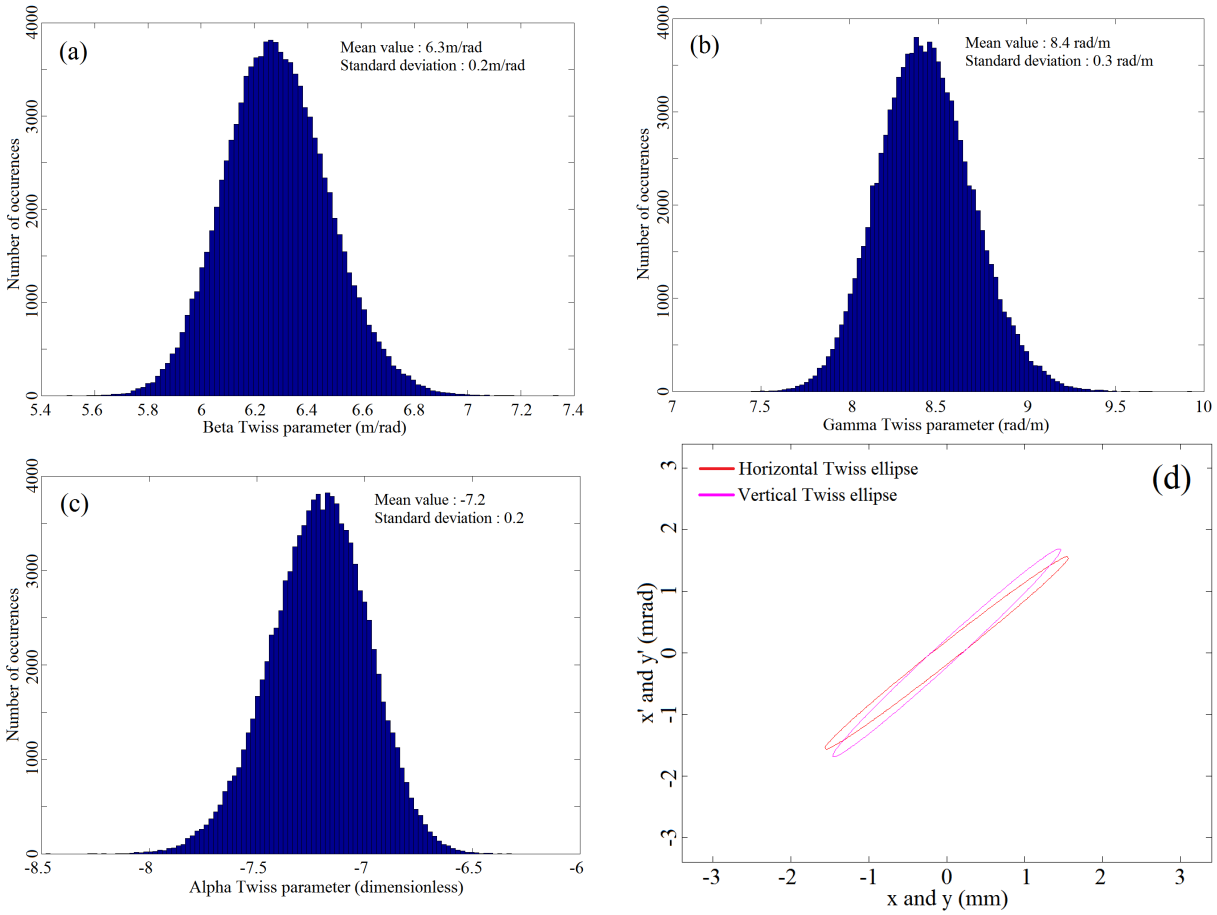

FIGURE *2.19 – Histograms obtained for β_y (a), γ_y (b) and α_y (c) from Fig. 2.17. Horizontal and vertical Twiss ellipses obtained from Fig. 2.17 (d). Experimental conditions : see Fig. 2.17.*

It is clearly visible in Fig. 2.19 (d) that the bunch is horizontally and vertically divergent at the entrance of the B5 solenoid magnet, and it has been indeed experimentally observed and predicted by the ASTRA simulation. It is also visible in Fig. 2.19 (d) that the orientations of the horizontal and vertical Twiss ellipses are not the same. It means that the divergences of the bunch are not the same along the horizontal and vertical transverse directions. This fact explains the different peak magnetic fields of B5 which are necessary to reach the minima of bunch rms transverse sizes on the YAG2 screen (0.134 T for the

horizontal direction and 0.138 T for the vertical direction). This asymmetry of the bunch along the two transverse directions is directly due to the asymmetry of the transverse profile of the laser pulse used to generate the bunch. In fact, it has rms transverse sizes of $\sigma_x = 0.360 \pm 0.003$ mm and $\sigma_y = 0.299 \pm 0.003$ mm (see Fig. 2.20).

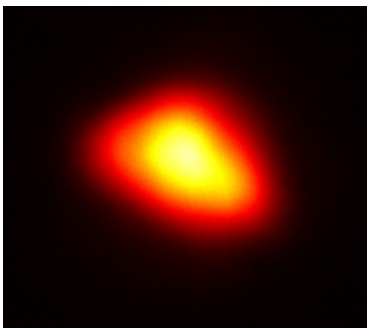

FIGURE *2.20 – Transverse profile of the laser pulse generating the bunch at PHIL for the measurement of Fig. 2.17. The image size is 171 ∗ 151 pixel* ^{2} *and one pixel corresponds to 15.5 µm.*

Systematic measurements

I then performed some systematic measurements of the bunch rms transverse emittance using the 3-gradient method, to see if I manage to retrieve the behavior predicted by the ASTRA simulations in Sec. 2.2.2.2.

I first measure ϵ_y, with the B5 solenoid magnet and the YAG2 screen, as a function of the bunch mean energy for two different bunch charge configurations. The first one with a low bunch charge, namely around 10 pC, for the following bunch energies : 4.47 MeV, 3.55 MeV and 2.95 MeV. The second one with a high bunch charge, namely around 100 pC, for the following bunch energies : 4.47 MeV, 3.55 MeV, 3.32 MeV and 3.09 MeV. Fig. 2.21 shows the obtained values for ϵ_y with the 3-gradient method, as well as the ones simulated with ASTRA, for the low bunch charge (a) and the high bunch charge (b).

Many things are notable in Fig. 2.21. The first one is that the behavior of the ϵ_y curves measured by the 3-gradient method relatively to the curves simulated by ASTRA is different between the two bunch charge configurations. On one hand, there is an almost constant gap of about 0.6 π.mm.mrad for the bunch charge around 10 pC, but the shapes of the curves are the same. On the other hand, the behavior is much more erratic for the bunch charge around 100 pC, since the measured ϵ_y curves cross two times the simulated one.

The most important thing to notice is the behavior of the relative discrepancy between ϵ_y measured by the 3-gradient method and the one simulated by ASTRA as a function of the bunch mean energy (blue curves in Fig. 2.21). It is clearly visible that it is decreasing when the bunch energy increases for the bunch charge around 100 pC, while it is increasing with the bunch energy for the bunch charge around 10 pC, namely with almost no space-charge forces. These two opposite behaviors have been predicted by the ASTRA si-

mulations in Sec. 2.2.2.2 (see Tab. 2.2 for the case with no space-charge forces and Tab. 2.3 for the case with a bunch charge of 100 pC). One can also see that the values of the relative discrepancy measured in Fig. 2.21 (a) for the bunch charge around 10 pC are very close to the ones predicted in Tab. 2.2 of Sec. 2.2.2.2 for the case with no space-charge forces. The fact that ϵ_y measured by the 3-gradient method is systematically higher than the one simulated by ASTRA has also been predicted in Tab. 2.2. The behavior is different for the relative discrepancy measured in Fig. 2.21 (b) for the bunch charge around 100 pC. In fact, it was predicted in Tab. 2.3 of Sec. 2.2.2.2 that ϵ_y measured by the 3-gradient method would be systematically lower than the one simulated by ASTRA. This is not what is experimentally observed in Fig. 2.21 (b). Most importantly, the experimentally measured relative discrepancies in Fig. 2.21 (b) are much lower than the ones predicted in Tab. 2.3 of Sec. 2.2.2.2, which is surprising but obviously a good thing.

Finally, the measurements shown in Fig. 2.21 (b) prove that the 3-gradient method, with the B5 solenoid magnet and the YAG2 screen, is perfectly suitable to perform the measurement of the bunch rms transverse emittance of a 100 pC and few MeV electron bunch generated by an RF-gun, despite the numerous approximations performed to establish it (see Sec. 2.2.2.1) and especially the omission of the space-charge forces. In fact, the discrepancy with the ASTRA simulations is lower than 50% above 3 MeV and becomes even lower than 20% above 3.6 MeV.

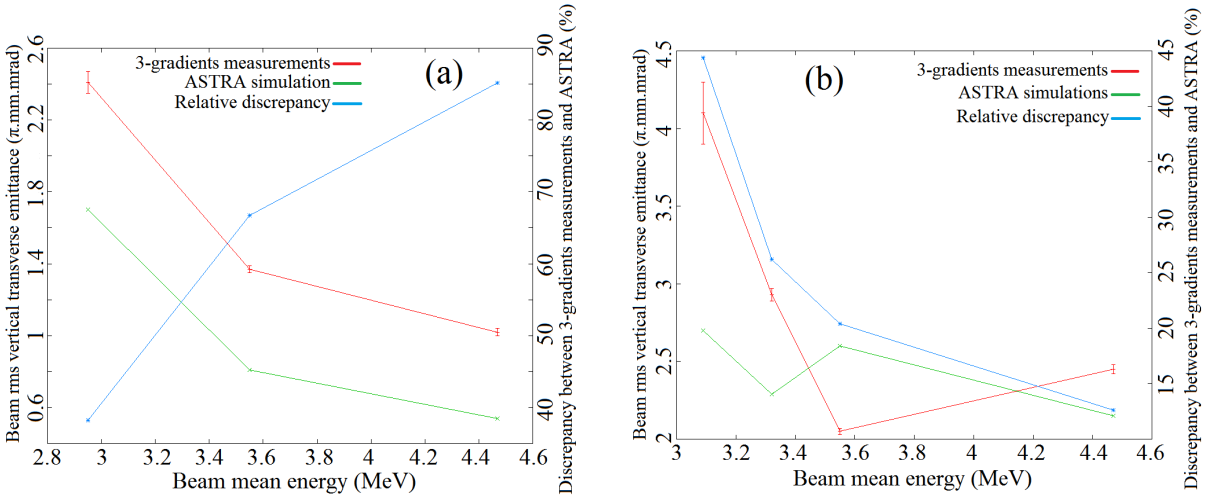

FIGURE *2.21 – Comparison between ϵ_y measured by the 3-gradient method, with B5 and the YAG2 screen, and the one simulated by ASTRA as a function of the bunch mean energy, for a bunch charge around 10 pC (a) and a bunch charge around 100 pC (b).*

I then compared the ϵ_y values measured by using the 3-gradient method with the YAG2 screen and the YAG3 screen, both in conjunction with the B5 solenoid magnet.

I first perform a comparison for a bunch charge around 100 pC and a bunch mean energy around 3.35MeV. In both cases, the current injected in the B3 solenoid magnet at the RF-gun exit was of 155 A. Fig. 2.22 shows the measured bunch rms transverse sizes, as a function of the current injected in the B5 solenoid magnet, on the two YAG screens.

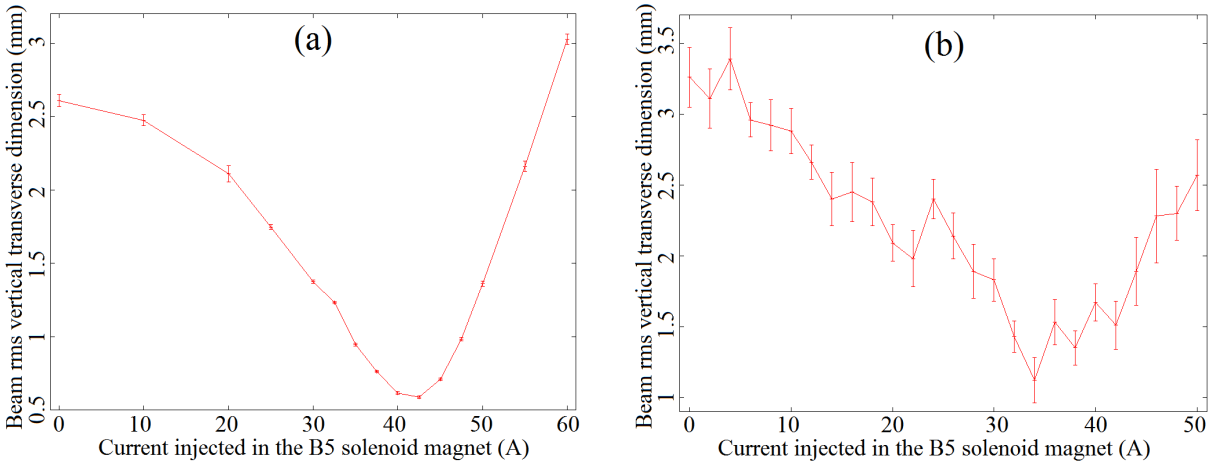

FIGURE *2.22 – Bunch transverse rms vertical sizes measured with the YAG2 screen (a) and YAG3 screen (b) as a function of the current injected in the B5 solenoid magnet. RF-gun peak accelerating field : 57.5 MV/m ; Gun RF-phase : minimizing the bunch energy spread ; Bunch energy : 3.35 MeV ; Bunch charge : 100 pC ; Current injected in B3 : 155 A.*

When using the YAG2 screen (see Fig. 2.22 (a)), the measured value of ϵ_y is 2.93 $\pm$ 0.04 π.mm.mrad and the ASTRA simulated one is 2.29 π.mm.mrad, resulting in a discrepancy of 26.2%. When using the YAG3 screen (see Fig. 2.22 (b)), the measured value of ϵ_y is 1.9 $\pm$ 0.1 π.mm.mrad and the ASTRA simulated one is 1.86 π.mm.mrad, resulting in a zero discrepancy. This lower discrepancy when using the YAG3 screen instead of the YAG2 screen, for a bunch around 3.35 MeV and 100 pC, has been predicted in Tab. 2.3 of Sec. 2.2.2.2.

One can note higher error bars on the measurements performed with the YAG3 screen. This is not due to the use of the YAG3 screen, but to the fact that the measurements on the two YAG screens have been performed on different days. The PHIL facility was simply less stable during the measurement with the YAG3 screen. The fact that the two measurements have been performed on different days also explains the different value of ϵ_y predicted by the ASTRA simulations. It is just due to the fact that the measured transverse size of the laser pulse driving the RF-gun was not exactly the same on these two days. However, these two facts do not call into question the conclusion of the comparison.

2.2.2.4 Conclusions

First and foremost, it has been demonstrated in this section that the 3-gradient method performed with a solenoid magnet (B5 at PHIL) and a YAG screen located around 1 m downstream (YAG2 at PHIL) is perfectly suitable to measure the rms transverse emittance of a 100 pC and few MeV electron bunch, which are the typical operation conditions of PHIL. In fact, the discrepancy with the ASTRA simulations is lower than 50% above 3 MeV and becomes even lower than 20% above 3.6 MeV (see Fig. 2.21 (b)). It has also been tested on one example, around 3.35 MeV and 100 pC, that performing

the 3-gradient method with a YAG screen located farther (YAG3 is 3 m away from B5 at PHIL) brings a benefit by decreasing the discrepancy with the ASTRA simulations. This is due to the fact that the magnetic field required to focus the bunch on this farther screen is lowered. Indeed, as it has previously been shown, the modeling of a solenoid magnet by its transfer matrix becomes more accurate when its magnetic field decreases.

Another very interesting important point which has been demonstrated in this section is that the measurement with the 3-gradient method at high bunch charge (100 pC) becomes more accurate when the bunch energy increases (see Fig. 2.21 (b)). It is explained by the fact that, for this high bunch charge, the dominant source of discrepancy with the ASTRA simulations is the space-charge forces, which are omitted in the 3-gradient method and reduced when the bunch energy increases. On the other hand, the 3-gradient method at low bunch charge, namely with almost no space-charge forces, becomes more accurate when the bunch energy decreases (see Fig. 2.21 (a)). It is explained by the fact that the dominant source of discrepancy with the ASTRA simulations becomes then the modeling of a solenoid magnet by its transfer matrix, which is more accurate when its magnetic field decreases therefore when the bunch energy decreases too. This different behavior as a function of the bunch charge has been first predicted by the ASTRA simulations in Sec. 2.2.2.2 and then experimentally proven in Sec. 2.2.2.3.

One can finally remark that the 3-gradient method is far more accurate than the classical 3-screen method presented in Sec. 2.2.1 [18]. In fact, for similar experimental conditions, the discrepancy with ASTRA simulations can be up to 900% for a 3.5 MeV and 100 pC bunch with the classical 3-screen method, while it is between 20% and 30% with the 3-gradient method. This major difference is due to the fact that I use only 3 measurement points, which is the minimum, to perform the 3-screen method, while I use more than ten points to perform the 3-gradient method thus improving its accuracy. It allows concluding that the 3-gradient method is more suitable than the 3-screen one to measure the bunch rms transverse emittance, since it is cheaper and technically easier to use one solenoid magnet and one YAG screen than using ten YAG screens or more.

18. The 3-screen method with a pure drift space between the three screens and without taking into account the space-charge force.

2.3 Longitudinal measurements

2.3.1 Measurement of the bunch kinetic energy thanks to a steerer magnet

Currently on PHIL (see Fig. 1.24), the bunch kinetic energy is measured thanks to the dipole magnet in 2 different ways. The first possibility is to search the dipole magnetic field for which the charge measured by the Faraday Cup n°2 is maximum after the slits system. We deduce then the bunch energy. This is equivalent to saying that the bunch energy corresponds to the maximum of the bunch energy spectrum. This choice is therefore strongly arguable in the cases where the bunch energy spectrum presents a wide summit plateau and/or is strongly asymmetric, which is for example the case as soon as one moves away from the RF-gun phase minimizing the bunch energy spread.

The second possibility is then to use the slit system located after the dipole magnet and to ramp its magnetic field to reconstruct the bunch energy spectrum thanks to a measurement by the Faraday Cup n°2, or by the YAG4 screen, of the charge passing the slits. One can then extract from this spectrum the mean energy which is a more relevant quantity than the energy at the intensity maximum. The problem is that, due to the lack of automating at PHIL, this measurement is quite long to obtain a good precision. In fact, more than half an hour is typically required to acquire one bunch energy spectrum.

There is another possibility to measure the bunch mean kinetic energy without reconstructing the bunch energy spectrum, therefore without the dipole magnet. This method consists in varying the magnetic field of a steering magnet, and to measure simultaneously the induced displacement of the bunch transverse barycenter on a YAG screen located downstream of this steerer. The advantage of this method is an important gain of time with respect to the acquisition of an energy spectrum. It also allows avoiding the problem of transverse alignment at the entrance of a dipole magnet, which is crucial for bunch energy measurement.

2.3.1.1 Theoretical calculation

Let consider a configuration of the used steerer magnet and YAG screen as depicted in Fig. 2.23. L is the distance between the steerer entrance and the YAG screen, l is the magnetic length of the steerer, θ is the deviation angle induced by the steerer on the bunch, ρ is the curvature radius of the bunch path in the steerer and x is the displacement generated on the YAG screen with respect to the case where the steerer is turned off.

The basic assumption of the method is to consider that the steerer has a negligible thickness and therefore acts as a thin lens. One has to be careful that this does not mean $l = 0$. This allows then assuming that the traveled distance in the steerer ($\rho\theta$) is equal to its magnetic length l, and that the bunch trajectory crossing the YAG screen forms a right-angled triangle with the trajectory in case of turned-off steerer (see Fig. 2.23). The validity criterion for this hypothesis can be explained by the following simple inequality : $L >> l$. Another important assumption is to keep small the θ angle. It is verified if L is

much greater than the YAG screen radius, which is around a few centimeters. However, it is convenient not to take too high a value for L. Otherwise the bunch would be visible on the YAG screen only for a very (too) small steerer field range, which would limit the energy measurement precision.

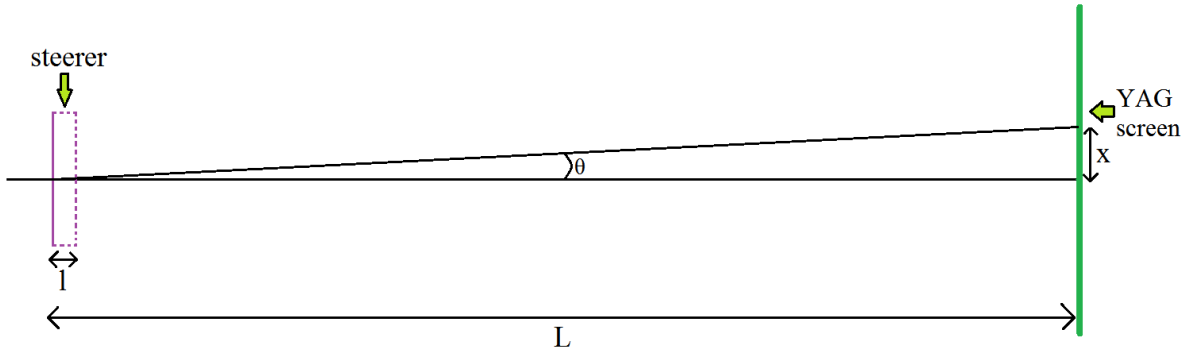

FIGURE *2.23 – Scheme of the considered situation; l = magnetic length of the steerer; L = distance between steerer center and YAG screen; θ = deviation angle induces by the steerer; x = bunch barycenter displacement on the YAG screen with respect to the case where the steerer is turned off.*

Starting from $l \approx \rho\theta$, we have to substitute ρ which is unknown. To do that it is sufficient to multiply by the steerer magnetic field B to recognize the bunch magnetic rigidity $B\rho$ which is equal to $\frac{p}{e}$, where p is the electron bunch mean momentum. We have then $p \approx \frac{eBl}{\theta}$. We still have to substitute θ, which can be written $\theta \approx arctan(\frac{x}{L}) \approx \frac{x}{L}$ taking into account the assumptions previously made. We then obtain the bunch mean momentum by $p \approx \frac{eBlL}{x}$, from which one easily obtains the bunch mean energy $E = \sqrt{p^2c^2 + m^2c^4} - mc^2$.

In practice, in order to minimize the uncertainty on E we do not measure only one value of x. We vary the B field to measure several values of x, then we plot the $x(B)$ curve. We then perform a linear fit on this curve, which has $d = \frac{elL}{p}$ as a slope. We finally extract p and E from this slope. It is noteworthy that the uncertainty on E will not take into account the various approximations used to establish this model.

2.3.1.2 Determination of the PHIL steerers magnetic length

One of the most difficult and hazardous steps of this study was to estimate the magnetic length of PHIL steerers, which is the same for both. The magnetic length of a magnetic element is by definition given by $l = \frac{1}{B_0}\int_{Oz-axis} B(z)\,\mathrm{d}z$, where Oz is the element axis, $B(z)$ is the field strength on this axis and B_0 the peak value of $B(z)$. To compute it, I had to use an axial profile of the PHIL steerers magnetic field [19]. It is shown in Fig. 2.24.

19. This field is perpendicular to the direction of the bunch propagation (namely transverse) to induce a deflection of the bunch trajectory.

By using the profile of Fig. 2.24, one obtains for the PHIL steerers a magnetic length $l = 147.5$ mm. However, it is obvious that the profile of Fig. 2.24 is cut at low field (around 12% of the maximum field value) and that the magnetic length is therefore a bit higher than 147.5 mm. In the absence of a complete file for the steerer magnetic field, I decided to fit the decrease of the field profile by decreasing exponential functions, in order to extend the profile that I arbitrarily cut at 1% of the maximal field value. The extended normalized profile obtained is shown in Fig. 2.25.

From the extended profile of Fig. 2.25 one obtains a magnetic length $l = 158$ mm for the PHIL steerers, namely a difference of +6.6% with the initial value deduced from Fig. 2.24.

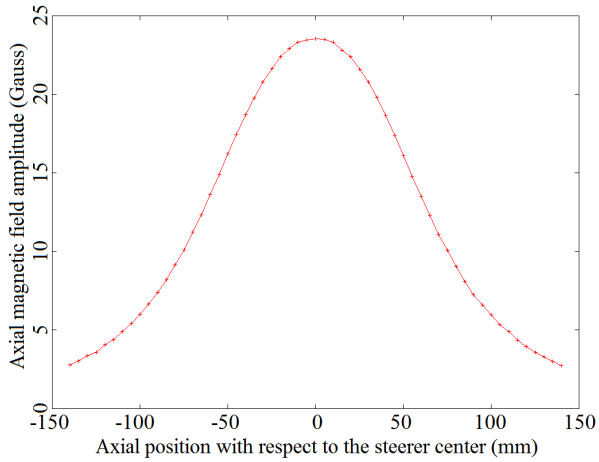

FIGURE *2.24 – Axial profile measurement of the PHIL steerers magnetic field for a current of 5 A (shape of the curve supposed to be independent on the current). Courtesy of R. Roux.*

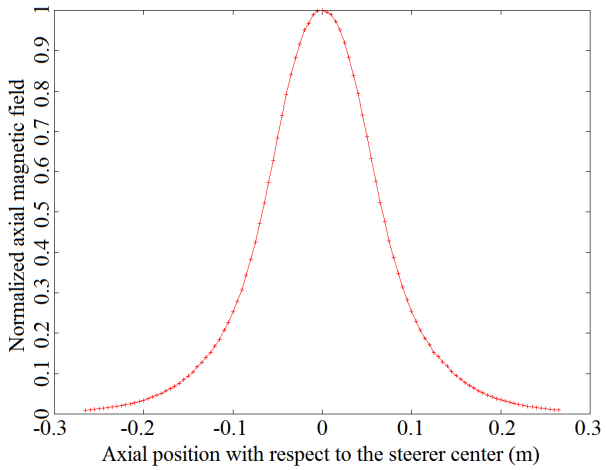

FIGURE *2.25 – Axial profile measurement of the PHIL steerers magnetic field, extended by exponential fit of the decreasing parts*

2.3.1.3 Experimental measurements on PHIL

On PHIL, there are 2 steerers and 3 YAG screens on the direct beamline (see Fig. 1.24). However, all the steerer-YAG configurations are not suitable to perform bunch energy measurement. The measurement on the YAG2 screen with the steerer n°2 was eliminated because of the very small distance between them ($L \approx 2l$). The measurement with the steerer n°1 on the YAG2 and YAG3 screens was eliminated because we use the B5 solenoid (see Fig. 1.24) to focus the bunch on these screens. A variation in the steerer n°1 magnetic field would then imply a change of the bunch entrance transverse point in the B5 field. This change would result in an additional displacement of the bunch barycenter on the YAG screen, not caused by the steerer n°1 but varying with the steerer n°1 magnetic field, which would completely distort the measurement. I chose therefore to perform the measurements with the steerer n°1 on the YAG1 screen and with the steerer n°2 on the YAG3 screen.

To perform the measurements we used the B3 and B5 solenoids to focus at maximum the bunch on the used YAG screen. It is done to entirely see the bunch on the YAG screen for the widest possible range of steerer magnetic field. It is an important condition to optimize the measurement and to obtain a low uncertainty on the computed bunch mean energy value. I choose to displace the electron bunch in the vertical direction and at the center of the YAG screen. The reason to choose the center is that the YAG screen is round, therefore it's there that it is the widest. The reason to choose the vertical direction is that there is a lot of parasitic light on the right and left edges of the YAG screen image (see Fig. 2.26), while there is far less at the top and bottom of the image. To choose the center of the YAG screen and the vertical direction allows therefore accessing the widest possible range of steerer magnetic field, while minimizing the inclusion of light parasites in the determination of the bunch barycenter position.

I first performed a proof-of-principle measurement with the steerer n°2 on the YAG3 screen with a current ramp of 0.1 A between 0 A and 1.1 A in the steerer n°2. In this configuration, we have $L = 2.491$ m and $l = 0.158$ m, so the condition $L >> l$ is verified. The RF-gun peak accelerating field was set around 50 MV/m and the RF-gun phase close to the one allowing the maximum energy gain. According to ASTRA beam dynamics simulations, the mean bunch energy in this case is 3.14 MeV.

Fig. 2.26 shows the recorded bunch positions on the YAG3 screen for some of the currents injected in the steerer n°2. Fig. 2.27 shows the bunch barycenter vertical displacement, with respect to the case where the steerer n°2 is turned off, as a function of the steerer n°2 magnetic field. I use the following formula to calculate the bunch barycenter vertical position $\bar{y}$:

$$\bar{y} = \frac{\sum y * I(x,y)}{\sum I(x,y)}$$

where y is the vertical coordinate on the bunch image, x is the horizontal coordinate on the bunch image, $I(x,y)$ is the intensity at the image point with coordinate (x,y) and $\sum$ denotes the sum over the region of interest in the image (namely the one containing the

bunch). The bunch barycenter vertical displacement is finally converted from pixel to mm by dividing by the magnification factor of the optical system imaging the screen, which is 0.16 for the YAG1 and YAG3 screens.

The error bars on the bunch barycenter vertical displacement have been determined from the fluctuations on the bunch barycenter position within a set of 10 images taken in the same conditions. A linear fit of the data is also plotted in Fig. 2.27 (green curve).

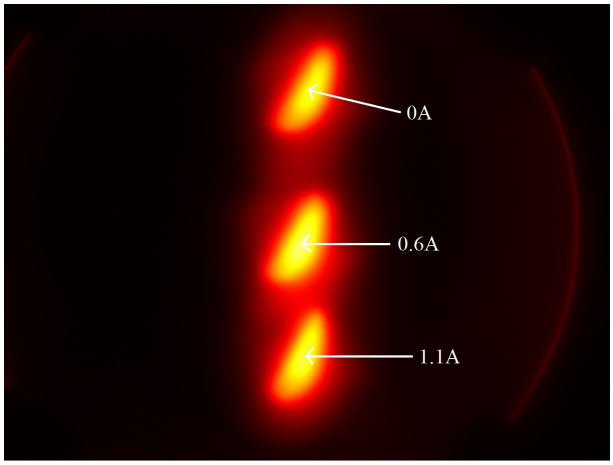

FIGURE *2.26 – Bunch vertical displacement on the YAG3 screen as a function of the current injected in the steerer n° 2. The size of the image is 1360∗1024 pixels (1 pixel is equivalent to a distance of 29 µm).*

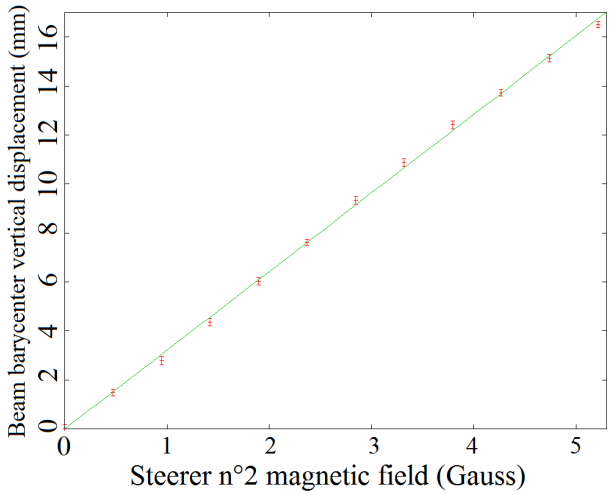

FIGURE *2.27 – Bunch vertical displacement on the YAG3 screen as a function of the current injected in the steerer n° 2*

The linear fit, by least-square method, gives a slope of $d = 32.3 \pm 0.3$ m.T^{-1}. Yet, we have $pc = \frac{elLc}{d}$. Besides, the uncertainty δp on the bunch mean momentum p is determined through the relation $\frac{\delta p}{p} = \frac{\delta d}{d}$. One then deduces $pc = 3.65 \pm 0.03$ MeV, corresponding

to a bunch mean kinetic energy $E = 3.17 \pm 0.03$ MeV. This value is consistent with the one coming from ASTRA simulation (3.14 MeV). It is nevertheless appropriate to more precisely estimate the quality of this measurement by comparing it with the mean bunch energy value extracted from a bunch energy spectrum measured by the dipole magnet under the same conditions.

Fig. 2.28 shows the bunch energy spectrum measured in the same RF-gun conditions than the ones where the measurement with the steerer n°2 and the YAG3 screen has been performed. One can note a characteristic shape with a shoulder towards the high energies, which indicates that the RF-gun phase is not the one minimizing (and also symmetrizing) the bunch energy spread.

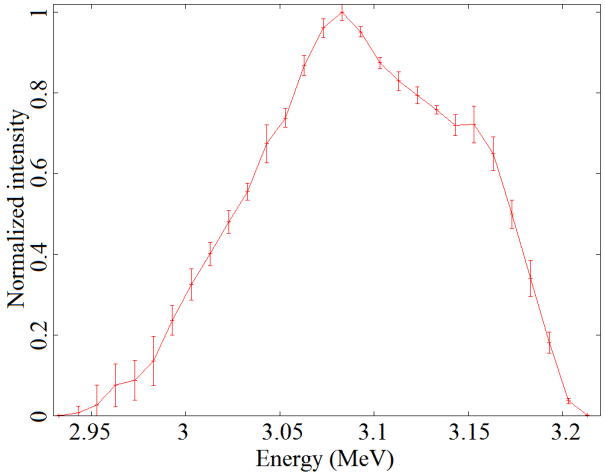

FIGURE *2.28 – Bunch energy spectrum measured with the dipole magnet using the slits system and the YAG4 screen*

The electron bunch mean energy extracted from this spectrum is $E = 3.090 \pm 0.005$ MeV. One can remark that the agreement between the bunch mean energy found by using the steerer n°2 and the YAG3 screen and the one extracted from the bunch energy spectrum is very good, since there is a relative deviation of only 2.5 %.

This discrepancy can be explained by several phenomena. First of all, the current really injected in the steerer magnet is probably not exactly the same as the one entered in the control panel. It would be necessary to perform in-situ measurements to quantify the difference between both. Then, the model developed above is only an approximation not taken into account in the error bars. Finally, it must not be forgotten that I have only approximate the steerer magnetic length l which is consequently non exact. The eventuality of a slight shift of the RF-gun phase between the two measurements is also not excluded.

The fact that the two values do not overlap each other within the error bars is not surprising, because these error bars are only statistical (namely they only take into account the shot-by-shot fluctuations). They do not take into account the systematics. For example the determination of the bunch barycenter position on the YAG3 screen can be distorted

by light not due to the electron bunch, which has not been evaluated for the moment.

I performed other measurements on PHIL for two different bunch energies, namely around 3.5 MeV and around 4.5 MeV, and for two different YAG-steerer configurations, namely YAG1-steerer1 ($L = 1.214$ m) and YAG3-steerer2 ($L = 2.491$ m). The measurement procedure and the precautions taken are the same as for the proof-of-principle measurement exposed above.

Fig. 2.29 shows the bunch barycenter vertical displacement, with respect to the case where the magnet steerer is turned off, as a function of the steerer magnetic field for the two cases with a bunch mean energy around 3.5 MeV. The bunch mean energy deduced in each case is also indicated on the figure. The mean bunch energy extracted from the bunch energy spectrum measured by the dipole magnet is $E = 3.547 \pm 0.001$ MeV.

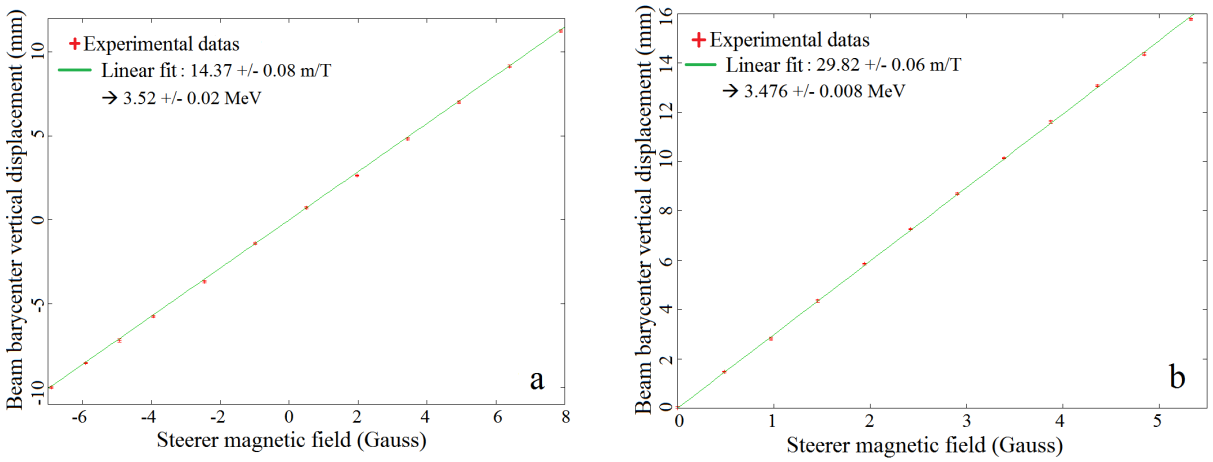

FIGURE *2.29 – Bunch barycenter vertical displacement on YAG1 (a) and YAG3 (b) as a function of the magnetic field generated by the steerer n°1 (a) and the steerer n°2 (b) for a bunch mean energy around 3.5 MeV*

The two mean bunch energy values shown in Fig. 2.29 are very close to each other (relative deviation of only 1.25%) but are not overlapping each other within the error bars. They are also very close to the value measured by the dipole magnet, since the discrepancy is 0.8% for the steerer1-YAG1 configuration and 2.0% for the steerer2-YAG3 configuration. However, it is noteworthy that the steerer1-YAG1 configuration is closer to the dipole magnet measurement than the steerer2-YAG3 configuration. Taking into account the bigger distance between the steerer n°2 and the YAG3 screen, it should be the opposite. It therefore raises some questions about the energy measurement with the dipole magnet. The discrepancies are however very small, therefore the questions remain marginal.

Fig. 2.30 shows the bunch barycenter vertical displacement, with respect to the case where the magnet steerer is turned off, as a function of the steerer magnetic field for two cases with a bunch mean energy around 4.5 MeV. The bunch mean kinetic energy deduced in each case is also indicated in the figure. The mean bunch energy extracted from the bunch energy spectrum measured by the dipole magnet is $E = 4.479 \pm 0.002$ MeV.

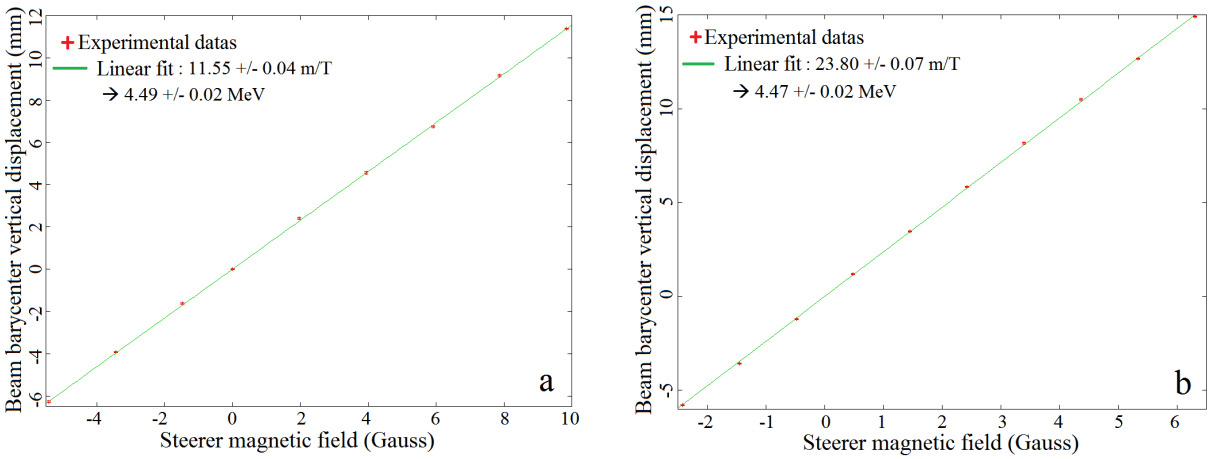

FIGURE *2.30 – Bunch barycenter vertical displacement on YAG1 (a) and YAG3 (b) as a function of the magnetic field generated by the steerer n°1 (a) and the steerer n°2 (b) for a bunch mean energy around 4.5 MeV*

The two mean bunch energy values shown in Fig. 2.30 are once again very close to each other (relative deviation of only 0.47%) and are overlapping each other within the error bars. They are also very close to the value measured by the dipole magnet, since the discrepancy is only 0.25% for the steerer1-YAG1 configuration and 0.2% for the steerer2-YAG3 configuration.

2.3.1.4 Measurement of the bunch mean energy with two bunch positions

The measurements exposed in Sec. 2.3.1.3 are performed with a large number (around 10) of different bunch positions on the YAG1 and YAG3 screens. The acquisition and analysis of the data is therefore rather time consuming in these cases. The linearity of the bunch displacement as a function of the steerer magnetic field is very good, as shown in Fig. 2.27, Fig. 2.29 and Fig. 2.30. It is therefore very interesting to study if the bunch mean energy measurement is possible by using only two different positions of the bunch taking at both extremities of the YAG screen, which is the minimum number to compute the bunch energy. It would significantly speed up the bunch mean energy measurement.

This study has been done by comparing the results obtained with all the acquired points with the ones obtained by using only the two extreme points of each set of data (see Fig. 2.29 and Fig. 2.30). This comparison is shown in Tab. 2.4.

The conclusion of this study is that the measurement of the bunch mean energy with a steerer magnet and a YAG screen can perfectly be performed with only two bunch

positions measured on the YAG screen. In fact, as it is shown in Tab. 2.4, the discrepancy between the measurement with all the bunch positions and the one with only the two extreme bunch positions is zero or almost zero for all the configurations tested in Sec. 2.3.1.3. Besides, the precision of the bunch energy measurement is not deteriorated by the fact of using only two bunch positions.

Configuration	Beam energy measured with the dipole	Beam energy measured with all the beam positions	Beam energy measured with the two extreme beam positions	discrepancy
Fig. 2.17 (a)	3.547 +/- 0,001 MeV	3.52 +/- 0,02 MeV	3.52 +/- 0,03 MeV	0%
Fig. 2.17 (b)	3.547 +/- 0,001 MeV	3.476 +/- 0,008 MeV	3.506 +/- 0,007 MeV	0.43%
Fig. 2.18 (a)	4.479 +/- 0,002 MeV	4.49 +/- 0,02 MeV	4.494 +/- 0,004 MeV	0%
Fig. 2.18 (b)	4.479 +/- 0,002 MeV	4.47 +/- 0,02 MeV	4.50 +/- 0,02 MeV	0%

TABLE *2.4 – Comparison between the bunch mean energy measured with all the acquired bunch positions and with only the two extreme bunch positions acquired in the configurations of Fig. 2.29 and Fig. 2.30*

2.3.1.5 Conclusions

The measurement of the bunch mean energy by means of a steerer magnet and a YAG screen gives very satisfactory results. The difference to the value extracted from the bunch energy spectrum is only 2.5% for an energy around 3.1 MeV. This discrepancy decreases to 0.2% as the energy increases around 4.5 MeV. Besides, I have shown that it is sufficient to acquire only two bunch positions at both extremities of the YAG screen to perform this measurement, which significantly speeds it up. This method is therefore a good alternative to the use of the dipole magnet in case of failure, but also because of its quickness making us less vulnerable to the varying experimental conditions, especially the Gun RF-phase, than during the acquisition of a bunch energy spectrum with the dipole magnet. However it gives only access to the mean bunch energy, while a bunch energy spectrum is a much richer source of informations (mean energy, energy spread, skewness, kurtosis ...).

It would be interesting to perform other measurements of this type, for example to evaluate the precision at other RF-gun phases than the one maximizing the energy, especially at RF-gun phases very far from this one.

2.3.2 Measurement of the bunch length thanks to the 3-phase method

2.3.2.1 Theoretical principles

The 3-phase method is a multiparametric method, which enables measuring the length of a particle bunch from 3 measurements (or more) of its energy spread in different acceleration conditions. The measured bunch length is then the one at the entrance of the accelerating structure from which we vary the parameters. It is theoretically possible to vary the RF phase or the peak accelerating field of this accelerating structure. In practical it is easier to vary the RF phase of the accelerating structure, which gives this method its name.

To establish the 3-phase model, it is essential to neglect the space-charge forces all along the bunch path after the accelerating structure entrance. This is a substantial approximation for the low-energy electron bunches studied in this thesis. In fact, the electron bunches generated by RF-guns typically have an energy lower than 6.5 MeV. We also assume that the non-linearities of the external electric and magnetic fields are negligible and that the transverse bunch motion is decoupled from the longitudinal one. This then allows assuming that the bunch transport is linear and can be described in the longitudinal phase-space by transfer matrices of the following form :

$$\begin{pmatrix} R_{11} & R_{12} \\ R_{21} & R_{22} \end{pmatrix}$$

with $\Delta t_f = R_{11}\Delta t_i + R_{12}\Delta E_i$ and $\Delta E_f = R_{21}\Delta t_i + R_{22}\Delta E_i$, where Δ represents the time and energy gaps between any electron of the bunch and the reference electron having the mean values. In the case where there is only a longitudinal drift between the accelerating structure and the system used to measure the bunch energy spread, we have $R_{22} = 1$. This is always the case in my measurements, therefore I will consider it always true hereafter.

The longitudinal beam matrix, gathering the statistical longitudinal properties of the bunch, is :

$$\begin{pmatrix} <\Delta t^2> & <\Delta E \Delta t> \\ <\Delta t \Delta E> & <\Delta E^2> \end{pmatrix} = \begin{pmatrix} \sigma_t^2 & \sigma_{Et} \\ \sigma_{Et} & \sigma_E^2 \end{pmatrix}$$

where $<>$ denotes the mean over all the electrons of the bunch, σ_t the rms bunch length, σ_E the rms bunch energy spread and σ_{Et} the rms bunch time/energy correlation.

The transport of this longitudinal beam matrix between the accelerating structure entrance (i subscripts) and the system measuring the bunch energy spread (f subscripts) is given by :

$$\begin{pmatrix} \sigma_{t_f}^2 & \sigma_{Et_f} \\ \sigma_{Et_f} & \sigma_{E_f}^2 \end{pmatrix} = \begin{pmatrix} R_{11} & R_{12} \\ R_{21} & 1 \end{pmatrix} \begin{pmatrix} \sigma_{t_i}^2 & \sigma_{Et_i} \\ \sigma_{Et_i} & \sigma_{E_i}^2 \end{pmatrix} \begin{pmatrix} R_{11} & R_{21} \\ R_{12} & 1 \end{pmatrix}$$

It leads to two equations which can be used experimentally :

$$\begin{cases} \sigma_{t_f}^2 = R_{11}^2\sigma_{t_i}^2 + 2R_{11}R_{12}\sigma_{Et_i} + R_{12}^2\sigma_{E_i}^2 \\ \\ \sigma_{E_f}^2 = R_{21}^2\sigma_{t_i}^2 + 2R_{21}\sigma_{Et_i} + \sigma_{E_i}^2 \end{cases}$$

The first equation requires to measure the final bunch length σ_{t_f} to deduce the initial bunch length σ_{t_i}. It is therefore not very useful experimentally speaking. The second equation is the one to use. The goal is to measure the final bunch energy spread σ_{E_f} for at least 3 different values R_{21_n} of R_{21}, which corresponds to different values of the RF phase of the accelerating structure. We then obtain a matrix system of the following form :

$$Y = AX, \text{ with } Y = \begin{pmatrix} \sigma_{E_{f_1}}^2 \\ ... \\ \sigma_{E_{fn}}^2 \end{pmatrix}, A = \begin{pmatrix} R_{21_1}^2 & 2R_{21_1} & 1 \\ ... & ... & ... \\ R_{21_n}^2 & 2R_{21_n} & 1 \end{pmatrix} \text{ and } X = \begin{pmatrix} \sigma_{t_i}^2 \\ \sigma_{Et_i} \\ \sigma_{E_i}^2 \end{pmatrix}$$

A least squares algorithm allows inverting the previous system and therefore calculating the values of σ_{t_i}, σ_{Et_i} and σ_{E_i} by :

$$X = \left(A^t A\right)^{-1} A^t Y$$

It is important to note that, to optimize the accuracy of the least squares method, it is necessary to maximize the number of different RF-phases used for the accelerating structure and to symmetrize these phases with respect to the one minimizing the bunch energy spread.

The rms bunch length σ_{t_i} at the entrance of the accelerating structure is then determined, but it remains to evaluate the error bars on it. To do that, I chose to use the 3-phase method explained above in combination with a Monte-Carlo algorithm. Concretely, I drew 100000 series of energy spread σ_{E_f} according to Gaussian distributions having for mean values the measured values of σ_{E_f} and for standard deviations the uncertainties on these measurements. I then applied the least squares algorithm introduced above for each of the 100000 series. I obtained in this way 100000 values of the bunch length σ_{t_i}. The value of σ_{t_i} is finally the mean of these 100000 values and the uncertainty on it is the standard deviation of these 100000 values.

2.3.2.2 The used longitudinal transfer matrices

The elements taken into account during my thesis for bunch length measurements by the 3-phase method are the longitudinal drift space, the traveling wave (TW) accelerating structure and the standing wave (SW) accelerating structure. In the following, their transfer matrices are established in the plane (ΔE,Δt), as defined in Sec. 2.3.2.1. In this section, the i subscript denotes a quantity at the entrance of the element considered and the f subscript the quantity at its exit.

The longitudinal drift space

Let start with the longitudinal drift space. As we neglect the effect of space-charge forces, the energy of an electron is then conserved and we have therefore $\Delta E_f = \Delta E_i$.

Consider now an electron with $\Delta t_i = 0$ and $\Delta E_i \neq 0$. We have to find the expression of Δt_f knowing that ΔE is a constant equal to ΔE_i. The time T taken by the electron with velocity v to travel through a drift space of length L is given by $T = \frac{L}{v}$. We have therefore $dT = \frac{\partial T}{\partial L} dL + \frac{\partial T}{\partial v} dv$, where the first term is zero since we suppose that all the electrons fly in straight line and travel the same distance, implying $dL = 0$. It leads to $\Delta T = -\frac{L}{v_0^2} \Delta v$, where $v_0 = \beta_0 c$ is the mean velocity of the bunch.

Knowing that $\Delta v = \frac{v_0}{\gamma_0(\gamma_0+1)} \frac{\Delta E}{E_0}$ and that $\Delta T = \Delta t_f - \Delta t_i$, we have :

$$\Delta t_f = \Delta t_i - \frac{L}{\gamma_0(\gamma_0+1)\beta_0 c E_0} \Delta E_i \tag{2.6}$$

By joining all the parts of the calculation, we find the longitudinal transfer matrix of a longitudinal drift space :

$$\begin{pmatrix} 1 & -\frac{L}{\gamma_0(\gamma_0+1)\beta_0 c E_0} \\ 0 & 1 \end{pmatrix}$$

The accelerating structures

To determine the longitudinal transfer matrix of accelerating structures, we have to suppose that the electron has a purely longitudinal motion along the structure Oz axis. We have also to suppose that the accelerating fields on these axes are purely sinusoidal. This is an approximation due to the fringe fields at the structure entrances and exits and also because of the irises between the cavities constituting the structures. The fields are therefore of the following form :

$$\begin{cases} E_z(z) = E_m \cos(2\pi f t - kz + \phi) \text{ for a TW structure} \\ \\ E_z(z) = E_m \sin(kz) \cos(2\pi f t + \phi) \text{ for a SW structure} \end{cases}$$

where E_m is the field amplitude, f is the frequency of the field, k is the wave vector of the field and ϕ its RF-phase.

In all my studies concerning the bunch length measurement by the 3-phase method, the electrons have at least a few MeV energy at the accelerating structure entrances and are therefore already relativistic. It allows assuming that their velocities are constant and equal to c all along their motions in the structures. In particular, it means that the relative

positions of the electrons remain the same in the structures [20]. It results first in $\Delta t_f = \Delta t_i$. It leads also to $2\pi ft = kz$ which enables simplifying the fields as :

$$\begin{cases} E_z(z) = E_m \cos(\phi) \text{ for a TW structure} \\ E_z(z) = E_m \sin(kz)\cos(kz+\phi) = \frac{E_m}{2}(\sin(2kz+\phi) - \sin(\phi)) \text{ for a SW structure} \end{cases}$$

We use then the relativistic kinetic power theorem $\frac{dE}{dt} = \vec{F}.\vec{v}$, where $E = (\gamma - 1)m_e c^2$ is the electron kinetic energy, $\vec{F} = -eE_z(z)\vec{e_z}$ is the force acting on it and $\vec{v} = c\vec{e_z}$ is its velocity. We obtain finally :

$$\begin{cases} E_f = E_i - eE_m L\cos(\phi) \text{ for a TW structure} \\ E_f = E_i - e\frac{E_m}{2}\left(\frac{1}{2k}\cos(\phi) - \frac{1}{2k}\cos(2kL+\phi) - \sin(\phi)L\right) \text{ for a SW structure} \end{cases}$$

where L is the length of the accelerating structure.

Differentiating E_f with respect to E_i and ϕ, and considering that $\Delta\phi = 2\pi f \Delta t_i$, we obtain :

$$\begin{cases} \Delta E_f = \Delta E_i + 2\pi f e E_m L \sin(\phi)\Delta t_i \text{ for a TW structure} \\ \Delta E_f = \Delta E_i + \pi f e E_m \left(\cos(\phi)L - \frac{1}{k}\cos(kL+\phi)\sin(kL)\right)\Delta t_i \text{ for a SW structure} \end{cases}$$

The longitudinal transfer matrix of a traveling wave accelerating structure is finally given by the following expression, often encountered in the literature :

$$\begin{pmatrix} 1 & 0 \\ 2\pi f e E_m L \sin(\phi) & 1 \end{pmatrix}$$

and the one of a standing wave accelerating structure by the following expression, which is not classical since it is often replaced by the one of a traveling wave accelerating structure in the literature :

$$\begin{pmatrix} 1 & 0 \\ \pi f e E_m \left(\cos(\phi)L - \frac{1}{k}\cos(kL+\phi)\sin(kL)\right) & 1 \end{pmatrix}$$

20. It is strictly speaking not true, since there are always velocity differences between the electrons of the bunch implying a variation of Δt. It can be taken into account to determine the bunch length variation in the accelerating structure (see the analytical modeling of the velocity bunching in Sec. 3.3.2). But it is of no importance for the bunch length measurement by the 3-phase method, where only the energy spread induced by the accelerating structure plays a role. I choose to therefore neglect here the variation of Δt.

As said in Sec. 2.3.2.1, all my 3-phase method measurements are performed with only a longitudinal drift between the system used to measure the bunch energy spread and the exit of the accelerating structure from which I vary the RF-phase. It implies that the term R_{21} of the longitudinal transfer matrix, which is the only one of interest for the 3-phase method, is only given by the one of the accelerating structure as a longitudinal drift has no impact on it.

2.3.2.3 Proof-of-principle measurement on the HELIOS Linac at SOLEIL

The HELIOS Linac is a good place to perform a proof-of-principle measurement of bunch length with the 3-phase method. First of all because a traveling wave accelerating structure, which is the simplest RF accelerating structure to analytically model, is used. Secondly because the effect of space-charge forces, not taken into account in the 3-phase method, is negligible on this facility at the entrance of the second traveling wave accelerating structure. Indeed, the beam is 67 MeV with 650 pC of charge, a bunch rms length of a few ps and an rms radius of the order of one millimeter. It is therefore the classical and optimal configuration to perform bunch length measurements by the 3-phase method.

It is noteworthy that, on HELIOS, the beam is made of a train of bunches (see Sec. 1.3.3). As a result, we do not measure the properties of each bunch separately by the 3-phase method but the properties of the mean bunch. However in the SP mode we use (see Sec. 1.3.3), there are only 5 bunches in the beam for a total charge of 650 pC at maximum. It allows neglecting the beam-loading phenomenon in the bunching and accelerating structures. It implies that the properties of the different bunches are very close to the ones of the mean bunch, which we measure.

On the HELIOS Linac (see Fig. 1.27), there are two traveling wave accelerating structures that we could in principle use to perform 3-phase measurements. However, it is practically only possible to use the second accelerating structure to perform this measurement. This is due to the fact that the RF-phase of the first accelerating structure is dependent on the one of the buncher located downstream. Thus, a change in the RF-phase of this first accelerating structure would also imply a change in the one of the buncher. It would result in a variation of the beam properties at the entrance of the first accelerating structure, which would prevent any application of the 3-phase method. The 3-phase measurement has therefore been performed by varying the RF-phase of the second accelerating structure and by measuring each time the beam energy spread.

To measure the beam energy spectrum, from which the beam energy spread can be extracted, we use the first dipole magnet, the slit system and the charge-meter n°2 (see Fig. 1.27). In fact for a fixed magnetic field B in the dipole magnet, the electrons are more or less deviated according to their energies. It is the famous formula $B\rho = \frac{p}{q}$, where ρ is the curvature radius of the electron path in the dipole magnet and p the momentum of the electron. Only those with an energy such that their radius of curvature ρ allows them to pass through the slits will be detected by the charge-meter n°2. It is sufficient to move the slits perpendicularly to the axis of beam propagation, to scan the electron energy passing the slits, and detecting them each time. Fig. 2.31 shows a schematic layout

of the situation.

The beam energy spectrum can then be reconstructed by knowing a reference value for the current I_{dip} in the dipole magnet and by calibrating the slit displacement. On HELIOS, a current of 197.5 A in the dipole magnet implies that electrons of 110 MeV travel on the accelerator axis and a slits displacement of +21 mm corresponds to an energy variation of +3 MeV. The detected energy as a function of the slit position is therefore given by :

$$\text{Energy(MeV)}=\frac{I_{dip}(A)}{197.5}*110+\frac{position(mm)}{21}*3$$

One has to note that there is another way to reconstruct the beam energy spectrum, which is to let the slits centered on the accelerator axis and to vary the magnetic field B in the dipole magnet to scan the electron energies. This solution is however not the standard solution adopted on HELIOS. We therefore choose not to use it.

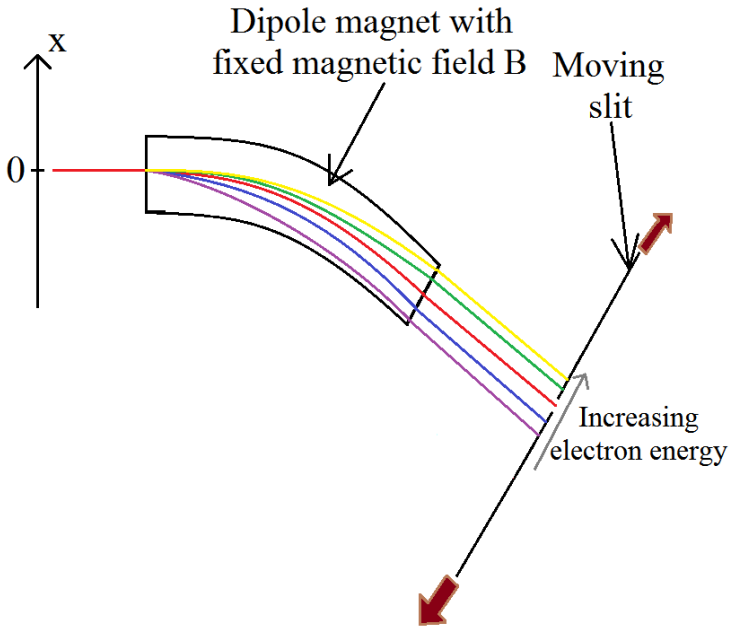

FIGURE *2.31 – Schematic layout of the beam energy spectrum measurement on the HELIOS Linac at Soleil. The different colors represent electrons of the beam with different energies.*

There is an uncertainty on the measured energy, due to the fact that the slit used after the dipole magnet to select the energy of the electrons detected by the charge-meter n°2 has a non-zero aperture. The goal is to reduce this aperture as much as possible, to lower the uncertainty on the measured energy. However it is noteworthy that it is not possible to reduce the slit aperture too much, otherwise the signal would not be sufficient to perform a correct measurement. There is therefore a compromise to find. During our measurements the slits aperture has been fixed to 2.5 mm, which corresponds to a resolution of $\frac{\Delta E}{E} = 0.4\%$ on the detected energy. The uncertainty on the charge

measured by the charge-meter n°2 varied between $\frac{\Delta Q}{Q} = 0.4\%$ and 0.6% depending on the measurement.

Knowing the energy/intensity couples $(E_k\,;\,I_k)$ constituting the beam energy spectrum together with the error bars on these points, it is possible to analyze it to determine the beam mean energy and the rms beam energy spread. The beam mean energy is statistically defined by :

$$\bar{E} = \frac{\sum_{k=1}^{n} E_k I_k}{\sum_{k=1}^{n} I_k}$$

The rms beam energy spread is then simply given by the statistical standard deviation of the beam energy spectrum around the beam mean energy :

$$\sigma_{E_f} = \sqrt{\frac{\sum_{k=1}^{n} I_k \left(E_k - \bar{E}\right)^2}{\sum_{k=1}^{n} I_k}}$$

To best determine the beam mean energy and rms energy spread and their uncertainties, I choose to use a Monte-Carlo algorithm. I perform 100000 random drawings of each couple $(E_k\,;\,I_k)$ constituting the beam energy spectrum, according to two Gaussian distributions having for means E_k and I_k and for standard deviations the uncertainties on E_k and I_k. I then obtained 100000 beam energy spectra randomly drawn. The beam mean energy (respectively rms energy spread) is finally defined as the mean of the energies (respectively energy spreads) of the 100000 distributions and its uncertainty as the standard deviation of these 100000 energies (respectively energy spreads).

The first measurement has been performed with a total beam charge of 650 $\pm$ 10 pC. Fig. 2.32 shows some examples of measured beam energy spectra for different RF-phase of the second traveling wave accelerating structure. Fig. 2.33 shows the beam mean energy and rms energy spread measured and used to perform the 3-phase method. The measurement of the beam mean energy is also essential to perform a bunch length measurement by the 3-phase method. In fact, a reference is needed to match the experimental RF-phase with the one of the 3-phase analytical model. This reference (0°) is chosen as the RF-phase allowing the maximum energy gain for the beam. The obtained results are the following [21] :

$$\begin{cases} \sigma_{t_i} = 4.0 \ \pm \ 0.2 \text{ ps} \\ \sigma_{Et_i} = 0.3 \ \pm \ 0.1 \text{ MeV.ps} \\ \sigma_{E_i} = 370 \ \pm \ 49 \text{ keV} \\ \epsilon_{z_i} = \sqrt{\sigma_{t_i}^2 \sigma_{E_i}^2 - \sigma_{Et_i}^2} = 1.5 \ \pm \ 0.2 \ \pi\text{.MeV.ps} \end{cases}$$

21. The uncertainty of ϵ_{z_i} is calculated by partial derivatives starting from the uncertainties on σ_{t_i}, σ_{Et_i} and σ_{E_i}.

where σ_{t_i} is the rms bunch length at the traveling wave accelerating structure entrance, σ_{E_i} its rms energy spread, σ_{Et_i} its rms time/energy correlation and ϵ_{z_i} its rms longitudinal emittance.

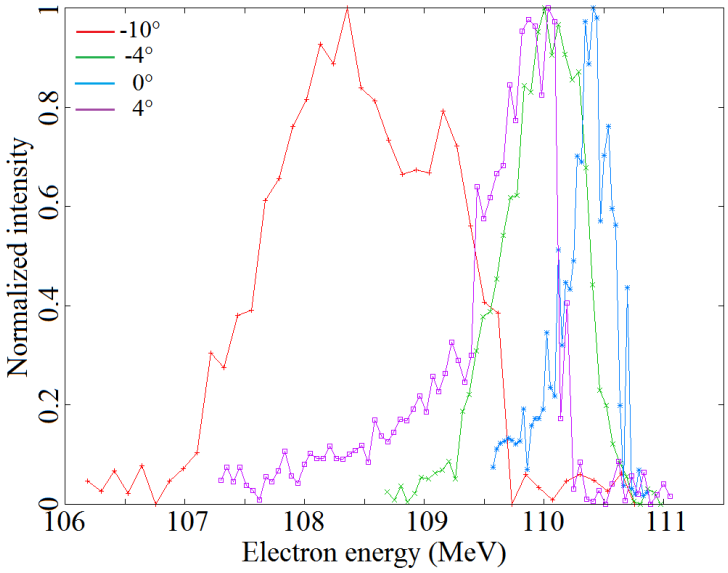

FIGURE *2.32 – Beam energy spectra measured after the second accelerating structure of the HELIOS Linac for different RF-phase of this structure ; 0° denotes the maximum mean beam energy.*

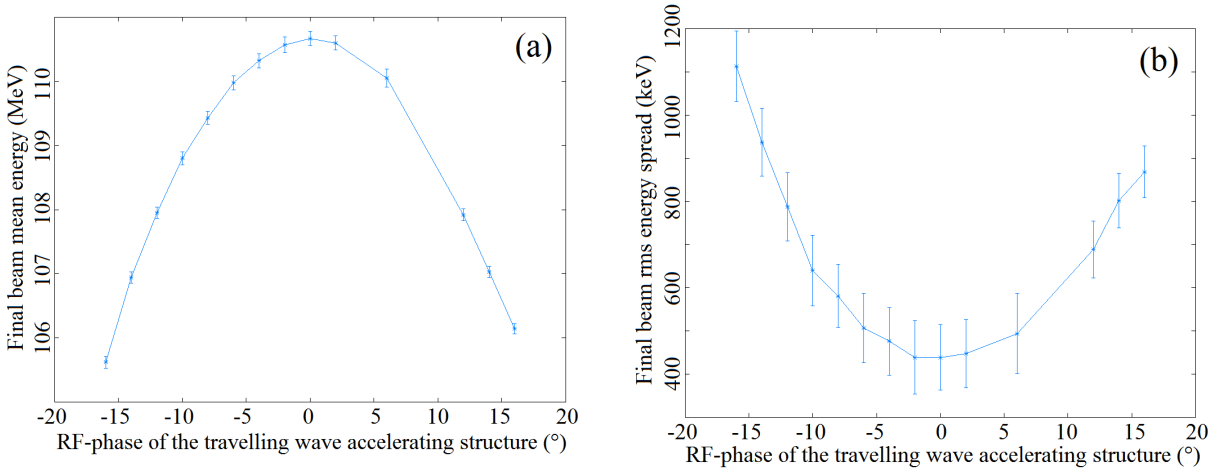

FIGURE *2.33 – Beam mean energy (a) and rms energy spread (b) measured after the second accelerating structure of the HELIOS linac as a function of its RF-phase ; Beam total charge : 650 pC. The point at +10° was not coherent with the others and has been discarded.*

Now it must be checked that the bunch length obtained by the 3-phase method on HELIOS is realistic. On HELIOS, the bunches are generated starting from a 1.4 ns

FWHM long initial beam injected in an RF-buncher (see Sec. 1.3.3). The length of the obtained bunches must then be compatible with the time period of the buncher RF-field. Its frequency being 2998.30 MHz, 1° of RF-phase corresponds to a duration of 0.93 ps. It means that the bunches spread on 26° of RF-phase at $\pm\ 3\sigma_t$, which is realistic with respect to the period of the buncher RF-field.

Moreover, the quantity σ_{E_i} can be directly measured on HELIOS. It is indeed sufficient to measure the beam rms energy spread, as previously explained, but with the second traveling wave accelerating structure switched off. The obtained result is $\sigma_{E_i} = 358\ \pm$ 64 keV. The discrepancy with the rms energy spread σ_{E_i} deduced from the 3-phase method is very low and widely included in the error bars. This is a further evidence for the consistency of the bunch length determined by the 3-phase method on HELIOS.

Another measurement has been performed with a lower total beam charge of 210 $\pm$ 10 pC. Fig. 2.34 shows the beam mean energy and rms energy spread measured and used to perform the 3-phase method.

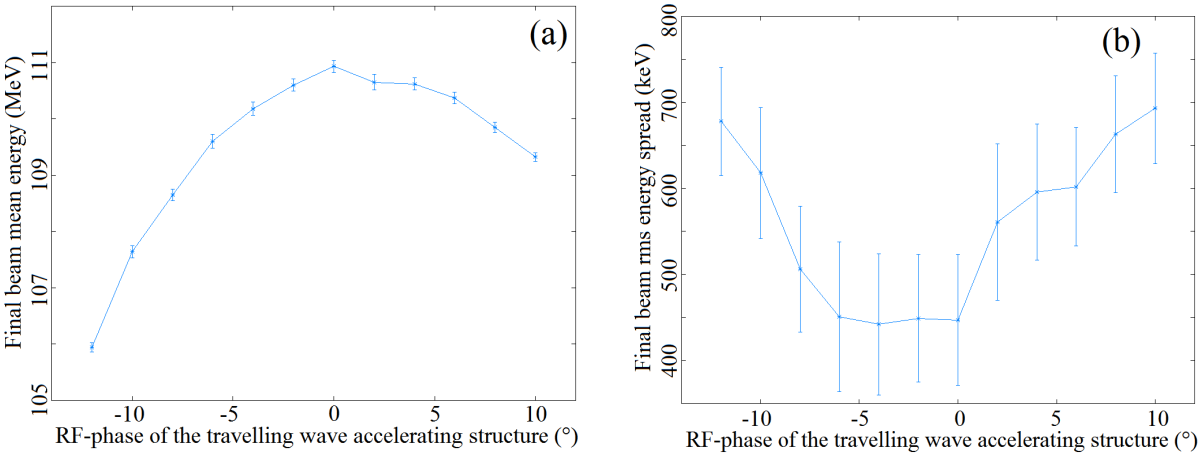

FIGURE *2.34 – Beam mean energy (a) and rms energy spread (b) measured after the second accelerating structure of the HELIOS linac as a function of its RF-phase ; Beam total charge : 210 pC.*

The obtained results are the following :

$$\begin{cases} \sigma_{t_i} = 3.3\ \pm\ 0.5 \text{ ps} \\ \sigma_{Et_i} = -0.3\ \pm\ 0.1 \text{ MeV.ps} \\ \sigma_{E_i} = 480\ \pm\ 37 \text{ keV} \\ \epsilon_{z_i} = \sqrt{\sigma_{t_i}^2 \sigma_{E_i}^2 - \sigma_{Et_i}^2} = 1.6\ \pm\ 0.3\ \pi\text{.MeV.ps} \end{cases}$$

One observes in particular a decrease in the rms bunch length σ_{t_i}, with respect to the total beam charge of 650 pC, which falls from 4 ps to 3.3 ps. This result was expected,

because the lower the beam charge, the less the space-charge force will counteract the bunching of the electron beam into bunches in the buncher. The bunching will then be more efficient and the obtained bunches have a lower rms length. One can observe that the longitudinal emittance ϵ_z is the same for the two beam charges. This is due to the fact that the lower rms bunch length at 210 pC is compensated by a higher rms energy spread than at 650 pC. This higher energy spread is explained by the different sign of the bunch rms time/energy correlation σ_{Et_i} between the two cases.

The 3-phase method is practicable in good conditions on the HELIOS Linac and provides a realistic and reliable measurement of the electron bunch rms length, which can be estimated to $\sigma_t = 4.0 \pm 0.2$ ps at 650 pC and 3.3 ± 0.5 ps at 210 pC. This result is interesting, since the bunch length has apparently never been measured before on HELIOS. This result will be to compared with the one of the SPESO experiment, which is implemented on HELIOS and aims at the measurement of electron bunch length using the Smith-Purcell radiation [91].

2.3.2.4 Measurements performed at PITZ, DESY, Zeuthen

On PITZ (see Fig. 1.25), the measurement of bunch length thanks to the 3-phase method can be performed with the CDS booster as phase-varying accelerating structure and the HEDA1 station to measure the energy spread after it. The deduced bunch length is then the one at the entrance of the CDS booster. It is noteworthy that this configuration is not at all the classical and optimal configuration for using the 3-phase method. In fact, the bunch is only at a few MeV and is quite short (850 fs rms at minimum) and we moreover use a standing wave accelerating structure and not a traveling wave structure to perform the measurements.

For these measurements the bunch charge has been adjusted to 20 pC, to minimize the effect of space-charge forces, which is not taken into account in the 3-phase method. The peak accelerating field has been fixed to 17.5 MV/m leading to a mean bunch energy around 22 MeV at the CDS booster exit. The measurements have been performed for 3 different time profiles of the laser pulse driving the RF-gun and also each time for several RF-phases of the RF-gun (0° denoting the RF-phase maximizing the energy gain of the bunch). Fig. 2.35 presents the 3 laser profiles. Fig. 2.36, Fig. 2.37 and Fig. 2.38 show the curves of bunch rms energy spread measured at the HEDA1 station, as a function of the CDS booster RF-phase, used to perform the bunch length measurement by 3-phase method. It is important to note that, contrary to the 3-phase measurements performed with the RF-gun (see Sec. 3.1.2.3 later), there are here no limitations due to the resolution of the bunch energy spread measurement system. In fact, the bunch energy spread at the CDS booster exit is always sufficiently high ($\geq$ 10 keV) to be properly measured by the HEDA1 station, which has a resolution of 5 keV [92].

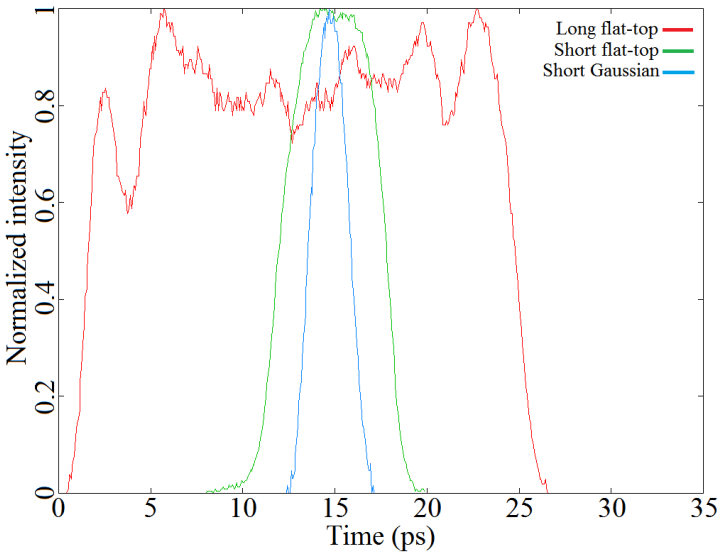

FIGURE 2.35 – *Laser time profiles used at PITZ : Long flat-top with 24 ps FWHM and 2 ps rise/fall time (σ_t = 6.8 ps rms) ; Short flat-top with 5.8 ps FWHM and 2 ps rise/fall time (σ_t = 1.9 ps rms) ; Short Gaussian with σ_t = 0.85 ps rms (2 ps FWHM).*

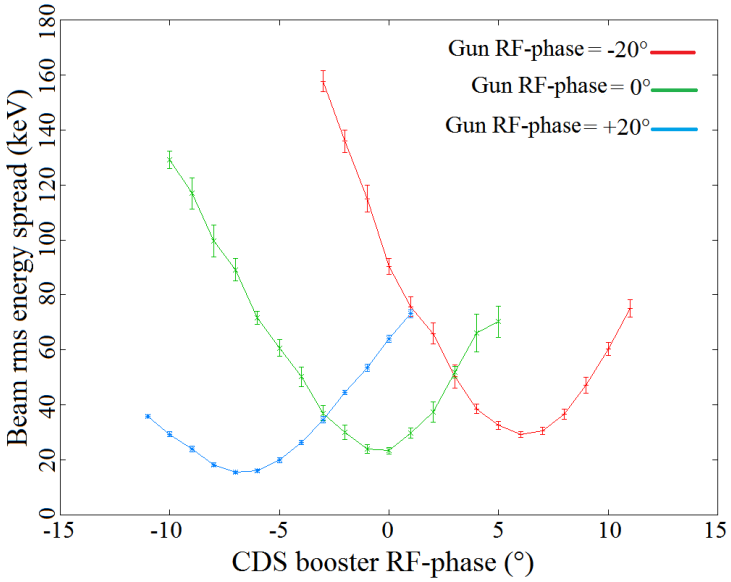

FIGURE 2.36 – *Bunch rms energy spread at HEDA1 station as a function of the CDS booster RF-phase ; Laser time profile : Long flat-top ; RF-gun peak accelerating field : 60 MV/m (Bunch energy around 6.2 MeV at the exit) ; CDS Booster peak accelerating field : 17.5 MV/m ; Bunch charge : 20 pC.*

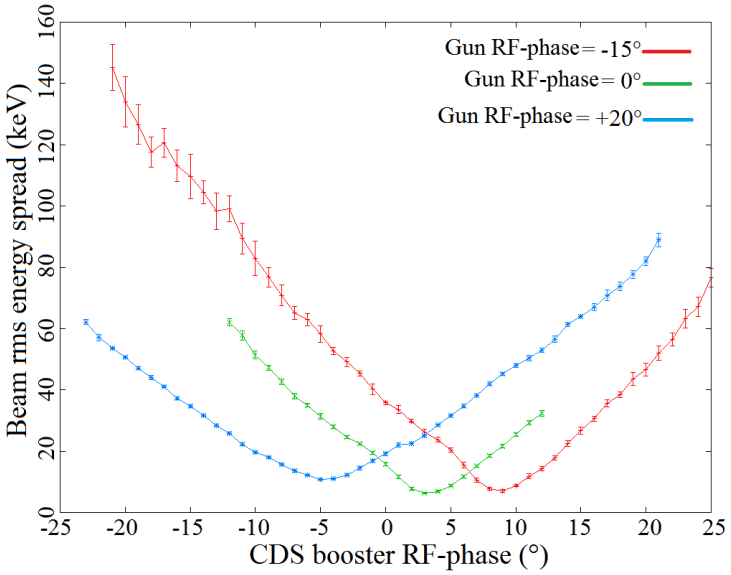

FIGURE 2.37 – *Bunch rms energy spread at HEDA1 station as a function of the CDS booster RF-phase ; Laser time profile : Short flat-top ; RF-gun peak accelerating field : 60 MV/m (Bunch energy around 6.2 MeV at the exit) ; CDS Booster peak accelerating field : 17.5 MV/m ; Bunch charge : 20 pC.*

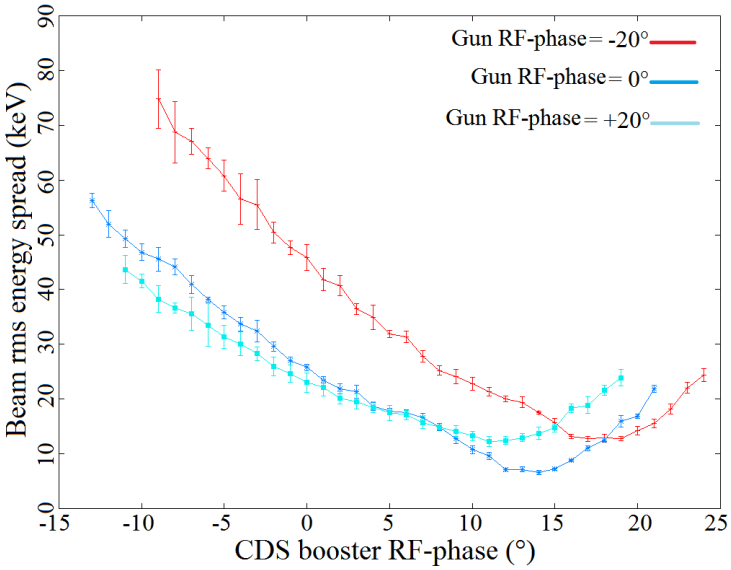

FIGURE 2.38 – *Bunch rms energy spread at HEDA1 station as a function of the CDS booster RF-phase ; Laser time profile : Short Gaussian ; RF-gun peak accelerating field : 60 MV/m (Bunch energy around 6.2 MeV at the exit) ; CDS Booster peak accelerating field : 17.5 MV/m ; Bunch charge : 20 pC. Measurements with Gun RF-phase of −15°, −10°, −5°, +5°, +10° and +15° have also been performed but are not shown here for visibility reason.*

Tab. 2.5 shows the results of the measurements performed with the CDS booster for the long and short flat-top laser time profiles. These results are also compared with the bunch length predictions coming from the ASTRA beam dynamics code.

Laser profile	Gun RF-phase	ASTRA predictions	3-phase method
Long flat-top	-20°	7.75 ps rms	7.5 +/- 0.2 ps rms
Long flat-top	0°	5.90 ps rms	6.0 +/- 0.2 ps rms
Long flat-top	+20°	3.99 ps rms	4.1 +/- 0.1 ps rms
Short flat-top	-15°	2.44 ps rms	2.2 +/- 0.1 ps rms
Short flat-top	0°	2.12 ps rms	1.8 +/- 0.1 ps rms
Short flat-top	+20°	1.85 ps rms	1.5 +/- 0.1 ps rms

TABLE *2.5 – 3-phase measurements performed with the CDS booster at PITZ for the short and long flat-top laser time profiles. RF-gun peak accelerating field : 60 MV/m (Bunch energy around 6.2 MeV at the exit) ; CDS Booster peak accelerating field : 17.5 MV/m ; Bunch charge : 20 pC.*

Tab. 2.5 shows that 3-phase method allows a good reconstruction of bunch length variations at the CDS booster entrance as a function of the Gun RF-phase for the long and short flat-top laser time profiles. Indeed, the discrepancy with the value predicted by ASTRA is below 3% for the long flat-top laser time profile. One can note that the measurements for the short flat-top profile are systematically lower, from 0.2 ps to 0.3 ps, than the ASTRA predictions. However it represents a discrepancy of only 13.5% at maximum, which remains fairly acceptable.

The most likely explanation of this discrepancy is the approximate modeling of the CDS booster accelerating field by a purely sinusoidal wave with no transverse components. I tested this hypothesis by applying the 3-phase method on data coming from ASTRA simulations. I computed the bunch energy spread as a function of the booster RF-phase with the real longitudinal profile of the booster accelerating field taken into account in ASTRA and with a perfectly sinusoidal longitudinal profile. I then compared in Tab. 2.6 the rms bunch length predicted by ASTRA simulations and the one computed by the 3-phase method (SCF stands for space-charge forces).

One can see in Tab. 2.6 that the rms bunch length computed by the 3-phase method is closer to the one predicted by ASTRA when the real longitudinal profile of the booster accelerating field is replaced by a purely sinusoidal one. In fact, the discrepancy decreases from 21% to 9% without space-charge forces and from 21% to 7% with space-charge forces. It therefore proves that the modeling of the CDS booster accelerating field by a purely sinusoidal wave with no transverse components can have a noticeable impact on the accuracy of the 3-phase method.

	case without SCF for the real booster field	case without SCF for the sinusoidal booster field	case with SCF for the real booster field	case with SCF for the sinusoidal booster field
expected length from simulation (fs)	186	186	353	357
reconstructed length from 3-phase method (fs)	225	203	428	381

TABLE *2.6 – rms bunch length predicted by the ASTRA simulations and computed by the 3-phase method. Bunch charge : 100 pC ; Bunch energy at the booster entrance : 6 MeV ; Booster peak accelerating field : 17.5 MV/m.*

Fig. 2.39 shows the results of the measurements performed with the CDS booster for the short Gaussian laser time profile. These results are also compared with the bunch length predictions coming from the ASTRA beam dynamics code.

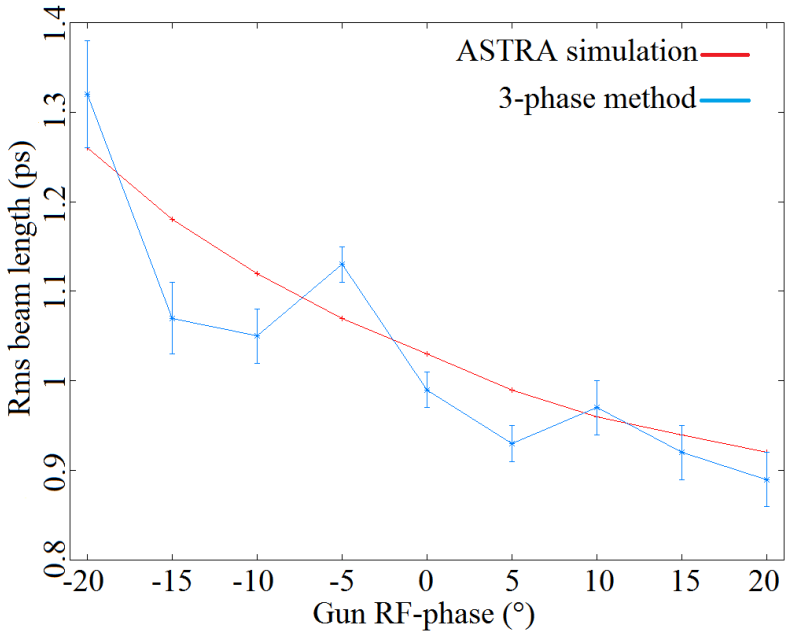

FIGURE *2.39 – 3-phase measurements performed with the CDS booster at PITZ for the short Gaussian laser time profile. RF-gun peak accelerating field : 60 MV/m (Bunch energy around 6.2 MeV at the exit) ; CDS Booster peak accelerating field : 17.5 MV/m ; Bunch charge : 20 pC.*

Fig. 2.39 shows that 3-phase method enables a very good reconstruction of bunch length at the CDS booster entrance as a function of the Gun RF-phase for the short Gaussian laser time profile. Indeed, the difference from the value extracted from the ASTRA simulation is only 9% (6% taking the error bars into account) at maximum.

The ASTRA predictions of the rms bunch length at the CDS booster entrance reported in Tab. 2.5 and Fig. 2.39 have been obtained with ideal initial electron time distri-

butions. Namely, the real long flat-top laser of PITZ (see Fig. 2.35) has been modeled in ASTRA by an ideal flat-top time profile with 24 ps FWHM and 2 ps rise and fall time, the real short flat-top by an ideal flat-top time profile with 5.8 ps FWHM and 2 ps rise and fall time and the real short Gaussian by an ideal Gaussian time profile with a standard deviation of 0.85 ps. To ensure that this approximation has no significant impact on the rms bunch length predicted by ASTRA, I choose to generate initial time distributions reproducing the ones of the real PITZ laser long and short flat-top pulses by using a Von Neumann algorithm. The used Von Neumann algorithm consists in the random generation of time positions uniformly distributed within the time extension of one of the PITZ laser pulse time distribution (see Fig. 2.35). For each time position a random number is generated between 0 and 1, which is the maximum value of the normalized time distribution of the PITZ laser pulse. If the generated random number is lower than the value of the time distribution at the generated time position, the time position is conserved. If the generated random number is higher than the value of the time distribution at the generated time position, the time position is not conserved. It ensures that the generated time distribution reproduces the one of the real PITZ laser pulse. I then use these Von Neumann generated time distributions to perform ASTRA simulations and I compare the results with those obtained with the ideal initial time distributions. Tab. 2.7 shows the result of this comparison for the cases of the Tab. 2.5.

Case	ASTRA predictions for ideal distributions	ASTRA predictions for Von Neumann distributions	discrepancy
Long flat-top +20° gun	3.99ps rms	3.95ps rms	1.00%
Long flat-top 0° gun	5.90ps rms	5.85ps rms	0.85%
Long flat-top -20° gun	7.75ps rms	7.67ps rms	1.03%
Short flat-top +20° gun	1.85ps rms	1.81ps rms	2.16%
Short flat-top 0° gun	2.12ps rms	2.06ps rms	2.83%
Short flat-top -15° gun	2.44ps rms	2.37ps rms	2.87%

TABLE *2.7 – Comparison of the rms bunch length predicted by ASTRA at the CDS booster entrance for ideal initial time distributions of the bunch and for initial time distributions reproducing the ones of Fig. 2.35 generated by a Von Neumann algorithm. The comparison has been performed for the cases shown in Tab. 2.5.*

Tab. 2.7 shows that the rms bunch length predicted by ASTRA when starting from an initial time distribution generated by the Von Neumann algorithm is different from the one predicted when starting from an ideal initial time distribution. However, the discrepancy remains small since it is 2.87% at maximum. One can remark that the discrepancy is lower for the long flat-top profile than for the short one. This is quite surprising since, as

it can be seen in Fig. 2.35, the long flat-top profile is not really flat but rather noisy on its top and one could therefore have expected a higher discrepancy between this profile and the ideal flat-top one. The conclusion of this study is that using initial time distributions generated by the Von Neumann algorithm to perform ASTRA simulations is not of a major interest, since the discrepancy with the ideal initial time distributions generated by ASTRA remains small.

The measurements performed at PITZ show that the 3-phase method, despite its numerous approximations, is very reliable and allows determining with a precision better than 15% the rms length of a few-MeV (around 6 MeV at PITZ) low-charge (20 pC) electron bunch generated by an RF-gun. The method has been validated in the sub-picosecond regime, since rms bunch length around 900 fs has been measured with a precision better than 5% (see Fig. 2.39).

Moreover, this is a cheap and technologically simple method. Indeed it requires only an RF accelerating structure and a system to measure the bunch energy spread, which are basic elements on an electron Linac. It is therefore a good alternative to the other classical bunch length measurement methods, like Cerenkov detector and transverse deflecting cavity, which are more expensive and technologically complicated to implement. But it doesn't allow determining the time profile of the bunch, contrary to Cerenkov detector and transverse deflecting cavity.

In my thesis, the 3-phase method has only been applied to low-charge electron bunches (20 pC). It would be interesting to develop a 3-phase method taking into account the space-charge force effects, to see if it is possible to apply it to very dense electron bunches. Measurements has been performed at PITZ with 1 nC bunches and could be used as a test for this new method.

2.3.3 Measurement of the bunch length thanks to a Cerenkov detector

2.3.3.1 Physical principle

One other way to measure the length of an electron bunch is to use a Cerenkov emitter placed in the path of the electron bunch. This radiation is emitted when a charged particle is traveling through a dielectric medium of refractive index n at a velocity v higher than the speed of light in the medium, which is equal to $\frac{c}{n}$. The charged particle will polarize the atoms along its path, such that they become electric dipoles. The time variation of the dipole field leads to the emission of electromagnetic radiation, the Cerenkov one. As long as $v < \frac{c}{n}$, the dipoles are disposed symmetrically around the charged particle path. The integrated dipole field over all the dipoles is then zero and there is no radiation emission. If $v > \frac{c}{n}$ this symmetry is broken, which results in a non-zero dipole moment leading to the Cerenkov radiation emission. These two cases are illustrated by Fig. 2.40.

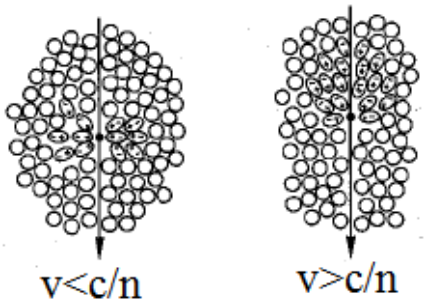

FIGURE *2.40 – Illustration of the Cerenkov effect [93].*

The Cerenkov light is emitted along a cone forming an angle $\theta_c = arcos(\frac{c}{nv})$ with the charged particle trajectory [93]. It has a continuous emission spectrum, for which the number N_ν of emitted photons per unit of length x in the wavelength range $[\lambda_1 ; \lambda_2]$ is given by the Frank-Tamm formula [93] :

$$\frac{dN_\nu}{dx} = 2\pi\alpha Z^2 \int_{\lambda_1}^{\lambda_2} \left(1 - \frac{c^2}{n^2 v^2}\right) \frac{d\lambda}{\lambda^2}$$

where Z is the charge of the particle (in terms of elementary charge $e = 1.6 * 10^{-19}$ C) and α the Fine-structure constant, approximately equal to 1/137.

One has to note that the refractive index n is a function of the emitted wavelength λ. It implies that the Frank-Tamm formula is relevant only in the wavelength range where $n(\lambda) > \frac{c}{v}$, the number of emitted photons being zero outside of this range. It means that there is a wavelength boundary below which no Cerenkov photons are emitted. In fact, n becomes equal to or lower than 1 in the X-ray region, implying that the condition $n(\lambda) > \frac{c}{v}$ cannot be fulfilled. Above this border the number of emitted photons scales like $\frac{1}{\lambda^2}$, meaning that most part is emitted at short wavelength, namely in the UV.

In the case of PHIL, only the Cerenkov photons between 400 nm and 800 nm will be detected. It allows assuming that the value of n is constant to the one at 524 nm ($n_0 = 1.77$). Indeed it is 1.7865 at 400 nm and 1.7601 at 800 nm, resulting in a variation lower than 1% with respect to n_0. The Frank-Tamm formula can be simply integrated in the case of a constant refraction index n :

$$N_\nu = 2\pi\alpha \left(\frac{1}{\lambda_1} - \frac{1}{\lambda_2}\right) \left(1 - \frac{c^2}{v^2 n^2}\right) L N_e \tag{2.7}$$

where L is the thickness of Cerenkov radiator crossed by the bunch (220 μm taking the 66° angle into account) and Z has been fixed to 1 since we will only consider the case of an electron bunch thereafter. N_e is the number of electrons in the bunch. Fig. 2.41 shows the number of Cerenkov photons emitted per unit of wavelength, as a function of the wavelength, between 400 nm and 800 nm for a constant refraction index $n = n_0 = 1.77$.

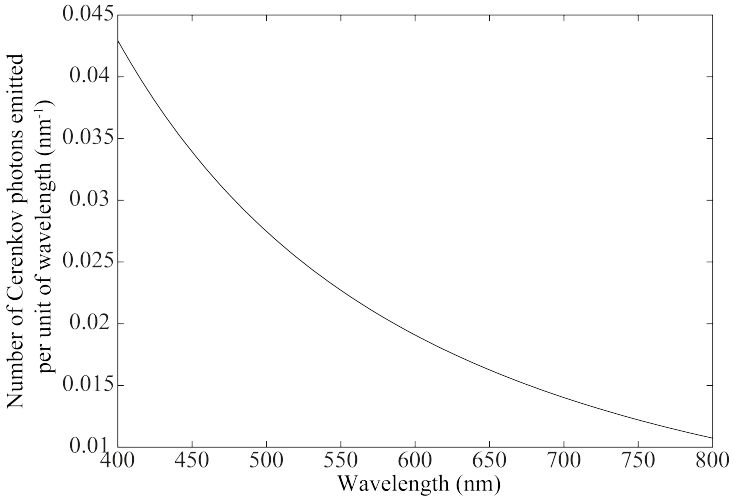

FIGURE *2.41 – Spectrum of the Cerenkov photons detected at PHIL*

The Cerenkov radiation is promptly emitted, namely within a few femtoseconds, after the passage of the particle. This is much shorter than the bunch produced at PHIL, which has an rms length of a few picoseconds. It implies that the emitted Cerenkov light reproduces the PHIL bunch time profile.

The Cerenkov radiation is then transported to a streak camera, in which the time profile is converted into a transverse profile thanks to the use of a fast time-sweeping transverse electric field. Fig. 2.42 depicts the operating principle of a streak camera. This section presents the different steps followed to develop and commission the Cerenkov detector and streak camera installed on the PHIL facility (see Fig. 1.24), in addition to the first measurements of the PHIL electron bunch length.

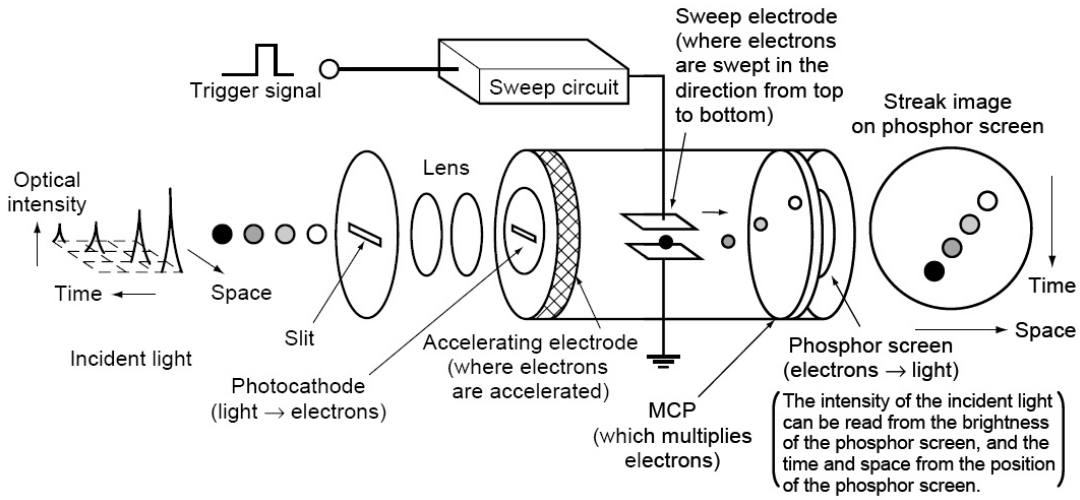

FIGURE *2.42 – Operating principle of a streak camera [94].*

2.3.3.2 Experimental layout

On the PHIL facility, the Cerenkov emitter is a Sapphire crystal of 200 μm thickness, having as a refraction index $n_0 = 1.77$ at a wavelength of 524 nm. The emitted Cerenkov light when the bunch passes through this crystal is extracted from the beamline at an angle of 90° with respect to the electron bunch path, as shown in Fig. 2.43. It requires the Sapphire crystal to form an angle of 66° with the electron bunch path, taking into account the refraction of Cerenkov light at the Sapphire exit. The angle between the Sapphire crystal and the electron bunch path is controlled by a step-by-step motor, allowing a resolution of 0.45° (one step of the motor).

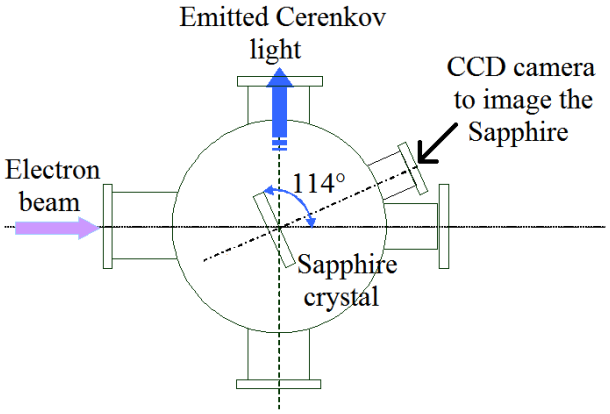

FIGURE *2.43 – Layout of the Cerenkov station mounted at the PHIL facility*

This Cerenkov light is then transported through a 15 m long path with 8 dielectric mirrors, 3 biconvex lenses with 75 mm diameter and 1.75 m focal and 2 achromatic lenses with 50 mm diameter and 12 cm and 20 cm focals. Two types of dielectric mirrors have been used successively. The first kind of mirror is produced by Laseroptik (B-08302 type) and offers a reflectivity higher than 99.8% at 550 nm and higher than 98.5% in the 510 nm-600 nm bandwidth for an incidence angle of 45°, as shown on the left plot of Fig. 2.44. It has a diameter of 2 inches (50.8 mm). The second kind of mirror has been purchased on my proposal. It is produced by Thorlabs (BB3-E02 type) and offers a reflectivity higher than 99% in the 400 nm-800 nm bandwidth for an incidence angle of 45°, as shown on the right plot of Fig. 2.44. It has a diameter of 3 inches (76.2 mm).

The Cerenkov light then goes into a streak camera to measure its time profile, which reproduces the one of the PHIL electron bunch. Two types of streak camera have been used successively at PHIL. The first type was an old streak camera, which allowed a time resolution of 3 ps rms, produced by ARP at the beginning of the 90s and used for the CANDELA experiment [95]. The second and current type is a streak camera produced by Hamamatsu (C10910-01 type), allowing an ultimate time resolution of 1 ps rms [94]. It will be used in the ThomX project [88].

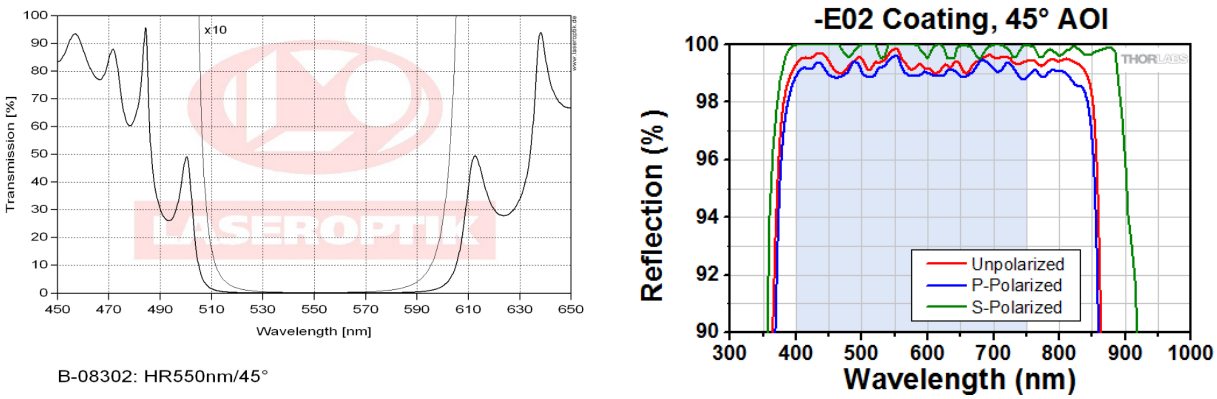

FIGURE 2.44 – *Reflectivity plots as a function of the incident wavelength for the two kind of dielectric mirror used at PHIL ; Left plot : Laseroptik B-08302 type ; Right plot : Thorlabs BB3-E02 type.*

2.3.3.3 Calibration of a CCD camera

To determine the number of Cerenkov photons at different points of the transport line, I choose to calibrate a CCD camera (MatrixVision BlueCougar S-123 [80]) by determining its number of generated signal units per incident photon. To do that, I used the green pulsed laser of PHIL which has a wavelength of 532 nm. The reason is that we can directly know the number of photons per pulse from a measurement of the pulse energy. This calibration will be used to study the number of extracted Cerenkov photons from the Cerenkov station (see Fig. 2.43) and also the number of photons transported along the transport line up to the streak camera.

This calibration has been performed at the gain 0 of the CCD camera and gives a result of $(3 \pm 0.2) * 10^{-2}$ signal units per 532 nm incident photon. It is important to note that this calibration is valid only for a wavelength of 532 nm. To determine the number of Cerenkov photons, which spread all over the visible wavelength range, it will be necessary to add a correction by taking into account the variation of the CCD spectral sensitivity with the incident wavelength. This spectral sensitivity is shown in Fig. 2.45.

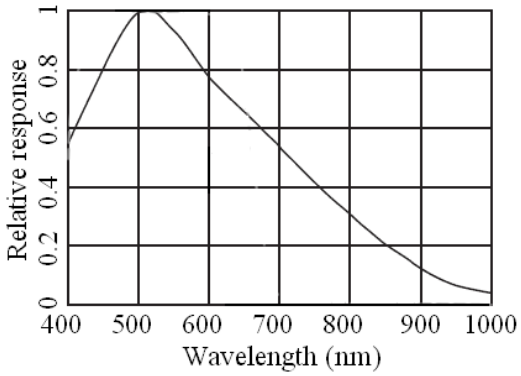

FIGURE 2.45 – *Spectral sensitivity of the MatrixVision BlueCougar S-123 CCD camera [80]*

Strictly speaking, the previous calibration is valid only at the gain 0 of the CCD camera. However, it is easily transposable to another gain X. In fact it is sufficient to take the same picture for both the gain 0 and the gain X and to determine the intensity ratio between the two images. The calibration ratio will then be the same between the gain 0 and the gain X.

2.3.3.4 Extraction of the Cerenkov photons from the Cerenkov station

I choose first to measure the number of Cerenkov photons extracted from the Cerenkov station, to compare it to the theoretical value given by the Frank-Tamm formula (see Eq. 2.7) and also to determine what are the best electron bunch transport conditions to optimize this number of extracted photons. To do that I placed the calibrated CCD camera just after the extraction window (see Fig. 2.43) with a 12 cm focal lens placed against this window, namely around 12 cm away from the Sapphire crystal, to focus the Cerenkov radiation on the CCD. I then tuned the bunch transport parameters of PHIL to obtain the most focused and intense Cerenkov photons beam possible on the CCD : $IB3$ (current injected in the B3 solenoid), $IB5$ (current injected in the B5 solenoid), steerer n°1 and Gun RF-phase (see Fig. 1.24).

Fig. 2.46 (left picture) shows the measured radiation. This measured radiation contains both the Cerenkov radiation and the fluorescence radiation emitted by the Sapphire crystal. It is therefore necessary to subtract the fluorescence radiation. It has been done by rotating the Sapphire crystal by an angle of 90° with respect to the configuration shown in Fig. 2.43. The thickness of Sapphire crosses by the electron bunch is then the same, but only the fluorescence radiation is extracted from the Cerenkov station. Fig. 2.46 (central picture) shows the measured fluorescence radiation and Fig. 2.46 (right picture) shows the Cerenkov radiation (subtraction of left and central picture). One remarks that the fluorescence radiation is far less intense than the Cerenkov one, greatly favoring the detection of the latter.

FIGURE *2.46 – Total radiation (left), fluorescence radiation (center) and Cerenkov radiation (right) measured after the Cerenkov station extraction window ; Conditions : 63 MV/m Gun peak accelerating field (3.5 MeV electron bunch) ; 350 pC bunch charge ; IB3 = 155 A ; IB5 = 45 A ; 6.3∗4.8 mm² CCD pad.*

It is now possible to determine the number of Cerenkov photons extracted from the

Cerenkov station and to compare it with the one predicted by the theory. I choose to limit the wavelength to the range 400 nm-800 nm, since the spectral sensitivity of the CCD camera becomes very weak outside (see Fig. 2.45). The bunch charge being of 350 pC ($2.2*10^9$ electrons) and the bunch energy of 3.5 MeV ($v = 0.992\ c$), the number of Cerenkov photons emitted by the Sapphire crystal between 400 nm and 800 nm can be estimated to $1.9*10^{10}$ by the Frank-Tamm formula (see Eq. 2.7).

The number of Cerenkov photons detected by the CCD camera, taking into account its spectral sensitivity (see Fig. 2.45), is estimated to $(1.9 \pm 0.3) * 10^8$. A factor of 100 is therefore lost with respect to the theory right out of the Cerenkov station. For the 3.5 MeV PHIL electrons, the angle of the Cerenkov emission cone is $\theta_c = 55.3°$, the extraction window of the Cerenkov station is placed 12 cm away from the Sapphire crystal and has a diameter of 7 cm. A simple geometrical calculation shows that only 6.6% of the Cerenkov cone passes through the extraction window for such a configuration. This explains a factor 15 of the Cerenkov radiation losses. Another cause of losses comes from the fact the collection lens placed just behind the extraction window is less wide than this one. Its diameter being 5 cm, it explains another factor 7/5 of losses. A factor 21 of losses is therefore only due to simple geometrical effects.

It is important to note that what has been developed previously is valid only for a perfect Cerenkov cone, namely emitted by a monochromatic point source into a Sapphire crystal of infinite sizes. This is not the case in our experiment, where the Sapphire crystal has finite sizes and the electron bunch is neither a point nor monochromatic or parallel. It implies a degradation of the quality of the emitted Cerenkov cone : refraction and reflection of the radiation at the Sapphire/air exit interface, nonzero thickness of the Cerenkov cone, divergence of the Cerenkov cone thickness. These effects, as well as the absorption of a part of the emitted Cerenkov radiation by the Sapphire crystal itself, can therefore be considered as responsible for the remaining loss factor of 5. It is also possible that the extraction window causes losses, by absorbing or scattering a part of the Cerenkov radiation. However these losses should be small, since the extraction window is transparent and doesn't distort the images.

These measurements allow concluding that the Sapphire crystal is of good quality from the point of view of the amount of produced Cerenkov radiation. However, only 1% can be extracted from the Cerenkov station.

I also performed this kind of measurement for different Gun RF-phases : The 0° phase maximizing the bunch charge (750 pC), the $-40°$ phase maximizing the bunch energy (480 pC) and the $-57°$ phase minimizing the bunch energy spread. For each measurement I optimized the bunch transport parameters ($IB3$, $IB5$ and steerer n°1) to obtain the most focused and intense Cerenkov beam possible on the calibrated CCD camera. Fig. 2.47 shows the measured Cerenkov radiations for these 3 configurations of Gun RF-phase (color scales are the same).

The numbers of measured photons for these 3 RF-phases are the following : $(2.4 \pm 0.1)*10^8$ at 0°, $(2.4 \pm 0.1)*10^8$ at $-40°$ and $(1.5 \pm 0.1)*10^8$ at $-57°$. These measurements highlight that the charge of the electron bunch is not the only important parameter to maximize the intensity of the Cerenkov radiation extracted from the Cerenkov station.

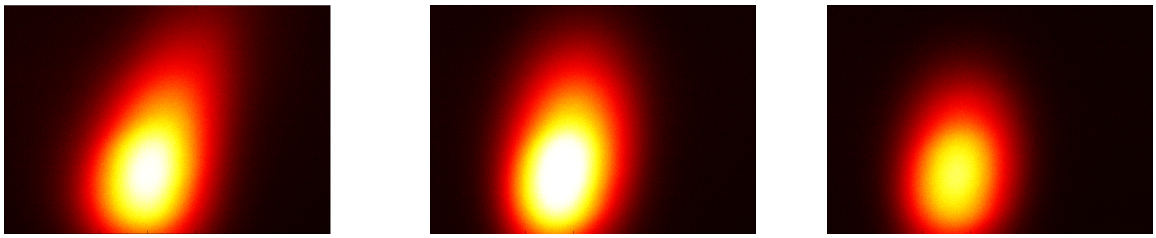

FIGURE 2.47 – *Cerenkov radiation measured after the Cerenkov station extraction window ; Conditions : 63 MV/m Gun peak accelerating field ; 0° (left), −40° (center) and −57° Gun RF-phase (0° = maximum of bunch charge) ; 2.8 MeV (left), 3.6 MeV (center) and 3.5 MeV (right) bunch energy ; 750 pC (left), 480 pC (center) and 230 pC (right) bunch charge ; IB3 = 118 A (left), 140 A (center) and 145 A (right) ; IB5 = 39 A (left), 41 A (center) and 41 A (right) ; 6.3∗4.8 mm² CCD pad.*

Indeed the numbers of extracted photons are the same at 0° and at −40°, despite the fact that the bunch charge and therefore the number of initially produced Cerenkov photons are 36% lower at −40°. The Gun RF-phase plays also an important role through the fact that, by dephasing with respect to the maximal bunch charge, the bunch energy spread and transverse emittance are lowered. It allows obtaining a more focused and symmetrical electron bunch on the Sapphire crystal, which consequently generates a cleaner Cerenkov cone (less thick and less divergent) therefore easier to extract and transport. Fig. 2.48 illustrates this fact by showing the measured electron bunch transverse profile on the PHIL YAG2 screen (see Fig. 1.24), located just after the Sapphire crystal, for each of these three cases. In each case, the bunch transport parameters (IB3, IB5 and steerer n°1) has been optimized to obtain the most focused and intense Cerenkov beam possible on the calibrated CCD camera. It is clearly visible that the electron bunch is more focused and symmetrical at −57° and −40° than at 0°. There is however a compromise to find since if the dephasing is too important the bunch charge becomes too low, and the number of extracted Cerenkov photons then decreases. It is visible in the measurement at −57° for which the number of extracted Cerenkov photons is lower than at −40°, because of the lower bunch charge.

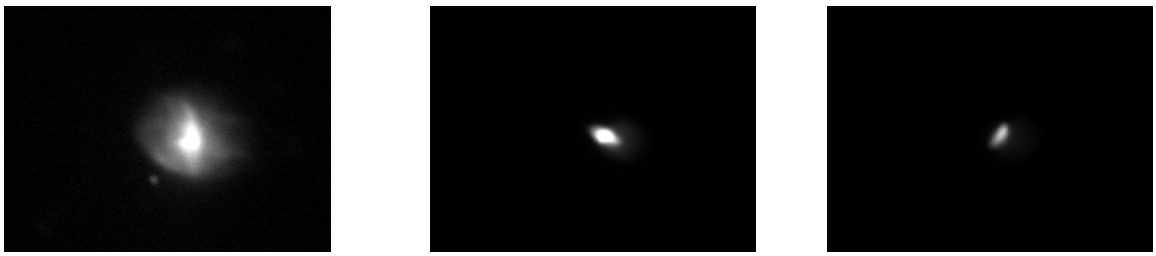

FIGURE 2.48 – *Electron bunch transverse profile measured on the PHIL YAG2 screen ; Conditions : 63 MV/m Gun peak accelerating field ; 0° (left), −40° (center) and −57° Gun RF-phase (0° = maximum of bunch charge) ; 2.8 MeV (left), 3.6 MeV (center) and 3.5 MeV (right) bunch energy ; 750 pC (left), 480 pC (center) and 230 pC (right) bunch charge ; IB3 = 118 A (left), 140 A (center) and 145 A (right) ; IB5 = 39 A (left), 41 A (center) and 41 A (right) ; 4.8∗3.6 mm² CCD pad.*

I choose therefore to work at a Gun RF-phase of $-40°$, with respect to the $0°$ phase maximizing the bunch charge, to perform the study of the transport of the Cerenkov radiation up to the streak camera entrance. The reason is that the transport of the Cerenkov radiation will be easier, because the electron bunch generating it is of better quality, and there will therefore be less losses.

2.3.3.5 Transport of the Cerenkov radiation up to the streak camera entrance

The calibrated CCD camera has then be placed just before the entrance of the streak camera, to measure again the number of Cerenkov photons. The goal of this measurement is to evaluate the efficiency of the 15 m long optical transport of the Cerenkov radiation.

It has been first performed with the Laseroptik mirrors (see Sec. 2.3.3.2 and Fig. 2.44 (left plot)). The measured Cerenkov radiation is shown in Fig. 2.49. The number of Cerenkov photons transported up to the streak camera entrance is $(2.5 \pm 0.4) * 10^6$ in this case. There is therefore a factor 100 of losses during the optical transport of the Cerenkov radiation between the exit of the Cerenkov station and the entrance of the streak camera. I proposed to perform again this measurement, in similar conditions, with the Thorlabs mirrors (see Sec. 2.3.3.2 and Fig. 2.44 (right plot)). The measured Cerenkov radiation is shown in Fig. 2.50. The number of Cerenkov photons transported up to the streak camera entrance is $(1.2 \pm 0.1) * 10^8$ in this case. It corresponds to losses of only 50% along the optical transport line, which is very good for a 15 m long transport of the Cerenkov radiation.

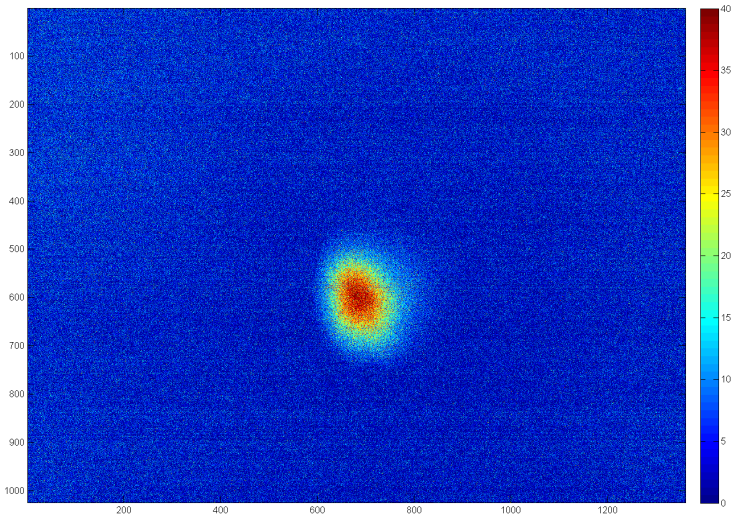

FIGURE *2.49 – Cerenkov radiation measured at the entrance of the streak camera with the Laseroptik mirrors ; Conditions : 63 MV/m Gun peak accelerating field ; −40° Gun RF-phase (0° = maximum of bunch charge) ; 3.6 MeV bunch energy ; 470 pC bunch charge ; IB3 = 137 A ; IB5 = 41 A ; 6.3∗4.8 mm² CCD pad ; Gain 18 of the CCD camera.*

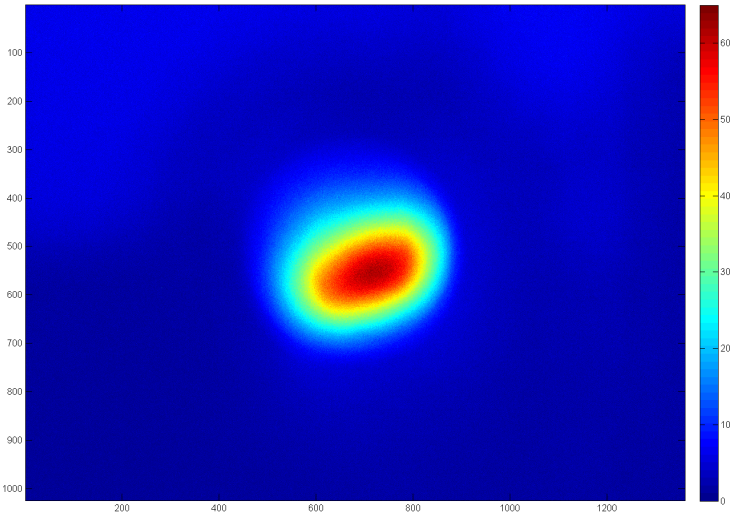

FIGURE *2.50 – Cerenkov radiation measured at the entrance of the streak camera with the Thorlabs mirrors ; Conditions : 63 MV/m Gun peak accelerating field ; −40° Gun RF-phase (0° = maximum of bunch charge) ; 3.6 MeV bunch energy ; 420 pC bunch charge ; IB3 = 138 A ; IB5 = 44 A ; 6.3∗4.8 mm² CCD pad ; Gain 0 of the CCD camera.*

The intensity gain due to the change of the optical transport line mirrors is therefore a factor of 48. It is noteworthy that this gain is explained by two phenomena. First, the increase in mirror bandwidth is responsible for a gain factor of 4. In fact, according to Eq. 2.7, 2.0 Cerenkov photons per electron are produced within the 510 nm-600 nm bandwidth of the Laseroptik mirrors and 8.5 Cerenkov photons per electron are produced within the 400 nm-800 nm bandwidth of the Thorlabs mirrors. The remaining, and main, gain factor of 12 is explained by the larger diameter of the Thorlabs mirrors (76.2 mm against 50.8 mm). It allows greatly reducing the geometrical losses of Cerenkov radiation along the optical transport line. The Thorlabs mirrors, that I proposed to purchase, are therefore used in the optical transport line instead of the initially intended Laseroptik mirrors.

2.3.3.6 Resolution of the measurement

An important point, before performing bunch length measurements with the streak camera, is to study the sources which limit the resolution of this kind of measurement by lengthening the Cerenkov signal. There are three main sources that are identified : the transverse size of the electron bunch impacting the Sapphire crystal, the difference of travel time between the electron bunch and the Cerenkov light in the Sapphire crystal and the aperture of the streak camera entrance slit.

Fig. 2.51 illustrates that there is a difference of travel time between the electron bunch and the emitted Cerenkov light in the Sapphire crystal. This difference corresponds to a lengthening of the Cerenkov radiation duration with respect to the electron bunch duration, since the travel time of the Cerenkov radiation is the longest.

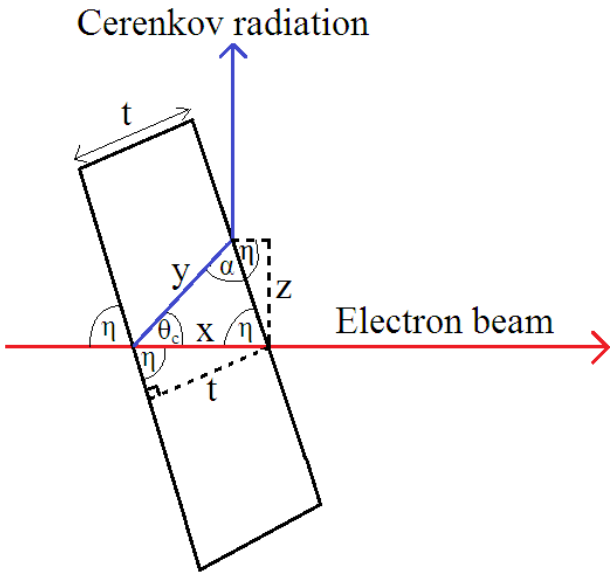

FIGURE 2.51 – *Illustration of the travel time difference of the electron bunch and Cerenkov radiation in the Sapphire crystal.* $\eta = 66°$; $t = 200\ \mu m$; $\theta_c = 55.3°$; $\alpha = 58.7°$.

The electrons travel the distance $x = \frac{t}{\sin(\eta)} = 220\ \mu m$ in the Sapphire crystal at a typical velocity of 0.992 c (energy of 3.5 MeV). I assume this velocity to be constant during all their motion in the Sapphire. It is justified since the energy loss in 220 μm of Sapphire for 3.5 MeV electrons is only 1.5 keV. The travel time of the electrons in the Sapphire crystal is therefore of $\Delta t_e = \frac{x}{0.992c} = 0.736\ ps$.

The Cerenkov photons emitted just at the entrance of the Sapphire crystal travels the distance $y = x\frac{\sin(\eta)}{\sin(\alpha)} = 235\ \mu m$ in the Sapphire crystal at a velocity of $\frac{c}{n_0}$. The travel time of these photons in the Sapphire crystal is therefore of $\Delta t_c = \frac{n_0 y}{c} = 1.382\ ps$.

The difference of travel time, between the first emitted Cerenkov radiation and the electron bunch, in the Sapphire crystal is finally given by $\Delta t_c - \Delta t_e = 0.646\ ps$. However, this is not equal to the final lengthening of the Cerenkov radiation with respect to the bunch one. In fact the last emitted Cerenkov radiation, that is to say the one emitted just before the electron bunch exits the crystal, has to travel a distance z in vacuum to reach the point where the first emitted Cerenkov radiation exits the crystal (see Fig. 2.51). This distance is traveled in a time $\Delta t_{cv} = \frac{x\sin(\eta)\sin(\theta_c)}{c\sin(\alpha)} = 0.642\ ps$. The lengthening of the Cerenkov radiation caused by the difference of the travel time in the Sapphire crystal with respect to the electron bunch is therefore given by $\delta t_{crystal} = \Delta t_c - \Delta t_e - \Delta t_{cv} = 4\ fs$.

This lengthening has to be expressed in rms terms, to be consistent with the measurements performed thereafter which are all expressed in rms terms. $\delta t_{crystal}$ is a uniformly distributed lengthening. The standard deviation σ of a uniform distribution of total width X is given by $\sigma = \frac{X}{2\sqrt{3}}$. The rms lengthening of the Cerenkov radiation caused by the difference of the travel time in the Sapphire crystal with respect to the electron bunch is therefore given by $\frac{\delta t_{crystal}}{2\sqrt{3}} = 1.15\ fs$. This lengthening is very small, far lower than the streak camera resolution, and will therefore not limit at all the bunch length measurement.

Fig. 2.52 shows a diagram explaining how the transverse size of the electron bunch causes an increase in the duration of the emitted Cerenkov radiation with respect to the electron bunch duration.

It is shown that two electrons A and B having the same phase, namely the same longitudinal position in the bunch, and separating by a distance Δx in the transverse plane will emit photons which wavefronts will be delayed with respect to each other. This corresponds to a lengthening of the Cerenkov radiation duration with respect to the electron bunch duration. The apparent lengthening Δt_x can be estimated as follows :

$$c\Delta t_x = d(B,C) + d(D,E) = \Delta x \left(\tan\left(\frac{\pi}{2} - \eta\right) + 1\right)$$

where d denotes the geometrical distances. It has been supposed that the electron travels from B to C with a velocity equal to c. This is justified since the typical energy of the PHIL electrons is 3.5 MeV, which corresponds to a velocity of 0.992 c.

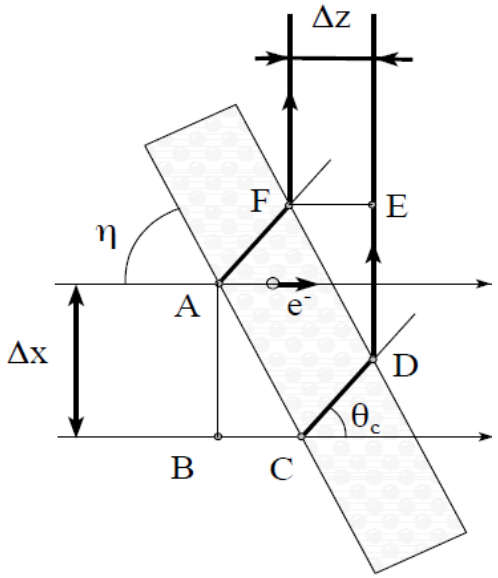

FIGURE *2.52 – Influence of the electron bunch transverse size on the emitted Cerenkov radiation duration*

At PHIL we have $\eta = 66°$, which corresponds to a lengthening of 4.8 ps per millimeter of transverse expansion Δx of the incident electron bunch. The typical transverse size of the electron bunch on the Sapphire crystal is almost the same as the one on the YAG2 screen, which is located only 20 cm behind. The rms transverse size for the bunch shown in Fig. 2.48 (center), and used in experiments, is 0.56 mm. It corresponds therefore to an rms lengthening of $\delta t_{transverse} = 2.7\ ps$ of the emitted Cerenkov radiation with respect to the real electron bunch rms duration.

This value of $\delta t_{transverse}$ is only a rough approximation, due to the slit at the entrance of the streak camera (see Fig. 2.42). This slit is typically closed down to an aperture of 100 μm and even less. This is much lower than the minimal transverse size at which the

Cerenkov radiation can be focused at the streak camera entrance. This minimal transverse size is indeed slightly lower than the electron transverse bunch size on the Sapphire crystal, therefore between 400 μm and 500 μm rms. It implies that the effective transverse size of the Cerenkov radiation on the Sapphire crystal, namely the one entering in the streak camera, is lower than the one of the electron bunch. A simple way to model and evaluate this phenomenon is to consider a parallel Cerenkov radiation, as shown in Fig. 2.53.

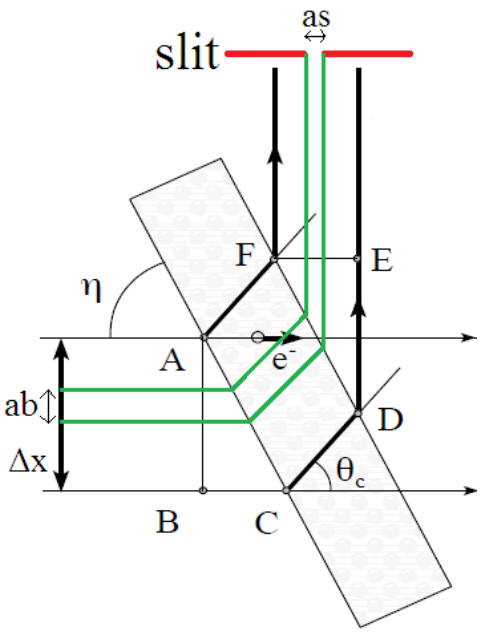

FIGURE *2.53 – Influence of the slit at the entrance of the streak camera on the measured Cerenkov radiation duration*

In this simple case, only the Cerenkov radiation delimited by the two green lines effectively enters in the streak camera. It implies that the effective transverse size of the Cerenkov radiation a_b is given by $a_b = \frac{a_s}{\tan(\frac{\pi}{2}-\eta)}$, where a_s is the aperture of the streak camera entrance slit. For the typical value of $a_s = 100\ \mu m$, we have $a_b = 225\ \mu m$. It corresponds therefore to a lengthening of $\delta t_{transverse} = 1.1\ ps$ of the emitted Cerenkov radiation with respect to the real electron bunch duration.

This value of $\delta t_{transverse}$ is also an approximation, because there are focusing elements along the optical transport line implying that the Cerenkov radiation is not parallel as shown in Fig. 2.53. However, this approximation remains accurate as long as the transverse size of the Cerenkov radiation coming at the streak camera entrance is about the order of the transverse size of the electron bunch on the Sapphire crystal, which is the case in our experiments.

The lengthening $\delta t_{transverse}$ has to be expressed in rms terms, to be consistent with the measurements performed thereafter which are all expressed in rms terms. To do that, we have to calculate the standard deviation of a Gaussian distribution cut at $\pm\frac{a_b}{2}$ (see Fig. 2.53). For the typical case previously exposed, namely a Gaussian distribution with a standard deviation of 0.56 mm and $a_b = 0.225\ mm$, the standard deviation of the cut

Gaussian distribution is 0.065 mm. It corresponds to an rms lengthening of $\delta t_{transverse} = 0.31$ ps of the emitted Cerenkov radiation with respect to the real electron bunch duration.

The aperture of the slit at the streak camera entrance plays a very important role in the resolution of the bunch length measurement. In fact, as shown in Fig. 2.42, the bunch length is deduced from the vertical bunch size measured after the fast-sweeping electric field in the streak camera. There is therefore a limitation in the resolution of the bunch length measurement, which is given by the vertical bunch size measured in the streak camera with the fast-sweeping electric field turned off. This is called the static slit size σ_{ss}. The static slit size is a function of the aperture of the slit at the streak camera entrance, which has therefore to be optimized before each session of measurements. The aperture must not be too large, otherwise the static slit size is too large and the measurement resolution is poor. But, the aperture cannot be reduced indefinitely for two reasons. Firstly, the signal intensity would become too low to perform a precise measurement. Secondly, diffraction of the incident signal would occur resulting in an increase in the static slit size. This phenomenon has been directly observed at PHIL. Indeed, Fig. 2.54 shows that, for the C10910-01 Hamamatsu streak camera, the rms static slit size is $\sigma_{ss} = 39$ pixels for an aperture of 45 μm (Fig. 2.54 (a)), while it is only $\sigma_{ss} = 26$ pixels for an aperture of 110 μm (Fig. 2.54 (b)). The typical slit aperture used during the experiments performed at PHIL is therefore around 100 μm, namely between 75 μm and 150 μm.

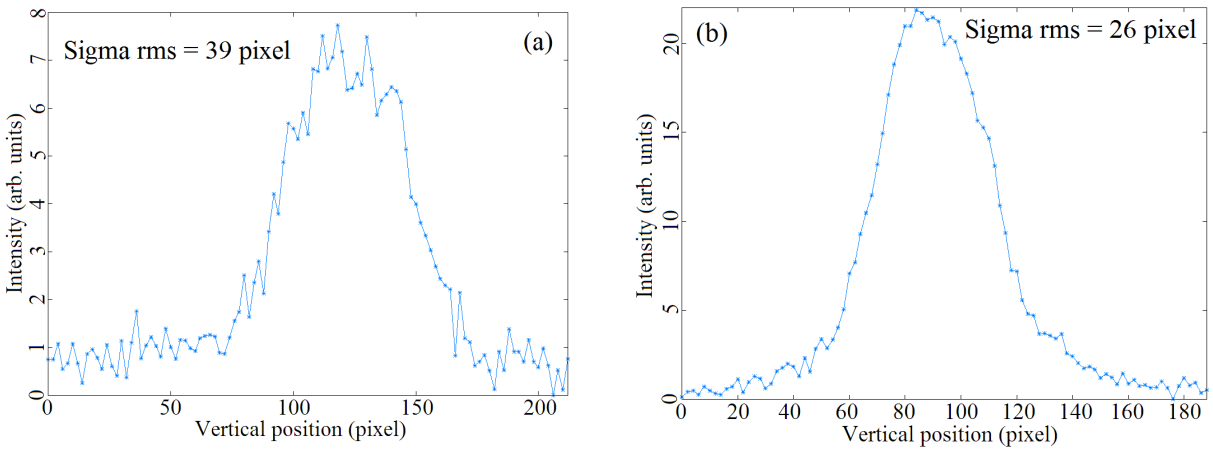

FIGURE 2.54 – *Static slit size σ_{ss} for an aperture of 45 μm (a) and of 110 μm (b) of the slit at the C10910-01 Hamamatsu streak camera entrance*

The static slit size is expressed in terms of pixel, because it is by definition independent on the sweeping speed of the electric field in the streak camera. Its conversion in terms of duration is dependent on the sweeping speed of the electric field in the streak camera and becomes therefore less important when the sweeping speed increases. For example, for the C10910-01 Hamamatsu streak camera, the fastest sweeping speed corresponds to a conversion of 71 fs/pixel between the measured vertical size in the streak camera and the duration of the incident Cerenkov radiation. In this case, the rms static slit size of 26 pixels previously mentioned will correspond to a resolution of 1.8 ps rms on the measurement of the Cerenkov radiation duration. The second fastest sweeping speed

corresponds to a conversion of 194 fs/pixel. In this case, the rms static slit size of 26 pixels previously mentioned will correspond to a resolution of 5.0 ps rms on the measurement of the Cerenkov radiation duration. It is therefore advantageous to perform the bunch length measurement with the fastest sweeping speed of the streak camera, to improve the resolution. However, if the bunch length is too large or the Cerenkov radiation intensity is too weak, it is sometimes inevitable to use a slower sweeping speed.

One has to be careful that these three limitations are not of the same type, and are therefore not applied in the same way on the value measured with the streak camera. $\delta t_{crystal}$ and $\delta t_{transverse}$ are pure lengthening of the Cerenkov radiation with respect to the electron bunch duration. They have therefore to be directly subtracted from the value measured with the streak camera. On the other hand, the time profile measured with the streak camera is a convolution of the incident Cerenkov radiation profile and of the static slit profile. The static slit size σ_{ss} has therefore to be quadratically subtracted from the rms length of the measured time profile σ_{meas} to obtain the rms length of the incident Cerenkov radiation σ_{Cer}. The rms length of the electron bunch impacting the Sapphire crystal σ_{t_e} is finally given by :

$$\sigma_{t_e} = \sqrt{\sigma_{meas}^2 - \sigma_{ss}^2} - \delta t_{transverse} - \delta t_{crystal} \tag{2.8}$$

In our case where σ_{ss}, $\delta t_{transverse}$ and $\delta t_{crystal}$ are much lower than σ_{t_e}, the three phenomena exposed above do not limit the resolution of the bunch length measurement with the streak camera. It is only when the addition of these three contributions starts to approach σ_{t_e} that the resolution of the measurement starts to be affected.

2.3.3.7 Bunch length measurement with the streak camera

Before measuring the PHIL electron bunch length, the length of the UV laser pulse driving the PHIL RF-gun has been measured with the streak camera. The result of this measurement is shown in Fig. 2.55. One has to note that the UV laser pulse has been directly sent into the streak camera. There are therefore no $\delta t_{transverse}$ and $\delta t_{crystal}$ lengthening contributions. The only limitation to the measurement resolution comes from the rms static slit size $\sigma_{ss} = 23$ pixels, which corresponds to a resolution of 1.6 ps rms for the fastest sweeping speed of the streak camera. The measured laser rms duration of 4.5 ± 0.3 ps is close to the manufacturer value of 3.8 ps.

During the session of electron bunch length measurements with the streak camera, the rms static slit size was $\sigma_{ss} = 24$ pixels which corresponds to a resolution of 1.7 ps rms for the fastest sweeping speed of the streak camera. One example of electron bunch length measurement at PHIL is shown in Fig. 2.56.

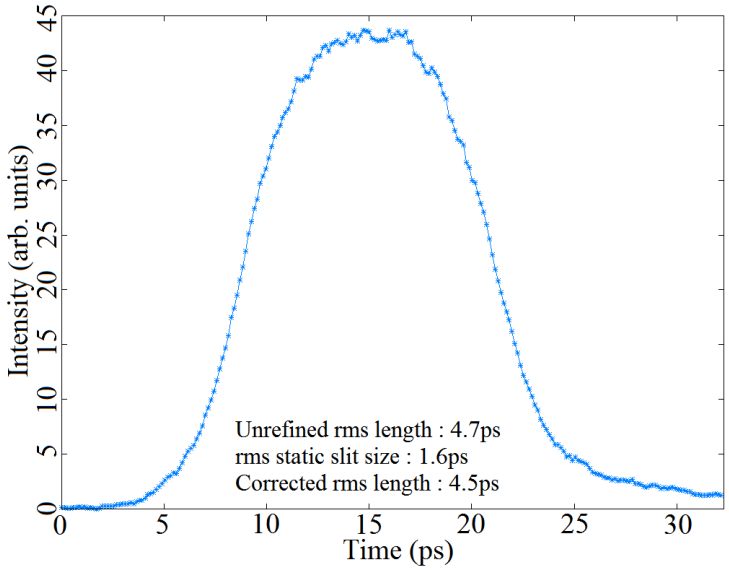

FIGURE *2.55 – Time profile of the UV laser pulse driving the PHIL RF-gun measured with the streak camera*

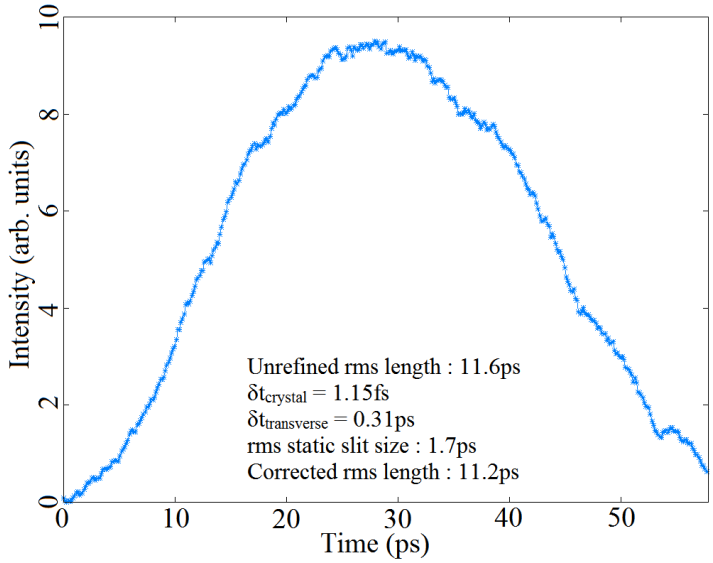

FIGURE *2.56 – Time profile of the Cerenkov radiation measured with the streak camera. Conditions : 62 MV/m Gun peak accelerating field ; −60° Gun RF-phase (0° = maximum of bunch charge) ; 3.5 MeV bunch energy ; 70 pC bunch charge ; IB3 = 148 A ; IB5 = 41 A.*

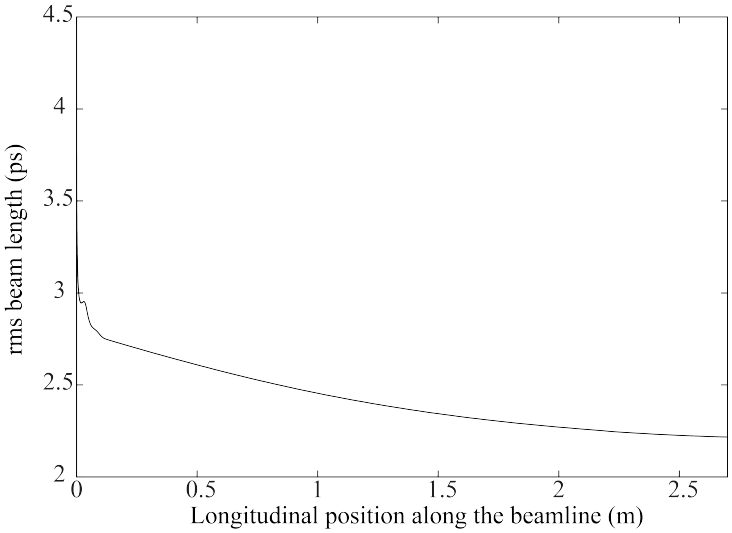

FIGURE *2.57 – Evolution of the rms bunch length predicted by ASTRA between the photocathode and the Sapphire crystal. Conditions : Conditions : 62 MV/m Gun peak accelerating field ; −60° Gun RF-phase (0° = maximum of bunch charge) ; 3.5 MeV bunch energy ; 70 pC bunch charge ; IB3 = 148 A ; IB5 = 41 A.*

The measured electron bunch rms length $\sigma_{t_e} = 11.2$ ps is significantly larger than the rms length predicted by the ASTRA simulations, which is about 2.2 ps at the level of the Sapphire crystal when starting from a 4.5 ps rms Gaussian electron distribution. Fig. 2.57 shows the evolution of the rms bunch length predicted by ASTRA between the photocathode and the Sapphire crystal. The reason of this large discrepancy has not been clearly determined yet and is still under investigation. However, several potential reasons are identified.

The main hypothesis is that the length of the electron bunch emitted from the photocathode is substantially larger than the 4.5 ps rms of the UV laser pulse impacting it and generating the electron bunch. There is currently no measurement device to directly test this hypothesis on PHIL. However, it can be indirectly tested through the measurement of the rms bunch energy spread with the dipole magnet (see Fig. 1.24). Indeed, for a fixed accelerating field in the RF-gun, the electron bunch energy spread varies with the length of the bunch. In particular, it is increasing when the electron bunch length is increasing. As shown in Sec. 2.3.2.1, the rms bunch energy spread at the RF-gun exit σ_{E_f} is given by :

$$\sigma_{E_f}^2 = R_{21}^2 \sigma_{t_i}^2 + 2R_{21}\sigma_{Et_i} + \sigma_{E_i}^2$$

where R_{21} is a coefficient of the RF-gun longitudinal transfer matrix (see Sec. 3.1.2.1) and σ_{t_i} is the rms length of the electron bunch at the moment of its emission from the photocathode. To simplify, the contribution σ_{E_i} of the initial rms bunch energy spread, which is about a few eV, can be neglected compared with σ_{E_f}, which is at least of a few keV. Assuming that the initial rms bunch time/energy correlation σ_{Et_i} is null, σ_{E_f} varies linearly with σ_{t_i} for fixed accelerating conditions (namely a fixed value of R_{21}).

Fig. 2.58 shows two electron bunch energy spectra measured with the dipole magnet on PHIL, each time at −60° from the Gun RF-phase maximizing the bunch charge. The major difference between the two measurement conditions is the photocathode. Fig. 2.58 (a) has been measured when using a polycrystalline Magnesium cathode. This is the cathode used during the electron bunch length measurement shown in Fig. 2.56. Fig. 2.58 (b) has been measured when using a Copper cathode.

Fig. 2.58 (b) shows a bunch rms relative energy spread of 0.15% at the −60° Gun RF-phase. This value totally agrees with the ASTRA simulations for a 62 MV/m Gun peak accelerating field and a 4.5 ps rms initial Gaussian electron distribution. On the contrary, Fig. 2.58 (a) shows a four times higher bunch rms relative energy spread of 0.63%, which is totally incompatible with a 62 MV/m Gun peak accelerating field and a 4.5 ps rms initial Gaussian electron distribution. This value would be consistent with an initial Gaussian electron distribution about four times longer, namely with an rms length around 18 ps. For this value, the ASTRA simulations predict an electron bunch rms length of 12.2 ps at the level of the Sapphire crystal (2.850 m after the photocathode). This value is close to the measured one, which is $\sigma_{t_e} = 11.2$ ps (see Fig. 2.56). It gives credence to the hypothesis of a 18 ps rms electron bunch emitted from the photocathode, substantially larger than the 4.5 ps rms of the UV laser pulse impacting it and generating the bunch. However, there are currently no identified mechanisms to explain such a lengthening of the electron bunch during its emission from the polycrystalline Magnesium photocathode.

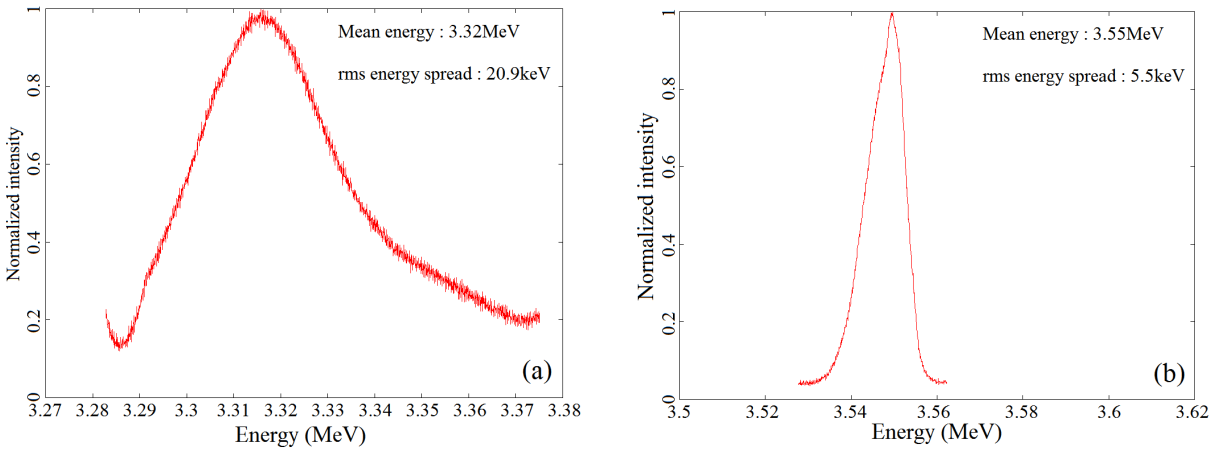

FIGURE *2.58 – Electron bunch energy spectrum measured in the same conditions than for the bunch length measurement of Fig. 2.56, namely with a Mg photocathode (a), and with a Copper photocathode in similar conditions (b)*

One way to simply test this hypothesis is to perform the electron bunch length measurement with a Copper photocathode mounted in the RF-gun. Before performing this measurement, I measure the bunch rms energy spread with the dipole magnet. The result of this measurement is shown in Fig. 2.59. The measured 4.36 keV bunch rms energy spread at 3.67 MeV is fully compatible with a 4.5 ps rms initial Gaussian electron distribution and an RF-gun peak accelerating field of 64 MV/m, implying that no lengthening of the electron bunch occurs during its emission from the Copper photocathode. Fig. 2.60

shows the bunch time profile measured with the streak camera in the same experimental conditions.

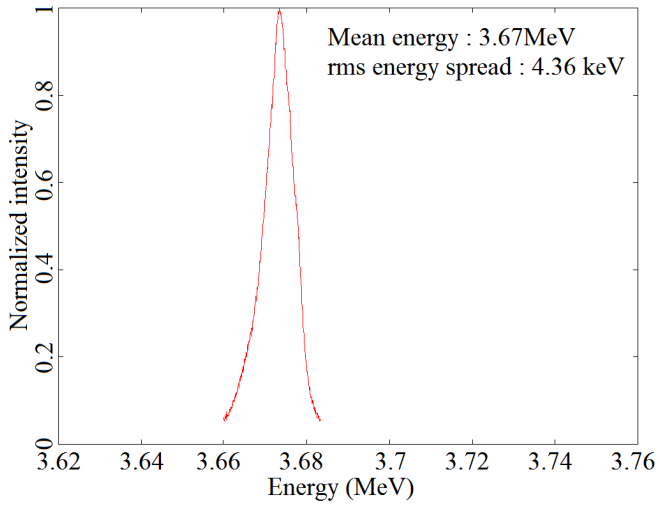

FIGURE *2.59 – Electron bunch energy spectrum for a Copper photocathode. RF-gun peak accelerating field : 64 MV/m ; Gun RF-phase : minimizing the energy spread ; Bunch charge : 45 pC.*

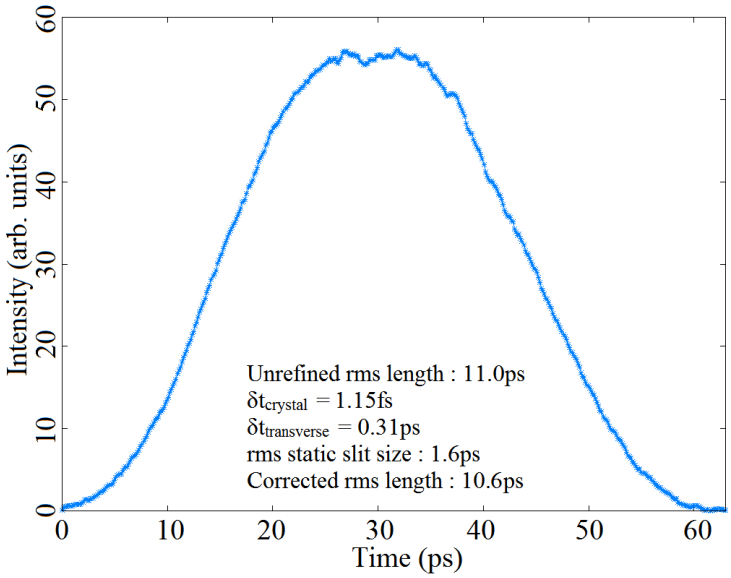

FIGURE *2.60 – Time profile of the Cerenkov radiation measured with the streak camera. Conditions : 64 MV/m Gun peak accelerating field ; Gun RF-phase : minimizing the bunch energy spread ; 3.67 MeV bunch energy ; 45 pC bunch charge ; IB3 = 148 A ; IB5 = 41 A.*

The measured rms bunch length in Fig. 2.60 is very close from the one measured in Fig. 2.56, and therefore still very far from the predictions of ASTRA. The previously

developed hypothesis of a lengthening of the electron bunch during its emission from the polycrystalline Magnesium photocathode is therefore not validated [22]. Other hypotheses have therefore to be investigated to explain the too long time profile measured with the streak camera. These hypotheses are three in number.

The first is that the Cerenkov radiation emission by the Sapphire crystal is lengthened with respect to the electron bunch duration far beyond the known contributions exposed in Sec. 2.3.3.6, which contributes only for 0.31 ps. It may come from a bad quality of the Sapphire crystal used on PHIL, or from the Sapphire properties itself. This hypothesis can be tested by replacing the current crystal by a new one, made of Sapphire or of another material like quartz.

The second is that the Cerenkov radiation is lengthened during its transportation up to the streak camera. Such a lengthening can be generated by the optical dispersion of the different elements constituting the optical transport line. The used lenses are achromatic and cannot therefore generate such a lengthening. The only elements which could be responsible would be the BB3-E02 dielectric mirrors (see Sec. 2.3.3.2). Unfortunately, Thorlabs does not have the dispersion data for this kind of mirror.

The third is that the streak camera cannot reproduce the time profile of the incident Cerenkov radiation and lengthens it. This may be due to chromatic effects of the optics inside the streak camera. A simple way to test this hypothesis is to put a filter at the entrance of the streak camera, to send only a narrow wavelength range in it. But this wavelength range should not be too narrow, otherwise the light intensity entering the streak camera would be too low to perform a precise measurement. It is also possible to use a polychromatic source with a known duration to test the response of the streak camera.

Depending on its availability, a comparison of bunch length measurements performed with a Cerenkov device and with the 3-phase method is intended on the ELYSE facility at LCP (Orsay). The 3-phase method having proved its accuracy (see Sec. 2.3.2.4), this comparison could be very helpful to understand and rule out some artificial bunch lengthening due to the Cerenkov device.

22. The explanation for the too high bunch rms energy spread measured with this photocathode is therefore still unknown.

Chapitre 3

Different methods for generating short electron bunches

Contents

3.1 Short laser pulse in an RF-gun 132
3.1.1 Principles and limitations 132
3.1.2 Analytical modeling of beam dynamics in an RF-gun 132
3.1.3 Simulations on PHIL 152
3.2 Magnetic compression in a chicane 170
3.2.1 Principles and limitations 170
3.2.2 Compression of a single electron bunch 171
3.2.3 Compression of a longitudinally modulated electron beam . . . 180
3.3 RF compression by velocity bunching in an accelerating cavity 197
3.3.1 Principles and limitations 197
3.3.2 Analytical modeling of the velocity bunching 199
3.3.3 Simulations on SPARC for the compression of a single bunch by velocity bunching 207
3.4 Conclusion : comparison of the three methods 228

This chapter describes the different methods currently used to produce short electron bunches. There are 3 methods currently used. The first one and most direct is to use a short laser pulse to drive an RF-gun, namely to generate a short electron bunch directly in the source. The two others consist in the compression of a pre-existent and already accelerated longer bunch, with either a magnetic structure (magnetic compression) or an RF accelerating electric field (velocity bunching).

3.1 Short laser pulse in an RF-gun

3.1.1 Principles and limitations

The electron bunches coming from an RF-gun (see Sec. 1.2.3 and 1.2.5) are generated by a laser pulse. They therefore have the particularity that their longitudinal and transverse profiles at the moment of their emission reproduce longitudinal and transverse profiles of the used laser pulse. A natural way to generate a short electron bunch is therefore to use a laser pulse with a very short duration, namely far lower than one picosecond.

For example, a research team from the Institute of Scientific and Industrial Research of Osaka University is currently using a 1.6 cells RF-gun and a femtosecond laser pulse to produce short electron bunches for electron microscopy [96, 97]. This team succeeded in generating an electron bunch of 3.5 pC with an rms length around 250 fs, starting with a laser pulse of 85 fs rms. It has as a goal to reach a bunch rms length of 100 fs by starting with a shorter laser pulse and by decreasing the bunch charge. The REGAE facility at Hamburg [98] and the PEGASUS facility at UCLA [99] aim to produce low-charge electron bunches with an rms length lower than 100 fs.

The main limitation of this method is the repulsive force between the electrons of the bunch, called the space-charge force, which tends to increase the length of the bunch. This force is proportional to the charge density of the bunch and scales like $\frac{1}{\gamma^2}$, where $\gamma = \frac{1}{\sqrt{1-\frac{v^2}{c^2}}}$ is the relativistic factor and v is the electron velocity. It is therefore particularly strong just after the electron emission from the photocathode, because they have a low energy at this moment ($\gamma \approx 1$), and can therefore generate a fast lengthening of the bunch at the very beginning of its path if it is initially very short. This force decreases rapidly thereafter because the acceleration of the electrons in the RF-gun, and in the accelerating sections eventually placed downstream, is fast. Indeed, for a typical energy of 2 MeV at the exit of the RF-gun first half-cell, therefore after a few cm, one has $\gamma \approx 5$ implying a space-charge force reduced by a factor around 25. This allows quickly reducing the bunch lengthening rate.

Thus, the short electron bunches generated by this method are limited to a low charge (a few pC) so that the initial lengthening of the bunch does not become too strong. But even with these low charges, this method does not currently allow to reach a bunch rms length under 100 fs. To obtain short electron bunches with a higher charge and/or an rms length lower than 100 fs, it is necessary to use other methods which shorten a longer pre-existent bunch.

3.1.2 Analytical modeling of beam dynamics in an RF-gun

3.1.2.1 Calculation of the RF-gun longitudinal transfer matrix

The main difficulty to derive an analytical modeling of beam dynamics in an RF-gun comes from the fact that the electrons start with an almost zero velocity at the photocathode and are relativistic (energy of several MeV) at the gun exit, therefore their

final velocities are very close to c. It is then impossible to consider the electron velocities as constant in the RF-gun, as it is usually done to derive analytical modeling of beam dynamics in accelerating section located after the electron source.

The key point is that the bunch is quickly accelerated to relativistic energy in the RF-gun. In fact, the beam energy exceeds the electron rest energy (511 keV) after typically only one tenth of the gun length. The velocity variation in the RF-gun can then be taken into account by splitting the gun into two zones. In the first zone, close to the photocathode, we neglect the electric field variation with time and space. We consider therefore that the beam is accelerated by an electrostatic field in this zone. In the second zone, farther from the photocathode, we consider the electrons ultra-relativistic, therefore with velocities constant and equal to c. These two zones are actually not separated but exhibit a fluent transition all along the gun, and the importance of the second zone grows when the beam energy increases. It is therefore noteworthy that the analytical model is by construction the most accurate when the beam energy gain is the highest in the gun. In fact, the higher the energy gain is the shorter the first zone is and the more valid the approximation of an electrostatic field is.

To establish the model, I consider electrons with a purely longitudinal motion on the RF-gun axis ($p_x = p_y = 0 \rightarrow p = p_z$). This is equivalent to neglecting the transverse electric field existing off-axis in the RF-gun, and therefore also the coupling existing between the electron transverse and longitudinal motion. I also consider a purely sinusoidal accelerating field given by $E_z(z,t) = E_m cos(kz)\sin(2\pi ft + \Phi_0)$. This is an approximation because the peak field is not exactly the same in each cell and the fringe fields at the gun exit deform the field with respect to a perfect sinusoid. I finally neglect the space-charge force all along the electron beam path in the RF-gun, which is a rather crude approximation since the electrons start with zero velocity from the photocathode.

We want to determine the longitudinal transfer matrix of the RF-gun :

$$\begin{pmatrix} R_{11} & R_{12} \\ R_{21} & R_{22} \end{pmatrix}$$

with $\Delta t_f = R_{11}\Delta t_i + R_{12}\Delta E_i$ and $\Delta E_f = R_{21}\Delta t_i + R_{22}\Delta E_i$, where Δ represents the time and energy differences between any electron of the beam and the reference electron having the mean values.

Define the variable $\Phi(z) = 2\pi ft - kz + \Phi_0$ which will be called phase of the accelerating field, by analogy with a traveling wave. One has to note that the RF-gun field is a standing wave and not a traveling wave. By definition, $\frac{dz}{dt} = \beta c = \frac{\sqrt{\gamma^2-1}}{\gamma}c$. One can then write $\Phi(z)$ in the following form :

$$\Phi(z) = \Phi_0 + k\int_0^z \left(\frac{\gamma}{\sqrt{\gamma^2-1}} - 1\right) \mathrm{d}z \tag{3.1}$$

Let $W = \gamma mc^2$ be the total energy of an electron, $\vec{F}$ the force applied to it and $\vec{v}$ its velocity. According to the kinetic power theorem, we have the following relation :

$\frac{dW}{dt} = \vec{F}.\vec{v}$. Knowing that $dz = \beta c dt$, one obtains the following differential equation for the relativistic factor γ :

$$\frac{d\gamma}{dz} = \frac{eE_m}{m_e c^2}\cos(kz)\sin(2\pi f t + \Phi_0) = \alpha k(\sin(\Phi(z)) + \sin(\Phi(z) + 2kz)) \tag{3.2}$$

where $\alpha = \frac{eE_m}{2m_e c^2 k}$.

If $z \approx 0$, therefore close to the photocathode, $\gamma \approx 1$ and therefore $\Phi(z) \approx \Phi_0$. Eq. 3.2 is then simplified : $\frac{d\widetilde{\gamma}}{dz} \approx 2\alpha k \sin(\Phi_0)$. It considers that the electron is accelerated by an electrostatic field with the value at the instant of its emission from the photocathode. We have then a simplified expression for γ, only valid close to the photocathode :

$$\widetilde{\gamma}(z) = \gamma_0 + 2\alpha k \sin(\Phi_0) z \tag{3.3}$$

$\Phi(z)$ can now be calculated by injecting Eq. 3.3 in Eq. 3.1. It is justified since the term in the integral decreases quickly towards 0 when z increases (because β quickly approaches 1). The fact that Eq. 3.3 is valid only close to the photocathode will have a reduced impact on the accuracy of the phase $\Phi(z)$ resulting from this calculation. It is convenient to replace the integration over z by an integration over $\widetilde{\gamma}$ to obtain :

$$\Phi(z) = \Phi_0 + \frac{1}{2\alpha\sin(\Phi_0)}\int_1^{\widetilde{\gamma}}\left(\frac{\widetilde{\gamma}}{\sqrt{\widetilde{\gamma}^2 - 1}} - 1\right)\mathrm{d}\widetilde{\gamma} = \Phi_0 + \frac{1}{2\alpha\sin(\Phi_0)}\left(\sqrt{\widetilde{\gamma}^2(z) - 1} - \widetilde{\gamma}(z) + 1\right)$$

By replacing $\widetilde{\gamma}(z)$, we have :

$$\Phi(z) = \Phi_0 + \frac{1}{2\alpha\sin(\Phi_0)}\left(\sqrt{(\gamma_0 + 2\alpha k\sin(\Phi_0)z)^2 - 1} - 2\alpha k\sin(\Phi_0)z - \gamma_0 + 1\right) \tag{3.4}$$

It is now possible to obtain a better approximation for γ than Eq. 3.3, namely an approximation taking into account what is happening far from the photocathode. What happened close to the photocathode has already been taken into account and one can remark that $\Phi(z)$ varies much more slowly after this zone, and less and less as z increases. I choose therefore to integrate Eq. 3.2 considering $\Phi(z)$ as a constant and then injecting Eq. 3.4 in the result. The integration is then simple and we obtain :

$$\gamma(z) = \gamma_0 + \alpha\left(k\sin(\Phi(z))z + \frac{1}{2}(\cos(\Phi(z)) - \cos(\Phi(z) + 2kz))\right) \tag{3.5}$$

The kinetic energy of the electron is simply given by :

$$E(z) = (\gamma_0 - 1)m_e c^2 + \alpha m_e c^2\left(k\sin(\Phi(z))z + \frac{1}{2}(\cos(\Phi(z)) - \cos(\Phi(z) + 2kz))\right) \tag{3.6}$$

It would be possible to pursue the process by injecting Eq. 3.5 in Eq. 3.1 to obtain an even more precise expression of $\Phi(z)$. However this calculation cannot be done in an analytical way and cannot be used to express the longitudinal transfer matrix of an RF-gun.

One remarks in Eq. 3.4 that the phase $\Phi(z)$ quickly tends towards an asymptotic value Φ_∞ as z increases. This value is equal to :

$$\Phi_\infty = \Phi_0 + \frac{1}{2\alpha \sin(\Phi_0)}$$

It is noteworthy that I consider $\gamma_0 = 1$ to establish Φ_∞. It is appropriate since the energy of the electrons emitted by the photocathode is very low (typically 1 eV). To determine the coefficients R_{11} and R_{12} of the RF-gun transfer matrix, I will consider that the phase $\Phi_f = \Phi(L)$ when the beam exits the gun is equal to the asymptotic value Φ_∞. We have :

$$\frac{d\Phi_\infty}{d\Phi_0} = 1 - \frac{\cos(\Phi_0)}{2\alpha \sin^2(\Phi_0)}$$

By replacing $\mathrm{d}\Phi_\infty$ and $\mathrm{d}\Phi_0$ by $\Delta\Phi_f$ and $\Delta\Phi_0$, we obtain :

$$\Delta\Phi_f = \left(1 - \frac{\cos(\Phi_0)}{2\alpha \sin^2(\Phi_0)}\right) \Delta\Phi_0$$

As we observe the beam at a fixed value of z (the RF-gun exit), we have $\Delta\Phi = 2\pi f \Delta t$ and therefore :

$$\Delta t_f = \left(1 - \frac{\cos(\Phi_0)}{2\alpha \sin^2(\Phi_0)}\right) \Delta t_0 \tag{3.7}$$

This allows deducing $R_{11} = 1 - \frac{\cos(\Phi_0)}{2\alpha \sin^2(\Phi_0)}$ and $R_{12} = 0$.

To determine the coefficients R_{21} and R_{22} of the RF-gun transfer matrix, we have to differentiate the following expression of $\gamma_f = \gamma(L)$ with respect to γ_0 and Φ_f :

$$\gamma_f = \gamma_0 + \alpha k L \sin(\Phi_f) + \frac{\alpha}{2}\cos(\Phi_f) - \frac{\alpha}{2}\cos(\Phi_f + 2kL)$$

where Φ_f is given by Eq. 3.4. We simply have $\Delta\gamma_f = \frac{\partial\gamma_f}{\partial\gamma_0}\Delta\gamma_0 + \frac{\partial\gamma_f}{\partial\Phi_f}\Delta\Phi_f$. By replacing Δt_f by Eq. 3.7 and $\Delta\gamma$ by $\frac{\Delta E}{m_e c^2}$ we obtain :

$$\Delta E_f = \Delta E_i + 2\pi f m_e c^2 \left(\alpha k L \cos(\Phi_f) - \frac{\alpha}{2}\sin(\Phi_f) + \frac{\alpha}{2}\sin(\Phi_f + 2kL)\right)\left(1 - \frac{\cos(\Phi_0)}{2\alpha \sin^2(\Phi_0)}\right)\Delta t_i$$

which allows deducing $R_{21} = 2\pi f m_e c^2(\alpha k L \cos(\Phi_f) - \frac{\alpha}{2}\sin(\Phi_f) + \frac{\alpha}{2}\sin(\Phi_f + 2kL))(1 - \frac{\cos(\Phi_0)}{2\alpha \sin^2(\Phi_0)})$ and $R_{22} = 1$.

By joining all the parts of the calculation, we obtain the following approximative expression for the RF-gun longitudinal transfer matrix :

$$\begin{pmatrix} 1 - \frac{\cos(\Phi_0)}{2\alpha \sin^2(\Phi_0)} & 0 \\ 2\pi f m_e c^2 \left(\alpha k L \cos(\Phi_f) - \frac{\alpha}{2}\sin(\Phi_f) + \frac{\alpha}{2}\sin(\Phi_f + 2kL)\right)\left(1 - \frac{\cos(\Phi_0)}{2\alpha \sin^2(\Phi_0)}\right) & 1 \end{pmatrix}$$

where $\Phi_f = \Phi(L)$ is given by Eq. 3.4.

The 3 following sections are intended to test the validity of this model on 3 different aspects : The beam mean energy aspect ; The time aspect ; The beam energy spread aspect.

3.1.2.2 Test of the analytical model on the beam mean energy aspect

To test the validity of the analytical model established in Sec. 3.1.2.1, I choose first to compare the maximum mean bunch energy coming from this model (see Eq. 3.5) with the one coming from ASTRA simulations as a function of the RF-gun peak accelerating field. The energy of the electrons emitted by the photocathode being very low (typically 1 eV) compared to the exit energy (a few MeV), I consider $\gamma_0 = 1$ in Eq. 3.5. The accelerating field used in ASTRA simulations is coming from SUPERFISH simulation. It therefore takes into account many effects that the analytical model does not : Fringe field at the RF-gun exit ; Difference of accelerating field amplitude between the different cells of the RF-gun ; Non-sinusoidality of the accelerating field longitudinal profile. The goal of the comparison is therefore to test the validity of neglecting these effects by considering a purely sinusoidal accelerating field in the analytical model.

This comparison has been performed for the 3 GHz 2.5 cells PHIL RF-gun, which has a mechanical length of 12.5 cm, and for the 1.3 GHz 1.6 cells PITZ RF-gun, which has a mechanical length of 18.45 cm. Fig. 3.1 shows the results of the comparison.

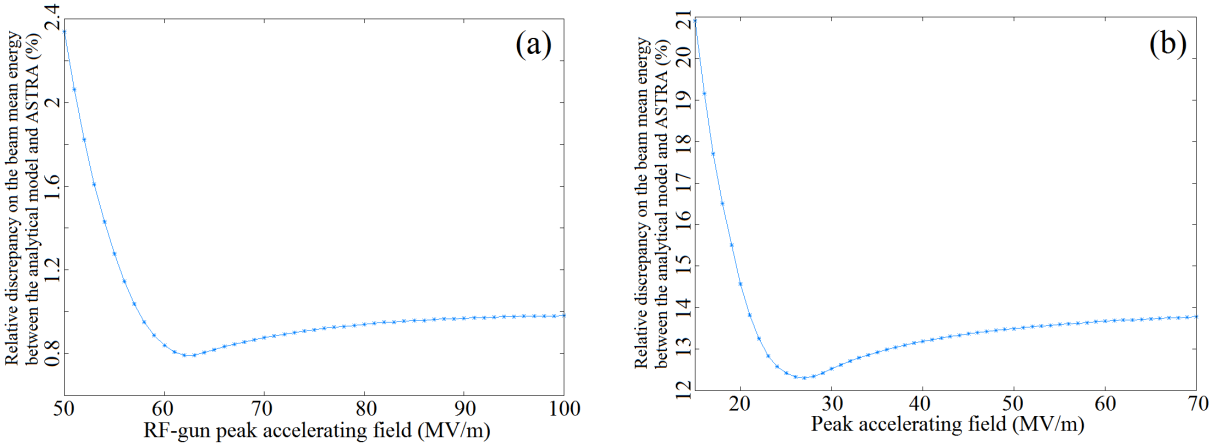

FIGURE *3.1 – Relative discrepancy* $\frac{E_m - E_a}{E_a}$ *between the maximum mean bunch energy coming from the analytical model developed in Sec. 3.1.2.1* E_m *and the one coming from ASTRA simulations* E_a *as a function of the RF-gun peak accelerating field. (a) : PHIL RF-gun ; (b) : PITZ RF-gun.*

The two curves present a similar behavior with a minimum, a sharp increase before the minimum and a slow rise after the minimum. The presence of a minimum can be explained by the combination of two effects. Firstly, at low RF-gun peak accelerating field, the bunch energy gain decreases and therefore the approximation used to establish the analytical model becomes more inaccurate, explaining the growing discrepancy. Secondly, at high RF-gun peak accelerating field, the fringe field leaking after the RF-gun exit (see Fig. 3.2) becomes more important and increases the bunch energy gain with respect to the purely sinusoidal accelerating field considered in the analytical model, leading to an increase in the relative discrepancy again.

Fig. 3.1 shows also that the relative discrepancy remains low for the PHIL RF-gun, since it is only about 2.3% at 50 MV/m and remains below 1% after 57 MV/m up to 100 MV/m. It means that considering a purely sinusoidal accelerating field in the analytical model is not a limitation for a 3 GHz 2.5 cells RF-gun from the maximum energy gain point of view. On the contrary the relative discrepancy is quite high for the PITZ RF-gun, since it is already of 12.3% at minimum. It demonstrates that considering a purely sinusoidal accelerating field in the analytical model is a priori an important limitation for a 1.3 GHz 1.6 cells RF-gun. This significant difference comes from the fact that the cells of a 1.3 GHz RF-gun are longer than the ones of a 3 GHz RF-gun (11.5 cm against 5 cm). It implies that the accelerating field is much less well-modeled by a purely sinusoidal wave, since it is flatter at the cell centers and the fringe field is more important at the RF-gun exit. This is shown in Fig. 3.2 where the accelerating field used in the ASTRA simulations (Superfish) and in the analytical model (sinus) are compared for the PHIL and PITZ RF-guns.

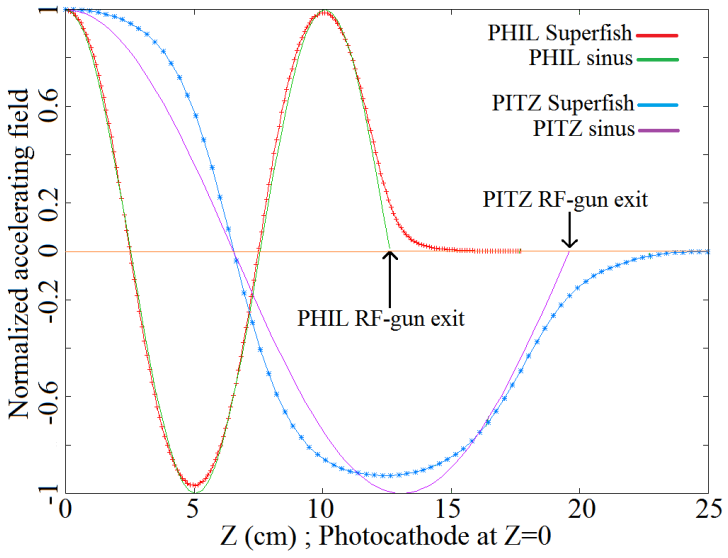

FIGURE *3.2 – Comparison between the accelerating field used in ASTRA simulations (Superfish) and in the analytical model (sinus) for the PHIL and PITZ RF-guns.*

However, there is one simple way to overcome this difficulty in the analytical modeling of a 1.3 GHz 1.6 cells RF-gun. In fact, it is sufficient to increase the length of the RF-gun

in the analytical model with respect to the real one. It corresponds to the virtual addition of a fraction of cell just after the exit of the real RF-gun.

To determine which increase of the RF-gun length is the best one, I compute the relative discrepancy between the maximum mean bunch energy coming from the analytical model and the one coming from the ASTRA simulations for several RF-gun lengths in the same accelerating field range as in Fig. 3.1 (b), namely between 15 MV/m and 70 MV/m. I then compute the mean relative discrepancy in this accelerating field range for the different RF-gun lengths (see Fig. 3.3). This study shows that an increase in the length of the PITZ RF-gun from 18.45 cm to 21.6 cm allows minimizing the mean relative discrepancy between 15 MV/m and 70 MV/m. It corresponds to the virtual addition of a fraction of cell of 3.15 cm, namely 27.4% of the length of a full cell, just after the exit of the real RF-gun.

For the optimum PITZ RF-gun length of 21.6 cm, the relative discrepancy between the maximum mean bunch energy coming from the analytical model and the one coming from the ASTRA simulations can be decreased below 2% for peak accelerating field between 15 MV/m and 70 MV/m, as it is shown in Fig. 3.4. This is larger than the typical range of operation for PITZ which is between 30 MV/m and 62 MV/m, where the relative discrepancy remains lower than 1%. I will therefore apply this change in the PITZ RF-gun length thereafter in the rest of Sec. 3.1.2.

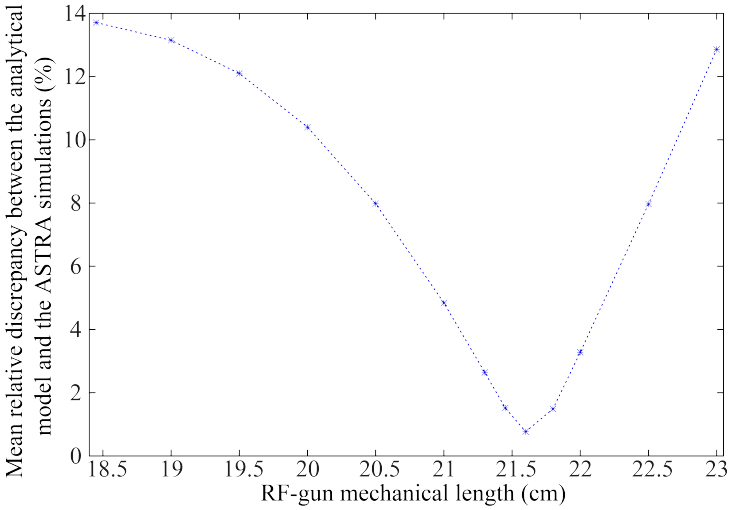

FIGURE *3.3 – Mean relative discrepancy between the maximum mean bunch energy coming from the analytical model and the one coming from the ASTRA simulations as a function of the RF-gun length. The average of the relative discrepancy has been performed for each gun length in the gun accelerating field range between 15 MV/m and 70 MV/m (step of 1 MV/m).*

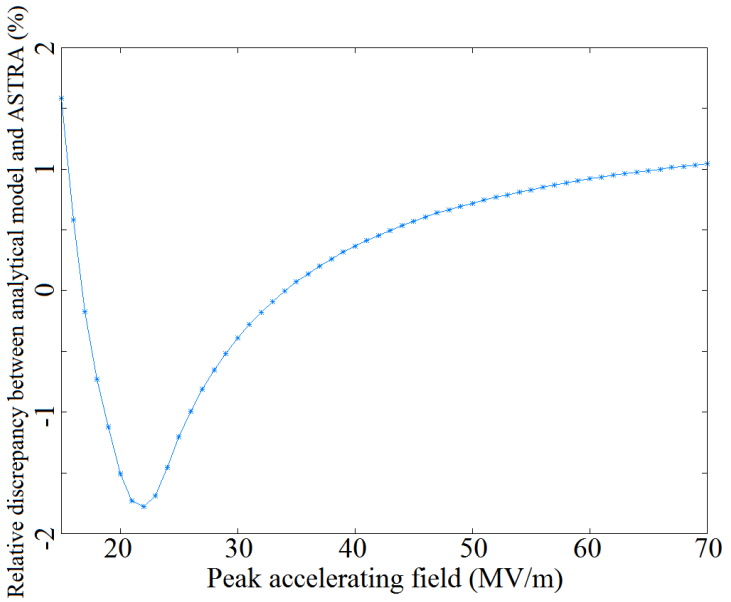

FIGURE *3.4 – Relative discrepancy between the maximum bunch energy coming from the analytical model developed in Sec. 3.1.2.1 and the one coming from ASTRA simulations as a function of the PITZ RF-gun peak accelerating field. The gun length has been increased from 18.45 cm to 21.6 cm in the analytical model compared to Fig. 3.1 (b).*

To test the validity of the model established in Sec. 3.1.2.1, it is also necessary to compare the bunch energy coming from this model (see Eq. 3.5) with experimental data acquired on the PITZ facility (see Fig. 1.25) at DESY, Zeuthen as a function of the gun RF-phase Φ_0. These experimental data have been acquired at the LEDA station, namely just after the RF-gun exit (see Fig. 1.25), for 3 different laser longitudinal profiles. The bunch charge was adjusted to 20 pC, to minimize the space-charge forces effects which are not taken into account in the analytical model. The RF-gun peak accelerating field was set around 60.5 MV/m (maximal value), implying a bunch energy around 6.25 MeV at the exit of the RF-gun. The energy of the electrons emitted by the photocathode being very low (typically 1 eV) compared to the exit energy (a few MeV), I consider $\gamma_0 = 1$ in Eq. 3.5.

Fig. 3.5, Fig. 3.6 and Fig. 3.7 show the results of this comparison for the 3 laser longitudinal profiles. The relative deviation between the analytical model and the measurements is also drawn.

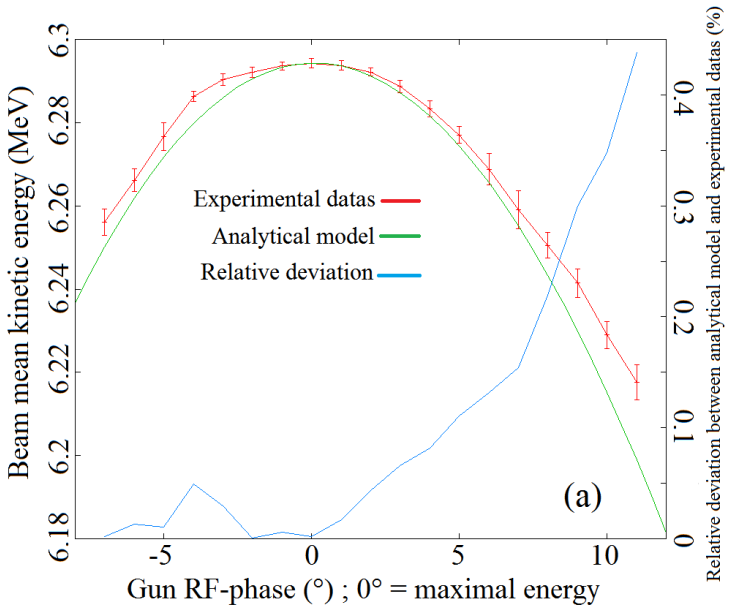

FIGURE *3.5 – Comparison between the bunch energy coming from the analytical model and from the measurements ; Laser time profile : Long flat-top with 24 ps FWHM and 2 ps rise/fall time (σ_t = 6.8 ps rms) ; Bunch charge : 20 pC ; RF-gun peak accelerating field : 60.5 MV/m (maximum mean bunch energy around 6.25 MeV).*

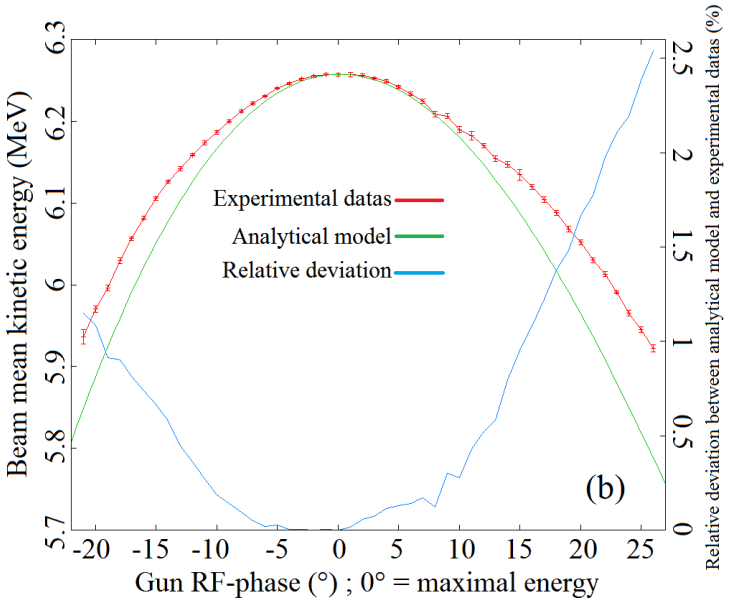

FIGURE 3.6 – *Comparison between the bunch energy coming from the analytical model and from the measurements ; Laser time profile : Short flat-top with 5.8 ps FWHM and 2 ps rise/fall time (σ_t = 1.9 ps rms) ; Bunch charge : 20 pC ; RF-gun peak accelerating field : 60.5 MV/m (maximum mean bunch energy around 6.25 MeV).*

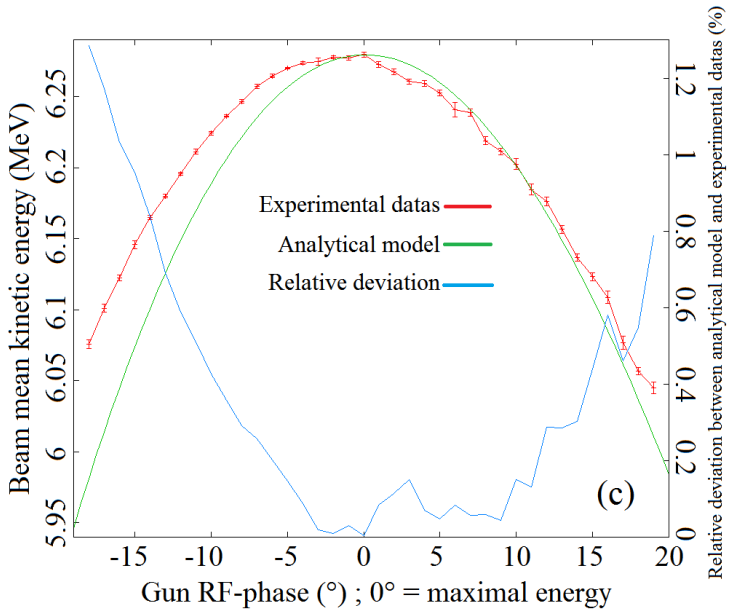

FIGURE 3.7 – *Comparison between the bunch energy coming from the analytical model and from the measurements ; Laser time profile : Short Gaussian with σ_t = 0.85 ps rms ; Bunch charge : 20 pC ; RF-gun peak accelerating field : 60.5 MV/m (maximum mean bunch energy around 6.25 MeV).*

One can see clearly that the bunch energy coming from the analytical model stays fairly close to the measurements over a quite wide range of RF-phases around the maximum energy. In fact, the relative deviation remains below 2% in a range of $\pm 20°$ around the maximal energy (0° phase). The fact that the relative deviation increases when the gun RF-phase moves away from the one maximizing the bunch energy is directly explained by the fact that the analytical model becomes less accurate when the bunch energy gain decreases.

We can conclude that the RF-gun analytical model developed in Sec. 3.1.2.1 is perfectly suitable to quickly and precisely compute the bunch energy at the RF-gun exit, if the RF-phase remains not too far from the one maximizing the bunch energy. However, it is important to take into account that the length of the RF-gun has to be increased with respect to the real one for the case of a 1.3 GHz 1.6 cells RF-gun.

3.1.2.3 Test of the analytical model on the time aspect

To test the analytical model developed in Sec. 3.1.2.1 with regards to the time aspect, it is possible to apply the 3-phase method presented in Sec. 2.3.2.1 directly with an RF-gun. In fact, by applying the 3-phase method to an RF-gun, the reconstructed bunch length is the one at the "entrance" of the gun, namely right at the moment of its emission by the photocathode. This length is known, since it is the one of the laser pulse used to generate the electron bunch. It is therefore a good way to test the validity of this analytical RF-gun longitudinal transfer matrix with respect to the time aspect for different experimental conditions, particularly various laser pulse lengths and RF-gun peak accelerating fields.

Measurements as a function of the laser pulse length and time profile have been performed at PITZ (see Fig. 1.25). The measurements has been done for 3 different laser time profiles. The bunch charge has been adjusted to 20 pC for these measurements, to minimize the effect of space-charge forces which are not taken into account in the 3-phase method. The RF-gun peak accelerating field was fixed to its maximal value of 60.5 MV/m, which corresponds to a mean bunch energy of 6.25 MeV at the gun exit, for the same reason. Fig. 3.8, Fig. 3.9 and Fig. 3.10 show the curves of bunch rms energy spread measured at the LEDA station (see Fig. 1.25), as a function of the gun RF-phase, used to perform the 3-phase method.

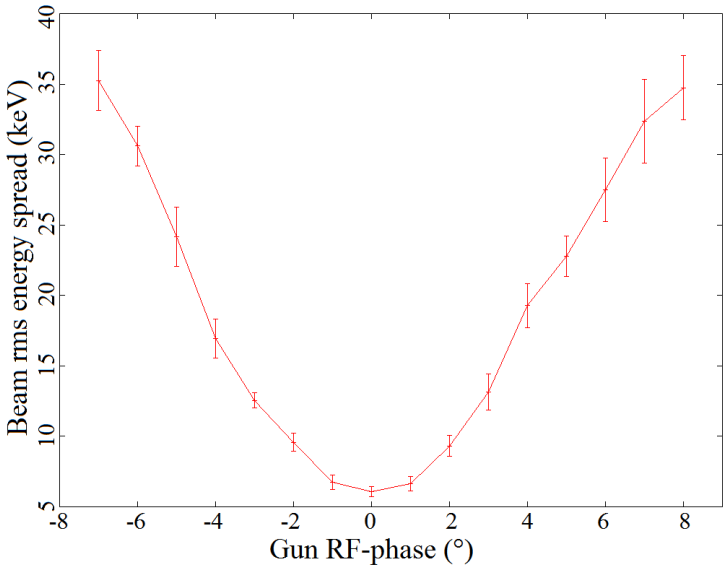

FIGURE *3.8 – Bunch rms energy spread at LEDA station as a function of the gun RF-phase ; Laser time profile : Long flat-top with 24 ps FWHM and 2 ps rise/fall time (σ_t = 6.8 ps rms) ; Bunch charge : 20 pC ; RF-gun peak accelerating field : 60.5 MV/m (maximum mean bunch energy around 6.25 MeV).*

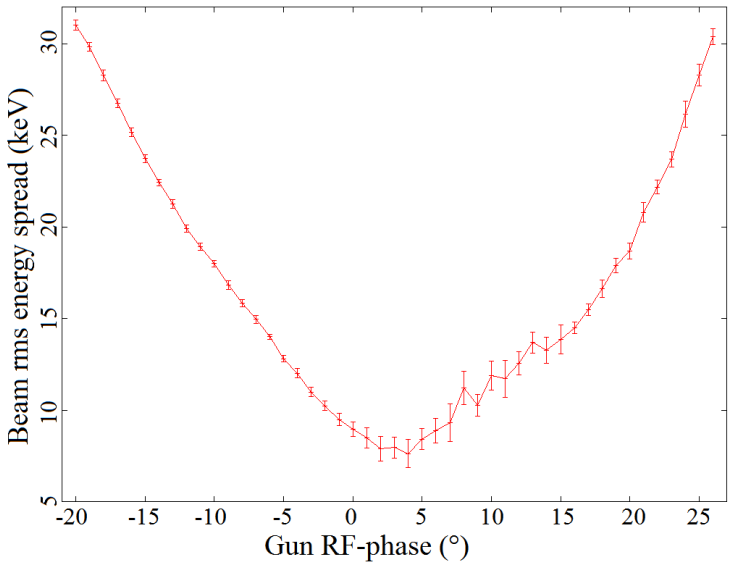

FIGURE *3.9 – Bunch rms energy spread at LEDA station as a function of the gun RF-phase ; Laser time profile : Short flat-top with 5.8 ps FWHM and 2 ps rise/fall time (σ_t = 1.9 ps rms) ; Bunch charge : 20 pC ; RF-gun peak accelerating field : 60.5 MV/m (maximum mean bunch energy around 6.25 MeV).*

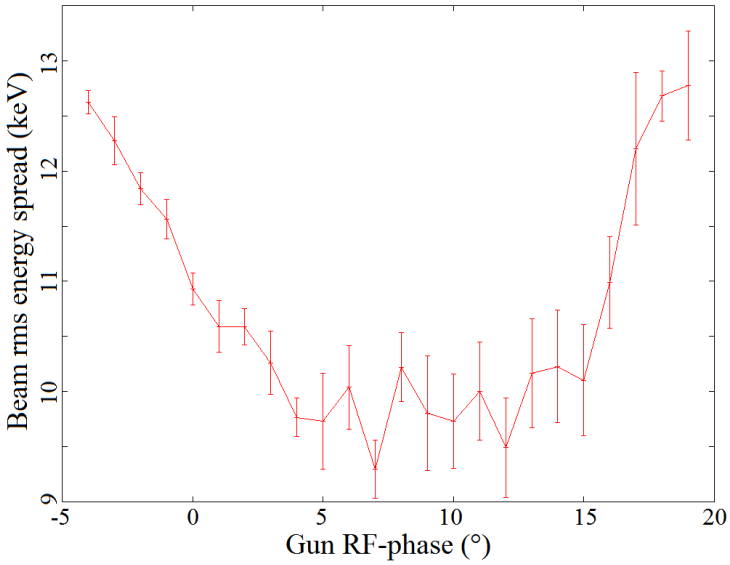

FIGURE *3.10 – Bunch rms energy spread at LEDA station as a function of the gun RF-phase ; Laser time profile : Short Gaussian with σ_t = 0.85 ps rms ; Bunch charge : 20 pC ; RF-gun peak accelerating field : 60.5 MV/m (maximum mean bunch energy around 6.25 MeV).*

Tab. 3.1 shows the reconstructed bunch length at the photocathode by the 3-phase method for each of the 3 laser time profile used in the experiments. We can see in it that the agreement is perfect for the short flat-top laser profile within the error bars, and that there are slight discrepancies for the long flat-top laser profile (4.5%) and mainly for the short Gaussian laser profile (29%). However, the main explanations for these discrepancies are not the same for the two profiles. For the long flat-top profile, the space-charge forces have a very weak effect. The main hypothesis to explain the discrepancy is therefore the approximate modeling of the gun accelerating field by a purely sinusoidal wave with no transverse components (see Tab. 2.6 in Sec. 2.3.2.4). In fact, the longer the bunch is, the more it will be sensitive to a wrong modeling of the accelerating field. This hypothesis cannot therefore be retained as the main one for the short Gaussian profile. For this profile, two explanations are involved. The first is the space-charge forces which become important again, despite the low bunch charge of 20 pC, because of the short bunch length (850 fs rms). The second is that the bunch energy spread becomes too small to be measured when the bunch becomes too short, since the resolution of the LEDA station is at best limited around 3 keV [100].

The measurements shown in Tab. 3.1 are in good agreement with the expected lengths. It shows that the RF-gun longitudinal transfer matrix developed in Sec. 3.1.2.1 is reliable and appropriate to model the time aspect of the dynamics of a 20 pC beam in an RF-gun, even close to the photocathode where the beam is non ultra-relativistic, down to a bunch length around one picosecond. Indeed, even in the non optimal measurement conditions encountered for the short Gaussian laser time profile, the discrepancy with respect to the expected length value is only 30%.

Laser profile	Expected length (Laser duration)	Length by 3-phase method
Long flat-top	6.8 ps rms	6.2 +/- 0.3 ps rms
Short flat-top	1.9 ps rms	1.8 +/- 0.1 ps rms
Short Gaussian	0.85 ps rms	1.14 +/- 0.04 ps rms

TABLE *3.1 – Summary of 3-phase measurements performed with the RF-gun at PITZ. Bunch charge : 20 pC; RF-gun peak accelerating field : 60.5 MV/m (maximum mean bunch energy around 6.25 MeV).*

Measurements as a function of the RF-gun peak accelerating field has been performed at PHIL (see Fig. 1.24) for bunch charges between 26 pC and 121 pC. The rms length of the UV laser pulse driven the RF-gun at PHIL, which is the length to reconstruct by the 3-phase method, is 4.5 $\pm$ 0.3 ps as shown in Fig. 3.11.

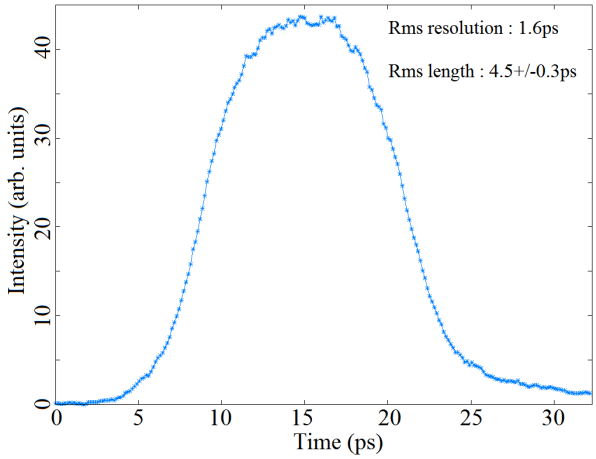

FIGURE *3.11 – Measurement of the PHIL laser time profile with a streak camera*

The results of 3-phase measurements as a function of the RF-gun peak accelerating field are shown in Fig. 3.12.

Fig. 3.12 shows 3-phase measurements below the expected value at low accelerating field, the discrepancy is about 38% at 51.9 MV/m, and converging towards the expected value when the peak accelerating field increases, the discrepancy being null at 84.9 MV/m. This behavior is explained by the space-charge forces, which are not taken into account in the 3-phase method. Indeed, they scale like the inverse of the square of the RF-gun accelerating field and becomes therefore stronger when the RF-gun accelerating field decreases, explaining the growing discrepancy.

It is important to note that the effect of space-charge forces was negligible for the 3-phase measurements performed with the RF-gun at PITZ and previously shown in this section. In fact the used PITZ RF-gun peak accelerating field of 60 MV/m is equivalent to a 98 MV/m accelerating field in the PHIL RF-gun in terms of bunch energy at the

RF-gun exit. This difference is due to the difference of operation frequency, 3 GHz at PHIL and 1.3 GHz at PITZ, implying that the PITZ RF-gun is longer than the PHIL one even if it has only 1.6 cells against the 2.5 cells at PHIL.

Measurements have also been performed at PHIL for RF-gun peak accelerating field of 70.5 MV/m and 81.2 MV/m. These measurements are excluded as results are not consistent with the others : 2.6 $\pm$ 1.6 ps at 70.5 MV/m and 2.3 $\pm$ 1.3 ps at 81.2 MV/m (see Fig. 3.12).

This is justified by an inaccuracy of the analytical model developed in Sec. 3.1.2.1 (see Eq. 3.5), which appears for a 3 GHz RF-gun when the accelerating field is such that its α parameter (see Eq. 3.2) becomes higher than 0.993. It corresponds to a peak accelerating field of 63.8 MV/m. At this field value, a second maximum appears on the curve representing the bunch energy at the RF-gun exit as a function of the gun RF-phase. This second maximum is unphysical and is not measured experimentally. The reason of its apparition hasn't been established yet and is still under investigation. Fig. 3.13 shows the top of this curve for RF-gun peak accelerating field of 57 MV/m, 65.2 MV/m and 84.9 MV/m. The apparition of the second maximum is clearly visible in this figure, as well as the fact that it moves away from the physical maximum when the RF-gun peak accelerating field increases.

The presence of this second maximum affects the R_{12} parameter of the RF-gun longitudinal transfer matrix, developed in Sec. 3.1.2.1, which is used in the 3-phase method. It explains why the measurements at 70.5 MV/m and 81.2 MV/m are inconsistent. The measurement at 84.9 MV/m is coherent because the unphysical maximum is sufficiently far from the physical one (see Fig. 3.13 (c)). It is therefore possible to perform a precise 3-phase measurement by using gun RF-phases sufficiently close to the physical maximum, namely not below $-20°$ of the physical maximum. The measurement at 65.2 MV/m is coherent, despite the presence of the unphysical maximum, because the two maxima are very close at this field (see Fig. 3.13 (b)). It is therefore possible to perform a precise 3-phase measurement by using gun RF-phases not too close to the unphysical maximum, namely below $-15°$ of the physical maximum.

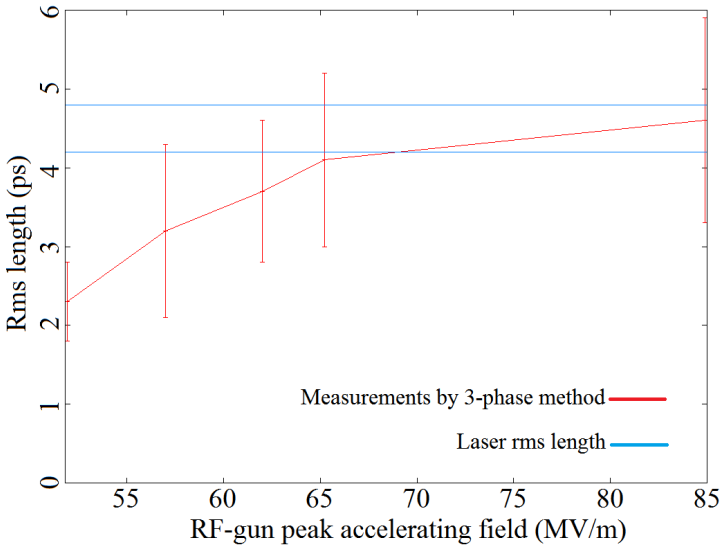

FIGURE *3.12 – Summary of 3-phase measurements performed with the RF-gun at PHIL as a function of the RF-gun peak accelerating field ; Bunch charge : 32 pC (51.9 MV/m), 26 pC (57 MV/m), 55 pC (62 MV/m), 73 pC (65.2 MV/m), 70 pC (70.5 MV/m), 110 pC (81.2 MV/m) and 121 pC (84.9 MV/m).*

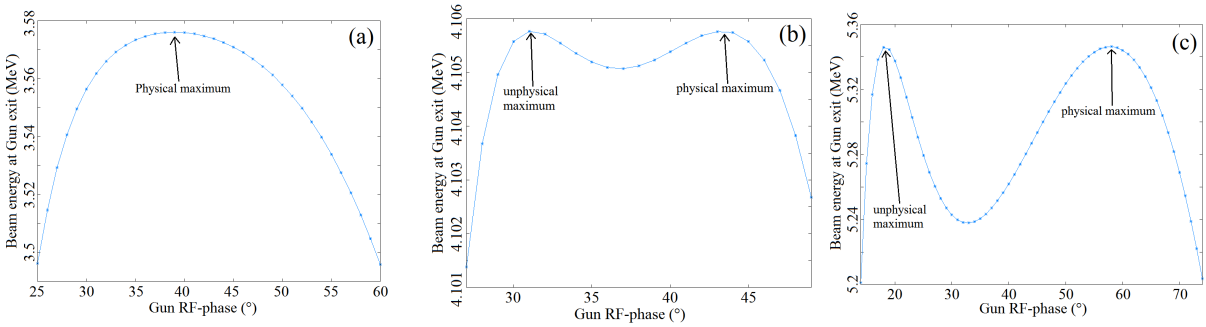

FIGURE *3.13 – Bunch energy at the PHIL RF-gun exit as a function of the Gun RF-phase for the analytical model developed in Sec. 3.1.2.1 (see Eq. 3.5) ; (a) : Peak accelerating field of 57 MV/m ; (b) : Peak accelerating field of 65.2 MV/m ; (c) : Peak accelerating field of 84.9 MV/m.*

This second maximum appears also for the 1.3 GHz PITZ RF-gun. But it appears when the accelerating field is such that its α parameter becomes higher than 0.858. It corresponds to a very low peak accelerating field of 23.9 MV/m. In practical, such a low accelerating field is not used in the experiments. The typical lowest used value is about 40 MV/m. Fig. 3.14 shows the top of the curve representing the bunch energy at the PITZ RF-gun exit as a function of the gun RF-phase for this field of 40 MV/m. At this value the two maxima are already well separated, even more than for the 3 GHz PHIL RF-gun at 84.9 MV/m, implying that the presence of the unphysical maximum is practically never a limitation to the use of 3-phase method with this RF-gun.

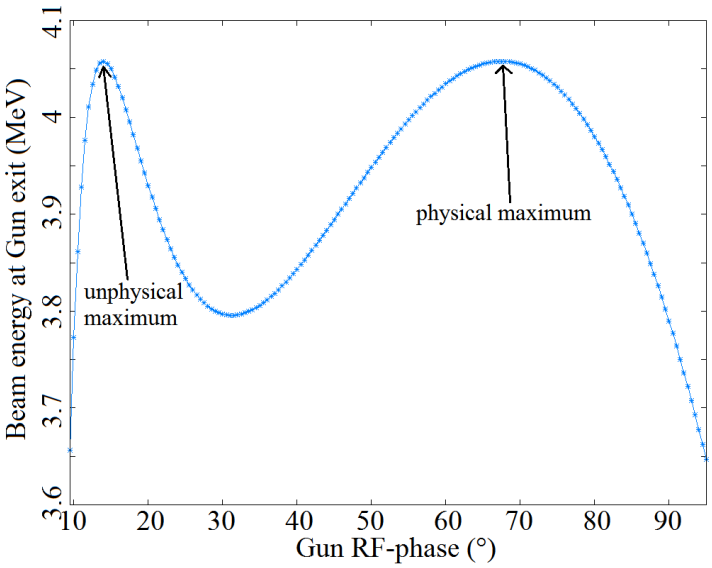

FIGURE *3.14 – Bunch energy at the PITZ RF-gun exit as a function of the Gun RF-phase for the analytical model developed in Sec. 3.1.2.1 (see Eq. 3.5); Peak accelerating field of 40 MV/m.*

3.1.2.4 Test of the beam energy spread dependence on the gun RF-phase

To test the validity of the analytical model developed in Sec. 3.1.2.1, I choose also to compare the bunch rms energy spread coming from this analytical model with the one coming from measurements performed on the PITZ facility (see Sec. 1.4.2) as a function of the Gun RF-phase. Starting from the RF-gun longitudinal transfer matrix M_{RF-gun} established at the end of Sec. 3.1.2.1, the bunch energy spread can be analytically calculated by transporting the longitudinal beam matrix Σ_l between the photocathode (i subscript) and the exit of the RF-gun (f subscript). In fact, in the transfer matrix formalism, the bunch energy spread is invariant, because the space-charge forces are neglected, in the drift space between the exit of the RF-gun and the LEDA station used at PITZ to measure the bunch energy spread (see Fig. 1.25). The bunch longitudinal transport is given by :

$$\Sigma_{l_f} = M_{RF-gun} \Sigma_{l_i} M^t_{RF-gun}$$

where the longitudinal beam matrix Σ_{l_α} is given by :

$$\begin{pmatrix} \sigma^2_{t_\alpha} & \sigma_{Et_\alpha} \\ \sigma_{Et_\alpha} & \sigma^2_{E_\alpha} \end{pmatrix}$$

with σ_{t_α} being the bunch rms length, σ_{E_α} being the bunch rms energy spread and σ_{Et_α} being the bunch rms time/energy correlation. The final bunch energy spread σ_{E_f} is finally given by :

$$\sigma_{E_f}^2 = A^2\sigma_{t_i}^2 + 2A\sigma_{Et_i} + \sigma_{E_i}^2 \tag{3.8}$$

As a reminder, the coefficient A is given by :

$$A = 2\pi f m_e c^2 \left(\alpha kL\cos(\Phi_f) - \frac{\alpha}{2}\sin(\Phi_f + 2kL)\right)\left(1 - \frac{\cos(\Phi_0)}{2\alpha\sin^2(\Phi_0)}\right)$$

where f is the RF-gun operation frequency, k is the wave vector of the RF-gun accelerating field, L is the RF-gun length, Φ_0 is the Gun RF-phase and $\alpha = \frac{eE_m}{2m_e c^2 k}$ with E_m being the RF-gun peak accelerating field. $\Phi_f = \Phi(L)$ is given by Eq. 3.4.

At the moment of its emission from the photocathode the electron bunch has almost zero energy spread. Actually, the initial energy spread is typically around 1 eV and it is therefore negligible compared to the one at the RF-gun exit which is about a few keV. The term $\sigma_{E_i}^2$ in Eq. 3.8 is therefore negligible. Moreover, at the moment of the bunch emission from the photocathode, there is no correlation between the time at which an electron is emitted and its initial energy. The time/energy correlation is only induced thereafter by the RF-gun accelerating field. The term σ_{Et_i} in Eq. 3.8 is therefore equal to zero and one obtains the following simplified equation :

$$\sigma_{E_f} = |A|\sigma_{t_i}$$

I then compute the rms bunch energy spread at the RF-gun exit, via this simplified equation, as a function of the Gun RF-phase and I compare it with the experimental data and the ASTRA simulations. The result of this comparison is shown in Fig. 3.15. Fig. 3.16 shows the discrepancy, as a function of the Gun RF-phase, between the bunch rms energy spread computed by the analytical model and the one experimentally measured.

One can see in Fig. 3.15 that the analytical model does not totally succeed in reproducing the experimental data. The agreement with the experimental data remains acceptable as long as the Gun RF-phase is not too close to the one minimizing the bunch energy spread. Indeed, as it is visible in Fig. 3.16, the discrepancy with the experimental data is between 10% and 40% as long as the Gun RF-phase is not in a range of $\pm 1^\circ$ around the one minimizing the bunch energy spread. In this range, the discrepancy dramatically increases up to more than 90%. This is due to the fact that, as shown in Fig. 3.15, the bunch rms energy spread computed by the analytical model becomes much too small in this range.

This discrepancy does not come from a measurement error. Indeed, as shown in Fig. 3.15, the experimental data and the ASTRA simulation agree very well each other. The origin of this high discrepancy close to the Gun RF-phase minimizing the bunch energy spread comes from the fact that my analytical model, describing the beam dynamics in an RF-gun, has been established starting from the motion equations for a single electron (see Eq. 3.1 and Eq. 3.2 in Sec. 3.1.2.1). Besides, the RF-gun longitudinal transfer matrix has been established by a simple linear differentiation of the solutions of these equations. The combination of these two facts imply that the model does not take well

into account the fact that the electron bunch is an electron distribution. As a result, in the analytical model, the minimal bunch rms energy spread is predicted to be zero, which is impossible when considering an electron distribution (even without interactions).

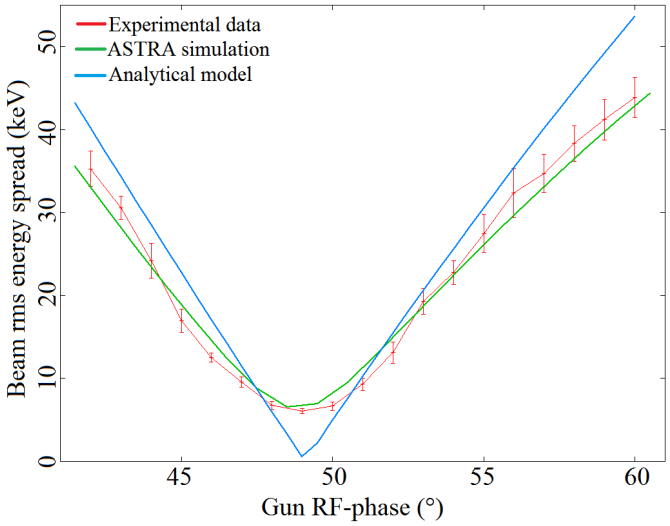

FIGURE *3.15 – Bunch rms energy spread at the PITZ LEDA1 station (see Fig. 1.25) as a function of the Gun RF-phase. RF-gun peak accelerating field : 62 MV/m ; Laser time profile : Long flat-top with 24 ps FWHM and 2 ps rise/fall time (σ_t = 6.8 ps rms) ; Bunch charge : 20 pC.*

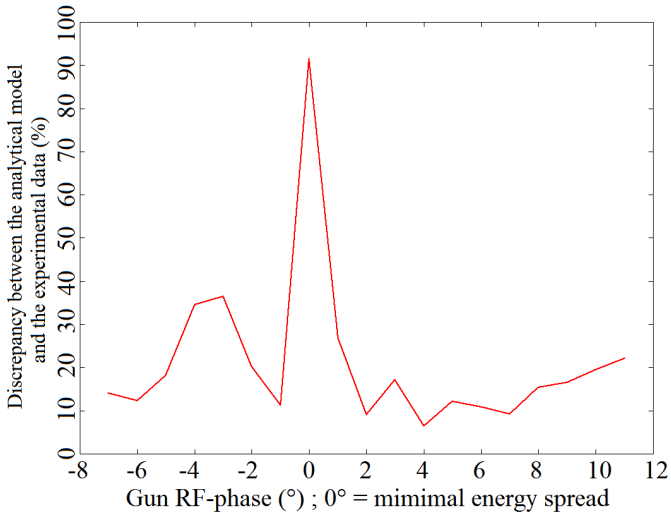

FIGURE *3.16 – Discrepancy between the bunch rms energy spread computed by the analytical model and the one experimentally measured. Simulation conditions : same as in Fig. 3.15.*

The way I choose to test this hypothesis on the discrepancy between the analytical model and the experimental data at Gun RF-phases close to the one minimizing the

energy spread is to generate 50000 electrons distributed according to the time profile of the long flat-top laser pulse of PITZ (see Fig. 2.35 red curve) with the Von Neumann algorithm (see Sec. 2.3.2.5). I then define the Gun RF-phase Φ_0 as the phase of the RF-gun accelerating field when the center of the bunch ($\equiv$ the mean position of the initial bunch time profile previously generated) is emitted from the photocathode. The frequency of the accelerating field at PITZ being of 1.3 GHz, one picosecond of delay between the emission of the electrons corresponds to a 0.468° variation of the phase of the RF-gun accelerating field when the electrons are emitted. I use this law to convert the time of emission of any electron of the bunch into the phase of the RF-gun accelerating field when this electron is emitted. I then compute the phases of the accelerating field when the electrons exit the RF-gun by using Eq. 3.4 and replacing z by the length L of the RF-gun (0.216 m for PITZ). It allows computing the kinetic energy of the electrons at the exit of the RF-gun by using Eq. 3.6. The bunch rms energy spread at the RF-gun exit is finally determined as the standard deviation of the kinetic energies of all the electrons generated at the beginning. Fig. 3.17 compares the bunch rms energy spread experimentally measured, previously shown in Fig. 3.15, with the ones coming from this analytical-numerical calculation and from the analytical model. Fig. 3.18 shows the discrepancy, as a function of the Gun RF-phase, between the bunch rms energy spread computed by the analytical-numerical calculation and the one experimentally measured.

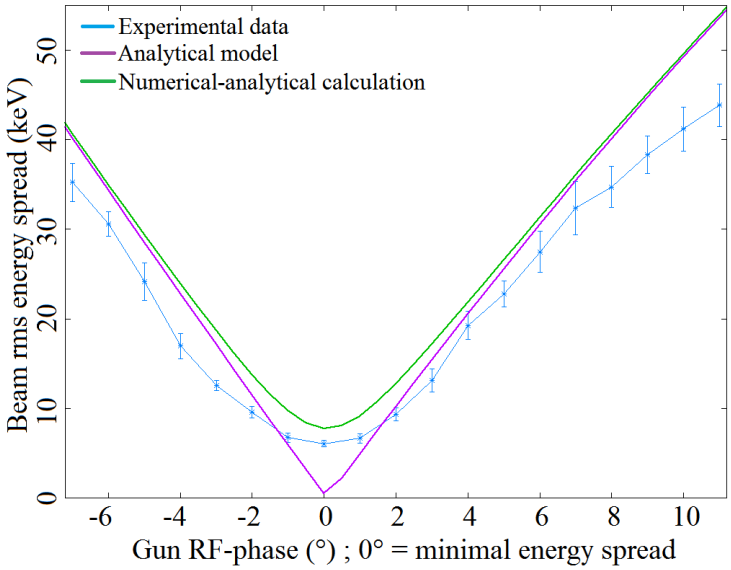

FIGURE *3.17 – Bunch rms energy spread at the PITZ LEDA1 station (see Fig. 1.25) as a function of the Gun RF-phase. Simulation conditions : see Fig. 3.15.*

It is visible in Fig. 3.17 that the analytical-numerical calculation reproduces much better the shape of the experimental bunch rms energy spread curve than the all analytical calculation. In fact, the curve coming from the analytical-numerical calculation is almost parallel to the experimental one with just a translation of a few keV above it, while the curve coming from the analytical model crosses the experimental one on both sides of the energy spread minimum. Besides, the analytical-numerical calculation does not show

anymore this dramatic decrease towards zero that the analytical model presents close from the Gun RF-phase minimizing the bunch rms energy spread. It allows asserting that the main deficiency of the analytical model to correctly model the evolution of the bunch rms energy spread is that it does not take well into account that the electron bunch is an electron distribution. The reason explaining the vertical translation of the curve coming from the analytical-numerical calculation compared to the experimental data is to be sought among the other approximations of the analytical model : Non inclusion of the space-charge forces and modeling of the real RF-gun accelerating field by a purely sinusoidal wave with no transverse components.

Fig. 3.18 summarizes the good performances of the analytical-numerical calculation previously described. It shows that its discrepancy with the experimental data is between 30% and 45% for the Gun RF-phases between $-4°$ and $+3°$ before decreasing to around 20% or lower for farther Gun RF-phases.

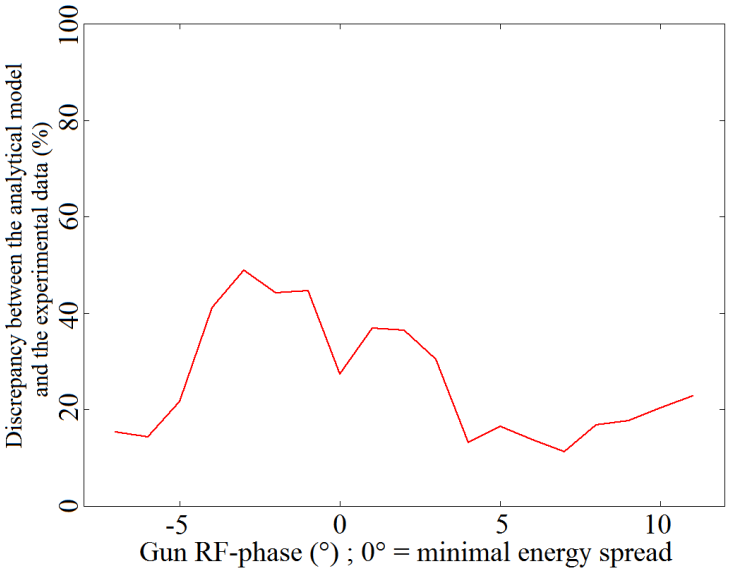

FIGURE *3.18 – Discrepancy between the bunch rms energy spread computed by the analytical-numerical calculation and the one experimentally measured. Simulation conditions : see Fig. 3.15.*

3.1.3 Simulations on PHIL

This section presents the results of beam dynamics simulations studying the generation of ultra-short electron bunches (around 100 fs rms) with the PHIN RF-gun currently mounted on PHIL at LAL (see Fig. 1.24). These simulations have been performed with the ASTRA code and have been used to test the impact of several parameters on the achievable rms bunch length and normalized transverse emittance : Gun peak accelerating field ; Gun RF-phase ; Laser pulse duration ; Transverse size of the laser pulse ; Bunch charge. The influence of the laser shape has also been studied since all the simulations have been performed for 3 different kind of laser shape : 3D Gaussian ; Beer can (longitudinal

cylinder with uniform distribution in the longitudinal direction and radial distribution in the transverse plane [23]); 3D ellipsoid (uniform distribution in all directions within an ellipsoid). I choose to study the effect of these parameters because they have a great impact on the space charge forces intensity, and therefore on the rms bunch length and normalized transverse emittance, at the bunch emission from the photocathode and all along its motion. The only parameter having a significant impact on the bunch rms normalized transverse emittance which has not been studied is the value of the magnetic field of the solenoid located at the exit of the PHIN RF-gun. This value is important to optimize the emittance compensation process [65, 66].

I consider the case of a 3 GHz standing wave booster located 30 cm after the photocathode, namely just after the RF-gun exit like on ELYSE facility at LCP [101]. This booster is 0.7 m long with a peak accelerating field of 38 MV/m, allowing a maximum mean bunch energy of 20.5 MeV at its exit for a 6 MeV bunch delivered by the RF-gun.

3.1.3.1 Influence of the Gun RF-phase

Fig. 3.19 shows the evolution of the rms bunch length at the Gun exit as a function of the Gun RF-phase (0° corresponds to the maximum energy gain) for the 3 different kind of laser shape.

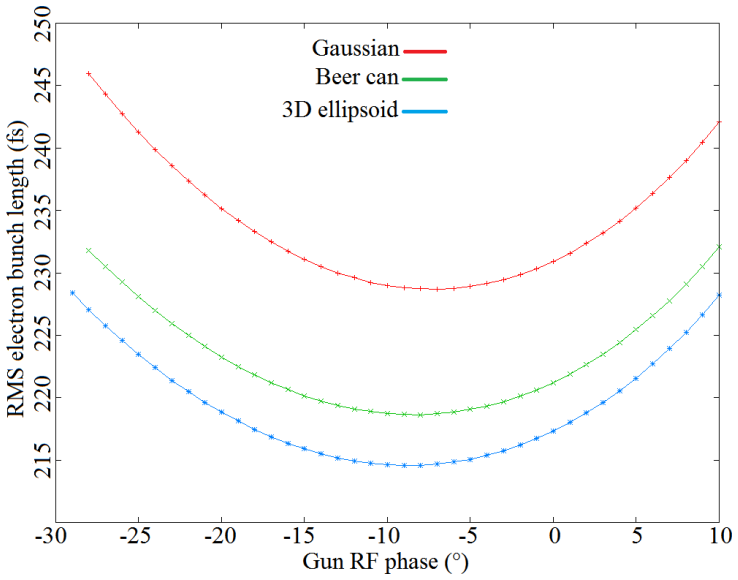

FIGURE *3.19 – Electron bunch rms length vs PHIN Gun RF-phase. Parameters of simulations : Charge 100 pC ; Laser rms duration 100 fs ; Laser rms transverse radius 0.8 mm ; Peak accelerating field 90 MV/m ; Simulation stops 30 cm after the photocathode.*

23. The radial distribution gives a parabolic distribution when projected along any direction of the transverse plane.

Fig. 3.19 shows the same behavior for the 3 shapes, with a minimum of rms bunch length for negative RF-phase values. The dependence of the bunch length on the RF-phase comes from the fact that, when the RF-phase is modified, the bunch undergoes a different accelerating field both in terms of value and of slope. It implies that the velocity differences created by the accelerating field along the bunch are different, and therefore the resulting bunch length at the RF-gun exit is also different when the RF-phase varies. There is one RF-phase value minimizing the rms bunch length, and it is not exactly the same for each shape. It is also function of the value of the peak accelerating field.

Fig. 3.19 also shows that a jitter of $\pm 10°$ on the Gun RF-phase, which corresponds to a 18 ps laser jitter, introduces a variation around 5 fs (so 2%) on the rms bunch length if we work at the RF-phase minimizing the bunch length and around 12 fs (so 5%) if we work at the 0° RF-phase maximizing the bunch energy. It is therefore clear that the stability of the phase between the laser pulse and the RF-wave injected in the RF-gun is not of a crucial importance for the rms bunch length at the exit of the Gun. The strong RF-phase jitter currently encountered on PHIL is therefore not a limitation to the generation of ultra-short electron bunches on this facility.

3.1.3.2 Influence of the Gun peak accelerating field

Fig. 3.20 shows the evolution of the rms bunch length at the Gun exit as a function of the peak accelerating field. The Gun RF-phase has each time been adjusted to the one minimizing the rms bunch length.

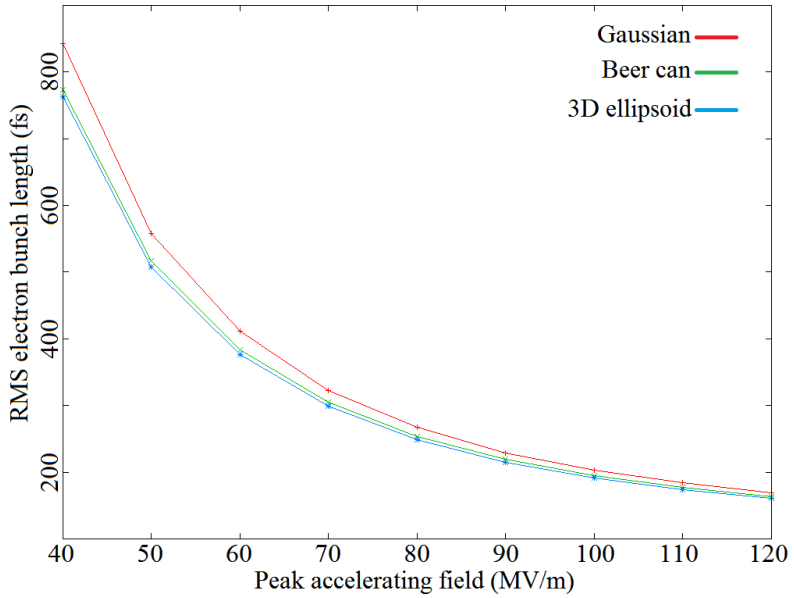

	3D Gaussian	Beer can	3D ellipsoid
40MV/m	+6°	+5°	+5°
50MV/m	0°	-1°	-1°
60MV/m	-2°	-3°	-3°
70MV/m	-4°	-5°	-5°
80MV/m	-5°	-6°	-7°
90MV/m	-8°	-8°	-9°
100MV/m	-10°	-10°	-11°
110MV/m	-12°	-12°	-13°
120MV/m	-15°	-14°	-15°

FIGURE *3.20 – Electron bunch length vs Gun peak accelerating field. Parameters of simulation : Charge 100 pC ; Laser rms duration 100 fs ; Laser rms transverse radius 0.8 mm ; RF-phase minimizing the bunch length (see the table) ; Simulation stops 30 cm after the photocathode.*

Fig. 3.20 shows clearly the importance to reach high peak accelerating field ($\geq$ 90 MV/m) to gain energy as quickly as possible in the RF-gun. The increase in Gun peak accelerating field allows a decrease in rms bunch length thanks to two different effects. First of all the effect of space-charge forces decreases when the peak accelerating field increases, which lowers the longitudinal explosion of the bunch in the RF-gun, especially just after its emission by the photocathode. Secondly, when the bunch energy increases, the velocity differences between the electrons constituting the bunch become smaller, which lowers the lengthening of the bunch due to the energy spread induced by the accelerating field.

The gain on rms bunch length diminishes as the peak accelerating field increases. In fact, the gain is around 45% between 60 MV/m and 90 MV/m and only around 25% between 90 MV/m and 120 MV/m. This latter gain remains however not negligible. Therefore, increasing the possible peak accelerating field is an interesting way to lower the rms bunch length. But it becomes very challenging to operate above 90 MV/m because of sparks and electrical breakdowns in the RF-gun.

3.1.3.3 Influence of the laser pulse duration

Fig. 3.21 shows the evolution of the rms bunch length at the Gun exit, as a function of the rms duration of the laser pulse driven the RF-gun.

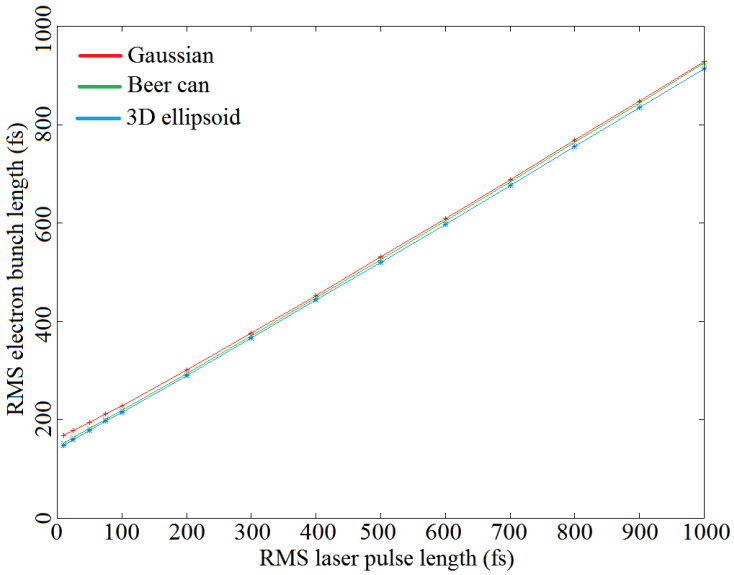

FIGURE *3.21 – Electron bunch length vs Laser rms duration. Parameters of simulation : Charge 100 pC ; Laser rms transverse radius 0.8 mm ; Gun peak accelerating field 100 MV/m ; RF-phase minimizing the bunch length ; Simulation stops 30 cm after the photocathode.*

The evolution of the rms bunch length is quite linear with the laser pulse rms duration. It is not surprising since the electron bunch at the photocathode reproduces the laser pulse

duration. However, one can observe in Fig. 3.21 that we cannot decrease indefinitely the rms bunch length by decreasing the laser pulse duration. Indeed the rms bunch length for very short laser pulse duration ($\leq$ 10 fs rms) reaches a limit which, for the laser rms transverse radius of 0.8 mm, is around 170 fs for the 3D Gaussian shape and around 150 fs for the Beer can and 3D ellipsoid shapes. This is explained by the increase in electron density with the decrease in laser pulse duration. It intensifies the space-charge forces, thus preventing to generate shorter bunches because of the longitudinal explosion just after the photocathode. One direct way to decrease the space-charge forces effect, and therefore to reach still lower bunch length, is then to increase the rms transverse radius of the laser pulse driving the RF-gun.

3.1.3.4 Influence of the laser pulse transverse radius

Fig. 3.22 shows the evolution of the rms bunch length at the Gun exit as a function of the rms transverse radius of the laser pulse driving the RF-gun. The bunch rms transverse emittance is also depicted.

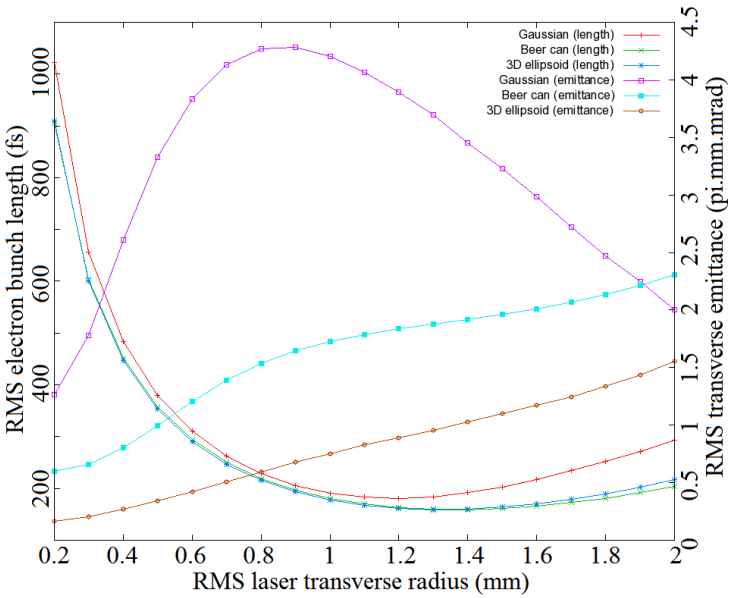

FIGURE *3.22 – Electron bunch length and transverse emittance vs Laser rms transverse radius. Parameters of simulation : Charge 100 pC ; Laser rms duration 100 fs ; Gun peak accelerating field 90 MV/m ; RF-phase minimizing the bunch length ; Simulation stops 30 cm after the photocathode.*

Fig. 3.22 shows clearly a gain on rms bunch length by increasing the laser rms transverse radius above 0.8 mm. In fact, the gain is between 20% and 25% between 0.8 mm and 1.2 mm. This is due, as previously explained, to the associated decrease in space-charge forces. However, there is an optimum value above which the rms bunch length starts to increase again because of optical effects in the magnetic field of the B3 solenoid (see Fig. 1.24). The laser rms transverse radius optimum values are around 1.2 mm for

the 3D Gaussian shape, around 1.4 mm for the Beer can shape and around 1.3 mm for the 3D ellipsoid shape. One can note that the laser rms transverse radius minimizing the rms bunch length is not at all the one minimizing the bunch rms transverse emittance, especially for the 3D Gaussian shape. It is therefore not possible to optimize both the rms bunch length and transverse emittance at the exit of the RF-gun.

3.1.3.5 Influence of the laser shape

In the case of an RF-gun, the electron density distribution is directly controlled by the energy density of the laser pulse impacting the photocathode. It is therefore important to have a precise control on the spatial and time shape of this laser pulse.

The effects of space-charge forces on the electron bunch depend strongly on the shape of the electron bunch density, especially at low energy namely close to the photocathode in the RF-gun. This fact is clearly depicted in Fig.3.23, where the time/energy phase-space of an electron bunch, at the exit of the RF-gun, is shown for the three different kind of laser shapes used in this section. The 3D Gaussian shape produces strong non-linear effects, resulting in a bunch time/energy phase-space deviating from the linearity very close from the bunch center (see Fig. 3.23 (a)). It is therefore the worst profile with respect to the space-charge forces. At the opposite extreme, the 3D ellipsoid shape generates completely linear space-charge fields along the bunch, resulting in an almost linear bunch time/energy phase-space (see Fig. 3.23 (c)). It is therefore the ideal distribution to minimize the effects of space-charge forces. The Beer can shape is an intermediate case. The non-linear effects are confined at the two edges of the cylinder, resulting in a bunch time/energy phase-space deviating from linearity only in the bunch head and bunch tail (see Fig. 3.23 (b)).

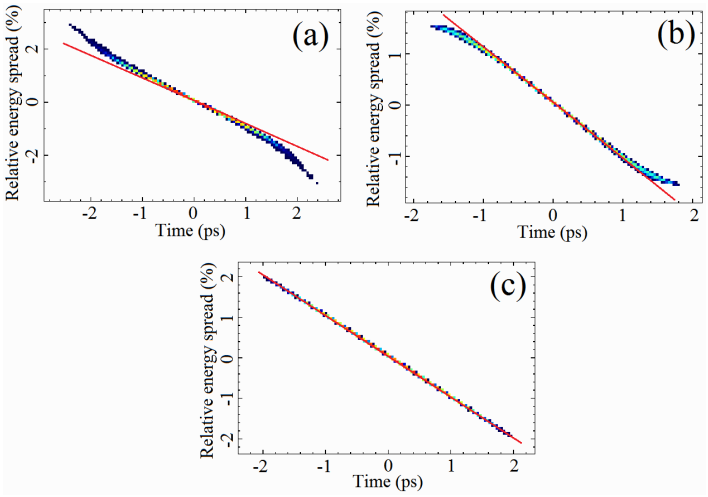

FIGURE *3.23 – Time/energy phase-space of the electron bunch at the exit of the RF-gun. Parameters of simulation : Charge 100 pC; Laser rms duration 1 ps; Gun peak accelerating field 80 MV/m; RF-phase minimizing the bunch length; Laser rms transverse radius 0.5 mm; Simulation stops 30 cm after the photocathode. (a) : 3D Gaussian laser shape; (b) : Beer can laser shape; (c) : 3D ellipsoid laser shape. The red line denotes a perfectly linear bunch phase-space.*

Fig. 3.19, Fig. 3.20, Fig. 3.21 and Fig. 3.22 show that the 3D ellipsoid shape allows reaching lower rms bunch length and transverse emittance than the Beer can shape allowing itself to achieve lower than the 3D Gaussian shape. It is interesting to quantify precisely the gain allowed by laser shaping. It can be done by doing simulations for each laser shape with the parameters minimizing the bunch length at the exit of the RF-gun. These optimum parameters can be derived from the simulations of Sec. 3.1.3.1, Sec. 3.1.3.2, Sec. 3.1.3.3 and Sec. 3.1.3.4. To stay realistic, I performed the simulations with a not too high peak accelerating field of 100 MV/m, which corresponds to the maximum value reached on PHIL until now. I choose also not too short a laser pulse duration of 50 fs rms, which corresponds to the specification of the LASERIX laser usable on PHIL [102]. Tab. 3.2 gathers the results of these simulations.

Laser shape	3D Gaussian	Beer can	3D ellipsoid
Laser rms transverse radius	1.2mm	1.4mm	1.3mm
Rms bunch length	140fs	121fs	119fs
Rms normalized transverse	3.8π.mm.mrad	2.0π.mm.mrad	1.0π.mm.mrad

TABLE *3.2 – Rms bunch length and transverse emittance for the 3 different kind of laser shape. Parameters of simulation : Charge 100 pC ; Laser rms duration 50 fs ; Peak accelerating field 100 MV/m ; RF-phase minimizing the bunch length ; Simulation stops 30 cm after the photocathode.*

Tab. 3.2 shows a quite small, but non negligible, gain on rms bunch length which is only of 17% between 3D ellipsoid shape and 3D Gaussian shape. The gain is above all observed on the bunch rms transverse emittance. Indeed it is around 75% between 3D ellipsoid shape and 3D Gaussian shape, and around 50% between 3D ellipsoid shape and Beer can shape. This more important gain in the transverse plane is explained by the fact that the space-charge forces have less effect in the longitudinal direction than in the transverse one [24].

The control of the laser pulse shape allows therefore reaching higher brilliance with a 100 pC electron bunch by improving the performances both in terms of duration and transverse emittance.

3.1.3.6 Influence of the bunch charge

It is obviously important to study the impact of bunch charge on the rms bunch length and transverse emittance, since the space-charge forces are directly proportional to the bunch charge. I choose to perform simulations for bunch charge between 1 nC, which is the maximum charge currently achievable on PHIL, and 100 fC which is more or less the lowest measurable charge currently on PHIL with a scintillating screen (see Sec. 2.1). Fig. 3.24 shows the results of these simulations.

24. The space-charge field scales as $\frac{1}{\gamma^2}$ in the transverse direction and as $\frac{1}{\gamma^3}$ in the longitudinal direction, where γ is the relativistic factor.

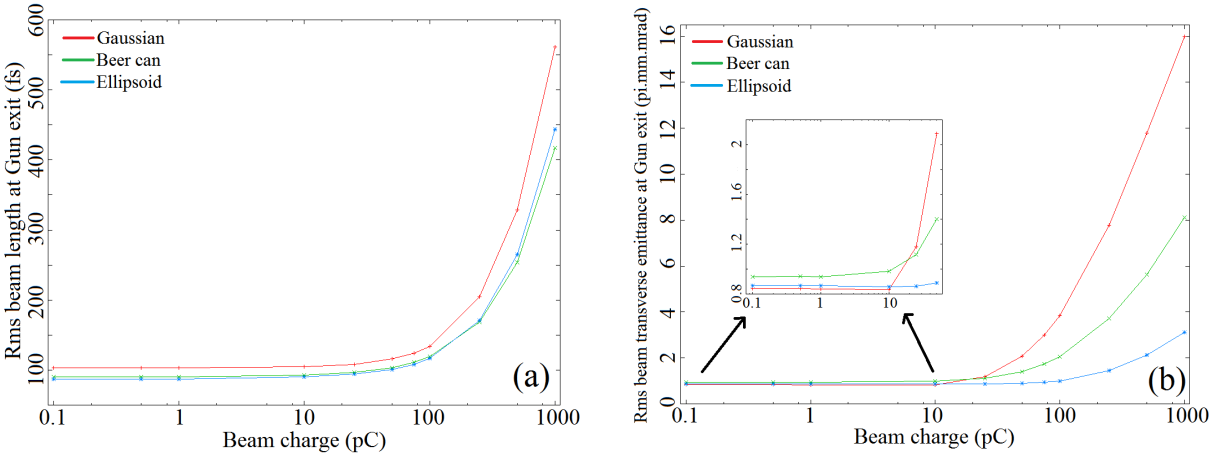

FIGURE *3.24 – Rms bunch length (a) and transverse emittance (b) vs Bunch charge. Parameters of simulation : Laser rms duration 50 fs ; Laser rms transverse radius 1.2 mm (3D Gaussian) 1.4 mm (Beer can) 1.3 mm (3D ellipsoid) ; Peak accelerating field 100 MV/m ; RF-phase minimizing the bunch length ; Simulation stops 30 cm after the photocathode.*

The rms bunch length shows a similar decrease towards different limit values for the 3 different laser shape. The limit values are of 103 fs (3D Gaussian), 90 fs (Beer can) and 87 fs (3D ellipsoid). One can observe that, for the used values of the laser rms transverse radii, the gain on rms bunch length becomes negligible below 10 pC of bunch charge. In fact, it is only of 3% between 10 pC and 1 pC and almost zero (less than 0.5%) below 1 pC. Therefore, for the used values of the laser rms transverse radii, it is not necessary to lower the bunch charge below 10 pC to optimize the rms bunch length. It is an interesting point since 10 pC are easily measurable with an ICT, which is not the case of sub-pC bunches. One has to note that if different values of the laser rms transverse radii was used, the behavior of Fig. 3.24 (a) would be the same but the value of the charge at which the gain on the rms bunch length becomes negligible would be different.

The rms bunch transverse emittance also reaches a limit value at low bunch charge. This value means that the space-charge forces have no more impact on the emittance and that it is only defined by the thermal emittance, namely the native emittance at the bunch emission from the photocathode. This thermal emittance $\epsilon_{th_{x,y}}$ is directly proportional to the laser pulse rms transverse radius $\sigma_{x,y}$ and is defined by [103, 86] :

$$\epsilon_{th_{x,y}} = 2\sigma_{x,y}\sqrt{\frac{2k_BT}{m_ec^2}} \tag{3.9}$$

where $k_B = 1.38 * 10^{-23}$ J/K is the Boltzmann constant and T is the temperature of the cathode. For $T = 300$ K, this formula is simplified as :

$$\epsilon_{th_{x,y}} = \sigma_{x,y}(mm) * 0.6463 \ \pi.mm.mrad$$

It explains why the rms bunch transverse emittance becomes lower at low bunch charge

for the 3D Gaussian shape than for the 3D ellipsoid shape and Beer can shape. The reason is simply that the used laser rms transverse radius is lower for the 3D Gaussian shape (1.2 mm) than for the 3D ellipsoid shape (1.3 mm) and the Beer can shape (1.4 mm). The hierarchy of the different laser shapes with respect to the space-charge forces appears only, for the used values of the laser rms transverse radii, for bunch charges higher than 25 pC, where one can see that the rms transverse emittance increases more quickly for 3D Gaussian shape than for Beer can shape than for 3D ellipsoid shape. Therefore, for the used values of the laser rms transverse radii, it is not necessary to lower the bunch charge below 10 pC to optimize the rms bunch transverse emittance and the shape of the laser pulse has no direct impact on the minimal achievable emittance. The only impact is the one of the laser pulse rms transverse radius. Once again it is interesting since 10 pC are easily measurable with an ICT, which is not the case of sub-pC bunches.

To conclude it can be said that, for the used values of the laser rms transverse radii, the laser shaping plays a significant role only for bunch charge higher than 10 pC. Below this value, the gain on the rms bunch length is only 15.5% between the 3D ellipsoid shape and the 3D Gaussian shape and the gain on the rms bunch transverse emittance is zero, since it is only defined by the rms transverse radius of the laser pulse. Shaping of the laser pulse is therefore necessary only when a high-charge bunch is required. It is noteworthy that if different values of the laser rms transverse radii were used, the behavior of Fig. 3.24 (b) would be the same but the value of the charge at which the rms transverse emittance becomes almost constant and defined by the laser pulse rms transverse radius would be different.

3.1.3.7 Influence of a booster cavity

The presence of a booster cavity just after the exit of the RF-gun is necessary since the bunch has only a mean energy of 6 MeV, implying that its length is not frozen at all and is still quickly increasing under the combined effects of space-charge forces and energy spread. Fig. 3.25 shows well this fact. One can see that the bunch length increases linearly after the RF-gun exit at 0.15 m. It has been calculated, between 0.15 m and 0.25 m, that the bunch lengthening rate is 174 fs/m at 10 pC and 143 fs/m at 100 pC. The initial bunch length being 134 fs at 100 pC and 105 fs at 10 pC, it is therefore clear that the bunch length cannot be maintained without a booster cavity after the RF-gun, since otherwise the bunch length is doubled in less than one meter.

The presence of a booster cavity can also be useful to freeze the bunch rms transverse emittance. Indeed, the rms transverse emittance is also still quickly increasing under the effect of space-charge forces when the bunch charge is high ($>$ 10 pC). Fig. 3.26 shows that the rms transverse emittance is almost constant at the thermal value after the RF-gun exit at 10 pC, but is increasing at a rate around 3.6 π.mm.mrad/m after the RF-gun exit at 100 pC. The initial value being of 3.84 π.mm.mrad, it corresponds once again to a doubling of the value in around one meter which highlights the necessity of a booster cavity.

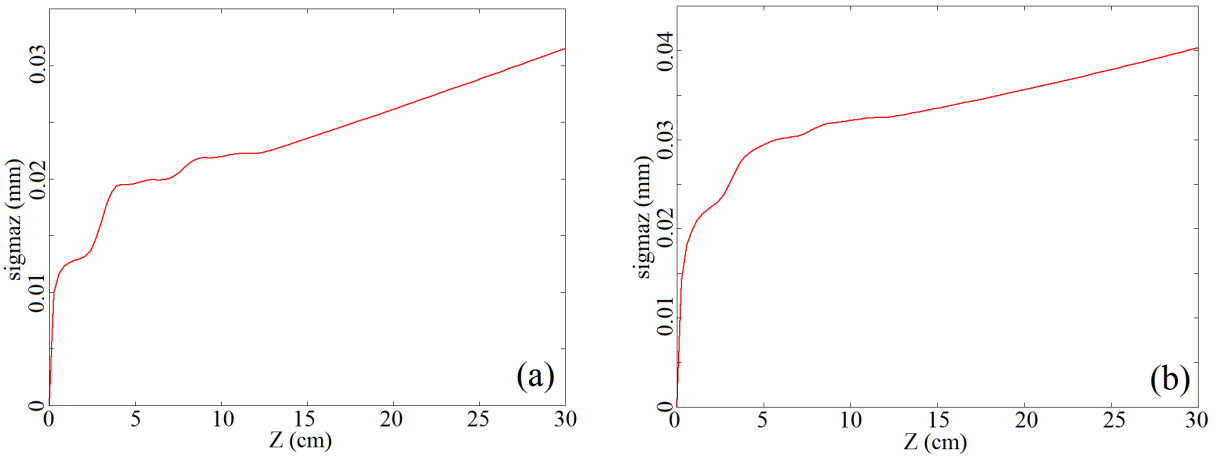

FIGURE *3.25 – Rms bunch length vs Bunch position. Parameters of simulation : Bunch charge 10 pC (a) and 100 pC (b) ; Laser rms duration 50 fs ; Laser rms transverse radius 1.2 mm (3D Gaussian) ; Peak accelerating field 100 MV/m ; RF-phase minimizing the bunch length ; Simulation stops 30 cm after the photocathode.*

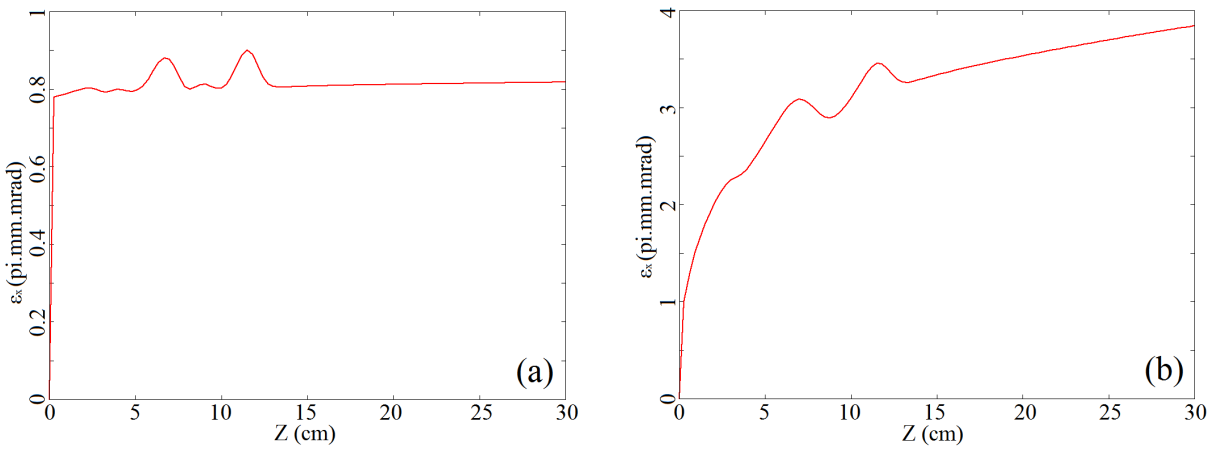

FIGURE *3.26 – Rms transverse emittance vs Bunch position. Parameters of simulation : Bunch charge 10 pC (a) and 100 pC (b) ; Laser rms duration 50 fs ; Laser rms transverse radius 1.2 mm (3D Gaussian) ; Peak accelerating field 100 MV/m ; RF-phase minimizing the bunch length ; Simulation stops 30 cm after the photocathode.*

To study the bunch performances after the booster cavity, I perform ASTRA simulations up to 1.5 m after the photocathode, namely 0.5 m after the exit of booster cavity. I study first the performances obtained for the bunch length at a high charge of 100 pC and at a low charge of 1 pC as a function of the RF-phase of the booster cavity. Fig. 3.27 shows the results of this study. It shows the same behavior for the 3 shapes, with a minimum of rms bunch length for negative booster RF-phase values. Fig. 3.28 shows the evolution of the bunch length along the beamline for the 3D gaussian laser shape and the Gun and Booster RF-phases minimizing the bunch length.

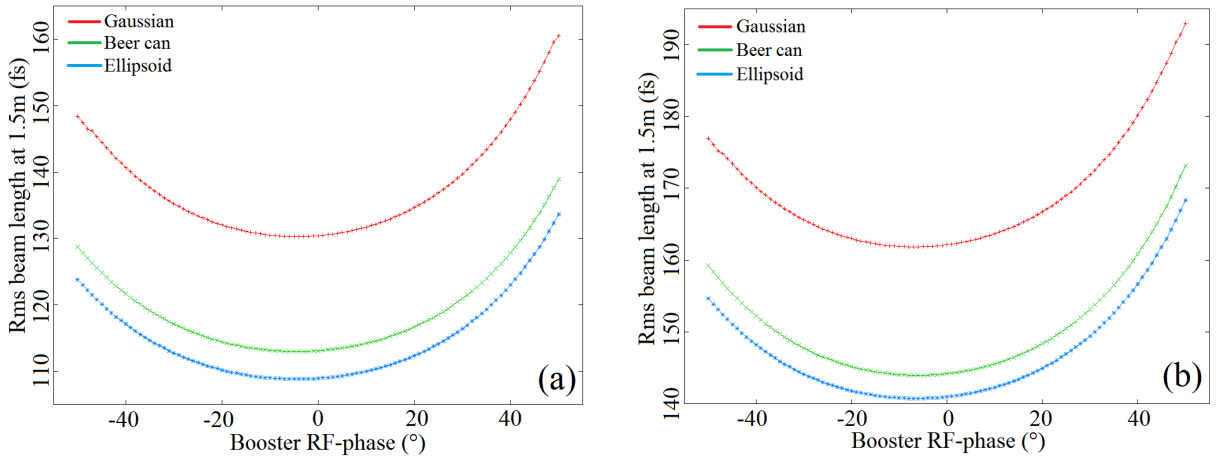

FIGURE 3.27 – *Rms bunch length vs Booster RF-phase. Parameters of simulation : Bunch charge 1 pC (a) and 100 pC (b) ; Laser rms duration 50 fs ; Laser rms transverse radius 1.2 mm (3D Gaussian) 1.4 mm (Beer can) 1.3 mm (3D ellipsoid) ; Gun peak accelerating field 100 MV/m ; Gun RF-phase minimizing the bunch length ; Booster peak accelerating field 38 MV/m ; Simulation stops 1.5 m after the photocathode.*

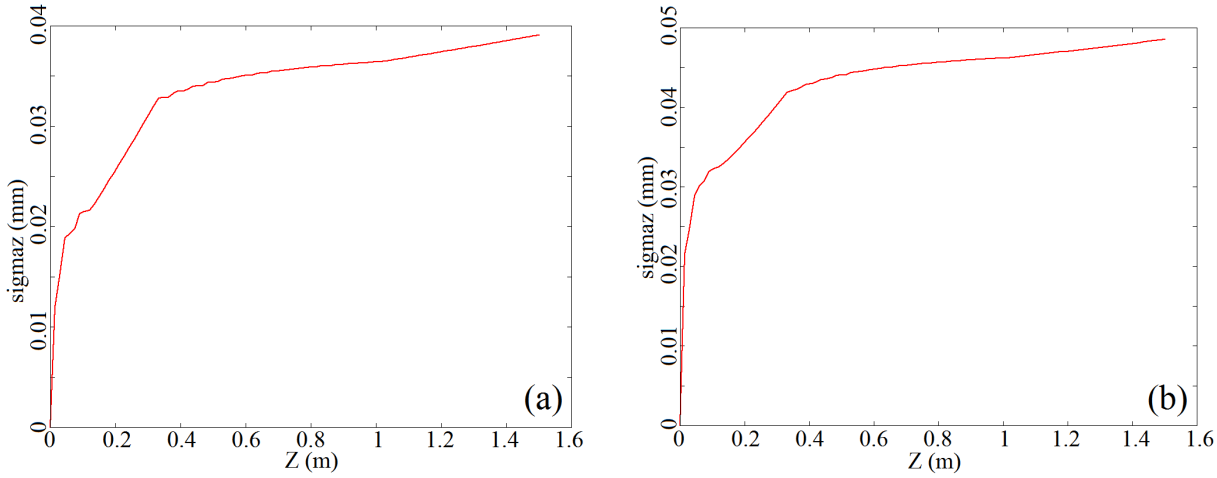

FIGURE 3.28 – *Rms bunch length vs Bunch position. Parameters of simulation : Bunch charge 1 pC (a) and 100 pC (b) ; Laser rms duration 50 fs ; Laser rms transverse radius 1.2 mm (3D Gaussian) ; Gun Peak accelerating field 100 MV/m ; Booster peak accelerating field 38 MV/m ; Booster and Gun RF-phase minimizing the bunch length ; Simulation stops 1.5 m after the photocathode.*

It is noteworthy that a jitter of ±10° on the booster RF-phase introduces a jitter of 0.7 fs (so 0.4%) if we work at the booster RF-phase minimizing the bunch length, and of 1.8 fs (so 1.1%) if we work at the 0° booster RF-phase maximizing the bunch energy. It is therefore clear that the stability of the booster RF-phase is not of a crucial importance to optimize the rms bunch length, even less than it is for the Gun RF-phase (see Sec. 3.1.3.1).

The booster cavity induces almost no change on the bunch length ratio between the 3 different kinds of laser shape with respect to the ratio at the RF-gun exit. In fact, the bunch length ratio between 3D ellipsoid and 3D Gaussian (Beer can) is 1.15 (1.02) while it was 1.17 (1.02) at the RF-gun exit (see Tab. 3.2).

The main effect of the booster cavity, concerning the rms bunch length, is the strong decrease observed in the bunch lengthening rate with respect to the one at the RF-gun exit. In fact, as shown in Fig. 3.28 the linear bunch lengthening rate (calculated between 1.1 m and 1.5 m) is 18.4 fs/m at 1 pC and 16.1 fs/m at 100 pC while it was around ten times higher at the RF-gun exit (174 fs/m at 10 pC and 143 fs/m at 100 pC). The booster cavity has therefore, as intended, a very beneficial effect on the bunch length conservation along the bunch propagation.

I then study the performances obtained for the bunch rms transverse emittance at a high charge of 100 pC and at a low charge of 1 pC as a function of the RF-phase of the booster cavity. Fig. 3.29 shows the results of this study. These two graphics confirm the emittance behavior observed at the RF-gun exit (see Fig. 3.24 (b)). Namely, it shows that at a low charge of 1 pC the rms transverse emittance is very close to the native thermal value for booster RF-phase around +10° and the emittance hierarchy is therefore the one of the laser pulse rms transverse radius. On the other hand, at a high charge of 100 pC, the emittance hierarchy is governed by the space-charge effect and shows a massive superiority of the 3D ellipsoid shape upon the Beer can shape and above all the 3D Gaussian shape in a large range of booster RF-phase around the 0° maximum energy gain.

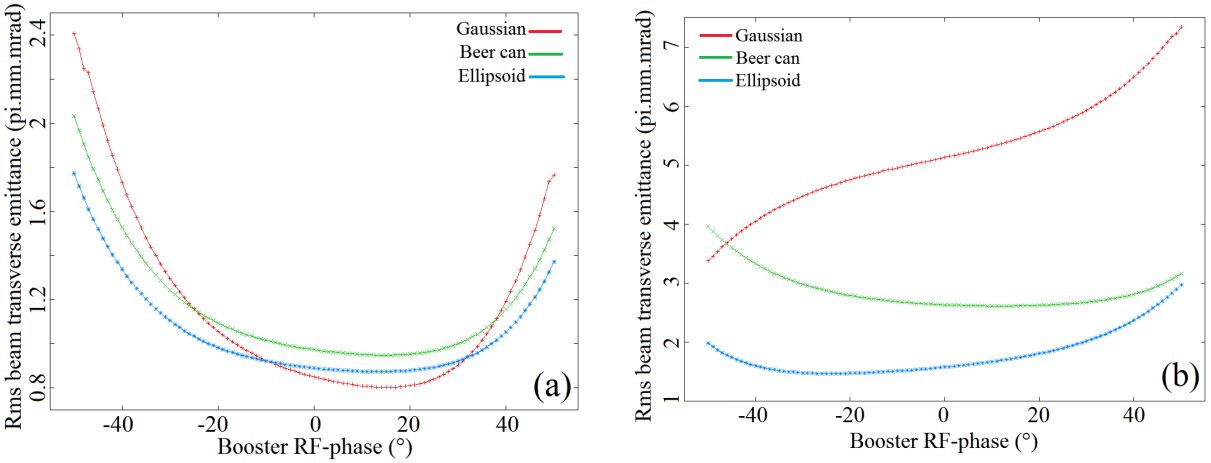

FIGURE *3.29 – Rms transverse emittance vs Booster RF-phase. Parameters of simulation : Bunch charge 1 pC (a) and 100 pC (b) ; Laser rms duration 50 fs ; Laser rms transverse radius 1.2 mm (3D Gaussian) 1.4 mm (Beer can) 1.3 mm (3D ellipsoid) ; Gun peak accelerating field 100 MV/m ; Gun RF-phase minimizing the bunch length ; Booster peak accelerating field 38 MV/m ; Simulation stops 1.5 m after the photocathode.*

The presence of a booster cavity plays also an important role for the rms transverse emittance conservation, by strongly reducing the effect of space-charge forces. Indeed, as

shown in Fig. 3.30 its linear increase rate (calculated between 1.1 m and 1.5 m) is about 0.48 π.mm.mrad/m at 100 pC, while it was 3.6 π.mm.mrad/m at the RF-gun exit.

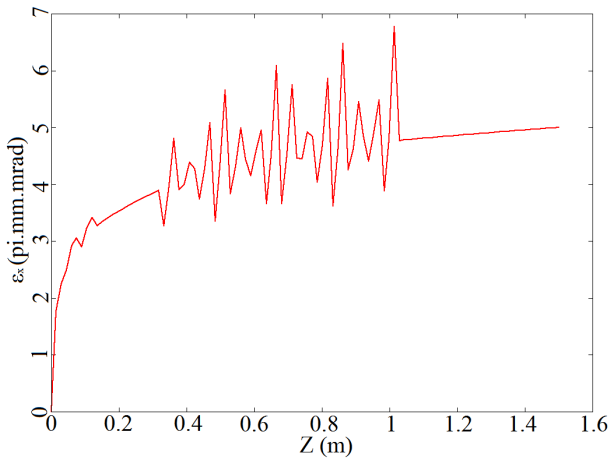

FIGURE *3.30 – Rms transverse emittance vs Bunch position. Parameters of simulation : Bunch charge 100 pC ; Laser rms duration 50 fs ; Laser rms transverse radius 1.2 mm (3D Gaussian) ; Gun peak accelerating field 100 MV/m ; Booster peak accelerating field 38 MV/m ; Booster and Gun RF-phase minimizing the bunch length ; Simulation stops 1.5 m after the photocathode.*

Tab. 3.3 shows a summary of the rms bunch length and transverse emittance, in the configurations minimizing the rms length, 1.5 m after the photocathode (namely around 0.5 m after the booster cavity exit) for the 3 different kind of laser shape and for the two bunch charges of 1 pC and 100 pC.

Laser shape /Beam charge	3D Gaussian /1pC	3D Gaussian /100pC	Beer can /1pC	Beer can /100pC	3D ellipsoid /1pC	3D ellipsoid /100pC
Rms bunch length	**130fs**	**162fs**	**113fs**	**144fs**	**109fs**	**141fs**
Linear lengthening rate	**18,4fs/m**	**16,1fs/m**	**15,7fs/m**	**16,1fs/m**	**14,9fs/m**	**14,7fs/m**
Rms transverse emittance	**0,875π.mm.mrad**	**5,006π.mm.mrad**	**0,987π.mm.mrad**	**2,659π.mm.mrad**	**0,900π.mm.mrad**	**1,534π.mm.mrad**
Linear emittance increase rate	**0,08π.mm.mrad/m**	**0,48π.mm.mrad/m**	**0,09π.mm.mrad/m**	**0,40π.mm.mrad/m**	**0,07π.mm.mrad/m**	**0,43π.mm.mrad/m**

TABLE *3.3 – Summary of bunch properties after the booster cavity. Parameters of simulation : Laser rms duration 50 fs ; Laser rms transverse radius 1.2 mm (3D Gaussian) 1.4 mm (Beer can) 1.3 mm (3D ellipsoid) ; Gun peak accelerating field 100 MV/m ; Booster peak accelerating field 38 MV/m ; Booster and Gun RF-phase minimizing the bunch length ; Simulation stops 1.5 m after the photocathode.*

3.1.3.8 Propagation of a longitudinally modulated electron beam

In addition to the single-bunch beam, I also simulate the propagation of a longitudinally modulated electron beam made of short bunches. This kind of beam can be generated by a THz temporally modulated laser pulse impacting a photocathode in an RF-gun. The temporally modulated laser pulse can be created by the "Pulse-Stacking" technique, which basically consists in copying a fs laser output several times and adding delays between the pulses [104]. It can also be generated by the "chirp pulse beating" technique [105, 7], where the laser pulse is stretched and chirped before passing through a third harmonic device. A Michelson interferometer allows creating two copies of the chirped pulse and combining them with a delay, thus creating a modulated pulse whose modulation frequency is a function of the delay. This kind of longitudinally modulated electron beam can be used for several applications : plasma acceleration (see Sec. 3.2.3), THz sources [7], Inverse Compton scattering sources [106] ....

In this part I will mainly be interested in the conservation of the beam modulation all along its propagation, since the properties of a single bunch have already been widely studied in the previous parts of Sec. 3.1.3. Fig. 3.31 shows the longitudinal profile I consider in this part, which is composed of 13 bunches symmetric with respect to the central one. Each bunch has an rms length of 100 fs and the spacing between the centers of two adjacent bunches is 1 ps. The charge ratio on each side with respect to the central bunch is 100%-96.2%-85.7%-70.7%-53.9%-38.1%-24.9%, thus following a Gaussian beam envelope.

In this part, the Gun RF-phase denotes the one at the moment of the emission of the first bunch of the beam. The delay time of 1 ps between the emission of two successive bunches corresponds to a shift of around 1° in the RF-phase of the 3 GHz accelerating field of the RF-gun.

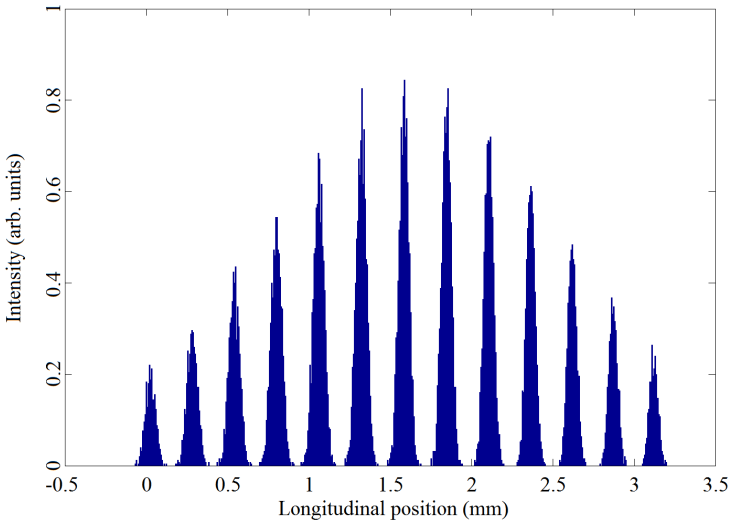

FIGURE *3.31 – Modulated longitudinal profile used for the simulations in this section*

My work consists in the study of the generation and propagation of the modulated beam in the PHIN RF-gun, currently mounted on the PHIL facility (see Sec. 1.4.1). I therefore stop the ASTRA simulations 30 cm after the photocathode. I perform this study for several total beam charges between 20 pC and 2 nC. Fig. 3.32 shows the longitudinally modulated beam, projected in a transverse/time plane, 30 cm after the photocathode for the studied charges. The RF-phase of the gun has each time been fixed to the one maximizing the beam energy.

It is clearly visible in Fig. 3.32 that for too high charges, roughly from 500 pC onward, the beam starts to visibly distort itself towards its tail. Namely, the bunches in the tail start to overlap each other implying a decrease in the contrast between the bunches. This is due to the effect of the space-charge forces of the first emitted bunches on the last emitted ones. One can also see that the spacings between the bunches and the lengths of the bunches becomes less and less uniform along the beam when the beam charge increases above 500 pC. It denotes a loss of the initial beam longitudinal modulation. For these reasons, I choose to perform a more detailed study of the beam properties only for the total beam charges of 20 pC and 200 pC, where the contrast between the bunches remains 100%. I study the evolution of the spacings between the bunches and of the rms lengths of the bunches for several Gun RF-phases. Fig. 3.33 shows the results of this study.

The graphics (a) and (c) of Fig. 3.33 show a different behavior than the graphics (b) and (d) of Fig. 3.33. This different behaviors are only caused by the space-charge forces effects, since the only difference between the two cases is the total beam charge which is increasing from 20 pC to 200 pC.

Fig. 3.33 (a) shows a linear increase of the spacing between the bunches from the beam head to the beam tail. This increase is due to the fact that, for the Gun RF-phases used in my simulations, the accelerating field on the photocathode is increasing in time. As a result, the successive bunches are more and more accelerated when they are emitted from the photocathode. It implies that the distance travels by one bunch before the emission of the next one is also increasing in time, which explains the increase of the spacing between the bunches observed in Fig. 3.33 (a). One can also see that the values of the spacings between the bunches depends on the Gun RF-phase. It is simply due to the fact that the value of the peak accelerating field on the photocathode depends on the Gun RF-phase, and it increases between $-5°$ and $+8°$.

Fig. 3.33 (b) shows a different behavior. Between the six or seven first bunches the spacing increases, for the same reasons as for Fig. 3.33 (a). Then it reaches an almost constant value, which is a function of the Gun RF-phase, between the six or seven last bunches. This is due to the space-charge electric field generated by the already emitted bunches. This field superimposes with the RF-gun accelerating field and reduces its value. This reduction compensates the increase in time of the RF-gun accelerating field, which results in an almost constant spacing between the last bunches of the beam. This effect is not observed in Fig. 3.33 (a) because the total charge is only of 20pC, implying very small space-charge forces effects.

Fig. 3.33 (c) shows that the rms lengths of the bunches increase with the Gun RF-phase in the studied range of Gun RF-phase. This is not surprising, since this behavior

has already been observed for one bunch of 100 pC in Fig. 3.19 of Sec. 3.1.3.1 (red curve). A direct consequence of this fact is that the rms lengths of the successive bunches increase from the beam head to the beam tail, since the Gun RF-phase increases.

Fig. 3.33 (d) shows a different and complicated behavior. This behavior is due to the space-charge forces, in each bunches and between the bunches, which can counteract the evolution of the bunches lengths along the beam due to the accelerating field (visible in Fig. 3.33 (c) for a beam charge of 20 pC). It can for example lead to an almost constant rms length for the ten first bunches at a Gun RF-phase of $-10°$. One can notice that, for the same Gun RF-phase, the rms bunches lengths are globally higher for the beam charge of 200 pC (Fig. 3.33 (d)) than the ones for the beam charge of 20 pC (Fig. 3.33 (c)), because of the higher intra-bunch space-charge forces.

The first conclusion which can be drawn from this study is that the 1 ps constant initial spacing between the bunches and the 100 fs constant initial rms length of the bunches along the beam cannot be conserved at the exit of the RF-gun, because of the time variation of the accelerating field in the RF-gun. This has been shown in Fig. 3.33 (a) and (c) where the beam charge is 20 pC, resulting in very small space-charge forces effects. This effect of the RF-gun accelerating field can, to some extent, be counteracted by the space-charge forces in the bunches and between the bunches, as it has been shown in Fig. 3.33 (b) and (d) for a beam charge of 200 pC. However, the space-charge force effect does not allow achieving a constant spacing between the bunches and a constant rms bunch length all along the beam, but only for parts of the beam.

The second important conclusion is that the spacing between the bunches and the rms length of the bunches cannot be optimized for the same Gun RF-phases. A compromise has therefore to be found between these two parameters, by setting the Gun RF-phase to an intermediate value.

For the beam charge of 20 pC, the spacing is optimum at $+8°$ since it varies from 0.94 ps to 1.05 ps between the beam head and tail, representing a maximal deviation of 6% from the 1 ps requirement. For this RF-phase, the rms length is not optimal at all since it varies from 110 fs to 121 fs, representing a maximal deviation of 21% from the 100 fs requirement. The rms length is optimal at $-4°$ where it varies from 96 fs to 105 fs, representing a maximal deviation of 5% from the 100 fs requirement. For this RF-phase, the spacing is not optimal since it varies from 0.82 ps to 0.93 ps, representing a maximal deviation of 18% from the 1 ps requirement.

For the beam charge of 200 pC, the spacing is optimum at $+6.5°$. It varies from 0.93 ps to 1.03 ps, representing a maximal deviation of 7% from the 1 ps requirement. For this RF-phase, the rms length varies from 109 fs to 126 fs, representing a maximal deviation of 26% from the 100 fs requirement. The rms length is optimal at $-15°$ where it varies from 97 fs to 108 fs, representing a maximal deviation of 8% from the 100 fs requirement. For this RF-phase, the spacing varies from 0.71 ps to 0.82 ps, representing a maximal deviation of 29% from the 1 ps requirement.

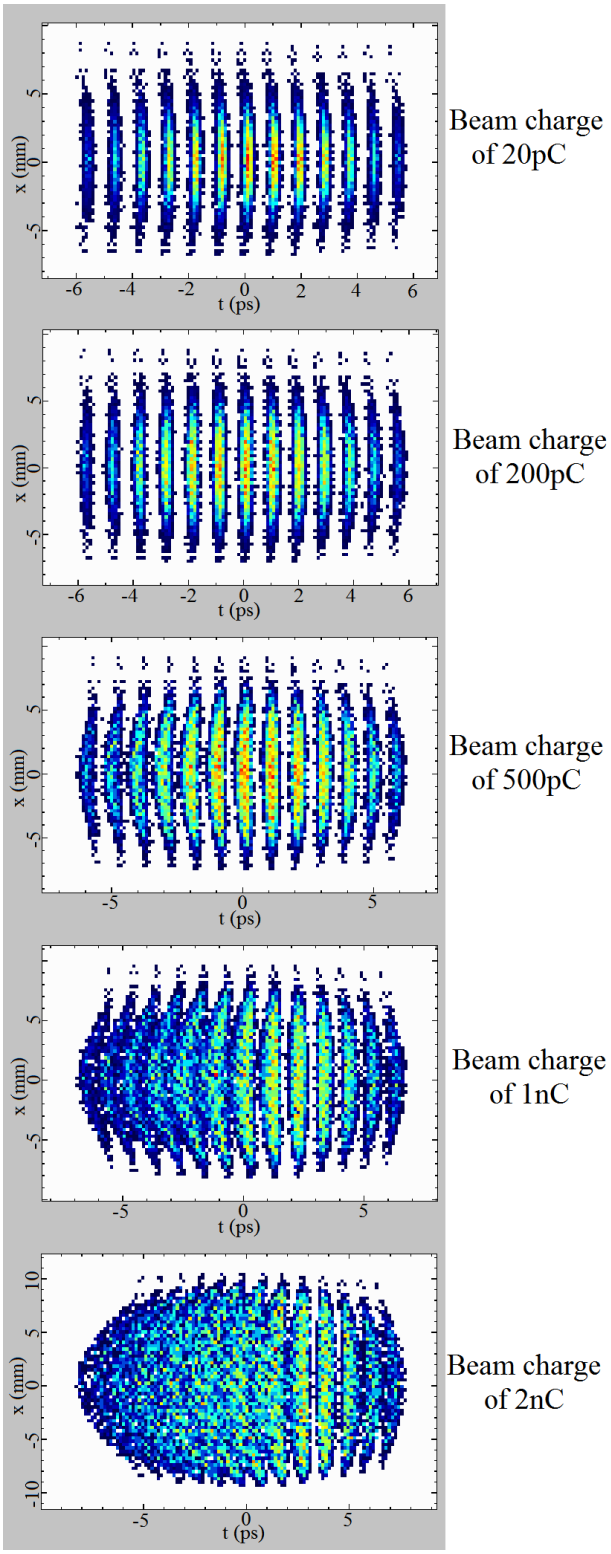

FIGURE 3.32 – *Longitudinally modulated beam at the entrance of the booster cavity for several total beam charges. RF-gun peak accelerating field : 90 MV/m ; Gun RF-phase : maximizing the beam energy ; Initial beam rms transverse radius : 0.8 mm.*

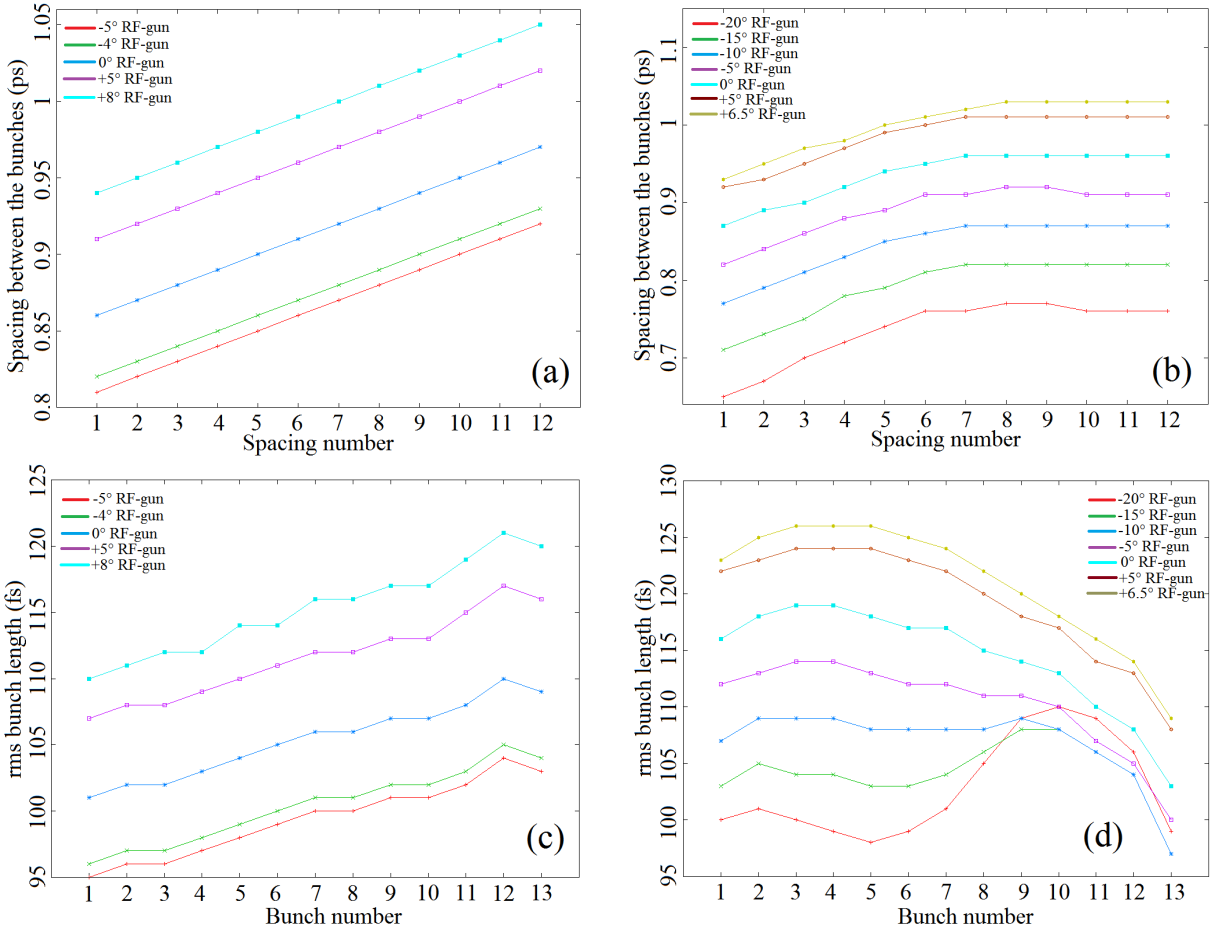

FIGURE *3.33 – Spacings between the bunches ((a) & (b)) and rms lengths of the bunches ((c) & (d)) of the modulated beam, at the RF-gun exit, for several Gun RF-phases (0° denotes the maximum energy gain in the RF-gun). The bunch n°1 is the first bunch emitted from the photocathode. Total beam charge : 20 pC ((a) & (c)) and 200 pC ((b) & (d)) ; RF-gun peak accelerating field : 90 MV/m ; Initial beam rms transverse radius : 0.8 mm.*

3.2 Magnetic compression in a chicane

3.2.1 Principles and limitations

The magnetic compression consists in using a static and uniform magnetic field to compress a pre-existent accelerated electron beam. The basic physical principle of this method is that the electrons with different energies constituting the beam will follow different paths, and therefore takes different travel times, to exit the area where the used magnetic field is located.

To shorten the beam length, it is sufficient to ensure that the electrons located in the beam tail before the magnetic compressor have such energies that their travel times in the compressor are lower than the ones of the electrons located in the beam head in order for them to catch up. A more energetic electron runs through a longer distance in the compressor, but it is also faster. Whether its travel time will be higher or lower than the one of a less energetic electron is therefore determined by a competition between these two effects.

The relative variation in travel time, in the magnetic compressor, between an electron with an energy E and a reference electron having the mean beam energy E_0 is given by the following approximate formula : $\frac{\Delta T}{T_0} = \eta \frac{E-E_0}{E_0}$, where $\eta = \alpha - \frac{1}{\gamma_0^2}$ with α a constant depending only on the magnetic compressor properties and $\gamma_0 = 1 + \frac{E_0}{mc^2}$. A demonstration and a formula for α are given in Appendix D.

One can see that if $\eta > 0$, the most energetic electrons have the highest travel time in the compressor, while they have the lowest time travel if $\eta < 0$. To shorten the beam length we must have, at the compressor entrance,, the most energetic electrons in the beam head if $\eta > 0$ or in the beam tail if $\eta < 0$. This correlation between the electrons energies and their longitudinal position in the beam is often realized thanks to an RF accelerating structure, placed before the compressor, which is used to accelerate differently the head and the tail of the beam. It is also sometimes directly generated in the electron source.

The magnetic compression is the currently most commonly used method to generate short electron beams. A good example is a research team from the Institute of Scientific and Industrial Research of Osaka University [107]. This team succeeded in generating by this method, at an energy of 32 MeV, electron bunches of 170 pC with an rms length of 98 fs and of 1 nC with an rms length of 400 fs.

The magnetic compression therefore allows generating shorter electron beams and/or with higher charge than an RF-gun driven by a femtosecond laser pulse. This is mainly due to the fact that it is performed on an already accelerated electron beam, which allows strongly decreasing the space-charge force effect on the beam length.

However this method has the drawback to induce a curved trajectory for the electrons, which implies the emission of synchrotron radiation by the electrons. The emission of synchrotron radiation can deteriorate in significant ways the beam properties, and especially its 3 emittances which correspond to the areas covered by the beam electrons in the two transverse phase-spaces and in the longitudinal phase-space. These emittances represent

the global quality of the beam and more precisely the easiness to focus the beam and therefore to transport it. The increase of the emittances in the magnetic compressor is therefore harmful, because it decreases the beam quality and make it harder to transport. This phenomenon is amplified by the fact that when the beam is very short, namely when its length is lower than the wavelength of the emitted synchrotron radiation, the different electrons of the beam emit their synchrotron radiation in a coherent way which amplifies its intensity and, therefore, its effect.

3.2.2 Compression of a single electron bunch

To perform the study of the compression of a single electron bunch in a magnetic chicane, I use a simple accelerator layout made of : The PHIN RF-gun mounted on PHIL, a 0.7 m long 3 GHz standing wave booster section whose entrance is located 1.2 m after the photocathode and a D-shape magnetic chicane whose entrance is located 2.5 m after the photocathode. The D-shape magnetic chicane is made of four dipole magnets arranged as shown in Fig. 3.34.

I choose to use the ASTRA beam dynamics code to perform the simulation between the photocathode and the entrance of the magnetic chicane, and the CSRtrack one to perform the simulation in the magnetic chicane. I use this latter because it is fully compatible with the ASTRA code. Another reason is that it takes into account the effects of the coherent synchrotron radiation and of the space-charge forces.

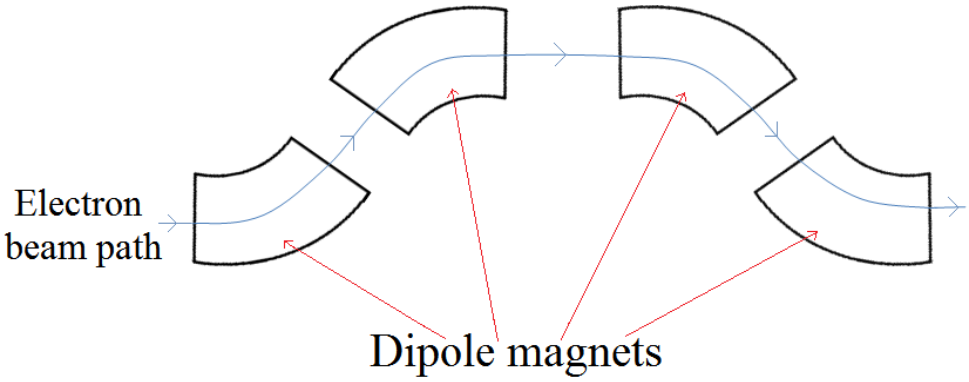

FIGURE *3.34 – Simplified layout of a D-shape magnetic chicane*

I set the peak accelerating field of the RF-gun to 80 MV/m, which is the current maximal value at PHIL, and the one of the booster section to 40 MV/m, thus allowing a maximum mean bunch energy around 21 MeV at its exit. In practical, the bunch mean energy will always be lower since the booster section, and potentially also the RF-gun, will work at an RF-phase different from the one maximizing the energy gain, to induce the bunch time/energy correlation (chirp) required to perform magnetic compression (see Sec. 3.2.1). I set the bunch charge to 100 pC, which is a typical value for a Copper photocathode in an RF-gun. I finally set the parameters of the laser pulse driving the RF-gun to the following : a 3D Gaussian shape, a 1 ps rms long time profile and a 0.5 mm rms transverse radius.

In the different studied configurations, I aimed to reach a final rms bunch length σ_t of 100 fs after compression. When it was not possible I just minimize the final rms bunch length. When it was possible, there were always two configurations of the magnetic chicane allowing reaching the 100 fs rms. In fact, if the maximal compression corresponds to a σ_t value lower than 100 fs, it is possible to reach the 100 fs rms either by undercompressing the bunch or by overcompressing it. I chose to always search for the bunch undercompression scheme, namely with a bunch continuing its compression in the longitudinal drift space following the magnetic chicane. The design of the magnetic chicane is different in each case. I will present in detail, at the end of this section, the properties of the magnetic chicane only for the best case I could find.

3.2.2.1 Evolution of the bunch mean energy

Fig. 3.35 shows the evolution of the bunch mean energy (a) and rms energy spread (b) at the magnetic chicane entrance, for several Gun RF-phases, as a function of the booster RF-phase.

These two parameters are important, since the combination of a high mean energy and of a low rms energy spread result in a low velocity spread between the electrons of the bunch. A low velocity spread implies a small lengthening rate of the bunch, and therefore a better conservation of the rms bunch length, in the longitudinal drift space following the magnetic chicane.

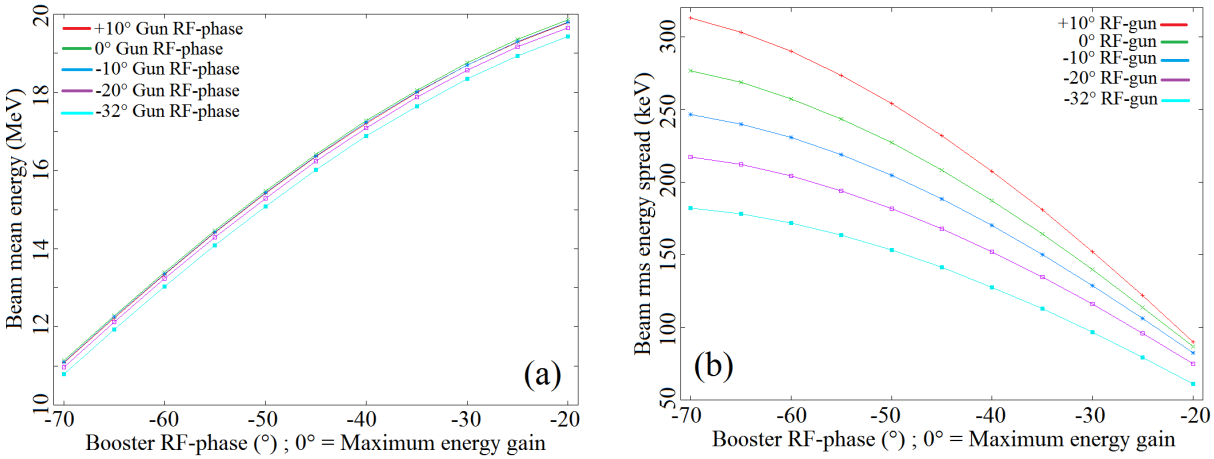

FIGURE *3.35 – Evolution of the bunch mean energy (a) and rms energy spread (b) at the magnetic chicane entrance as a function of the booster RF-phase, for several Gun RF-phases. Bunch charge : 100 pC ; RF-gun peak accelerating field : 80 MV/m ; Booster peak accelerating field : 40 MV/m ; Current injected in the B3 solenoid at the RF-gun exit : 177 A.*

3.2.2.2 Evolution of the final rms bunch length

I first study the evolution of the final rms bunch length after compression, for several RF-phases of the RF-gun, as a function of the RF-phase of the booster section. Fig. 3.36 shows the results of this study. Fig. 3.37 shows, for the same cases, the rms bunch length at the entrance of the magnetic chicane.

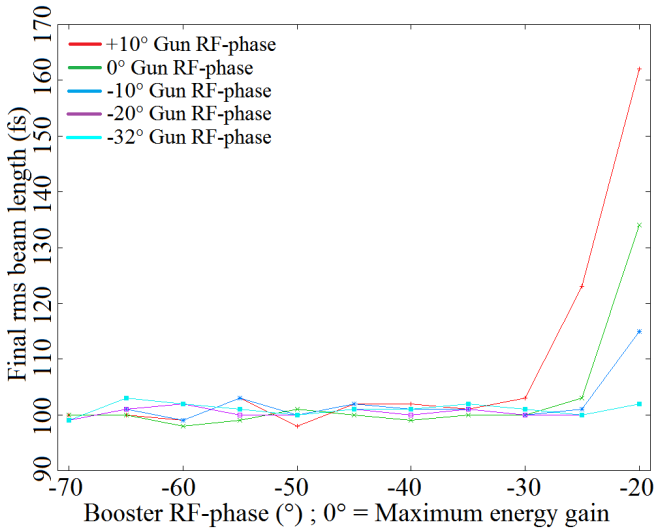

FIGURE *3.36 – Final rms bunch length, for several Gun RF-phases, as a function of the booster RF-phase. Bunch charge : 100 pC ; RF-gun peak accelerating field : 80 MV/m ; Booster peak accelerating field : 40 MV/m ; Current injected in the B3 solenoid at the RF-gun exit : 177 A.*

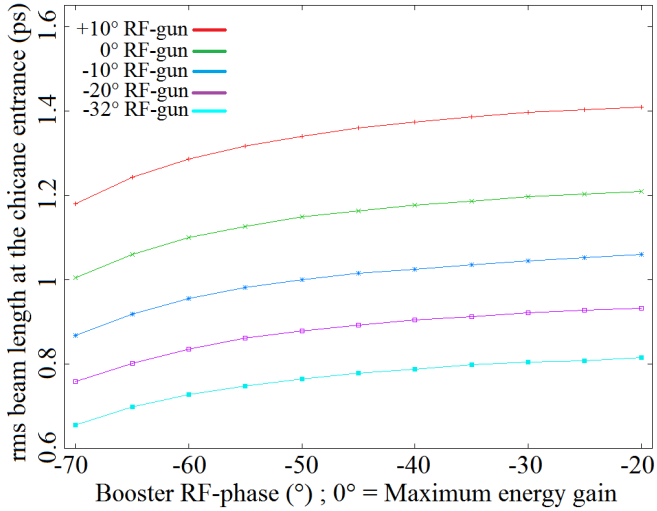

FIGURE *3.37 – rms bunch length at the chicane entrance, for several Gun RF-phases, as a function of the booster RF-phase. Bunch charge : 100 pC ; RF-gun peak accelerating field : 80 MV/m ; Booster peak accelerating field : 40 MV/m ; Current injected in the B3 solenoid at the RF-gun exit : 177 A.*

It is clearly visible in Fig. 3.36 that the goal of a 100 fs final rms bunch length cannot be achieved in all the configurations of gun and booster RF-phases. Indeed, one can see that when the gun and/or booster RF-phases are not sufficiently negative with respect to the ones maximizing the energy gain, the minimal achievable value of σ_t remains above 100 fs. This is due to the fact that the bunch time/energy correlation, induced by the accelerating electric fields of the RF-gun and of the booster section, is not sufficiently pronounced to reach the 100 fs rms, even in the configuration of the magnetic chicane allowing a maximal compression. This is accentuated by the fact that the rms bunch length at the chicane entrance increases with the booster RF-phase (see Fig. 3.37). One can also see that the threshold of booster RF-phase below which the 100 fs rms can be achieved moves towards 0° when the gun RF-phase decreases. In fact, it is about −35° for a gun RF-phase of +10° and about −20° for a gun RF-phase of −20°. This is due to the fact that the rms bunch length at the chicane entrance decreases with the Gun RF-phase (see Fig. 3.37).

3.2.2.3 Evolution of the final bunch rms transverse emittance

I then study the variation of the bunch rms horizontal transverse emittance ϵ_x during the compression process in the magnetic chicane, for several RF-phases of the RF-gun, as a function of the RF-phase of the booster section (see Fig. 3.38). Indeed, the dispersive direction is the horizontal one in the dipole magnets constituting the chicane. Therefore, the horizontal bunch rms transverse emittance is the one which can be affected during the bunch magnetic compression.

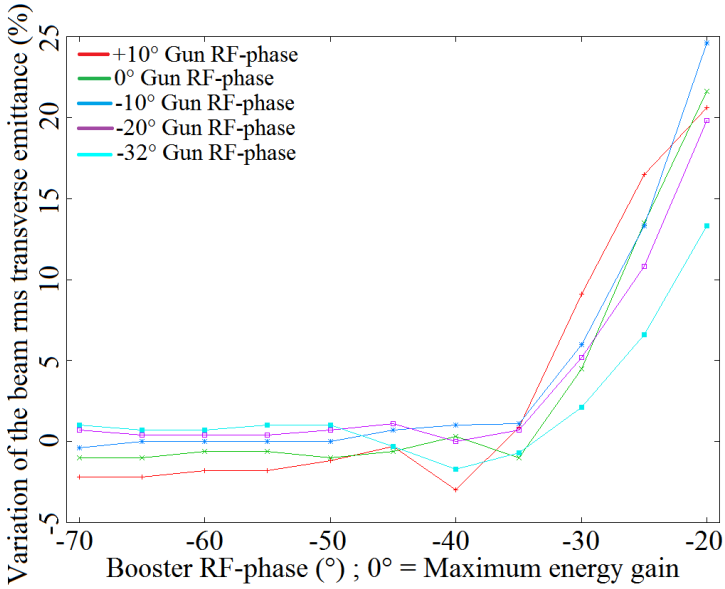

FIGURE *3.38 – Variation of the horizontal bunch rms transverse emittance during the magnetic compression, for several Gun RF-phases, as a function of the booster RF-phase. Bunch charge : 100 pC ; RF-gun peak accelerating field : 80 MV/m ; Booster peak accelerating field : 40 MV/m ; Current injected in the B3 solenoid at the RF-gun exit : 177 A.*

Fig. 3.38 shows that the behavior of the variation of ϵ_x with the booster RF-phase, during the magnetic compression process, is the same for all the Gun RF-phases tested in my study. Namely, ϵ_x shows an increase during the magnetic compression process for booster RF-phases above $-35°$. This increase can be significant, since it can be up to 25% for a booster RF-phase of $-20°$ and a Gun RF-phase of $-10°$. For the "low" booster RF-phases, below $-35°$, ϵ_x is nearly not affected by the magnetic compression process.

The reason of the increase of ϵ_x at "high" booster RF-phases is the emission of synchrotron radiation (coherent and incoherent) by the bunch during the compression process, and also the interaction of the bunch with this radiation. This is called the self-forces and it is taken into account in the CSRtrack code. Fig. 3.39 demonstrates this assertion by comparing ϵ_x at the entrance of the magnetic chicane and at its exit, with and without taking into account the self-forces. It is visible that ϵ_x remains the same at the chicane entrance and exit when the self-forces are not taken into account. On the opposite, ϵ_x is affected when they are taken into account. It is also visible that the effect of the self-forces increases when the booster RF-phase increases. This is due to two facts. First of all, it is due to the increase of the bunch mean kinetic energy E_c (see Fig. 3.35 (a)). In fact, the emitted power of synchrotron radiation in the chicane scales like E_c^4 [108] leading to a strong increase in the self-forces when E_c increases. The second reason is that the bunch time/energy correlation becomes less important, as it is visible in Fig. 3.35 (b) where the booster induced energy spread decreases. As a result the strength of the magnetic field required to perform the bunch compression increases, implying a decrease of the curvature radius ρ of the bunch trajectory in the magnets of the chicane. Since the emitted power of synchrotron radiation scales like ρ^{-2} [108], this also leads to an increase in synchrotron radiation emission and in the self-forces. At "low" booster RF-phases, below $-35°$, the self-forces effect becomes minor and ϵ_x is nearly not affected by the magnetic compression process. This is enhanced by the fact that the bunch is initially shorter at the chicane entrance for "low" booster RF-phases, thus requiring a smaller magnetic strength to compress it down to 100 fs rms which results in a decrease in synchrotron radiation and in self-forces.

Fig. 3.40 shows the final bunch rms transverse emittance, as a function of the booster RF-phase, for the Gun RF-phase of $-20°$. It shows well that only the horizontal bunch rms transverse emittance is degraded during the magnetic compression process. It also shows that the value achievable for the bunch rms transverse emittance is around 2.7 π.mm.mrad both in the horizontal and in the vertical transverse phase-space, which corresponds to the value at the entrance of the magnetic chicane as shown in Fig. 3.38. It is noteworthy that I use a 3D Gaussian laser pulse to generate the bunch in the RF-gun. The final bunch rms transverse emittance can of course be improved by using a different laser shape, 3D ellipsoid for example, as it has been shown in Sec. 3.1.3.

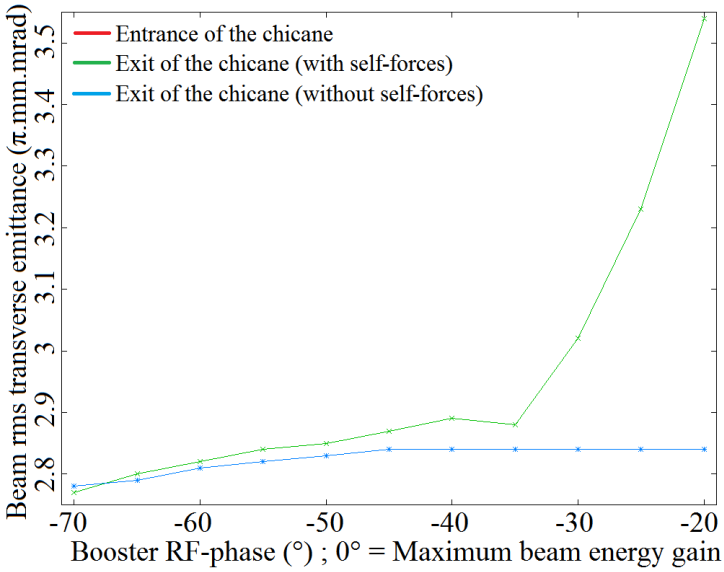

FIGURE *3.39 – Horizontal bunch rms transverse emittance as a function of the booster RF-phase. Bunch charge : 100 pC ; RF-gun peak accelerating field : 80 MV/m ; Gun RF-phase : −10° ; Booster peak accelerating field : 40 MV/m ; Current injected in the B3 solenoid at the RF-gun exit : 177 A. The red and blue curves are superimposed.*

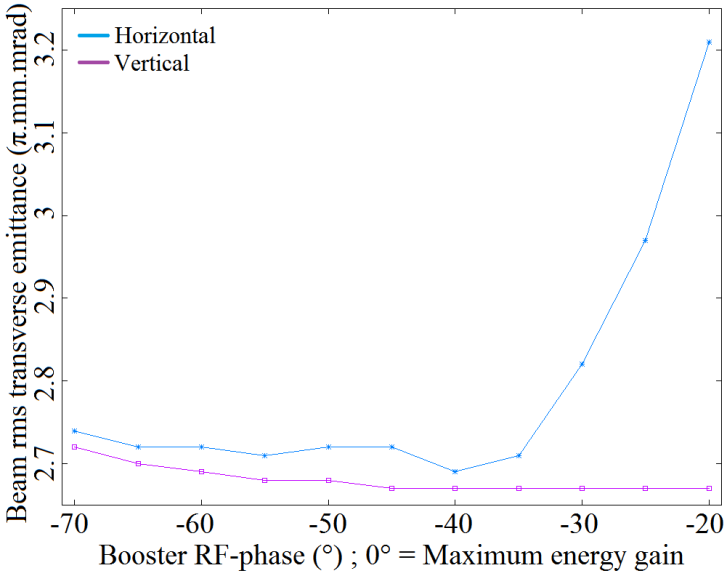

FIGURE *3.40 – Final bunch rms transverse emittance as a function of the booster RF-phase. Bunch charge : 100 pC ; RF-gun peak accelerating field : 80 MV/m ; Gun RF-phase : −20° ; Booster peak accelerating field : 40 MV/m ; Current injected in the B3 solenoid at the RF-gun exit : 177 A.*

3.2.2.4 Evolution of the bunch time profile and longitudinal phase-space

Another important aspect to study is the evolution of the bunch time profile and longitudinal phase-space during the magnetic compression process. Fig. 3.43 shows the evolution of the bunch time profile and of the bunch longitudinal phase-space, as a function of the booster RF-phase, for the Gun RF-phase of $-20°$.

It is clearly visible in Fig. 3.43 that the bunch longitudinal phase-space acquires a characteristic "S-shape" during the magnetic compression process, whatever the booster RF-phase. This is due to the fact that the bunch longitudinal phase-space has non linearities at the entrance of the magnetic chicane. These non-linearities come from several effects. In my study, they are first and mainly due to the space-charge forces effects between the photocathode and the chicane entrance. They can also come from the RF accelerating fields in the RF-gun and in the booster, which induce a curvature (called RF-curvature) on the bunch longitudinal phase-space. Finally the beam-loading phenomenon can also generate non-linearities in the bunch longitudinal phase-space, but it is negligible in my study. The non-linearities are clearly visible at the two edges of the bunch longitudinal phase-space shown in Fig. 3.41. They are amplified during the magnetic compression process, by the non-linearities generated by the chicane itself, to finally give the "S-shape" observed in Fig. 3.43 after compression.

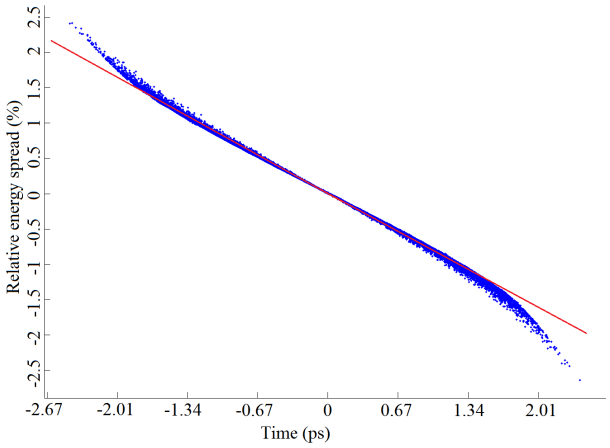

FIGURE *3.41 – Bunch longitudinal phase-space at the magnetic chicane entrance (the red line represents the linear one). Bunch charge : 100 pC ; RF-gun peak accelerating field : 80 MV/m ; Gun RF-phase : $-20°$; Booster peak accelerating field : 40 MV/m ; Booster RF-phase : $-35°$; Current injected in the B3 solenoid at the RF-gun exit : 177 A.*

Fig. 3.42 demonstrates this assertion by showing the bunch longitudinal phase-space after magnetic compression when the bunch longitudinal phase-space is perfectly linear at the chicane entrance. This perfectly linear bunch longitudinal phase-space has been created via Matlab and has replaced the real one in the CSRtrack input file. One can see by comparing this longitudinal phase-space with the one in Fig. 3.43, for the booster RF-phase of $-35°$, that the "S-shape" has vanished.

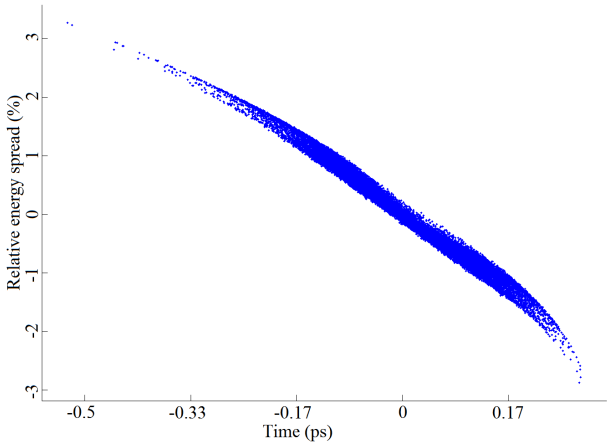

FIGURE *3.42 – Bunch longitudinal phase-space at the magnetic chicane exit, with a perfectly linear one at the entrance. Bunch charge : 100 pC ; RF-gun peak accelerating field : 80 MV/m ; Gun RF-phase : −20° ; Booster peak accelerating field : 40 MV/m ; Booster RF-phase : −35° ; Current injected in the B3 solenoid at the RF-gun exit : 177 A.*

It is also visible in Fig. 3.43 that the shape of the bunch time profile evolves with the booster RF-phase. Indeed, the bunch time profile remains quite symmetric for booster RF-phases higher than −35°, it is even rather uniform between −25° and −35° which is strange because it was Gaussian at the chicane entrance. For booster RF-phases lower than −35° the bunch time profile starts to distort itself with the appearance of a spike of current, which becomes more and more important when the booster RF-phase decreases.

Taking into account the considerations on the bunch mean energy, on the achievement of the final rms bunch length, on the conservation of the bunch rms transverse emittance and on the bunch time profile, the best configuration to perform a magnetic compression down to 100 fs rms on the considered setup is for a Gun RF-phase around −20° and a booster RF-phase around −35°. In this case, the bunch mean energy is 17.9 MeV (see Fig. 3.35 (a)), the 100 fs rms bunch length is easily achieved (see Fig. 3.36), the bunch rms transverse emittance is around 2.7 π.mm.mrad (see Fig. 3.40) and almost not affected by the compression in the chicane (see Fig. 3.38) and the bunch time profile remains symmetric (see Fig. 3.43).

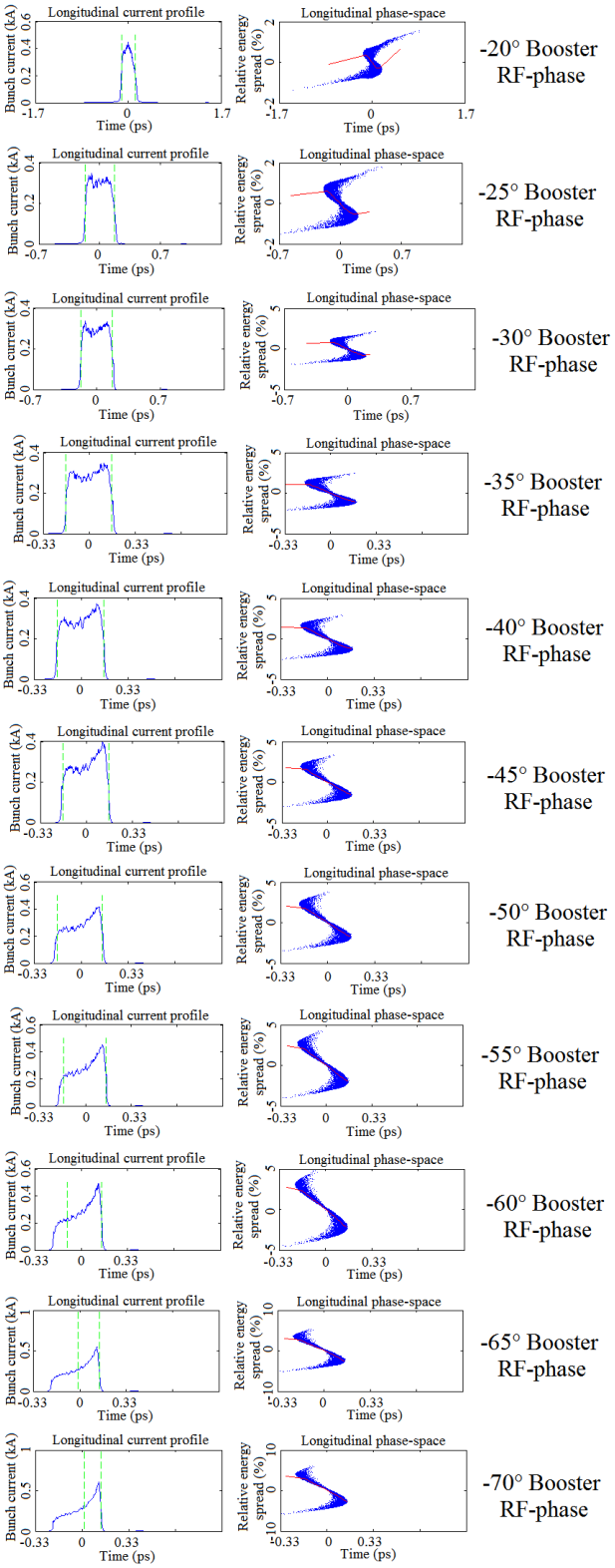

FIGURE *3.43 – Evolution of the bunch time profile and longitudinal phase-space as a function of the Booster RF-phase. Bunch charge : 100 pC ; RF-gun peak accelerating field : 80 MV/m ; Gun RF-phase : −20° ; Booster peak accelerating field : 40 MV/m ; Current injected in the B3 solenoid at the RF-gun exit : 177 A.*

3.2.2.5 Design of the magnetic chicane

The last step of the study is to determine what is the design of the magnetic D-shape chicane (see Fig. 3.34) for the case with a Gun RF-phase of $-20°$ and a booster RF-phase of $-35°$. The mechanical length of the four dipole magnets is already fixed at 25 cm. The projected distance between the dipole magnets is also fixed. It is 50 cm between the first and second dipole magnets and also between the third and fourth dipole magnets, while it is 75 cm between the second and third dipole magnets.

In practice, the curvature radius ρ of the bunch trajectory is fixed by the wanted final rms length of 100 fs for the bunch. It cannot be practically determined through the R_{56} parameter of the dipole magnet transfer matrix, because of the space charge forces. It has therefore been determined by trying different values of ρ in the CSRtrack code and choosing the one allowing a final rms bunch length of 100 fs. For the case with a Gun RF-phase of $-20°$ and a booster RF-phase of $-35°$, a curvature radius $\rho = 1.6944$ m and a deviation angle of $\theta = 8.5°$ in each dipole magnet have been found.

This value of ρ can then be used in combination with the bunch mean kinetic energy T to determine the strength B of the magnetic field which has to be generated by the dipole magnets :

$$B = \frac{\sqrt{T(T + 2m_e c^2)}}{q\rho c}$$

For the studied case, $T = 17.9$ MeV which implies $B = 0.0362$ T $= 362$ G.

The bunch deviation angle of $\theta = 8.5°$ in each dipole magnet allows computing that the shift between the center of the first and second dipole magnet and between the third and fourth dipole magnet is $75 * \tan(\theta) = 11.2$ cm. Fig. 3.44 shows a simplified layout of the magnetic chicane design.

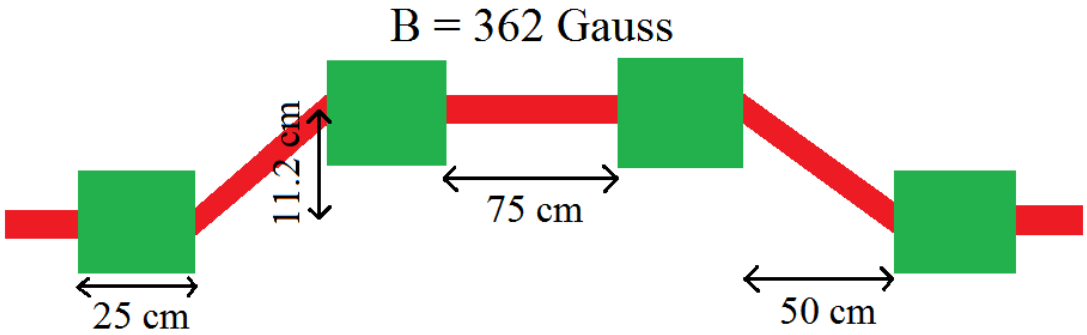

FIGURE *3.44 – Simplified design of the magnetic chicane.*

3.2.3 Compression of a longitudinally modulated electron beam

In addition to the single-bunch beam, I also simulate the propagation and the magnetic compression of a longitudinally modulated electron beam. In this part I will mainly be

interested in the conservation of the beam modulation all along its propagation and after its magnetic compression, since the properties of a single bunch have already been widely studied in the previous parts of Sec. 3.2.2. Fig. 3.45 shows the modulated time profile of the laser pulse used in this section to generate the longitudinally modulated electron beam in an RF-gun. It is composed of five bunches, spaced from each other by 6 ps and having each an rms length σ_t of 1 ps. The first four bunches present a linear increase in current, and the last one has a charge equal to the one of the first one. Such a time profile will be used at the PITZ facility (see Sec. 1.4.2) to perform a plasma acceleration experiment [109]. The intended charge repartition between the bunches is 10 pC-30 pC-50 pC-70 pC-10 pC. The first four bunches will be used to excite a plasma contained in a plasma cell, thus creating an electromagnetic wave in the plasma cell. This is called the high-transformer ratio process [110, 111, 112]. The last bunch will then be used as a probe and accelerated by this wave.

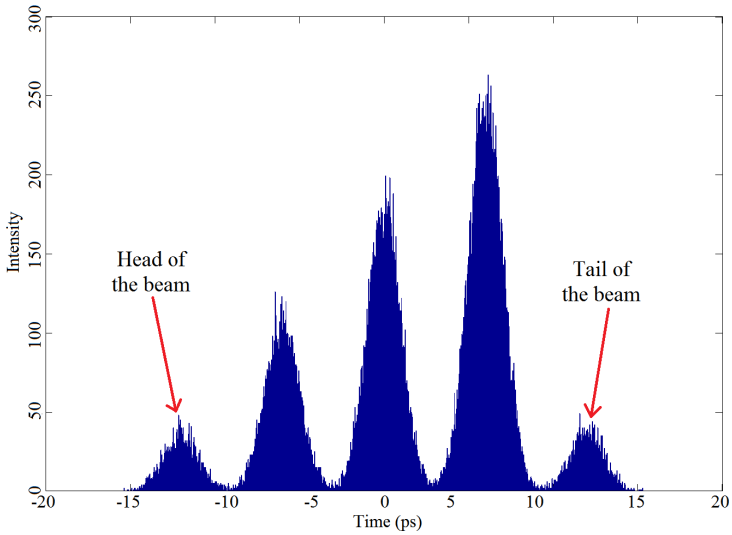

FIGURE *3.45 – Time profile of the laser pulse used to generate the electron beam in an RF-gun in Sec. 3.2.3*

The previously mentioned modulated time profile of the electron beam has to be uniformly compressed by a factor of four before interacting with the plasma cell. It means that after the compression, the spacing between the bunches has to be of 1.5 ps and the rms length of the bunches has to be of 250 fs. The linear increase in current within the first four bunches has also to be preserved after the compression. This compression is intended, at the PITZ facility (see Fig. 1.25), by using a D-shape magnetic chicane. This type of magnetic compressor is constituted of four dipole magnets arranged as shown in Fig. 3.34 of Sec. 3.2.2. The entrance of the chicane will be located 5.84 m after the photocathode, just after the first EMSY station (see Fig. 1.25), and its exit will be located 2.75 m away, just after the 180° dipole magnet of the HEDA1 station (see Fig. 1.25).

I choose to simulate the compression of the beam in this magnetic chicane with the CSRtrack code [113], for the same reasons as for the compression of a single bunch beam (see Sec. 3.2.2).

3.2.3.1 Compression of a "perfect" modulated electron beam

To test if the magnetic compression of such a modulated electron beam is feasible and so find what the better conditions to perform it are, I choose in a first time to neglect the propagation of the electron beam between the photocathode and the entrance of the magnetic compressor. Namely, I consider a beam with the exact longitudinal profile of the laser pulse (see Fig. 3.45) and with a perfectly linear correlation (also called chirp) in the time/energy phase space. The main interest of this study is to investigate what the possible beam performances are after compression, both in terms of spacing between the bunches, of length of the bunches and of conservation of the linear increase in current between the first four bunches.

The method I use to create this perfectly linear correlation is to simply rotate each electron position in the time/energy phase space by the same angle with respect to the beam center. I choose to apply this rotation on a monokinetic distribution of electrons with 16 MeV energy. Fig. 3.46 shows the beam mean energy and rms energy spread as a function of the angle of rotation [25]. This value of 16 MeV is dictated by the capacities of the PITZ accelerator. In fact, the maximum energy at the exit of the CDS booster cavity (see Fig. 1.25) is around 22 MeV. However, to induce the required correlation in the time/energy phase space, the RF-phase of the CDS booster has to be set at a value different from the one maximizing the beam energy. The value of 16 MeV allows taking some margin and therefore testing several initial conditions for the beam compression.

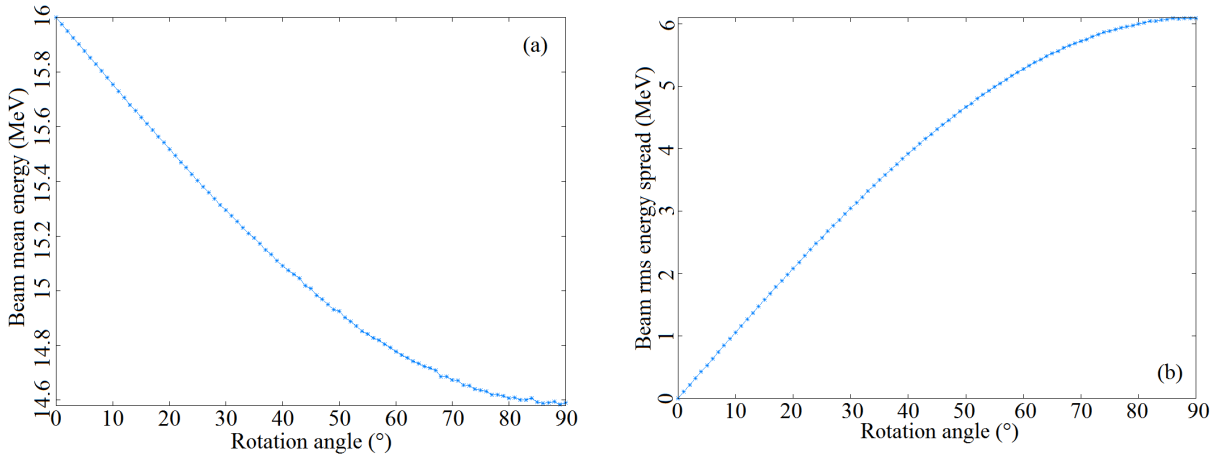

FIGURE *3.46 – Electron beam mean energy (a) and rms energy spread (b), as a function of the angle of rotation in the time/energy phase space, for an initial monokinetic 16 MeV energy distribution with the time profile shown in Fig. 3.45*

I then perform the magnetic compression of these "perfect" electron beams with the CSRTrack code. The results show to be very dependent on the rotation angle I give to the beam in the time/energy phase space, namely to its relative energy spread, which was expected. Fig. 3.47, Fig. 3.48 and Fig. 3.49 show respectively the longitudinal beam

25. The beam mean energy varies as a function of the rotation angle because the charge distribution is asymmetric with respect to the beam center.

properties after magnetic compression for rotation angles of 9°, 5° and 1.5° corresponding to energies of 15.78 MeV, 15.88 MeV and 15.96 MeV and to rms relative energy spreads of 6.02%, 3.33% and 1.00%.

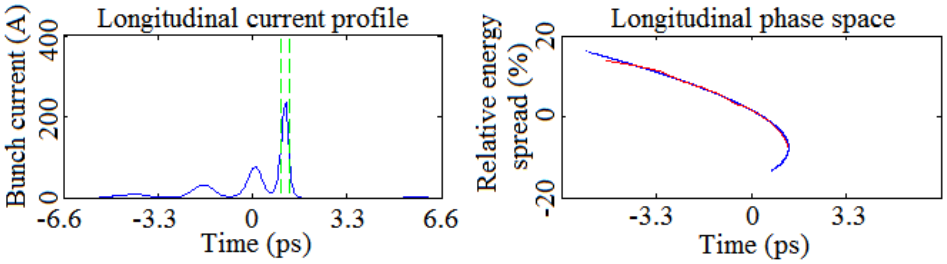

FIGURE *3.47 – Beam longitudinal properties after compression for an rms relative energy spread of 6.02% (15.78 MeV)*

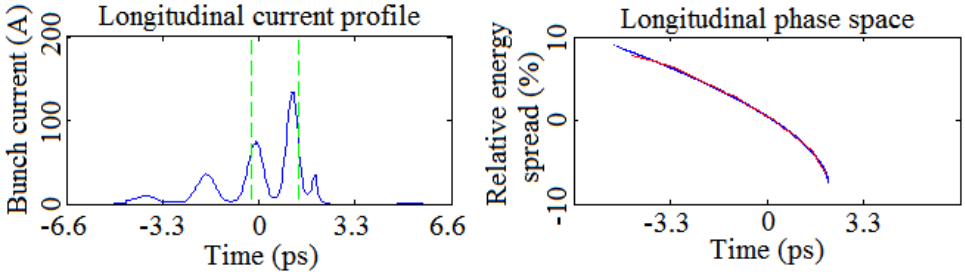

FIGURE *3.48 – Beam longitudinal properties after compression for an rms relative energy spread of 3.33% (15.88 MeV)*

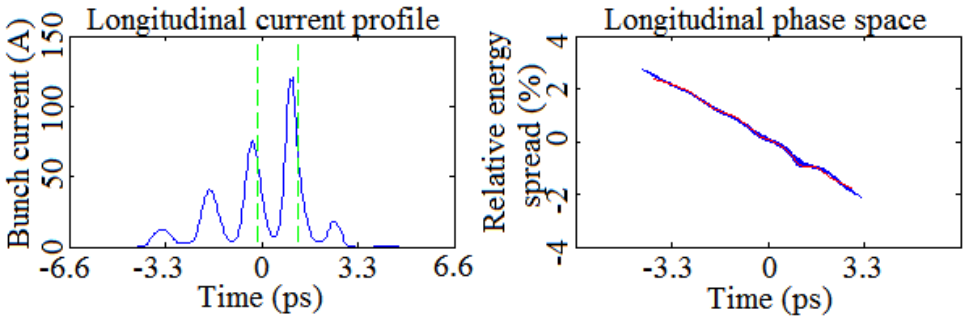

FIGURE *3.49 – Beam longitudinal properties after compression for an rms relative energy spread of 1.00% (15.96 MeV)*

Fig. 3.47, Fig. 3.48 and Fig. 3.49 show that the conservation of the longitudinal modulation during the compression is better when the relative beam energy spread decreases. In other words, the spacing between the bunches and the compression factor of each bunch are more uniform. Besides, the linear increase in current between the first four bunches is also better preserved, although it is still not perfect for an rms relative energy spread of 1.00% (see Fig. 3.49).

I measure in Fig. 3.49 the bunches longitudinal parameters, namely the spacing between the bunches and their respective rms length. These are approximate values, especially for the rms length measurement, since the beam current does not fall down to zero between the bunches. The results are shown in Tab. 3.4.

bunch	charge	spacing with previous bunch	gap with the requirement (1,5ps)	rms length	gap with the requirement (250fs)
1	10pC	X	X	335fs	34%
2	30pC	1,69ps	12,67%	287fs	14,80%
3	50pC	1,46ps	2,67%	255fs	2%
4	70pC	1,39ps	7,33%	207fs	17,20%
5 (probe)	10pC	1,46ps	2,67%	239fs	4,40%

TABLE *3.4 – Bunches longitudinal parameters after compression for an rms energy spread of 1.00% (15.96 MeV)*

Finally, this study with "perfect" electron beams has shown that the uniform compression by a factor of four of the longitudinally modulated electron beam shown in Fig. 3.45 is theoretically possible, within the limits exposed in Tab. 3.4, with a fine-tuning of the beam relative energy spread. Concerning the spacing between the bunches, the values remain quite close to the requirement since the difference is only 12.7% at maximum. It seems rather more difficult to reach the requirements for the rms lengths of the bunches, since the variation increases up to 34% for the first bunch. A solution to better preserve the linear increase in current between the first four bunches also has to be investigated thereafter.

3.2.3.2 Compression of a longitudinally modulated electron beam coming from ASTRA simulations

I try first to perform the magnetic compression of a longitudinally modulated beam coming from ASTRA simulations with an rms relative energy spread of 3% (beam mean energy of 15.82 MeV). Fig. 3.50 shows the beam longitudinal properties at the entrance of the magnetic compressor. The contrast of the successive bunches is also shown next to the longitudinal current profile. The contrast C_o of one bunch is defined as :

$$C_o = 100 * \frac{I_{max} - I_{min}}{I_{max}}$$

where I_{max} is the peak current of the bunch and I_{min} is the maximum of the two minima of current found on both sides of the peak current. Fig. 3.51 shows the beam longitudinal properties after magnetic compression for the initial conditions of Fig. 3.50.

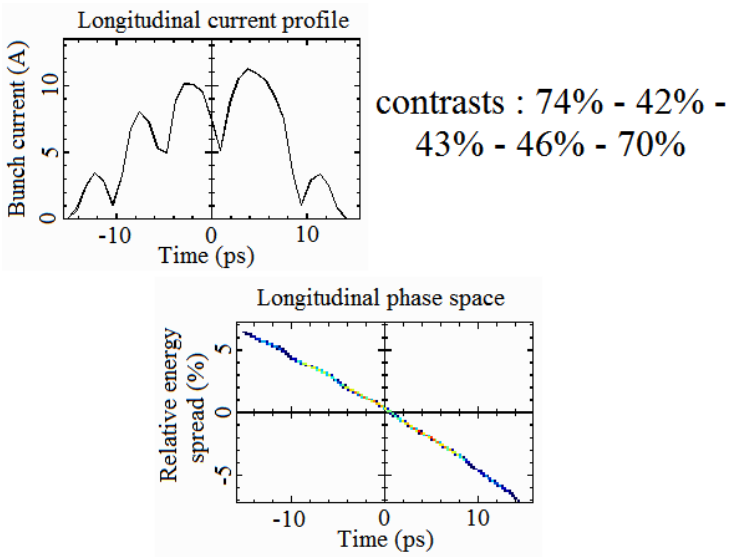

FIGURE *3.50 – Beam longitudinal properties at the compressor entrance. ASTRA conditions : 60.5 MV/m RF-gun peak accelerating field ; +10° Gun RF-phase (0° = maximal energy) ; 0.2 T peak field of the Gun solenoid magnet ; 16 MV/m CDS booster peak accelerating field ; −47° CDS booster RF-phase (0° = maximal energy) ; 3% rms relative energy spread (15.82 MeV beam mean energy).*

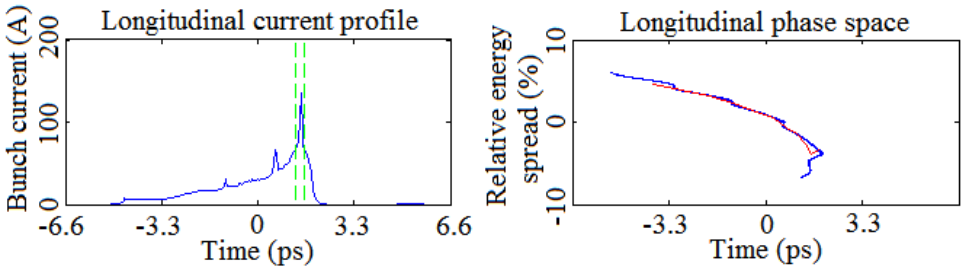

FIGURE *3.51 – Beam longitudinal properties after magnetic compression. ASTRA conditions : 60.5 MV/m RF-gun peak accelerating field ; +10° Gun RF-phase (0° = maximal energy) ; 0.2 T peak field of the Gun solenoid magnet ; 16 MV/m CDS booster peak accelerating field ; −47° CDS booster RF-phase (0° = maximal energy) ; 3% rms relative energy spread (15.82 MeV beam mean energy).*

One can see in Fig. 3.51 that the magnetic compression has completely destroyed the longitudinal modulation of the electron beam. To determine the reasons of this destruction, it is interesting to compare Fig. 3.51 with the beam properties obtained after magnetic compression for a ”perfect” modulated beam in similar conditions of energy and energy spread (see Fig. 3.48).

The comparison of Fig. 3.51 and Fig. 3.48 shows that the beam longitudinal modulation is far better preserved for the ”perfect” beam than for the beam coming from ASTRA simulations. This ascertainment allows us asserting that the destruction of the

beam longitudinal modulation during its magnetic compression comes from two main facts.

Firstly, it is clearly visible in Fig. 3.50 that the beam longitudinal modulation is already destroyed at the entrance of the chicane, because of the long transport from the photocathode (5.84 m). Indeed, in addition to the overlap of the bunches, the increase in current between the first four bunches is clearly no more linear. This is both due to the effect of space-charge forces during the beam transport up to the chicane entrance. It is possible to overcome it both by increasing the spacing between the bunches, to reduce the inter-bunches forces, and by decreasing the charges of the bunches, to reduce the intra-bunches forces too. Remarking that the beam current is shifting towards the beam tail during the transport up to the chicane entrance, it will also be interesting to start with a non linear increase in current between the first four bunches, in order that it becomes linear at the chicane entrance.

Secondly, the correlation in the time/energy phase space, mainly induced by the CDS booster, is not appropriate to perform a uniform compression of the beam. In fact the beam is shrunk towards its tail at the end of the compression, with a bump always pointing towards the positive values of energy and time differences in the beam time/energy phase-space, implying a big spike. I will call that "positive curvature" of the time/energy phase-space thereafter. This is true with the perfectly linear correlation of the time/energy phase space, at the chicane entrance, studied in Sec. 3.2.3.1 (see Fig. 3.48) and with the correlation coming from ASTRA simulations (see Fig. 3.51), which shows a slightly positive curvature at the chicane entrance. This is due to the non-linearities, induced by the chicane during the compression process, which create or amplify the positive curvature of the time/energy phase-space. A simple idea, at least in principle, to preserve the modulated longitudinal profile during the compression is therefore to start the compression with a "negative curvature" of the correlation in the time/energy phase space, namely with a bump pointing towards the negative values of energy and time differences. The goal is to compensate the non-linearities induced by the chicane, and to therefore exit the chicane with the most linear beam time/energy phase-space possible. This kind of curvature can practically be generated with a third order harmonic cavity [114, 115].

3.2.3.3 Use of a negative curvature for the correlation in the time/energy phase space

I start first to perform simulation with a "perfect" modulated electron beam at the entrance of the magnetic chicane (see Fig. 3.45). To create a negative curvature of the correlation in the time/energy phase space, I use a distribution of monokinetic electrons and then apply the following transformation to obtain the energy E of each electron :

$$E = E_0 + C * |t|^2$$

where E_0 is the initial energy of the electrons (16 MeV in my case), t is the time of the electron and C is a parameter I will call curvature which has to be positive to induce a negative curvature (and negative to induce a positive curvature). This transformation

corresponds to a simple parabolic curvature of the correlation in the time/energy phase-space. One can remark that C has the dimension of an energy divided by time square, in my case MeV/ps^2. Finally, I give a uniform rotation to this distribution in the longitudinal phase-space to create the time/energy correlation.

I take the same simulation conditions as the one used to obtain Fig. 3.48 and vary the value of C. The results are shown in Fig. 3.52. The relative fluctuations ΔS in the spacing between the successive bunches are also reported in Fig. 3.52 for each value of C. ΔS is defined as :

$$\Delta S = 100 * \frac{S_{max} - S_{min}}{S_{min}}$$

where S_{max} and S_{min} are respectively the largest and smallest spacings between two successive bunches. This calculation has been done by computing the mean center of each bunch. The gaps between these centers are then defined as the spacings between the bunches.

One can see clearly in Fig. 3.52 that if C is too low, namely here $C < 0.0006$, the beam modulation is shrinking towards its tail resulting in high relative fluctuations in the spacing between the bunches. This is due to the fact that the longitudinal phase-space acquires a positive curvature at the end of the magnetic compression. Conversely if C is too high, namely here $C > 0.0006$, the beam modulation is shrinking towards its head resulting once again in high relative fluctuations in the spacing between the bunches. This is due to the fact that the longitudinal phase-space keeps a negative curvature at the end of the magnetic compression. In the region of C values around 0.0006 the beam longitudinal modulation is preserved, resulting in relative fluctuations in the spacing between the bunches close to zero and in a conservation of the linear increase in current between the first four bunches. This is due to the fact that the longitudinal phase-space becomes almost linear, namely with zero curvature, at the end of the magnetic compression.

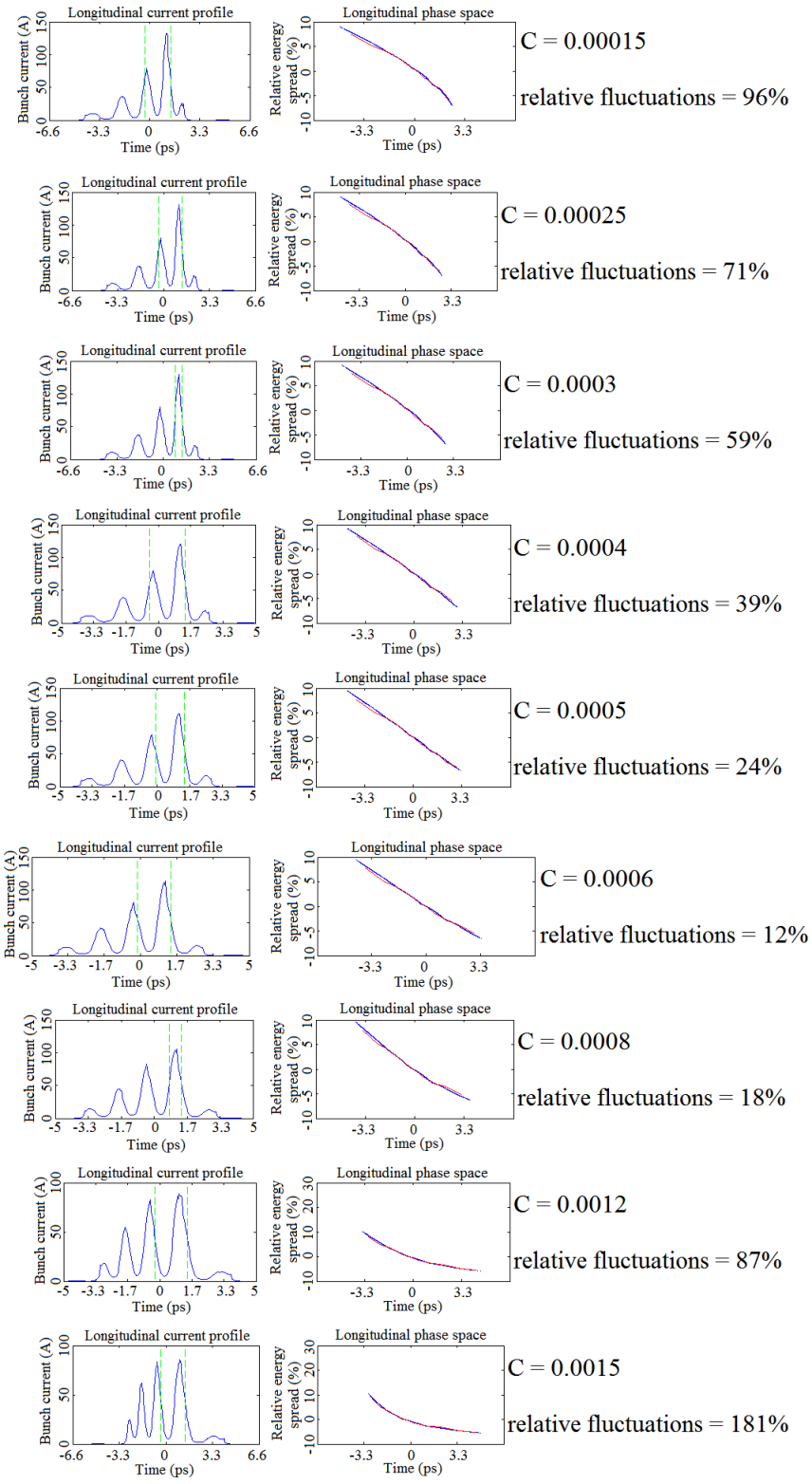

FIGURE *3.52 – Beam longitudinal properties after magnetic compression as a function of C. Initial time profile given by Fig. 3.45 and rms relative energy spread of 3.33% (15.88 MeV).*

One interesting feature to observe in Fig. 3.52 is that, for the optimal value of $C = 0.0006$, the two most charged bunches have clearly lost their Gaussian shape and acquired a marked asymmetrical "triangle" shape at the end of the magnetic compression. The next step is therefore to study the evolution of the beam time profile after compression, for the appropriate value of the curvature C, as a function of the beam energy spread to see if the Gaussian shape of the bunches can be better preserved for certain values of the energy spread. Two particularly suitable parameters for this study are the skewness α_3 and the kurtosis α_4, which respectively characterize the symmetry and the flattening of the electron distribution in the bunches. They are respectively defined by :

$$\alpha_3 = \frac{n\sum_{i=0}^{n}(t_i - \bar{t})^3}{(n-1)(n-2)}\frac{1}{\sigma_t^3}$$

$$\alpha_4 = \frac{n(n+1)\sum_{i=0}^{n}(t_i - \bar{t})^4 - 3(n-1)\sum_{i=0}^{n}(t_i - \bar{t})^4}{(n-1)(n-2)(n-3)}\frac{1}{\sigma_t^4}$$

where n is the number of electrons in the bunch, $\bar{t}$ is the time center of the bunch and σ_t is the standard deviation of the time distribution of the bunch (namely the rms bunch length). $\alpha_3 = 0$ means a perfectly symmetric electron distribution, $\alpha_4 = 0$ means that the electron distribution has the same flattening as a Gaussian distribution and $\alpha_3 = \alpha_4 = 0$ defines a perfectly Gaussian electron distribution. Fig. 3.53 shows the results of this study as well as the values of α_3 and α_4 for the two most charged bunches of the beam.

We can see in Fig. 3.53 that for rms relative energy spread higher than 4.7% the symmetry of the two most charged bunches is preserved, at the end of the magnetic compression, since α_3 becomes close to zero. It corresponds also to the vanishing of the clearly visible local non-linearities of the longitudinal phase-space at lower energy spread. However, it is not the case for the flattening of the bunches. Indeed, in spite of the slight decrease in α_4 up to the rms relative energy spread of 4.7%, the values of α_4 remain largely higher than 0, meaning that the bunches are heavily sharper than a Gaussian distribution.

We can conclude that the use of an appropriate curvature C of the correlation in the time/energy phase-space at the entrance of the magnetic compressor allows performing a good compression of the "perfect" modulated electron beam for sufficiently high rms relative energy spread values ($\geq 4.7\%$). Concretely, it allows preserving the linear increase in current between the first four bunches (but this point has still to be improved), the uniform spacing between the bunches and the symmetry in the bunches distributions. The flattening of the bunches distributions is however not Gaussian anymore after magnetic compression.

One can remark that this need of high rms relative energy spread values runs counter to the assumption made in Sec. 3.2.3.1 with "perfect" beam, which was to minimize the beam energy spread. However, this assumption has been established with $C = 0$. But, it has been explained in Sec. 3.2.3.2 that the introduction of a negative curvature of the longitudinal phase-space ($C \neq 0$) is required to preserve the longitudinal modulation of a "real" beam coming from ASTRA simulations. These non zero values of C introduce the deformations of the bunches observed for the low beam energy spreads in Fig. 3.52, and

therefore the need of increasing the beam energy spread.

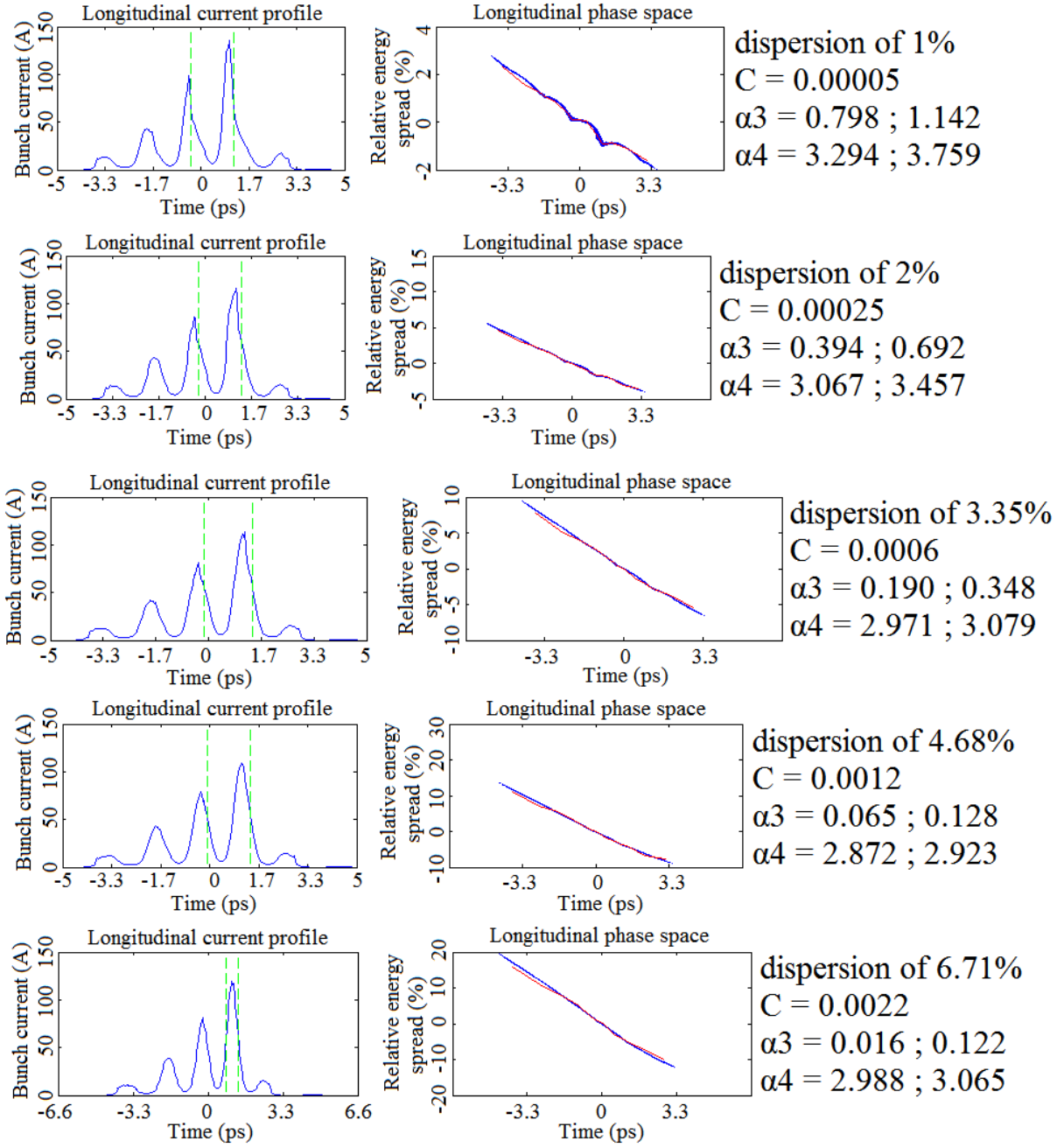

FIGURE *3.53 – Beam longitudinal properties after magnetic compression as a function of the beam rms relative energy spread. Initial time profile given by Fig. 3.45.*

To test the validity of the approach with negative curvature of the longitudinal phase-space, I then study the magnetic compression of a modulated beam coming from ASTRA simulations with artificially implemented negative curvature of the correlation in the time/energy phase-space. Fig. 3.54 and Fig. 3.55 show respectively the beam longitudinal properties at the entrance of the chicane and after compression, after fine-tuning

of the curvature C of the longitudinal phase-space at the chicane entrance. Fig. 3.56 shows the beam longitudinal properties after compression without applying any artificial curvature to the longitudinal phase-space ($C = 0$).

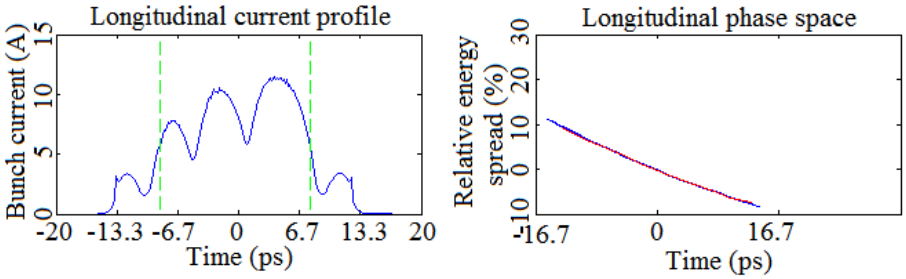

FIGURE *3.54 – Beam longitudinal properties at the compressor entrance. ASTRA conditions : 60.5 MV/m RF-gun peak accelerating field ; +10° Gun RF-phase (0° = maximal energy) ; 0.2 T peak field of the Gun solenoid magnet ; 20.8 MV/m CDS booster peak accelerating field ; −58° CDS booster RF-phase (0° = maximal energy) ; 4.7% rms relative energy spread (16.08 MeV beam mean energy).*

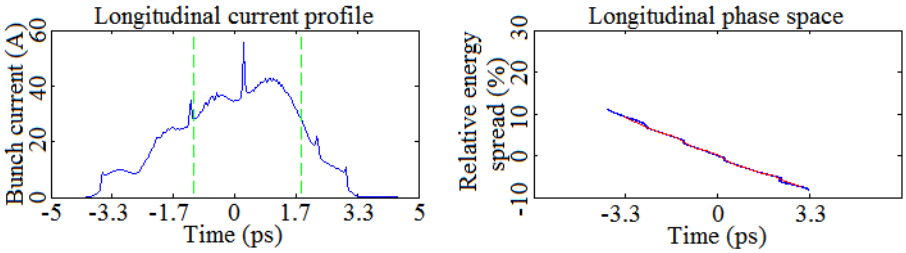

FIGURE *3.55 – Beam longitudinal properties after compression with fine-tuning of the value of C. ASTRA conditions : 60.5 MV/m RF-gun peak accelerating field ; +10° Gun RF-phase (0° = maximal energy) ; 0.2 T peak field of the Gun solenoid magnet ; 20.8 MV/m CDS booster peak accelerating field ; −58° CDS booster RF-phase (0° = maximal energy) ; 4.7% rms relative energy spread (16.08 MeV beam mean energy).*

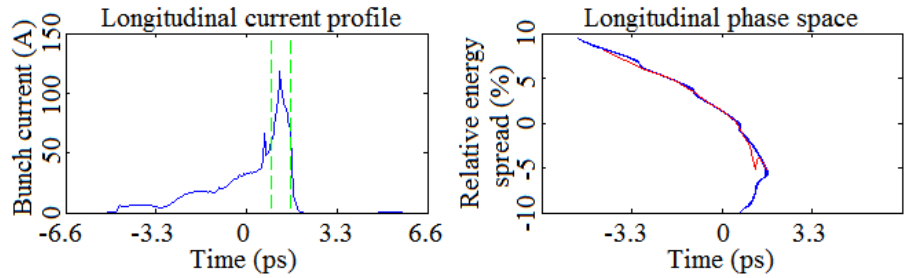

FIGURE *3.56 – Beam longitudinal properties after compression with C = 0. ASTRA conditions : 60.5 MV/m RF-gun peak accelerating field ; +10° Gun RF-phase (0° = maximal energy) ; 0.2 T peak field of the Gun solenoid magnet ; 20.8 MV/m CDS booster peak accelerating field ; −58° CDS booster RF-phase (0° = maximal energy) ; 4.7% rms relative energy spread (16.08 MeV beam mean energy).*

One can see by comparing Fig. 3.55 and Fig. 3.56, obtained in the same simulation conditions, that the use of a negative curvature of the longitudinal phase-space implies a visible improvement in the conservation of the beam time modulation during the compression. Indeed, there is no more a big current spike at the beam tail when appropriate negative curvature is applied. However, it is obvious that the longitudinal modulation is still not preserved during the compression. In fact the contrasts of the different bunches are respectively of 19%, 5%, 9%, 16% and 6% after compression (see Fig. 3.55), while they were of 81%, 43%, 43%, 45% and 80% at the chicane entrance (see Fig. 3.54). Moreover, the increase in current between the first four bunches is not linear at the end of the compression. The difficulty comes from the fact that the beam longitudinal modulation is already destroyed at the chicane entrance (see Fig. 3.54), due to the 5.84 m long transport. This also comes from the local (not global) non-linearities of the longitudinal phase-space. They amplify themselves during the compression, because of the non-linearities induced by the chicane itself, thus creating the "stairs-structure" observed in the longitudinal phase-space at the chicane exit (see Fig. 3.55).

To optimize the compression, it is therefore necessary to adjust the initial spacing between the bunches and their charges. This will allow reducing the space-charge forces and therefore to better preserve the beam longitudinal modulation during the transport up to the chicane entrance. It will also limit the appearance of local non-linearities in the longitudinal phase-space. By comparing Fig. 3.45 and Fig. 3.54, it is visible that the beam current is concentrating towards the beam tail during the transport up to the chicane entrance. It is therefore interesting to start with a non linear increase in current between the first four bunches, in order that it becomes linear at the chicane entrance.

3.2.3.4 Optimization of the compression of a modulated beam coming from ASTRA simulations

I choose to test two spacings between the bunches, namely 6 ps and 8 ps, for two configurations of beam charge, namely 10 pC-20 pC-30 pC-50 pC-10 pC and half-charge 5 pC-10 pC-15 pC-25 pC-5 pC. Fig. 3.57 shows the beam longitudinal properties at the chicane entrance for the 10 pC-20 pC-30 pC-50 pC-10 pC charge configuration and Fig. 3.58 the ones for the 5 pC-10 pC-15 pC-25 pC-5 pC charge configuration. In each case, the CDS booster peak accelerating field and RF-phase have been adjusted to enter in the chicane with an energy around 16 MeV and rms energy spread around 750 keV, namely an rms relative energy spread around 4.7% which has been shown to be optimal in Sec. 3.2.3.3. The contrast of each bunch is also indicated in Fig. 3.57 and Fig. 3.58.

One can see by comparing Fig. 3.54, Fig. 3.57 and Fig. 3.58 that the reduction of bunches charges and the increase in bunches spacing enables a better preservation of the beam longitudinal modulation during the transport from the photocathode up to the chicane entrance. Indeed the bunches are less overlapping each other, which is visible through the increase in bunches contrasts. It is explained by the reduction of the space charge forces effects. It is also visible, by comparing Fig. 3.54 and Fig. 3.57 or Fig. 3.58, that the increase in current between the first four bunches becomes far more linear. This fact is not only due to the space charge forces effects, but also to the fact that the initial

increase in current has intentionally been taken to be non linear for Fig. 3.57 and Fig. 3.58. As previously explained, it allows a linearization of the current profile during the transport of the beam from the photocathode up to the chicane entrance.

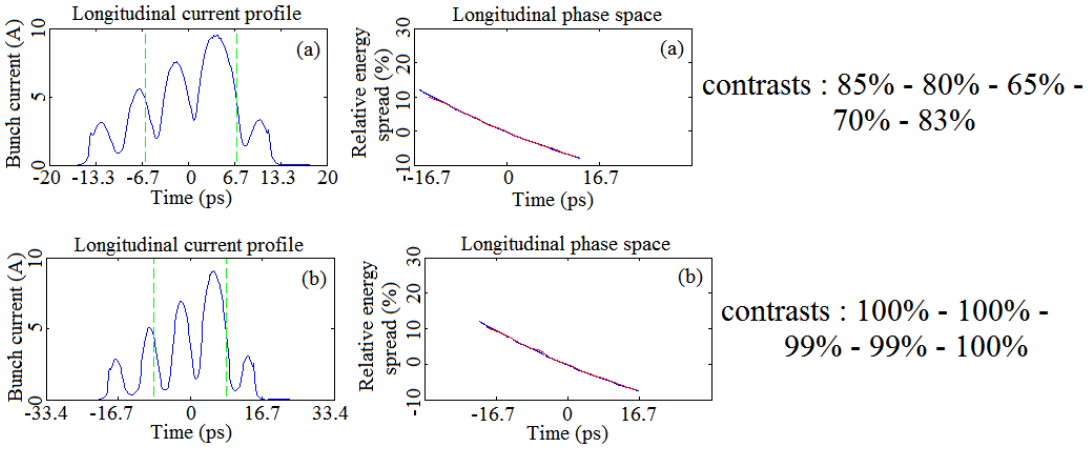

FIGURE *3.57 – Beam longitudinal properties at the compressor entrance for the 10 pC-20 pC-30 pC-50 pC-10 pC charge configuration and 6 ps (a) and 8 ps (b) initial spacings between the bunches. ASTRA conditions : 60.5 MV/m RF-gun peak accelerating field ; +10° Gun RF-phase (0° = maximal energy) ; 0.2 T peak field of the Gun solenoid magnet ; 20.8 MV/m (a) and 17.75 MV/m (b) CDS booster peak accelerating field ; −58° (a) and −51° (b) CDS booster RF-phase (0° = maximal energy) ; 4.8% (a) and 4.73% (b) rms relative energy spread (16.00 MeV (a) and 16.02 MeV (b) beam mean energy).*

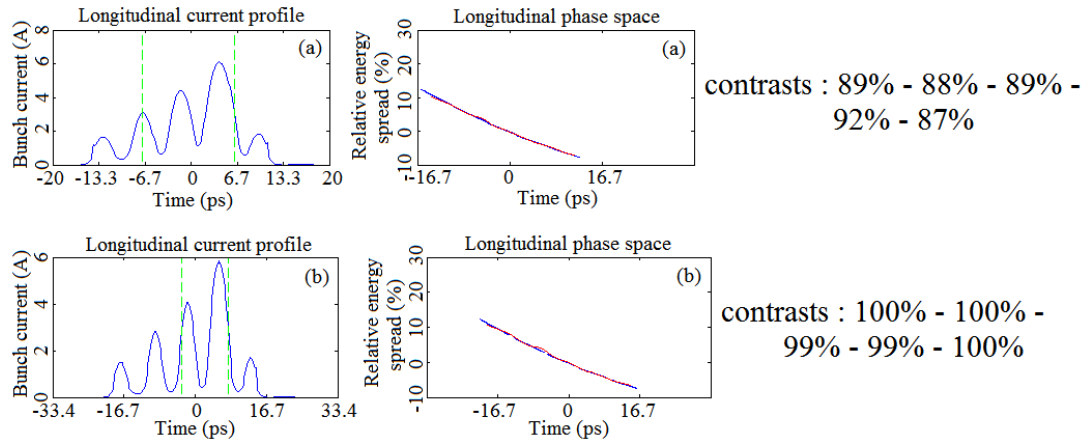

FIGURE *3.58 – Beam longitudinal properties at the compressor entrance for the 5 pC-10 pC-15 pC-25 pC-5 pC charge configuration and 6 ps (a) and 8 ps (b) initial spacings between the bunches. ASTRA conditions : 60.5 MV/m RF-gun peak accelerating field ; +10° Gun RF-phase (0° = maximal energy) ; 0.2 T peak field of the Gun solenoid magnet ; 20.8 MV/m (a) and 17.75 MV/m (b) CDS booster peak accelerating field ; −58° (a) and −51° (b) CDS booster RF-phase (0° = maximal energy) ; 4.73% (a) and 4.74% (b) rms relative energy spread (15.93 MeV (a) and 15.97 MeV (b) beam mean energy).*

Fig. 3.59 shows the beam longitudinal properties after magnetic compression for the 10 pC-20 pC-30 pC-50 pC-10 pC charge configuration and Fig. 3.60 the ones for the 5 pC-10 pC-15 pC-25 pC-5 pC charge configuration. The contrast of each bunch is also indicated in Fig. 3.59 and Fig. 3.60.

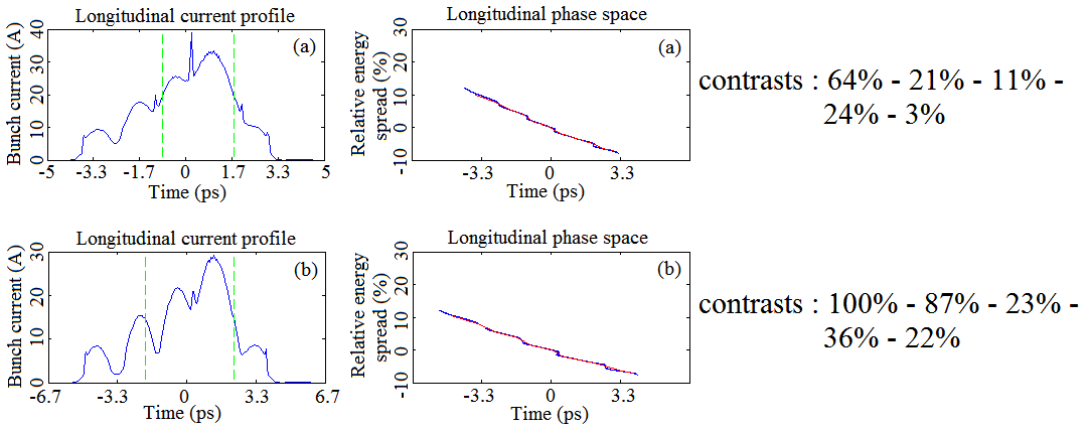

FIGURE *3.59 – Beam longitudinal properties after magnetic compression for the 10 pC-20 pC-30 pC-50 pC-10 pC charge configuration and 6 ps (a) and 8 ps (b) initial spacings between the bunches. ASTRA conditions : 60.5 MV/m RF-gun peak accelerating field ; +10° Gun RF-phase (0° = maximal energy) ; 0.2 T peak field of the Gun solenoid magnet ; 20.8 MV/m (a) and 17.75 MV/m (b) CDS booster peak accelerating field ; −58° (a) and −51° (b) CDS booster RF-phase (0° = maximal energy) ; 4.8% (a) and 4.73% (b) rms relative energy spread (16.00 MeV (a) and 16.02 MeV (b) beam mean energy).*

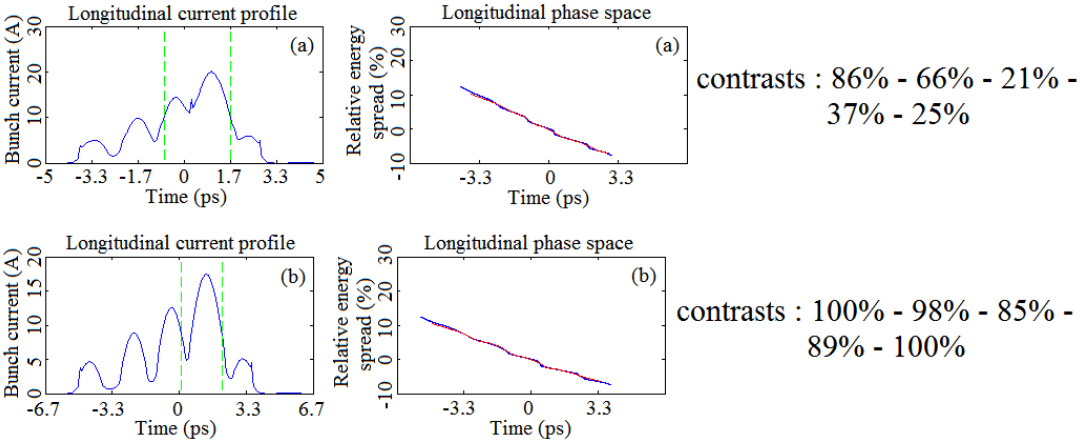

FIGURE *3.60 – Beam longitudinal properties after magnetic compression for the 5 pC-10 pC-15 pC-25 pC-5 pC charge configuration and 6 ps (a) and 8 ps (b) initial spacings between the bunches. ASTRA conditions : 60.5 MV/m RF-gun peak accelerating field ; +10° Gun RF-phase (0° = maximal energy) ; 0.2 T peak field of the Gun solenoid magnet ; 20.8 MV/m (a) and 17.75 MV/m (b) CDS booster peak accelerating field ; −58° (a) and −51° (b) CDS booster RF-phase (0° = maximal energy) ; 4.73% (a) and 4.74% (b) rms relative energy spread (15.93 MeV (a) and 15.97 MeV (b) beam mean energy).*

The 5 pC-10 pC-15 pC-25 pC-5 pC charge configuration is clearly better than the 10 pC-20 pC-30 pC-50 pC-10 pC charge configuration from the bunches contrasts point of view. This is directly due to the reduction of space charge forces. Tab. 3.5 shows, for the two aforementioned cases of the 5 pC-10 pC-15 pC-25 pC-5 pC charge configuration, the spacing between the bunches after compression, the rms length of each bunch after compression and also the relative fluctuations between the bunch spacings and between the bunch rms lengths.

initial bunches spacing	1st final gap	2nd final gap	3rd final gap	4th final gap	gap relative fluctuations	1st bunch rms length	2nd bunch rms length	3rd bunch rms length	4th bunch rms length	5th bunch rms length	rms length relative fluctuations
6ps	1,55ps	1,40ps	1,29ps	1,36ps	20%	419fs	452fs	565fs	565fs	419fs	35%
8ps	2,19ps	1,88ps	1,72ps	1,82ps	27%	421fs	488fs	532fs	643fs	421fs	53%

TABLE *3.5 – Final bunches longitudinal parameters of the beams shown in Fig. 3.60*

The greater initial bunches spacing (8 ps) enables to have far less overlap between the bunches after magnetic compression (see contrasts in Fig. 3.59 (b) and Fig. 3.60 (b)) than the design spacing (6 ps), which is desired. However, the relative fluctuations in the bunch spacings and in the bunch rms lengths after compression become bigger when the initial bunches spacing increases (see Tab. 3.5). Therefore, the initial bunches spacing of 6 ps is more suitable than 8 ps. In fact, the most important point to excite the plasma and create the electromagnetic wave is to have the smallest possible relative fluctuations in the bunch spacings and rms lengths.

On the first line of Tab. 3.5, it is clearly visible that the final bunches spacings are quite close to the requirement (1.5 ps), since there is a discrepancy of only 14% at maximum (1.29 ps). This is not the case for the final bunches rms lengths. In fact, the requirement is 250 fs and the discrepancy for this value varies between 68% and 126%. It is important to note that this strong discrepancy is not mainly created during the magnetic compression. Indeed, Tab. 3.4 obtained for a "perfect" modulated time profile shows that the discrepancy is only of 34% at maximum in this case. It already exists at the chicane entrance and is due to the intra-bunch space charge forces, especially just after the beam emission from the photocathode where they are very strong. The solution to reduce them would be to decrease the bunches charges. One has then to pay attention to the measurement of the probe bunch charge [26]. In fact, since the charge of the probe bunch would be below 5 pC, the electronic devices like ICT or Faraday Cup would be close or below their resolution limit because of the electronic noise. A solution could be to measure the probe bunch charge thanks to the intensity of the light emitted by a scintillating screen hit by the beam, as it has been studied in Sec. 2.1.

3.2.3.5 Design of the magnetic chicane

The last step of the study is to determine what is the design of the magnetic D-shape chicane (see Fig. 3.34) for the cases studied in the previous sections. The mechanical length

26. The probe bunch can be separated from the other bunches, and thereby measured independently, by the use of a dipole magnet because it has a higher energy (up to a factor of 8) after acceleration.

of the four dipole magnets is already fixed to 25 cm. The projected distances between the dipole magnets are also fixed. It is 50 cm between the first and second dipole magnets and also between the third and fourth dipole magnets, while it is 75 cm between the second and third dipole magnets.

In practice, the curvature radius ρ of the beam trajectory is fixed by the wanted factor four of compression for the beam. It cannot be practically determined through the R_{56} parameter of the dipole magnet transfer matrix, because of the space charge forces and above all because of the fact that the beam to compress is a modulated beam and not a single beam. It has therefore been determined by trying different values of ρ in the CSRtrack code and choosing the one allowing a compression factor of four. For the case shown in Fig. 3.58 (chicane entrance) and Fig. 3.60 (chicane exit), a curvature radius $\rho = 1.909$ m and a deviation angle of $\theta = 7.5°$ in each dipole magnet have been found.

This value of ρ can then be used in combination with the beam mean kinetic energy T to determine the strength B of the magnetic field that has to be generated by the dipole magnets :

$$B = \frac{\sqrt{T(T + 2m_e c^2)}}{q\rho c}$$

For the case shown in Fig. 3.58 (chicane entrance) and Fig. 3.60 (chicane exit), $T = 15.93$ MeV which implies $B = 0.0287$ T $= 287$ G.

The beam deviation angle of $\theta = 7.5°$ in each dipole magnet allows computing that the shift between the center of the first and second dipole magnet and between the third and fourth dipole magnet is $75 * \tan(\theta) = 9.9$ cm. Fig. 3.61 shows a simplified layout of the magnetic chicane design.

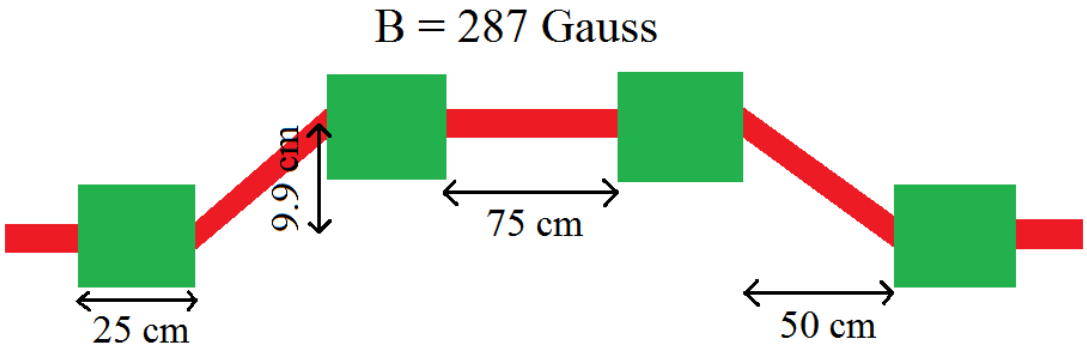

FIGURE *3.61 – Simplified design of the magnetic chicane.*

3.3 RF compression by velocity bunching in an accelerating cavity

3.3.1 Principles and limitations

The velocity bunching, also called RF compression, is a technique allowing one to compress a pre-existent accelerated electron beam while keeping it on a linear trajectory. This technique allows therefore avoiding the synchrotron radiation emission, inherent in the use of magnetic compression, and the degradation of the beam properties coming with this. It is most often performed with a traveling wave accelerating structure, where the electron beam is accelerated by a traveling wave whose phase velocity is ideally equal to c. Practically it is in most cases different, but still very close to c. Fig. 3.62 shows a diagram explaining the velocity bunching. It is assumed in Fig. 3.62 that the traveling wave is sinusoidal, which is not always the case.

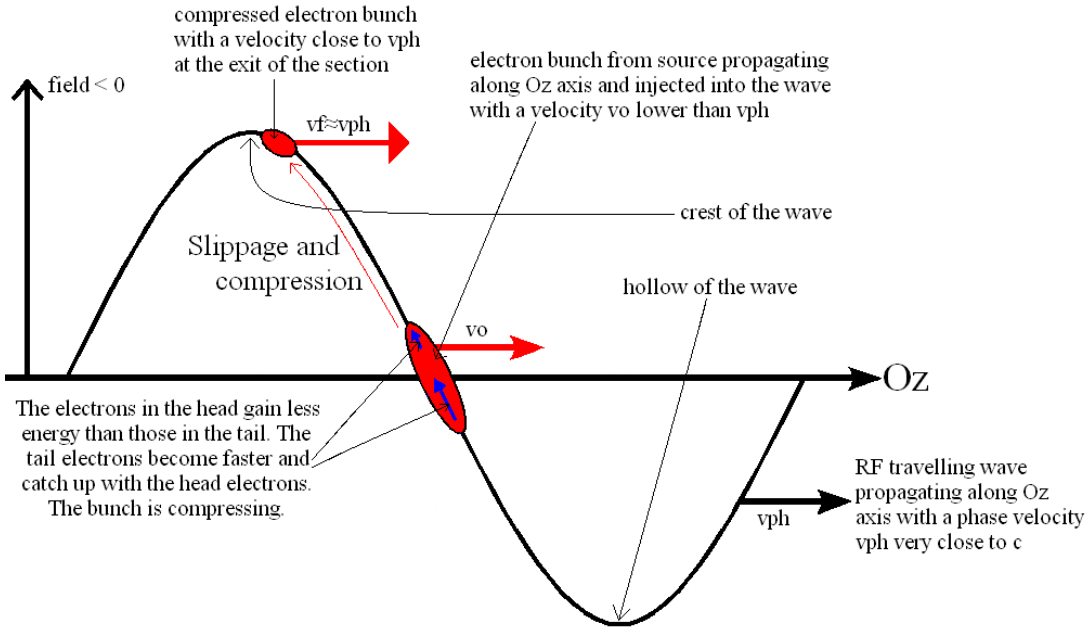

FIGURE *3.62 – Explanatory diagram of the velocity bunching process in a traveling wave*

The basic physical principle of this method is to submit the electron beam to a differential acceleration along its longitudinal direction, such that the electrons in the beam tail gain more energy than the ones in the beam head. Thus the electrons in the tail will become faster than the ones in the head and will catch up with them. The beam will be then compressed. To achieve this, it is most efficient to inject the electron beam in the accelerating section at a traveling wave phase where its field is close to zero. The reason is that it is at these phases that the slope of the wave field is the highest, so that the differential acceleration is the most pronounced along the beam. It is important to note that there are two phases of the traveling wave where its field is zero, but only one of these implies a compression of the beam (see Fig. 3.62). The other implies a longitudinal

stretching of the beam and is therefore unsuitable to perform velocity bunching.

The injected electron beam being slower than the traveling wave, it will slip relative to it and therefore experience an evolving field along its path. If injected at the previously mentioned correct phase to perform velocity bunching, it will slip towards the accelerating field of the wave (see Fig. 3.62) therefore allowing for both compression and acceleration of the beam in the section. This acceleration is of course lower than the maximal acceleration achieved by injecting the beam near the crest of the wave (see Fig. 3.62), but this maximal acceleration doesn't involve any compression of the beam.

It is important to note that the velocity bunching works only with non ultra-relativistic electron beams, namely with a mean beam energy E_0 typically lower than 20 MeV. The reason is that at too high energies ($E_0 >> mc^2$ therefore $\gamma >> 1$) the energy differential induced during the acceleration implies a velocity differential, and therefore a compression, of almost zero because the electrons all have velocities very close to c whatever their energies. This is a drawback with respect to the magnetic compression, which can be performed with ultra-relativistic and non ultra-relativistic electron beams [116].

This specificity implies that, in practice, the velocity bunching is performed in the accelerating sections directly following the source, because afterwards the electrons have too high energies and the induced velocity difference becomes too small to significantly compress the beam. It is difficult to define a precise energy border because there is always an induced velocity difference, it just becomes smaller, but 20 MeV is a typical border value. The following sections are used to accelerate the beam to make it ultra-relativistic and thus almost cancel the velocity differential. It is often necessary because otherwise this velocity differential, created to compress the beam, will imply a beam lengthening once past the point of maximum compression. As we will see later, it is however possible to obtain non ultra-relativistic compressed beams. This requires a very low residual velocity differential at the exit of the accelerating sections used to perform the velocity bunching.

The velocity bunching has begun to be used quite recently and quite few research teams have generated short electron beams using this method. Nevertheless, one can quote as an example a research team of the LNLL (Lawrence Livermore National Laboratory) which uses velocity bunching to generate short electron bunches, with the aim to produce X-rays by interaction of electrons with a laser (Thomson scattering) [117]. This facility succeeded in generating bunches with a charge of 250 pC, an energy of 50 MeV and an rms length lower than 300 fs [27].

There is a variation of velocity bunching, called ballistic bunching, where the velocity differential is created by differential acceleration in a short standing wave accelerating section and the compression of the beam takes place in the following drift space. This is the principle of the thin lens applied to particle beam longitudinal dynamics. Accelerating sections are placed just before the point of maximum compression to accelerate the beam and freeze its length by making it ultra-relativistic, thus preventing that its length increases again once past the point of maximum compression. This technique has been for example used at the NEPTUNE laboratory (UCLA), to produce 7 MeV electron bunches

27. 300 fs corresponds to the ultimate resolution of the diagnostic used in this facility to measure the length of the bunch.

with a charge of 300 pC and an rms length around 400 fs [118].

3.3.2 Analytical modeling of the velocity bunching

To my knowledge, there is currently only one approach allowing an analytical description of the velocity bunching phenomenon in a traveling wave accelerating section. This approach leads to different models, depending on the approximations performed for the beam energy at the exit of the section. For example, L.Serafini [119] fixes it such that the beam γ factor is equal to the one of the traveling wave. P.Piot [14] considers it very high compared to the entrance energy.

In a first time I re-established the model of P.Piot, which is more general, in order to highlight all the approximations necessary to its establishment. In doing so I find a sign fault in this model. Then, I compared the results from this model with PARMELA simulations to assess its possibilities. Finally, to improve the quantitative aspect and to obtain access to the beam length evolution all along the section, I developed a model resulting in a more accurate but more complicated equation.

3.3.2.1 Model of P.Piot

To establish this model, it is necessary to perform several approximations. First of all one has to consider that the traveling wave field is purely longitudinal, which is true only if the beam stays not too far from the section axis Oz. Then it is considered that the wave is purely sinusoidal and is not deforming during its propagation, which is false (see Appendix III) but allows analytically solving the problem. The field of the wave is then given by $E(z,t) = E_0 \sin(2\pi f t - kz + \Psi_0) = E_0 \sin(\Phi)$, where E_0 is the wave peak field and k its wave vector. Φ is the phase of the electron, namely the wave phase at the electron place. Ψ_0 is the origin phase, or RF-phase, of the traveling wave. Ψ_0 is by definition equal to the phase Φ_0 of the electron at its injection in the traveling wave structure. I choose therefore to replace Ψ_0 by Φ_0 thereafter.

The dynamics fundamental principle then allows deriving :

$$\frac{dp_z}{dt} = eE_0 \sin(\Phi) \Rightarrow m_e c \frac{d\beta_z \gamma_z}{dt} = eE_0 \sin(\Phi),$$

where p_z is the electron momentum along Oz and $\beta_z = \frac{v_z}{c}$ is the usual relativistic factor. In the PARMELA simulations I considered positrons for simplicity reasons. I will therefore do the same to establish the analytical models. It does not change anything to the physics, since it is sufficient to change the RF-phase Φ_0 by 180° to find the same results as for electrons. Two other approximations are then still necessary. Firstly, one has to consider that the electron motion is essentially along Oz and that the projections β_z and γ_z can be replaced by the total values β and γ. This is very justified because we typically have $\gamma_z = 0.998\gamma$, the same for β, in an accelerator. Secondly, one has to consider that the electrons are relativistic and therefore can approximate $\beta = 1$. This is acceptable since the energy at the exit of an RF-gun, therefore at the entrance of the accelerating section

used to perform velocity bunching, is typically about 5 MeV so $\beta = 0.9957$. It allows approximating $\frac{dz}{dt} \approx c$. One then obtains :

$$\frac{d\gamma}{dz} = \frac{eE_0}{m_e c^2} \sin(\Phi) = \alpha k \sin(\Phi), \text{ where } \alpha = \frac{eE_0}{m_e c^2 k} \text{ is dimensionless}$$

One also has $\frac{d\Phi}{dz} = 2\pi f \frac{dt}{dz} - k$. In this equation one cannot consider $\beta = 1$ since it is this difference which implies the slippage of the electrons with respect to the wave, which is an important phenomenon in velocity bunching (see Sec. 3.3.1). One then has $\frac{dz}{dt} = \beta c$, where β depends on z (or t). Strictly speaking $2\pi f = k v_\phi$, where v_ϕ is the wave phase velocity. But in a large majority of traveling wave accelerating section, $v_\phi \approx c$. I will therefore consider $v_\phi = c$ thereafter. One then obtains :

$$\frac{d\Phi}{dz} = k\left(\frac{1}{\beta} - 1\right) = k\left(\frac{\gamma}{\sqrt{\gamma^2 - 1}} - 1\right)$$

This equation highlights the fact that when the electron becomes very energetic (β very close to 1) it undergoes almost no slippage relative to the wave and stays at an almost constant phase Φ (because $\frac{d\Phi}{dz}$ becomes almost zero) during the rest of its motion. This is explained by the fact that its velocity becomes very close to the wave phase velocity.

The longitudinal dynamics of an electron in the traveling wave is therefore determined by the following coupled equations :

$$\frac{d\gamma}{dz} = \alpha k \sin(\Phi) \tag{3.10}$$

$$\frac{d\Phi}{dz} = k\left(\frac{\gamma}{\sqrt{\gamma^2 - 1}} - 1\right) \tag{3.11}$$

By dividing Eq. 3.11 by Eq. 3.10, one obtains :

$$\frac{d\Phi}{d\gamma} = \frac{1}{\alpha \sin(\Phi)}\left(\frac{\gamma}{\sqrt{\gamma^2 - 1}} - 1\right) \Rightarrow \alpha \sin(\Phi) d\Phi = \left(\frac{\gamma}{\sqrt{\gamma^2 - 1}} - 1\right) d\gamma$$

We obtain from integration $-\alpha \cos(\Phi) + C = \sqrt{\gamma^2 - 1} - \gamma$, where C is a constant determined by the initial conditions namely at the entrance of the accelerating section considered [28]. We have therefore $C = \alpha \cos(\Phi_0) + \sqrt{\gamma_0^2 - 1} - \gamma_0$, which allows obtaining the expression of Φ as a function of γ :

$$\Phi(\gamma) = \arccos\left(\frac{\alpha \cos(\Phi_0) + \sqrt{\gamma_0^2 - 1} - \gamma_0 - \sqrt{\gamma^2 - 1} + \gamma}{\alpha}\right) \tag{3.12}$$

28. There is a sign mistake in the article [14] published by P. Piot.

To simplify the expression of $\Phi(\gamma)$, one can consider that γ^2 remains still big with respect to 1 in the section. It is justified since $\gamma = 10.8$ for the typical energy of 5 MeV at the section entrance. One can then develop $\sqrt{\gamma^2 - 1} \approx \gamma - \frac{1}{2\gamma}$, which allows obtaining :

$$\Phi(\gamma) = \arccos\left(\cos(\Phi_0) + \frac{1}{2\alpha\gamma} - \frac{1}{2\alpha\gamma_0}\right) \tag{3.13}$$

The phase of the electron at the exit of the section is therefore given by :

$$\Phi_f = \arccos\left(\cos(\Phi_0) + \frac{1}{2\alpha\gamma_f} - \frac{1}{2\alpha\gamma_0}\right)$$

We will also consider that γ_f is sufficiently greater than γ_0 to neglect the term in γ_f with respect to the one in γ_0 in the expression of Φ_f. The phase Φ_f then becomes :

$$\Phi_f = \arccos\left(\cos(\Phi_0) - \frac{1}{2\alpha\gamma_0}\right) \tag{3.14}$$

This approximation is rather crude, because when the beam is compressed in the traveling wave section it is injected close to the phase where the wave field is zero. The electrons therefore undergo quite small an acceleration in the section. Consequently, γ_f is not much greater than γ_0. In practice, the factor between both remains below 5 when performing velocity bunching in a 3 m long SLAC-type section. The limits of this approximation will be highlighted in Sec. 3.3.2.3 and an evolved analytical model, freed from this approximation, will be developed in Sec. 3.3.2.2. The improvements brought by this evolved model will also be introduced in Sec. 3.3.2.3.

Differentiating Eq. 3.14, we obtain the rms phase extension of the beam at the exit of the section σ_{Φ_f}. We have :

$$\sigma_{\Phi_f} = \frac{\partial\Phi_f}{\partial\Phi_0}\sigma_{\Phi_0} + \frac{\partial\Phi_f}{\partial\gamma_0}\sigma_{\gamma_0} = \frac{\sin(\Phi_0)}{\sin(\Phi_f)}\sigma_{\Phi_0} - \frac{1}{2\alpha\gamma_0^2\sin(\Phi_f)}\sigma_{\gamma_0} \tag{3.15}$$

where σ_{Φ_0} is the initial rms phase extension of the beam and σ_{γ_0} is the initial standard deviation of the beam γ distribution. Dividing σ_{Φ_f} by $2\pi f$, where f is the traveling wave frequency, allows obtaining the rms beam length σ_{t_f} at the section exit.

3.3.2.2 Evolution of the model of P.Piot

To obtain an analytical model giving the evolution of the electron beam length all along the accelerating structure, and not only at the exit of the accelerating structure like in the model of P.Piot, it is necessary to determine an expression of $\gamma(z)$ as a function of the initial conditions Φ_0 and γ_0 and to insert it in Eq. 3.13 to deduce $\Phi(z)$. To do that, I approximate a linear variation for the electron phase Φ in the accelerating structure. Eq. 3.11 then becomes :

$$\frac{d\Phi}{dz} = \frac{\Phi_f - \Phi_0}{L} \tag{3.16}$$

where L is the length of the accelerating structure used to perform velocity bunching and Φ_f is given by Eq. 3.13. I integrate Eq. 3.16 and injected the result in Eq. 3.10 that I integrate again to obtain :

$$\gamma(z) = \gamma_0 + \frac{\alpha k L}{\Phi_f - \Phi_0}\left(\cos(\Phi_0) - \cos\left(\Phi_0 + \frac{\Phi_f - \Phi_0}{L}z\right)\right) \tag{3.17}$$

To test the validity of this approximation, I choose to use a typical electron bunch of 50 pC and 5.72 MeV generated by the SPARC RF-gun injected in the first traveling wave accelerating structure of the SPARC facility (see Fig. 1.28 and Sec. 1.3.4), which is 3 m long. I compare the bunch mean energy as a function of the RF-phase Φ_0 at the traveling wave accelerating structure exit coming from the analytical model (Eq. 3.17) with the one coming from the PARMELA beam dynamics code and also with the one coming from numerical integration with Matlab of the motion equations Eq. 3.10 and Eq. 3.11. Fig. 3.63 shows the results of this comparison for a wave peak field of $E_0 = 10.68$ MV/m, corresponding to $\alpha = 0.349$.

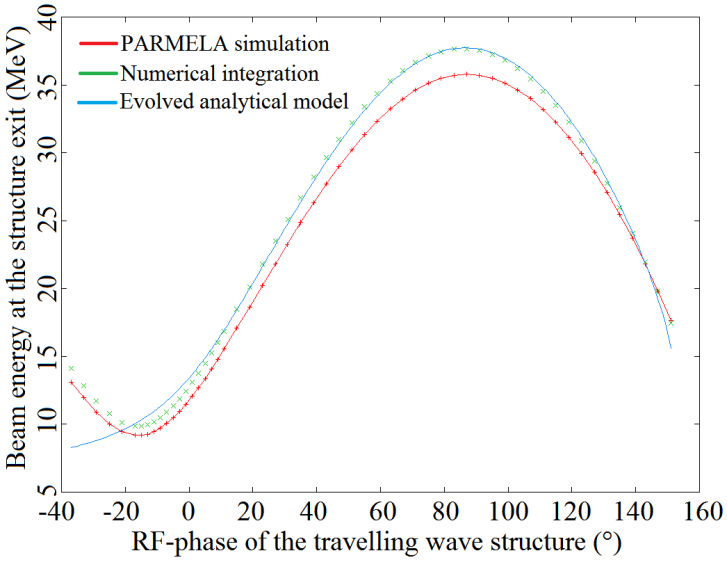

FIGURE *3.63 – Bunch mean energy at the exit of the traveling wave accelerating structure as a function of the injection phase Φ_0 for a wave peak field of 10.68 MV/m*

One can see two zones for the bunch energy gain in Fig. 3.63.

The first zone is between $\Phi_0 = 10°$ and $\Phi_0 = 150°$. In this zone, we can see that the analytical model overestimated by 5% to 10% the bunch energy at the accelerating structure exit with respect to PARMELA simulation. But it matches with the numerical integration of the motion equations. It means that the discrepancy in this zone doesn't come from the approximation of a linear variation of the electron phase Φ in the accelerating structure, but from the expressions used for the motion equations. Especially,

the approximation to consider a purely sinusoidal traveling wave not deforming along its propagation is involved to explain this discrepancy. The analytical model is therefore valid in this range of RF-phase Φ_0.

The second zone is below $\Phi_0 = 10°$. In this zone, we can see that the analytical model matches neither with PARMELA simulations nor with numerical integration of the motion equations. Especially, the bunch energy rise for Φ_0 lower than $-15°$ is not predicted by the analytical model. It means that the approximation of a linear variation of the electron phase Φ is not accurate in this range of RF-phase Φ_0. It is explained by the fact that the electron bunch has quite a low energy at the accelerating structure entrance (5.72 MeV). As a result, when the bunch is injected in the traveling wave structure at an RF-phase Φ_0 close to the one of zero field ($\Phi_0 = 0°$) or implying decelerating field ($\Phi_0 < 0°$) there are significant variations of the bunch velocity which imply strongly non-linear variations of the electron phase Φ (linear variation corresponding to a constant bunch velocity) leading to the inaccuracy of the analytical model. This inaccuracy is increasing when Φ_0 decreases because the bunch velocity variations are then increasing. For Φ_0 higher than 10°, there still are bunch velocity variations. But the accelerating field is high enough and these variations are concentrated in a short zone after the accelerating structure entrance implying that the approximation of a linear variation of the electron phase Φ is valid.

I injected Eq. 3.17 in Eq. 3.13 that I differentiated with respect to Φ_0 and γ_0 to obtain the expression of the beam length along the accelerating structure :

$$\sigma_\Phi(z) = \frac{2\alpha\gamma(z)^2(\Phi_f - \Phi_0)\sin(\Phi_0) + (\gamma(z) - \gamma_0) + \alpha kL\left(-\sin(\Phi_0) + \left(1 - \frac{z}{L}\right)\sin\left(\Phi_0 + \frac{\Phi_f - \Phi_0}{L}z\right)\right)}{2\alpha\gamma(z)^2(\Phi_f - \Phi_0)\sin\left(\arccos\left(\cos(\Phi_0) - \frac{1}{2\alpha\gamma_0} + \frac{1}{2\alpha\gamma(z)}\right)\right)}\sigma_{\Phi_0} - \frac{2\alpha\left(\gamma(z)^2 - \gamma_0^2\right)}{4\alpha^2\gamma_0^2\gamma(z)^2\sin\left(\arccos\left(\cos(\Phi_0) - \frac{1}{2\alpha\gamma_0} + \frac{1}{2\alpha\gamma(z)}\right)\right)}\sigma_{\gamma_0} \tag{3.18}$$

where $\gamma(z)$ is given by Eq. 3.17. Φ_f is given by Eq. 3.13, in which γ is calculated with Eq. 3.17. Dividing $\sigma_\Phi(z)$ by $2\pi f$, where f is the traveling wave frequency, allows obtaining the rms beam length $\sigma_t(z)$. However it is noteworthy that to simplify I perform the approximation to not differentiate Φ_f (see Eq. 3.13), which depends yet on Φ_0 and γ_0, to establish Eq. 3.18.

3.3.2.3 Comparison of the analytical models with PARMELA simulations

I compare the bunch length coming from the analytical models developed in Sec. 3.3.2 with the one coming from the beam dynamics code PARMELA (Phase And Radial Motion in Electron Linear Accelerators) [120], to test the validity and the accuracy of these models.

I also numerically integrated Eq. 3.10 and Eq. 3.11, with Matlab, for a Gaussian particle distribution where the faster electrons are initially located in the bunch tail, as it is the case in my PARMELA simulations. The results coming from this numerical integration are very useful for several reasons. First of all it gives a more precise idea of the way the bunch length evolved than with the analytical model, while remaining faster and

far simpler than the PARMELA simulations. Then, by comparing the results coming from this numerical integration with those coming from the analytical model, it will be possible to evaluate the impact of neglecting the term in γ_f with respect to the one in γ_0 to obtain Eq. 3.14. Finally, by comparing the results coming from this numerical integration with those coming from PARMELA simulations, it will be possible to determine the impact on the longitudinal beam dynamics of the space-charge force (not taken into account in the numerical integration and in the analytical model) and of the fact that the traveling wave is not sinusoidal and is deforming along its propagation.

To perform this comparison, I choose once again to use a typical electron bunch generated by the SPARC RF-gun injected in the first traveling wave accelerating structure of the SPARC facility (see Fig. 1.28 and Sec. 1.3.4), which is 3 m long. The bunch properties at the entrance of the accelerating structure are the following : Bunch charge of 50 pC ; Bunch mean energy of 5.72 MeV ($\gamma_0 = 12.194$) ; $\sigma_{\Phi_0} = 0.0284$ rad (namely $\sigma_{t_0} = 1.58$ ps) ; Bunch relative energy spread of 0.2% (namely $\sigma_{\gamma_0} = 0.0243$).

Model of P. Piot

I choose first to compare the rms bunch length at the traveling wave structure exit as a function of the RF-phase Φ_0, which corresponds to the injection phase of the electron bunch in the structure, with the corrected analytical model of P. Piot. 0° denotes the RF-phase where the electric field of the traveling wave is zero and where the electron bunch slips towards the accelerating fields (see the initial position of the electron bunch in Fig. 3.62). Fig. 3.64 shows the results of this comparison for a wave peak field of $E_0 = 10.68$ MV/m, corresponding to $\alpha = 0.349$.

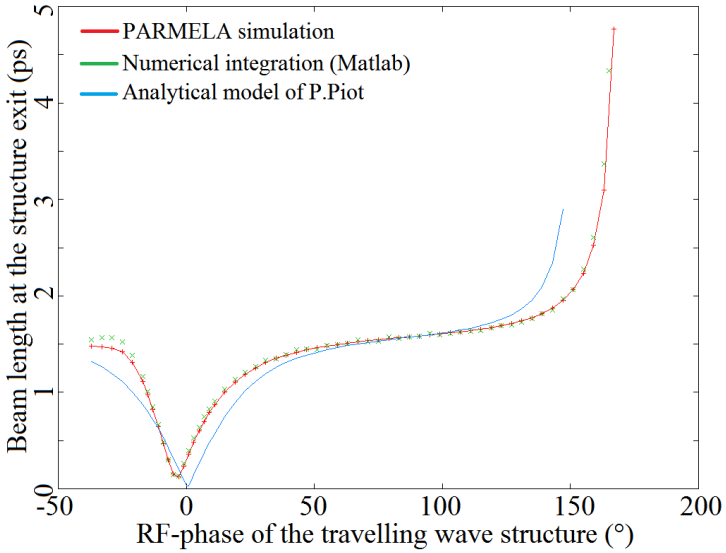

FIGURE *3.64 – Rms bunch length at the exit of the traveling wave accelerating structure as a function of the injection phase Φ_0 for a wave peak field of 10.68 MV/m*

Fig. 3.64 shows well that the bunch is compressed, as intended, for injection phase

Φ_0 close to 0° and on a relatively small phase range of the order of 40°. Besides it shows that, close to the optimal compression, the bunch length is quickly varying with Φ_0. To perform a precise bunch compression by velocity bunching, it is therefore necessary to have a good control of the bunch injection phase Φ_0 (typically better than 1°).

We also observe that the results coming from PARMELA simulations and those coming from Matlab numerical integration are very close, since the discrepancy remains lower than 13% in the studied range of Φ_0. It allows concluding that the space-charge force and the fact that the traveling wave is not sinusoidal and is deforming along its propagation have only a weak combined effect on the bunch length at the traveling wave structure exit, therefore on the bunch compression by velocity bunching. Besides, we can say that this effect changes only a little with the injection phase Φ_0.

We finally observe that the analytical model of P. Piot allows a good reproduction of the shape of the evolution of the bunch length as a function of the injection phase Φ_0. Besides, it allows also a rather good prediction of the RF-phase of maximal bunch compression Φ_{0_m}. In fact, it predicts $\Phi_{0_m} = 0.5°$ while PARMELA and the Matlab numerical integration predicts $\Phi_{0_m} = -3°$ so a discrepancy of only 3.5°.

However, one can observe in Fig. 3.64 that the analytical model of P. Piot is not well-adapted to compute the value of the bunch length in the range of phase where the bunch is compressed (between $-20°$ and 20°). There is in fact up to a factor 9 of difference, at $\Phi_0 = 1°$, between this model and the PARMELA results.

A part of this discrepancy is due to the fact that the assumption to neglect the term in γ_f with respect to the one in γ_0 to obtain Eq. 3.14 is not valid in this range of RF-phase Φ_0. In fact, it can be seen in Fig. 3.63 that the bunch energy gain in this range is weak, since the bunch mean energy is 5.72 MeV at the traveling wave accelerating structure entrance. This is supported by the fact that in the RF-phase range where the bunch energy gain is important (between 30° and 130°), the analytical model of P. Piot predicts the bunch length with a far better accuracy since the discrepancy with the PARMELA simulations remains below 10% in this range.

There is another reason explaining the length values discrepancy between PARMELA and the analytical model of P. Piot in the RF-phase range where the bunch is compressed. The analytical model of P. Piot has been established starting from the equations of motion Eq. 3.10 and Eq. 3.11 for a single electron, and the expression of the bunch length σ_{Φ_f} (Eq. 3.15) has been established by a simple linear differentiation of the solution Φ_f (Eq. 3.14) of these equations. As a result, the analytical model of P. Piot does not take into account the fact that the electron bunch is an electron distribution, and the bunch maximum compression therefore corresponds to a zero bunch length. This is impossible when considering an electron distribution, even without interactions as it is the case in the Matlab numerical integration of the equations of motion (which does not exhibit a zero bunch length). It especially explains why the minimal rms bunch length in the analytical model of P. Piot (27.7 fs) [29] is far lower than in the PARMELA simulations (124 fs).

29. This length is not zero because I perform my calculations with a 2° step for the injection phase Φ_0. A more small step shows that for $\Phi_0 = 0.4724°$ the rms bunch length predicted by the analytical model of P. Piot is 2.7 as.

To remedy this and to develop a more accurate and realistic analytical model, it would be necessary to start with an electron distribution and not with a single electron. This is for example possible by using a beam envelope equation for the longitudinal motion of the bunch in the accelerating section, since this equation directly propagate the second moment of the longitudinal electron distribution which is the bunch length. This is also possible by using the Vlasov equation, since this equation directly propagate a distribution of electrons through magnetic and electric field. However, it is not possible to analytically solve these two equations in the general case and numerous approximations have to be performed to do so. The equations of motions of a single electron are analytically solvable under few assumptions and are therefore more suitable to the establishment of a first simple analytical model.

Evolved analytical model

It is now interesting to compare the evolution of the analytical model of P. Piot (named evolved analytical model) with PARMELA simulations and numerical integration of the motion equations by Matlab, to see if it leads to some improvements in the velocity bunching modeling. Fig. 3.65 shows the result of this comparison.

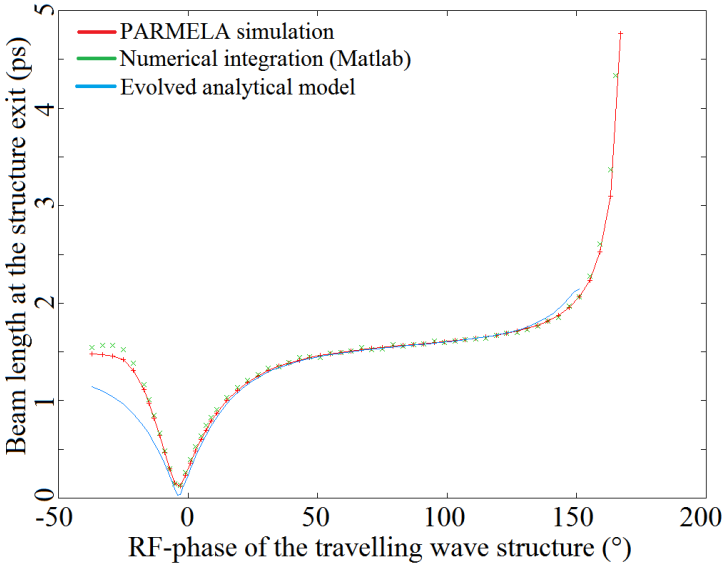

FIGURE *3.65 – Rms bunch length at the exit of the traveling wave accelerating structure as a function of the injection phase Φ_0 for a wave peak field of 10.68 MV/m*

One can clearly see by comparing Fig. 3.65 with Fig. 3.64 that the evolved analytical model leads to two major improvements with respect to the analytical model of P. Piot. The first is that the RF-phase Φ_0 leading to the maximum bunch compression at the traveling wave structure exit is perfectly predicted by the evolved analytical model, which is not the case for the analytical model of P. Piot. The second is that the agreement with PARMELA simulations for the RF-phase Φ_0 above the bunch maximum compression is

far better in the evolved analytical model than in the analytical model of P. Piot. These improvements are due to the fact that the evolved analytical model is freed from the hypothesis to neglect γ_0 in front of γ_f, which is strongly limiting in the analytical model of P. Piot.

However, the agreement between the evolved analytical model and PARMELA simulations is also not good for the RF-phase Φ_0 below the maximum bunch compression. It is due to the fact that the approximation of a linear variation of the electron phase Φ is inaccurate in this range of RF-phase Φ_0, as explained in Sec. 3.3.2.2.

Besides, as for the analytical model of P. Piot, the evolved analytical model fails in predicting the rms bunch length at the RF-phase Φ_0 of maximum bunch compression. In fact, it predicts $\sigma_t = 30.3$ fs [30] while PARMELA simulation predicts $\sigma_t = 124$ fs. The reason is the same as for the analytical model of P. Piot, namely that I start from the equations of motion Eq. 3.10 and Eq. 3.11 for a single electron, and the expression of the bunch length σ_Φ (Eq. 3.18) has been established by a simple linear differentiation of the solutions Φ (Eq. 3.13) and γ (Eq. 3.17) of these equations. As a result, the evolved analytical model does not take into account the fact that the electron bunch is an electron distribution, and the bunch maximum compression therefore corresponds to a zero bunch length. As previously mentioned, it can be remedy by using a beam envelope equation or the Vlasov equation for the longitudinal motion of the bunch.

3.3.3 Simulations on SPARC for the compression of a single bunch by velocity bunching

I choose to perform simulations of the generation of short electron bunches by the velocity bunching method on the SPARC layout (see Sec. 1.4.4 and Fig. 1.28), within the framework of a starting collaboration between the Laboratoire de Physique des Gaz et des Plasmas of the Université Paris Sud, the LAL and the INFN of Frascati about a laser-plasma acceleration experiment. This experiment requires ultra-relativistic electron bunches with a very short duration, namely a few tens of femtoseconds rms. The goal is to inject these bunches in an electromagnetic wave, created in a plasma by interaction with an intense laser pulse, with a very high accelerating field (of the GV/m order) and a very short wavelength (a few tens of micrometers) to accelerate the bunch. One has to note that the electron bunch has to be very short, namely much shorter than the wavelength of the accelerating wave, in this scheme of plasma acceleration. Otherwise, the different electrons of the bunch would be subject to very different accelerating field values (even of opposite sign). This would strongly deteriorate the quality of the bunch, especially its energy spread. The fact that 30 μm of wavelength corresponds to a duration of 100 fs for an ultra-relativistic electron bunch explains the required rms duration of a few tens of femtoseconds for the electron bunch in this experiment.

I use the PARMELA beam dynamics code [120] to perform all the simulations presen-

30. This length is once again not zero because I perform my calculations with a 2° step for the injection phase Φ_0. A more small step shows that for $\Phi_0 = -3.5468°$ the rms bunch length predicted by the evolved analytical model is about 0.9 as.

ted in this section. The reason is that the accelerating structures on SPARC are traveling wave ones, and this kind of structure is easier to include in PARMELA than in ASTRA. For simplicity reasons, I simulate the dynamics of positron bunches in PARMELA. It does not matter since it is sufficient to change the RF-phases Ψ_i of all the accelerating structures by 180° to retrieve the same dynamics for electron bunches with the same charges. Concerning the RF-phase Ψ_i of the traveling wave accelerating structure, which is nothing else than the injection phase of the bunch in the structure, I use the convention shown in Fig. 3.66. Namely the +90° phase is the on-crest acceleration phase for a positron bunch, the −90° phase is the one for an electron bunch and the 0° phase is the phase of zero field. As a reminder, the compression of the bunch by the velocity bunching process is the most efficient when the bunch is injected in a structure close to the 0° phase (see Sec. 3.3.1).

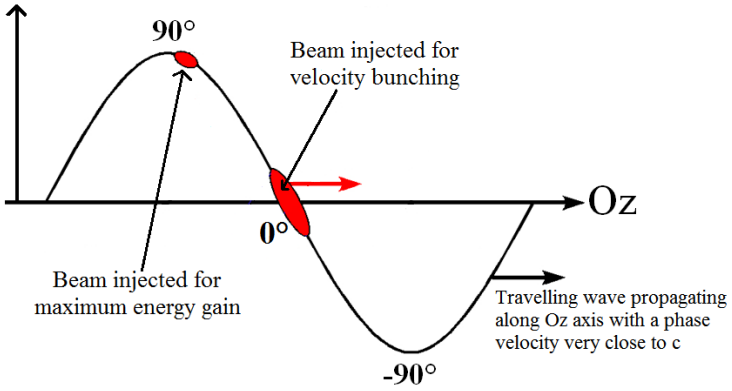

FIGURE *3.66 – Phase convention used for the traveling wave accelerating structures*

The laser pulse used to drive the SPARC RF-gun has a uniform transverse profile and a Gaussian time profile. In all the simulations presented in this section, the current injected in the solenoid surrounding the first SLAC section has been fixed to 50 A and I did not use the one surrounding the second one. Only the current I_p injected in the solenoid at the RF-gun exit has been varied.

SPARC containing three successive SLAC sections, that I will call S1, S2 and S3 thereafter, it allows two different ways to generate ultra-short electron bunches by velocity bunching to be tested. The first way consists in a fast bunch compression in S1, followed by a strong acceleration of the bunch in S2 and S3 to freeze its length by making it ultra-relativistic[31]. The second way consists in the compression of the bunch in S1 and S2, namely a slower compression, followed by a strong acceleration in S3 to freeze the bunch length.

31. It is said that the length is frozen for an ultra-relativistic electron bunch, because the energy differences between the electrons of the bunch translate into almost zero velocity differences, resulting in an almost constant length.

3.3.3.1 Influence of the Gun RF-phase

The first step is to study the influence of the SPARC Gun RF-phase φ (see Sec. 1.2.5) on the velocity bunching process in S1, to determine in which configuration I will use it thereafter. The velocity bunching process is indeed impacted by the Gun RF-phase, because the correlation between the longitudinal positions of the electrons in the bunch and their energies at the entrance of S1 is a function of the Gun RF-phase.

I choose to work with a high value of the mean accelerating field in the RF-gun, namely 50 MV/m [32], to have a high bunch mean energy at its exit (around 5.7 MeV). The reason of this choice is that it allows minimizing the influence of space-charge forces. It therefore eases the transport of the electron bunch up to S1, which is located quite far from the RF-gun exit (1.45 m). I choose to use two different Gun RF-phases, namely $\varphi = +10°$ and $\varphi = -10°$ with respect to the one maximizing the bunch energy at the RF-gun exit (0°). Fig. 3.67 shows the evolution of the rms bunch length up to the exit of S1 for these two Gun RF-phases. In each cases, the injection phase of the bunch in S1 has been tuned to maximize the compression of the bunch.

One can see in Fig. 3.67 that for $\varphi = -10°$ the maximum compression factor in S1 (14.5) is higher than the one for $\varphi = +10°$ (10.4). Thus, this study shows that to have a better longitudinal compression in S1, it is necessary to fix the Gun RF-phase at a value lower than the one maximizing the bunch energy. $\varphi = -10°$ is not a generality, it is dependent of the other experimental conditions, especially the bunch charge and the sizes of the laser pulse driving the RF-gun.

The explanation of this better compression factor can be found in the time/energy correlation of the bunch at the entrance of S1. It is shown, for $\varphi = +10°$ and $\varphi = -10°$, in Fig. 3.68. One can see clearly that the most energetic electrons are in the head of the bunch for $\varphi = +10°$, while they are in the tail for $\varphi = -10°$. When the most energetic electrons are in the bunch tail, the differential acceleration induces by the traveling wave (see Fig. 3.62) allows a compression of the bunch right from the beginning of S1. On the opposite, when the most energetic electrons are in the head of the bunch, the energy between the head and the tail of the bunch has first to be inverted in S1. As a result, the bunch compression does not start at the very beginning of S1 (see Fig. 3.67 red curve) and the compression factor is lower. In addition to this better compression factor, the bunch length is also already lower at the entrance of S1 for $\varphi = -10°$. This is also due to the time/energy correlation induced by the RF-gun, and this also constitutes a reason to work at $\varphi = -10°$ rather than at $\varphi = +10°$.

32. It corresponds to a peak field of 122 MV/m.

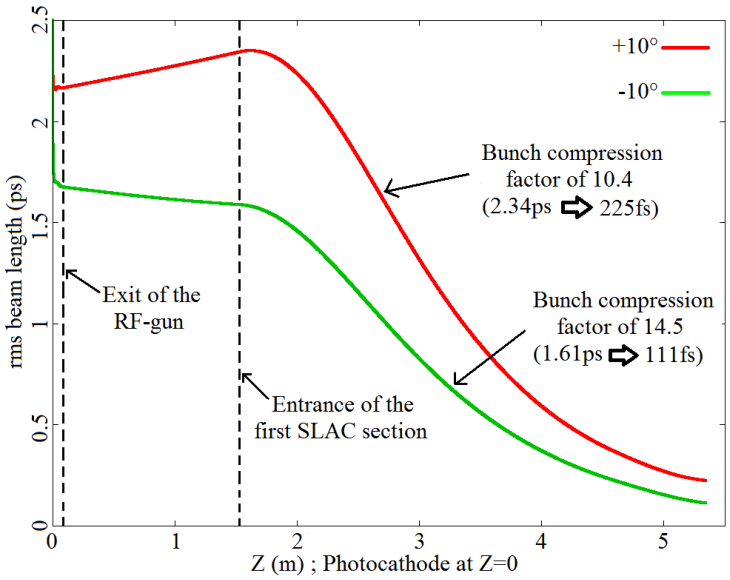

FIGURE *3.67 – Evolution of the rms bunch length up to the exit of S1. Bunch charge : 50 pC ; RF-gun mean accelerating field : 50 MV/m ; Laser pulse driving the RF-gun : 0.6 mm transverse radius and 2.5 ps rms duration ; I_p : 201 A ; S1 mean accelerating field : 10 MV/m ; Injection phase in S1 : −2° (red) and −0.5° (green).*

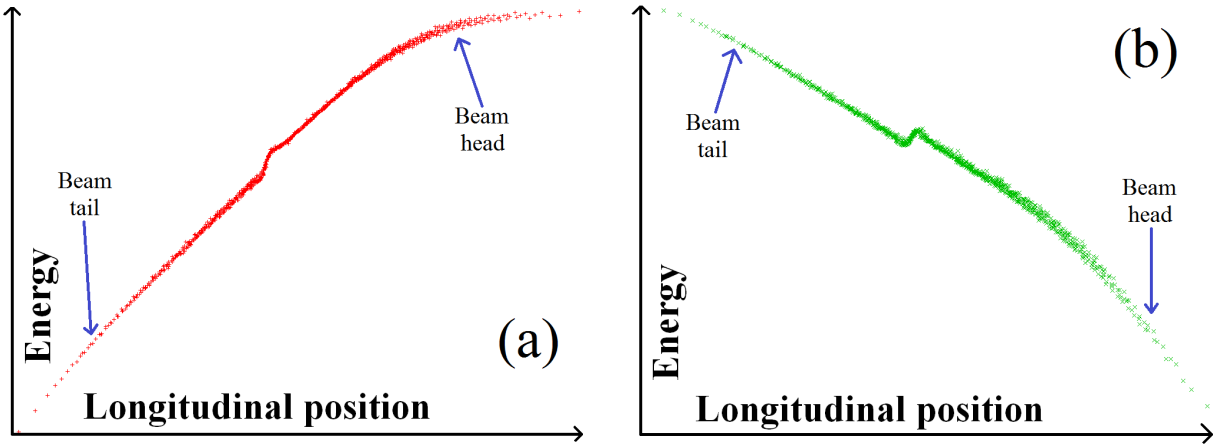

FIGURE *3.68 – Bunch time/energy phase-space at the entrance of S1. Bunch charge : 50 pC ; RF-gun mean accelerating field : 50 MV/m ; Gun RF-phase : +10° (a) and −10° (b) ; Laser pulse driving the RF-gun : 0.6 mm transverse radius and 2.5 ps rms duration ; I_p : 201 A.*

3.3.3.2 First scheme of ultra-short electron bunch generation

Influence of the injection phase in S1

As shown in Fig. 3.65, the bunch compression by velocity bunching is very dependent on the injection phase Ψ_1 in S1 since there are fast variations of the bunch length around the injection phase Ψ_{1_m} allowing the maximal compression at its exit (see Fig. 3.65 in Sec. 3.3.2.3). Ψ_1 has therefore to be adjusted very precisely. The reason explaining the existence of this phase of maximal compression is shown in Fig. 3.69.

As it is visible in Fig. 3.69, if the injection phase is too low (red curve), there is an overcompression of the bunch in S1 and the bunch length increases again. This is due to the fact that the differential acceleration is too marked along the bunch, implying that the electrons in the bunch tail overtake the ones in the bunch head. On the opposite, if the injection phase is too high (blue curve), there is an undercompression of the bunch in S1. This is due to the fact that the differential acceleration is not sufficiently marked along the bunch, implying that the compression is not achieved at the exit of S1.

In practice, to optimize the bunch compression by velocity bunching, Ψ_1 must not be chosen equal to Ψ_{1_m}. It is necessary because, at this injection phase, the bunch is not yet ultra-relativistic at the exit of S1. The typical bunch energy is indeed between 8 MeV, for a mean accelerating field of 5 MV/m, and 17 MeV, for a mean accelerating field of 20 MV/m. The high energy spread value, induced by the compression via velocity bunching, would then imply a lengthening of the bunch in the drift space up to the entrance of S2 (see Eq. 2.6 in Sec. 2.3.2.2 and Fig. 3.70 (red curve)).

Ψ_1 has typically to be chosen between 2° and 4° higher than Ψ_{1_m}, depending on the value of the mean accelerating field in S1. This allows achieving the bunch compression during its motion in S2 (see Fig. 3.70 (green curve)). Ψ_1 has to be precisely adjusted, namely with a precision of the order of 1°. In fact, if Ψ_1 is not sufficiently higher than Ψ_{1_m}, the bunch compression will end too soon. In other words, the bunch will not have gained enough energy in S2 to become ultra-relativistic before reaching its point of maximal compression. The bunch length will then increase a bit, due to the bunch energy spread, after passing the point of maximal compression in S2. On the opposite, if Ψ_1 is too much higher than Ψ_{1_m}, the bunch compression will end too late. In other words, the bunch will have gained energy too fast in S2 and will become ultra-relativistic before reaching its point of maximal compression. The bunch length will then be frozen before reaching the point of maximal compression and will be therefore not minimal.

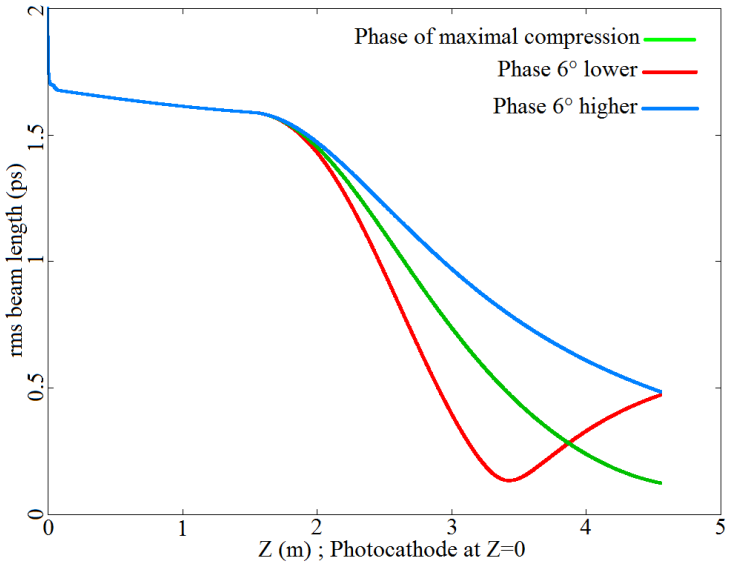

FIGURE *3.69 – Evolution of the rms bunch length up to the exit of S1. Bunch charge : 50 pC ; RF-gun mean accelerating field : 50 MV/m ; Gun RF-phase : −10° ; Laser pulse driving the RF-gun : 0.6 mm transverse radius and 2.5 ps rms duration ; I_p : 196 A ; S1 mean accelerating field : 10 MV/m ; Ψ_1 : −1.5° (green), −7.5° (red) and +4.5° (blue).*

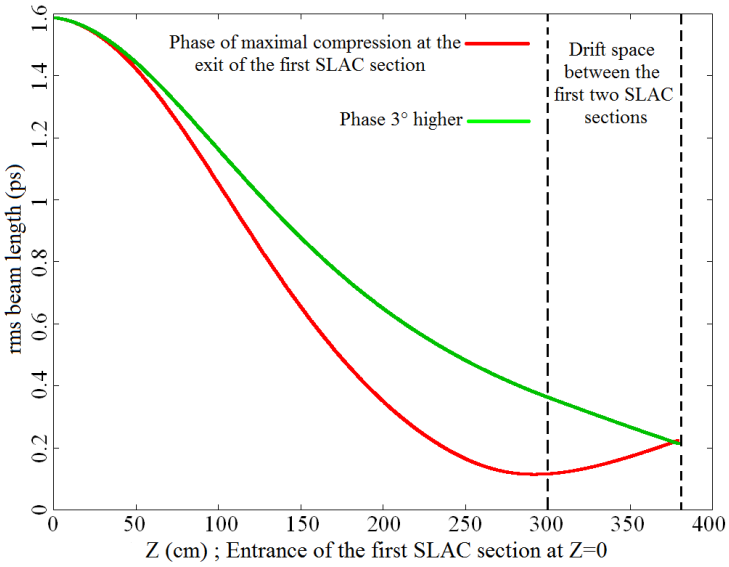

FIGURE *3.70 – Evolution of the rms bunch length up to the entrance of S2. Bunch charge : 50 pC ; RF-gun mean accelerating field : 50 MV/m ; Gun RF-phase : −10° ; Laser pulse driving the RF-gun : 0.6 mm transverse radius and 2.5 ps rms duration ; I_p : 196 A ; S1 mean accelerating field : 10 MV/m ; Ψ_1 : −1.5° (red) and +1.5° (green).*

Influence of the S1 and S2 mean accelerating field

The following step has been to study the evolution of the minimum achievable rms bunch length, at the exit of S3, as a function of the mean accelerating field in S1 and S2 [33]. For each case, the injection phases Ψ_i in the three SLAC sections has been optimized to obtain the lowest possible bunch length at the exit of S3. Fig. 3.71 shows the rms bunch length obtained as a function of the mean accelerating field in S1 and S2, and Tab. 3.6 shows the bunch properties in these configurations of minimal bunch length.

One can observe in Fig. 3.71 that the rms bunch length at the exit of S3 shows a minimum for a mean accelerating field around 10 MV/m in S1 and S2. It is also visible that there is a quick increase in the bunch length when the mean accelerating field decreases, the increase being of 66% between 10 MV/m and 5 MV/m. The increase is much slower when the mean accelerating field increases, the increase being of 8% between 10 MV/m and 20 MV/m. It is therefore not necessary to precisely optimize the mean accelerating field value in S1 and S2. It is sufficient to ensure to not be below the optimal value to have a bunch length close from its minimum.

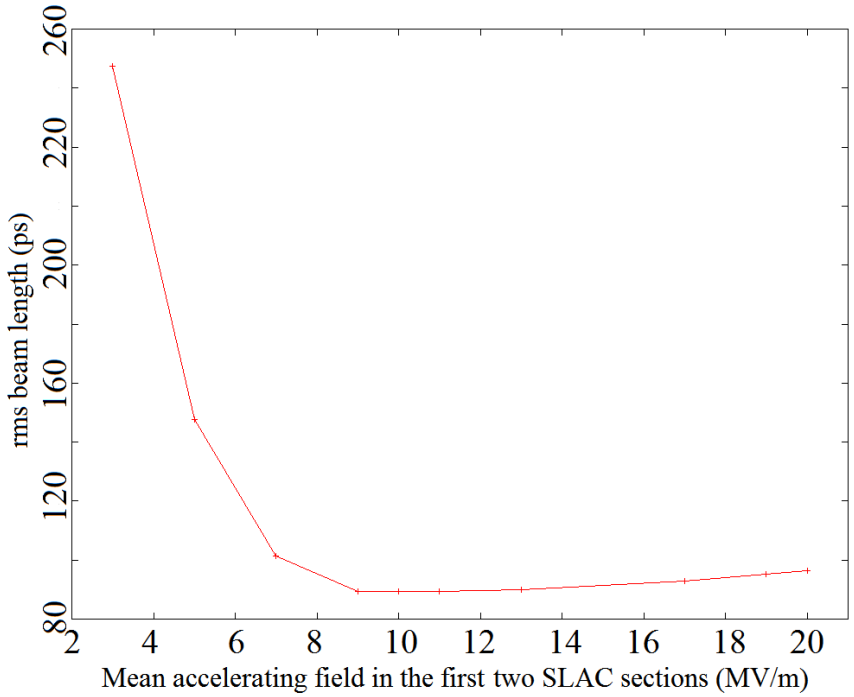

FIGURE *3.71 – rms bunch length at the exit of S3 as a function of the mean accelerating field in S1 and S2. Bunch charge : 50 pC ; RF-gun mean accelerating field : 50 MV/m ; Gun RF-phase : −10° ; Laser pulse driving the RF-gun : 0.6 mm transverse radius and 2.5 ps rms duration ; Other conditions : see Tab. 3.6.*

33. As a reminder, it is necessarily the same (see Sec. 1.4.4).

Mean accelerating field in the first two SLAC sections	Current injected in the solenoid at the RF-gun exit	$\Psi_1/\Psi_2/\Psi_3$	Mean energy (MeV)	rms relative energy spread (%)	rms length (fs)	rms transverse radius (mm)	rms transverse emittance (π.mm.mrad)	rms longitudinal emittance (π.mm.mrad)
3MV/m	194A	-12,5° / 78,8° / 49,2°	**42,27**	**0,156**	**267**	**1,74**	**1,433**	**10,63**
5MV/m	194A	-4,5° / 81,5 ° / 73,4°	**57,53**	**0,31**	**148**	**1,23**	**1,716**	**13,11**
7MV/m	194A	-0,5° / 41,6° / 66,4°	**56,98**	**0,443**	**102**	**1,12**	**1,563**	**15,45**
9MV/m	194A	1,5° / 23,9° / 82,2°	**58,59**	**0,639**	**89,3**	**0,95**	**1,802**	**19,88**
10MV/m	196A	1,5° / 25,1° / 80,7°	**60,57**	**0,683**	**89,3**	**0,89**	**1,826**	**22,33**
11MV/m	196A	1,5° / 24,4° / 79,6°	**61,74**	**0,709**	**89,4**	**0,82**	**1,721**	**23,44**
13MV/m	196A	1,5° / 25,1° / 77,5°	**65,11**	**0,775**	**90,1**	**0,76**	**2,111**	**27,79**
17MV/m	198A	1,5° / 25,1° / 54,6	**65,27**	**0,972**	**93**	**0,74**	**2,025**	**36,69**
19MV/m	198A	1,5° / 24,3° / 53,5°	**67,28**	**1,032**	**95,3**	**0,64**	**2,25**	**41,2**
20MV/m	198A	1,5° / 23,9° / 53,0°	**68,27**	**1,079**	**96,5**	**0,56**	**2,589**	**45,16**

TABLE *3.6 – Bunch properties at the exit of S3 for the configurations minimizing the bunch length. Bunch charge : 50 pC ; RF-gun mean accelerating field : 50 MV/m ; Gun RF-phase : −10° ; Laser pulse driving the RF-gun : 0.6 mm transverse radius and 2.5 ps rms duration ; Mean accelerating field in S3 : 12 MV/m.*

To understand the existence of the observed optimal mean accelerating field in Fig. 3.71, it is relevant to superimpose the rms length curves for mean accelerating fields of 5 MV/m, 10 MV/m and 20 MV/m in S1 and S2. It is shown in Fig. 3.72 (a). Fig. 3.72 (b) shows the evolution of the bunch mean energy for these three cases.

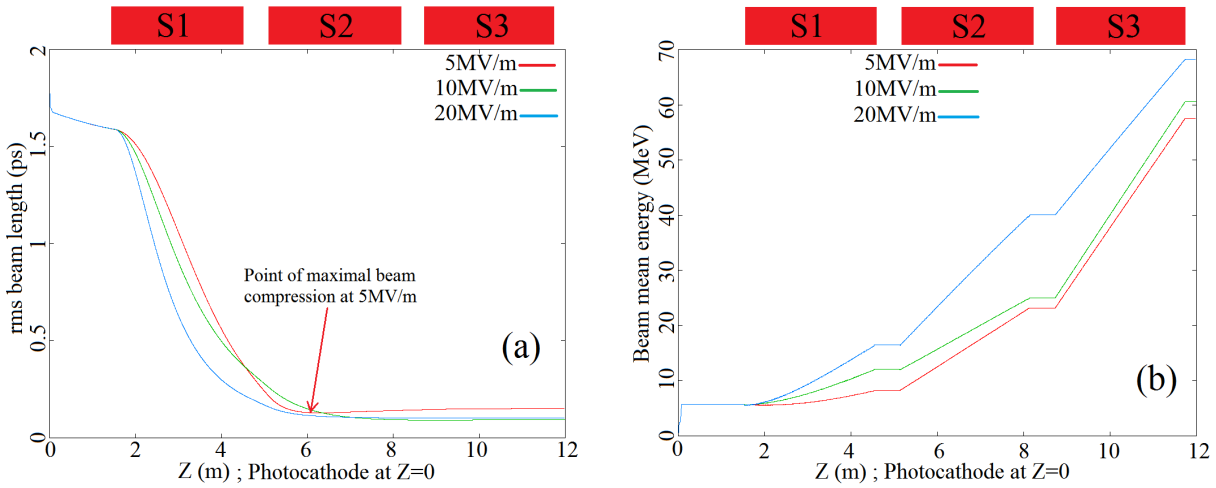

FIGURE *3.72 – Bunch rms length (a) and mean energy (b) up to the exit of S3 for different values of the mean accelerating field in S1 and S2. Simulation conditions : see Tab. 3.6.*

One can observe in Fig. 3.72 (a) that, compared to the optimal mean accelerating field of 10 MV/m, the bunch compression at 20 MV/m is faster in S1 (between 1.55 m and 4.55 m). This is simply due to the fact that this higher field value induces a higher

relative energy spread, and therefore a higher relative velocity spread. Nevertheless, the bunch lengths for these two fields then cross together in the middle of S2. This is explained by the fact that, as shown in Fig. 3.72 (b), the bunch energy gain is faster at 20 MV/m. The electrons become therefore too quickly ultra-relativistic and the bunch length is frozen before reaching the point of maximal compression. It explains the slight increase observed in Fig. 3.71 beyond the optimal mean accelerating field.

The sharp rise observed at lower mean accelerating fields is more complex, because it is due to the combination of two phenomena : the differential of velocity and the space-charge forces. First of all the point of maximal compression at 5 MV/m, pointed out in Fig. 3.72 (a) at Z =6.3 m, is located far upstream the one at 10 MV/m which is located at Z =8.8 m namely after the exit of S2. This is due to the fact that, as shown in Fig. 3.72 (b), the energy gain is faster at 10 MV/m in S1 thus resulting in a faster attenuation of the differential of velocity created by the differential acceleration along the bunch. It implies that the bunch compression at 10 MV/m, initially faster, becomes slower than at 5 MV/m around the exit of S1 at Z =4.5 m. The combination of this nearest position of the point of maximal compression and of the slowest energy gain implies that the electrons have not become sufficiently energetic at 5 MV/m to enable the freezing of the bunch length at the point of maximal compression. This leads to an increase in the bunch length once passed this point, which is clearly visible in Fig. 3.72 (a). The second phenomenon explaining the higher bunch lengths at mean accelerating fields lower than the optimal one is the space-charge forces. Indeed, one observes in Fig. 3.72 (a) that the rms bunch length at the point of maximal compression at 5 MV/m (130 fs at Z =6.3 m) is already higher than the one at 10 MV/m (91 fs at Z =8.8 m). This is due to the repulsive space-charge forces between the electrons of the bunch. They scale like the inverse square of the bunch energy and are therefore stronger at 5 MV/m than at 10 MV/m, because the energy at the point of maximal compression is lower (13 MeV at Z =6.3 m versus 26.5 MeV at Z =8.8 m, representing a factor of four on the intensity of the space-charge forces).

All the phenomena previously described are involved in the existence of an optimal mean accelerating field value in S1 and S2 to obtain the lowest possible bunch length at the exit of S3. It is important to note that the value of this optimum is dependent on the simulation conditions. For example, it will move towards higher values when the bunch charge increases. It is visible in Tab. 3.7, where it can be seen that for a bunch charge of 250 pC the minimal bunch length is for a mean accelerating field of 15 MV/m in S1 and S2. This is due to the space-charge forces which, being more intense, move the optimum towards higher field values where the bunch energy is higher.

Tab. 3.6 shows that the bunch rms relative energy spread is increasing with the mean accelerating field in S1 and S2. However it does not matter for the conservation of the bunch length, as shown in Fig. 3.72 (a) between Z =10 m and Z =12 m, because the bunch is ultra-relativistic (see Tab. 3.6). It is also visible in Tab. 3.6 that the bunch rms transverse radius decreases when the mean accelerating field in S1 and S2 increases. This is due to the transverse component of the traveling wave field, which has a focusing effect on the bunch. It becomes stronger, and therefore more focusing, when the wave amplitude increases. Finally, Tab. 3.6 shows that the bunch rms normalized transverse emittance increases with the mean accelerating field value in S1 and S2, which is a drawback for the

transport of the bunch after the exit of the third SLAC section. This increase is due to the stronger transverse components of the accelerating field when its amplitude increases.

Influence of the bunch charge

The next step has been to study the impact of the bunch charge on the bunch compression by the velocity bunching process. Tab. 3.7 shows the bunch properties at the exit of S3, in the configurations minimizing the rms bunch length, for three different bunch charges (250 pC, 50 pC and 10 pC). For each of these bunch charges, the mean accelerating field in S1 and S2 has been optimized as well as the three injection phases Ψ_i.

Beam charge	Current injected in the solenoid at the RF-gun exit	Mean accelerating field in the first two SLAC sections	$\Psi_1/\Psi_2/\Psi_3$	Mean energy (MeV)	rms relative energy spread (%)	rms length (fs)	rms transverse radius (mm)	rms transverse emittance (π.mm.mrad)	rms longitudinal emittance (π.mm.mrad)
250pC	198A	15MV/m	0.1° / 50° / 7°	**51,33**	**1,071**	**126**	**2,06**	**5,547**	**40,24**
50pC	196A	10MV/m	1.5° / 25.1° / 80.7°	**60,57**	**0,683**	**89,3**	**0,89**	**1,826**	**22,33**
10pC	196A	10MV/m	2.3° / 32.2° / 69.2°	**61,92**	**0,75**	**79,8**	**0,19**	**0,854**	**21,96**

TABLE *3.7 – Bunch properties at the exit of S3 for the configurations minimizing the bunch length. RF-gun mean accelerating field : 50 MV/m ; Gun RF-phase : −10° ; Laser pulse driving the RF-gun : 0.6 mm transverse radius and 2.5 ps rms duration ; Mean accelerating field in S3 : 12 MV/m.*

As expected, the minimum achievable rms bunch length decreases when the bunch charge decreases. This is due to the simultaneous decrease in the space-charge forces. However, it is relevant to notice that the decrease in the minimum achievable rms bunch length is only around 30% between 250 pC and 50 pC and around 10% between 50 pC and 10 pC whereas the bunch charge decreases by a factor of five in each case. Tab. 3.7 therefore shows that reducing the bunch charge is not a very efficient way to shorten it. This result is explained by the fact that the decrease in the space-charge forces due to the decrease in the bunch charge is partially compensated by the increase in the space-charge forces due to the decrease in the bunch transverse radius, clearly visible in Tab. 3.7. This decrease in the bunch rms transverse radius is explained by the fact that the focusing effect due to the transverse component of the traveling wave in the SLAC sections is more efficient when the bunch charge decreases, because of the decrease in the space-charge forces. An expected decrease in the bunch rms transverse emittance with the bunch charge, due to the decrease in the space-charge forces, is also observed in Tab. 3.7. It is a positive effect, since it will ease the transport of the bunch after S3.

Influence of the laser pulse parameters

The last approach I investigated to further lower the final bunch length is to decrease the bunch length at the entrance of S1, namely before compression by the velocity bunching process. This optimization is quite difficult since it is interrelated with the length

and transverse radius of the laser pulse driving the RF-gun, the Gun RF-phase φ and the current I_p injected in the solenoid at the RF-gun exit. The way I choose to perform this study is to more or less fix the laser properties, to have a certain number of cases, and to optimize for each case φ and I_p. I choose to increase the laser transverse radius up to 3 mm or 4 mm, to strongly decrease the space-charge forces in the RF-gun compared to the case with the typical 0.6 mm transverse radius of SPARC. I then optimize the mean accelerating field in S1 and S2 and the injection phases in the three SLAC sections [34] to have the lowest possible final rms bunch length, except for the case with a 1 ps laser rms length where I try to optimize the bunch rms transverse emittance. Tab. 3.8 shows the bunch properties at the exit of S3 for the studied laser configurations.

Laser rms length	Laser transverse radius	Gun RF-phase	Current injected in the solenoid at the RF-gun exit	Mean accelerating field of the SLAC sections (MV/m)	Mean energy (MeV)	rms relative energy spread (%)	rms length (fs)	rms transverse radius (mm)	rms transverse emittance (π.mm.mrad)	rms longitudinal emittance (π.mm.mrad)
2ps	3mm	-19°	171A	20 / 20 / 12	**68.72**	**0.555**	**51.3**	**0.3**	**6.738**	**11.06**
1.8ps	3mm	-20°	162A	20 / 20 / 12	**68.23**	**0.354**	**63.7**	**0.49**	**6.686**	**8.46**
1.5ps	4mm	-21°	156A	20 / 20 / 12	**47.48**	**0.283**	**70.7**	**0.16**	**6.576**	**4.66**
1ps	4mm	-14°	151A	20 / 20 / 12	**111.82**	**0.189**	**78.0**	**1.65**	**3.795**	**4.14**
500fs	4mm	-25°	146A	10 / 10 / 12	**43.13**	**0.373**	**78.7**	**0.37**	**9.899**	**5.46**
100fs	4mm	-25°	144A	15 / 15 / 12	**44.60**	**0.395**	**82.8**	**0.86**	**11.904**	**4.89**

TABLE *3.8 – Bunch properties at the exit of S3 for the configurations minimizing the bunch length or the transverse emittance (case at 1 ps). RF-gun mean accelerating field : 50 MV/m ; Bunch charge : 50 pC.*

It is visible by comparing Tab. 3.8 with Tab. 3.7 that the bunch rms transverse emittance has strongly increased. Indeed, for the bunch charge of 50 pC, it grows up from 1.8 π.mm.mrad in Tab. 3.7 to 6.7 π.mm.mrad for the laser pulse length of 2 ps rms in Tab. 3.8, representing an increase of 270%. To understand this increase, it is relevant to both superimpose the bunch rms transverse emittance and bunch rms transverse radius curves for these two cases. This is shown in Fig. 3.73.

In Fig. 3.73 it is visible that the increase in the bunch transverse emittance for the case with a 2 ps - 3 mm laser pulse compared to the case with a 2.5 ps - 0.6 mm laser pulse takes place at two specific locations of the beamline : the RF-gun and S1 (between Z =1.55 m and Z =4.55 m).

At the exit of the gun, the rms bunch transverse emittance is already 3.7 π.mm.mrad for the 2 ps - 3 mm laser pulse, while it is only of 0.9 π.mm.mrad for the 2.5 ps - 0.6 mm laser pulse. This is due to the higher transverse radius of the laser pulse, which implies an increase in the thermal emittance at the bunch emission from the photocathode (see Eq. 3.9). The bunch has also a higher rms transverse radius during its motion in the RF-gun. It implies that higher transverse electric fields are applied to the electrons, resulting

34. For the laser pulse rms length of 500 fs and 100 fs, the compression by velocity bunching does not correspond anymore to the first compression scheme or to the second one described in the introduction of Sec. 3.3.3. I simply optimized the mean accelerating fields of the SLAC sections and the injection phases in them to minimize the final rms bunch length.

also in an increase in the bunch transverse emittance.

The strong increase in the bunch transverse emittance observed in S1, for the case with a 2 ps - 3 mm laser pulse, is explained by the fact that the values of the Gun RF-phase φ and of the current I_p injected in the solenoid at the RF-gun exit are not suited to perform the bunch emittance compensation process [121, 66]. One can note that this increase in the bunch transverse emittance also appears, to a smaller extent, for the case with a 2.5 ps - 0.6 mm laser pulse.

This increase in the bunch rms transverse emittance in S1 can be avoided by a correct tuning of φ and I_p. This is called the bunch emittance compensation process. I optimize φ and I_p in this way for the case with a 1 ps - 4 mm laser pulse (see Tab. 3.8 fourth line). Fig. 3.74 shows the evolution of the bunch rms transverse emittance for this case. It is clearly visible that, opposite to Fig. 3.73, there is no increase of the bunch transverse emittance in S1 (there is even a decrease). It results in a much lower final bunch transverse emittance than for the case with a 2 ps - 3 mm laser pulse.

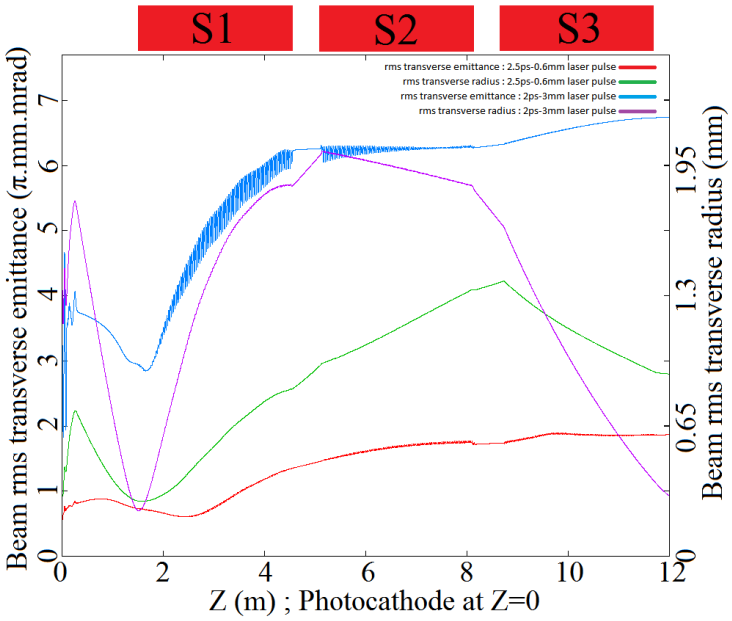

FIGURE *3.73 – Bunch rms transverse emittance and bunch rms transverse radius up to the exit of S3. Simulation conditions : see Tab. 3.7 second line for the blue and green curves ; see Tab. 3.8 first line for the red and purple curves.*

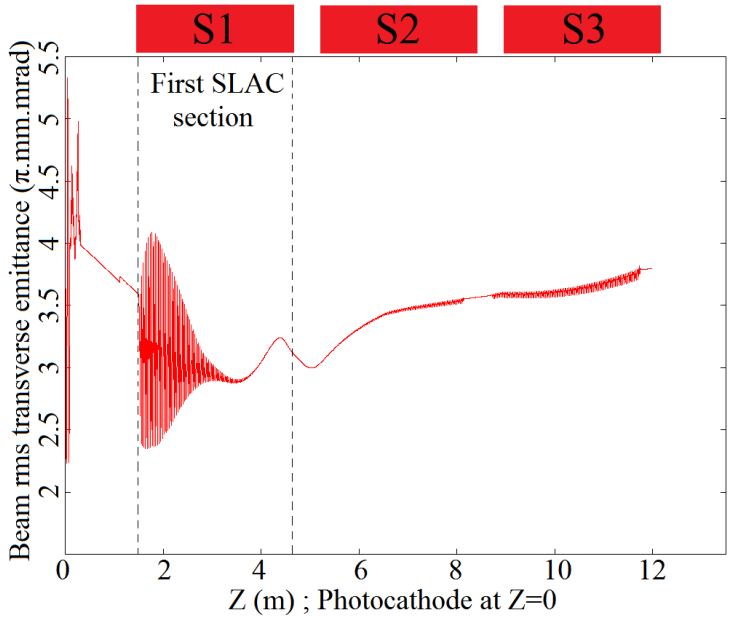

FIGURE *3.74 – Bunch rms transverse emittance up to the exit of S3. Simulation conditions : see Tab. 3.8 fourth line.*

Comparing Tab. 3.8 with Tab. 3.7, it appears that the rms bunch length decreases significantly between the case with a 2.5 ps - 0.6 mm laser pulse (89.3 fs rms for a bunch charge of 50 pC) and the one with a 2 ps - 3 mm laser pulse (51.3 fs rms for a bunch charge of 50 pC), the decrease being of 42.6%. This decrease is not due to the decrease in the laser pulse length since, as it can be seen in Tab. 3.8, the minimum achievable final rms bunch length increases when the laser pulse length decreases. To understand the nature of this decrease it is relevant to superimpose the rms bunch length curves for the two aforementioned cases. It is shown in Fig. 3.75.

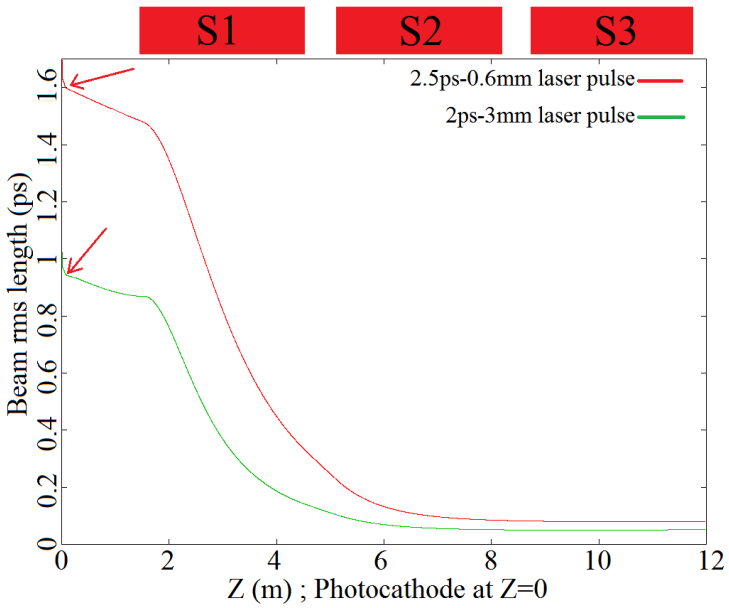

FIGURE *3.75 – Bunch rms length up to the exit of S3. Simulation conditions : see Tab. 3.7 second line (red curve) ; see Tab. 3.8 first line (green curve). Red arrows mark the exit of the RF-gun.*

It is clearly visible in Fig. 3.75 that, at the exit of the RF-gun, the discrepancy on the bunch rms length between the case with a 2.5 ps - 0.6 mm laser pulse (red curve) and the one with a 2 ps - 3 mm laser pulse (green curve) is about 41% (1.6 ps versus 0.95 ps), which is almost equal to the final discrepancy of 42.6%. The discrepancy on the bunch rms length between the two cases is therefore completely created in the RF-gun and is not compensated thereafter during the compression process by velocity bunching.

This discrepancy is due to the much larger transverse radius, which is 3 mm for the 2 ps laser pulse and 0.6 mm for the 2.5 ps laser pulse. The space-charge forces in the RF-gun are therefore less intense. As a result the bunch compression in the RF-gun, mainly induced by the fact that the electric field on the photocathode is increasing in time during the bunch emission, is stronger. In fact, the bunch compression factor in the RF-gun is 2.11 for the case with a 2 ps - 3 mm laser pulse (2 ps $\Rightarrow$ 0.95 ps) while it is only 1.56 for the case with a 2.5 ps - 0.6 mm laser pulse (2.5 ps $\Rightarrow$ 1.6 ps).

The fact that a lower rms bunch length at the RF-gun exit and at the entrance of S1 leads to a lower final rms bunch length at the exit of S3 is actually not always true. It

is true only when the longitudinal space-charge forces are not too strong, namely when the laser pulse driving the RF-gun is not too short (this is the case at 2.5 ps and 2 ps for example). When it is too short, the longitudinal space-charge forces create strong non-linearities in the bunch time/energy phase-space, which become more important when the laser pulse is shorter. These non-linearities prevent one from reaching a shorter final rms bunch length, even when it is initially shorter at the beginning of the compression by velocity bunching. It is visible in Tab. 3.8 where the case with a laser pulse of 100 fs rms does not allow reaching a lower final rms bunch length (82.8 fs rms versus 78.7 fs rms) than the case with a laser pulse of 500 fs rms, even though the rms bunch length at the entrance of the first SLAC section is 250 fs for the 100 fs rms laser pulse and 300 fs for the 500 fs rms laser pulse.

It is noteworthy in Tab. 3.8 that I did not succeed in optimizing the laser pulse parameters to obtain the lowest possible final rms bunch length. In fact, as previously mentioned, the final rms bunch length decreases when the laser pulse length increases up to 2 ps and I did not use higher values of the laser pulse length (at least not with a 3 mm transverse radius). It will therefore be interesting to use a laser pulse longer than 2 ps rms, but with a transverse radius significantly higher than the 0.6 mm previously used at 2.5 ps, to see if it brings some improvement in the final rms bunch length. However one should not forget, as previously said, that this increase in the laser pulse transverse radius comes with an unavoidable increase in the bunch rms transverse emittance due to the increase of the thermal emittance and to the beam dynamics in the RF-gun. This increase in the bunch rms transverse emittance can also be amplified in S1 if the bunch emittance compensation process is not correctly performed (see Fig. 3.73).

Study at 10 pC with a 1 ps - 4 mm laser pulse

Another way to further decrease the final rms bunch length is to redo the study as a function of the laser parameters for a bunch charge of 10 pC. For time reason, I choose to only study the case with a 1 ps rms length and 4 mm transverse radius laser pulse driving the RF-gun. After optimization of the mean accelerating fields in the SLAC sections (20 MV/m ; 20 MV/m ; 13 MV/m) and of the injection phases in them (1.1° ; 30.0° ; 84.8°), I obtained the following bunch properties : Mean energy of 84.53 MeV ; rms relative energy spread of 0.225% ; rms length of 27.1 fs ; rms transverse radius of 1.65 mm ; rms transverse emittance of 4.53 π.mm.mrad.

The achieved rms length of 27.1 fs represents a significant gain compared to the 78.0 fs rms obtained with the same laser parameters for a bunch charge of 50 pC (see Tab. 3.8 fourth line), the decrease being close to a factor of three (65%). This gain is much more important than the one obtained when I used a small laser transverse radius of 0.6 mm. In fact, it was only of 10% (89.3 fs rms at 50 pC and 79.8 fs rms at 10 pC). The increase in the laser transverse radius therefore increases the gain provided by a decrease in the bunch charge.

One can note that the final rms transverse emittance of 4.53 π.mm.mrad is slightly higher than the 3.80 π.mm.mrad obtained with a bunch charge of 50 pC (see Tab. 3.8

fourth line). This is due to the fact that I have less well optimized the bunch emittance compensation process for this case at 10 pC than for the one at 50 pC. It demonstrates once again that the bunch rms transverse emittance is very sensitive to the optimization of the bunch emittance compensation process.

3.3.3.3 Second scheme of ultra-short electron bunches generation

As a reminder, this second scheme consists in a bunch compression taking place in S1 and S2, namely in a slower compression than for the first scheme presented in Sec. 3.3.3.2.

To perform this slower compression, the injection phase Ψ_1 in S1 has to be set around 6° higher than the one Ψ_{1_m} allowing a maximal bunch compression at its exit, while it is only around 3° higher in the first scheme. This choice of Ψ_1 results in a strong undercompression of the bunch in S1. This undercompression corresponds to the fact that the differential acceleration is not sufficiently marked along the bunch to achieve its compression. The injection phase Ψ_2 in S2 has then to be optimized in the same way, and for the same reasons, as Ψ_1 has been optimized in the first compression scheme (see Sec. 3.3.3.2). The only new fact to take into account is that, in the second compression scheme, the bunch has already gained energy in S1. It is therefore necessary to ensure that it loses energy or gains only a little energy in S2. This means injecting the bunch in S2 at a phase Ψ_2 close to 0°, where the accelerating field is zero. Otherwise, the bunch would become too quickly ultra-relativistic and its length would be frozen before the end of the compression. In the first compression scheme, the compression is almost finished at the end of S1 and the bunch is injected in S2 at a phase Ψ_2 closer from 90°, where the accelerating field is maximal, to freeze its length.

Influence of the S1 and S2 mean accelerating field

To study the performances allowed by this second scheme of bunch compression by velocity bunching, I follow the same approach as for the first scheme. I therefore start by searching the configurations allowing a minimal rms bunch length at the exit of S3 for several mean accelerating field values in S1 and S2. Tab. 3.9 shows the obtained bunch properties at the exit of S3 for these configurations.

One observes in Tab. 3.9 the existence of an optimal value of the mean accelerating field in S1 and S2 to obtain a minimum bunch rms length at the exit of S3. The phenomena responsible of the existence of this optimal value are the same as in the first compression scheme (see Sec. 3.3.3.2 and Tab. 3.6). The only difference is that the compression now takes place in S1 and S2 and not only in S1.

Mean accelerating field in the first two SLAC sections	Current injected in the solenoid at the RF-gun exit	Mean accelerating field in the third SLAC section	$\Psi_1/\Psi_2/\Psi_3$	Mean energy (MeV)	rms relative energy spread (%)	rms length (fs)	rms transverse radius (mm)	rms transverse emittance (π.mm.mrad)	rms longitudinal emittance (π.mm.mrad)
5MV/m	194A	13MV/m	4.6° / 8.8° / 74.9°	**50.8**	**0.533**	**85.2**	**0.87**	**1.288**	**13.54**
10MV/m	196A	12MV/m	5.4° / 8.0° / 69.1°	**51.56**	**1.099**	**76.8**	**0.55**	**1.723**	**25.57**
15MV/m	198A	12MV/m	6.4° / 6.1° / 33.3°	**52.95**	**1.894**	**85.2**	**0.24**	**1.918**	**43.27**
20MV/m	198A	12MV/m	5.4° / 4.6° / 31.1°	**41.32**	**3.04**	**87.2**	**0.32**	**2.115**	**65.24**

TABLE *3.9 – Bunch properties at the exit of S3 for the configurations minimizing the bunch length. Bunch charge : 50 pC; RF-gun mean accelerating field : 50 MV/m; Gun RF-phase : −10° ; Laser pulse driving the RF-gun : 0.6 mm transverse radius and 2.5 ps rms duration.*

Comparison of the two compression schemes

Comparing Tab. 3.9 with Tab. 3.6 it is visible that the compression along S1 and S2 allows obtaining a substantial gain on the final rms bunch length compared to the compression along S1. In fact, at the optimal mean accelerating field of 10 MV/m in S1 and S2, the final rms bunch length decreases from 89.3 fs to 76.8 fs between the two schemes, namely a decrease of 14%. It is relevant to superimpose the rms bunch length curves for these two cases, to visualize the differences between the two compression schemes. It is shown in Fig. 3.76 (a). Fig. 3.76 (b) shows the evolution of the bunch mean energy and rms relative energy spread for these two cases. It is helpful to understand how the second compression scheme works and why it allows reaching lower final rms bunch length.

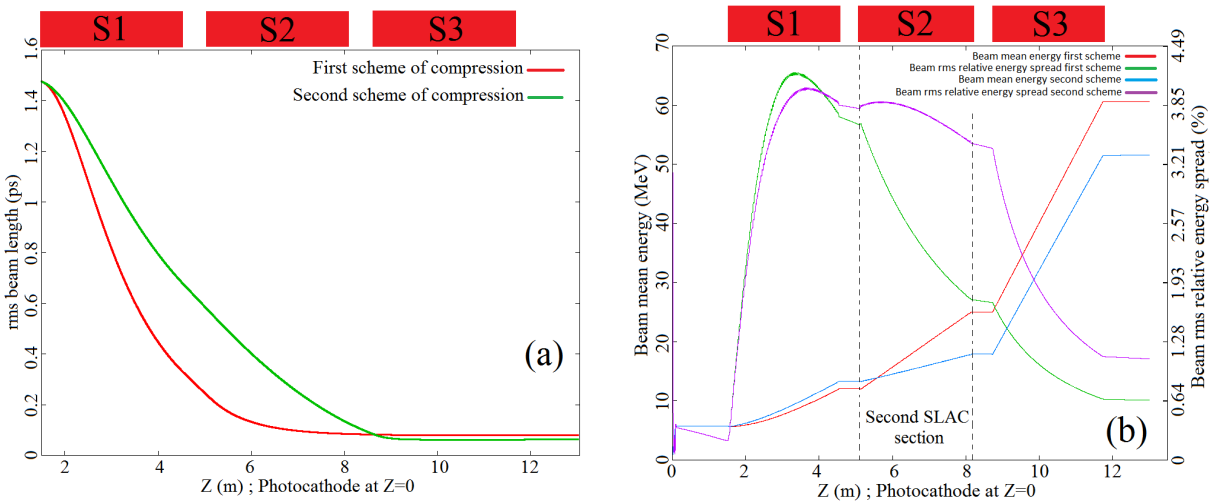

FIGURE *3.76 – Bunch rms length up to the exit of S3 (a). Bunch mean energy and rms relative energy spread up to the exit of S3 (b). Simulation conditions : see Tab. 3.6 fifth line for the red curve (a) and (b) and for the green curve (b); see Tab. 3.9 second line for the green curve (a), the blue curve (b) and the purple curve (b).*

Fig. 3.76 (a) highlights very well the fact that the bunch compression is slower in the second compression scheme than in the first one. Fig. 3.76 (b) shows that, for the second compression scheme, the bunch energy gain is very low and the relative energy spread is kept to a high value in S2. This is explained by the injection of the bunch in S2 at phase Ψ_2 close to 0°. The combination of these two phenomena allows pursuing the bunch compression in S2.

The reason explaining the lower final rms bunch length achievable in the second compression scheme is precisely that the bunch compression is slower. This allows moving away the point of maximal compression. Indeed, this point is at Z =8.8 m (shortly after the exit of S2) in the first compression scheme (see Fig. 3.76 (a) red curve), while it is at Z =11.5 m (shortly before the exit of S3) in the second compression scheme (see Fig. 3.76 (a) green curve). It allows the bunch to gain much more energy in the successive SLAC sections before reaching the point of maximal compression. In fact, the bunch mean energy at the point of maximal compression is 27.9 MeV in the first compression scheme (see Fig. 3.76 (b) red curve), while it is 48.3 MeV in the second compression scheme (see Fig. 3.76 (b) blue curve). This higher energy induces less intense space-charge forces around the point of maximal compression [35], which allows reaching a lower rms bunch length at this point.

Influence of the bunch charge

Then, I vary the bunch charge to evaluate the achievable gain on the rms bunch length. For each of the selected bunch charges, the mean accelerating field in S1 and S2 has been optimized as well as the three injection phases Ψ_i in the SLAC sections to minimize the final rms bunch length. Tab. 3.10 presents the results of the simulations for different bunch charges.

Beam charge	Current injected in the solenoid at the RF-gun exit	Mean accelerating field in the first two SLAC sections	Mean accelerating field in the third SLAC section	$\Psi_1/\Psi_2/\Psi_3$	Mean energy (MeV)	rms relative energy spread (%)	rms length (fs)	rms transverse radius (mm)	rms transverse emittance (π.mm.mrad)	rms longitudinal emittance (π.mm.mrad)
250pC	200A	15MV/m	12MV/m	6.1° / 2.9° / 74.8°	**53.79**	**2.129**	**115**	**0.92**	**5.226**	**77.03**
50pC	198A	10MV/m	12MV/m	5.4° / 8.0° / 69.1°	**51.56**	**1.099**	**76.8**	**0.55**	**1.723**	**25.57**
10pC	196A	5MV/m	13MV/m	7.3° / 10.6° / 77.7°	**51.98**	**0.583**	**62.4**	**0.33**	**0.673**	**11.02**

TABLE *3.10 – Bunch properties at the exit of S3 for the configurations minimizing the bunch length. RF-gun mean accelerating field : 50 MV/m ; Gun RF-phase : −10° ; Laser pulse driving the RF-gun : 0.6 mm transverse radius and 2.5 ps rms duration.*

One can see in Tab. 3.10 that the final rms bunch length decreases when the bunch charge decreases. The reason is, as for the first compression scheme (see Sec. 3.3.3.2 and Tab. 3.7), the decrease in the space-charge forces. As for the first compression scheme, the decrease in the final rms bunch length (18.8% between 50 pC and 10 pC) is quite small

35. In the developed example there is a factor of three between the space-charge forces.

compared to the one in the bunch charge. This is due to the decrease in the bunch rms transverse radius when the bunch charge decreases, as previously shown in Sec. 3.3.3.2.

Influence of the laser pulse parameters

The next step to further lower the final rms bunch length obtained with the second compression scheme has been to increase the transverse radius of the laser pulse driving the RF-gun, from 0.6 mm to 3 mm or 4 mm, and to vary the rms length of this laser pulse. Tab. 3.11 shows the results of the simulations for different laser pulse parameters.

Laser rms length	Laser transverse radius	Gun RF-phase	Current injected in the solenoid at the RF-gun exit	Mean accelerating field of the three SLAC sections	Mean energy (MeV)	rms relative energy spread (%)	rms length (fs)	rms transverse radius (mm)	rms transverse emittance (π.mm.mrad)	rms longitudinal emittance (π.mm.mrad)
2ps	3mm	-19°	171A	20 / 20 / 12	**56.40**	**1.25**	**42.8**	**0.42**	**8.282**	**13.28**
1.5ps	4mm	-21°	156A	20 / 20 / 13	**55.01**	**0.69**	**37.6**	**0.31**	**7.511**	**7.12**
1ps	4mm	-14°	151A	20 / 20 / 13	**56.94**	**0.61**	**31.8**	**0.25**	**6.815**	**6.25**

TABLE *3.11 – Bunch properties at the exit of S3 for the configurations minimizing the bunch length. RF-gun mean accelerating field : 50 MV/m ; Bunch charge : 50 pC. For each laser pulse length, I optimized the mean accelerating field in S1 and S2 and the injection phases Ψ_i in the three SLAC sections to have the lowest possible final rms bunch length.*

Comparing Tab. 3.11 with Tab. 3.8, it clearly appears that the behaviors of the two compression schemes with the rms length of the laser pulse driving the RF-gun are very different regarding the minimization of the final rms bunch length. Indeed, the first compression scheme is optimized for long laser pulse rms length ($\geq$ 2 ps see Tab. 3.8) while the second one is optimized for short laser pulse rms length ($\leq$ 1 ps see Tab. 3.11).

The comparison of Tab. 3.10 and Tab. 3.11 shows that, for the bunch charge of 50 pC, the combined increase in the laser pulse transverse radius (from 0.6 mm to 4 mm) and decrease in the laser pulse rms length (from 2.5 ps to 1 ps) allows a significant gain on the final rms bunch length achieved with the second compression scheme. In fact, it decreases from 76.8 fs rms for the 2.5 ps - 0.6 mm laser pulse (see Tab. 3.10 second line) to 31.8 fs rms for the 1 ps - 4 mm laser pulse (see Tab. 3.11 third line), namely a decrease of 58.6%.

The evolution of the final rms bunch length indicates that the optimal value of the laser pulse rms length for the second compression scheme is probably below 1 ps. A trail to further shorten the final rms bunch length in the second compression scheme is therefore to further pursue the optimization of the rms laser pulse length below 1 ps.

However it is already possible to say that, for the bunch charge of 50 pC, this optimal laser pulse rms length is higher than 500 fs. In fact, for a laser pulse rms length of 500 fs and a laser transverse radius of 4 mm, the bunch compression by velocity bunching does not correspond anymore to the first compression scheme developed in Sec. 3.3.3.2 or to the second compression scheme developed in Sec. 3.3.3.3. The reason is that, for these short laser pulse rms length, the correlation of the bunch time/energy phase-space at the

entrance of S1 is not optimal to perform the velocity bunching. Namely, because of the strong space-charge forces, the most energetic electrons are in the bunch head while the less ones are in the bunch tail, as in the example of Fig. 3.68 (a). As a result, a significant part of the time in S1 is used to reverse this correlation. Then the compression slowly starts between the end of S1 and the beginning of S2. Finally, it ends very quickly between the end of S2 and the entrance of S3. All these facts are clearly visible in Fig. 3.77 which shows the evolution of the rms bunch length up to the exit of S3.

For the laser pulse rms length of 500 fs, the final bunch rms length after optimization is of 78.7 fs and therefore far higher than the 31.8 fs obtained with the 1 ps - 4 mm laser pulse in the second compression scheme. It implies that, for the laser transverse radius of 4 mm, the optimal laser pulse rms length for the second compression scheme is between 1 ps and 500 fs.

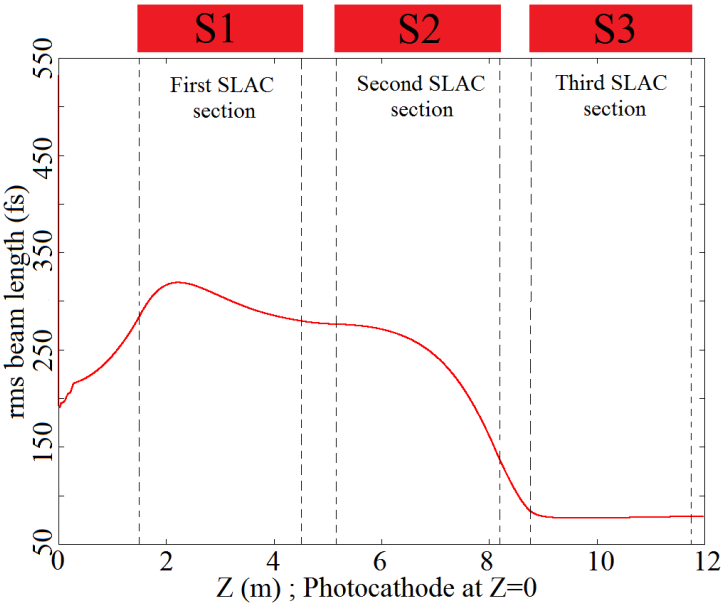

FIGURE *3.77 – Bunch rms length up to the exit of S3. Simulation conditions : see Tab. 3.8 fifth line. I optimize the mean accelerating field in S1 and S2 and of the injection phases Ψ_i in the three SLAC sections.*

Study at 10 pC with a 1 ps - 4 mm laser pulse

I choose to only study the case with a 1 ps rms length and 4 mm transverse radius laser pulse driving the RF-gun for a bunch charge of 10 pC. After optimization of the mean accelerating fields in the SLAC sections (20 MV/m ; 20 MV/m ; 13 MV/m) and of the injection phases in them (5.1° ; 3.6° ; 50.3°), I obtained the following bunch properties : Mean energy of 51.32 MeV ; rms relative energy spread of 0.792% ; rms length of 19.4 fs ; rms transverse radius of 0.68 mm ; rms transverse emittance of 6.80 π.mm.mrad.

The achieved bunch rms transverse emittance of 6.80 π.mm.mrad is significantly higher than the one of 4.53 π.mm.mrad obtained in the first compression scheme with a

bunch charge of 10 pC and a 1 ps - 4 mm laser pulse at the end of Sec. 3.3.3.2. It does not mean that the second compression scheme deteriorates the bunch transverse emittance with respect to the first one. Actually, this is only due to the fact that I do not perform at all the bunch emittance compensation process for the case studied at 10 pC in the second compression scheme, while I try to optimize it a little for the case studied at 10 pC in the first compression scheme. Comparing Tab. 3.9 with Tab. 3.6 and Tab. 3.10 with Tab. 3.7 one can see that the bunch rms transverse emittances are of the some order between the second and the first bunch compression scheme, and even slightly lower for the second one. The key point to optimize the bunch rms transverse emittance is not the bunch compression scheme, but the optimization of the bunch emittance compensation process.

3.3.3.4 Conclusions and prospects

The second bunch compression scheme, involving a slow compression of the bunch in S1 and S2, is more favorable than the first one, involving a fast compression of the bunch in S1, to minimize the final rms bunch length. In fact, the obtained final rms bunch length is of 31.8 fs at 50 pC and of 19.4 fs at 10 pC for the second compression scheme while it is of 51.3 fs at 50 pC and of 27.1 fs at 10 pC for the first compression scheme.

The final bunch rms transverse emittance is of the same order in the first and in the second compression scheme. None of the two compression schemes is favorable concerning the bunch rms transverse emittance. The key factor to optimize the bunch transverse emittance is to fine-tune the current injected in the solenoid at the RF-gun exit and in the solenoids surrounding S1 and S2, to optimize the bunch emittance compensation process.

The achieved final rms bunch length of 19.4 fs is still a little too high for an optimal acceleration of the bunch in the plasma acceleration scheme described in the introduction of Sec. 3.3.3. Indeed, this rms bunch length corresponds to 6 μm and the wavelength of the accelerating wave created in the plasma by the laser is below a few tens of micrometers. It implies that the different electrons of the bunch will still be subject to significantly different accelerating fields in the plasma wave, and that the rms bunch length has to be further decreased to optimize the plasma acceleration of the bunch.

The main trail to further decrease the final rms bunch length is to better optimize the rms length and the transverse radius of the laser pulse driving the RF-gun. Indeed, as shown in Tab. 3.8 and Tab. 3.11, the gain is already quite significant compared to the standard laser pulse of SPARC (2.5 ps of rms length and 0.6 mm of transverse radius). A fine tuning of the laser pulse parameters can further improve the achievable rms bunch length. It is also relevant to redo this optimization for a bunch charge of 10 pC, or lower, since the gain on the final rms bunch length due to the decrease in the bunch charge is more significant once the laser pulse is optimized compared to the gain when the standard laser pulse of SPARC is used.

3.4 Conclusion : comparison of the three methods

In the simulations performed in Chapter 3, I was mainly interested in the rms length and in the rms transverse emittance of the electron bunch. The comparison that I will draw in this section between the three methods used to generate short electron bunches will therefore rely on these two parameters. A particular attention has also been given to the generation of a longitudinally modulated electron beam made of short bunches.

The rms bunch length

Concerning the rms length, the use of a short laser pulse ($<$ 100 fs rms) directly in the RF-gun has shown some limits for the generation of very short electron bunches ($<$ 100 fs rms). This limitation is due to the very strong effects of the space-charge forces, just after the bunch emission from the photocathode, which blow up the bunch and prevent to translate the duration of the laser pulse into the duration of the electron bunch. Indeed, when using a 50 fs rms laser pulse, the bunch rms length cannot be lowered below 100 fs at the exit of a booster cavity located 30 cm after the photocathode and allowing increasing the bunch mean energy up to 20 MeV. This is the case even when the bunch charge is very low (1 pC), and when shaping of the laser pulse (3D ellipsoid) is performed to reduce the effects of space-charge forces (see Tab. 3.3 in Sec. 3.1.3.7). A value of 109 fs rms is reached, at the exit of the booster cavity, for a 1 pC electron bunch generated by a 50 fs rms 3D ellipsoid laser pulse.

The magnetic compression and RF-compression (velocity bunching) methods have shown the capability to generate electron bunches with a much shorter rms length. The reason is that the compression is performed on a longer and already accelerated electron bunch, which allows reducing the effects of space-charge forces and therefore reaching shorter rms lengths. The velocity bunching technique is indeed able to produce electron bunches with an rms length of 19.4 fs for a bunch charge of 10 pC and of 31.8 fs for a bunch charge of 50 pC (see Tab. 3.11 in Sec. 3.3.3.3). It has also shown its ability to produce high-charge short electron bunches, since 115 fs rms are achieved without total optimization for a bunch charge of 250 pC (see Tab. 3.10 in Sec. 3.3.3.3). The magnetic compression can easily produce 100 fs rms electron bunches with a charge of 100 pC and a mean energy below 20 MeV (see Fig. 3.36 and Fig. 3.35 in Sec. 3.2.2.2). It has not been shown in this thesis, because it was not the approach of my study [36], but the magnetic compression can of course be used to reach shorter bunch rms length. For instance, 45 fs rms are achievable for a 16.2 MeV and 100 pC electron bunch, starting from a 1ps rms 3D Gaussian laser pulse, when the Gun RF-phase is set to $-20°$ and the booster one to $-45°$.

The bunch rms transverse emittance

36. The approach was to set the final rms bunch length to 100 fs and to study in which conditions the bunch transverse emittance was not deteriorated.

Concerning the bunch rms transverse emittance, each of the three methods developed in Chapter 3 have features which can deteriorate it in different conditions. For each of the three methods, the bunch rms transverse emittance is also not optimized in the same conditions as the bunch rms length. In my study, I mainly optimize the bunch rms length. It is therefore difficult to perform a direct comparison of the achieved bunch rms transverse emittances between the three methods. I therefore simply study individually for each method the mechanisms degrading the bunch transverse emittance.

When using a short laser pulse in an RF-gun, the rms transverse emittance can be heavily deteriorated by the strong effects of space-charge forces just after the bunch emission from the photocathode. For instance, it can be up to 5 π.mm.mrad for 100 pC electron bunch generated by a 3D Gaussian laser pulse (see Tab. 3.3 in Sec. 3.1.3.7). This limitation can be overcome either by lowering the bunch charge, the rms transverse emittance decreasing to 0.88 π.mm.mrad at 1 pC, or by using a laser shape reducing the effects of space-charge forces by linearizing them, the rms transverse emittance decreasing to 1.53 π.mm.mrad for a 100 pC electron bunch generated by a 3D ellipsoid laser pulse. Another limitation is that the bunch rms length is optimized for a quite large laser rms transverse radius, between 1.2 mm and 1.4 mm for a 100 pC electron bunch depending on the laser shape. It implies an increase of the thermal emittance (see Eq. 3.9 in Sec. 3.1.3.6), and therefore of the ultimate achievable bunch rms transverse emittance.

The transverse emittance can be deteriorated during the magnetic compression process by the emission of synchrotron radiation (coherent and incoherent) by the bunch and by the interaction of the bunch with this radiation. This effect can be massively lowered if the bunch has a strong time/energy correlation (chirp) at the chicane entrance. In this case, the magnetic strength required to compress the bunch and the bunch mean kinetic energy decrease implying a decrease in the emission of synchrotron radiation. This chirp can be controlled by using a booster RF-phase far away from the one maximizing the energy gain (see Fig. 3.39 in Sec. 3.2.2.3). The bunch rms transverse emittance after compression is then almost the same as at the chicane entrance. The typical achieved value, which can be improved by using a different laser pulse shape, is about 2.7 π.mm.mrad for a 100 pC and 100 fs rms electron bunch generated by a 1 ps rms 3D Gaussian laser pulse (see Fig. 3.40 in Sec. 3.2.2.3). This is much lower than when it is directly generated by an RF-gun, because of the lower effects of space-charge forces just after the bunch emission from the photocathode.

The compression of an electron bunch by the velocity bunching technique may be accompanied by a large degradation of its rms transverse emittance, if the emittance compensation process is not performed correctly [121, 66]. This is the case when the current injected in the solenoid magnets located at the RF-gun exit and around S1 have not the correct values. It is visible in Fig. 3.73 (blue curve) of Sec. 3.3.3.2, where the bunch rms transverse emittance is doubled in the accelerating section S1 where the velocity bunching is performed (between 1.5 m and 4.5 m). On the opposite, it shows no increase when the emittance compensation process is better performed (see Fig. 3.74 in Sec. 3.3.3.2). Another limitation is that the bunch rms length obtained by the velocity bunching process is optimized for a large transverse radius of the laser pulse driving the RF-gun, about 3 mm or 4 mm (see Fig. 3.75 in Sec. 3.3.3.2). It implies an increase of the thermal emittance (see

Eq. 3.9 in Sec. 3.1.3.6), and therefore of the achievable bunch rms transverse emittance. For instance, an rms value of 1.72 π.mm.mrad is obtained for a 50 pC and 77 fs rms electron bunch generated by a 2.5 ps rms and 0.6 mm transverse radius laser pulse (see Tab. 3.10 in Sec. 3.3.3.3). It increases up to 6.82 π.mm.mrad for the 50 pC and 32 fs rms electron bunch generated by a 1 ps rms and 4 mm transverse radius laser pulse (see Tab. 3.11 in Sec. 3.3.3.3).

The case of a longitudinally modulated electron beam

A last important point is the generation of a longitudinally modulated electron beam made of short bunches. As shown in Sec. 3.2.3, the conservation of the beam longitudinal modulation during the magnetic compression process is very complicated and requires a fine tuning of the beam longitudinal phase-space shape at the entrance of the magnetic chicane, in order to compensate the non-linearities introduce by the chicane during the compression process. In Sec. 3.2.3, the intended compression factor was only four and only for a train of five bunches. The difficulty will increase with the number of bunches and the desired compression factor. The compression of a longitudinally modulated electron beam by the velocity bunching technique has not been tested in my thesis. However, like the magnetic compression technique, the velocity bunching uses the time/energy correlation to compress the beam. As a result, a fine tuning of the beam longitudinal phase-space shape at the entrance of the accelerating section used to perform compression by velocity bunching is also necessary to preserve the beam longitudinal modulation during its compression.

It is highly preferable to generate a longitudinally modulated electron beam directly in an RF-gun by using a longitudinally modulated laser pulse to drive it. In fact, it has been shown in Sec. 3.1.3.8 that the initial parameters (the spacing between the bunches and the bunch rms length) of a modulated beam with thirteen bunches can be preserved at the RF-gun exit better than 15% for a total charge of 20 pC and better than 20% for a total charge of 200 pC when fine-tuning the Gun RF-phase. The relative fluctuations in the spacing and in the length of the bunches are less important than in the magnetic compression of a longitudinally modulated beam.

Conclusion

The scope of this thesis was the study of the generation of short electron beams and their diagnostics.

A method allowing measuring the bunch charge with a scintillating screen has been developed. This method has proven to be suitable to measure very low bunch charges ($<$ 100 fC), which are not measurable with the classical beam charge measurement devices used on low energy electron accelerators (ICT and Faraday Cup). A lowest bunch charge of 15 $\pm$ 10 fC has been measured by using a LANEX screen on PHIL. This value has been confirmed by two independent measurements : a direct charge measurement with a diamond detector and an indirect charge estimation from the measurement of the energy of the laser pulse driving the PHIL RF-gun. It can be further improved by shielding the CCD camera imaging the scintillating screen against the X-rays and by cooling it down to reduce the thermal noise. This single-shot measurement is perfectly suitable to be used in laser-plasma acceleration experiments where the beam properties, and therefore the beam charge, can strongly vary from one beam to the next.

I applied the 3-screen and 3-gradient methods, classically used to measure the rms transverse emittance of high energy electron beams, to few MeV electron bunches generated by an RF-gun. The measurements performed on the PHIL facility have shown that the 3-gradient method performed with a solenoid magnet is perfectly suitable to measure the rms transverse emittance of this kind of bunch. In fact, for a 100 pC electron bunch, the discrepancy with the ASTRA beam dynamics simulations is below 50% above 3 MeV and becomes lower than 20% above 3.6 MeV. It has also been experimentally verified that for a lower charge electron bunch of 10 pC the discrepancy with the ASTRA simulations is higher and increases with the bunch energy. The classical 3-screen method, without inclusion of the space-charge forces and with a pure drift space between the screens, has shown to be totally unsuitable to perform the measurement of the rms transverse emittance of a few MeV and 100 pC electron bunch at PHIL, the discrepancy with the ASTRA simulations being typically of a factor of ten. The inclusion of the space-charge forces, assuming a 3D Gaussian bunch charge density, via the formalism of the beam envelope equation leads to a significant gain by strongly decreasing the discrepancy with the ASTRA simulations (64% for a 4.5 MeV and 135 pC electron bunch). However, the test of this evolved 3-screen method has been severely restricted by the uncertainties on the real bunch length at PHIL. Measurements have therefore to be performed on other facilities to fully evaluate

the potential of this evolved 3-screen method.

I developed a method to measure the beam mean energy through the beam transverse displacement on a scintillating screen induced by a steering magnet. The results coming from this method have been compared with the ones coming from bunch energy spectra measured with the dipole magnet at PHIL. The agreement has shown to be very satisfactory, since the discrepancy is 2.5% at 3.1 MeV and falls down to 0.2% at 4.5 MeV, proving that this method is a good alternative to the use of a dipole magnet. It has also been demonstrated that only two bunch position measurements at both extremities of the scintillating screen are sufficient to perform this measurement without losing accuracy, which makes it very fast.

After a check of its validity on a high energy (67 MeV) electron beam at the HELIOS Linac of SOLEIL, I applied the 3-phase method to measure the rms length of a few MeV electron bunch generated by an RF-gun. Measurements have been performed on the PITZ facility for a 20 pC electron bunch with several time profile of the laser pulse driving the RF-gun. The accuracy of the 3-phase method has proven to be very good, since the discrepancy with the ASTRA simulations remains below 15% in the tested configurations. It is also true in the subpicosecond range, since an rms bunch length of 900 fs has been measured with a precision better than 5%. It demonstrates that the 3-phase method, because of its cheap and technologically simple aspects, is a good alternative to the classical bunch length measurement methods, more expensive and technologically complicated to implement. A further study will be to apply the 3-phase method on electron bunches with a lower rms length, a few hundred of femtoseconds, to investigate its possibilities in this bunch length range. Measurements of this type will soon be possible on the PHIL facility, thanks to the implementation of a booster cavity and to the use of a 100 fs rms laser pulse, coming from the Laserix facility, to drive the RF-gun. Another further study will be to develop a 3-phase method taking into account the effects of space-charge forces, to see if it is possible to apply it to very dense electron bunches. Measurements have been performed at PITZ with 1 nC electron bunches and could be used as a test for this new method.

The 3-gradient method, the 3-phase method and the measurement of the beam mean energy with a steering magnet are very cheap and technologically simple methods, but they proved to be reliable for the measurement of few MeV electron bunches generated by an RF-gun. They will therefore be very useful for the daily operation of the PHIL facility, and also for the commissioning of the THOMX facility, which is intended to start at the end of 2016.

I greatly contributed to the development and test on the PHIL facility of a bunch length measurement device using the Cerenkov light emitted when the electron bunch goes through a Sapphire crystal. I especially established the electron bunch transport conditions to maximize the intensity of the Cerenkov light extracted from the beamline and transported up to the streak camera. I also participated in the development of the optical transport line between the Sapphire crystal and the streak camera, by purchasing a new type of mirror which led to a significant gain of a factor 48 on the Cerenkov light at the streak camera entrance. Before this change, the signal was too low to perform a

measurement with the streak camera. The measurements performed with this device have given much larger rms bunch lengths than the ones predicted by the ASTRA simulations (10.5 ps versus 2.2 ps). This large discrepancy is still not understood, and several hypotheses are currently under investigation to explain it. The experience acquired on the PHIL facility will be very helpful to implement the same type of Cerenkov based bunch length measurement device on the THOM-X facility. In particular, the streak camera will be exactly the same.

Starting from the model of K. J. Kim [13], I developed and tested an analytical model describing the beam dynamics in an RF-gun with a simple transfer matrix. This model has proven to be very accurate for the prediction of the bunch mean energy, the relative deviation with measurements performed at PITZ remaining below 2% in a range of $\pm$ 20° around the Gun RF-phase maximizing the bunch energy. For a 1.3 GHz RF-gun, the mechanical length has to be increased with respect to the real one to achieve this accuracy. The model has also been tested on the time aspect by applying the 3-phase method with an RF-gun, which should lead to retrieve the duration of the laser pulse driving the RF-gun, and has shown to be accurate on this aspect. The measurements performed at PITZ, for different time profiles of the laser pulse, show in fact a discrepancy lower than 30% at 6.2 MeV. The measurements performed at PHIL, as a function of the bunch energy, show a perfect agreement at 5 MeV and a discrepancy growing to 38% at 3 MeV because of the growing effects of space-charge forces. In contrast, the model has shown to be unsuitable to reproduce the bunch rms energy spread close to the Gun RF-phase minimizing it. This limitation is intrinsic to the model, because it has been established starting from the motion equations for one single electron and the RF-gun longitudinal transfer matrix has then been established by a simple linear differentiation of the solutions of these equations. As a result, the model does not take well into account the fact that the electron bunch is an electron distribution and predicts a zero minimal bunch rms energy spread. Away from this area, the model is suitable since the discrepancy with the measurement decreases and can be below 20%.

Starting from the model of P. Piot [14], I developed and tested an evolved analytical model describing the compression of an electron beam by velocity bunching in a traveling wave accelerating structure. This model leads to significant progress compared to the one of P. Piot. It predicts with a precision far better than 1° the RF-phase of the traveling wave accelerating structure allowing the maximum compression of the bunch, while the precision of the model of P. Piot is about a few degrees. This is important because the control of the RF-phase, to a precision better than 1°, is a crucial point to optimize the bunch compression by velocity bunching. The evolved analytical model also leads to a far better reproduction of the evolution of the final rms bunch length as a function of the RF-phase of the traveling wave accelerating structure. However, this model does not succeed in quantitatively reproducing the value of the bunch length close to the RF-phase of the traveling wave accelerating structure maximizing the bunch compression. This is due to the fact that it has been established starting from the equations of motion of a single electron, and that the expression of the bunch length has been established by a

simple linear differentiation of the solutions of these equations. Therefore, the model does not take well into account the fact that the electron bunch is an electron distribution and predicts a zero minimal rms bunch length. A way to overcome this limitation in the future would be to start from a beam envelope equation or from the Vlasov equation for describing the bunch longitudinal motion.

Simulations performed with ASTRA have shown that the use of a short laser pulse (50 fs rms) to drive an RF-gun does not allow generating very short electron bunches ($<$ 100 fs rms), even when the bunch charge is very low and when laser shaping is performed to reduce the effects of space-charge forces just after the bunch emission from the photocathode. A value of 109 fs rms is indeed reached for a 1 pC electron bunch generated by a 3D ellipsoid laser pulse. On the opposite, the reduction of the bunch charge and the laser shaping lead to a large improvement in the bunch rms transverse emittance. In fact, in the conditions minimizing the rms bunch length, it can be reduced from 5 π.mm.mrad for a 100 pC electron bunch generated by a 3D Gaussian laser pulse to 0.88 π.mm.mrad at 1 pC or to 1.53 π.mm.mrad for a 100 pC electron bunch generated by a 3D ellipsoid laser pulse. These simulations pave the way for the upcoming use of a femtosecond laser pulse, coming from the Laserix facility, to drive the RF-gun of the PHIL facility. Simulations have also been performed to study the generation in an RF-gun of a longitudinally modulated electron bunch with short bunches. They have shown that, by fine-tuning the Gun RF-phase, the initial modulation of a laser pulse with thirteen bunches of 100 fs rms each spaced by 1 ps can be preserved better than 15% for a total charge of 20 pC and better than 20% for a total charge of 200 pC.

Simulations performed with ASTRA and CSRtrack have shown that the emission of synchrotron radiation (coherent and incoherent) by the bunch during its compression in a magnetic chicane, and also its interaction with this radiation, can strongly deteriorate the bunch transverse emittance. An increase potentially up to 25% is indeed predicted during the compression of a 3D Gaussian electron bunch from 1 ps rms to 100 fs rms. However, this effect can be massively lowered if the bunch has a strong time/energy correlation (chirp) at the chicane entrance. In this case, the bunch mean kinetic energy and the magnetic strength required to compress the bunch decrease implying a decrease in the emission of synchrotron radiation. The bunch rms transverse emittance can then be conserved during the magnetic compression.

I studied the conditions allowing preserving the longitudinal modulation of an electron beam during the magnetic compression process. This study proved to be very complicated. I demonstrated that the longitudinal modulation can be preserved, if a fine-tuning of the beam longitudinal phase-space shape is performed before the entrance of the magnetic chicane. However, the way to practically perform this shaping of the beam longitudinal phase-space with a third order harmonic cavity has not been studied in my thesis. These simulations constitute a preliminary study for the implementation of a magnetic chicane on the PITZ facility. The compressed longitudinally modulated electron beam exiting the chicane is intended to be used in a laser-plasma acceleration experiment based on the high-transformer ratio process.

I performed simulations with the PARMELA beam dynamics code on the SPARC facility to study the achievable bunch properties with two different schemes of velocity bunching : the first one with a fast compression in one 3 m long traveling wave accelerating structure, and the second one with a slow compression in two of these structures. The scheme with a slow compression allows reaching shorter bunch rms length, because of the lower effects of space-charge forces at the focal point level. In fact, the minimal rms bunch length achieved in my study is 19.4 fs for a bunch of 10 pC (31.8 fs at 50 pC) in the slow compression scheme, while it is 27.1 fs for a bunch of 10 pC (51.3 fs at 50 pC) in the fast compression scheme. These rms bunch lengths are not ultimate and can be further improved by a fine optimization of the parameters, length and transverse radius, of the laser pulse driving the RF-gun. The other important result of my study is that the bunch rms length and transverse emittance cannot be simultaneously optimized when performing velocity bunching. The reason is that the velocity bunching is optimized when a large transverse radius of the laser pulse driving the RF-gun is used, which leads to a large increase of the thermal emittance at the bunch emission from the photocathode. For instance, an rms value of 1.72 π.mm.mrad is obtained for a 50 pC and 77 fs rms electron bunch generated by a 2.5 ps rms and 0.6 mm transverse radius laser pulse. It increases up to 6.82 π.mm.mrad for the 50 pC and 32 fs rms electron bunch generated by a 1 ps rms and 4 mm transverse radius laser pulse.

Annexe A

Demonstration of the beam magnetic rigidity

We consider here an electron with a charge q moving with a velocity $\vec{v}$ and a momentum $\vec{p}$, which are initially contained in a plane perpendicular to a static and uniform magnetic field $\vec{B}$. The force $\vec{F}$ acting on the electron is given by the Lorentz relation :

$$\vec{F} = q\vec{v} \wedge \vec{B}$$

One can clearly see that $\vec{F}$ is always perpendicular to $\vec{v}$. It implies that the power of $\vec{F}$ $(\vec{F}.\vec{v})$ is zero by definition. The kinetic energy T of the electron is therefore a constant of the motion [37]. The fundamental principle of dynamics gives the following relation :

$$\frac{d\vec{p}}{dt} = q\vec{v} \wedge \vec{B} \;\Rightarrow\; \gamma m \frac{d\vec{v}}{dt} = q\vec{v} \wedge \vec{B}$$

where m is the electron mass and $\gamma = 1 + \frac{T}{mc^2}$ is the Lorentz relativistic factor and is a constant of the motion in the present case.

It is visible that the variation of $\vec{v}$ $\left(\frac{d\vec{v}}{dt}\right)$ are always perpendicular to $\vec{B}$. It implies that the electron trajectory is contained in a plane perpendicular to $\vec{B}$, the one initially containing $\vec{v}$ and $\vec{p}$. It is therefore possible to use the Frenet-Serret formulas to describe the electron motion :

$$\gamma m \left(\frac{dv}{dt}\vec{t} + \frac{v^2}{\rho}\vec{n} \right) = q\vec{v} \wedge \vec{B}$$

where ρ is the local curvature radius of the electron motion. $\vec{t}$ is the unitary vector parallel to $\vec{v}$ and pointing in the same direction than $\vec{v}$, and $\vec{n}$ is the unitary vector perpendicular to $\vec{v}$ and pointing towards the local center of curvature of the electron motion.

37. We do not consider here the kinetic energy potentially lost by the electron through synchrotron radiation

The kinetic energy T being conserved, one has $\frac{dv}{dt} = 0$. It implies that the electron trajectory is circular with a curvature radius ρ. Knowing that $\vec{v}$ and $\vec{B}$ are perpendicular and that $p = \gamma mv$, one obtains :

$$\frac{pv}{\rho} = qvB$$

Since $pc = \sqrt{T(T + 2mc^2)}$, one finally obtains the relation defining the beam magnetic rigidity :

$$B\rho = \frac{p}{q} = \frac{\sqrt{T(T + 2mc^2)}}{qc}$$

Annexe B

Additional information on the modes

Let consider a closed cylindrical cavity, also called a pillbox cavity. The electromagnetic modes which can be established are of two major types : the TE_{mnp} modes (TE standing for Transverse Electric) and the TM_{mnp} modes (TM standing for Transverse Magnetic). The TE_{mnp} modes cannot be used to accelerate the electrons, because the electric field of these modes is perpendicular to the Oz symmetry axis of the pillbox cavity, which is the wanted direction of acceleration for the electrons. It is therefore necessarily a TM_{mnp} mode which has to be used. It is noteworthy that the electric field of these modes is purely longitudinal only on the Oz axis, its transverse component becoming more and more important as one moves away from Oz.

The subscripts m, n and p are each associated with one coordinate and give informations on the field variations along these coordinates. In cylindrical coordinates $(r; \theta; z)$, m is associated with θ, n is associated with r and p is associated with z. A zero value means that the electric and magnetic field of the mode are invariant along the associated coordinate. A value $q \neq 0$ means that the fields vary and cross q times zero along the associated coordinate.

The TM_{010} mode used in the RF-guns is therefore invariant by translation along Oz and by rotation around Oz. One has to be careful that it is only true for a closed cylindrical cavity. The RF-guns correspond to the case of several open cylindrical cavities linked together via apertures called irises. It implies that, in an RF-gun, the TM_{010} mode is actually divided into several sub-modes having very close resonant frequencies. These sub-modes present variations by translation along Oz , because the cavities are open and linked together along Oz. On the opposite, they remain invariant by rotation around Oz.

In a 1.6 cells RF-gun, two sub-modes appear. The $TM_{010-\pi}$ mode (see Fig.1.7 in Sec. 1.2.5), which is the mode used to accelerate the electrons. In this mode the electric field is phase-shifted by π, therefore at any time of opposite signs, between the two cells. The other sub-mode is the TM_{010-0} mode where the electric field is phase-shifted by 0, therefore of the same sign and amplitude, between the two cells. The profile of the longitudinal electric field on the Oz axis of the RF-gun for the mode TM_{010-0} is shown in Fig. B.1 (the time is fixed).

The TM_{010-0} mode is not suitable to accelerate the electrons. In fact, since the electric

field is of the same sign in the two cells and the second cell is longer than the first, the electrons would be submit to a decelerating field in the second cell and would start to longitudinally oscillate in the RF-gun or would go back to the photocathode.

In a 2.5 cells RF-gun, three sub-modes appear. The $TM_{010-\pi}$ and TM_{010-0} modes are still present and have profiles similar to the ones encountered in a 1.6 cells RF-gun, except that there is one more cell. The additional sub-mode is the $TM_{010-\frac{\pi}{2}}$ mode, where the electric field is at any time almost equal to zero in the second cell. The profile of the longitudinal electric field on the Oz axis of the RF-gun for the mode $TM_{010-\frac{\pi}{2}}$ is shown in Fig. B.2 (the time is fixed).

The $TM_{010-\frac{\pi}{2}}$ mode does not allow an optimal acceleration of the electrons, because the accelerating field is at any time almost zero in the second cell.

The TM_{010-0} and $TM_{010-\frac{\pi}{2}}$ modes are therefore not suitable to accelerate the electrons. However, they have resonant frequencies very close to the one of the $TM_{010-\pi}$ mode of interest. It is therefore essential that the frequency of the signal generated by the klystron and fed into the RF-gun is very sharply selected, in order that only the $TM_{010-\pi}$ mode resonates in the RF-gun, otherwise the acceleration of the electrons would be much less efficient.

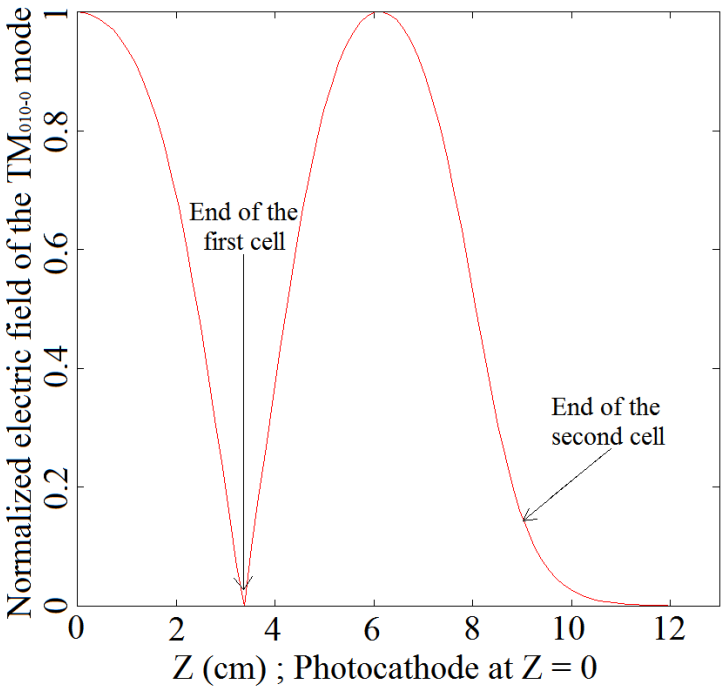

FIGURE *B.1 – Normalized profile of the longitudinal electric field of the TM_{010-0} mode on the Oz axis of a 1.6 cells RF-gun.*

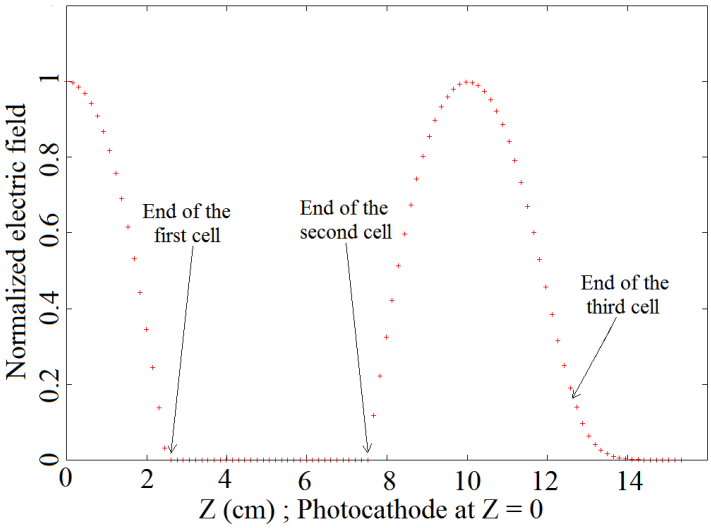

FIGURE *B.2 – Normalized profile of the longitudinal electric field of the $TM_{010-\frac{\pi}{2}}$ mode on the Oz axis of a 2.5 cells RF-gun.*

Annexe C

Code for the analysis of the images produced by the YAG screens of the PHIL facility

I used Matlab and Gnuplot to develop a code allowing the extraction of the bunch transverse sizes from the images produced by the YAG screens of the PHIL facility. This code is easily transferable to any facility, since the only parameters dependent on the facility are : the size of the pixel of the CCD camera imaging the scintillating screen and the magnification of the optical line between the scintillating screen and the CCD camera.

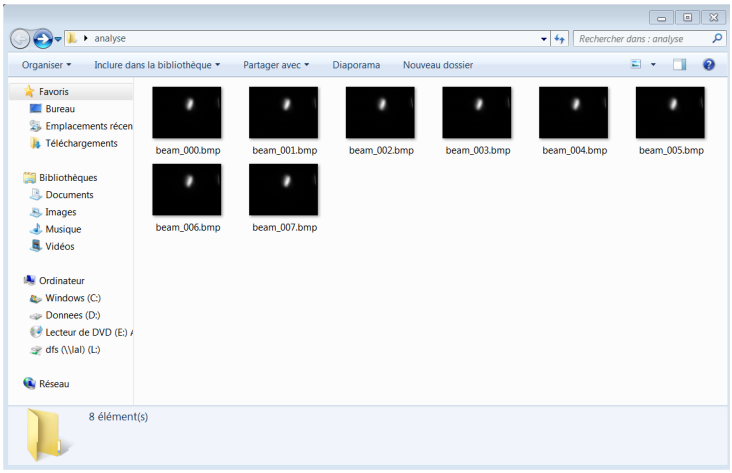

FIGURE *C.1 – Folder containing the bunch images before analysis.*

The first step is to place the bunch images in a dedicated folder, as shown in Fig. C.1, because the code uses all the images in the folder to perform the analysis [38]. The code offers the possibility to take into account or not the dark current, namely the electrons emitted without laser pulse driving the RF-gun. In the case it is taken into account, the

38. There are no constraints on the number of images, on the name of the images and on the folder used to store the images.

bunch and dark current images have to be stored in two different folders. The code then computes the mean of the dark current images and subtract it from each bunch images to obtain images with only the photoemitted electrons.

The user has then to select on these images, as shown in Fig. C.2, a region of interest (ROI) containing the image of the bunch and excluding the potential parasitic lights often encountered at the edges of the scintillating screens. The code then computes for each images the projected horizontal and vertical intensity profiles inside the ROI. These projected intensity profiles are obtained, for one image, by averaging all the intensity profiles along the two directions inside the ROI. Fig. C.3 shows an example of such a profile, in the horizontal direction, extracted from Fig. C.2.

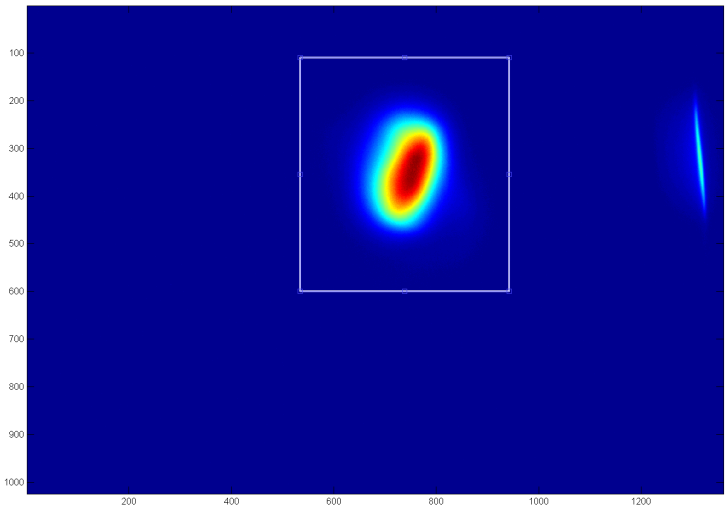

FIGURE *C.2 – Selection of the region of interest (ROI) on the bunch images.*

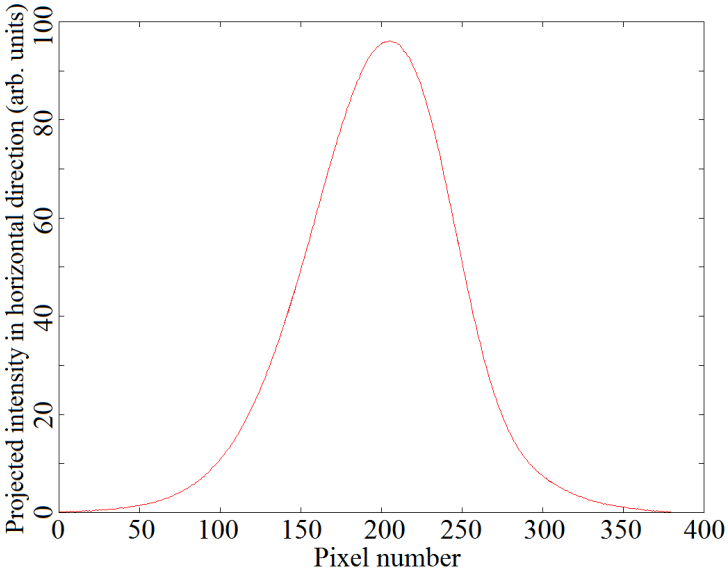

FIGURE *C.3 – Example of projected intensity profile in the horizontal direction.*

The code finally computes, from the projected intensity profiles, the bunch horizontal and vertical transverse sizes by three different methods.

The first one is to perform a Gaussian fit, with Gnuplot, of the projected intensity profiles with the following function $f(x)$ where a, b and σ_g are the parameters of the fit :

$$f(x) = \frac{a}{\sigma_g\sqrt{2\pi}} e^{-\frac{(x-b)^2}{2\sigma_g^2}}$$

The bunch transverse sizes are then defined as the two σ_g parameters, which are the standard deviations of the Gaussian distributions best fitting the projected intensity profiles.

The second one is to compute the Full Widths at Half-Maximum (FWHM) of the projected intensity profiles. The projected intensity profiles can sometimes be rather noisy, implying that the FWHMs cannot be unequivocally determined. I choose to always search for the pixels having half-intensity, with respect to the maximum, which are located the farther from the maximum. It corresponds actually to compute the largest possible FWHMs. The obtained FWHMs are then divided by $2\sqrt{2\ln(2)}$ to define the bunch transverse sizes σ_F [39].

The third one is to compute the statistical standard deviation σ_{rms} of the projected intensity profiles, which is defined by the following equation :

$$\sigma_{rms} = \sqrt{\frac{\sum_{k=1}^{n} I_k (k-\bar{k})^2}{\sum_{k=1}^{n} I_k}}$$

where the k subscript denotes the pixel number along the projected intensity profiles and I_k the intensity for the pixel number k. $\bar{k}$ is the mean pixel of the projected intensity profile, given by :

$$\bar{k} = \frac{\sum_{k=1}^{n} k I_k}{\sum_{k=1}^{n} I_k}$$

At this step of the analysis, the three computed bunch transverse sizes σ_g, σ_F and σ_{rms} are expressed in terms of a number of pixels of the CCD camera. They have to be finally converted into millimeters. This is done by multiplying them by the size of the CCD camera pixel, and dividing them by the magnification of the optical line between the scintillating screen and the CCD camera. One has to note that, in case of a perfectly Gaussian transverse distribution for the electron bunch, the three bunch transverse sizes computed by the code are the same.

Fig. C.4 shows the contents, after the end of the analysis, of the folder initially containing the bunch images.

39. I choose the factor $2\sqrt{2\ln(2)}$ because for a Gaussian distribution it is the ratio between the FWHM and the standard deviation.

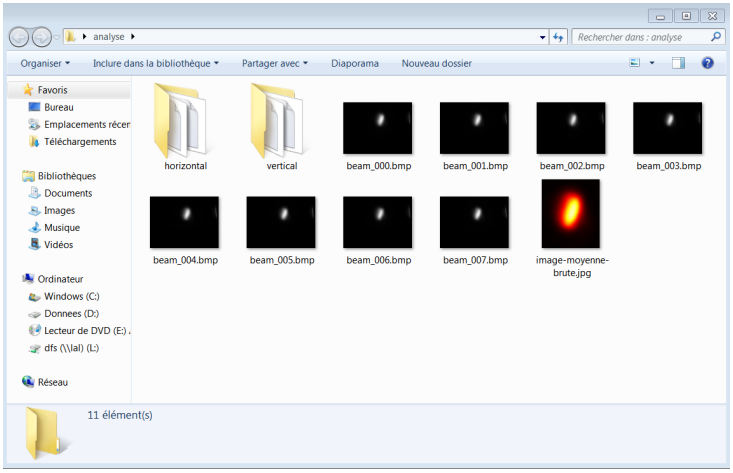

FIGURE *C.4 – Folder containing the bunch images after analysis.*

In addition to the mean of the bunch images (”image-moyenne-brute.jpg” file), the folder contains two new folders (”horizontal” and ”vertical”) which contains the results of the analysis. Fig. C.5 shows as an example the contents of the folder ”horizontal”.

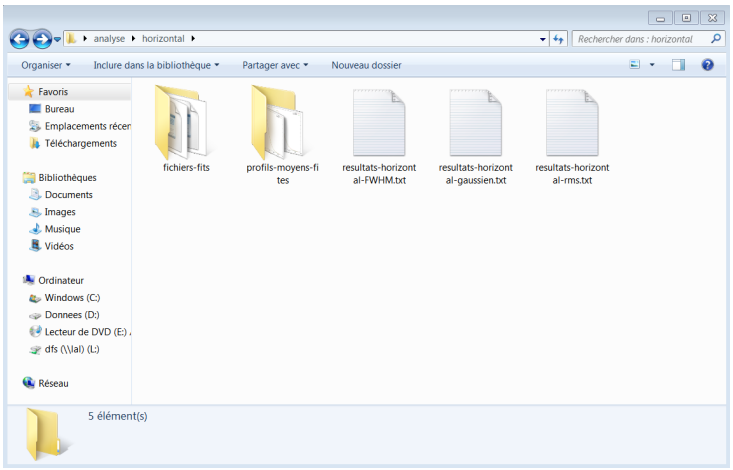

FIGURE *C.5 – Contents of the folder ”horizontal” of Fig. C.4.*

The folder ”fichiers-fits” contains the mathematical results (final parameters, correlation matrix, residuals ...) of the Gaussian fits performed on the projected intensity profiles. The folder ”profils-moyens-fites” contains the graphics where the projected intensity profiles and their Gaussian fits by Gnuplot are superimposed. Fig. C.6 shows an example of such a graphic. The three text files contain the bunch transverse sizes computed by the three methods : ”resultats-horizontal-gaussien” $\rightarrow \sigma_g$, ”resultats-horizontal-FWHM” $\rightarrow \sigma_F$ and ”resultats-horizontal-rms” $\rightarrow \sigma_{rms}$. They are all organized in the same way (Fig. C.7 shows as an example the contents of a ”resultats-horizontal-rms” file). They first contain the bunch transverse sizes for each bunch images. Then, they show the mean and standard deviation of these bunch transverse sizes. Finally, the bunch transverse sizes computed on the mean of the bunch images are written.

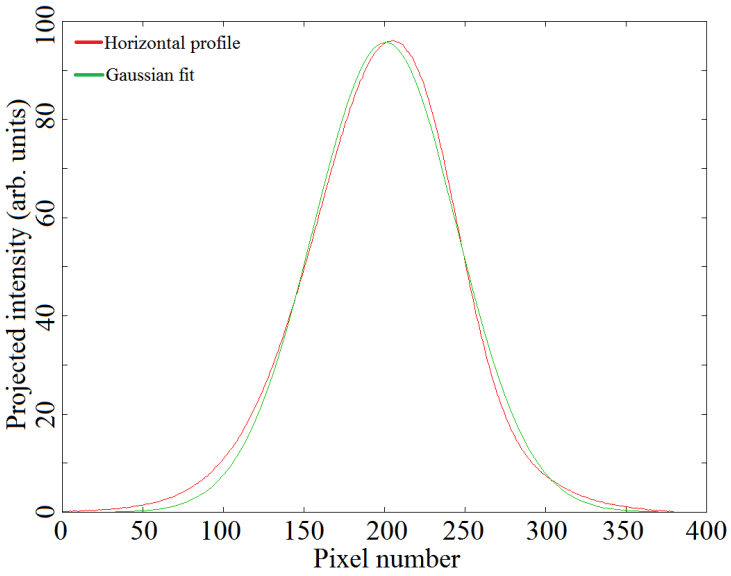

FIGURE *C.6 – Example of a Gaussian fit of a projected horizontal intensity profile.*

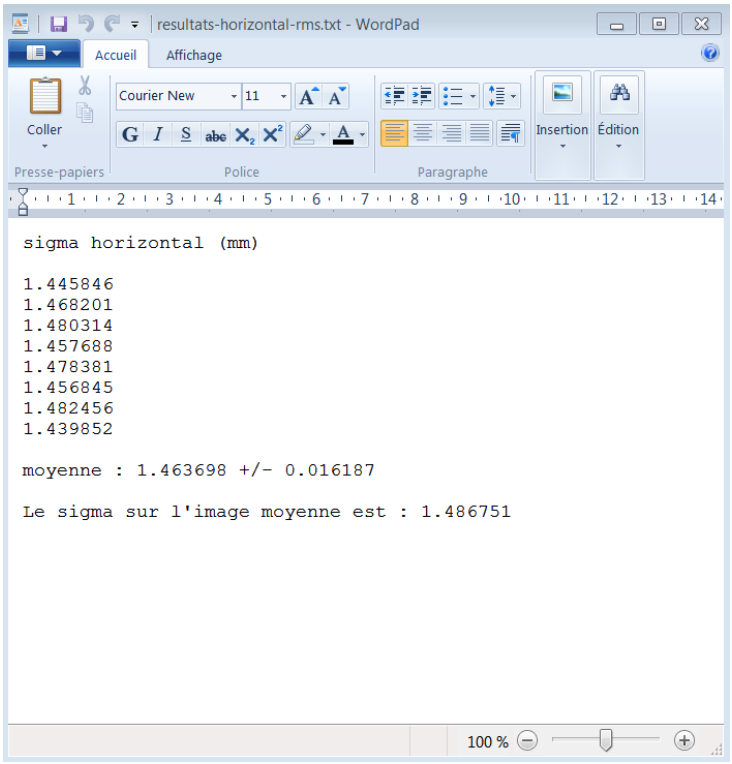

FIGURE *C.7 – Example of a text file containing the results for* σ_{rms}.

Annexe D

Relative variation of the travel time in a magnetic structure between electrons of different energies

The travel time T of an electron in a magnetic structure is given by $T = \frac{L}{v}$, where v is the velocity of the electron (constant in the magnetic structure) and L is the length of its path in the magnetic structure. It is very important to note that L is dependent on v. One has $dT = \frac{\partial T}{\partial L}dL + \frac{\partial T}{\partial v}dv$, which implies :

$$\frac{dT}{T} = \frac{dL}{L} - \frac{dv}{v}$$

Considering that the velocity and trajectory differences, respectively Δv and ΔL, between the different electrons of the beam remain small compared to the quantities v_0 and L_0, associated to the reference particle of the beam, one can write :

$$\frac{\Delta T}{T_0} = \frac{\Delta L}{L_0} - \frac{\Delta v}{v_0}$$

, where $\Delta T = T - T_0$ is the difference of travel time between any electron of the beam and the reference particle.

The total energy of an electron is given by $W = \gamma m_e c^2$, where $\gamma = \frac{1}{\sqrt{1-\frac{v^2}{c^2}}}$. We have therefore $dW = m_e c^2 d\gamma$ and $d\gamma = \gamma^3 \frac{v}{c^2} dv$, which allows obtaining :

$$\frac{dv}{v} = \frac{1}{\gamma^2}\frac{c^2}{v^2}\frac{dW}{W}$$

Considering that the energy and velocity differences, respectively ΔW and ΔT, between the different electrons of the beam remain smal compared to the quantities W_0 and v_0, associated to the reference particle of the beam, one can write :

$$\frac{\Delta v}{v_0} = \frac{1}{\gamma_0^2}\frac{c^2}{v_0^2}\frac{\Delta W}{W_0} \tag{D.1}$$

In the case where the electrons are ultra-relativistic, namely when $\gamma >> 1$, one can replace the total energy W by the kinetic energy $E = (\gamma - 1)m_e c^2$ and approximate $v \approx c$. This allows obtaining :

$$\frac{\Delta v}{v_0} = \frac{1}{\gamma_0^2}\frac{\Delta E}{E_0} = \frac{1}{\gamma_0^2}\frac{E - E_0}{E_0} \tag{D.2}$$

In most cases the electrons are ultra-relativistic when the magnetic compression is used. However, it is not always the case. For example a team of the Chiang Maï university performed the magnetic compression, with an alpha magnet, on electrons having energies between 1 MeV and 3 MeV, corresponding to γ between 3 and 7 [116]. In these rare cases the simplification given by Eq. D.2 is not relevant and Eq. D.1 must be employed.

The difference of trajectory between any electron of the beam and the trajectory of the reference electron, which is defined as the reference trajectory of the beam, comes from two phenomena. First of all, the energy difference implies that the reference trajectory associated to the electron of energy E is different from the one of the beam, associated to the beam mean energy E_0. Let assume that the motion of the electrons is contained in an horizontal plane. The local gap between the two trajectories is then given by :

$$x_\epsilon = D_x \frac{E - E_0}{E_0}$$

, where D_x is the horizontal dispersion function which depends only on the elements constituting the magnetic structure. For example, in a dipole magnet (see Fig. D.1) with a deviation angle θ, a curvature radius ρ, a zero index and no edge angles one has :

$$D_x(s) = \rho\left(1 - \cos\left(\frac{s}{\rho}\right)\right)$$

, where s is the curvilinear abscissa along the reference trajectory and therefore varies from zero to $L = \rho\theta$ for a dipole magnet.

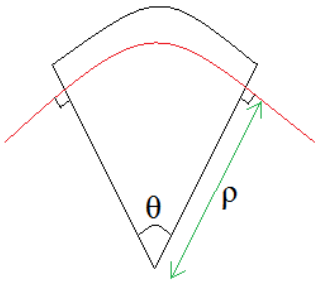

FIGURE *D.1 – Dipole magnet with a deviation angle θ, a curvature radius ρ, a zero index and no edge angles. The reference trajectory associated to the energy E_0 is depicted by the red line.*

Then there are the betatron oscillations of the electron around the reference trajectory associated to its energy E. I neglect this term, because at first order the betatron oscillation generates a zero mean displacement with respect to the reference trajectory associated to the energy E of the electron. I will therefore only consider the difference of trajectory due to the difference of energy, that is to say the difference between the reference trajectories associated to the different energies.

Besides, I will consider only this difference in the horizontal plane (Oxs), since in the ideal case the elements constituting the magnetic structure have a zero vertical dispersion function D_y. In practical, there is always a small residual vertical dispersion due to a coupling between the horizontal plane (Oxs) and the vertical plane (Oys) coming from the non-perfect positioning of the elements of the magnetic structure (slightly skew quadrupole magnet for example). However, these couplings remain small and I will therefore neglect them hereafter.

Fig. D.2 shows a scheme of reference trajectories associated to the mean beam energy E_0 and to the energy E of any electron of the beam. The infinitesimal lengths ds and dl traveled on these trajectories during dt are also shown (ρ_0 is the local curvature radius of the reference trajectory associated to the energy E_0).

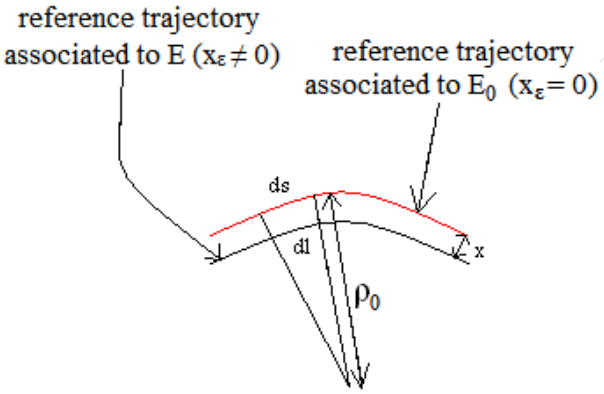

FIGURE *D.2 – Reference trajectories associated to the beam mean energy E_0 (red line) and to any energy E of the beam (black line). Note : x_ϵ is negative on this picture.*

The displacements ds and dl being infinitesimal, one can approximate them as straight lines. It is therefore possible to use the Thales theorem to obtain :

$$\frac{ds}{dl} = \frac{\rho_0}{\rho_0 + x_\epsilon} \text{ or } dl = ds\left(1 + \frac{x_\epsilon}{\rho_0}\right)$$

The length of the trajectory traveled by an electron with the energy E in the magnetic structure is therefore given by :

$$\int_{structure} \mathrm{d}l = \int_{structure} \left(1 + \frac{x_\epsilon}{\rho_0}\right) \mathrm{d}s = L_0 + \Delta L$$

, where the integral over ds denotes an integral over the reference trajectory associated to the beam mean energy E_0. L_0 is the length of this trajectory and ΔL is the length difference between the references trajectories associated to E and to E_0. ΔL is given by :

$$\Delta L = \int_{structure} \frac{x_\epsilon}{\rho_0} \mathrm{d}s = \frac{E - E_0}{E_0} \int_{structure} \frac{D_x(s)}{\rho_0(s)} \mathrm{d}s$$

It follows :

$$\frac{\Delta L}{L_0} = \alpha \frac{E - E_0}{E_0} \text{ with } \alpha = \frac{1}{L_0} \int_{structure} \frac{D_x(s)}{\rho_0(s)} \mathrm{d}s$$

, where α depends only on the properties of the magnetic structure. One finally obtains :

$$\frac{\Delta T}{T_0} = \frac{\Delta L}{L_0} - \frac{\Delta v}{v_0} = \left(\alpha - \frac{1}{\gamma_0^2} \right) \frac{E - E_0}{E_0} = \eta \frac{E - E_0}{E_0}$$

Annexe E

The ASTRA beam dynamics code

The ASTRA (A Space-charge TRacking Algorithm) code is a beam dynamics code developed at DESY (Hamburg) since 1997 [42]. It is made of three main parts.

The first part is the program *generator*, which may be used to generate the initial particle distribution. Fig. E.1 shows an example of commented input file for the program *generator*.

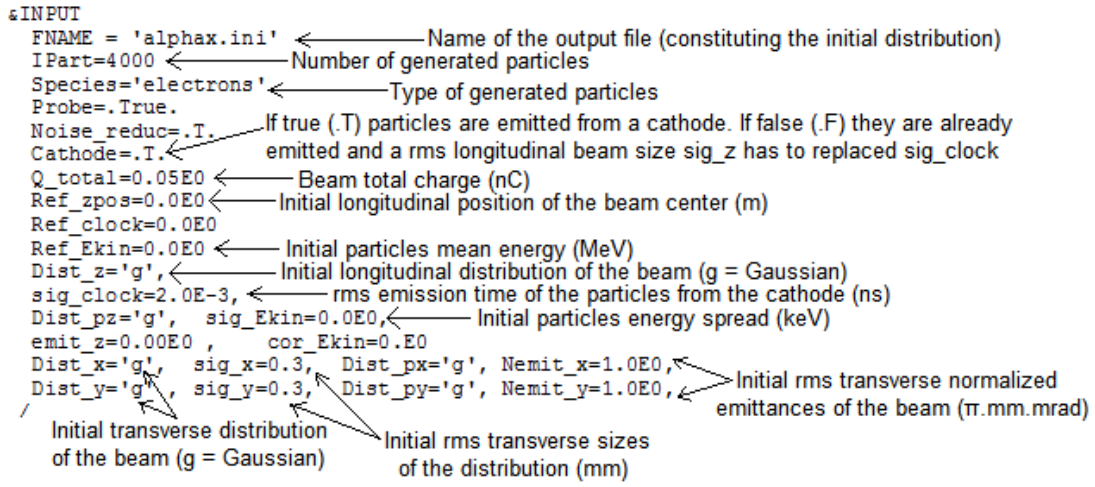

FIGURE *E.1 – Example of commented input file for the program generator generating the initial particle distribution for ASTRA.*

The program *generator* allows setting all the initial transverse and longitudinal parameters of the particle distribution, as shown in Fig. E.1. It also allows defining the shape of the initial distribution of the particles within the beam. The distribution can be Gaussian (with eventually a cutoff radius), uniform, flat-top (uniform plateau with exponential rise and fall), inverted parabola (only for the longitudinal distribution), radial (2D transverse

uniform distribution within a circle [40]) and 3D uniformly filled ellipsoid [41].

The second part contains three programs which are used to analyze the results of the ASTRA simulation. The first one is the *fieldplot* program, which is used to display the electromagnetic fields of the elements constituting the beamline (accelerating sections, focusing elements, etc.) and the electromagnetic fields generated by the particle distribution itself (the so-called space-charge fields). The second one is the *lineplot* program, which is used to display the evolution of the beam properties (rms transverse size, emittance, rms bunch length, energy, etc.) as a function of the longitudinal position along the beamline or as a function of other parameters which can be scanned in ASTRA (RF-phases of accelerating structures, focusing strength of magnetic elements, etc.). The third one is the *postpro* program, which is used to display numerous phase-spaces of the particle distribution at several longitudinal positions along the beamline. It can also be used to perform a detailed analysis of these phase-spaces.

The third and central part is the *Astra* program itself, which computes the beam dynamics by solving the equations of motion with a Runge-Kutta method of fourth order. The program *Astra* tracks individually each particle of the beam through the external electromagnetic fields defined by the user, mainly accelerating sections and focusing elements (but special features like dipole magnets and wakefields can also be taken into account). It also computes the space-charge fields generated by the beam during its motion and takes into account their effects on the beam dynamics. *astra* also allows defining physical apertures beyond which the particles of the beam are lost. It is noteworthy that the sample of macroparticles (typically between 10^3 and 10^5) used to perform the simulation is much smaller than the real number of particles in the beam (typically higher than 10^7), otherwise the simulation will be too long. The charge q and mass m of the macroparticles are adjusted to have the same ratio $\frac{q}{m}$ as for the real particles constituting the beam, in order to have the same dynamics in the electromagnetic fields. It is important to take the number of macroparticles sufficiently high to statistically correctly represent the real beam.

To take into account the accelerating and focusing fields, *astra* offers the possibility to use either 1D maps of the longitudinal fields along the propagation axis of the beam or full 3D maps of the fields. In the case of the 1D maps, the off-axis components of the fields are calculated by a Taylor-expansion of the 1D longitudinal fields on the axis. This Taylor-expansion can be user-defined as being of the first or third order. The 1D maps are used when the field are (almost) cylindrically symmetric, while the 3D ones are used when the field asymmetry starts to play a significant role or when the third order Taylor-expansion of the 1D maps is not accurate enough to model the real fields.

To compute the space-charge fields ASTRA offers two differents algorithms : the cylindrical grid algorithm and the 3D cartesian algorithm. During my simulations I used only the cylindrical grid algorithm, because the beam in my simulations was always cylin-

40. The projection of such a distribution along the horizontal and vertical directions of the transverse plane are half-ellipses.

41. The projection of such a distribution along the horizontal, vertical and longitudinal directions are inverted parabolas.

drically symmetric (or only slightly asymmetric) and because the 3D cartesian algorithm requires a higher number of simulated particles, a higher number of grid cells and a finer grid step to be accurate, which increases the computing time. I will therefore only present the cylindrical algorithm hereafter.

To compute the space-charge fields through the cylindrical grid algorithm the space over the extension of the bunch has to be divided into cells to form a grid. These cells consist in concentric rings along the radial direction and in slices in the longitudinal direction. The number of cells in the radial and longitudinal directions have to be specified by the users, but the total extension of the grid is dynamically adjusted by ASTRA during the beam motion. A Lorentz transformation of this grid is performed to pass into the average rest system of the beam. In this system, the motion of the particles can be considered non-relativistic. The space-charge fields can therefore be computed at the center of each cell [42] with a classical static field calculation (solving of the Poisson equation) by numerically integrating over the contributions of all the cells (the charge density in a cell is assumed constant). The space-charge fields are then calculated into the laboratory system by an inverse Lorentz transformation. Finally, the space-charge fields are applied on each particle of the beam by means of a cubic spline interpolation between the centers of the cells, where the space-charge fields have been computed. The space-charge fields are not calculated by this cylindrical algorithm at each time step of the computation of the beam dynamics by ASTRA, otherwise the simulation would be too long. Instead of that they are scaled at each time step by the coefficients shown in the page 12 of [42]. The space-charge fields are fully calculated again by the cylindrical algorithm when the scaling factor of the longitudinal or radial space-charge field exceeds a user-defined value (for example 5% of variation with respect to the previous calculation with the cylindrical algorithm). It is noteworthy that a compromise has to be found between the number of cells constituting the grid and the number of macroparticles constituting the beam. Indeed, the number of cells has to be sufficiently high to allow a precise spatial calculation of the space-charge fields. But it has to be taken into account that each cell must contain a substantial number of macroparticles to allow a precise calculation of the space-charge fields on the statistical point of view (if the number of macroparticles in each cell is too low, noise will be introduced). As a result the number of cells cannot be too high otherwise the number of macroparticles necessary to fill all the cells would be too high and the simulation would become too long.

Finally, The *astra* program pays particular attention to the emission of the particles and especially in an RF-gun. First of all, it allows emitting the particles from the photocathode according to the initial time spread defined in the program *generator* (see parameter sig_clock in Fig. E.1). It takes into account the effect of the space-charge fields of the already emitted particles on the emission of the following particles. This effect may prevent the emission of new particles and reduce the beam charge. It also takes into account the effect of the mirror charge created in the photocathode by the emitted charge. The field of this mirror charge is superimposed to the space-charge fields of the emitted particles. The calculation of the mirror charge is switched off when its field decreases below 1 of

42. The centers of the cells are concentric circles, where the space-charge fields are constant because of the assumed cylindrical symmetry.

the beam space-charge fields. Then, it allows taking into account the Schottky effect [22] during the emission of the beam from a photocathode. This corresponds to the fact that the work function of the photocathode material is varying with time in an RF-gun, because the electric field on the photocathode varies with time, implying that the emitted charge is a function of the instant of emission, which is equivalent to the RF-phase of the RF-gun. ASTRA allows taking this effect into account by calculating the emitted charge Q via the following formula :

$$Q = Q_0 + Srt\_Q\_Schottky\sqrt{E} + Q\_SchottkyE$$

, where Q_0 is the charge initially defined in the program *generator* and E is the total field (field of the RF-gun and space-charge fields) applied on the photocathode. $Q\_Schottky$ and $Srt\_Q\_Schottky$ are two parameters which allows respectively modeling the linear and square-root variation of the emitted charge with the field E. They can be set to zero to turn off the Schottky effect. Finally, the *astra* program allows including the secondary electron emission which occurs when a particle of the beam hits a physical aperture of the beamline defined by the users, and also the enhancement of this effect by an applied electric field. Several parameters can be used to reproduce the properties of the used materials and therefore fine-tune the yield of the secondary electron emission as a function of the kinetic energy of the particle hitting the aperture.

During my thesis, I mainly use the ASTRA code to perform my simulations. I also use the CSRTrack code [113], which is fully compatible with the ASTRA code, to perform the simulations of beam magnetic compression. I finally use the PARMELA code [120] to perform the simulation of beam compression by the velocity bunching phenomenon in traveling wave accelerating sections. The reason is that it is easier to include traveling wave accelerating sections in the PARMELA code than in the ASTRA code.

Bibliographie

[1] S. A. Aseyev, P. M. Weber, and A. A. Ischenko. Ultrafast Electron Microscopy for Chemistry, Biology and Material Science. Journal of Analytical Sciences, Methods and Instrumentation, 3(1) :30, 2013.

[2] R. Hajima, M. Shimada, and N. Nakamura. Generation and applications of ultra-short electron beams in energy-recovery linacs. Nuclear Instruments and Methods in Physics Research Section A : Accelerators, Spectrometers, Detectors and Associated Equipment, 637(1) :S37, 2011.

[3] J. B. Rosenzweig, D. Alesini, G. Andonian, M. Boscolo, M. Dunning, L. Faillace, M. Ferrario, A. Fukusawa, L. Giannessi, E. Hemsing, et al. Generation of ultra-short, high brightness electron beams for single-spike SASE FEL operation. Nuclear Instruments and Methods in Physics Research Section A : Accelerators, Spectrometers, Detectors and Associated Equipment, 593(1) :39, 2008.

[4] `http://www.xfel.eu/overview/facts_and_figures/`.

[5] R. Hettel and M. Borland. Perspectives and Challenges for Diffraction-Limited Storage Ring Light Sources. In Proceedings of PAC, page 19, 2013.

[6] G. L. Carr, M. C. Martin, W. R. McKinney, K. Jordan, G. R. Neil, and G. P. Williams. High-power terahertz radiation from relativistic electrons. Nature, 420(6912) :153, 2002.

[7] Y. Shen, X. Yang, G. L. Carr, Y. Hidaka, J. B. Murphy, and X. Wang. Tunable few-cycle and multicycle coherent terahertz radiation from relativistic electrons. Physical review letters, 107(20) :204801, 2011.

[8] J. Yang, K. Kan, T. Kondoh, N. Naruse, Y. Murooka, K. Tanimura, Y. Yoshida, J. Urakawa, et al. Photocathode femtosecond electron beam applications : Femtosecond pulse radiolysis and femtosecond electron diffraction. In Proceedings of IPAC, page 4113, 2010.

[9] S. Bayesteh, H. Delsim-Hashemi, and K. Floettmann. Beam Profile Monitors at REGAE. In Proceedings of IBIC, page 212, 2013.

[10] D. Lipka, J. Lund-Nielsen, and M. Seebach. Resonator for charge measurement at REGAE. In Proceedings of IBIC, page 872, 2013.

[11] F. Chautard. Un Compresseur de Paquets d'Electrons Fortement Chargés au CERN. PhD thesis, Paris U., IV, 1996.

[12] C. Rechatin. Accélération d'électrons dans l'interaction laser-plasma : développement et caractérisation d'un injecteur optique. PhD thesis, Ecole Polytechnique X, 2009.

[13] K. J. Kim. RF and space-charge effects in laser-driven RF electron guns. Nuclear Instruments and Methods in Physics Research Section A : Accelerators, Spectrometers, Detectors and Associated Equipment, 275(2) :201, 1989.

[14] P. Piot, L. Carr, W. S. Graves, and H. Loos. Subpicosecond compression by velocity bunching in a photoinjector. Physical Review Special Topics-Accelerators and Beams, 6(3) :033503, 2003.

[15] O. Sise, M. Ulu, and M. Dogan. Multi-element cylindrical electrostatic lens systems for focusing and controlling charged particles. Nuclear Instruments and Methods in Physics Research Section A : Accelerators, Spectrometers, Detectors and Associated Equipment, 554(1) :114, 2005.

[16] F. Loehl, I. Bazarov, S. Belomestnykh, M. Billing, E. Chojnacki, Z. Conway, J. Dobbins, B. Dunham, R. Ehrlich, M. Forster, et al. High current and high brightness electron sources. In Proceedings of IPAC, page 45, 2010.

[17] K. Smolenski, I. Bazarov, B. Dunham, H. Li, Y. Li, X. Liu, D. Ouzounov, and C. Sinclair. Design and performance of the Cornell ERL DC photoemission gun. In AIP Conference Proceedings, volume 1149, page 1077, 2009.

[18] T. Taniuchi, T. Asaka, H. Dewa, H. Hanaki, T. Kobayashi, A. Mizuno, S. Suzuki, and H. Tomizawa. Upgrade of a Photocathode RF Gun at SPring-8. In Proceedings of FEL, page 431, 2004.

[19] N. Pichoff. Dynamique des faisceaux de particules chargées en présence de charge d'espace. Master de Physique Spécialité Rayonnements et Energie, Université Paris Sud.

[20] C. Kittel. Introduction to solid state physics. Wiley, 2005.

[21] O. W. Richardson. Thermionic phenomena and the laws which govern them. Nobel Lecture, December, 1929.

[22] J. Orloff. Handbook of charged particle optics. CRC press, 2008.

[23] H. Monard. Les sources d'électrons. Master de Physique Spécialité Accélérateurs de Particules et Interaction avec la Matière, Université Paris Sud, 2012.

[24] B. Anderberg, Å. Andersson, M. Demirkan, M. Eriksson, L. Malmgren, and S. Werin. The design of a 3GHz thermionic RF-gun and energy filter for MAX-lab. Nuclear Instruments and Methods in Physics Research Section A : Accelerators, Spectrometers, Detectors and Associated Equipment, 491(1) :307, 2002.

[25] J. W. Lewellen. Energy-spread compensation of a thermionic-cathode RF gun. In Proceedings of PAC, page 2035. IEEE, 2003.

[26] H. Tong-Ning, C. Qu-Shan, P. Yuan-Ji, L. I. Ji, and Q. Bin. Physical design of FEL injector based on the performance-enhanced EC-ITC RF gun. Chinese Physics C, 38(1) :018101, 2014.

[27] R. A. Powell, W. E. Spicer, G. B. Fisher, and P. Gregory. Photoemission studies of cesium telluride. Physical review B, 8(8) :3987, 1973.

[28] P. Musumeci, L. Cultrera, M. Ferrario, D. Filippetto, G. Gatti, M. S. Gutierrez, J. T. Moody, N. Moore, J. B. Rosenzweig, C. M. Scoby, et al. Multiphoton photoemission from a copper cathode illuminated by ultrashort laser pulses in an RF photoinjector. Physical review letters, 104(8) :084801, 2010.

[29] R. P. Brogle. Studies of linear and nonlinear photoemission processes in metals and semiconductors. 1996.

[30] R. A. Loch. Cesium-Telluride and Magnesium for high quality photocathodes. Masterdiploma thesis, University of Twente, 2005.

[31] K. Aulenbacher, J. Schuler, D. V. Harrach, E. Reichert, J. Röthgen, A. Subashev, V. Tioukine, and Y. Yashin. Pulse response of thin III/V semiconductor photocathodes. Journal of applied physics, 92(12) :7536, 2002.

[32] D. Janssen, A. Arnold, H. Buttig, U. Lehnert, P. Michel, P. Murcek, C. Schneider, R. Schurig, F. Staufenbiel, J. Teichert, et al. Review on superconducting RF guns. In Proceedings of the International SRF Workshop, Cornell University, page 433, 2005.

[33] A. Brachmann, J. E. Clendenin, E. L. Garwin, K. Ioakeimidi, R. E. Kirby, T. Maruyama, C. Y. Prescott, J. Sheppard, J. Turner, F. Zhou, et al. The Polarized Electron Source for the International Collider (ILC) Project. In Proceedings of the 17 th International Spin Physics Symposium (AIP Conference Proceedings Volume 915), page 1091, 2007.

[34] S. Di Mitri. On the Importance of Electron Beam Brightness in High Gain Free Electron Lasers. In Photonics, volume 2, page 317. Multidisciplinary Digital Publishing Institute, 2015.

[35] J. Arthur et al. Linac Coherent Light Source (LCLS) Conceptual Design Report. SLAC-R-593, 2002.

[36] M. Vogt, B. Faatz, J. Feldhaus, K. Honkavaara, S. Schreiber, R. Treusch, and DESY Deutsches Elektronensynchrotron. Status of the free electron laser user facility FLASH. In Proceedings of IPAC, page 938, 2014.

[37] J. W. Wang and G. A. Loew. Field emission and rf breakdown in high-gradient room-temperature linac structures. SLAC PUB, 7684, 1997.

[38] X. Li, M. Li, L. Dan, Y. Liu, and C. Tang. Cold cathode rf guns based study on field emission. Physical Review Special Topics-Accelerators and Beams, 16(12) :123401, 2013.

[39] S. V. Baryshev et al. Planar ultrananocrystalline diamond field emitter in accelerator radio frequency electron injector : Performance metrics. Applied Physics Letters, 105(20) :203505, 2014.

[40] T. Vinatier, C. Bruni, R. Roux, J. Brossard, S. Chancé, J. N. Cayla, V. Chaumat, G. Xu, and H. Monard. Performances of the Alpha-X RF-gun on the PHIL accelerator at LAL. Nuclear Instruments and Methods in Physics Research Section A : Accelerators, Spectrometers, Detectors and Associated Equipment, 797 :222, 2015.

[41] R. H. Varian and S. F. Varian. A high frequency oscillator and amplifier. Journal of Applied Physics, 10(5) :321, 1939.

[42] K. Flöttmann. ASTRA : A space charge tracking algorithm, 2011.

[43] P. Forck. Lecture notes on beam instrumentation and diagnostics. 2015.

[44] A. Buck, K. Zeil, A. Popp, K. Schmid, A. Jochmann, S. D. Kraft, B. Hidding, T. Kudyakov, C. M. S. Sears, L. Veisz, et al. Absolute charge calibration of scintillating screens for relativistic electron detection. Review of Scientific Instruments, 81(3) :033301, 2010.

[45] U. Iriso, G. Benedetti, and F. Pérez. Experience with YAG and OTR screens at ALBA. In Proceedings of DIPAC, page 200, 2009.

[46] `http://www.crytur.cz/pages/33/crytur-materials`.

[47] S. Bhadra, M. Cadabeschi, P. De Perio, V. Galymov, M. Hartz, B. Kirby, A. Konaka, A. D. Marino, J. F. Martin, D. Morris, et al. Optical transition radiation monitor for the T2K experiment. Nuclear Instruments and Methods in Physics Research Section A : Accelerators, Spectrometers, Detectors and Associated Equipment, 703 :45, 2013.

[48] C. Couillaud, A. Loulergue, and G. Haouat. Electron beam transverse emittance measurement using optical transition radiation interferometry. In Proceedings of EPAC, page 1594, 1996.

[49] M. C. Ross, D. McCormick, E. Bong, D. Arnett, W. Inmam, S. Horton-Smith, R. Alley, R. K. Jobe, T. Kotseroglou, M. Scheeff, et al. A high performance spot size monitor. In Proceedings of LINAC, page 308. CERN, 1996.

[50] S. Liu. Development of Diamond Sensors for Beam Halo and Compton Spectrum Diagnostics after the Interaction Point of ATF2. PhD thesis, Université Paris Sud, 2015.

[51] F. Burkart, R. Schmidt, E. Griesmayer, O. Stein, and D. Wollmann. Experimental Results from the Characterization of Diamond Particle Detectors with a High Intensity Electron Beam. In Proceedings of IPAC, page 3671, 2014.

[52] A. Shapovalov and L. Staykov. Emittance measurement wizard at PITZ. In Proceedings of BIW, page 282, 2010.

[53] K. T. McDonald and D. P. Russell. Methods of emittance measurement. In Frontiers of particle beams ; observation, diagnosis and correction, page 122. Springer, 1989.

[54] `http://www.hamamatsu.com/resources/pdf/sys/e_c6138.pdf`.

[55] M. Tordeux, M. Labat, F. Dohou, and O. Marcouillé. Bunch length measurements from the incoherent synchrotron radiation fluctuation at SOLEIL. In Proceedings of IPAC, page 1159, 2011.

[56] Y. Otake, S. Matsubara, H. Maesaka, K. Tamasaku, T. Togashi, K. Togawa, H. Tanaka, M. Goto, KK Hamamatsu Photonics, and Higashi-ku Joko-cho. Bunch length measurements at scss test accelerator toward XFEL/SPring-8. In Proceedings of BIW, volume 10, 2010.

[57] P. Emma, J. Frisch, and P. Krejcik. A transverse RF deflecting structure for bunch length and phase space diagnostics. LCLS Technical Note, 12, 2000.

[58] P. Krejcik, C. Behrens, F. J. Decker, Y. Ding, J. Frisch, Z. Huang, J. R. Lewandowski, H. Loos, J. Turner, J. W. Wang, et al. Commissioning the new LCLS X-band transverse deflecting cavity with femtosecond resolution. In Proceedings of IBIC, page 308, 2013.

[59] R. Akre, L. Bentson, P. Emma, and P. Krejcik. Bunch length measurements using a transverse RF deflecting structure in the SLAC linac. In Proceedings of EPAC, page 1882, 2002.

[60] J. Frisch, H. Loos, P. Emma, T. Raubenheimer, P. Krejcik, T. Maxwell, and S. Smith. Electron Beam Diagnostics and Feedback for the LCLS-II. In Proceedings of FEL, page 666, 2014.

[61] A. E. Wheelhouse, R. K. Buckley, S. R. Buckley, L. Cowie, P. Goudket, L. Ma, and J. McKenzie. Commissioning of the Transverse Deflecting Cavity on VELA at Daresbury Laboratory. In Proceedings of IPAC, page 3239, 2015.

[62] H. G. Jerrard. Optical compensators for measurement of elliptical polarization. Journal of the Optical Society of America, 38(1) :35, 1948.

[63] I. Wilke, A. M. MacLeod, W. A. Gillespie, G. Berden, G. M. H. Knippels, and A. F. G. Van Der Meer. Single-shot electron-beam bunch length measurements. Physical review letters, 88(12) :124801, 2002.

[64] M. Alves et al. PHIL photoinjector test line. Journal of Instrumentation, 8(01) :T01001, 2013.

[65] L. Serafini and J. B. Rosenzweig. Envelope analysis of intense relativistic quasilaminar beams in rf photoinjectors : mA theory of emittance compensation. Physical Review E, 55(6) :7565, 1997.

[66] B.E. Carlsten. New photoelectric injector design for the Los Alamos National Laboratory XUV FEL accelerator. Nuclear Instruments and Methods in Physics Research Section A : Accelerators, Spectrometers, Detectors and Associated Equipment, 285(1) :313, 1989.

[67] M. Krasilnikov et al. PITZ experience on the experimental optimization of the RF photo injector for the european XFEL. In Proceedings of FEL, volume FEL Technology II, page 161, 2013.

[68] `http://www.synchrotron-soleil.fr/portal/page/portal/Recherche/LignesLumiere`.

[69] `http://www.synchrotron-soleil.fr/Recherche/LignesLumiere/CRISTAL`.

[70] `http://www.synchrotron-soleil.fr/Recherche/LignesLumiere/GALAXIES`.

[71] `http://www.synchrotron-soleil.fr/Recherche/LignesLumiere/AILES`.

[72] `http://www.synchrotron-soleil.fr/Recherche/LignesLumiere/DESIRS`.

[73] `http://www.synchrotron-soleil.fr/Recherche/LignesLumiere/CASSIOPEE`.

[74] `http://www.synchrotron-soleil.fr/portal/page/portal/Recherche/LignesLumiere/METROLOGIE`.

[75] http://www.synchrotron-soleil.fr/Recherche/LignesLumiere.

[76] M. Ferrario, D. Alesini, M. Bellaveglia, R. Boni, M. Boscolo, M. Castellano, E. Chiadroni, A. Clozza, L. Cultrera, G. Di Pirro, et al. Recent results of the SPARC project. In Proceedings of FEL, page 359, 2008.

[77] L. Palumbo et al. Status of SPARX project. In Proceedings of EPAC, page 121, 2008.

[78] S. V. Milton, E. Gluskin, N. D. Arnold, C. Benson, W. Berg, S. G. Biedron, M. Borland, Y. C. Chae, R. J. Dejus, P. K. Den Hartog, et al. Exponential gain and saturation of a self-amplified spontaneous emission free-electron laser. Science, 292(5524) :2037, 2001.

[79] K. J. Kim. Three-dimensional analysis of coherent amplification and self-amplified spontaneous emission in free-electron lasers. Physical review letters, 57(15) :1871, 1986.

[80] http://www.matrix-vision.com/camera-GigE-Vision-mvbluecougar-s.html.

[81] http://www.thorlabs.de/NewGroupPage9_PF.cfm?Guide=10&Category_ID=220&ObjectGroup_ID=3193.

[82] http://www.cividec.at.

[83] J. H. Park and T. S. Sudarshan. Chemical vapor deposition. ASM international, 2001.

[84] Y. Glinec, J. Faure, H. Monard, J. P. Larbre, M. Mostafavi, A. Guemnie-Tafo, J. L. Marignier, V. Malka, and V. De Waele. Broadrange single shot electron spectrometer. Technical report, CARE, 2006.

[85] A. Chancé, O. Delferrière, J. Schwindling, C. Bruni, N. Delerue, A. Specka, B. Cros, G. Maynard, B. S. Paradkar, and P. Mora. Transport line for a multi-staged laser-plasma acceleration : Dactomus. Nuclear Instruments and Methods in Physics Research Section A : Accelerators, Spectrometers, Detectors and Associated Equipment, 740 :158, 2014.

[86] M. Reiser. Theory and design of charged particle beams. John Wiley & Sons, 2008.

[87] I. Borchardt, E. Karantzoulis, H. Mais, and G. Ripken. Calculation of transverse and longitudinal space charge effects within the framework of the fully six-dimensional formalism. Zeitschrift für Physik C Particles and Fields, 41(1) :25, 1988.

[88] C. Bruni, Y. Fedala, J. Haissinski, M. Lacroix, B. Mouton, R. Roux, A. Variola, F. Zomer, E. Bressi, P. Brunelle, et al. A Compact Ring for Thom X-Ray Source. In Proceedings of PAC, page 1372. Triumf Vancouver, 2009.

[89] K.L. Brown, F. Rothacker, D.C. Carey, and F.C. Iselin. Transport : A Computer Program for Designing Charged Particle Beam Transport Systems, 1977.

[90] S. M'Garrech. Utilisation de faisceaux d'électrons pour la production des noyaux radioactifs par photo-fission. PhD thesis, Université Paris Sud-Paris XI, 2004.

[91] N. Delerue, J. Barros, S. Jenzer, M. Vieille-Grosjean, L. Cassinari, M. Labat, G. Doucas, I. V. Konoplev, A. Reichold, A. Faus-Golfe, et al. Presentation of the Smith-Purcell Experiment at SOLEIL. In Proceedings of IBIC, page 460. Joint Accelerator Conferences Website, 2013.

[92] D. Malyutin, M. Gross, I. Isaev, M. Khojoyan, G. Kourkafas, M. Krasilnikov, B. Marchetti, F. Stephan, and G. Vashchenko. First results of a longitudinal phase space tomography at PITZ. In Proceedings of FEL, page 334, 2013.

[93] C. Grupen and B. Shwartz. Particle detectors, volume 26. Cambridge university press, 2008.

[94] http://www.hamamatsu.com/resources/pdf/sys/SHSS0016E_C10910s.pdf.

[95] G. Devanz, B. Leblond, B. Mouton, and C. Travier. Bunch length measurement on CANDELA photo-injector. In Proceedings of LINAC, page 761. CERN, 1996.

[96] J. Yang, K. Kan, N. Naruse, Y. Murooka, Y. Yoshida, K. Tanimura, and J. Urakawa. Femtosecond Photoinjector And Relativistic Electron Microscopy. In Proceedings of IPAC, page 1126, 2011.

[97] J. Yang, K. Kan, T. Kondoh, Y. Yoshida, and J. Urakawa. Photoinjector Based MeV Electron Microscopy. In Proceedings of DIPAC, page 503, 2011.

[98] S. Bayesteh and H. Delsim-Hashemi. Diagnostics of Femtosecond Low-Charge Electron Bunches at Regae. In Proceedings of IPAC, page 1192, 2011.

[99] http://pbpl.physics.ucla.edu/Research/Facilities/PEGASUS/.

[100] M. Hänel, J. Rönsch, G. Klemz, M. Krasilnikov, and F. Stephan. Electron Bunch Momentum Distribution Modulations at PITZ. In Proceedings of FEL, page 247, 2009.

[101] J. Belloni, H. Monard, F. Gobert, J. P. Larbre, A. Demarque, V. De Waele, I. Lampre, J. L. Marignier, M. Mostafavi, J. C. Bourdon, et al. ELYSE, A picosecond electron accelerator for pulse radiolysis research. Nuclear Instruments and Methods in Physics Research Section A : Accelerators, Spectrometers, Detectors and Associated Equipment, 539(3) :527, 2005.

[102] O. Guilbaud, D. Ros, S. Kazamias, B. Zielbauer, J. Habib, M. Pittman, K. Cassou, F. Ple, M. Farinet, A. Klisnick, et al. LASERIX : premier bilan du fonctionnement de l'installation. In UVX-Colloque sur les Sources Cohérentes et Incohérentes UV, VUV et X : Applications et développements récents, page 57. EDP Sciences, 2009.

[103] J. Arianer. Les sources de particules chargées. DEA de Physique et Technologie des Grands Instruments, Université Paris Sud, 2005.

[104] L. Yan, Y. Du, C. Liao, J. Hua, Q. Du, W. Huang, and C. Tang. Ultrashort electron bunch train production by UV laser pulse stacking. In Proceedings of IPAC, page 3210, 2010.

[105] A. S. Weling, B. B. Hu, N. M. Froberg, and D. H. Auston. Generation of tunable narrow-band THz radiation from large aperture photoconducting antennas. Applied physics letters, 64(2) :137, 1994.

[106] S. Kashiwagi, R. Kato, G. Isoyama, R. Kuroda, J. Urakawa, K. Sakaue, A. Masuda, T. Nomoto, T. Gowa, and M. Washio. Compact EUV source based on laser Compton scattering between micro-bunch electron beam and CO2 laser pulse. In Proceedings of EPAC, page 1869, 2008.

[107] K. Kan, J. Yang, T. Kondoh, K. Norizawa, and Y. Yoshida. Effects of emittance and space-charge in femtosecond bunch compression. Nuclear Instruments and Methods in Physics Research Section A : Accelerators, Spectrometers, Detectors and Associated Equipment, 597(2) :126, 2008.

[108] P. Puzo. Dynamique des particules chargées en présence de rayonnement synchrotron. Master de Physique Spécialité Accélérateurs de Particules et Interaction avec la Matière, Université Paris Sud, 2012.

[109] `http://laola.desy.de/e93663/index_eng.html`.

[110] R. J. England, J. Frederico, M. J. Hogan, C. Joshi, W. An, W. Lu, W. Mori, and P. Muggli. A High Transformer Ratio Plasma Wakefield Accelerator Scheme for FACET. In Proceedings of PAC, page 265, 2011.

[111] R.D. Ruth, P.L. Morton, P.B. Wilson, and A.W. Chao. A plasma wake field accelerator. Part. Accel., 17(SLAC-PUB-3374) :171, 1984.

[112] K.L.F. Bane, P. Chen, and P.B. Wilson. On Collinear Wake Field Acceleration. Technical Report, (SLAC-PUB-3662), 1985.

[113] M. Dohlus and T. Limberg. CSRtrack Version 1.2 User's Manual, 2007.

[114] K. Togawa, T. Hara, and H. Tanaka. Electron-bunch compression using a dynamical nonlinearity correction for a compact x-ray free-electron laser. Physical Review Special Topics-Accelerators and Beams, 12(8) :080706, 2009.

[115] F. Zimmermann and T.O. Raubenheimer. Compensation of longitudinal nonlinearities in the NLC bunch compressor. In AIP Conference Proceedings, page 84. IOP INSTITUTE OF PHYSICS PUBLISHING LTD, 1996.

[116] C. Thongbai, K. Kusoljariyakul, S. Rimjaem, M. W. Rhodes, J. Saisut, P. Thamboon, P. Wichaisirimongkol, and T. Vilaithong. Femtosecond electron bunches, source and characterization. Nuclear Instruments and Methods in Physics Research Section A : Accelerators, Spectrometers, Detectors and Associated Equipment, 587(1) :130, 2008.

[117] S. G. Anderson, W. Brown, A. M. Tremaine, P. Musumeci, and J. B. Rosenzweig. Pulse Compression via Velocity Bunching with the LLNL Thomson X-ray Source Photoinjector. In Proceedings of PAC, page 2957, 2003.

[118] P. Musumeci, R. Yoder, and J. B. Rosenzweig. Velocity bunching experiment at the Neptune Laboratory. In Proceedings of PAC, volume 3, page 2117. IEEE, 2003.

[119] L. Serafini and M. Ferrario. Velocity bunching in photo-injectors. In AIP conference proceedings, page 87. IOP INSTITUTE OF PHYSICS PUBLISHING LTD, 2001.

[120] L. M. Young and J. H. Billen. PARMELA Version 3.40 User's Manual, 2005.

[121] C. Ronsivalle et al. Simulations of the Emittance Compensation in Photoinjectors and comparison with SPARC measurements. In Proceedings of EPAC, page 21, 2008.

Table des figures

1.1 Simplified layout of an electron gun. 5

1.2 The basic physical principle of the thermionic emission. W is the work function of the material and ϵ_f is the Fermi level. Blue curve : 0 K ; Orange curve : 2000 K ; Red curve : 5000 K. 6

1.3 The basic physical principle of the photoelectric emission. W_{eff} is the effective work function of the material and $h\nu$ is the photon energy, with ν the photon frequency and the Planck constant h = $6.626 * 10^{-34}$ J.s. Blue curve : 0 K ; Orange curve : 2000 K. [23]. 9

1.4 Basic physical principles of the field emission. W_{eff} is the material effective work function, δW is the variation of W_{eff} due to the applied electric field E (see Eq. 1.2) and ϵ_f is the material Fermi energy. 12

1.5 Dark current measurement performed at the PHIL facility, as a function the photocathode RF-gun peak accelerating field, for a Copper photocathode. The duration of the dark current pulse is given by the one of the RF power pulse fed into the photocathode RF-gun. 13

1.6 Section of the Alpha-X photocathode RF-gun and of its coupling system to the klystron [40]. L = 5 cm ; R = 42 mm ; r = 12 mm ; ra = 7.4 mm. Note that the first cell is half the length of the other. 14

1.7 Normalized profile of the longitudinal electric field E_z along the Oz axis of the SPARC 1.6 cells photocathode RF-gun. 15

1.8 Dephasing curve acquired on the PHIL facility, with a Copper photocathode, compared with some coming from ASTRA simulations. RF-gun peak accelerating field : 56.7 MV/m. Red curve : Experimental data ; Purple curve : ASTRA curve with Q_0 = 60 pC ; Cyan curve : ASTRA curve with Q_0 = 85 pC ; Brown curve : ASTRA curve with Q_0 = 110 pC ; Blue curve : ASTRA curve with no Schottky effect ; Green curve : Accelerating field on the photocathode at the moment of the beam emission. 17

1.9 Schematic layout and working principle of a Faraday Cup [43]. 18

1.10 Typical signal produced by a Faraday Cup on the PHIL facility (see Fig. 1.24 in Sec. 1.4.1). 19

1.11 Schematic layout and working principle of a current transformer [43]. . . . 20

1.12 Simplified equivalent circuit for the secondary transformer side [43]. 21
1.13 Time response of a current transformer to a temporally rectangular beam and to a temporally Gaussian beam [43]. 22
1.14 Scheme of a typical current transformer housing [43]. 23
1.15 Typical signal (green curve) produced by an ICT on the PHIL facility (see Fig. 1.24 in Sec. 1.4.1). 23
1.16 The two typical setups for beam transverse profile measurements using a scintillating screen. 24
1.17 Beam transverse profile measured with the YAG1 screen of PHIL (see Sec. 1.4.1). 24
1.18 Scheme of the Optical Transition Radiation emission [47]. 26
1.19 Example of a SEM grid device [43]. 27
1.20 Example of a wire scanner device [43]. 28
1.21 Schematic layout of a moving slit device for the measurement of the beam transverse emittance [43]. 31
1.22 Simplified layout of a pepper-pot device for the measurement of the beam transverse emittance [53]. 32
1.23 Working principle of a transverse deflecting cavity (TDC) used for the bunch length measurement [43]. 36
1.24 Layout of the PHIL accelerator at LAL with the PHIN RF-gun. 38
1.25 Layout of the first part of the PITZ accelerator at DESY, Zeuthen [67]. . . 39
1.26 Layout of SOLEIL at Saint-Aubin, France [75]. 40
1.27 Simplified layout of the HELIOS Linac at SOLEIL. 41
1.28 Simplified layout of the SPARC photo-injector. 42
1.29 Normalized magnetic field on the SPARC accelerator Oz axis ; (a) : Solenoid at the RF-gun exit (maximum current of 250 A $\rightarrow$ peak field of 0.4 T) , (b) : Solenoid around the first SLAC section (maximum current of 180 A $\rightarrow$ peak field of 0.3 T). 43

2.1 Scheme of the experimental setup located just after the exit window 47
2.2 Comparison of light yields between a LANEX screen (b) and a 100 μm thickness YAG screen (a). RF-gun peak accelerating field : 62 MV/m ; Gun RF-phase : maximizing the bunch energy ; Bunch energy : 3.55 MeV ; CCD gain = 10. 49
2.3 Calibration of the LANEX screen without collimator (a) and with collimator (b). All the intensities are normalized to be bring back to the same scale as for the gain 0 of the CCD. RF-gun peak accelerating field : 62 MV/m ; Gun RF-phase : maximizing the bunch energy ; Bunch mean energy : 3.55 MeV. 50

2.4 Bunch charge measurement by a LANEX screen, without collimator, as a function of the optical density (Thorlabs NDUV [81]) placed in the path of the laser pulse (4th April 2014). Calibration of Fig. 2.3 (a) used. Fit via Gnuplot. RF-gun peak accelerating field : 62 MV/m ; Gun RF-phase : maximizing the bunch energy ; Bunch mean energy : 3.55 MeV. 52

2.5 Bunch charge measurement by a LANEX screen, with collimator, as a function of the optical density (Thorlabs NDUV [81]) placed in the path of the laser pulse (25th April 2014). Calibration of Fig. 2.3 (b) used. Fit via Gnuplot. RF-gun peak accelerating field : 62 MV/m ; Gun RF-phase : maximizing the bunch energy ; Bunch mean energy : 3.55 MeV. 53

2.6 Comparison of the bunch charge measured with the LANEX screen and the diamond detector. (a) : Logarithmic scale ; (b) : Linear scale. RF-gun peak accelerating field : 62 MV/m ; Gun RF-phase : maximizing the bunch energy ; Bunch mean energy : 3.55 MeV. 54

2.7 Simulation of the energy deposited by an electron in the scintillator layer of the Kodak Lanex fine screen as a function of its energy [84]. The red line corresponds to an energy of 2 MeV for the incident electron. 55

2.8 The 3 focusing cases studied in ASTRA 64

2.9 Histogram of ϵ_y obtained with the classical 3-screen method in the selected example. RF-gun peak accelerating field : 62 MV/m ; Gun RF-phase : minimizing the bunch energy spread ; Bunch energy : 3.55 MeV ; Bunch charge : 100 pC ; Current injected in B3 : 165 A. 66

2.10 Histograms obtained for β_y (a), γ_y (b) and α_y (c) with the classical 3-screen method in the selected example. Vertical Twiss ellipse obtained (d). Experimental conditions : see Fig. 2.9. 67

2.11 Determination of ϵ_y by the 3-screen method using the beam envelope equation, without space-charge forces included, for the selected example. Experimental conditions : see Fig. 2.9. 68

2.12 Determination of ϵ_y by the 3-screen method using the beam envelope equation without space-charge forces included. RF-gun peak accelerating field : 62 MV/m ; Gun RF-phase : minimizing the bunch energy spread ; Bunch energy : 3.55 MeV ; Bunch charge : 8 pC ; Current injected in B3 : 150 A. . 69

2.13 Determination of ϵ_y by the 3-screen method using the beam envelope equation, with space-charge forces included assuming a 3D ellipsoid uniform bunch charge density (see Eq. 2.4), for the selected example. Experimental conditions : see Fig. 2.9. 70

2.14 Determination of ϵ_y by the 3-screen method using the beam envelope equation, with space-charge forces included assuming a 3D Gaussian bunch charge density (see Eq. 2.5), for the selected example. Experimental conditions : see Fig. 2.9. 70

2.15 Determination of ϵ_y by the 3-screen method using the beam envelope equation, with space-charge forces included assuming a 3D Gaussian bunch charge density (see Eq. 2.5). RF-gun peak accelerating field : 62 MV/m ; Gun RF-phase : minimizing the bunch energy spread ; Bunch energy : 3.55 MeV ; Bunch charge : 100 pC. 72

2.16 Determination of ϵ_y by the 3-screen method using the beam envelope equation, with space-charge forces included assuming a 3D Gaussian bunch charge density (see Eq. 2.5). RF-gun peak accelerating field : 62 MV/m (red curve) and 78 MV/m (blue curve) ; Gun RF-phase : minimizing the bunch energy spread ; Bunch charge : 100 pC (red curve) and 135 pC (blue curve). Current injected in the B3 solenoid magnet at the RF-gun exit : 165 A (red curve) and 205 A (blue curve). 73

2.17 Bunch transverse rms sizes σ_x and σ_y measured with the YAG2 screen as a function of the peak magnetic field generated by the B5 solenoid magnet. RF-gun peak accelerating field : 63 MV/m ; Gun RF-phase : minimizing the bunch energy spread ; Bunch energy : 3.67 MeV ; Bunch charge : 46 pC ; Current injected in B3 : 155 A. 80

2.18 Histogram of ϵ_y obtained after application of the Monte-Carlo algorithm described in Sec. 2.2.2.1 on the data of Fig. 2.17. Experimental conditions : see Fig. 2.17. 80

2.19 Histograms obtained for β_y (a), γ_y (b) and α_y (c) from Fig. 2.17. Horizontal and vertical Twiss ellipses obtained from Fig. 2.17 (d). Experimental conditions : see Fig. 2.17. 81

2.20 Transverse profile of the laser pulse generating the bunch at PHIL for the measurement of Fig. 2.17. The image size is $171 * 151$ pixel ^{2} and one pixel corresponds to 15.5 μm. 82

2.21 Comparison between ϵ_y measured by the 3-gradient method, with B5 and the YAG2 screen, and the one simulated by ASTRA as a function of the bunch mean energy, for a bunch charge around 10 pC (a) and a bunch charge around 100 pC (b). 83

2.22 Bunch transverse rms vertical sizes measured with the YAG2 screen (a) and YAG3 screen (b) as a function of the current injected in the B5 solenoid magnet. RF-gun peak accelerating field : 57.5 MV/m ; Gun RF-phase : minimizing the bunch energy spread ; Bunch energy : 3.35 MeV ; Bunch charge : 100 pC ; Current injected in B3 : 155 A. 84

2.23 Scheme of the considered situation ; l = magnetic length of the steerer ; L = distance between steerer center and YAG screen ; θ = deviation angle induces by the steerer ; x = bunch barycenter displacement on the YAG screen with respect to the case where the steerer is turned off. 87

2.24 Axial profile measurement of the PHIL steerers magnetic field for a current of 5 A (shape of the curve supposed to be independent on the current). Courtesy of R. Roux. 88

2.25 Axial profile measurement of the PHIL steerers magnetic field, extended by exponential fit of the decreasing parts 88

2.26 Bunch vertical displacement on the YAG3 screen as a function of the current injected in the steerer n°2. The size of the image is 1360∗1024 pixels (1 pixel is equivalent to a distance of 29 μm). 90

2.27 Bunch vertical displacement on the YAG3 screen as a function of the current injected in the steerer n°2 90

2.28 Bunch energy spectrum measured with the dipole magnet using the slits system and the YAG4 screen 91

2.29 Bunch barycenter vertical displacement on YAG1 (a) and YAG3 (b) as a function of the magnetic field generated by the steerer n°1 (a) and the steerer n°2 (b) for a bunch mean energy around 3.5 MeV 92

2.30 Bunch barycenter vertical displacement on YAG1 (a) and YAG3 (b) as a function of the magnetic field generated by the steerer n°1 (a) and the steerer n°2 (b) for a bunch mean energy around 4.5 MeV 93

2.31 Schematic layout of the beam energy spectrum measurement on the HELIOS Linac at Soleil. The different colors represent electrons of the beam with different energies. 100

2.32 Beam energy spectra measured after the second accelerating structure of the HELIOS Linac for different RF-phase of this structure ; 0 ° denotes the maximum mean beam energy. 102

2.33 Beam mean energy (a) and rms energy spread (b) measured after the second accelerating structure of the HELIOS linac as a function of its RF-phase ; Beam total charge : 650 pC. The point at +10 ° was not coherent with the others and has been discarded. 102

2.34 Beam mean energy (a) and rms energy spread (b) measured after the second accelerating structure of the HELIOS linac as a function of its RF-phase ; Beam total charge : 210 pC. 103

2.35 Laser time profiles used at PITZ : Long flat-top with 24 ps FWHM and 2 ps rise/fall time ($\sigma_t = 6.8$ ps rms) ; Short flat-top with 5.8 ps FWHM and 2 ps rise/fall time ($\sigma_t = 1.9$ ps rms) ; Short Gaussian with $\sigma_t = 0.85$ ps rms (2 ps FWHM). 105

2.36 Bunch rms energy spread at HEDA1 station as a function of the CDS booster RF-phase ; Laser time profile : Long flat-top ; RF-gun peak accelerating field : 60 MV/m (Bunch energy around 6.2 MeV at the exit) ; CDS Booster peak accelerating field : 17.5 MV/m ; Bunch charge : 20 pC. 105

2.37 Bunch rms energy spread at HEDA1 station as a function of the CDS booster RF-phase ; Laser time profile : Short flat-top ; RF-gun peak accelerating field : 60 MV/m (Bunch energy around 6.2 MeV at the exit) ; CDS Booster peak accelerating field : 17.5 MV/m ; Bunch charge : 20 pC. 106

2.38 Bunch rms energy spread at HEDA1 station as a function of the CDS booster RF-phase ; Laser time profile : Short Gaussian ; RF-gun peak accelerating field : 60 MV/m (Bunch energy around 6.2 MeV at the exit) ; CDS Booster peak accelerating field : 17.5 MV/m ; Bunch charge : 20 pC. Measurements with Gun RF-phase of $-15\,^\circ$, $-10\,^\circ$, $-5\,^\circ$, $+5\,^\circ$, $+10\,^\circ$ and $+15\,^\circ$ have also been performed but are not shown here for visibility reason. 106

2.39 3-phase measurements performed with the CDS booster at PITZ for the short Gaussian laser time profile. RF-gun peak accelerating field : 60 MV/m (Bunch energy around 6.2 MeV at the exit) ; CDS Booster peak accelerating field : 17.5 MV/m ; Bunch charge : 20 pC. 108

2.40 Illustration of the Cerenkov effect [93]. 111

2.41 Spectrum of the Cerenkov photons detected at PHIL 112

2.42 Operating principle of a streak camera [94]. 112

2.43 Layout of the Cerenkov station mounted at the PHIL facility 113

2.44 Reflectivity plots as a function of the incident wavelength for the two kind of dielectric mirror used at PHIL ; Left plot : Laseroptik B-08302 type ; Right plot : Thorlabs BB3-E02 type. 114

2.45 Spectral sensitivity of the MatrixVision BlueCougar S-123 CCD camera [80] 114

2.46 Total radiation (left), fluorescence radiation (center) and Cerenkov radiation (right) measured after the Cerenkov station extraction window ; Conditions : 63 MV/m Gun peak accelerating field (3.5 MeV electron bunch) ; 350 pC bunch charge ; IB3 = 155 A ; IB5 = 45 A ; 6.3∗4.8 mm^2 CCD pad. 115

2.47 Cerenkov radiation measured after the Cerenkov station extraction window ; Conditions : 63 MV/m Gun peak accelerating field ; $0\,^\circ$ (left), $-40\,^\circ$ (center) and $-57\,^\circ$ Gun RF-phase ($0\,^\circ$ = maximum of bunch charge) ; 2.8 MeV (left), 3.6 MeV (center) and 3.5 MeV (right) bunch energy ; 750 pC (left), 480 pC (center) and 230 pC (right) bunch charge ; IB3 = 118 A (left), 140 A (center) and 145 A (right) ; IB5 = 39 A (left), 41 A (center) and 41 A (right) ; 6.3∗4.8 mm^2 CCD pad. 117

2.48 Electron bunch transverse profile measured on the PHIL YAG2 screen ; Conditions : 63 MV/m Gun peak accelerating field ; $0\,^\circ$ (left), $-40\,^\circ$ (center) and $-57\,^\circ$ Gun RF-phase ($0\,^\circ$ = maximum of bunch charge) ; 2.8 MeV (left), 3.6 MeV (center) and 3.5 MeV (right) bunch energy ; 750 pC (left), 480 pC (center) and 230 pC (right) bunch charge ; IB3 = 118 A (left), 140 A (center) and 145 A (right) ; IB5 = 39 A (left), 41 A (center) and 41 A (right) ; 4.8∗3.6 mm^2 CCD pad. 117

2.49 Cerenkov radiation measured at the entrance of the streak camera with the Laseroptik mirrors ; Conditions : 63 MV/m Gun peak accelerating field ; $-40\,^\circ$ Gun RF-phase ($0\,^\circ$ = maximum of bunch charge) ; 3.6 MeV bunch energy ; 470 pC bunch charge ; IB3 = 137 A ; IB5 = 41 A ; 6.3∗4.8 mm^2 CCD pad ; Gain 18 of the CCD camera. 118

2.50 Cerenkov radiation measured at the entrance of the streak camera with the Thorlabs mirrors ; Conditions : 63 MV/m Gun peak accelerating field ; $-40\,^\circ$ Gun RF-phase ($0\,^\circ$ = maximum of bunch charge) ; 3.6 MeV bunch energy ; 420 pC bunch charge ; IB3 = 138 A ; IB5 = 44 A ; 6.3∗4.8 mm^2 CCD pad ; Gain 0 of the CCD camera. 119

2.51 Illustration of the travel time difference of the electron bunch and Cerenkov radiation in the Sapphire crystal. $\eta = 66\,^\circ$; t = 200 μm ; $\theta_c = 55.3\,^\circ$; $\alpha = 58.7\,^\circ$. 120

2.52 Influence of the electron bunch transverse size on the emitted Cerenkov radiation duration 121

2.53 Influence of the slit at the entrance of the streak camera on the measured Cerenkov radiation duration 122

2.54 Static slit size σ_{ss} for an aperture of 45 μm (a) and of 110 μm (b) of the slit at the C10910-01 Hamamatsu streak camera entrance 123

2.55 Time profile of the UV laser pulse driving the PHIL RF-gun measured with the streak camera 125

2.56 Time profile of the Cerenkov radiation measured with the streak camera. Conditions : 62 MV/m Gun peak accelerating field ; $-60\,^\circ$ Gun RF-phase ($0\,^\circ$ = maximum of bunch charge) ; 3.5 MeV bunch energy ; 70 pC bunch charge ; IB3 = 148 A ; IB5 = 41 A. 125

2.57 Evolution of the rms bunch length predicted by ASTRA between the photocathode and the Sapphire crystal. Conditions : Conditions : 62 MV/m Gun peak accelerating field ; $-60\,^\circ$ Gun RF-phase ($0\,^\circ$ = maximum of bunch charge) ; 3.5 MeV bunch energy ; 70 pC bunch charge ; IB3 = 148 A ; IB5 = 41 A. 126

2.58 Electron bunch energy spectrum measured in the same conditions than for the bunch length measurement of Fig. 2.56, namely with a Mg photocathode (a), and with a Copper photocathode in similar conditions (b) . . . 127

2.59 Electron bunch energy spectrum for a Copper photocathode. RF-gun peak accelerating field : 64 MV/m ; Gun RF-phase : minimizing the energy spread ; Bunch charge : 45 pC. 128

2.60 Time profile of the Cerenkov radiation measured with the streak camera. Conditions : 64 MV/m Gun peak accelerating field ; Gun RF-phase : minimizing the bunch energy spread ; 3.67 MeV bunch energy ; 45 pC bunch charge ; IB3 = 148 A ; IB5 = 41 A. 128

3.1 Relative discrepancy $\frac{E_m - E_a}{E_a}$ between the maximum mean bunch energy coming from the analytical model developed in Sec. 3.1.2.1 E_m and the one coming from ASTRA simulations E_a as a function of the RF-gun peak accelerating field. (a) : PHIL RF-gun ; (b) : PITZ RF-gun. 136

3.2 Comparison between the accelerating field used in ASTRA simulations (Superfish) and in the analytical model (sinus) for the PHIL and PITZ RF-guns. 137

3.3 Mean relative discrepancy between the maximum mean bunch energy coming from the analytical model and the one coming from the ASTRA simulations as a function of the RF-gun length. The average of the relative discrepancy has been performed for each gun length in the gun accelerating field range between 15 MV/m and 70 MV/m (step of 1 MV/m). 139

3.4 Relative discrepancy between the maximum bunch energy coming from the analytical model developed in Sec. 3.1.2.1 and the one coming from ASTRA simulations as a function of the PITZ RF-gun peak accelerating field. The gun length has been increased from 18.45 cm to 21.6 cm in the analytical model compared to Fig. 3.1 (b). 139

3.5 Comparison between the bunch energy coming from the analytical model and from the measurements ; Laser time profile : Long flat-top with 24 ps FWHM and 2 ps rise/fall time (σ_t = 6.8 ps rms) ; Bunch charge : 20 pC ; RF-gun peak accelerating field : 60.5 MV/m (maximum mean bunch energy around 6.25 MeV). 140

3.6 Comparison between the bunch energy coming from the analytical model and from the measurements ; Laser time profile : Short flat-top with 5.8 ps FWHM and 2 ps rise/fall time (σ_t = 1.9 ps rms) ; Bunch charge : 20 pC ; RF-gun peak accelerating field : 60.5 MV/m (maximum mean bunch energy around 6.25 MeV). 141

3.7 Comparison between the bunch energy coming from the analytical model and from the measurements ; Laser time profile : Short Gaussian with σ_t = 0.85 ps rms ; Bunch charge : 20 pC ; RF-gun peak accelerating field : 60.5 MV/m (maximum mean bunch energy around 6.25 MeV). 141

3.8 Bunch rms energy spread at LEDA station as a function of the gun RF-phase ; Laser time profile : Long flat-top with 24 ps FWHM and 2 ps rise/fall time (σ_t = 6.8 ps rms) ; Bunch charge : 20 pC ; RF-gun peak accelerating field : 60.5 MV/m (maximum mean bunch energy around 6.25 MeV). . . . 143

3.9 Bunch rms energy spread at LEDA station as a function of the gun RF-phase ; Laser time profile : Short flat-top with 5.8 ps FWHM and 2 ps rise/fall time (σ_t = 1.9 ps rms) ; Bunch charge : 20 pC ; RF-gun peak accelerating field : 60.5 MV/m (maximum mean bunch energy around 6.25 MeV). 143

3.10 Bunch rms energy spread at LEDA station as a function of the gun RF-phase ; Laser time profile : Short Gaussian with σ_t = 0.85 ps rms ; Bunch charge : 20 pC ; RF-gun peak accelerating field : 60.5 MV/m (maximum mean bunch energy around 6.25 MeV). 144

3.11 Measurement of the PHIL laser time profile with a streak camera 145

3.12 Summary of 3-phase measurements performed with the RF-gun at PHIL as a function of the RF-gun peak accelerating field ; Bunch charge : 32 pC (51.9 MV/m), 26 pC (57 MV/m), 55 pC (62 MV/m), 73 pC (65.2 MV/m), 70 pC (70.5 MV/m), 110 pC (81.2 MV/m) and 121 pC (84.9 MV/m). . . . 147

3.13 Bunch energy at the PHIL RF-gun exit as a function of the Gun RF-phase for the analytical model developed in Sec. 3.1.2.1 (see Eq. 3.5) ; (a) : Peak accelerating field of 57 MV/m ; (b) : Peak accelerating field of 65.2 MV/m ; (c) : Peak accelerating field of 84.9 MV/m. 147

3.14 Bunch energy at the PITZ RF-gun exit as a function of the Gun RF-phase for the analytical model developed in Sec. 3.1.2.1 (see Eq. 3.5) ; Peak accelerating field of 40 MV/m. 148

3.15 Bunch rms energy spread at the PITZ LEDA1 station (see Fig. 1.25) as a function of the Gun RF-phase. RF-gun peak accelerating field : 62 MV/m ; Laser time profile : Long flat-top with 24 ps FWHM and 2 ps rise/fall time (σ_t = 6.8 ps rms) ; Bunch charge : 20 pC. 150

3.16 Discrepancy between the bunch rms energy spread computed by the analytical model and the one experimentally measured. Simulation conditions : same as in Fig. 3.15. 150

3.17 Bunch rms energy spread at the PITZ LEDA1 station (see Fig. 1.25) as a function of the Gun RF-phase. Simulation conditions : see Fig. 3.15. 151

3.18 Discrepancy between the bunch rms energy spread computed by the analytical-numerical calculation and the one experimentally measured. Simulation conditions : see Fig. 3.15. 152

3.19 Electron bunch rms length vs PHIN Gun RF-phase. Parameters of simulations : Charge 100 pC ; Laser rms duration 100 fs ; Laser rms transverse radius 0.8 mm ; Peak accelerating field 90 MV/m ; Simulation stops 30 cm after the photocathode. 153

3.20 Electron bunch length vs Gun peak accelerating field. Parameters of simulation : Charge 100 pC ; Laser rms duration 100 fs ; Laser rms transverse radius 0.8 mm ; RF-phase minimizing the bunch length (see the table) ; Simulation stops 30 cm after the photocathode. 154

3.21 Electron bunch length vs Laser rms duration. Parameters of simulation : Charge 100 pC ; Laser rms transverse radius 0.8 mm ; Gun peak accelerating field 100 MV/m ; RF-phase minimizing the bunch length ; Simulation stops 30 cm after the photocathode. 155

3.22 Electron bunch length and transverse emittance vs Laser rms transverse radius. Parameters of simulation : Charge 100 pC ; Laser rms duration 100 fs ; Gun peak accelerating field 90 MV/m ; RF-phase minimizing the bunch length ; Simulation stops 30 cm after the photocathode. 156

3.23 Time/energy phase-space of the electron bunch at the exit of the RF-gun. Parameters of simulation : Charge 100 pC ; Laser rms duration 1 ps ; Gun peak accelerating field 80 MV/m ; RF-phase minimizing the bunch length ; Laser rms transverse radius 0.5 mm ; Simulation stops 30 cm after the photocathode. (a) : 3D Gaussian laser shape ; (b) : Beer can laser shape ; (c) : 3D ellipsoid laser shape. The red line denotes a perfectly linear bunch phase-space. 157

3.24 Rms bunch length (a) and transverse emittance (b) vs Bunch charge. Parameters of simulation : Laser rms duration 50 fs ; Laser rms transverse radius 1.2 mm (3D Gaussian) 1.4 mm (Beer can) 1.3 mm (3D ellipsoid) ; Peak accelerating field 100 MV/m ; RF-phase minimizing the bunch length ; Simulation stops 30 cm after the photocathode. 159

3.25 Rms bunch length vs Bunch position. Parameters of simulation : Bunch charge 10 pC (a) and 100 pC (b) ; Laser rms duration 50 fs ; Laser rms transverse radius 1.2 mm (3D Gaussian) ; Peak accelerating field 100 MV/m ; RF-phase minimizing the bunch length ; Simulation stops 30 cm after the photocathode. 161

3.26 Rms transverse emittance vs Bunch position. Parameters of simulation : Bunch charge 10 pC (a) and 100 pC (b) ; Laser rms duration 50 fs ; Laser rms transverse radius 1.2 mm (3D Gaussian) ; Peak accelerating field 100 MV/m ; RF-phase minimizing the bunch length ; Simulation stops 30 cm after the photocathode. 161

3.27 Rms bunch length vs Booster RF-phase. Parameters of simulation : Bunch charge 1 pC (a) and 100 pC (b) ; Laser rms duration 50 fs ; Laser rms transverse radius 1.2 mm (3D Gaussian) 1.4 mm (Beer can) 1.3 mm (3D ellipsoid) ; Gun peak accelerating field 100 MV/m ; Gun RF-phase minimizing the bunch length ; Booster peak accelerating field 38 MV/m ; Simulation stops 1.5 m after the photocathode. 162

3.28 Rms bunch length vs Bunch position. Parameters of simulation : Bunch charge 1 pC (a) and 100 pC (b) ; Laser rms duration 50 fs ; Laser rms transverse radius 1.2 mm (3D Gaussian) ; Gun Peak accelerating field 100 MV/m ; Booster peak accelerating field 38 MV/m ; Booster and Gun RF-phase minimizing the bunch length ; Simulation stops 1.5 m after the photocathode. 162

3.29 Rms transverse emittance vs Booster RF-phase. Parameters of simulation : Bunch charge 1 pC (a) and 100 pC (b) ; Laser rms duration 50 fs ; Laser rms transverse radius 1.2 mm (3D Gaussian) 1.4 mm (Beer can) 1.3 mm (3D ellipsoid) ; Gun peak accelerating field 100 MV/m ; Gun RF-phase minimizing the bunch length ; Booster peak accelerating field 38 MV/m ; Simulation stops 1.5 m after the photocathode. 163

3.30 Rms transverse emittance vs Bunch position. Parameters of simulation : Bunch charge 100 pC ; Laser rms duration 50 fs ; Laser rms transverse radius 1.2 mm (3D Gaussian) ; Gun peak accelerating field 100 MV/m ; Booster peak accelerating field 38 MV/m ; Booster and Gun RF-phase minimizing the bunch length ; Simulation stops 1.5 m after the photocathode. 164

3.31 Modulated longitudinal profile used for the simulations in this section . . . 165

3.32 Longitudinally modulated beam at the entrance of the booster cavity for several total beam charges. RF-gun peak accelerating field : 90 MV/m ; Gun RF-phase : maximizing the beam energy ; Initial beam rms transverse radius : 0.8 mm. 168

3.33 Spacings between the bunches ((a) & (b)) and rms lengths of the bunches ((c) & (d)) of the modulated beam, at the RF-gun exit, for several Gun RF-phases (0 ° denotes the maximum energy gain in the RF-gun). The bunch n°1 is the first bunch emitted from the photocathode. Total beam charge : 20 pC ((a) & (c)) and 200 pC ((b) & (d)) ; RF-gun peak accelerating field : 90 MV/m ; Initial beam rms transverse radius : 0.8 mm. 169

3.34 Simplified layout of a D-shape magnetic chicane 171

3.35 Evolution of the bunch mean energy (a) and rms energy spread (b) at the magnetic chicane entrance as a function of the booster RF-phase, for several Gun RF-phases. Bunch charge : 100 pC ; RF-gun peak accelerating field : 80 MV/m ; Booster peak accelerating field : 40 MV/m ; Current injected in the B3 solenoid at the RF-gun exit : 177 A. 172

3.36 Final rms bunch length, for several Gun RF-phases, as a function of the booster RF-phase. Bunch charge : 100 pC ; RF-gun peak accelerating field : 80 MV/m ; Booster peak accelerating field : 40 MV/m ; Current injected in the B3 solenoid at the RF-gun exit : 177 A. 173

3.37 rms bunch length at the chicane entrance, for several Gun RF-phases, as a function of the booster RF-phase. Bunch charge : 100 pC ; RF-gun peak accelerating field : 80 MV/m ; Booster peak accelerating field : 40 MV/m ; Current injected in the B3 solenoid at the RF-gun exit : 177 A. 173

3.38 Variation of the horizontal bunch rms transverse emittance during the magnetic compression, for several Gun RF-phases, as a function of the booster RF-phase. Bunch charge : 100 pC ; RF-gun peak accelerating field : 80 MV/m ; Booster peak accelerating field : 40 MV/m ; Current injected in the B3 solenoid at the RF-gun exit : 177 A. 174

3.39 Horizontal bunch rms transverse emittance as a function of the booster RF-phase. Bunch charge : 100 pC ; RF-gun peak accelerating field : 80 MV/m ; Gun RF-phase : −10 ° ; Booster peak accelerating field : 40 MV/m ; Current injected in the B3 solenoid at the RF-gun exit : 177 A. The red and blue curves are superimposed. 176

3.40 Final bunch rms transverse emittance as a function of the booster RF-phase. Bunch charge : 100 pC ; RF-gun peak accelerating field : 80 MV/m ; Gun RF-phase : −20 ° ; Booster peak accelerating field : 40 MV/m ; Current injected in the B3 solenoid at the RF-gun exit : 177 A. 176

3.41 Bunch longitudinal phase-space at the magnetic chicane entrance (the red line represents the linear one). Bunch charge : 100 pC ; RF-gun peak accelerating field : 80 MV/m ; Gun RF-phase : −20 ° ; Booster peak accelerating field : 40 MV/m ; Booster RF-phase : −35 ° ; Current injected in the B3 solenoid at the RF-gun exit : 177 A. 177

3.42 Bunch longitudinal phase-space at the magnetic chicane exit, with a perfectly linear one at the entrance. Bunch charge : 100 pC ; RF-gun peak accelerating field : 80 MV/m ; Gun RF-phase : −20 ° ; Booster peak accelerating field : 40 MV/m ; Booster RF-phase : −35 ° ; Current injected in the B3 solenoid at the RF-gun exit : 177 A. 178

3.43 Evolution of the bunch time profile and longitudinal phase-space as a function of the Booster RF-phase. Bunch charge : 100 pC ; RF-gun peak accelerating field : 80 MV/m ; Gun RF-phase : −20 ° ; Booster peak accelerating field : 40 MV/m ; Current injected in the B3 solenoid at the RF-gun exit : 177 A. 179

3.44 Simplified design of the magnetic chicane. 180

3.45 Time profile of the laser pulse used to generate the electron beam in an RF-gun in Sec. 3.2.3 181

3.46 Electron beam mean energy (a) and rms energy spread (b), as a function of the angle of rotation in the time/energy phase space, for an initial monokinetic 16 MeV energy distribution with the time profile shown in Fig. 3.45 182

3.47 Beam longitudinal properties after compression for an rms relative energy spread of 6.02 % (15.78 MeV) 183

3.48 Beam longitudinal properties after compression for an rms relative energy spread of 3.33 % (15.88 MeV) 183

3.49 Beam longitudinal properties after compression for an rms relative energy spread of 1.00 % (15.96 MeV) 183

3.50 Beam longitudinal properties at the compressor entrance. ASTRA conditions : 60.5 MV/m RF-gun peak accelerating field ; +10 ° Gun RF-phase (0 ° = maximal energy) ; 0.2 T peak field of the Gun solenoid magnet ; 16 MV/m CDS booster peak accelerating field ; −47 ° CDS booster RF-phase (0 ° = maximal energy) ; 3 % rms relative energy spread (15.82 MeV beam mean energy). 185

3.51 Beam longitudinal properties after magnetic compression. ASTRA conditions : 60.5 MV/m RF-gun peak accelerating field ; +10 ° Gun RF-phase (0 ° = maximal energy) ; 0.2 T peak field of the Gun solenoid magnet ; 16 MV/m CDS booster peak accelerating field ; −47 ° CDS booster RF-phase (0 ° = maximal energy) ; 3 % rms relative energy spread (15.82 MeV beam mean energy). 185

3.52 Beam longitudinal properties after magnetic compression as a function of C. Initial time profile given by Fig. 3.45 and rms relative energy spread of 3.33 % (15.88 MeV). 188

3.53 Beam longitudinal properties after magnetic compression as a function of the beam rms relative energy spread. Initial time profile given by Fig. 3.45. 190

3.54 Beam longitudinal properties at the compressor entrance. ASTRA conditions : 60.5 MV/m RF-gun peak accelerating field ; +10 ° Gun RF-phase (0 ° = maximal energy) ; 0.2 T peak field of the Gun solenoid magnet ; 20.8 MV/m CDS booster peak accelerating field ; −58 ° CDS booster RF-phase (0 ° = maximal energy) ; 4.7 % rms relative energy spread (16.08 MeV beam mean energy). 191

3.55 Beam longitudinal properties after compression with fine-tuning of the value of C. ASTRA conditions : 60.5 MV/m RF-gun peak accelerating field ; +10 ° Gun RF-phase (0 ° = maximal energy) ; 0.2 T peak field of the Gun solenoid magnet ; 20.8 MV/m CDS booster peak accelerating field ; −58 ° CDS booster RF-phase (0 ° = maximal energy) ; 4.7 % rms relative energy spread (16.08 MeV beam mean energy). 191

3.56 Beam longitudinal properties after compression with $C = 0$. ASTRA conditions : 60.5 MV/m RF-gun peak accelerating field ; +10 ° Gun RF-phase (0 ° = maximal energy) ; 0.2 T peak field of the Gun solenoid magnet ; 20.8 MV/m CDS booster peak accelerating field ; −58 ° CDS booster RF-phase (0 ° = maximal energy) ; 4.7 % rms relative energy spread (16.08 MeV beam mean energy). 191

3.57 Beam longitudinal properties at the compressor entrance for the 10 pC-20 pC-30 pC-50 pC-10 pC charge configuration and 6 ps (a) and 8 ps (b) initial spacings between the bunches. ASTRA conditions : 60.5 MV/m RF-gun peak accelerating field ; +10 ° Gun RF-phase (0 ° = maximal energy) ; 0.2 T peak field of the Gun solenoid magnet ; 20.8 MV/m (a) and 17.75 MV/m (b) CDS booster peak accelerating field ; −58 ° (a) and −51 ° (b) CDS booster RF-phase (0 ° = maximal energy) ; 4.8 % (a) and 4.73 % (b) rms relative energy spread (16.00 MeV (a) and 16.02 MeV (b) beam mean energy). . . 193

3.58 Beam longitudinal properties at the compressor entrance for the 5 pC-10 pC-15 pC-25 pC-5 pC charge configuration and 6 ps (a) and 8 ps (b) initial spacings between the bunches. ASTRA conditions : 60.5 MV/m RF-gun peak accelerating field ; +10 ° Gun RF-phase (0 ° = maximal energy) ; 0.2 T peak field of the Gun solenoid magnet ; 20.8 MV/m (a) and 17.75 MV/m (b) CDS booster peak accelerating field ; −58 ° (a) and −51 ° (b) CDS booster RF-phase (0 ° = maximal energy) ; 4.73 % (a) and 4.74 % (b) rms relative energy spread (15.93 MeV (a) and 15.97 MeV (b) beam mean energy). . . 193

3.59 Beam longitudinal properties after magnetic compression for the 10 pC-20 pC-30 pC-50 pC-10 pC charge configuration and 6 ps (a) and 8 ps (b) initial spacings between the bunches. ASTRA conditions : 60.5 MV/m RF-gun peak accelerating field ; +10 ° Gun RF-phase (0 ° = maximal energy) ; 0.2 T peak field of the Gun solenoid magnet ; 20.8 MV/m (a) and 17.75 MV/m (b) CDS booster peak accelerating field ; −58 ° (a) and −51 ° (b) CDS booster RF-phase (0 ° = maximal energy) ; 4.8 % (a) and 4.73 % (b) rms relative energy spread (16.00 MeV (a) and 16.02 MeV (b) beam mean energy). . . 194

3.60 Beam longitudinal properties after magnetic compression for the 5 pC-10 pC-15 pC-25 pC-5 pC charge configuration and 6 ps (a) and 8 ps (b) initial spacings between the bunches. ASTRA conditions : 60.5 MV/m RF-gun peak accelerating field ; +10 ° Gun RF-phase (0 ° = maximal energy) ; 0.2 T peak field of the Gun solenoid magnet ; 20.8 MV/m (a) and 17.75 MV/m (b) CDS booster peak accelerating field ; −58 ° (a) and −51 ° (b) CDS booster RF-phase (0 ° = maximal energy) ; 4.73 % (a) and 4.74 % (b) rms relative energy spread (15.93 MeV (a) and 15.97 MeV (b) beam mean energy). . . 194

3.61 Simplified design of the magnetic chicane. 196

3.62 Explanatory diagram of the velocity bunching process in a traveling wave . 197

3.63 Bunch mean energy at the exit of the traveling wave accelerating structure as a function of the injection phase Φ_0 for a wave peak field of 10.68 MV/m 202

3.64 Rms bunch length at the exit of the traveling wave accelerating structure as a function of the injection phase Φ_0 for a wave peak field of 10.68 MV/m 204

3.65 Rms bunch length at the exit of the traveling wave accelerating structure as a function of the injection phase Φ_0 for a wave peak field of 10.68 MV/m 206

3.66 Phase convention used for the traveling wave accelerating structures 208

3.67 Evolution of the rms bunch length up to the exit of S1. Bunch charge : 50 pC ; RF-gun mean accelerating field : 50 MV/m ; Laser pulse driving the RF-gun : 0.6 mm transverse radius and 2.5 ps rms duration ; I_p : 201 A ; S1 mean accelerating field : 10 MV/m ; Injection phase in S1 : −2 ° (red) and −0.5 ° (green). 210

3.68 Bunch time/energy phase-space at the entrance of S1. Bunch charge : 50 pC ; RF-gun mean accelerating field : 50 MV/m ; Gun RF-phase : +10 ° (a) and −10 ° (b) ; Laser pulse driving the RF-gun : 0.6 mm transverse radius and 2.5 ps rms duration ; I_p : 201 A. 210

3.69 Evolution of the rms bunch length up to the exit of S1. Bunch charge : 50 pC ; RF-gun mean accelerating field : 50 MV/m ; Gun RF-phase : $-10\,^\circ$; Laser pulse driving the RF-gun : 0.6 mm transverse radius and 2.5 ps rms duration ; I_p : 196 A ; S1 mean accelerating field : 10 MV/m ; Ψ_1 : $-1.5\,^\circ$ (green), $-7.5\,^\circ$ (red) and $+4.5\,^\circ$ (blue). 212

3.70 Evolution of the rms bunch length up to the entrance of S2. Bunch charge : 50 pC ; RF-gun mean accelerating field : 50 MV/m ; Gun RF-phase : $-10\,^\circ$; Laser pulse driving the RF-gun : 0.6 mm transverse radius and 2.5 ps rms duration ; I_p : 196 A ; S1 mean accelerating field : 10 MV/m ; Ψ_1 : $-1.5\,^\circ$ (red) and $+1.5\,^\circ$ (green). 212

3.71 rms bunch length at the exit of S3 as a function of the mean accelerating field in S1 and S2. Bunch charge : 50 pC ; RF-gun mean accelerating field : 50 MV/m ; Gun RF-phase : $-10\,^\circ$; Laser pulse driving the RF-gun : 0.6 mm transverse radius and 2.5 ps rms duration ; Other conditions : see Tab. 3.6. 213

3.72 Bunch rms length (a) and mean energy (b) up to the exit of S3 for different values of the mean accelerating field in S1 and S2. Simulation conditions : see Tab. 3.6. 214

3.73 Bunch rms transverse emittance and bunch rms transverse radius up to the exit of S3. Simulation conditions : see Tab. 3.7 second line for the blue and green curves ; see Tab. 3.8 first line for the red and purple curves. 219

3.74 Bunch rms transverse emittance up to the exit of S3. Simulation conditions : see Tab. 3.8 fourth line. 219

3.75 Bunch rms length up to the exit of S3. Simulation conditions : see Tab. 3.7 second line (red curve) ; see Tab. 3.8 first line (green curve). Red arrows mark the exit of the RF-gun. 220

3.76 Bunch rms length up to the exit of S3 (a). Bunch mean energy and rms relative energy spread up to the exit of S3 (b). Simulation conditions : see Tab. 3.6 fifth line for the red curve (a) and (b) and for the green curve (b) ; see Tab. 3.9 second line for the green curve (a), the blue curve (b) and the purple curve (b). 223

3.77 Bunch rms length up to the exit of S3. Simulation conditions : see Tab. 3.8 fifth line. I optimize the mean accelerating field in S1 and S2 and of the injection phases Ψ_i in the three SLAC sections. 226

B.1 Normalized profile of the longitudinal electric field of the TM_{010-0} mode on the Oz axis of a 1.6 cells RF-gun. 241

B.2 Normalized profile of the longitudinal electric field of the $\mathrm{TM}_{010-\frac{\pi}{2}}$ mode on the Oz axis of a 2.5 cells RF-gun. 241

C.1 Folder containing the bunch images before analysis. 243

C.2 Selection of the region of interest (ROI) on the bunch images. 244

C.3 Example of projected intensity profile in the horizontal direction. 244
C.4 Folder containing the bunch images after analysis. 246
C.5 Contents of the folder "horizontal" of Fig. C.4. 246
C.6 Example of a Gaussian fit of a projected horizontal intensity profile. 247
C.7 Example of a text file containing the results for σ_{rms}. 247

D.1 Dipole magnet with a deviation angle θ, a curvature radius ρ, a zero index and no edge angles. The reference trajectory associated to the energy E_0 is depicted by the red line. 250
D.2 Reference trajectories associated to the beam mean energy E_0 (red line) and to any energy E of the beam (black line). Note : x_ϵ is negative on this picture. 251

E.1 Example of commented input file for the program *generator* generating the initial particle distribution for ASTRA. 253

Liste des tableaux

1.1 Some properties of common scintillation screens used for beam transverse profile measurements [46]. 25

2.1 Results of ASTRA simulations for evaluating the classical 3-screen method (without space-charge forces included and with a pure drift space) accuracy. Bunch charge : 100 pC ; Gun RF-phase : maximizing the bunch mean energy. 63

2.2 Results of ASTRA simulations for evaluating the 3-gradient method accuracy without space-charge forces. Gun RF-phase : maximizing the bunch mean energy. 78

2.3 Results of ASTRA simulations for evaluating the 3-gradient method accuracy with space-charge forces. Bunch charge : 100 pC ; Gun RF-phase : maximizing the bunch mean energy. 78

2.4 Comparison between the bunch mean energy measured with all the acquired bunch positions and with only the two extreme bunch positions acquired in the configurations of Fig. 2.29 and Fig. 2.30 94

2.5 3-phase measurements performed with the CDS booster at PITZ for the short and long flat-top laser time profiles. RF-gun peak accelerating field : 60 MV/m (Bunch energy around 6.2 MeV at the exit) ; CDS Booster peak accelerating field : 17.5 MV/m ; Bunch charge : 20 pC. 107

2.6 rms bunch length predicted by the ASTRA simulations and computed by the 3-phase method. Bunch charge : 100 pC ; Bunch energy at the booster entrance : 6 MeV ; Booster peak accelerating field : 17.5 MV/m. 108

2.7 Comparison of the rms bunch length predicted by ASTRA at the CDS booster entrance for ideal initial time distributions of the bunch and for initial time distributions reproducing the ones of Fig. 2.35 generated by a Von Neumann algorithm. The comparison has been performed for the cases shown in Tab. 2.5. 109

3.1 Summary of 3-phase measurements performed with the RF-gun at PITZ. Bunch charge : 20 pC ; RF-gun peak accelerating field : 60.5 MV/m (maximum mean bunch energy around 6.25 MeV). 145

3.2 Rms bunch length and transverse emittance for the 3 different kind of laser shape. Parameters of simulation : Charge 100 pC ; Laser rms duration 50 fs ; Peak accelerating field 100 MV/m ; RF-phase minimizing the bunch length ; Simulation stops 30 cm after the photocathode. 158

3.3 Summary of bunch properties after the booster cavity. Parameters of simulation : Laser rms duration 50 fs ; Laser rms transverse radius 1.2 mm (3D Gaussian) 1.4 mm (Beer can) 1.3 mm (3D ellipsoid) ; Gun peak accelerating field 100 MV/m ; Booster peak accelerating field 38 MV/m ; Booster and Gun RF-phase minimizing the bunch length ; Simulation stops 1.5 m after the photocathode. 164

3.4 Bunches longitudinal parameters after compression for an rms energy spread of 1.00 % (15.96 MeV) 184

3.5 Final bunches longitudinal parameters of the beams shown in Fig. 3.60 . . 195

3.6 Bunch properties at the exit of S3 for the configurations minimizing the bunch length. Bunch charge : 50 pC ; RF-gun mean accelerating field : 50 MV/m ; Gun RF-phase : $-10\,^\circ$; Laser pulse driving the RF-gun : 0.6 mm transverse radius and 2.5 ps rms duration ; Mean accelerating field in S3 : 12 MV/m. 214

3.7 Bunch properties at the exit of S3 for the configurations minimizing the bunch length. RF-gun mean accelerating field : 50 MV/m ; Gun RF-phase : $-10\,^\circ$; Laser pulse driving the RF-gun : 0.6 mm transverse radius and 2.5 ps rms duration ; Mean accelerating field in S3 : 12 MV/m. 216

3.8 Bunch properties at the exit of S3 for the configurations minimizing the bunch length or the transverse emittance (case at 1 ps). RF-gun mean accelerating field : 50 MV/m ; Bunch charge : 50 pC. 217

3.9 Bunch properties at the exit of S3 for the configurations minimizing the bunch length. Bunch charge : 50 pC ; RF-gun mean accelerating field : 50 MV/m ; Gun RF-phase : $-10\,^\circ$; Laser pulse driving the RF-gun : 0.6 mm transverse radius and 2.5 ps rms duration. 223

3.10 Bunch properties at the exit of S3 for the configurations minimizing the bunch length. RF-gun mean accelerating field : 50 MV/m ; Gun RF-phase : $-10\,^\circ$; Laser pulse driving the RF-gun : 0.6 mm transverse radius and 2.5 ps rms duration. 224

3.11 Bunch properties at the exit of S3 for the configurations minimizing the bunch length. RF-gun mean accelerating field : 50 MV/m ; Bunch charge : 50 pC. For each laser pulse length, I optimized the mean accelerating field in S1 and S2 and the injection phases Ψ_i in the three SLAC sections to have the lowest possible final rms bunch length. 225